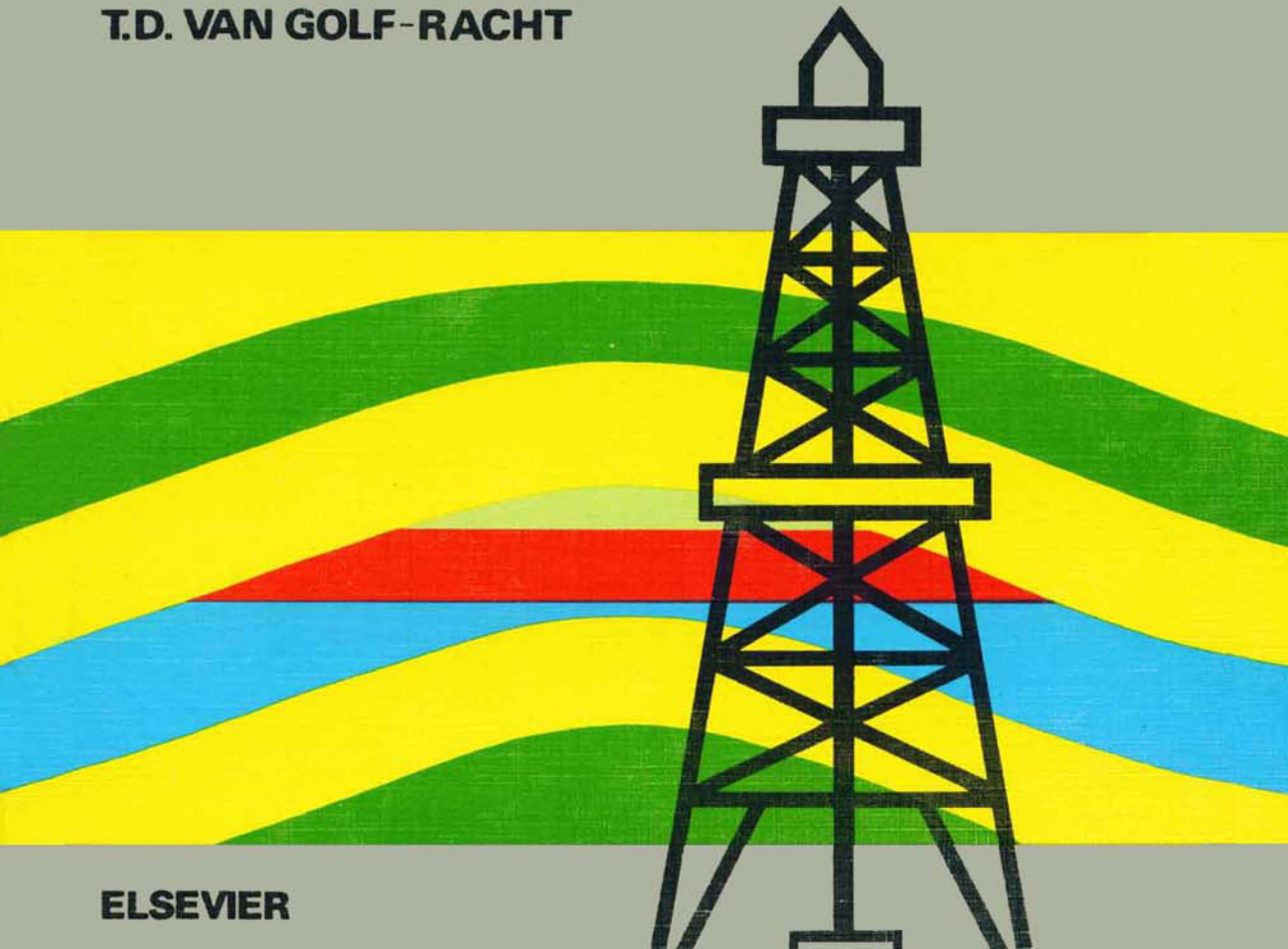


**DEVELOPMENTS IN PETROLEUM SCIENCE 12**

# **fundamentals of fractured reservoir engineering**

**BY**

**T.D. VAN GOLF-RACHT**



**ELSEVIER**

Developments in Petroleum Science, 12

# **fundamentals of fractured reservoir engineering**

*FURTHER TITLES IN THIS SERIES*

1 A. GENE COLLINS  
GEOCHEMISTRY OF OILFIELD WATERS

2 W.H. FERTHL  
ABNORMAL FORMATION PRESSURES

3 A.O. SZILAS  
PRODUCTION AND TRANSPORT OF OIL AND GAS

4 C.E.B. CONYBEARE  
GEOMORPHOLOGY OF OIL AND GAS FIELDS IN  
SANDSTONE BODIES

5 T.F. YEN and G.V. CHILINGARIAN (Editors)  
OIL SHALE

6 D.W. PEACEMAN  
FUNDAMENTALS OF NUMERICAL RESERVOIR SIMULATION

7 G.V. CHILINGARIAN and T.F. YEN (Editors)  
BITUMENS, ASPHALTS AND TAR SANDS

8 L.P. DAKE  
FUNDAMENTALS OF RESERVOIR ENGINEERING

9 K. MAGARA  
COMPACTION AND FLUID MIGRATION

10 M.T. SILVIA and E.A. ROBINSON  
DECONVOLUTION OF GEOPHYSICAL TIME SERIES IN THE  
EXPLORATION FOR OIL AND NATURAL GAS

11 G.V. CHILINGARIAN and P. VORABUTR  
DRILLING AND DRILLING FLUIDS

Developments in Petroleum Science, 12

# **fundamentals of fractured reservoir engineering**

by

T.D. VAN GOLF-RACHT

- Manager Reservoir Engineering Dept.  
Petroleum Division, Norsk Hydro  
Oslo, Norway
- Professor of Reservoir Engineering  
University of Trondheim  
Trondheim, Norway
- Member of Norwegian  
Academy of Science



ELSEVIER SCIENTIFIC PUBLISHING COMPANY  
AMSTERDAM — OXFORD — NEW YORK 1982

ELSEVIER SCIENTIFIC PUBLISHING COMPANY  
Molenwerf 1  
P.O. Box 211, 1000 AE Amsterdam, The Netherlands

*Distribution for the United States and Canada:*

ELSEVIER/NORTH-HOLLAND INC.  
52, Vanderbilt Avenue  
New York, N.Y. 10017

**Library of Congress Cataloging in Publication Data**

Golf-Racht, T. D. van (Theodor D. van), 1924-  
Fundamentals of fractured reservoir engineering.

(Developments in petroleum science ; 12)  
Includes bibliographical references and index.  
1. Oil reservoir engineering. 2. Rock mechanics.  
3. Fracture mechanics. I. Title. II. Series.  
TN87L.G6924 622'.3382 81-19416  
ISBN 0-444-42046-0 (U.S.) AACR2

ISBN 0-444-42046-0 (Vol. 12)

ISBN 0-444-41625-0 (Series)

© Elsevier Scientific Publishing Company, 1982

All rights reserved. No part of this publication may be reproduced, stored in a retrieval system or transmitted in any form or by any means, electronic, mechanical, photocopying, recording or otherwise, without the prior written permission of the publisher, Elsevier Scientific Publishing Company, P.O. Box 330, 1000 AH Amsterdam, The Netherlands

Printed in The Netherlands

This book is dedicated  
to my wife Annabel  
and my daughter Barbara

The author would like to extend his gratitude to

Torvild Aakvaag  
Executive Vice-President of Norsk Hydro

Hans Bjøntegard  
Vice-President and General Manager  
of Petroleum Division, Norsk Hydro

Einar Wathne  
Assistant Vice-President  
of Petroleum Division, Norsk Hydro

for the encouragement received during the preparation of this book.

## FOREWORD

The history of fractured reservoirs is probably as long as the history of petroleum itself. During the Los Angeles Panel Discussion on Fractured Reservoirs (March 1952) Levorsen mentioned that the notion "fractured porosity" was introduced only two years after Drake's discovery in 1861 by the geologist E.B. Andrews who wrote that if fractures are numerous along the anticline axis it represents the primary cause of an accumulation, and also that a law of proportionality was observed between the oil produced and the amount of fissures. But it was only in the early nineteen fifties, with the important discoveries in the Spraberry trend of West Texas and giant fields in the Middle East that an increasing interest for this type of fields started. In continuation in the late fifties, but especially in the last two decades, various concepts have been developed in various areas such as geology, reservoir description, flow toward the well, reservoir mechanisms, etc. But the studies and papers published in the literature presented single problems in a limited area and unrelated to a *global concept* of fractured reservoirs. Therefore, in order to integrate the existent published material and my personal views on natural fractured reservoirs, I have tried to write a self-contained book where the reader can find the necessary tools for the evaluation of fractures by processing the observed data, examining the flow behaviour towards a well and analysing reservoir behaviour during a field's entire history, through its specific production mechanisms.

By establishing new principles and laws which govern the dynamic phenomena in fractured reservoirs, an engineer or geologist will *no longer be constrained to use the conventional reservoir procedures* in order to solve any problem in this special kind of field. The use of procedures valid for fractured wells (by stimulation) in the case of well-transient analysis for a natural fractured reservoir has to be avoided, since the conditions of flow are completely different. It is also unacceptable to use simple conventional drives (water-drive and/or solution-gas drive) as basic drives when the fractured reservoir is producing mainly under the control of gravity-capillary forces, including all implications related to imbibition and drainage processes. For a better understanding of various concepts, the material here presented is along the modern outlines of reservoir analysis. Thus,

- the first part is devoted to reservoir description;
- the second part to flow towards a well and,
- the third part to the flow mechanism in a fractured reservoir.

The generation of fractures, their detection and the procedure to describe them by appropriate processing of all types of information is discussed in detail in the first part.

The flow in fractures, as well as the simultaneous flow of matrix-fracture systems is the basis of radial-symmetrical flow which is developed in detail in the second part.

In the third part, the complex flow mechanism and new concepts are presented in a unitarian approach for the three phases, gas-oil-water, where the role of gravitational and capillary forces show that the conventional roles of water-drive or solution gas-drive are completely modified in a fractured reservoir.

The material presented in this book is the result of my personal involvement in fractured reservoir studies in Europe and the Middle East during the last two decades. The results obtained in various studies and the continuous attempt to reconcile field behaviour with theoretical work presented in various papers have been the basis of the elaboration of specific fractured reservoir production mechanisms. In addition, discussion with specialists during the examination of various projects improved the concepts which are introduced in the present book. I am proud to mention that the basis of the third part of the book is the result of a meeting with M. Muskat in London (1963), where both of us were involved in the evaluation of the future behaviour of Ragusa Field (Sicily). Muskat's concepts on matrix-fracture flow mechanisms and rate sensitivity vs. water-table advancement are the basic approach of the material developed in chapters 9 and 10. Later, in the last decade, while elaborating the fundamental concepts of natural fractured reservoirs, I had the opportunity to present and debate various parts of the book in a series of conferences. A part of it was presented in my course at the Geological Institute, University of Milano (1968–1973) and another part in my course at the Petroleum Institute, the University of Trondheim (1973–1980). Other parts have been presented to the students of the Mining Institute of Turin (1972), to the engineers of YPF (Buenos Aires), and to petroleum engineers of Petrobras (Rio de Janeiro) and Statoil (Stavanger), etc.

In the meantime, the encouraging results obtained from comparison of field data with theoretical reservoir behaviour forecasts reinforced my conviction that a book treating the fundamental of fractured reservoirs may open *a new scientific area in petroleum science and fluid mechanics*. With this aim in mind, the book was developed as basic scientific material on fractured reservoirs for the education of students in Universities, and for the geologist and engineer involved in field operations.

By using the new concepts discussed in this book, it may become possible to avoid the errors occurring when conventional reservoir approaches are applied instead of specific fractured reservoir methods, as for example when induced fracturing process procedures are used for the evaluation of naturally fractured reservoir behaviour. And finally, I should like to men-

tion that through the scientific basis of fractured reservoir research developed in this book, I hope that further contributions in this field will be encouraged.

I take this opportunity to thank all these collaborators who have helped me in publishing this book. First I mention David Nicklin who contributed to chapter 3, and his wife Patricia who took care of the first preparatory draft. I should also like to thank Ellen Damsleth for typing the largest part of the book, Grethe Glasse for checking the printers proofs and Kari Anderson for drawings. Grateful appreciation goes to *Impact Graphic* for the final lay-out of the entire printed material.

Special gratitude goes to the Society of Petroleum Engineers for allowing reproduction of illustrations and tables.

Paris, May 1981

Prof. Dr. Theodor van Golf-Racht

This Page Intentionally Left Blank

## LIST OF CONTENTS

### **FIRST PART : RESERVOIR DESCRIPTION**

#### **CHAPTER 1** *BASIC GEOLOGY*

	Page
1.1. Introduction .....	5
1.1.1. What is a fracture?.....	5
1.1.2. Origin of fractures.....	6
1.2. Geological conditions of fracturing.....	7
1.2.1. Rock mechanics vs. fracturing.....	8
1.2.2. Fracturing under geological events .....	14
1.2.3. Rock characteristics vs. fracturing.....	20
1.3. Geological model for the simulation of fracturing.....	24
1.3.1. Modeling based on finite element method.....	25
1.3.2. Formulation of a finite element in the case of a visco-plastic material .....	26
1.3.3. Numerical solutions.....	27
1.3.4. Programs .....	27
1.4. Influence of stylolitization and jointing .....	30
1.4.1. Stylolites and stylolitization .....	30
1.4.2. Development of stylolitization .....	33
1.4.3. Joints and their formations.....	36
1.5. Quantitative evaluation of fracturing.....	38
1.5.1. Fractured reservoir productivity .....	38
1.5.2. Model of a large North Sea fractured structure .....	42
List of Symbols.....	49
References.....	50

#### **CHAPTER 2** *FRACTURE DETECTION AND EVALUATION*

2.1. Classification and definitions.....	51
2.1.1. Classification on the basis of descriptive criteria .....	51
2.1.2. Classification based on geological criteria .....	53

	Page
2.2. Basic parameters of fractures .....	54
2.2.1. General discussion .....	54
2.2.2. Single fracture parameters .....	55
2.2.3. Multi-fracture parameters .....	57
2.3. Direct evaluation of fracturing .....	66
2.3.1. Outcrop fractures .....	67
2.3.2. Fracture evaluation through core examination .....	68
2.4. Processing of data .....	84
2.4.1. Tabulation and classification of data .....	84
2.4.2. Representation of data .....	86
2.5. Application of fracturing studies .....	95
2.5.1. Tectonophysic study in southern Germany .....	97
2.5.2. Evaluation of matrix block units .....	99
2.5.3. Iranian structure studied through outcropping .....	102
List of Symbols .....	108
References .....	109

## **CHAPTER 3**

### ***FRACTURED RESERVOIRS, CASE HISTORY***

3.1. Fractured carbonate reservoirs .....	111
3.1.1. General .....	111
3.1.2. Ain Zalah field, Iraq .....	112
3.1.3. Kirkuk field, Iraq .....	116
3.1.4. Dukhan field, Qatar .....	120
3.1.5. Southwest Iran, the Asmari Formation .....	124
3.1.6. Gela and Ragusa fields, Sicily .....	127
3.2. Fractured silt/sand reservoirs .....	131
3.2.1. General .....	131
3.2.2. Spraberry Trend, Midland Basin, West Texas .....	131
3.3. Fractured shale reservoirs .....	136
3.3.1. General .....	136
3.3.2. Californian fractured shale reservoir .....	137
3.3.3. Big Sandy gas field, eastern Kentucky .....	140
3.4. Fractured «basement» reservoirs .....	142

<b>CHAPTER 4</b>		<b>Page</b>
<i>PHYSICAL PROPERTIES OF ROCKS</i>		
4.1.	Introduction . . . . .	147
4.2.	Porosity. . . . .	147
4.2.1.	Definition of double porosity . . . . .	148
4.2.2.	Qualitative description of secondary porosity $\Phi_f$ . . . . .	150
4.2.3.	Quantitative evaluation of $\Phi_f$ . . . . .	151
4.3.	Permeability . . . . .	156
4.3.1.	Intrinsic fracture permeability $K_{ff}$ . . . . .	156
4.3.2.	Conventional fracture permeability $K_f$ . . . . .	158
4.3.3.	Permeability of fracture-matrix system . . . . .	158
4.3.4.	Permeability $K_f$ in simplified models. . . . .	161
4.3.5.	Permeability $K_f$ evaluated through permeameters . . . . .	163
4.3.6.	Permeability $K_f$ from thin sections (micro-sections) . . . . .	169
4.3.7.	Permeability $K_f$ from structural geological data . . . . .	172
4.3.8.	Permeability $K_f$ vs. overburden pressure. . . . .	174
4.4.	Discussion concerning basic parameters ( $K$ , $\Phi$ , $S_{wi}$ ) . . . . .	176
4.4.1.	Fluid saturation in a fractured reservoir . . . . .	177
4.4.2.	Relationship of permeability vs. porosity . . . . .	178
4.4.3.	Data and examples of basic parameters . . . . .	193
4.4.4.	Variation of $\Phi_f$ and $K_f$ with reservoir pressure decline. . . . .	196
4.5.	Compressibility in a fractured rock . . . . .	199
4.5.1.	Rock compressibility. . . . .	200
4.5.2.	Fluid compressibility. . . . .	202
4.5.3.	Total compressibility (rock and fluids) . . . . .	204
4.6.	Relative permeability in a fractured reservoir . . . . .	208
4.6.1.	Review of basic concepts. . . . .	209
4.6.2.	Evaluation of relative permeability in homogeneous rock. . . . .	213
4.6.3.	Evaluation of relative permeability in heterogeneous rock . . . . .	219
4.7.	Capillary pressure curve. . . . .	233
4.7.1.	Review of conventional capillary curve . . . . .	234
4.7.2.	Composite capillary imbibition curve . . . . .	241

<b>CHAPTER 5</b>		
<i>LOGGING VS. FRACTURE EVALUATION</i> . . . . .		
5.1.	Introduction . . . . .	255
5.2.	Lithology logs . . . . .	256
5.2.1.	Spontaneous potential S.P. log . . . . .	256
5.2.2.	Gamma ray log . . . . .	256

	Page
5.3. Caliper logs .....	257
5.4. Temperature logs.....	258
5.5. Resistivity logs .....	260
5.5.1. Classification.....	260
5.5.2. Resistivity vs. measurement conditions.....	261
5.5.3. Role of short and long normal.....	262
5.5.4. Discussion of combined tools .....	262
5.6. Dipmeter logs .....	264
5.6.1. Idealized cases.....	264
5.6.2. Tools and applications.....	267
5.7. Porosity logs .....	270
5.7.1. Density log .....	271
5.7.2. Neutron log.....	271
5.7.3. Sonic log.....	272
5.7.4. Secondary porosity .....	281
5.7.5. Role of lithoporosity cross plot.....	281
5.8. Borehole televIEWER.....	285
5.9. Discussion .....	286
5.9.1. Logging programs .....	286
5.9.2. Logging results vs. other information .....	288
5.10. Quantitative interpretation .....	290
5.10.1. Interpretation approach .....	290
5.10.2. Applications .....	291
List of Symbols.....	293
References.....	294

**SECOND PART: WELL DYNAMICS**  
*FLOW OF HOMOGENEOUS FLUIDS  
 TOWARD A WELL*

PREFACE.....	295
--------------	-----

**CHAPTER 6**  
*FLOW OF FLUIDS TOWARDS A WELL IN NON-POROUS FRACTURED  
 ROCK*

	Page
6.1. Law of flow of homogeneous liquids.....	299
6.1.1. Flow of homogeneous liquids through an individual fracture.....	299
6.1.2. Flow through a network of fractures.....	293
6.1.3. Turbulence in fractures.....	294
6.2. Steady-state flow of homogeneous liquids through fractures toward a well.....	311
6.2.1. Modelling of fracture networks.....	311
6.2.2. Modelling of a radial symmetrical flow .....	317
6.2.3. Practical application of modelling.....	320
6.3. Flow of gas through fractures toward a well .....	338
6.3.1. Basic concepts in fractured reservoir.....	338
6.3.2. Radial geometrical flow of gas toward a well.....	341
6.4. Transient flow in a non-porous fractured rock .....	347
List of Symbols.....	350
References.....	351

## CHAPTER 7

### *FLOW TOWARDS A WELL IN FRACTURED ROCK OF DOUBLE POROSITY*

7.1. Basic equations of flow.....	355
7.1.1. The Barenblatt <sup>7</sup> approach .....	355
7.1.2. Warren and Root <sup>1</sup> solution.....	358
7.1.3. Other models and solutions.....	366
7.1.4. Special model – the Pollard model .....	372
7.2. Discussion of the Warren and Root <sup>1</sup> model.....	375
7.2.1. Basic dimensional equations .....	375
7.2.2. Basic dimensionless parameters .....	376
7.2.3. Pressure drawdown behaviour in the case $R = \infty$ .....	378
7.2.4. Pressure drawdown behaviour in the case $R = R_o$ .....	392
7.2.5. Pressure build-up behaviour in the case $R = \infty$ .....	395
7.2.6. Pressure build-up behaviour in the case $R = R_o$ .....	401
7.2.7. Evaluation of $\lambda$ and $\omega$ through dimensionless diagrams ..	403
7.3. Discussion of Pollard method .....	407
7.3.1. Data processing.....	407
7.3.2. Basic parameters .....	408
7.3.3. Additional parameters obtained by analogy .....	409
List of Symbols.....	415
References.....	417

<b>CHAPTER 8</b>		<b>Page</b>
<i>SPECIAL PROBLEMS OF FLOW TOWARD A WELL</i>		
8.1. Introduction .....	419	
8.2. Well interference .....	419	
8.2.1. Interference effects under pressure drawdown conditions .....	419	
8.2.2. Interference effects under pressure build-up conditions ..	431	
8.3. Evaluation of anisotropy in a fractured reservoir.....	434	
8.3.1. Theoretical review.....	434	
8.3.2. Anisotropy and flow toward a well .....	435	
8.3.3. Anisotropy evaluation.....	440	
8.4. Use of type-curves for analysis of flow toward a well .....	453	
8.4.1. Type-curve of a producing well under constant rate conditions .....	453	
8.4.2. Case of production under constant pressure drop conditions.....	455	
List of Symbols.....	458	
References.....	459	

## **THIRD PART : RESERVOIR DYNAMICS**

<b>CHAPTER 9.</b>		
<i>FLUID DISPLACEMENT IN A SINGLE MATRIX BLOCK</i>		
9.1. Introduction .....	465	
9.2. Simplified dynamic approach to matrix fluid displacement....	465	
9.2.1. Basic model.....	467	
9.2.2. Displacement of oil by water.....	468	
9.2.3. Displacement of oil by gas.....	477	
9.2.4. Conclusions .....	481	
9.3. Simplified physical approach to fluid displacement in matrix block.....	482	
9.3.1. Basic discussion of displacement process.....	482	
9.3.2. Analysis of the displacement process.....	485	
9.4. Concepts and experiments : single block imbibition displacement .....	495	
9.4.1. Concepts of a simplified model.....	495	
9.4.2. Recovery versus time : basic theory and basis of experiments.....	500	

	Page
9.4.3. Recovery versus time : scaling laws .....	510
9.4.4. Recovery versus time : critical discussion .....	519
9.4.5. Observation and conclusions : single block imbibition..	528
9.5 Other aspects of single block fluid displacement.....	530
9.5.1. Drainage displacement.....	530
9.5.2. Production by water injection.....	531
9.6. Oil produced from a single block : theoretical approach .....	536
9.6.1. Barenblatt's <sup>18</sup> continuum approach for simultaneous flow of immiscible fluids in fractured reservoirs .....	536
9.6.2. Braester's <sup>19</sup> theoretical approach.....	540
List of Symbols.....	547
References.....	548

## **CHAPTER 10.**

### *PRODUCTION MECHANISM OF A FRACTURED RESERVOIR*

10.1. Introduction .....	551
10.2. Reservoir description during depletion .....	554
10.2.1. Reservoir zoning .....	554
10.2.2. Zoning vs. pressure distribution.....	557
10.3. Reservoir zoning vs. production mechanism .....	560
10.3.1. Production mechanism in the gas-invaded zone.....	564
10.3.2. Production mechanism in the gasing zone.....	574
10.3.3. Production mechanism in the undersaturated zone...	585
10.3.4. Convection process in gasing and undersaturated zones.....	587
10.3.5. Production mechanism in the water-invaded zone....	590
10.4. Specific aspects of a fractured reservoir.....	594
10.4.1. Material balance relationship.....	594
10.4.2. Migration of hydrocarbons in a fractured reservoir ...	597
List of Symbols.....	603
References.....	605

<b>CHAPTER 11</b>		<b>Page</b>
<i>NUMERICAL SIMULATION OF FRACTURED RESERVOIRS</i>		
11.1. Introduction . . . . .	607	
11.2. Phase flow simulation . . . . .	608	
11.2.1. One-phase flow simulator . . . . .	608	
11.2.2. Two-phase simulators . . . . .	612	
11.2.3. Three-phase simulators . . . . .	617	
11.3. Compositional simulators . . . . .	632	
11.3.1. Yamamoto's model . . . . .	633	
11.3.2. Saidi's model . . . . .	637	
List of Symbols . . . . .	639	
References . . . . .	640	
 <b>CHAPTER 12</b>		
<i>FRACTURED RESERVOIR EXAMPLES</i>		
12.1. Basic data and history of certain fractured reservoirs . . . . .	641	
12.1.1. Iranian reservoirs . . . . .	641	
12.1.2. Irakian reservoir . . . . .	650	
12.2. Simplified examples of reservoir calculations . . . . .	651	
Application A : Dimensional and dimensional single block rate and recovery . . . . .	651	
Application B : Well rate evaluation . . . . .	672	
Application C : Well rate under combined drive mechanism . . . . .	677	
Application D : Combined drive mechanism behaviour . . . . .	684	
Application E : Reservoir past history and reservoir behaviour prediction . . . . .	692	
List of Symbols . . . . .	703	
References . . . . .	705	
 <b>SUBJECT INDEX . . . . .</b>		707

## **FIRST PART**

This Page Intentionally Left Blank

# Reservoir Description

In the modern language of reservoir engineering by *reservoir description* is understood the totality of basic local information concerning the reservoir rock and fluids which by various procedures are extrapolated over the entire reservoir.

Since the fractured reservoir is different from the conventional reservoir, the description will have to be related to its specific features. Among these it is the correlation between fracturing process and geological events that is extensively discussed in Chap. 1. The condition of fracturing, associated to mechanical rock properties and type of stresses helps in the evaluation of highly fractured zones, and this may be improved by use of reservoir simulation through mathematical models.

Fracture detection, evaluation and processing is another essential step in the process of fractured reservoir description. In chapter 2, all parameters related to fracture density and fracture intensity, together with various procedures of data processing are discussed in detail. After a number of field examples, developed in Chap. 3, the main objective remains the quantitative evaluation of physical properties. This is done in Chap. 4, where the evaluation of fractures porosity and permeability, their correlation and the equivalent ideal geometrical models versus those parameters are discussed in great detail. Special rock properties such as capillary pressure and relative permeability are reexamined in the light of a double-porosity reservoir rock.

In order to complete the results obtained by direct measurements on rock samples, Chap. 5 examines fracturing through indirect measurements from various logging results.

The entire material contained in these five chapters defines the basic physical parameters and indicates procedures for their evaluation which may be used further in the description of fractured reservoirs.

This Page Intentionally Left Blank

# CHAPTER 1

## BASIC GEOLOGY

The study of the geology of a fractured reservoir requires the study of the relationship between the fracturing process and the geological events which took place during this phase. This includes the elaboration of a correct theory of fracturing and a valid diagnosis of the features of a fractured reservoir. Rock fracturing will most commonly have a tectonic origin, developing in folded beds or in connection with faulting or joint patterns. Sometimes it may also be caused by differential rates of diagenesis and lithification.

In general, the understanding of the fracturing process has recently progressed from an empirical to a more scientific approach, and therefore, reservoir description and reservoir modeling has benefited.

It is, however, necessary to remember that the evaluation of fracturing is far more complex than the evaluation of porosity and permeability in a conventional reservoir. In fact, the fracturing depends on the pattern of mechanical stresses of the rock material and rock properties. Hence, the results of fracturing, such as fracture openings, size, distribution, orientation, etc., will be related to stresses and type of rock (brittle or ductile), structural conditions, depth (overburden stress), lithology, bed thickness, etc.

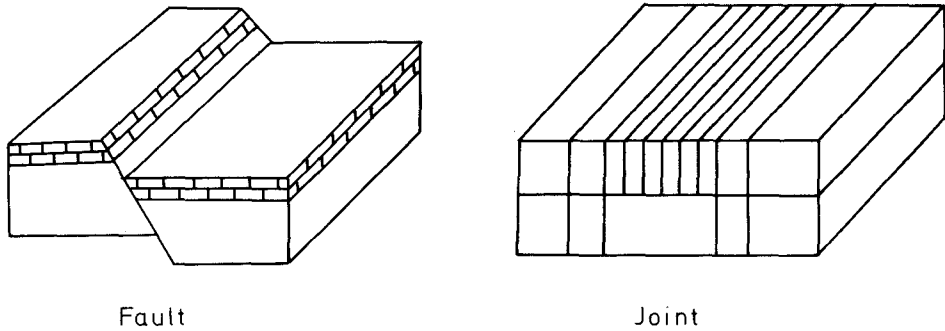
In this chapter, the geological conditions of fracturing are examined, including rock mechanics vs. geological events (faulting, folding, etc) and the rock characteristics and their variations vs. fracturing. In order to develop a valid geological model of a fractured reservoir, various geological events and fracturing developments are examined in detail. The results obtained offer many possibilities for further development.

### **1.1. INTRODUCTION**

Before entering into a detailed analysis of fracture phenomena, it is essential that certain terms are defined and a few basic statements elaborated on.

#### ***1.1.1. What is a fracture?***

According to different points of view various definitions can be given, but from a



1.1 – Schematic presentation of a fault and a joint.

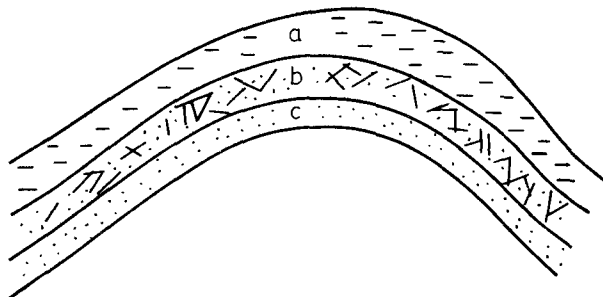
strictly geo-mechanical point of view a fracture is the surface in which a loss of cohesion has taken place. Since rupture refers to a process which results in the loss of cohesion of a given material, a fracture is then the result of a rupture. In general, a fracture in which relative *displacement has occurred* can be defined as a *fault*, while a fracture in which *no noticeable displacement* has occurred can be defined as a *joint* (figure 1.1).

A fracture can also be defined, in a more general way, as the discontinuity which breaks the rock beds into blocks along cracks, fissures, joints or whatever they may be referred to as, and along which there is no displacement parallel with the planes of discontinuity.

Basically, whether a fracture is considered a joint or a fault depends on the scale of investigation, but in general, that which is called a *fracture* corresponds to a *joint*.

### 1.1.2. Origin of fractures

Referring to the definition of rupture as the loss of cohesion along a plane which separates the material into discrete parts, the extrapolation of this process is more complex<sup>2</sup> for sedimentary rocks in the earth's crust. This is due to the fact that the



1.2 – Non-fractured layers a and c, and interbedded fractured layer b.

geological environment plays an essential role in the development of reservoir fracturing.

Among the three layers *a*, *b* and *c* in a reservoir (figure 1.2), rock layer *b* may lose cohesion at a lower stress than layers *a* and *c*. Therefore, while *b* is fractured, *a* and *c* can withstand further stress loading without developing fractures. In this case, nevertheless, the individual layer *b* is *fractured*, but the bulk behaviour of the entire sedimentary section is considered *non-fractured*.

The origin of fractures and their relationship with structural-tectonic events has been very much debated in the literature, especially with respect to the intensity of fractures and their significance for reservoir trapping.

Stearns and Friedman<sup>2</sup> recognized two classes of fractures, those *genetically* related to folding and those related to local structures (regional fractures).

Hodgson<sup>3</sup>, from the joint study made in Arizona and Utah, rejected the theory of a genetic relationship between joints and folds. He believed that joints were formed in the early stage of sedimentary diagenesis as the result of fatigue developed by semidiurnal earth tides.

Price<sup>4</sup> mentioned that even though joints have been observed in a number of more recent sediments, it is difficult to believe that early formed joints could survive the post-depositional processes of compaction and diagenesis.

Cook<sup>5</sup>, from the studies conducted in the Sidney Basin sediments, reached the conclusion that early formed joints can persist during later geological phases, such as burial and consolidation.

Harris<sup>6</sup>, after analysing the relationship between fracture density and layer thickness, supported the idea of a direct correlation between them.

It might be concluded that the structure-fracturing relationships must be associated to the division of fractures in two different categories<sup>1</sup> since field observations show that:

- a. *structure-related fractures* are those which show a consistency of orientation and regularity over a given field of observation. This relationship with the structure refers to localized prefolding features;
- b. *structure-unrelated fractures* are those which include irregular or curved discontinuous breaks that show no consistency of orientation. Such fractures are related to various superficial surface features (landslides, gravitational slump sheets, etc.).

## 1.2. GEOLOGICAL CONDITIONS OF FRACTURING

From examination of the fractured reservoir case histories<sup>2</sup> the most probable fractured reservoirs are expected to occur in brittle reservoir rock of low porosity where favourable tectonic events have developed. In this case, the re-

sulting fractures are large and very extended and are, therefore, called *macrofractures*. If the rock is less brittle and has a high intergranular porosity, the fractures are generally of limited extent and with relatively small openings and are, therefore, called *microfractures* or *fissures*.

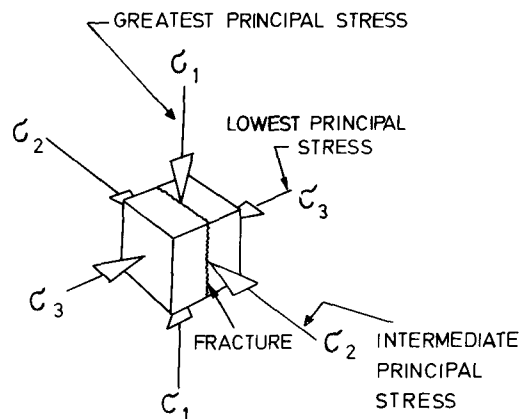
Fractures which are generated as the result of stress which reduces rock cohesion can be attributed to various geological events, such as:

- a. diastrophism in the case of folding and faulting,
- b. deep erosion of the overburden, which will cause a differentiated stress on the rock through the planes of weakness,
- c. rock volume shrinkage as a result of loss of water when pertaining to shale or shaly sands.
- d. rock volume shrinkage in the case of a variation of temperature in igneous rocks.

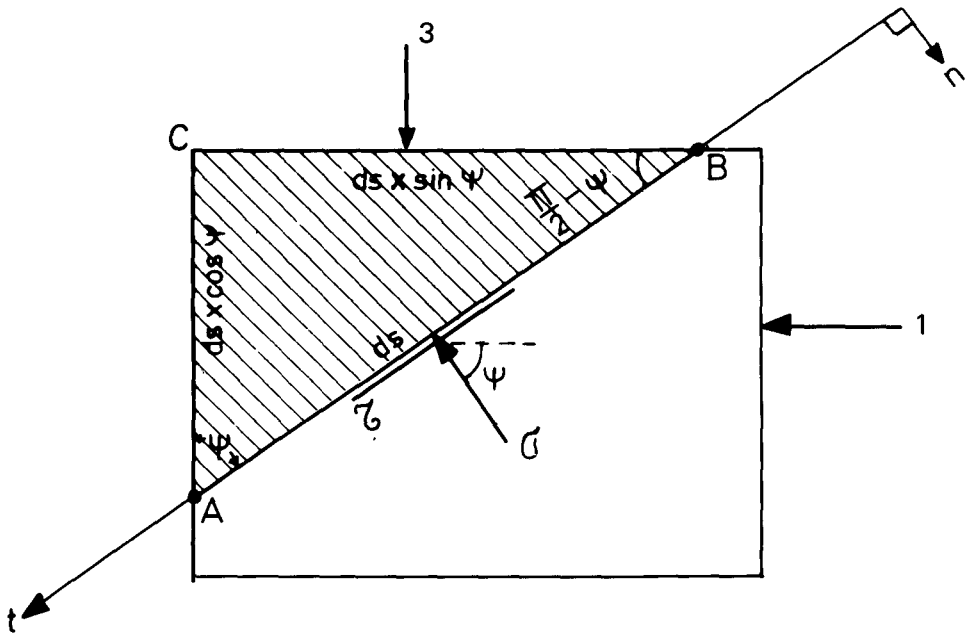
### 1.2.1. Rock mechanics vs. fracturing

#### 1.2.1.1. Basic equations

In reservoir conditions an elementary rock volume is in a state of stress provoked by overburden (geostatic) pressure, confining pressure, fluid (pore) pressure and, in addition, tectonic forces. Adopting the usual representation of forces by three normal directions and designating the three normal vectors as the principal stresses, the components  $\sigma_1, \sigma_2, \sigma_3$  are the greatest, intermediate and lowest stresses, respectively (figure 1.3). Often from these three stresses, the vertical stress  $\sigma_1$  reproduces the overburden pressure due to the overlying rock, while the horizontal stresses  $\sigma_2$  and  $\sigma_3$  may work as compressive or tension stresses.



1.3 – Stress element and preferred plane of fracturing



1.4 –  $\sigma$  and  $\tau$  on a plane of angle  $\psi$  (King Hubert<sup>7</sup>, Courtesy AAPG).

The relationship of the normal stress  $\sigma$  and shear stress  $\tau$  acting across a plane perpendicular to  $\sigma_1$  and  $\sigma_3$  is expressed as a function of the angle  $\psi$ , between the direction of the greatest principal stress  $\sigma_1$  and the plane AB (figure 1.4). The equilibrium of forces acting on a triangular prism ABC results as calculated below.

Solving the forces equilibrium in directions n and t

$$\sum_i F_{i,n} = 0; \sum_i F_{i,t} = 0$$

results in direction n

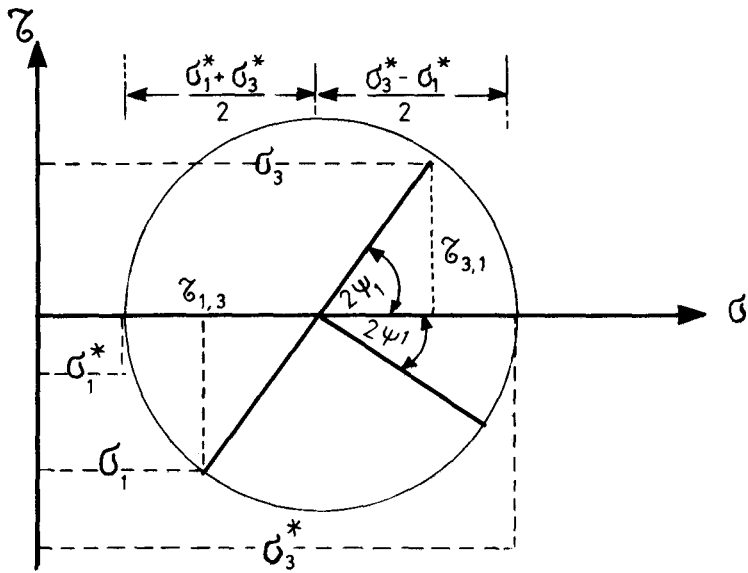
$$\sigma = \frac{\sigma_3 + \sigma_1}{2} + \frac{\sigma_3 - \sigma_1}{2} \cos 2\psi + \tau_{3,1} \sin 2\psi \quad (1.1)$$

and in direction t

$$\tau = \frac{\sigma_1 - \sigma_3}{2} \sin 2\psi + \tau_{3,1} \cos 2\psi \quad (1.2)$$

By using the Mohr's diagram (fig. 1.5) due to the variation of angle  $\psi$ , equations 1.1 and 1.2 may be rewritten as a function of principal stresses  $\sigma_1^*$  and  $\sigma_3^*$  (acting on the principal planes) indicated by the directions  $\psi = \psi_1$  and  $\psi = \psi_2 = \psi_1 + 90^\circ$ .

If  $\psi_1$ ,  $\psi_2$ , directions of the main stresses and the principal stresses,  $\sigma_1^*$  and  $\sigma_3^*$ , are known, equations 1.1 and 1.2 will become



1.5 – Mohr's diagram for normal stress  $\tau$  and shear stress, on a plane of orientation  $\psi$  (King Hubert<sup>7</sup>, Courtesy AAPG)..

$$\sigma = \frac{\sigma_1^* + \sigma_3^*}{2} + \frac{\sigma_1^* + \sigma_3^*}{2} \cos 2\psi^1 \quad (1.1')$$

$$\tau = \frac{\sigma_1^* + \sigma_3^*}{2} \sin 2\psi^1 \quad (1.2')$$

where

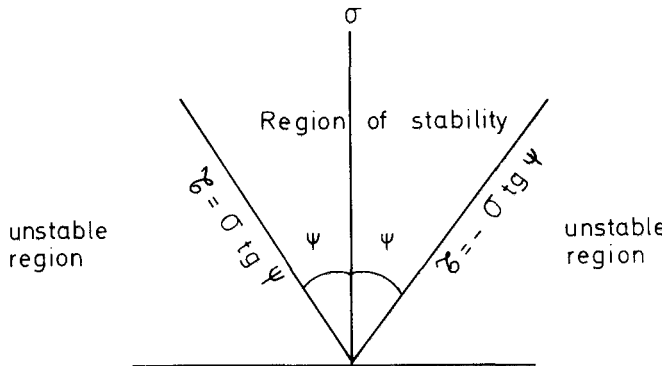
$$\psi = \psi_1 + \psi' \quad (1.3)$$

In order to determine the relationship  $\tau$  vs  $\sigma$ , it is necessary to refer to the experimental results which show that the shear stress is directly proportional to the normal stress through the equation:

$$\frac{\tau}{\sigma} = \tan \psi = \tan(\psi_1 + 45^\circ) \quad (1.4)$$

where  $\psi$  is the internal friction of the material. By using the Mohr envelope, faulting will occur on a plane making an angle of  $45^\circ + \psi/2$ . Since sand has an internal friction angle of  $\psi = 30^\circ$ , the normal fault will have a dip of  $60^\circ$ , an observation which was discussed in various geological works<sup>2 7 8</sup>.

For sand formations which have an internal friction angle of  $30^\circ$ , a failure will occur when  $\sigma_1 = \sigma_3$  along a plane making a  $45^\circ$  angle with the lowest principal stress (figure 1.6). In similar conditions (figure 1.6), if the vertical stress is constant a



1.6 –  $\sigma$ ,  $\tau$ ,  $\psi$  relationship for fracture planes in sand.

failure will occur if the horizontal stress takes values between one third and three times the vertical stress.

The above analysis could be further extended to consolidated rocks. In general, such predictions are obtained in the laboratory through triaxial compression tests on rock samples.

By using the maximum and minimum stresses  $\sigma_1^*$  and  $\sigma_3^*$  it was observed that at high values of  $\sigma_1^*$  nearly all rocks deform plastically and Mohr envelopes become approximately parallel to the  $\sigma$  axis. At lower pressure most rocks fail as the result of brittle fractures. The basic equation governing this state is:

$$\tau = \pm (\tau_0 + \sigma \operatorname{tg} \psi) \quad (1.4)$$

where  $\tau_0$  is the shearing strength for zero normal stress and  $\psi$ , the friction angle which varies between  $20^\circ - 50^\circ$ , but most commonly is around  $30^\circ$ . This equation is generally applicable to all rocks of geological interest, except salt and plastic clay.

It is possible to modify the above rock behaviour analysis by taking into consideration the role of the fluid saturation of the pores. In this case, the effective stress  $\sigma$  must be expressed as the difference between the total axial stress  $S$  and pore pressure  $P$ :

$$\sigma = S - p \quad (1.5)$$

while the shear stress  $\tau$  remains independent of pressure  $P$ . In fact, pressure  $P$  does not produce shear stress since it works on the fluid and solid simultaneously and, therefore,  $\sigma$  in triaxial testing of cores offers satisfactory conditions of simulation for the reservoir rock stress/strain conditions.

In order to evaluate the vertical stress in reservoir conditions, it is necessary to express  $\sigma_z$  by the following equation:

$$\sigma_z = S_z - P = h\gamma_r - h\gamma_w = h \times \Delta\gamma \quad (1.6)$$

in the absence of reservoir overpressure. If the formation is faulted and a significant overpressure has been developed in the fluid saturating the pores, the value  $\gamma_w$  is considered to be the local pore pressure gradient  $G_w$  and not the water density. In this case of abnormally high pore pressure  $P$ , the reduction of  $\sigma_1$  may become important, as has been observed in the North Sea (Jurassic formations) and Gulf Coast.

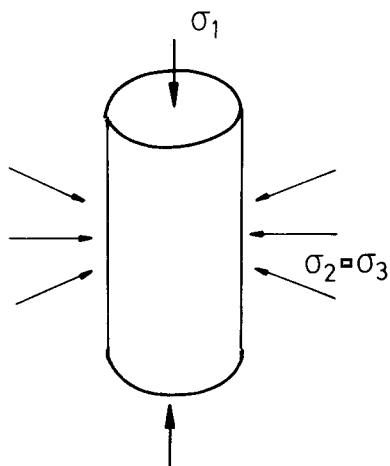
### 1.2.1.2. Testing of rock material

The most common testing procedure of rock failure is the conventional triaxial test.

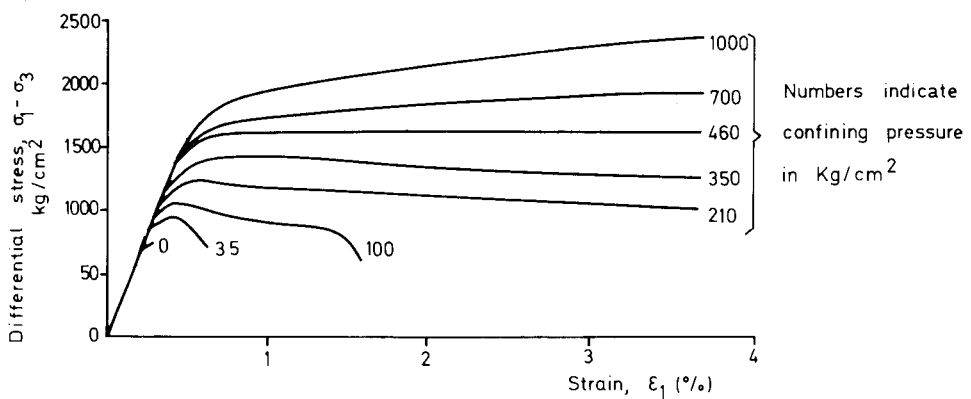
The experiments are made on a cylindrical sample subjected to an axial force (maximum principal stress  $\sigma_1$ ) acting along the axis of the cylinder and to a lateral confining fluid pressure (so that the two minimum stresses are equal,  $\sigma_2 = \sigma_3$ ) directed normal to the axis of the cylinder (figure 1.7).

The general procedure is to apply a hydrostatic pressure equal to the confining pressure and then to increase the axial loading by keeping the confining pressure constant. This combined state of stress for the evaluation of deformation properties has been extensively debated in the literature. The main result of this procedure is that the yield and ultimate strength increase as the confining pressure increases. An example is shown in figure 1.8 where the differential stress  $\sigma_1 - \sigma_3$  is plotted vs. longitudinal strain  $\epsilon$ , for different confining pressures.

As illustrated, the shape of the curves  $\sigma_1 - \sigma_3$  vs.  $\epsilon$ , is influenced by the confining pressure. At a low confining pressure a brittle fracture is obtained with an evident strength drop when failure occurs, while for a high confining pressure a large deformation may occur without any strength drop.

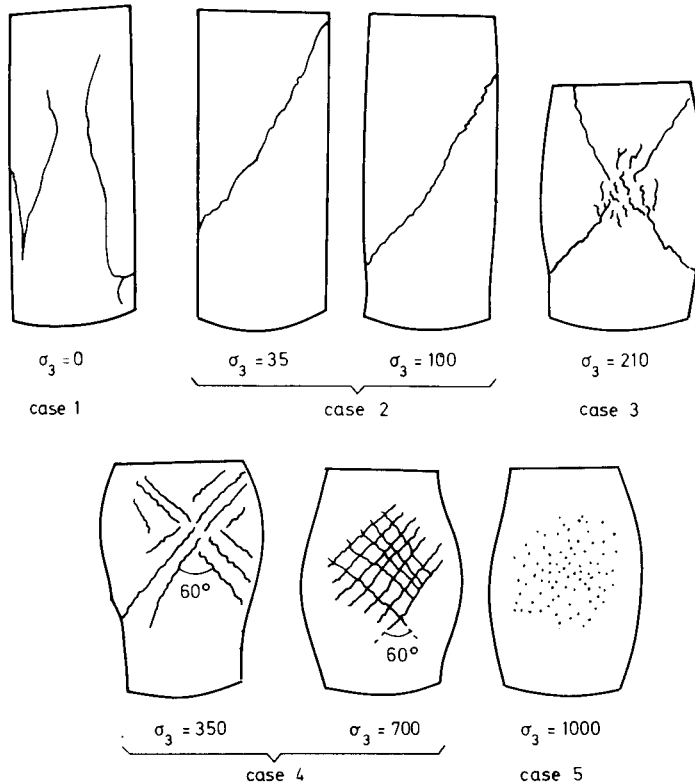


1.7 – Triaxial test for a cylindrical specimen (axial compression  $\sigma_1$  and fluid confining pressure  $\sigma_2 = \sigma_3$ ).

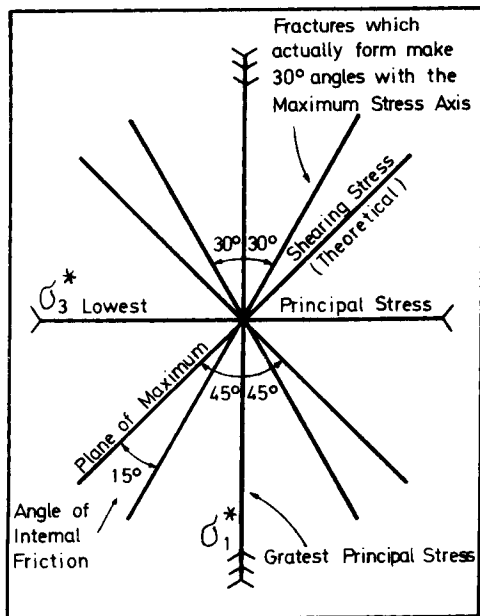


1.8 – Differential stress  $\sigma_1 - \sigma_2$  vs. strain  $\epsilon$  for various confining pressures.

The fracture pattern is very much influenced by the confining pressure (figure 1.9). If the confining pressure is low (below 35  $\text{Kg}/\text{cm}^2$ ) fractures are irregular (case 1, figure 1.9). If the confining pressure is over 35  $\text{Kg}/\text{cm}^2$  or 100  $\text{Kg}/\text{cm}^2$  net fractures



1.9 – Triaxial testing results for various confining pressures  $\sigma_3$  ( $\text{kg}/\text{cm}^2$ ).



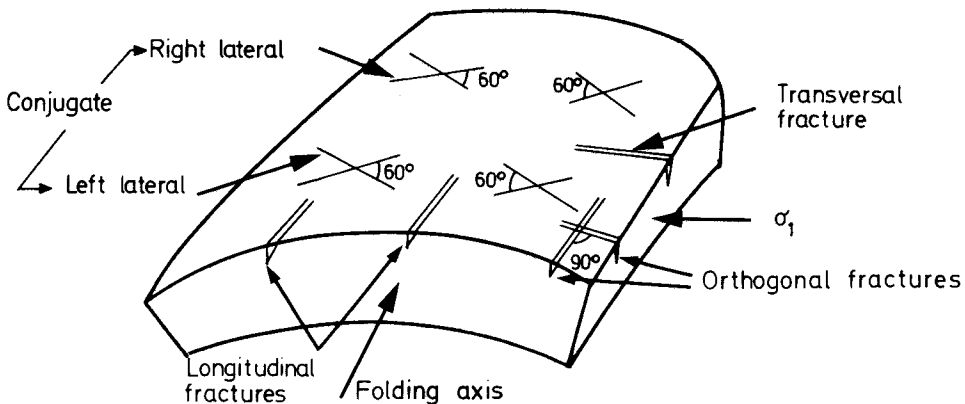
1.10 – Schematization of principal stress and shear stress.

result from triaxial tests (case 2). Over 200 Kg/cm<sup>2</sup> the fractures intersect symmetrically (case 3). For further increments of confining pressure (300–700 Kg/cm<sup>2</sup>) symmetrical abundant *conjugate* fractures are associated to a substantial reduction of sample height (case 4). For a high confining pressure (over 1000 Kg/cm<sup>2</sup>) fractures do not develop at all.

The relationship between stress direction, shear stress and fractures is presented schematically for a sandstone (figure 1.10). The two main directions, vertical and horizontal, show the greatest principal stress ( $\sigma_1$ ) axis and the lowest principal stress ( $\sigma_3$ ) axis. The plane of maximum shear stress indicates an angle of 30° with the greatest principal stress axis. The angle between the maximum and actual shear stress (30°), represents the angle of internal friction.

### 1.2.2. Fracturing under geological events

Fractures, as defined by Stearns and Friedman<sup>2</sup>, may have a common origin if they have been developed under a single state of stress. This type of fracture is called *conjugate*. In this case (figure 1.11) the fracture pattern contains a left-lateral shear fracture and a right-lateral shear fracture as a result of the greatest principal stress which coincides with the transversal fracture. The conjugate shear fractures form a pattern of fracture planes intersecting at 60°. The important advantage of such a



1.11 – Conjugate and orthogonal fractures referred to the folding axis.

fracture pattern is that it is sufficient to know only one orientation of a system of fractures in order to build the whole pattern of fractures and stress distribution.

On the contrary, the orthogonal fractures with an intersection angle of 90° will be the result of more than one single state of stress even if it is not excluded that the fracturing has a common geological origin for both groups of fractures.

#### 1.2.2.1. Fractures vs. faulting

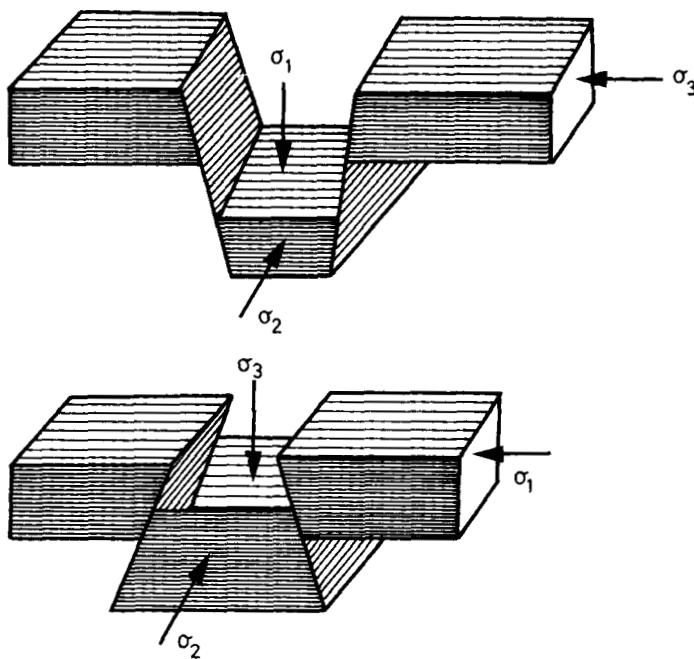
In order to understand the manner in which the three principal stresses ( $\sigma_1 > \sigma_2 > \sigma_3$ ) influence the various geological deformations, a series of examples are given. In these examples the distribution of stresses is related to faults and shear fractures.

Case 1: If the principal stress  $\sigma_1$  has vertical orientation and  $\sigma_2$  and  $\sigma_3$  a horizontal orientation (figure 1.12), normal faulting will result where two conjugate faults form an angle of 60°. This illustrates the development of normal faults by extension. Therefore, based on what was previously discussed the greatest stress  $\sigma_1$  is approximately vertical and equal to the overburden stress, while the lowest stress  $\sigma_3$  should be horizontal. Thus, the relationship between  $\sigma_1$  and  $\sigma_3$  during the fracturing process has a variation range of,

$$\sigma_3 \cong \frac{1}{2}\sigma_1 \div \frac{1}{3}\sigma_1$$

Case 2: During geological history when the bed was shortened by the effect of folding or overthrusting, the lowest stress  $\sigma_3$  would be vertical while the greatest stress  $\sigma_1$  would be horizontal (figure 1.12b). Therefore, in this case the variation range of  $\sigma_1$  is,

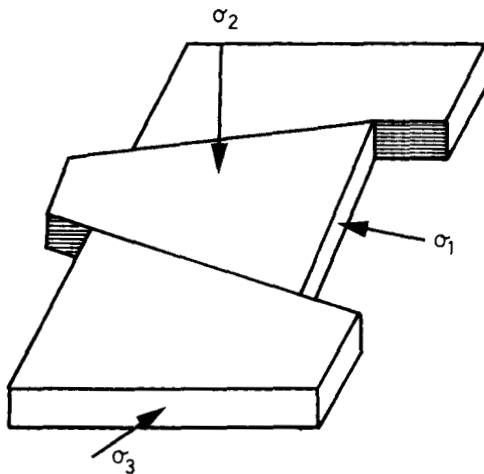
$$\sigma_1 \cong 2\sigma_3 \div 3\sigma_3$$



1.12 – Faulting: a) Extension and normal fault and b) compression of inverse fault.

The result as observed in figure 1.12 b is inverse faulting as the result of compression due to  $\sigma_1$  and overburden  $\sigma_3$ .

Case 3: A different situation will arise if the greatest and lowest principal stresses ( $\sigma_1$ ,  $\sigma_3$ ) are both horizontal and the vertical stress is  $\sigma_2$ . Compression followed by shear fracturing occurs as in figure 1.13. In this zone of transcurrent faulting where both



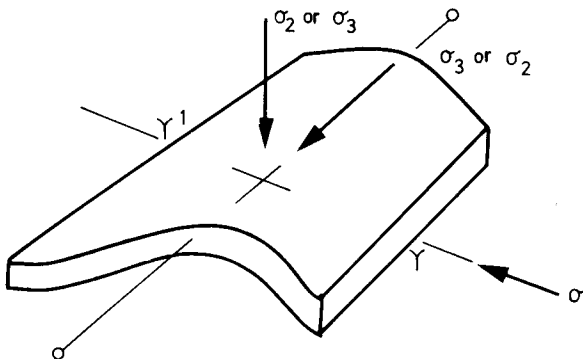
1.13 – Compression and shear fracturing.

the greatest and the lowest stresses ( $\sigma_1, \sigma_3$ ) are horizontal and the intermediate stress ( $\sigma_2$ ) is vertical, two fracturing surfaces forming an angle of  $60^\circ$  will result (figure 1.13). The following examples are based on field observations and have been discussed in the literature:

1. During the Tertiary period normal faulting occurred in Texas and the Louisiana Gulf Coast. The normal fault stress system is cyclic since the stresses build up until a breaking point is reached, followed by a relaxed period and again by a period of pressure build up. Since the faults are mostly parallel with the strike, the lowest stress must be oriented parallel with the dip, having an order of magnitude of  $1/2 - 1/3$  of the overburden effective pressure.
2. Contrary to this, in California where tectonic deformation took place recently and is still continuing, slippage movements along faults and elevation movements under a global overthrusting deformation are observed. Compression still takes place and the greatest principal stress  $\sigma_1$  will be horizontal while the lowest stress  $\sigma_3$  of the effective overburden will be vertical (figure 1.14).

From the examples and cases examined the relationship between fractures and faults could be resumed<sup>1</sup> as follows:

- a. fractures associated with the fault have a common stress origin;
- b. the orientation of fractures (strike and dip) can, therefore, be predicted if the orientation of the fault is known, and inversely from fracture orientation the fault strike and dip can be determined;
- c. it is not possible to evaluate fracture density from fault data;
- d. the strikes of all three potential fractures and their intersection can be predicted;
- e. for normal faults it is necessary to know the relative development of the two shear fractures;
- f. if the fractures are conjugate to the fault it is possible for the well drilled in the reverse direction of the two blocks to intersect a great number of fractures.



1.14 – Folding compression

The understanding of the relationship between fractures and faulting can become complicated if folding events have occurred in addition to the faulting process.

#### 1.2.2.2. Fractures vs. folding

In the case of folding, fractures cannot be associated with a single state of stress (as in the case of faulting), but instead, to several states of stresses which took place during the folding history.

The examples of folding shown in figure 1.14 and 1.15 represent the two cases when the greatest principal stress is acting parallel and normal to the formation bedding.

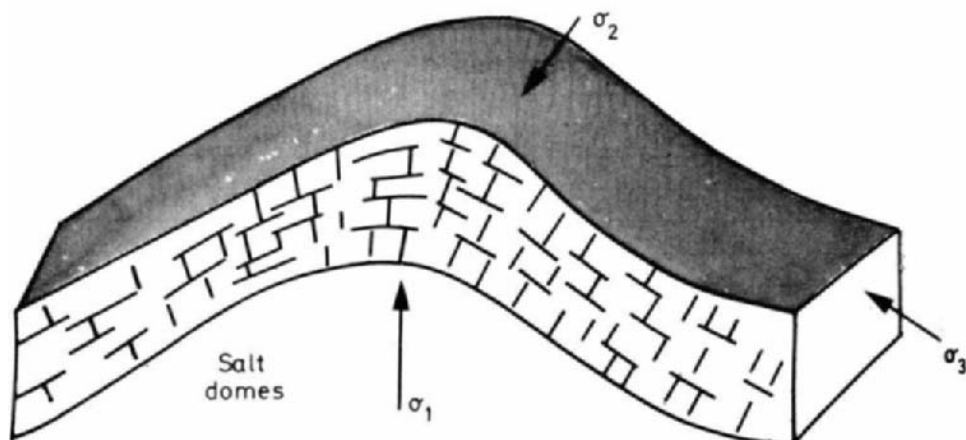
In figure 1.14 the lateral stress  $\sigma_1$  acts only on one side of the bed ( $Y'$ ) and is practically immobile on the other side ( $Y'$ ). The folding will, therefore, generate a series of fractures as the result of compression and tension stresses.

Figure 1.15 presents the case where  $\sigma_1$  acts vertically as a result of salt dome rising. The structure is uplifted and the reservoir layers are under compression and tension stresses.

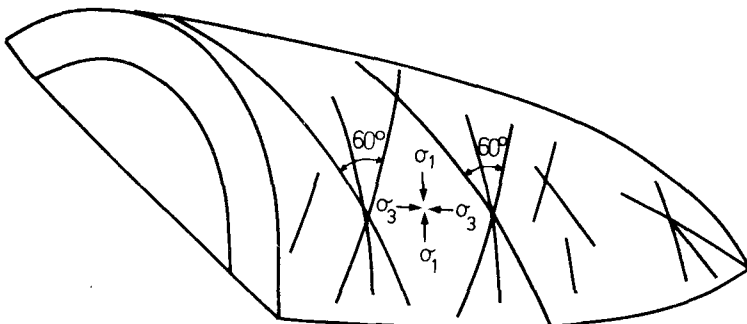
During the folding process a series of fracture patterns are generated under various conditions of distribution of the principal stress. Of these patterns, two have been retained as the most important and are described below:

##### a. Pattern 1 (figure 1.16)

In this case the three principal stresses work in the following directions:  $\sigma_1$  and  $\sigma_3$  along the bedding plane and  $\sigma_2$  normal on the bedding plane. Due to the direction of the greatest principal stress  $\sigma_1$  along the structure dip, a series of transversal fractures and the respective conjugate fractures will occur. This observation is of major interest when studying the outcropping data in a folded structure. Based on the observed conjugate fractures, it becomes possible to understand what direction  $\sigma_1$



1.15 – Folding due to salt dome uplift.



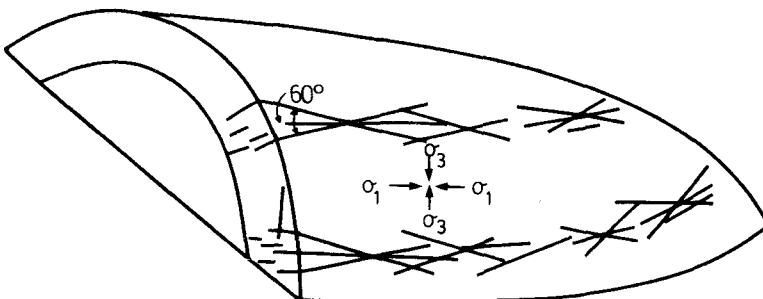
1.16 – Fracture Pattern 1:  $\sigma_1$ ,  $\sigma_3$  acting in the bedding plane and  $\sigma_3$  acting normal to the bedding plane ( $\sigma_3$  – dip direction:  $\sigma_1$  – strike direction). (Stearns<sup>2</sup>, Courtesy AAPG).

had during folding and also, to establish the normal direction in the same bedding plane where  $\sigma_3$  has worked. The dip of the anticline is then given by  $\sigma_1$  and the strike is given by  $\sigma_3$ .

#### b. Pattern 2 (figure 1.17)

This fracture pattern is similar to Pattern 1 with  $\sigma_2$  normal to the bedding plane and  $\sigma_1$  and  $\sigma_3$  in the bedding plane. The only difference is that the greatest principal stress  $\sigma_1$  acts in a direction parallel to the folding axis. Therefore, the result will be a series of conjugate fractures which will indicate  $\sigma_1$  along the longitudinal direction which represents strike direction, while the lowest principal stress  $\sigma_3$  will indicate the dip.

A shortening and an elongation of the anticline will occur on the anticline folding in these two cases. The shortening due to  $\sigma_1$  will be on a dip direction in Pattern 1 and on a strike direction in Pattern 2, and vice-versa for the elongation. Except for fracturing, no change such as shortening or elongation normal to bedding will occur.



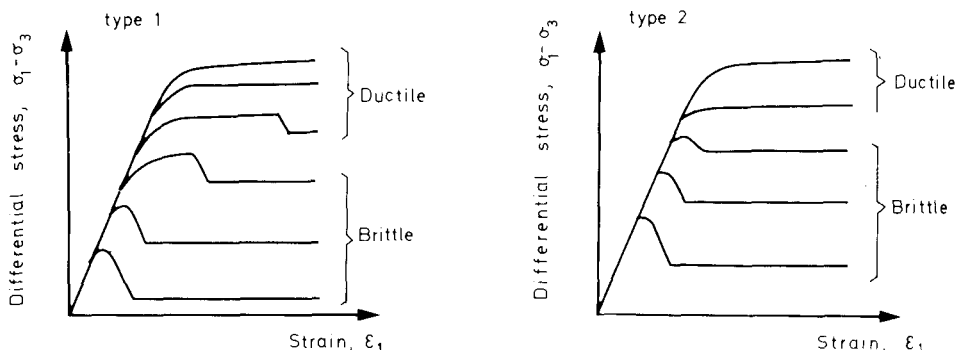
1.17 – Fracture pattern 2:  $\sigma_1$ ,  $\sigma_3$  acting in the bedding plane and  $\sigma_1$  acting normal to the bedding plane ( $\sigma_3$ -dip direction,  $\sigma_1$ -strike direction). (Stearns<sup>2</sup>, Courtesy AAPG.)

Stearns and Friedman<sup>2</sup> have mentioned a series of examples of these two patterns and have made a number of observations:

- a. the two patterns may be developed in the same bed;
- b. in general, Pattern 1 will precede Pattern 2, which means that folding must develop to a sufficient degree so that fracturing can occur. In such a case fractures will be normal to the anticline trend;
- c. the fractures of Pattern 1 are often developed on long distances such as single breaks. In general the fractures are large with a homogeneous orientation, which may aid fluid movement over large areas;
- d. the fractures of Pattern 2 are of reduced length, often varying between a few inches and a few feet. The fractures are aligned with the folding axis and usually contain fractures in all three principal directions;
- e. the extension fractures in Pattern 1 may terminate in lateral fractures (left or right), and the shear fractures may terminate in extension fractures or in their conjugates;
- f. without it being demonstrated, it seems that there are more chances of having continuity of a single fracture in the case of Pattern 1, but the fracture density of Pattern 2 may be more effective for the fluid flow;
- g. in a well intersecting the fractures of Pattern 1 there are three possible directions for the well to intersect the fractures, but in the case of Pattern 2 the most favoured communication will be in the direction parallel to the structural trend.

### 1.2.3. Rock characteristics vs. fracturing

The deformation curve, expressed for a given rock as a variation of differential yield stress ( $\sigma_1 - \sigma_3$ ), vs. confining pressure ( $\sigma_3$ ), has demonstrated a different behaviour for different types of rocks. Testing was done by grouping the rocks into two categories, Type 1 where large permanent strain can occur before fracturing, and Type 2 where permanent deformation occurs in the post-yield region (figure 1.18).



1.18 – Strain/stress curve for different confining pressures.

As observed, *Type 1* rock in the high pressure region does not describe the strength of the material, therefore, the Coulomb law is not valid. However, since almost all reservoir rocks are of *Type 2*, the Coulomb criteria remains valid for fracture prediction of rock reservoir behaviour.

#### 1.2.3.1. Brittle-ductile state transition

As already discussed, a rock could pass from the brittle state to a ductile state when the confining pressure is very elevated, and reach a state of permanent deformation without fracturing (figure 1.9). The transition from the brittle state to the ductile state is not sharp. In general, it was observed that the changes in deformation mechanisms in *Type 2* reservoir rock are associated to a cataclastic flow which corresponds to the crushing of grains and formation of fractures along the grain boundaries. In various states the maximum strain is variable. During the brittle state the maximum strain is below 3%, while in a ductile state it is over 5%. In the transition state the maximum strain varies between 3% and 5%. The determination of the deformation mechanism of rock was accomplished by the examination of the volumetric differences of the rock sample. These observations have shown a clear differentiation for the two states, especially in the case of rocks of low porosity. A volumetric increase of a specimen corresponds to a cataclastic deformation and a volumetric reduction, and indicates an intercrystalline plastic flow. The main problem in the case of highly porous rocks is that the dilatancy during cataclastic deformation may reduce the pore volume and alter the results.

#### 1.2.3.2. Deformational properties

In order to examine a rock in the laboratory and use the results for field fracturing behaviour, a number of factors must be examined such as time expressed by loading rate, reservoir temperature, confining pressure and type of rock.

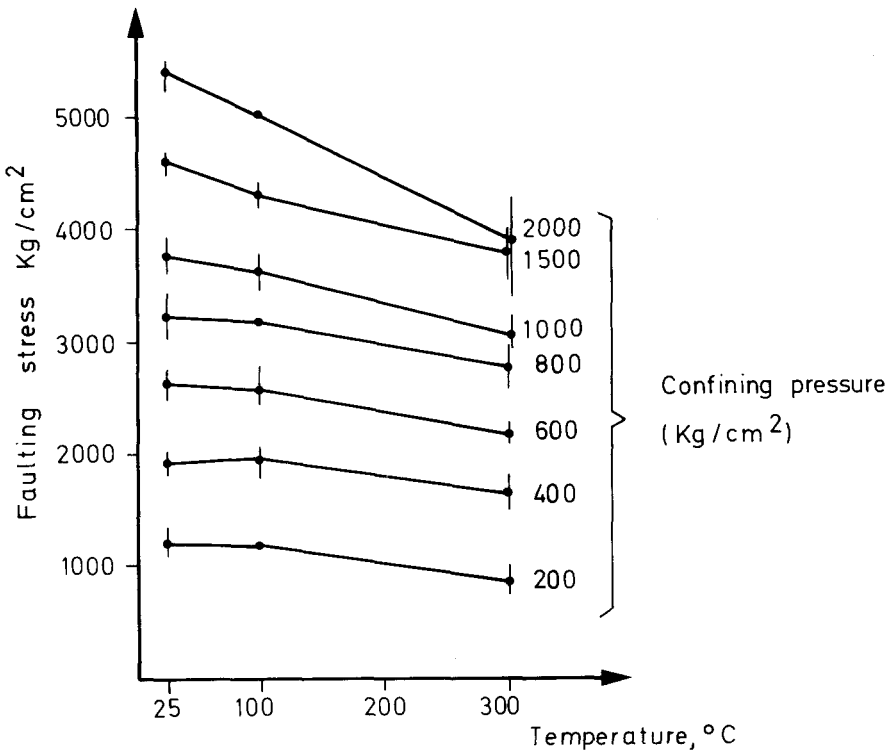
The brittle-ductility relationship should be related essentially to the type of rock which will show a different behaviour under similar environmental conditions.

##### a. Loading rate

In general, a decrease in the strain rate will cause an increase in ductility, but the strain rate is in itself a function of rock deformation mechanism, temperature and confining pressure. Laboratory observation has shown in any case that for sandstone and compact limestone the long-time strength of rock will not vary much from the laboratory experimental data.

##### b. Temperature effect

Temperature effect was examined in detail by Handin<sup>10</sup>. He examined rock specimens in the laboratory under temperature variations ranging from 25 °C to 300 °C. The conclusion reached after many experiments was that, in general, the increment in temperature is followed by a reduction in yield and ultimate strength



1.19 – Faulting stress vs. temperature for various confining pressures.

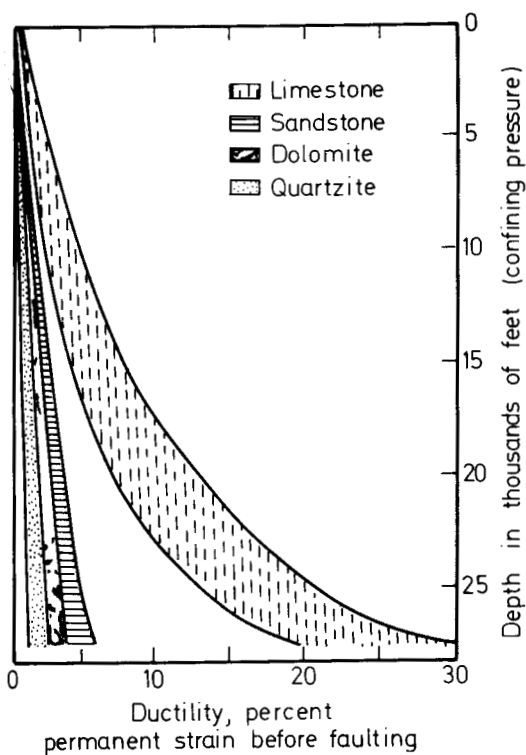
and an increase in ductility. The temperature effect also seemed to be more sensitive in carbonate rocks than in silicate rocks. The effect of temperature on a limestone is shown in figure 1.19.

### c. Type of rock

The mechanical properties of sedimentary rocks have been studied in detail<sup>10</sup>, but it is still premature to give a precise relationship for various rock materials<sup>1</sup>.

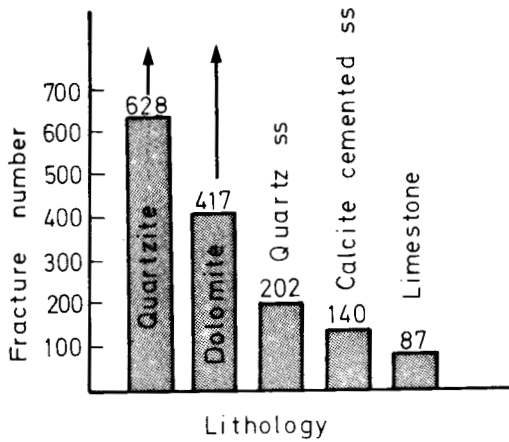
In general, it can be stated that by increasing the confining pressure and the temperature but decreasing the strain rate, an increment in ductility will result. Quartzite and dolomite never become as ductile in the same environment as limestone. The degree of cementation in sandstones is somewhere between limestones and dolomites. In figure 1.20, the change in ductility is associated with the burial depth by using normal pressure (due to overburden) gradients and normal temperature gradients. Therefore, the difference in ductility is negligible at a low depth, but at a depth of several thousand feet an impressive differentiation will result.

The variations in ductility could substantially influence the number of fractures when the rock is buried at a given depth as mentioned in relation to figure 1.20. The results

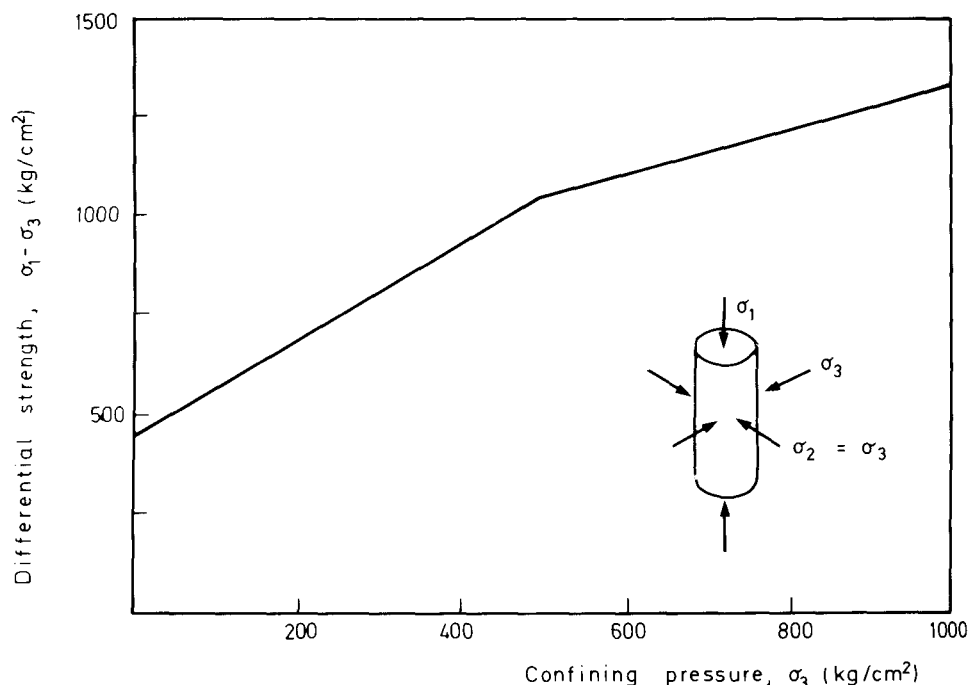


1.20 – Ductility vs. depth (water saturated rock)<sup>10</sup> (Courtesy AAPG).

obtained in the laboratory show a substantial difference in the number of fractures for various rocks (figure 1.21).



1.21 – Average number of fractures vs. lithology<sup>10</sup> (Courtesy AAPG).



1.22 – Long-time strength of limestone vs. confining pressure.

#### d. Fracture or yield data

Since the estimation of long term rock properties from short term triaxial compression tests performed in the laboratory is uncertain, it was proposed to use an elastic limit. In other words, to utilise the fact that in a strain-stress curve there is a limit in stress over which the linear strain-stress relationship is no longer valid. This limit, which is called a *marked non-linearity in the stress-strain curve*, begins before fracturing as a result of a considerable microcracking process inside the rock.

When plotting the differential  $\sigma_1 - \sigma_3$  vs. confining pressure  $\sigma_3$  as in the curve illustrated in figure 1.22, the fracture curve for the material in the reservoir will result. The state of stress exceeding this curve will occur in rock fracturing. The curve can be represented in a simplified form by two straight lines, where the change in slope corresponds to the brittle-ductile transition zone. By use of this method a fracture criterion is established for all principal stresses in compression or tension conditions.

#### 1.3. GEOLOGICAL MODEL FOR THE SIMULATION OF FRACTURING

Models of the fracturing process have been developed recently by Quiblier<sup>11</sup> and Ramstad<sup>8</sup>. The main objective of the model developed by Quiblier was to find the

areas of highest fracture density or highest probability of fracturing by computing a series of iso-risk maps for fracture development. His basic idea was that the tectonic stresses in the reservoir could be computed by using the present shape of different layers and assuming that the material was deformed from an original undeformed plane state. The total stresses are resulting from the superpositions of the tectonic stresses and overburden (gravity) stresses. From the total stresses and the fracturing criteria the density and distribution of fractures will result.

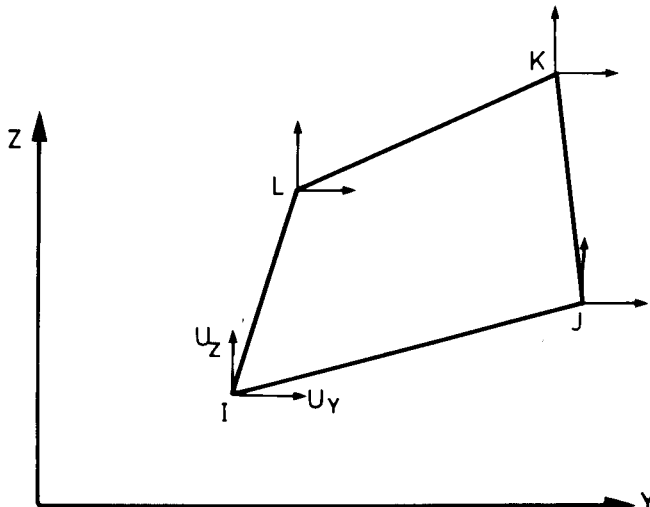
From this method the critical modulus of elasticity has been calculated for each point and evaluated to see if it was high enough to create fractures for a given displacement. The points with the lowest critical modulus would then increase their fracturing possibility and vice-versa. This model has been applied to Iranian reservoirs.

Ramstad's model retains Quiblier's basic idea of prescribing a known displacement, but the method in this case is different. He used the finite element method in conditions of linearly elastic and elasto-visco-plastic materials law.

### *1.3.1. Modeling based on the finite element method*

This method consists of dividing the total domain of the reservoirs into subdomains and expressing the field functions as polynomial expansions within each element. The continuity between the elements is also expressed by the field functions.

This is a very advantageous method for complicated geometry in non-homogeneous materials, and it is also very suitable for treating problems concerning visco-plastic analysis. The element in the present work is a quadrilateral plane strain element having two degrees of freedom at each corner or nodal point (figure 1.23).



1.23 – Quadrilateral plane element.

The rigidity of the matrix is obtained by using  $2 \times 2$  Gauss integration, while the stresses in the visco-plastic analysis are computed at the four Gauss integration points and at the center of the element in the linearly elastic analysis<sup>8</sup>.

### 1.3.2. Formulation of a finite element in the case of a visco-plastic material

When dividing a structure into finite elements the displacement field ( $U$ ) inside an element is expressed by means of nodal point values ( $V$ ) and interpolation functions. The basic equations for a discrete system of an ordinary differential equation is given by the following:

1. The relationship between incremental nodal displacements and increments in load is obtained by,

$$K\Delta r - \sum_{i=1}^{n_2} a_i^T \int_{\Gamma_i} B_i^T \Delta \varepsilon_i^{\text{VP}} dV - \Delta R = 0 \quad (1.7)$$

where  $K$  is the matrix stiffness for the whole model.

2. The expression of the visco-plastic strain rate  $\varepsilon^{\text{VP}}$ , which is equal to a symmetric matrix depending on the current state of stress  $\sigma$  for an isotropic material  $\Gamma$ , is,

$$\varepsilon^{\text{VP}} = \bar{\Gamma} \bar{\sigma} \quad (1.8)$$

3. For finite increments the relationship between stress increment and strain difference is expressed by,

$$\Delta \sigma = D(\Delta \varepsilon - \Delta \varepsilon^{\text{VP}}) \quad (1.9)$$

where  $D$  is the plane strain elasticity matrix for each element. This indicates that the variation of stress is equal to the plane strain elasticity of matrix  $D$  obtained under the assumption of zero elastic strain in the  $Z$ -direction.

#### 1.3.2.1. The role of pore pressure

If the pore pressure due to the fluid contained is taken into consideration, the effective stress  $\sigma'$  will result as the difference between the total stress  $\sigma$  and the pore pressure  $\sigma^h$ , hence,

$$\sigma' = \sigma - \sigma^h \quad (1.10)$$

and thus, the total stress can be expressed by,

$$\sigma = D(\varepsilon - \varepsilon^{\text{VP}}) - M \times p \quad (1.11)$$

where  $M$  is a vector defined by,

$$M = [1, 1, 0] \quad (1.12)$$

and  $D$  is the elasticity of the matrix, while  $\varepsilon$  and  $\varepsilon_{VP}$  are the vectors of strain components and the vectors of the visco-plastic strain components, respectively.

### 1.3.3. Numerical solutions

Two solutions to the fracturing problem (which results from salt dome uprise) have been found through two different computer programs, for linear elastic material and for elasto-visco-plastic material.

### 1.3.4. Programs

#### 1.3.4.1. Linear elastic programs

The stresses are composed of tectonic stress (due to salt dome rising) and gravity stress (caused by the weight of the overburden). The different stresses are computed separately and later superimposed in order to give the total amount of stress. The vertical component of the gravity stress is directly computed from the overburden weight, while the horizontal component is assumed to be a certain fraction of the vertical component (in the range of 60%–80% of the vertical component). The role of sediments due to the deposition above the reservoir during the salt dome rising is modelled by adding more layers during the calculation. The increments of gravity stress and pore pressure are computed as a result of the addition of new sediments, and the equation system is solved by finding the increment of tectonic stress due to this deformation.

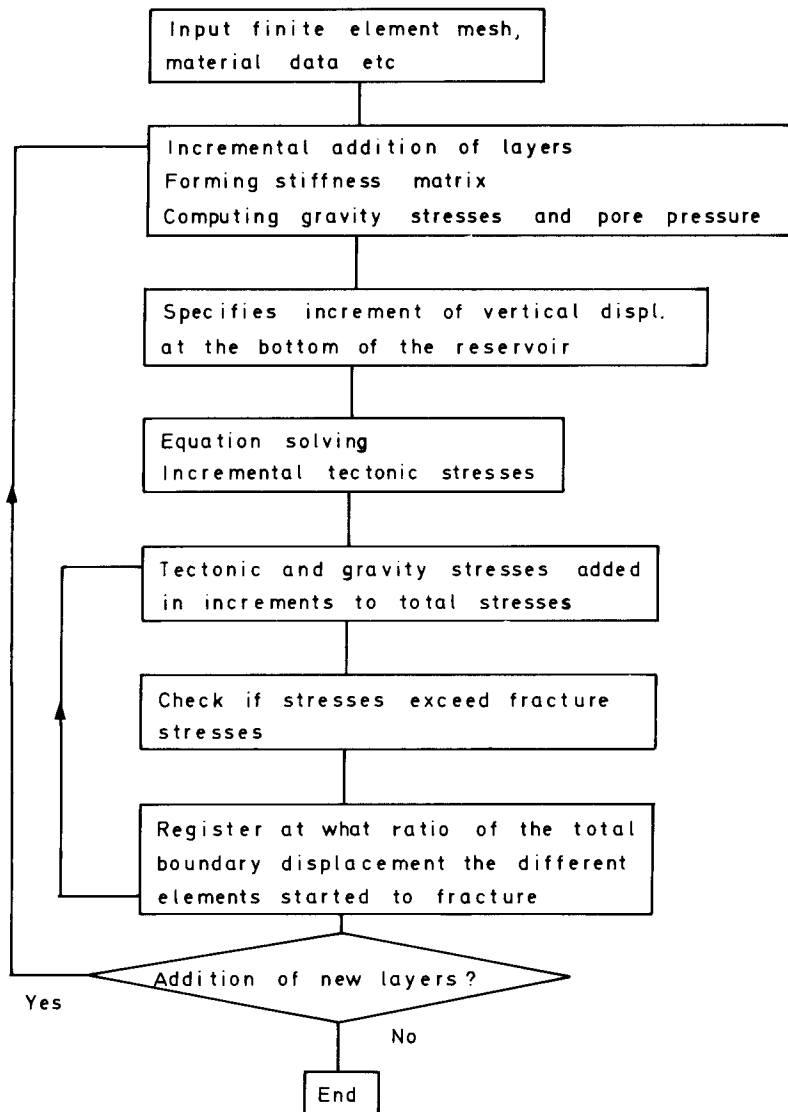
The stress increments are added to the total stresses, and for each element the stress is checked against a fracture criterion to *discover* if the elements are fractured or not.

The ratio of the total displacement at which the different elements start to fracture is found and this is used as a relative measure for fracture density, assuming that the elements which first start to fracture have the highest fracture density or highest probability of fracturing<sup>8</sup>.

The detailed simulation program is shown in the flow chart of figure 1.24.

#### 1.3.4.2. Elasto-visco-plastic program.

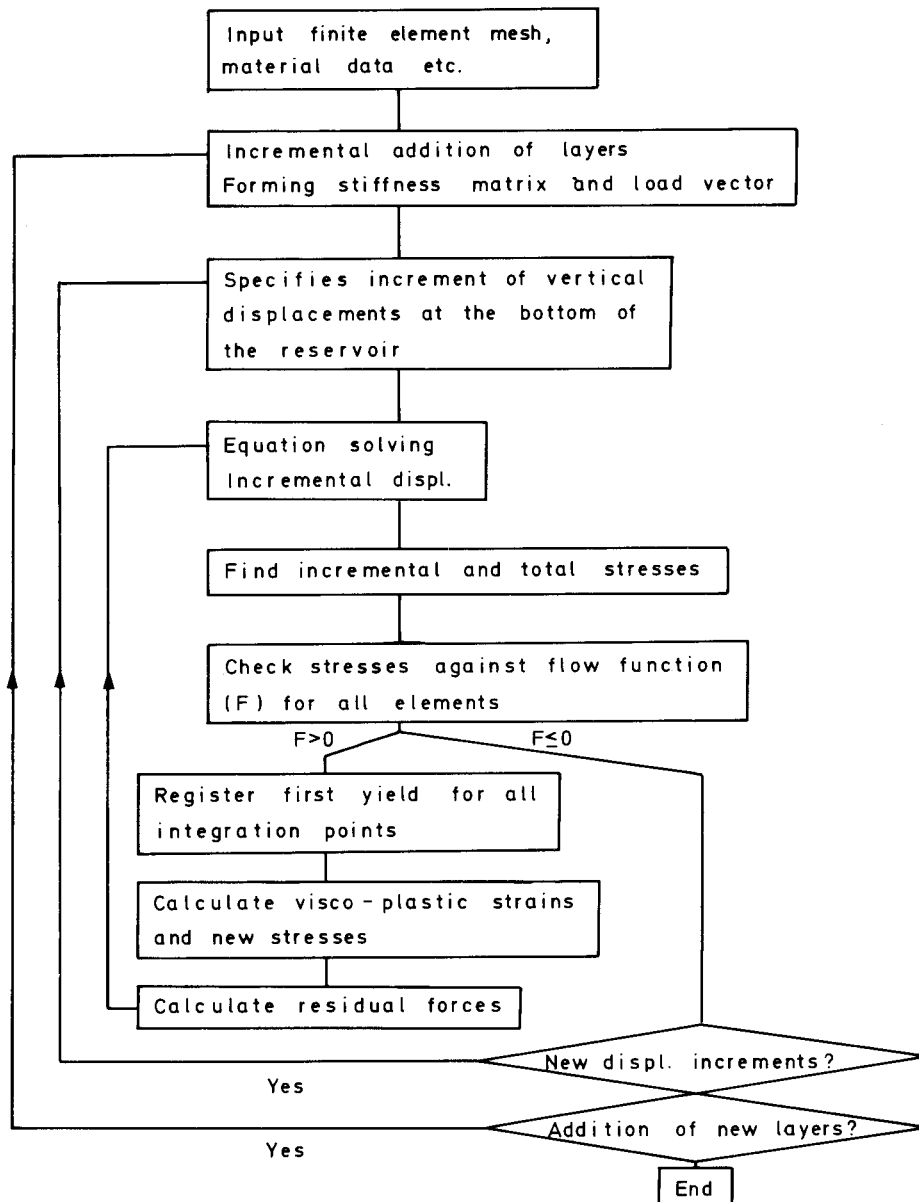
The program shown in the flow chart in figure 1.25 is designed for elasto-plastic problems, but with minimum changes it could be adapted for elasto-visco-plastic



1.24 – Flow chart for the case of linear elasticity model.

problems. In this program the gravitational and tectonic stresses are computed together and the horizontal component is higher than the value computed for the elastic case. The stresses calculated as an effect of the salt dome rising and overburden sediments are checked against a flow function. By checking the stresses against the flow function for all elements the two resulting cases are:

- a. if the flow function  $F>0$ , the visco-plastic strains and new stresses are calculated,



1.25 – Flow chart for the case of elasto-visco plasticity model.

then the residual forces are reintroduced into the basic equation solving the incremental displacement until a stationary situation  $F < 0$  is reached;  
 b. if  $F < 0$  a new displacement might occur and in this case the specific increment of vertical displacement at the bottom of the reservoir must be reviewed until a

stationary situation is reached. If not, new over-layers will have to be considered until a stationary situation is reached.

#### ***1.4. INFLUENCE OF STYLOLITIZATION AND JOINTING***

The largest majority of fractured reservoirs are located in limestone rocks in which both joints and stylolites have considerable influence on reservoir quality.

Stylolites occur as irregular planes of discontinuity passing through the rock matrix, generally roughly parallel to bedding (figure 1.29 illustrates the main types), and their presence normally reduces the intercommunicability of the reservoir fracture system. Understanding the importance of stylolites to fractured reservoirs, depends more on understanding the *timing* of their origin relative to that of fracturing and hydrocarbon migration, than on their actual origin.

Joints are more common than stylolites, and are normally associated with the structural history of the area and may be rationalized in terms of angularity to the principal stresses resulting in regional folding and faulting trends.

##### ***1.4.1. Stylolites and stylolitization***

The presence of stylolites in limestones is a common feature independent of rock facies and geologic age. In general, they are easily recognizable as irregular planes of discontinuity or sutures, along which two rock units appear to be interlocked or mutually interpenetrating<sup>12</sup>. These planes are usually characterized by the accumulation of insoluble residues which form the stylolite seams, which may be found to terminate laterally or converge into residual clay seams.

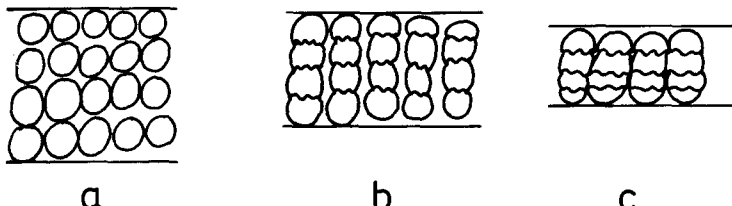
Although their origin has in the past given rise to considerable debate, it is now generally accepted as being the result of either a contraction-pressure process, and/or a pressure-solution process. Observations by a number of workers (Wagner<sup>13</sup>, Stockdale<sup>14</sup>) tend to give greater support to the latter.

Pressure-solution then, is a diagenetic process in which significant reduction (up to 40%) of the initial rock volume takes place by thinning. This appears to begin before cementation and continues until either the cementation process is completed, or all of the carbonate dissolved in the interstitial fluids has been precipitated.

The presence of stylolites and reprecipitated cements, especially if continuous, causes considerable reduction in reservoir quality since they act as barriers to hydrodynamic systems, intergranular pores and fracture networks.

###### ***1.4.1.1. Schematic description of stylolitization***

In the case of pressure-solution the process of stylolitization could be simplified as shown in figure 1.26. The original grains of phase a, due to increasing fluid pressure



1.26 – Schematization of stylolitization with thinning.

(as a result of increasing overburden with deepening burial), will reach a state of high solubility. Furthermore, this will be greatest at the grain extremities and point to point contacts between grains.

Phase b in figure 1.26 represents the carbonate material which will be transported, and if dissolution continues the new phase c will be reached.

The thinning process has been examined by Dunnington<sup>15</sup>, who described a reduction in volume by dissolution of up to 30% (figure 1.27). This can be expressed in the following equations:

$$\Phi_i = TH + \Phi - \Phi \times TH \quad (1.13)$$

$$TH = \frac{\Phi_i - \Phi}{1 - \Phi} \quad (1.14)$$

where TH is the percentage of thinning,  $\Phi_i$  is the initial porosity and  $\Phi$  the resulting porosity after thinning.

*Example:* If the present porosity is 0.2 and the initial porosity 0.4, the following thinning will result:

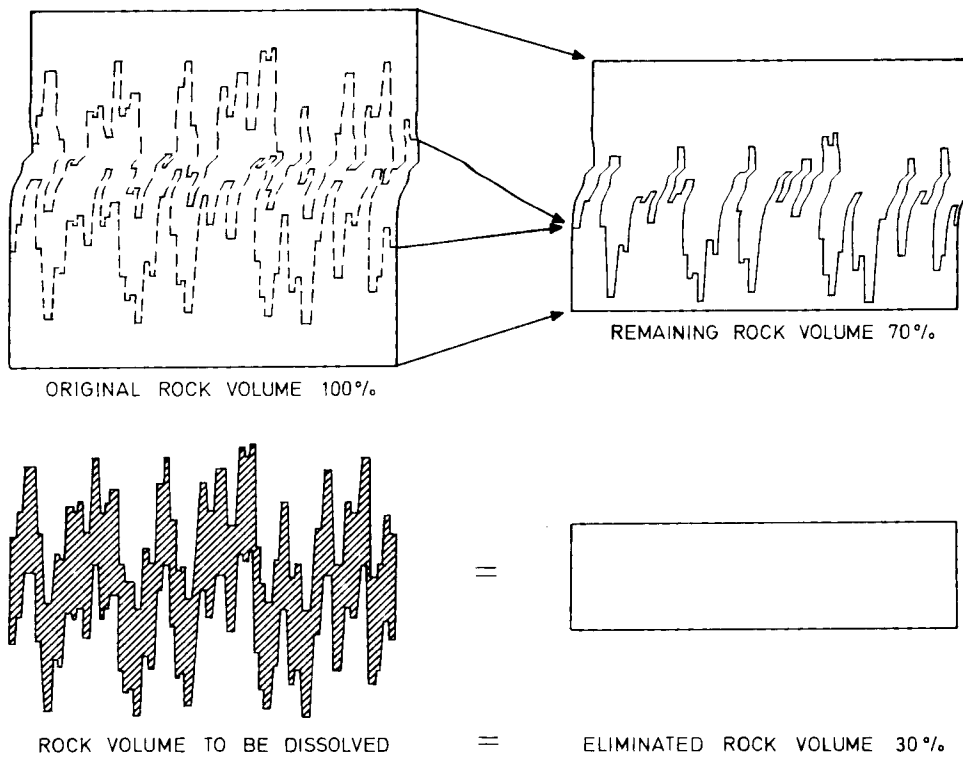
$$TH = \frac{.4 - .2}{1 - .2} = .25$$

From observations made on various rocks the dissolved material was transported and redeposited only short distances away from the site of its original dissolution, and in general, it was observed that the stylolite seams are best developed in high porosity areas, whereas redeposition is more common in areas of low porosity.

#### 1.4.1.2. Classification of stylolites

Stylolites turn out to be most easily described in terms of their relationship to the fabric of the host rock, and two main types are described by Park in this manner:

1. *Intergranular stylolites*; in which case the amplitude of the seam is smaller than the grain size in the host rock, and



1.27 – Schematization of rock volume changes due to stylolitization (Courtesy Dunnington<sup>12</sup>).

2. *Aggregate stylolites*; where a seam departs from the line of the bedding plane, and has an amplitude greater than the width of the individual columns making up the seam.

Two schemes are then used to classify stylolites: *geometrically* and *genetically*.

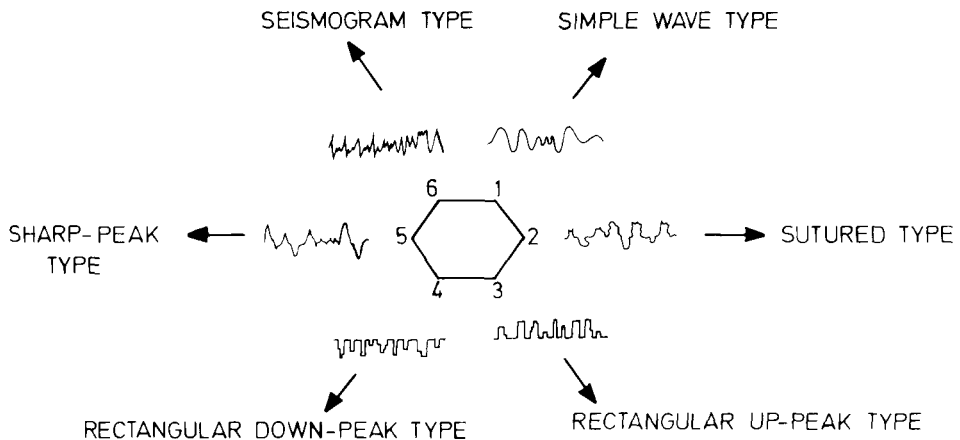
- a. *Geometric classification*: this includes two divisions:

1. stylolites described by means of their two dimensional geometry, and
2. stylolites described by means of the congruency of the stylolite seams to bedding (figures 1.28 and 1.29).

From figure 1.28 types 1, 5 and 6 are observed in  $.1\mu - 10\mu$  grain size; types 2, 3 and 4 are observed in bio-oospatic, and types 5 and 6 are described as highly inclined to vertical.

- b. *Genetic classification*: this again contains two divisions, depending on whether or not the stylolites were formed as diagenetic or tectonic features.

In the case of diagenesis, a further differentiation of early and late diagenesis is possible on the basis of detailed studies of the fabric changes within the host rock.

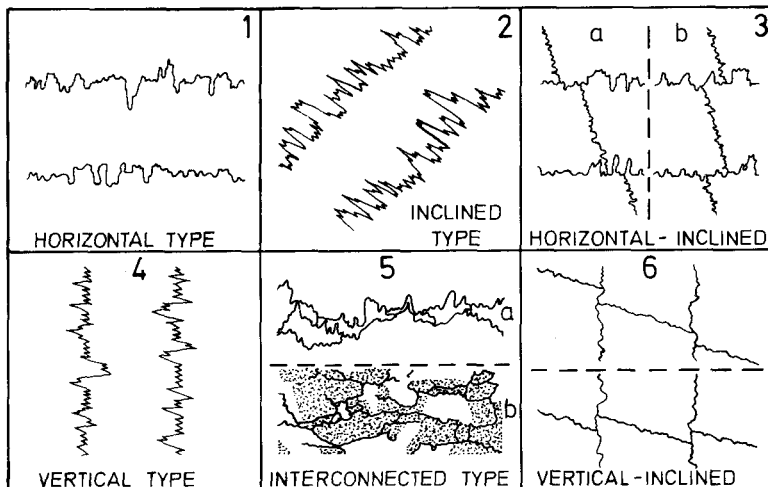


1.28 – Classification of stylolites based on stylolitic seam (Park<sup>15</sup>, Courtesy AAPG).

Diagenetic stylolites may include virtually all those described in figure 1.29; whereas tectonic stylolites may include types 4, 5 and 6 only.

#### 1.4.2. Development of stylolitization relative to the compaction and diagenetic history of limestone

As discussed, stylolitization is the only process other than erosion which introduces changes in volume and shape of limestone after an initial induration. Stylolites influence bulk volume, porosity, and even permeability.



1.29 – Classification of stylolites vs. bedding (Park<sup>15</sup>, Courtesy AAPG).

It was demonstrated<sup>1</sup> that stylolites tend to develop in hard rocks (mainly limestones) along a particular plane (often parallel to bedding), sometimes after the initial rock induration, and generally when the fluid (water) reaches a particular critical pressure (associated to dissolution pressure of reservoir rock). The simplified history of a sediment from deposition to stylolithification is schematized in figure 1.30 as a function of depth.

*Phase 1* – deposition of sediments represents very loose packing. Initially the grains are fluid supported, but closer packing develops with depth variation.

*Phase 2* – due to the continuously increasing overburden load, a tighter packing of grains takes place. Large amounts of water have been expelled, but sediments are still highly porous. Porosity is still 100% water unsaturated.

During the phase 1/phase 2 interval, the rock is submitted to *compaction*.

*Phase 3* – compaction continues, together with hardening, lithification and a slight cementation.

During the phase 2/phase 3 interval, the rock is submitted to *induration*, when the sediments are hardened and lithified.

*Phase 4* – pressure solution at grain to grain contact is reached and  $\text{CaCO}_3$  is dissolved. Water in the pore space moves from high pH zones to low pH zones. *Stylolitization* is completed by the removal of bulk volume and replacement by stylolites, such as microstylolites and megastylolites. Megastylolites often displace microstylolites during mechanical interdigitation.

*Phase 5* – cement is deposited in the area surrounding the stylolites, and *stylolithification* takes place. The material may be transported by diffusion and then precipitated; or if the material is insoluble it may become concentrated on the seam as the rock progressively dissolves.

#### General Observations:

The most formative pressure of stylolites is the weight of the overburden pressure when the sediments are located at approximately 2000–3000 feet deep.

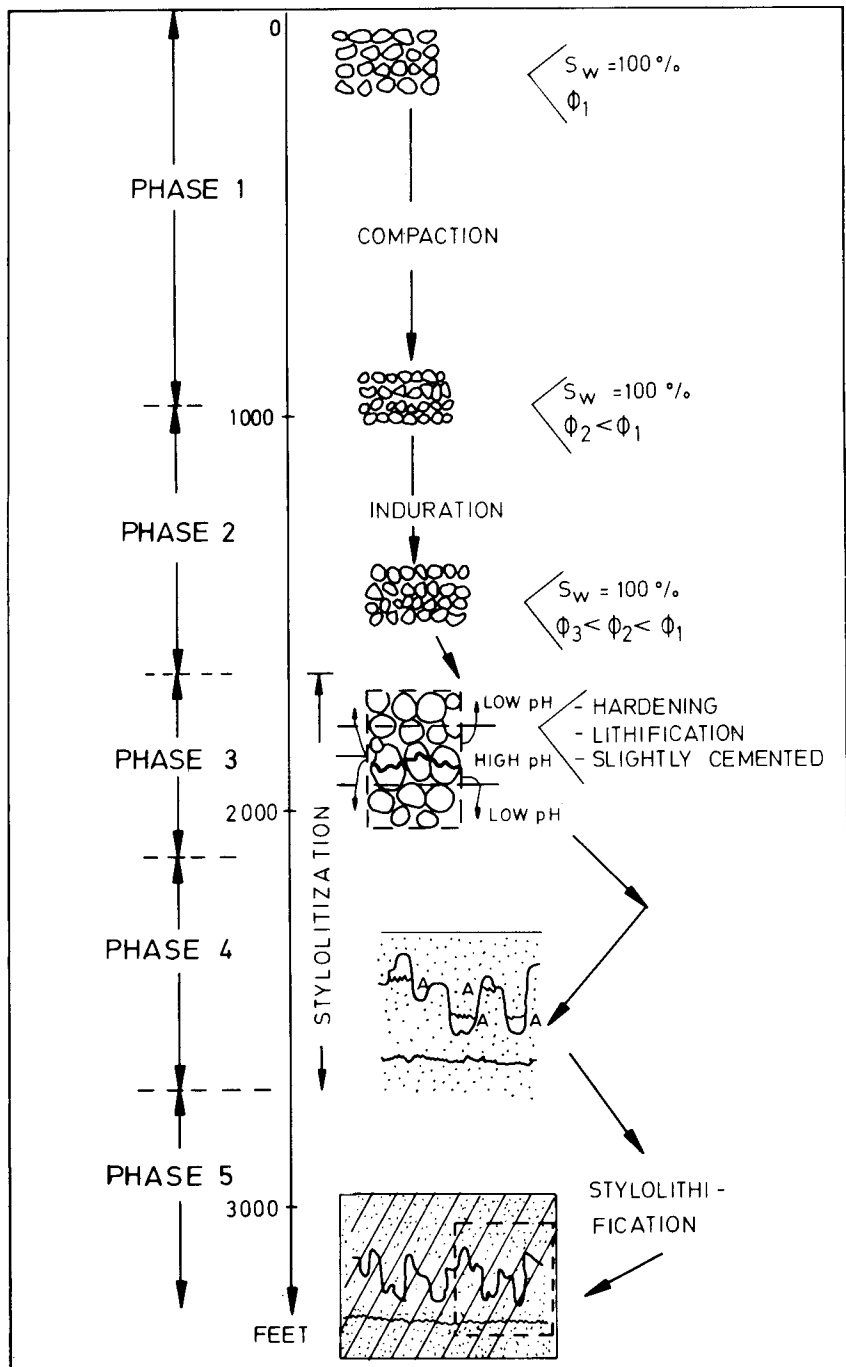
Water passing into and/or out of the system, as well as the water remaining in the rock after stylolite development, should have the same constituents in solution before and after stylolite formation.

The end of the stylolitization process is due to various conditions, but it is certain that in the absence of water (hydrocarbons substitute water), or in the case of complete cementation of the pore space by calcite, stylolitization ceases.

Slickolites are microfault (fault) surfaces where a solution-pressure-diffusion process has sculptured their surfaces. In general, slickolitic surfaces show displacements of millimeters, centimeters, and in extremely rare cases, layer dimensions.

#### Field example:

The presence of oil or gas in a stylolitic zone can be recognized if stylolitization is interrupted in the same reservoir without any additional changes. An interesting



1.30 – Schematization of stylolitization and stylolithification.

example is a chalky limestone anticline in the North Sea, where the lower part of the actual reservoir has an average density of 10–15 stylolites per foot, while the upper part has almost no stylolites at all. This anomaly of two different stylolitized zones may be the result of a migration in stages, which should show that during the stylolitization of the lower part of the reservoir, the upper part already contains oil in place, which inhibits the formation of stylolites.

The Dukhan field (Quatar peninsula) is formed by three overlying Jurassic reservoirs which contain stylolite networks. The initial development of stylolites is believed to have occurred shortly after oil began to accumulate in the structure and solution-pressure processes continued to operate when accumulation continued. This was evident in the lower part of the structure where stylolite density was highly developed, and their presence considerably reduced well productivity. The aquifer is virtually closed by the presence of stylolites in the entire transition water-oil zone.

The Bab Dome of Murban field in Abu Dhabi is formed by several superimposed reservoirs, among which the thickest is the B zone. The thickness of the reservoir varies from 170 feet at the crest, to 150 feet below the oil-water transition zone as a result of stylolitic thinning. This confirms the presence of single stylolites in the crestral zone and the role of the interpenetration of each seam, which increases with depth.

#### *1.4.3. Joints and their formation*

Joints are considered to be structural features, but their origin remains controversial. In general, the theories concerning their formation are associated to the observation and interpretation of the more obvious features, such as parallelism, angular relations between joint sets, and other structural features (folds and faults).

Joints are *systematic* when they occur in sets where the respective composing joints are parallel or sub-parallel. In addition, one joint set may intersect other joint sets<sup>16</sup>.

Joints can also be *non-systematic*, and in this case they are less oriented and more randomly distributed. Curvilinear patterns are the most representative of non-systematic joints.

The following list will help to distinguish systematic from non-systematic joints:

##### *Systematic Joints:*

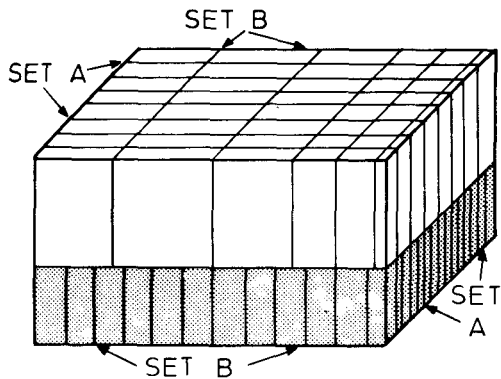
- occur as planar traces on surfaces
- occur as broadly curved surfaces
- occur on oriented surface structures

##### *Non-systematic Joints:*

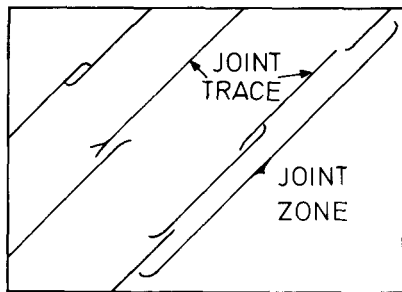
- meet but do not cross other joints
- are strongly curved in plan
- terminate at bedding surface

Joints are roughly *equidistant* and in thin-bedded rocks extend across many layers, but very few joints completely extend through very thick units.

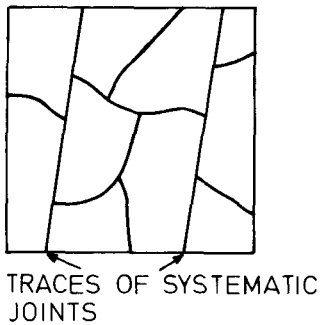
The main characteristic of joints is their *parallelism*, being grouped into sets where each joint is parallel or sub-parallel to the other.



1.31 – Variation of joint spacing vs. bed thickness (Hodgson<sup>3</sup>, Courtesy AAPG).



1.32 – Systematic joint pattern (Hodgson<sup>3</sup>, Courtesy AAPG).



1.33 – Non-systematic joint termination in systematic joint pattern.

A number of schematic relationships<sup>16</sup> between systematic and non-systematic joints are shown in figures 1.31 and 1.32. In figure 1.31 it is observed that for a thicker layer, the joints have a wider spacing than in a thinner layer. In figure 1.32 a plan view of systematic joint behaviour is illustrated, while in figure 1.33 the areal

view of a typical pattern of non-systematic joints and their termination against a systematic joint pattern is illustrated. In figure 1.33 a schematic block<sup>16</sup> shows the relationship between cross-joints and systematic joints, and cross-joints and the bedding surface. It is observed that cross-joints do not intersect systematic joints and terminate against large bedding. In general, these joints are more irregular, sinuous or rough than systematic joints.

#### Conclusions:

Both categories of joints, systematic and non-systematic, do not show any evidence of movement. The joint surface suggests that joints are fractures that began at a given point of the rock and propagated far into the rock mass. Experiments have been carried out on steel and glass, where the concentration of stress at the edges of such a small crack was observed. Propagation of the crack primarily depends on abnormal concentration of stress. It is also important in aggregates of discrete grains (similarly to the sedimentary rocks bonded by cement), that there are a large number of points within a rock unit where a fracture could start. It is also important that *fatigue fracture* and *cyclic stresses* help the formation of fractures and propagation in the rock material.

The regional joint pattern may be explained, not only by simple shear and tension, but also by other mechanisms as a result of fatigue and cyclic stresses.

### ***1.5. QUANTITATIVE EVALUATION OF FRACTURING***

In recent years there has been a greater tendency to further develop the quantitative evaluation procedure of fracturing; this includes fracture density or the basic physical parameters of fractures. Two studies have been retained; one concerning the relationship between folding on fracture parameters through a mathematical model (Murray<sup>17</sup>), and another concerning the evaluation of fracture density under certain conditions of reservoir and stress (Ramstad<sup>8</sup>).

#### ***1.5.1. Fractured reservoir productivity***

An analysis of reservoir productivity as a function of the fractured zone has been developed by Murray on the Devonian Sanish Pool of the Antelope field (North Dakota). The theoretical method developed tried to establish a relationship between fracturing, porosity and permeability associated to bed thickness and structural curvature.

##### ***1.5.1.1. Theoretical background***

If a bed with a thickness  $H$  is folded so that a curvature of radius  $R$  could be

determined, a series of stresses should develop in the formation. If a transverse section (figure 1.34) shows that the fractures developed as a result of structural folding, a fracture at each interval  $\Delta S$  will result, with its extension increasing with radius  $R$ . The result obtained per unit of section in the plane  $XOZ$  may be extended along the axis  $OY$ .

### a. Porosity

Porosity is the result of the pore volume divided by the bulk, which may be expressed by using the notations from figure 1.34.

The fracture pore volume is,

$$V_{pf} = \frac{[(R+H)\Delta\Theta - R\Delta\Theta] \times H}{2} = \frac{H^2\Delta\Theta}{2} \quad (1.15)$$

while the equivalent bulk is,

$$V_B = \frac{[(R+H)\Delta\Theta + R\Delta\Theta] \times H}{2} = \frac{2RH\Delta\Theta + H^2\Delta\Theta}{2} \quad (1.16)$$

the result will then be,

$$\Phi_f = \frac{V_{pf}}{V_B} = \frac{H}{2R+H}$$

Since the curvature radius  $R$  is always considerably larger than pay  $H$ , ( $R \gg H$ ), it results that

$$\Phi_f \approx \frac{H}{2R} \quad (1.17)$$

If the curvature  $R$  is expressed as the reciprocal derivative of the structural curvature slope,

$$R = 1/(d^2z/dx^2) \quad (1.18)$$

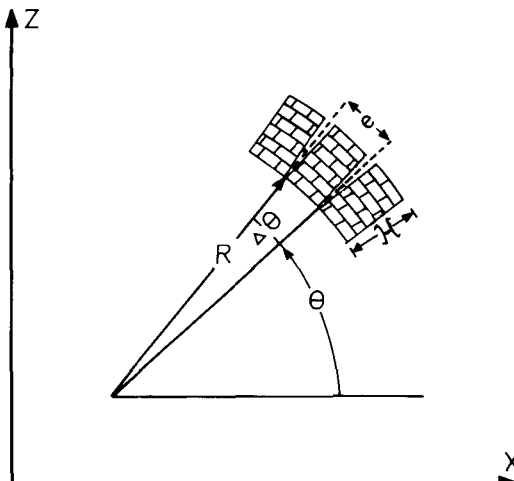
it is possible to write the porosity as,

$$\Phi_f = \frac{1}{2} H \left( \frac{d^2z}{dx^2} \right) \quad (1.19)$$

### b. Permeability

Permeability of fractures may be obtained by using the flow in a single fracture with a variable  $b$  opening, and the extension along the axis  $OY$  considered unitary,

$$q = b \times 1 \times \frac{b^2}{12} \frac{1}{\mu} \frac{dp}{dy} \quad (1.20)$$



1.34 – Simplified folding cross-section (Murray<sup>16</sup>, Courtesy AAPG).

The total rate for the entire pay varying from zero to H will be,

$$Q = \int_0^H q dH = -\frac{1}{12\mu} \frac{dp}{dy} \int_0^H b^3 dH$$

If  $b$  varies with the pay through a constant  $a$  the result will be ( $b=aH$ ), and so

$$Q = a \frac{a^3}{12\mu} \frac{dp}{dy} \int_0^H H^3 dH = \frac{a^3 H^4}{48\mu} \frac{dp}{dy} \quad (1.21)$$

and filtration velocity (for flowing section S),

$$V = \frac{Q}{S} = \frac{1}{S} \times \frac{a^3 H^4}{48\mu} \frac{dp}{dy} \quad (1.22)$$

Based on the relationship between  $H$ ,  $R$  and  $d^2z/dx^2$ , the permeability from equations 1.19 and 1.22 results as,

$$K_f = \frac{S^2}{48H^2} \left( H \times \frac{d^2z}{dx^2} \right)^3 = \frac{1}{48} e^2 \left( H \frac{d^2z}{dx^2} \right)^3 \quad (1.23)$$

which could be further reduced in dimensional parameters,

$$K_f \approx 2 \times 10^{11} [H(d^2z/dx^2)]^3 \times e^2 \quad (1.24)$$

where,  $K_f$ (md) and fracture interval  $e$  (feet).

c. Minimum fracturing stress.

The minimum stress necessary<sup>17</sup> to develop fractures is expressed by the relationship between principal stress  $\sigma_1$ , elasticity modulus  $E$ , pay  $H$ , and curvature  $R$ ,

$$\sigma_1 > E \left( H \frac{d^2z}{dx^2} \right) \quad (1.25)$$

where  $H d^2z/dx^2$  has the significance of a pseudo-curvature. A critical value of a limestone pseudo-curvature, above which fractures are developed, is estimated in the range of  $10^{-4}$ . Based on these empirical limits, fracturing may be expected at any time when the ratio  $1/E$  is greater than  $10^{-4}$ .

*Example:*

These calculations have been applied in Sanish Pool (figure 1.35) where the reservoir is formed by a dolomitic sandstone of  $\Phi = 5-6\%$  and  $K < lmD$ , while water saturation is very high. Well productivity appeared to be unrelated to the lithology variation, since the wells in the best developed sand were the poorest and vice-versa, the best wells were located in thin sands. It was evident that productivity was controlled by fracturing and verification was done by using the above methodology.

The reservoir cross-section A-B (figure 1.35) was represented at the top of the structure (figure 1.36).

The points showing main change in curvature are E, D and C (section 1, figure 1.36).

The dip magnitude is further shown in section 2 of figure 1.36, while the curvature in section 3 indicates the maximum values in section E and C.

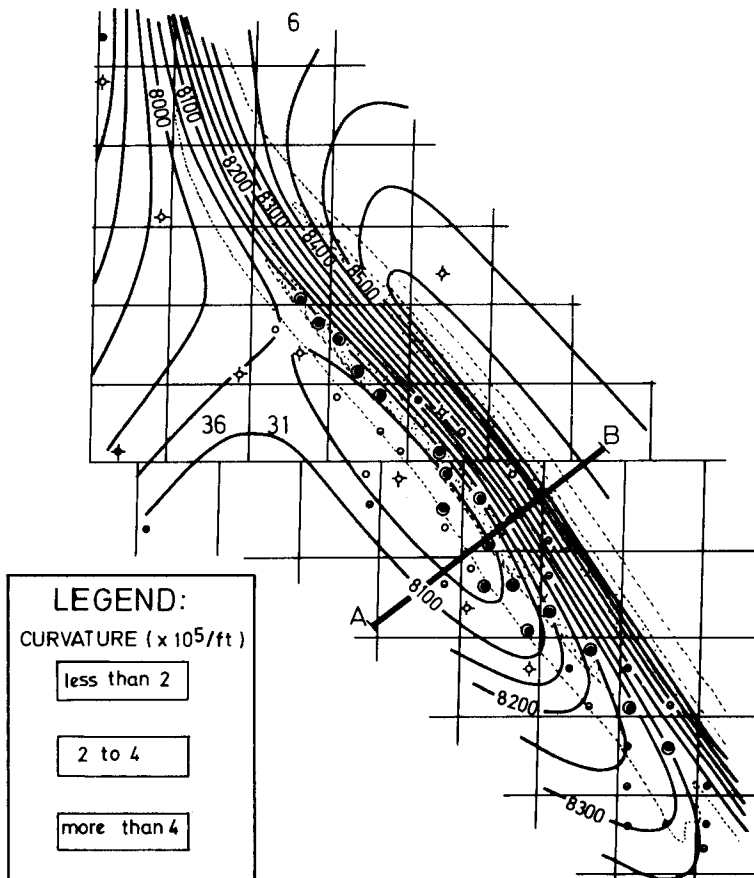
From the pay of approximately 20 feet and the average curvature of approximately  $5 \times 10^{-5}$  the result is,

$$\left( H \frac{d^2z}{dx^2} \right) = 20 \times 5 \times 10^{-5} \cong 10^{-3}$$

If the fracture interval is assumed  $e = 0.5$  foot the permeability becomes, from equation 1.24,

$$K(mD) = 2 \times 10^{11} \times 0.5 \times 10^{-9} = 50mD$$

This indicates that the conditions for fracturing were achieved mostly in the central part of zones E and C which are very fractured and probably the most productive. They correspond to the best well location for a high productivity. These zones have



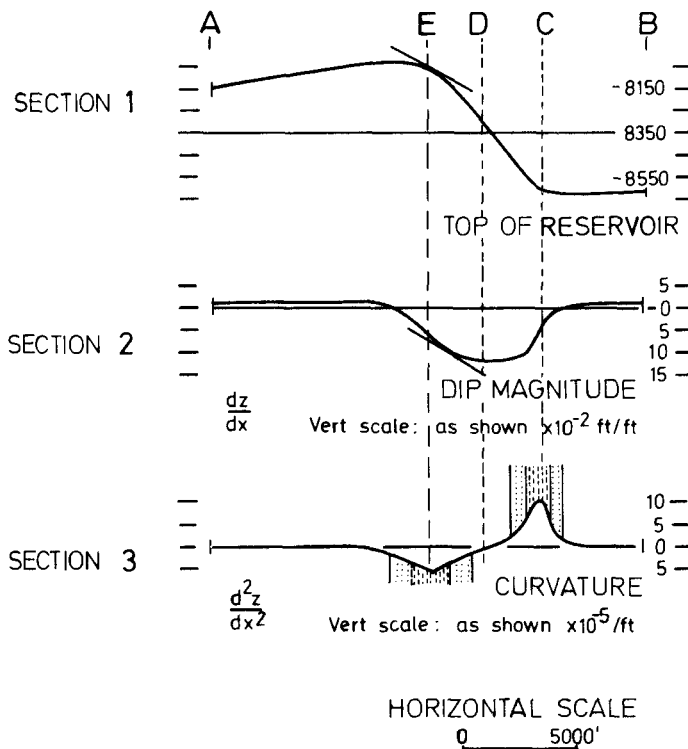
1.35 – Structural contour maps, Antelope Sanish Pool, North Dakota. Contour interval 50 ft. (Murray<sup>16</sup>, Courtesy AAPG).

been further verified in the field through well productivity tests, and it was confirmed that the highest productivity corresponded to the highest curvature sections.

### 1.5.2. Fracturing model of a large North Sea structure

A simulation of Danian limestone, in which deposition took place during the Cretaceous period in the North Sea reservoir, was made by using the Ramstad model<sup>18</sup>. It appeared that during its deposition and also at a later stage, the underlying salt dome was growing and, as observed in figure 1.37, the thickness in the center was very much reduced if compared with its original thickness which is actually on the flanks.

From a seismic survey the shape of the top of the reservoir is drawn as iso-

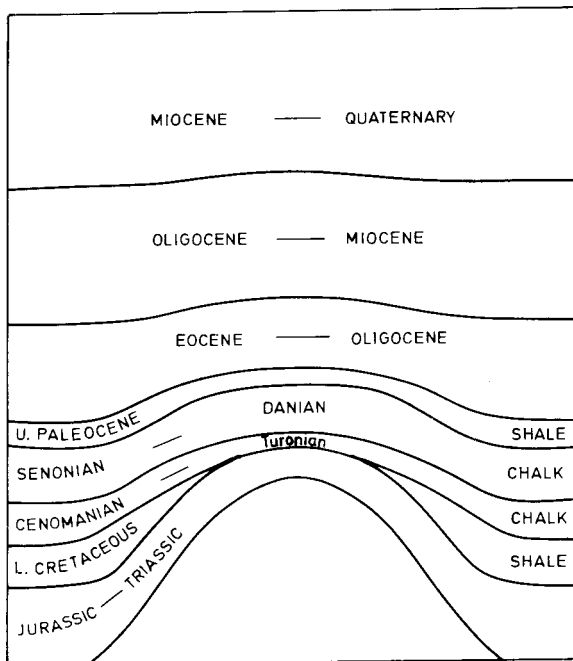


1.36 – Cross-section A-B. Section 1: Top of structure. Section 2: Dip magnitude. Section 3: Curvature (Murray<sup>16</sup>, courtesy AAPG).

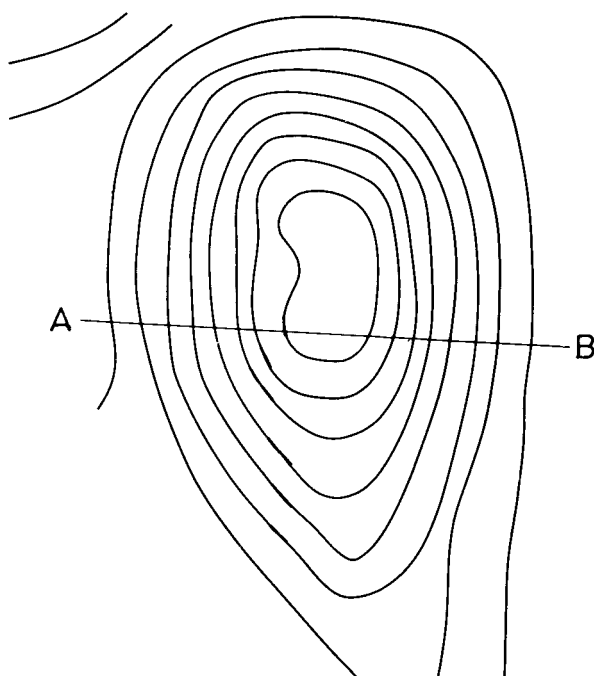
bathic lines (figure 1.38), which may be approximated to an elliptical shape. Cross-section A–B, along the shortest ellipsoid axes, has been examined first, and later additional cross-sections have integrated the results for an integrated volumetric distribution of fracturing.

The model (as represented in figure 1.39) is formed by the oil zone (2 layers) having a total pay of 300m, while the depth to the salt dome was assumed to be 2000m. Beneath the oil reservoir the rock was divided into two layers of 1000m each, while above the reservoir the overburden is formed by 3080m of pay up to the sea bottom. As boundary conditions, it was assumed that the vertical boundaries have a free movement in the vertical direction, but in the horizontal direction no movement was assumed. At the upper level of the model (sea bottom) movements are free in both directions, while at the lowest boundary (contact with the salt dome) free gliding against the salt layer was assumed.

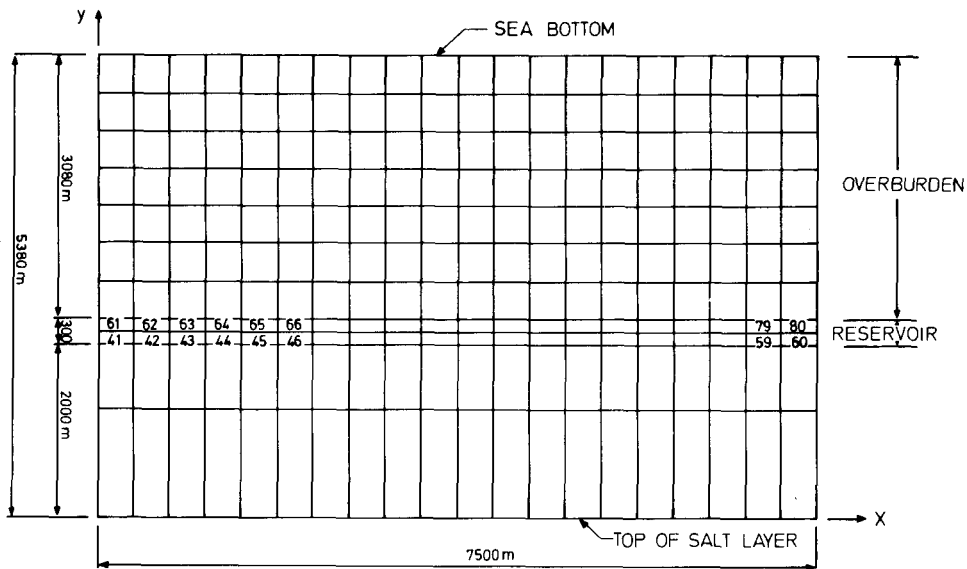
Since locating the absolute stresses is difficult, only relative stress distribution in the fracture was computed. For simplification purposes the initial reservoir shape is considered to be the same as the actual bottom reservoir shape. Only the first order



1.37 – North Sea structure folded by salt dome rising.



1.38 – Structural contour map.



1.39 – Finite element mesh for cross-section A-B.

terms of the strain-displacement equation  $\varepsilon_x = du/dx$  have been included in the study, while the second order terms

$$\frac{1}{2} \left[ \left( \frac{dv}{dx} \right)^2 + \left( \frac{du}{dy} \right)^2 \right]$$

were neglected.

A relative arbitrary elasticity module has been used in order to create fractures for a specific displacement. The upper layer material was considered to have a module ten times higher than that of the overlying layer. As Poisson's ratio, 0,25 was used for the elasto-visco-plastic calculation and 0,35 for plastic effects.

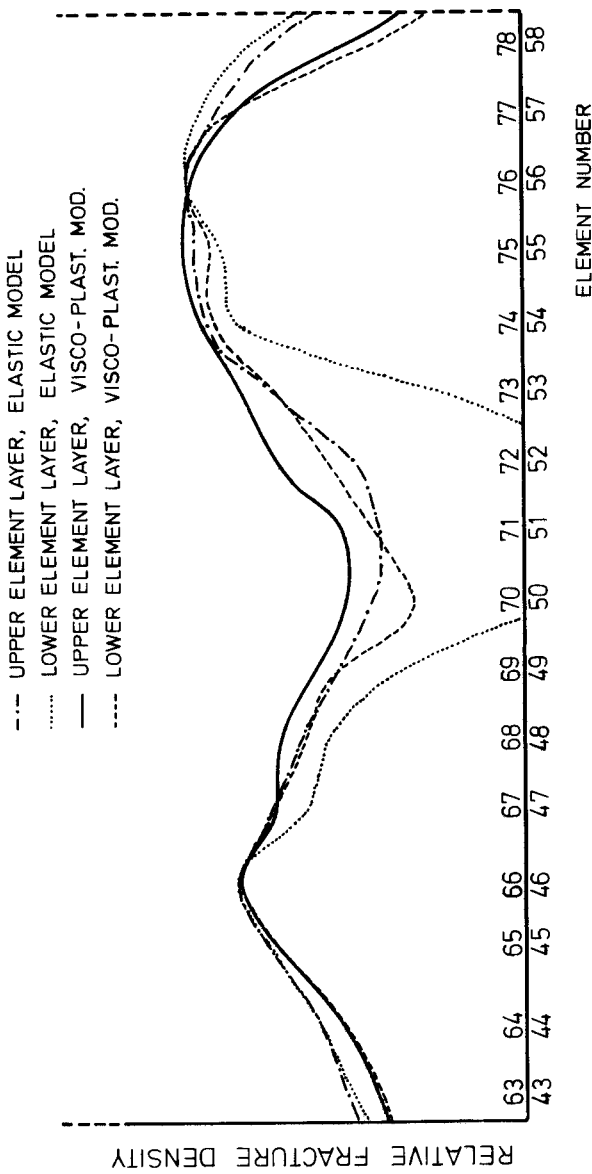
Other input parameters are porosity 30% and rock density 2,650 gr/cm<sup>3</sup>.

#### *Results obtained:*

*Comparison between elastic and elasto-plastic model.* The results obtained have been presented as the *relative fracture density* for different elements in the reservoir which correspond to the reciprocal value of the total displacement of fracturing. The results are, in the last analysis, a probabilistic result since this indicates only a degree of probability to develop fractures in the respective element, which may be assumed as proportional to the *relative fracture density*.

The results are very similar for both elastic and visco-plastic models, with the

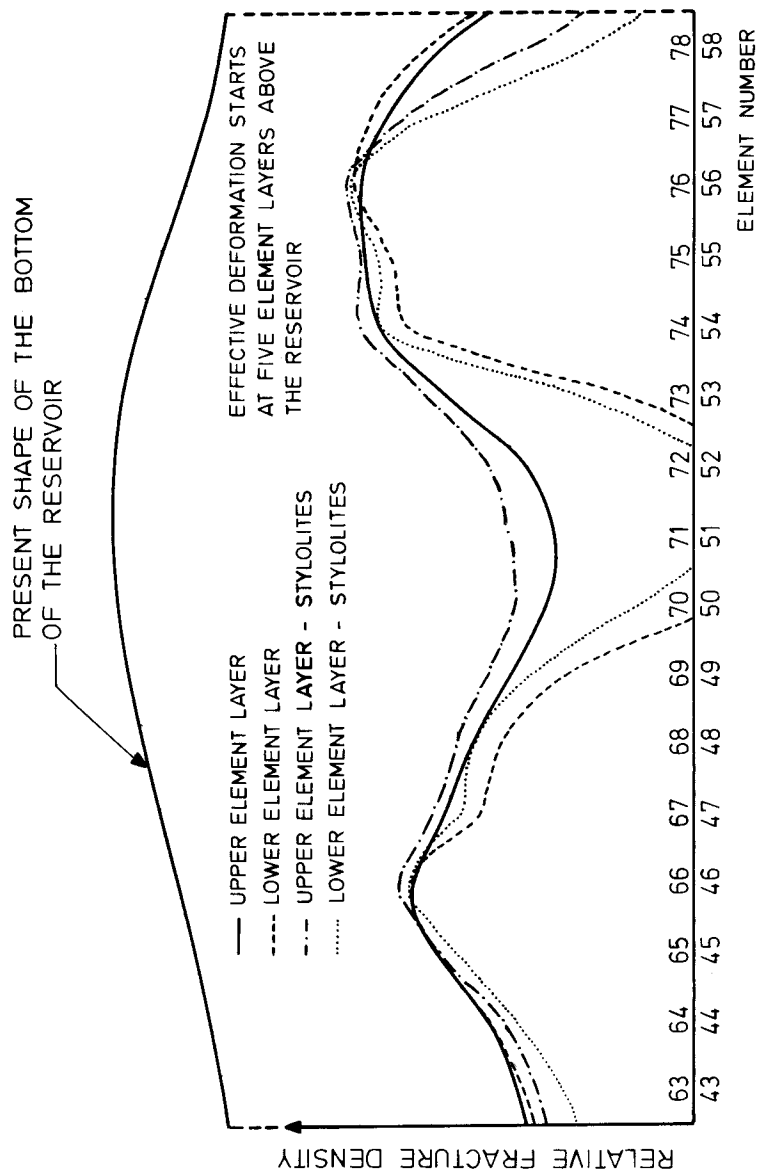
PRESENT SHAPE OF THE BOTTOM  
OF THE RESERVOIR



1.40 – Relative fracture density. Comparison between linear-elastic and elasto-visco-plastic case.

exception of the lower layer, which deviates in the central zone (figure 1.40). This is due to a redistribution of stresses in the visco-plastic analysis as a result of fracturing, and consequently, in a higher stress zone in the central part of the structure.

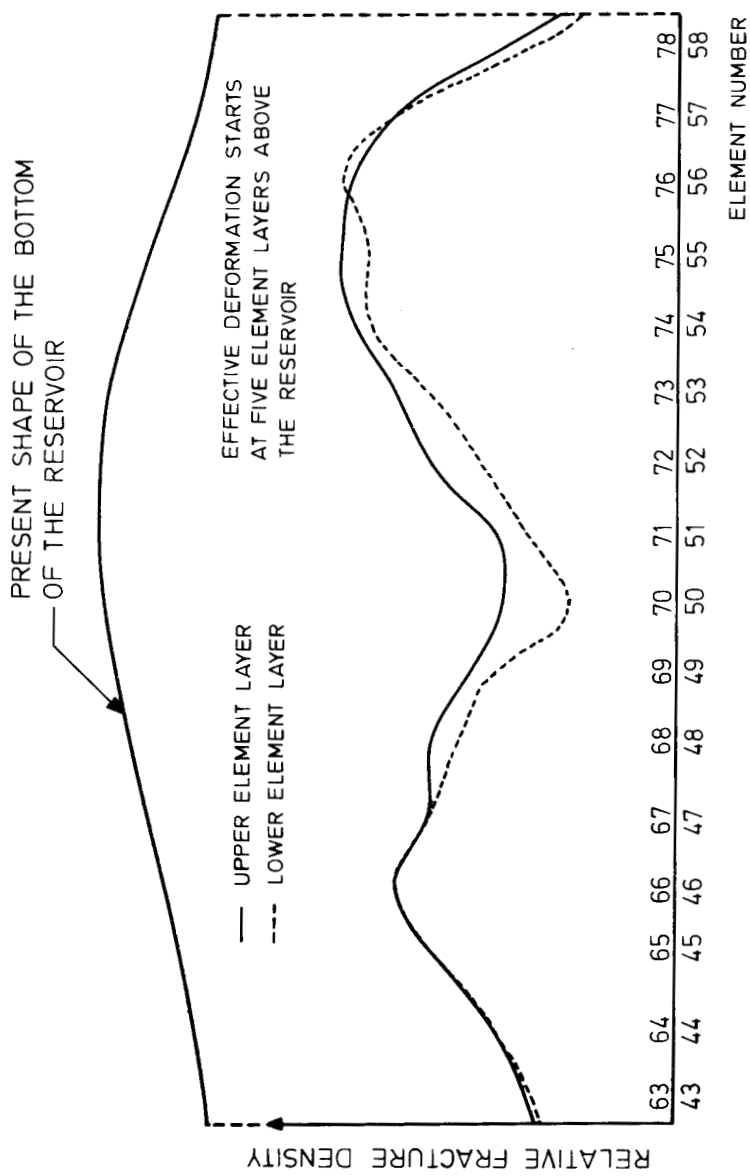
*Simulations of stylolites;* Since the effective stresses influence rock strains, the value of pore pressure must be accurately considered. In general, for a fully drained deformation, pore pressure remains independent of deformations. In the case of stylolitiza-



1.41 – Relative fracture density in the presence of stylolites.

tion the hypothesis was that through stylolitization a network of impermeable surfaces will be generated in the reservoir where the pore fluid is trapped. The undrained pore fluid, in this case, will increase its pressure with deformation, expressed by a relation,

$$\Delta P = \frac{C_f}{\Phi} \varepsilon_v$$



1.42 – Result of best matching (elasto-visco-plastic model).

where  $\Delta P$  is the pressure increment,  $C_f$  the compressibility of the fluid,  $\Phi$  the porosity, and  $\epsilon_v$  the volumetric strain.

The effect of stylolites is shown in figure 1.41. However, although the effect is not very important, in the presence of stylolites (as a result of the undrained pore fluid) in both upper and lower layers, an increasing relative fracture density results in the central zone and a decreasing effect in the flanks. These results were found to be similar with the results from wells drilled in the center and flanks of this structure.

*Fracturing hypothesis for model matching;* Since the relative fracture density in the cross-section is controlled by a number of wells drilled on the structure, various hypotheses should be elaborated relative to the geological history of the reservoir. As in figure 1.42 two basic variables have been examined:

- the height of underlying layers (HUL)
- salt dome rise after deposition of the overlying layer (SDR).

The cases examined included HUL – 500m; 1000m; 2000m; and SDR – 400m; 800m; 1100m (respectively, first, second and third layers).

The best match of fracturing distribution was obtained in the case presented in figure 1.42. The examination of a number of cross-sections obtained after a limited number of wells were drilled gives a better understanding of the overall fracture distribution of the reservoir, which later can help to optimize the location of the undrilled wells.

## SYMBOLS

### Latin Letters:

a	— connectivity matrix
$a_i$	— relationship between nodal displacement vector of the element and of the whole model
B	— matrix relating strain on nodal displacement
D	— elasticity modulus
K	— assembly stiffness matrix
M	— vector defined equation 1.12
R	— assembly load vector
r	— assembly displacement factor
P	— pore pressure
S	— total axis stress
T	— transpose of a matrix
TH	— percentage of thinning
V	— volume of a body

### Greek letters:

$\epsilon$	— vector of strain component
$\epsilon_{vp}$	— vector of visco-plastic component
$\Gamma$	— matrix indicating relationship between visco-plastic strain rate and stresses
$\psi$	— internal friction angle
$\Phi, \Phi_i$	— porosity and initial porosity
$\sigma$	— vector of stress components (equation 1.10)
$\sigma^e$	— vector of effective stress components
$\sigma^h$	— vector of pore fluid pressure components
$\tau$	— shear stress
$\tau_0$	— shear stress for normal stress «zero».

## Subscripts

- 1, 2 — reference number  
vp — visco-plastic

## REFERENCES

1. McQuillan, H., 1973. Small-scale fracture density in Asmari Formation of southwest Iran and its relation to bed thickness and structural setting. Am. Assoc. Petroleum Geologists. Bull., V 45, No. 1, p 1–38.
2. Stearns, D.W. and Friedman, M., 1972. Reservoirs in fractured rock in stratigraphic oil and gas fields classification, exploration methods and case histories. Am. Assoc. Petroleum Geologists. Mem. 16, p 82–106.
3. Hodgson, R.A., 1961. Regional study of jointing of Comb Ridge-Navajo Mountain area, Arizona and Utah. Am. Assoc. Petroleum Geologists. Bull., V 45, No. 1, p 1–38.
4. Price, N.J., 1966. Fault and joint development in brittle and semi-brittle rock. London, Pergamon Press, 176 pp.
5. Cook, A.C. and Johnson, K.R., 1970. Early joint formation in sediments. Geol. Mag., V 107, No. 4, p 361–368.
6. Harris, J.F., Taylor, G.L. and Walper, J.H., 1960. Relation of deformation fractures in sedimentary rock to regional and local structure. Am. Assoc. Petroleum Geologists. Bull., V 44, No. 12, p 1853–1873.
7. King Hubert, M. and Willis, D.G., 1972. Mechanics of hydraulic fracturing. Am. Assoc. Petroleum Geologist. Reprinting series, 21.
8. Ramstad, L.R., 1977. Geological modelling of fractured hydrocarbon reservoirs. Univ. of Trondheim, report No. 77-4.
9. Mogi, K., 1971. Fracture and flow of rocks under high triaxial compression. Journal of Geophysics. Res., V 76, No. 5, pp 1255–1296.
10. Handin, J.W., 1966. Strength and ductility. Sec. 11 in Handbook of physical constants. Geol. Soc. America. Mem. 97, p 223–289.  
Handin et al, 1963. Experimental deformation of sedimentary rocks under confining pressure. Am. Assoc. Petroleum Geologists. Bull., V 47, p 717–75.
- Handin, and Hager, R.V., 1957. Experimental deformation of sedimentary rocks under confining pressure tests at room temperature on dry sample. Am. Assoc. Petroleum Geologists. Bull., V 41, p 1–50.
11. Quiblier, 1971. Contribution à la prévision de la fissuration en zone faiblement tectonisée. Thesis presented at Univ. of Paris.
12. Dunnington, H.V., 1967. Aspects of diagenesis and shape change in stylolitic limestone reservoirs. Proc. VII World Petr. Congr., Mexico, 2, Panel Discussion, No. 3.
13. Wagner, G., 1913. Stylolithen und drucksuturen. Geol. Paleontol. Abhandl, N.F. 11 (15), 1–30.
14. Stockdale, P.B., 1922. Styolites: Their nature and origin. Indiana Univ. Studies. 9, 55, 1–97.
15. Park, W.C. and Schott, E.H., 1968. Stylolitization in carbonate rocks. Recent developments in carbonate sedimentology in Central Europe. Springer.
16. Murray, G.H., 1977. Quantitative fracture study, Sanish Pool. Fracture-controlled production, AAPG Reprint Series 21.
17. Van Golf-Racht, T.D. and Ramstad, L.J. Modelling North Sea fractured limestone reservoir. Offshore North Sea proceedings, 1976, Stavanger, Norway.

# CHAPTER 2

## FRACTURE DETECTION AND EVALUATION

Fracture detection and evaluation is accomplished during the various operations in both the exploration and production phases of oilfield development. Methods and techniques include operations such as drilling, logging, coring and testing.

In this chapter the basic parameters of a single fracture and group of fractures are defined in detail. These include the opening, size, nature and orientation of a single fracture, and distribution, density and intensity of multi-fractures. Particular attention is given to the evaluation of the matrix block unit.

The best quantitative information concerning fracture parameters is obtained by direct measurement on *outcrops* (if available) and on *cores* obtained during drilling operations. The procedures of evaluation are discussed and the data processing is examined through various types of representations: statistic (histograms and stereograms), geometric representations (stereograms, schematic models) etc. Some examples illustrate the procedures discussed.

The above procedures, if used correctly, may help in the description of fractured reservoirs through local correlations which can be further extrapolated throughout the entire reservoir.

### *2.1. CLASSIFICATION AND DEFINITIONS*

The basic definitions of a natural fracture have been given in chapter 1, however, variations in fracture characteristics provide a basis for more detailed descriptions and classification.

#### *2.1.1. Classification based on descriptive criteria*

##### *2.1.1.1. Natural fracture vs. induced fracture*

A natural fracture is any break or crack occurring in the rock, including those cracks which can be identified by the presence of slickensides and mineralization. On the other hand, induced fractures are all those cracks which result during coring (such as breaks along the bedding plane) or from mishandling of cores.

The classification of fractures based on their appearance and morphology has been elaborated by Stearns<sup>1</sup> through the following categories:

- a. *Unequivocal natural fractures*; those which are partially filled or totally filled by vein material and also those which are opened and lie on a parallel trend to partially or totally filled fractures.
- b. *Very probable natural fractures*; fractures with slickensided surfaces and also those parallel to them.
- c. *Probable natural fractures*; fractures with clean, fresh surfaces accompanied by small fractures which are parallel to the unequivocal fractures.
- d. *Induced fractures*; generally recognized as fresh, clean fractures parallel or normal to the core axis as a result of bending or twisting of the core during coring.

#### 2.1.1.2. Measurable and non-measurable fractures

Measurable fractures are visible fractures which may be defined by width, length, orientation (dip and strike angle), while non-measurable fractures are only traces across the core which end within the core. Any reference to fracture density or intensity, etc., should refer to the visible natural fracture which indicates a certain dip angle and direction.

In addition, there are broken cores with fractures which are not measurable either because they are too dense and irregular or because there is no criterion of evaluation. There are two types of such fractures and they are denominated *breccia* and *rubble*. Breccia is formed by acute angled pieces of similar sized pseudo-prismatic matrix blocks which fit together, often forming hundreds of mini blocks per foot. In general, *breccia* is considered to be any fractured rocks which have over 50 fractures/foot. The other type of fractured rock denominated *rubble* represents an irregular broken core where the individual pieces do not fit together and no criteria exist to evaluate the fracture density.

#### 2.1.1.3. Macrofractures and microfractures

The difference between these two categories mainly concerns the dimensions of the fractures. In general, *macrofracture* corresponds to a fracture with a large width (over 100 microns) and considerable length, while *microfracture* applies to a fracture of limited length and width (sometimes microfractures form a continuous network which is hydrodynamically very similar to a porous medium). In the literature it is often possible to come across terms such as, macrofractures = fractures while microfractures = fissures.

The division of the same categories of fractures may be interpreted differently when referring to a genetic criterion. In this case, macrofractures may refer to large or cavernous openings resulting from dissolution-erosion (karst), whereas microfractures with dimensions below 100 microns will develop in response to structural and tectonic events.

#### 2.1.1.4. Open and closed fractures

Based on direct examination, there are two categories of fractures – *open* fractures and *closed* fractures; these depend mainly on circulating water and precipitation, which is capable of plugging the fractures with anhydrite, minerals, etc. On the other hand, fractures which are closed in surface conditions may often be open or partially open in reservoir conditions where pore pressure acts on fracture walls.

#### 2.1.2. Classification of fractures based on geological criteria

As discussed in chapter 1, the geological history of a reservoir is directly related to the fracturing process. Since the major role in generating fractures is played by tectonic events and the geological environment (lithology) as already discussed in chap. 1, any classification of fractures has to take these criteria into consideration.

##### 2.1.2.1. Fractures associated with folding

In general, fractures are related to the *folding axis*<sup>3</sup> (figure 2.1) and therefore are denominated:

- a. *longitudinal fractures* – along the folding axis
- b. *transversal fractures* – perpendicular to the folding axis
- c. *diagonal fractures* – in relation with the folding axis

##### 2.1.2.2. Fractures and the stress state

If fractures are associated to one or more states of stress they are divided into two groups:

- a. *conjugate fractures*
- b. *non-conjugate* (orthogonal) fractures

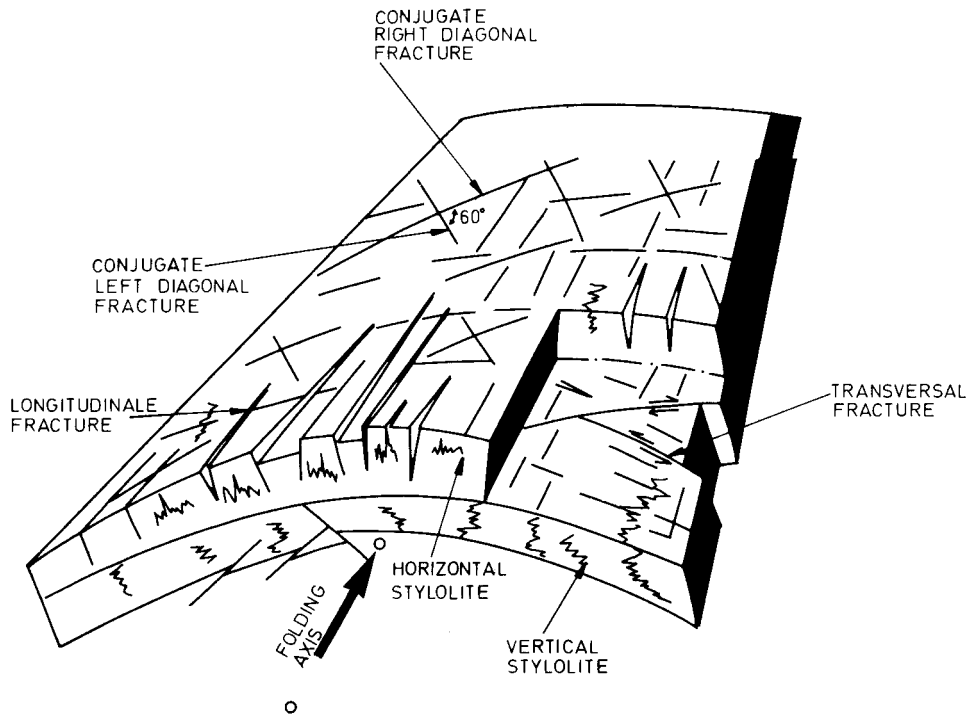
where conjugate fractures are those which have been developed from a unique state of stress (figure 2.1).

The totality of the fractures could be associated with their direction and therefore:

- a. The *fracture system* is formed by all fractures having the same mutually parallel direction.
- b. the *fracture network* is the result of various fracture systems.

##### 2.1.2.3. Fractures associated with stratigraphy

The variations of dimensions and density of fractures depend on lithology and thickness of the layer in which the fractures are developed. The results obtained will divide the fractures into two categories:



2.1 – Various types of fractures generated by folding (courtesy of Leroy<sup>2</sup>).

- a. *first-order* fractures
- b. *second-order* fractures

*First-order* fractures are those which cut through several layers of rock, while *second-order* fractures are limited to a single layer of rock.

## 2.2. BASIC PARAMETERS OF FRACTURES

### 2.2.1. General discussion

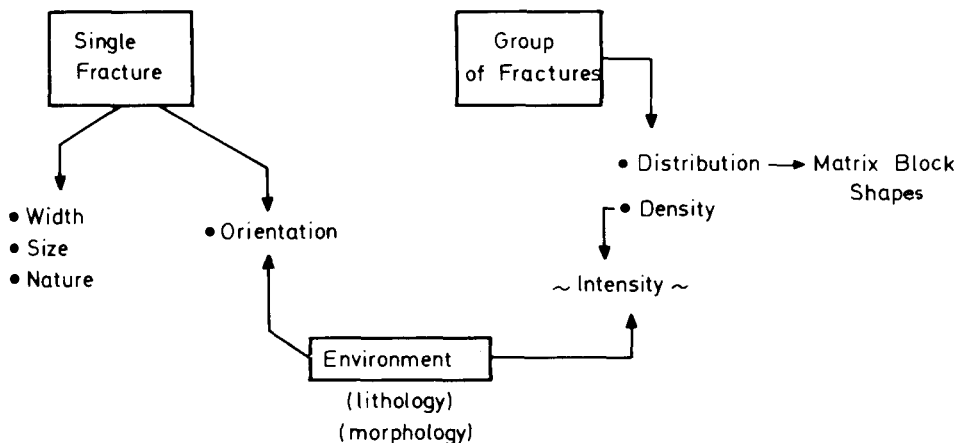
The variations in space of fracture characteristics, such as size, orientation and description, are so irregular and complicated that the description of such a reservoir is substantially more difficult than that of a conventional reservoir. Therefore, the study of a fractured reservoir must follow a special pattern, beginning with the examination of local basic characteristics of single fractures, only afterwards continuing with the examination of a multifracture system. In establishing the relationship among the various groups of fractures, the local relationships are examined at reservoir scale by comparison, trends and extrapolation of parameters.

Single fracture parameters refer to the *intrinsic* characteristics, such as *opening*

(width), size and nature of fracture. If the single fracture is associated with the reservoir environment, another essential characteristic, the fracture orientation, will result.

The multi-fracture parameters refer to the fracture arrangement (geometry) which further generates the bulk unit, called the *matrix block*. The number of fractures and their orientation are directly related to fracture distribution and density. When fracture density is related to lithology, another parameter of particular interest, called fracture intensity, is obtained.

The basic parameters and their relationships are illustrated below:

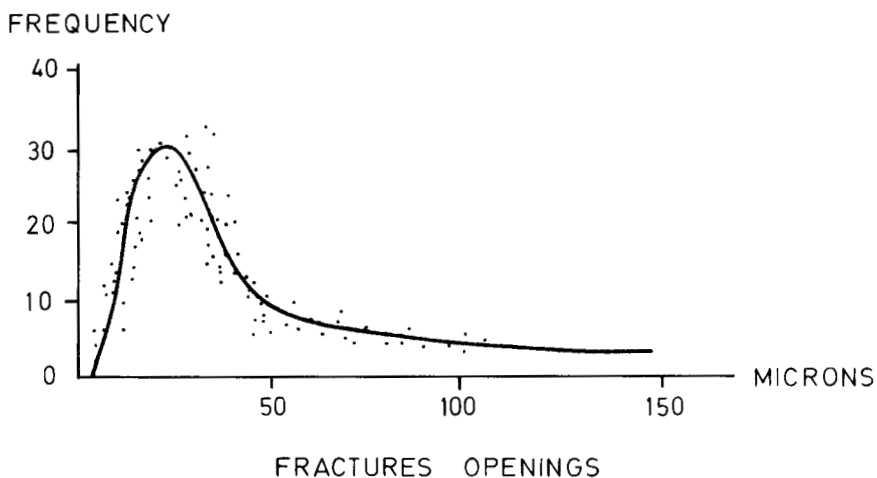


## 2.2.2. Single fracture parameters

### 2.2.2.1. Fracture opening

Fracture *opening* or fracture *width* is represented by the distance between the fracture walls. The width of the opening may depend (in reservoir conditions) on depth, pore pressure and type of rock. The fracture width varies between 10–200 microns, but statistics have shown that the most frequent range is between 10–40 microns (figure 2.2).

The fracture opening depends on the lithological-petrographic characteristics of the rock, nature of stresses and reservoir environment. Often the difference between the width of the fracture in reservoir conditions and surface conditions (laboratory) is the result of the release of confining and pore pressure on the sample in laboratory conditions. In reservoir conditions where the confined pressure  $\sigma$  (overburden pressure) remains constant, but the initial pore pressure  $P_i$  is reduced (during reservoir depletion) to  $P_f$ , the width  $b$  will become smaller (figure 2.3), as effect of rock expansion.

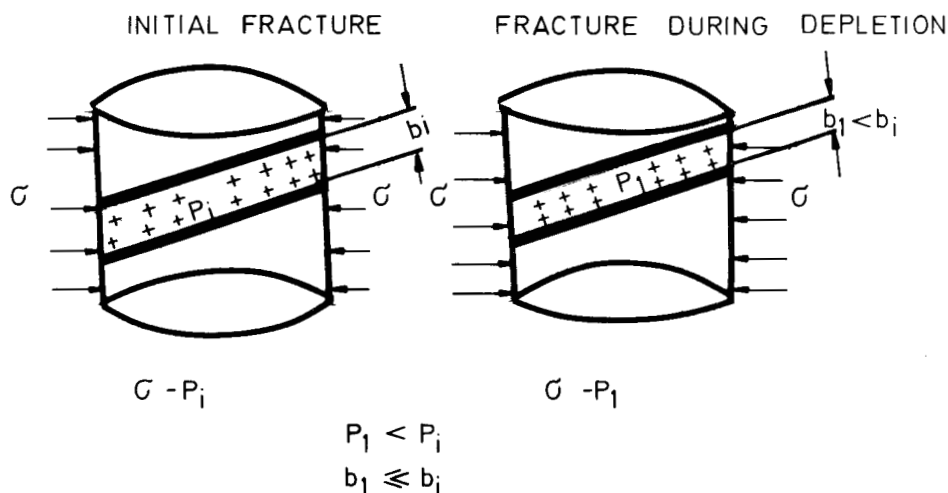


2.2 – Statistical frequency curve of opening width

#### 2.2.2.2. Fracture size

Fracture size refers to the relationship between fracture length and layer thickness, especially if a qualitative evaluation is to be formulated. In this case fractures can be evaluated as minor, average and major<sup>3</sup>:

- a. *minor* fractures have a length less than the single layer pay
- b. *average* fractures traverse more layers
- c. *major* fractures have a very large extension, often tens or even hundreds of meters.



2.3 – Reduction of fracture width as an effect of reservoir pressure depletion

Minor fractures are equivalent to the previously defined second-order fractures, while average and major fractures are equivalent to first-order fractures.

According to Rhuland's<sup>3</sup> observations, minor fractures generally have smaller openings and are often filled, while major fractures have large openings and are rarely mineralized or filled.

#### 2.2.2.3. Nature of fracture

The nature of fractures mainly concerns the state of fractures under observation with reference to opening, filling and wall characteristics, and is generally discussed in the following terms:

- a. opening – open, joint, closed
- b. filling – mineral, various minerals
- c. closed by – homogeneous or diffused filling material
- d. fracture walls – rugose, smooth, polished, creeping

#### 2.2.2.4. Fracture orientation

Fracture orientation is the parameter which connects the single fracture to the environment. The fracturing plane can be defined (as in classic geological practice<sup>4</sup>) by two angles, dip azimuth  $\delta$  and dip angle  $\omega$  (figure 2.4).

The orientation of the plane can also be determined vectorially by the three directions corresponding to the angles  $2_1$ ,  $2_2$ ,  $2_3$  between  $x_1$ ,  $x_2$  and  $x_3$  and the unit vector. The directions  $x_1$ ,  $x_2$  and  $x_3$  are oriented towards east, north and zenith, therefore:

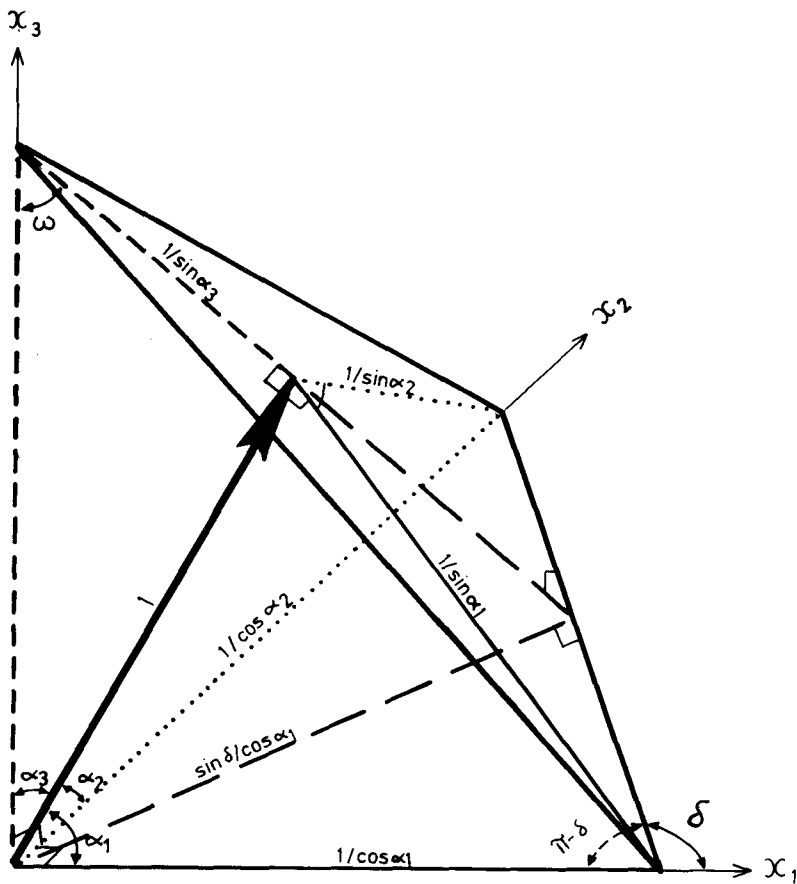
$$\begin{aligned}\cos \alpha_1 &= \sin \delta \times \cos \omega \\ \cos \alpha_2 &= -\cos \delta \times \cos \omega \\ \cos \alpha_3 &= \sin \omega\end{aligned}\tag{2.1}$$

From comparison of the orientation of the various single fractures it follows that all parallel fractures belong to a *fracture system*. If more intercommunicating fracture systems are recognized in a reservoir, those systems will form the fractured reservoir *network*.

### 2.2.3. Multi-fracture parameters

#### 2.2.3.1. Fracture distribution

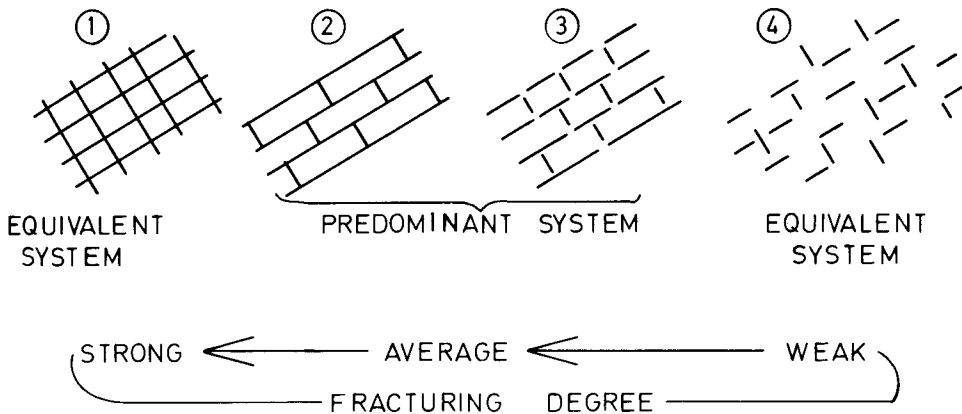
In a fracture network which contains two or more fracture systems, each fracture system will generally be generated by a certain state of stress. Pairs of conjugate fractures which have been generated by the same stress state are an exception (see chapter 1). Fracture distribution is then expressed by a



2.4 – Fracture oriented in a cartesian coordinate system ( $\delta$ -azimuth angle,  $\omega$ -dip angle)

degree of fracturing factor. This factor will be *stronger* if there is continuous intercommunication among the fracture systems and if the systems are equivalent to each other. The degree of fracturing will be weaker if the intercommunication among the fracture systems is interrupted and if the fracturing of one system prevails over the other.

As an example<sup>3</sup> two orthogonal fracture systems are shown in figure 2.5. In case 1 the fracture densities of the two systems are equivalent and are continuously intercommunicating. This corresponds to a strong degree of fracturing. The interrupted fracture network in case 4 corresponds to a weak degree of fracturing. In cases 2 and 3 where one of the two systems is predominant and the other partially interrupted, the degree of fracturing is qualified as average.



2.5 – Various combinations of orthogonal fracture systems and the qualitative evaluation of the degree of fracturing (Ruhland<sup>3</sup>)

#### 2.2.3.2. Matrix block unit (trapped bulk)

The fractures which cut the reservoir rock in various directions, delineate a bulk unit referred to as the *matrix block unit* or simply the *matrix block*. Since around any single block a *continuum* (formed by the fracture network) exists, each single block will be hydrodynamically separated from the adjacent blocks. It is thus correct to consider that each bulk unit is, in fact, *trapped* inside the fracture network. In reality these blocks are in contact through leaning points, but the hydrodynamic communication between blocks remains practically interrupted.

The matrix blocks are defined by shape, volume and height, in relation to the fracture system's dip, strike and distribution. The shape of the matrix block is irregular, but for practical work the block units are reduced to simplified geometrical volumes, such as cubes or as elongated or flat parallelepipeds.

Various block shapes have been described by Ruhland<sup>3</sup> through simplified geometrical models as shown in table 2.2., where a qualitative description of shape can be attached to the basic dimensions of each block.

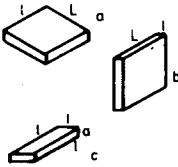
The spatial aspect of a block unit may be further associated with tectonic events and the predominance of one or another of the stresses. In reference to the models shown in table 2.2., it may be stated that:

- a. column block unit (case 1 and 2) – the principal stress parallel with the bedding generated higher fracture density
- b. flat block unit (case 4 and 5) – the principal stress normal to the bedding generated a higher fracture density
- c. cube block unit (case 3) – orthogonal equivalent stresses took place

If, in addition, the orientation of the fracture is known, an improved understanding of structural-tectonic events may become possible.

Table 2.1.

Matrix block unit description

Case	BLOCK SHAPE	RATIO $\frac{L}{c} \frac{l}{c} \frac{l}{l}$	SCALE		
			100cm	100 - 10cm	10cm
1		$a < \frac{1}{5} \quad 1$ $b = \frac{1}{5} \quad 1 \quad \frac{1}{5}$	COLUMN	SMALL COLUMN	PENCIL MATCHES
2		$\frac{1}{5} \text{ to } \frac{1}{2} \quad 1$	BIG BLOCK PARALLELIPIPED	AVERAGE BLOCK PARALLELIPIPED	SMALL BLOCK PARALLELIPIPED
3		1	METRIC CUBE	DECIMETRIC CUBE	CENTIMETRIC CUBE
4		$2 \text{ to } 5 \quad 1$	SLAB	AVERAGE SLAB	SMALL SLAB
5		$a > 5 \quad 1$	PLATE	AVERAGE PLATE	SMALL PLATE
		$b \quad 1 \quad \frac{1}{5} > 5$		AVERAGE PLATE	PLATELET
		$c > 5 \quad \frac{5}{2} \quad 2$	BOARD	AVERAGE BOARD	RULER

### 2.2.3.3. Fracture density

Fracture density expresses the degree of rock fracturing through various relative ratios. If the ratio refers to the bulk volume the fracture density is called *volumetric fracture density*. If the ratio refers to the area or to a length the fracture density is called *areal or linear fracture density*. The analytical expressions of these densities are as follows:

Volumetric fracture density; the ratio between fracture-bulk surface S and matrix bulk volume:

$$V_{fD} = \frac{S}{V_B} \quad (2.2)$$

Areal fracture density; the ratio between the cumulative length of the fractures  $l_t = \sum_i^n l_i = n_f x l$  and matrix (bulk area  $S_B$  in a cross flow section,

$$A_{fD} = \frac{n_f x l}{S_B} = \frac{l_t}{S_B} \quad (2.3)$$

Linear fracture density; the ratio between the number (n) of fractures intersecting a straight line (normal on flowing direction) and the length of the straight line:

$$L_{fD} = \frac{n_f}{L_B} \quad (2.4)$$

The linear fracture density is also called fracturing rate, fracture frequency or linear frequency.

OBSERVATION: All three fracture densities are expressed by a reciprocal length. The volumetric density is a static parameter (similar to the porosity), while the areal and linear densities are associated to direction of fluid flow.

#### a. Fracture interval

*Fracture interval* is a parameter often used in substitution of linear density. This parameter represents the length of the matrix between two consecutive fractures and, thus, the reciprocal value of the linear density is,

$$e = 1/L_{fD} \quad (2.5)$$

Often this value is expressed as an average value  $\bar{e}$  between the  $L_{fd}$  max and  $L_{fd}$  min.

#### b. Fracture density of a cube

If a matrix block has the shape of a cube of length  $a$  so that the fluid flows parallel to the horizontal faces (figure 2.6), the results will be as follows:

Volumetric fracture density:

- contact fracture surface – matrix ( $a^2$ )
- total surface – matrix ( $6a^2$ )
- bulk volume – matrix ( $a^3$ )

$$V_{fD} = \frac{6a^2}{a^3} = \frac{6}{a} \quad (2.6)$$

Areal fracture density:

Since the flow is horizontal the fluid will be in contact with two fractures of length  $a$ ,

$$n \times l = 2a$$

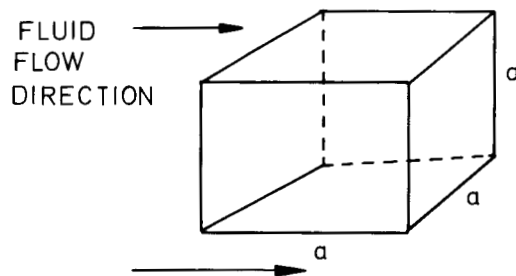
The cross section area is  $a^2$ , therefore,

$$A_{fD} = \frac{n \times l}{s} = \frac{2a}{a^2} = \frac{2}{a} \quad (2.7)$$

Linear fracture density:

- On a vertical line normal to the horizontal direction of flow, only two fractures will intersect the vertical line and, therefore, the matrix length between the two fractures is  $a$ ,

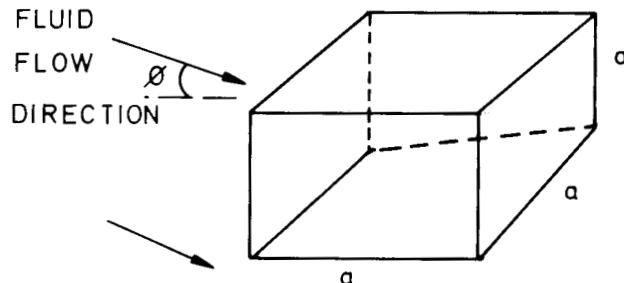
$$L_{fD} = \frac{n_f}{L_B} = \frac{2}{a} \quad (2.8)$$



2.6 – Horizontal flow around a cubic matrix block unit

- If in a cubic matrix block the flow direction forms the angle  $\theta$  with the base of the cube (figure 2.7), only the areal and linear densities will need to be corrected with angle  $\theta$ ,

$$\begin{aligned} V_{fD} &= \frac{6a^2}{a^3} = \frac{6}{a} \\ A_{fD} &= \frac{2a \cos\theta}{a^2} = \frac{2}{a} \times \cos\theta \\ L_{fD} &= \frac{2}{a \cos\theta} \end{aligned} \quad (2.9)$$



2.7 – Flow around a cubic matrix block unit (angle  $\alpha$  between flow direction and cube base)

c. Fracture density of a fracture system.

If the reference plane  $ox$  direction forms an angle  $\theta$  with the number  $n$  of fracture systems (where all fractures are parallel), then,

the areal density is,

$$A_{fD} = \frac{\cos\theta \sum_i^n l}{S} \quad (2.10)$$

· and the linear density is,

$$L_{fD} = \frac{n}{\cos\theta \times l} \quad (2.11)$$

d. Fracture density of a fracture network.

If there are  $m$  fracture systems inside the fracture network, and if each forms an angle  $\theta$  with the flow (reference) plane, the density parameters will result as the summation of system densities:

· volumetric fracture density,

$$V_{fD} = \sum_i^m \frac{A_{fD,i}}{\cos\theta_i} \quad (2.12)$$

· areal fracture density,

$$A_{fD} = \sum_i^m (L_{fD,i} \times \cos\theta_i) \quad (2.13)$$

· which will reduce the volumetric density to,

$$V_{fD} = \sum_i^m L_{fD,i} \quad (2.14)$$

If, among the fractures examined, it is difficult to identify systems of fractures, a random distribution of fractures should be considered where the basic relationship refers to all single fractures<sup>4</sup>. In this case, the areal fracture density will be,

$$(A_{fD})_j = (V_{fD})_j \cos\theta_j \quad (2.15)$$

Between the two parameters, volumetric and areal fracture density, the following relationship will result,

$$A_{fD} = \frac{2}{\pi} V_{fD} \quad (2.16)$$

e. Fracture density vs. lithology (example)

In the outcrops of Yuzhno-Minusiuskaya (Devonian) sediments in the USSR, the fracture density vs. rock lithology was recorded as listed below<sup>3</sup>:

Table 2.2.

Rock lithology	Fracture density 1/m
Medium-grained sandstone	9.0
Fine-grained sandstone	50.0
Glauconitic sandstone	19.5
Calcareous sandstone	9.5
Flaggy bedded limestone	30.0
Algal limestone	33.0
Massive limestone	12.3
Medium-grained limestone	12.0
Fine-grained limestone	27.0
Thick-bedded limestone	24.0
Argillaceous siltstone	60.0
Argillite	56.0
Volcanic rock	48.0
Thin-bedded marl	20.0
Massive porphyrite	36.4
Conglomerate	44.0

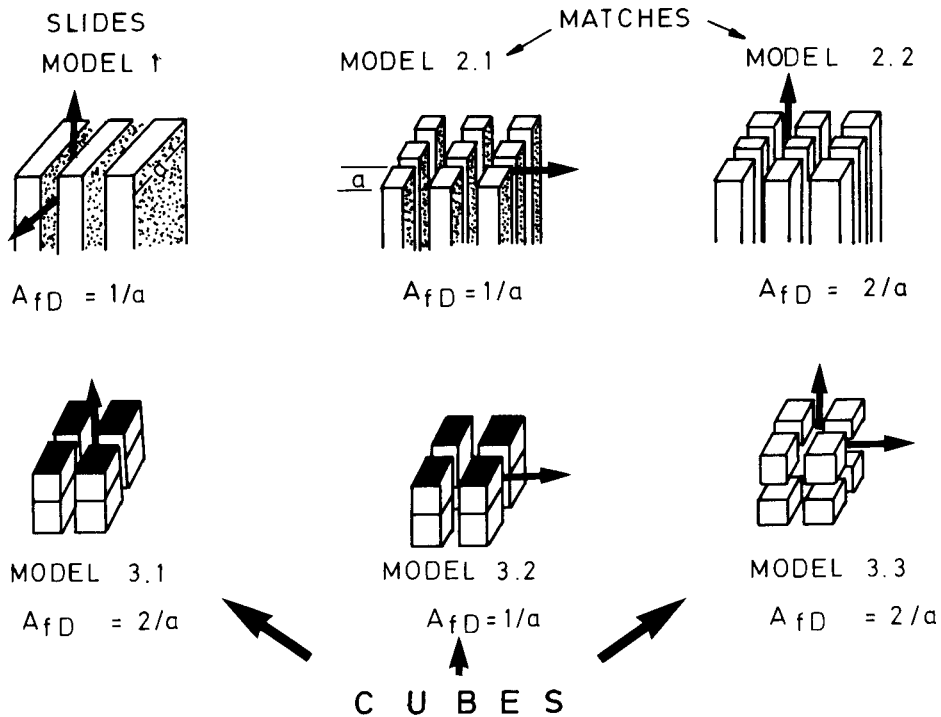
f. Fracture density vs. idealized model

If various matrix block units are grouped into certain geometrical distributions, a number of idealized fractured networks can be obtained. If the models are as shown in figure 2.8 (Reiss<sup>4</sup>), the volumetric, areal and linear densities are modified according to the flow direction and to the impermeability of the block faces.

As observed, model 1 *slides* have only one fracturing plane independent of the flow direction. The blocks which are match-shaped (model 2) have a fracture density associated to the flowing direction, horizontal or vertical. The cubes (model 3) have, according to impermeable horizontal planes (case 3.1 and 3.2), different fracture densities if the flow is towards a vertical or horizontal direction, or if the cubes are completely permeable on all faces (model 3.3).

#### 2.2.3.4. Fracture intensity

If a quantitative analysis of fractures has to be carried out it is necessary to associate the fractures with the lithology, pay and tectonic mechanisms of the layers which contributed to the formation of the fractures. In order to make the tectonic examina-



2.8 – Idealized models and fracture density expressed as a function of flowing direction (Reiss<sup>5</sup>)

tion of this problem possible, it is necessary to weight the fracture parameters with the thickness and lithology. Since areal and linear fracture densities and cumulative frequencies are used for the same layers or for similar layers, it is necessary to use another parameter, labeled by Ruhland<sup>3</sup> as *fracture intensity*, if the pay is very much contrasted.

This parameter may define the role played by the intrinsic characteristics of each layer (permeability, porosity, cementation, etc.) during the fracturing process, by the thickness of the layer and by its structural location (top, center, or bottom of the structure).

According to Ruhland, this parameter expresses the ratio between fracture frequency (FF) and layer thickness frequency (THF),

$$FINT = \frac{\text{fracture frequency}}{\text{thickness frequency}} = \frac{FF}{THF} \quad (2.17)$$

If there exists only one layer of pay  $L_B$ , the intensity is practically similar to the linear fracture density (equation 2.4):

$$L_{fD} = \frac{n_f}{L_B}$$

Fracture intensity may be applied either to open or closed fractures, and under specific conditions to the totality of the fractures, therefore:

$$\begin{aligned} \text{total fracture intensity } FINT_f &= FF_t/THF_t \\ \text{open fracture intensity } FINT_o &= FF_o/THF_o \\ \text{closed fracture intensity } FINT_c &= FF_c/THF_c \end{aligned} \quad (2.18)$$

If the two parameters FF and THF are plotted on a log-log diagram (figure 2.9), where the point of the same fracturing intensity is on a straight line of slope 1, the increase and decrease of FINT along such a line correlates the proportionality between vertical fracture frequency and pay.

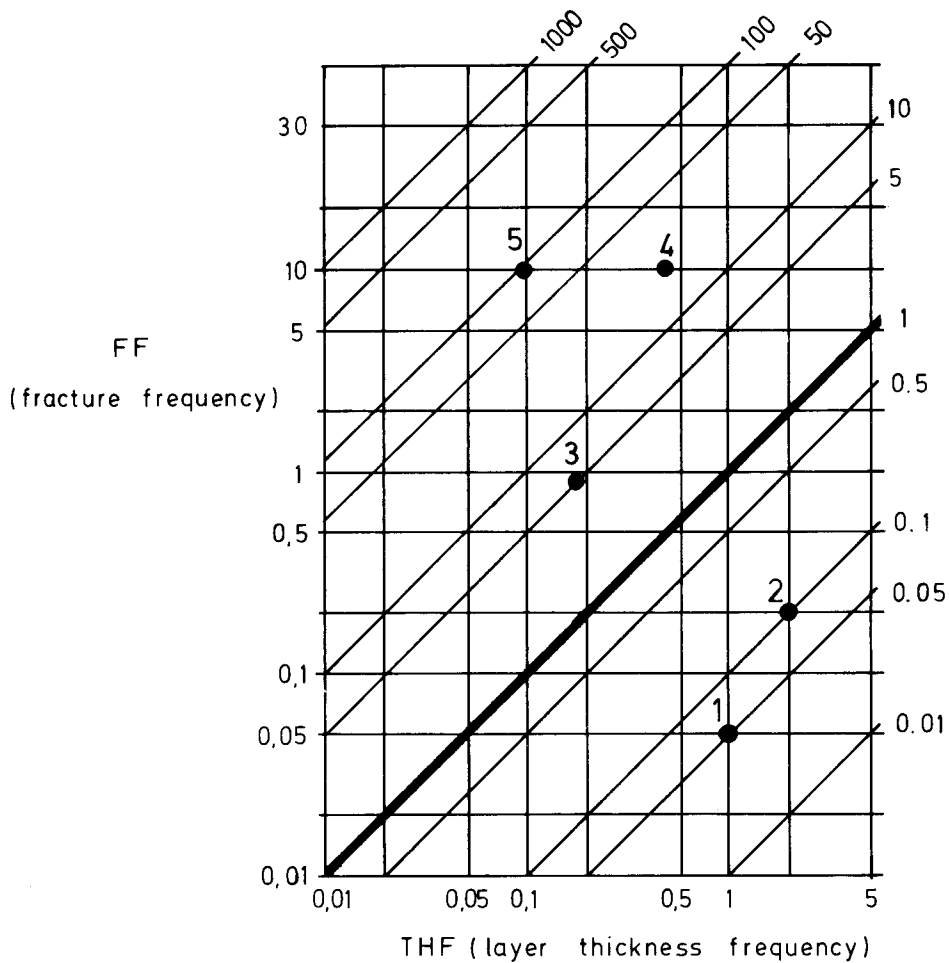
As mentioned by Ruhland<sup>3</sup>, the fracture intensity parameter generally varies between 0.01 and 100. The magnitude of FINT is significant because there is a possibility of qualitative evaluation of the fracturing process as shown below:

	category
If $FINT \geq 0.05$	1
If $FINT \sim 0.1$	2
If $FINT = 5$ to $10$	3
If $FINT = 20$ to $50$	4
If $FINT \geq 100$	5

The category of fractures from 1 to 5 are presented in figure 2.9 as examples of various ratios of two frequency parameters, FF and THF.

### 2.3. DIRECT EVALUATION OF FRACTURING

The detection and evaluation of fractures is the result of information<sup>6</sup> obtained during various phases of field work, such as exploration, drilling, logging, coring and testing. Some of these results represent *direct information*, such as observations on outcrops during the exploration phase, core examination in the laboratory, and the use of a televiwer in the well during logging operations. The other category, *indirect information*<sup>5</sup>, is obtained during various operations, such as drilling, testing, logging, etc.



2.9 – Fracture intensity diagram (Ruhland<sup>3</sup>) for estimation of fracturing process (cases 1, 2, 3, 4 and 5 discussed in section 2.2.3.4)

Direct evaluation (on site or in the laboratory) on outcrops and on cores is mainly oriented towards the determination of the basic characteristics of single fractures, such as width, orientation, length, etc. In addition, the group of fractures is examined in order to evaluate their communicability, geometry and distribution, and eventually their density and intensity.

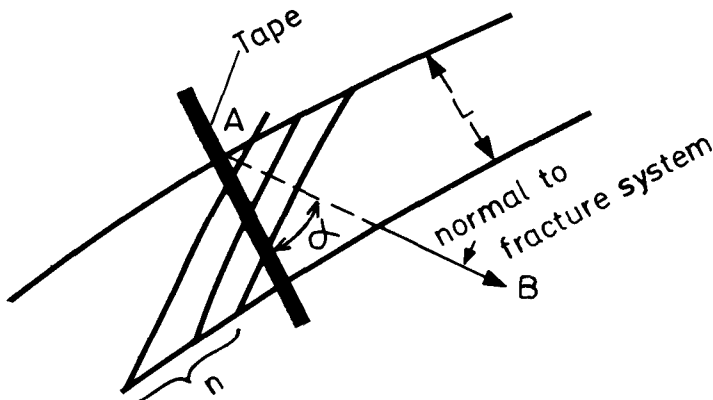
### 2.3.1. Outcrop fractures

Studying fractures in outcrops involves the collection of various information, such as the relative position of layers, the orientation of fracture systems, the number of

fractures in each system, the lithological data, the fracture morphology, etc., which, in a transect over an area under study is best obtained by setting up a number of conventionally positioned observation stations.

The easiest method of measuring fractures is to mark an outcrop with a tape in any convenient direction, independent of the orientation of the fracture system. Based on the orientation of the fracture system and measuring of the azimuth, it is possible to calculate the angle between the tape line and the plane normal to the fracture (AB). The fracture density  $L_{FD}$  will result from the number of fractures  $n_f$  which intersect the straight line AB (figure 2.10). The length along the line AB will be corrected to the tape direction through the angle  $\alpha$ . The linear fracture density in this case is,

$$L_{FD} = \frac{n_f}{L/\cos\alpha} \quad (2.19)$$

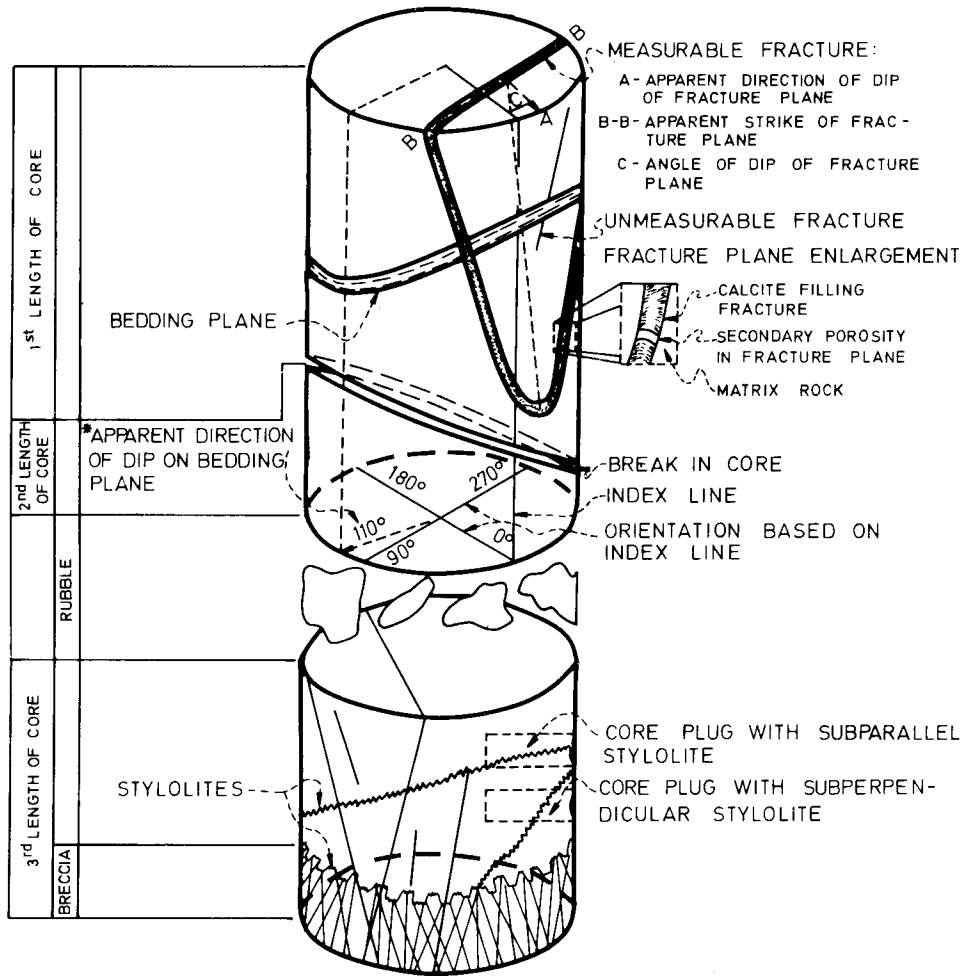


2.10 – Evaluation of fracture density in an outcrop

In order to normalize different fracture systems it may be preferable to rotate the strike of the beddings to a common strike, which is the *reference strike*. It is important to gather the data from more stations in order to recognize the fracture patterns which tend to group around the dip and strike of the anticline. If the beds at most of the stations dip more than 5°, they must be rotated to a horizontal plane in order to unitize the observations.

### 2.3.2. Fracture evaluation through core examination

From core examination maximum information is expected, such as width, dip and strike for measurable fractures, and filling material in unmeasurable fractures. A composite core is shown in Fig. 2.11.



\*TRUE DIRECTION OF DIP ON BEDDING PLAN FROM DIPMET IS 200°

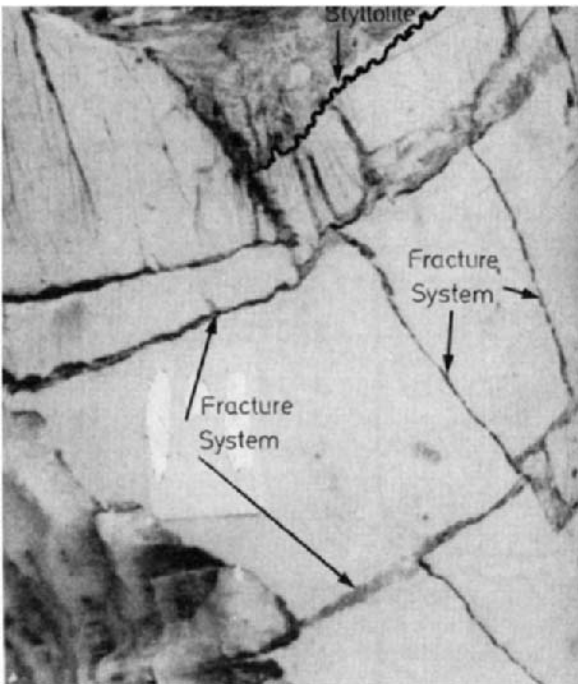
### 2.11 – Composite core of a fractured reservoir

Orientation of the core can be obtained by scribe lines on cores which form an angle of 110° with the oriented zero line (figure 2.11).

With a core it is important to evaluate the bedding plane and its dip in order to avoid confusion between the real bedding plane and any apparent breakage plane in the core.

If a highly fractured material is found (rubble, breccia), it is necessary to estimate the percentage of fractures with reference to core length (Fig. 2.11).

The type of fracture (unequivocal or probable) is established through visual examination. According to figure 2.12 the fractures are parallel and filled with migrated oil. The fractures can be open and then filled with oil (figure 2.12), closed



2.12 – Picture of a fractured core

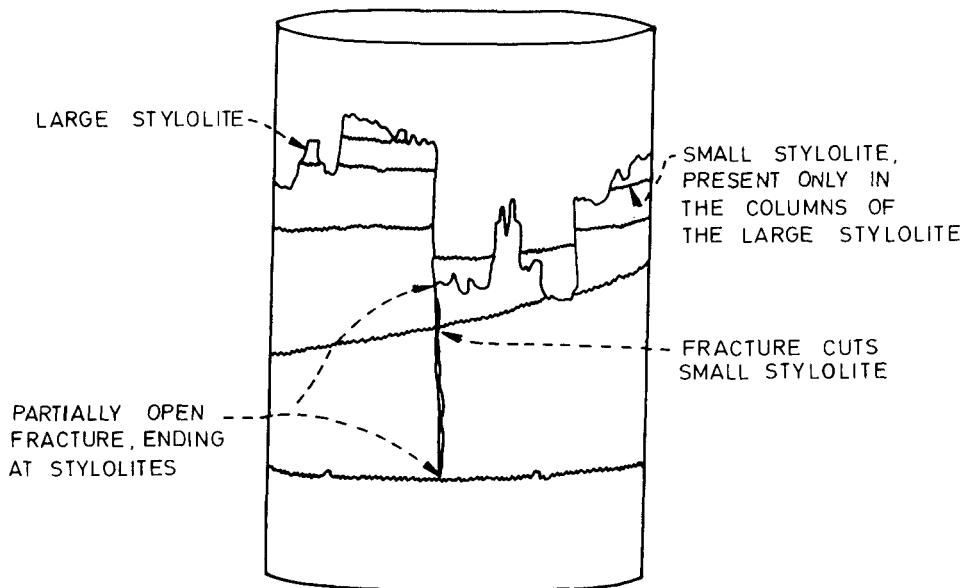
and filled with calcite (figure 2.11) or partially open. The evaluation of fracture characteristics, such as open or filled, and the nature of the material is essential in a further description of a fracture network.

Stylolites are another very important core feature and should be described by a procedure similar to that used to describe the fractures. Stylolite orientation (figure 2.11), subvertical or subparallel to the bedding, and their intersection with the fractures especially when interrupting the fracture intercommunication (figure 2.12), is considered to represent an essential observation. A schematization of stylolites in a core, including their magnitude (small, large), opening, etc., is shown in figure 2.13.

### 2.3.2.1. Single fracture parameters

#### a. Evaluation of fracture width

The width of the fracture is obtained by microscopic examination of thin sections. This method is considered to be the most effective since it is the only one which permits a direct measurement of the opening size. The width is measured at several openings of the thin section and the results are then averaged. Based on a number of thin sections, the results will again be averaged and finally corrected with the angle  $\theta$



2.13 – Stylolites in a fractured core

between the plane of the thin section and the fracture. If the angle varies during each measurement, a random variation from 0 to  $\pi/2$  is used in the calculation, therefore,

$$b_{\text{real}} = b_{\text{measured}} \times \cos\theta \quad (2.20)$$

and for a random distribution the averaged  $b_{\text{real}}$  is a function of the averaged  $b$  measured,

$$\bar{b}_{\text{real}} = \bar{b}_{\text{measured}} \times \frac{2}{\pi} \quad (2.21)$$

The data acquired from the evaluation of fracture openings indicates that the opening size is generally less than 0.1mm = 100 microns. However, if the openings are large, some difficulties may arise if the entire fracture opening is not included in the thin section under examination.

#### Example:

In a well having 1110 cores, the open unequivocal fractures of different widths were measured and are presented in table 2.3.

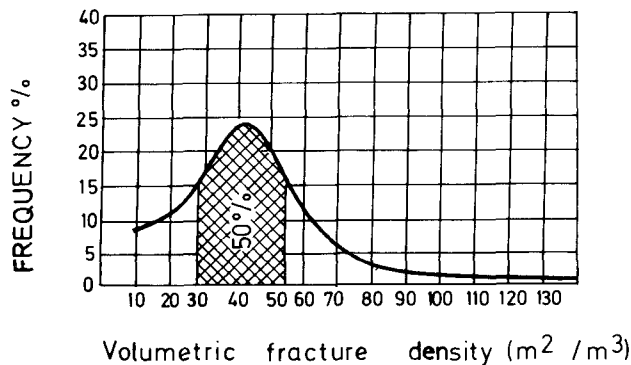
Table 2.3.

Class of width, mm	Average width	Number	Frequency %
< .01	.01	430	39%
.01 – .03	.02	80	7%
.03 – .07	.05	180	16%
.07 – .113	.10	270	24%
.113 – .117	.15	10	1%
.117 – .23	.20	20	2%
.23 – .27	.25	30	3%
.33 – .33	.30	60	5%
.33 – .67	.50	30	3%

The results are presented as a frequency curve as shown in figure 2.14.

The average opening size is,

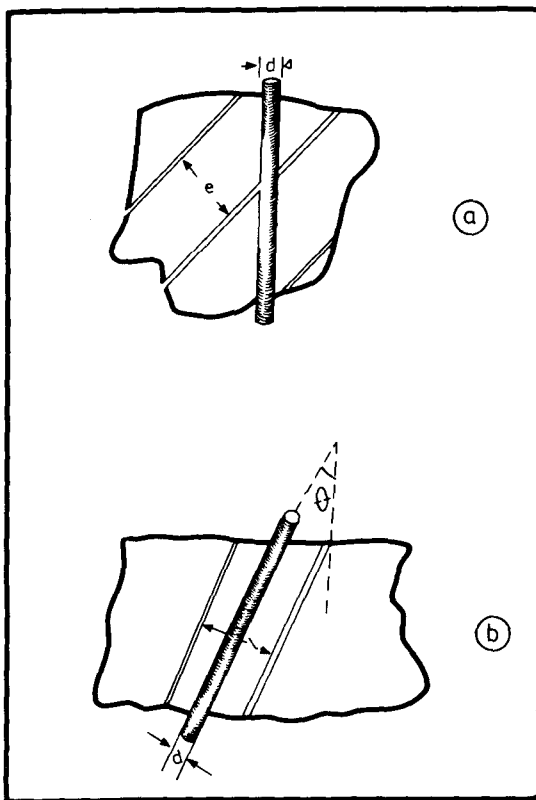
$$\bar{b} = .079 \text{ mm} \cong .08 \text{ mm}$$



2.14 – Opening width obtained from Basquiria Middle Cretaceous<sup>4</sup>

#### b. Evaluation of fracture size

In general, from coring data it is easier to record all microfractures than it is to identify all macrofractures. In fact, the detection of some macrofractures could be biased by sampling conditions as a result of the relationship between fracture spacing vs. core diameter (figure 2.15a), and fracture orientation vs. hole deviation (figure 2.15b). As observed, fracture spacing in subvertical fractures and deviated holes may avoid the identification of fractures (figure 2.15b). On the other hand, the distance between the adjacent fractures might reduce the detection of the fracture system in cores (figure 2.15b)



2.15 – Well and fracture system. a) Fracture interval larger than core height b) Fracture and well parallel

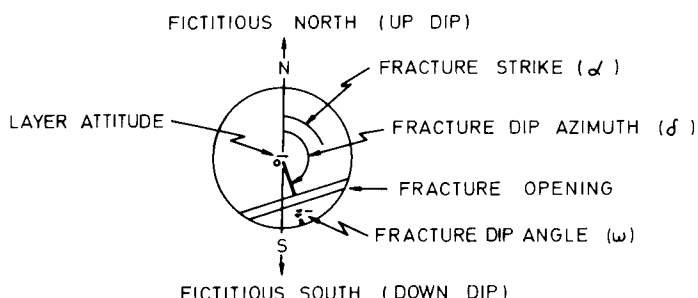
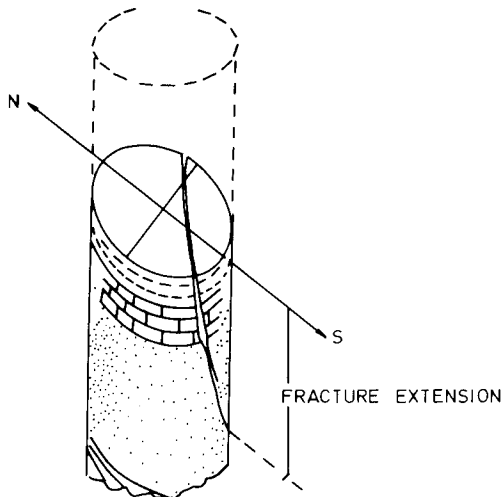
#### c. Evaluation of fracture orientation

In order to establish the orientation of fractures it is necessary to orient the core itself during coring operations by continuously recording the polar orientation.

The method for evaluating fracture orientation (which associates it to the directional features of the layers) was proposed by Vieira<sup>6</sup>. The orientation lines on the core are obtained by three scribes which form, respectively, angles of  $288^\circ$ ,  $144^\circ$  and  $72^\circ$  with the fictitious North-South reference line.

In correcting the fictitious orientation to the true polar values, the measurable features above and below the survey depth are adjusted in reference to the respective azimuth and depth (figure 2.16).

In order to transform the fictitious dip and azimuth into real values of the slope and direction (referred to as the North direction), core orientation may be difficult. It is therefore useful to correlate the results of the log dip and observed core dip to achieve a successful correlation. If the log dip is not available, a more approximate result may be obtained from structural mapping.



2.16 – Relationship between fictitious north and fracture strike, dip azimuth (courtesy of Vieira<sup>6</sup>)

A method described by Vieira for finding fracture orientation is based on core description and on continuous dipmeter logs or structural maps and their correlation with the fictitious North-South direction and the layer dip. As illustrated in figure 2.16 the fictitious North is the up-dip and the fictitious South the down-dip; the fracture orientation data will be the the strike, dip and opening correlated to the extension of the fracture.

When considering the following three parameters which define the dip angle, a number of cases can be examined (figure 2.17) where,

$\alpha$  – is the apparent dip angle of the layer as a result of the core being in a vertical position

$i$  – is the inclination from the well dipmeter

$B$  – is the true dip angle obtained either from the dipmeter or structural interpretation.

Case 1: Orientation is impossible in a vertical or deviated well if combined with a horizontal bed, since  $B = 0$ .

Case 2: If the well is vertical, but the layer dips with an angle  $B$ , orientation is possible.

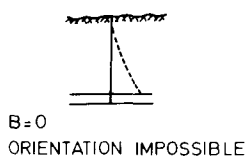
Case 3: If wells are deviating in the direction opposite to the direction of dip, orientation is impossible only in the case of  $i = B$ , which corresponds to a well penetrating the layer normally.

If  $i < B$  the apparent core dip angle  $\alpha$  will decrease with the increase of  $i$  and orientation is possible.

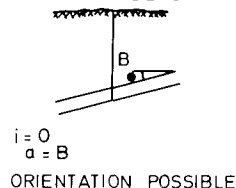
If  $i > B$ , angle  $\alpha$  will increase with increase of  $i$  and orientation is possible.

Case 4: If a well deviates in the same direction as the dip of the bed, angle  $\alpha$  will increase with  $i$  and orientation is possible.

1. VERTICAL OR DEVIATED WELL  
HORIZONTAL BEDS

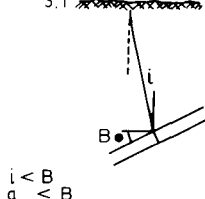


2 VERTICAL WELL  
INCLINED BEDS

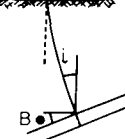


3. WELL DEVIATED IN OPPOSITE DIRECTION FROM THE DIP OF THE LAYER (GENERAL CASE)

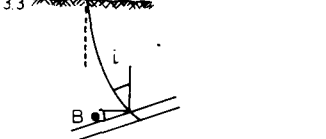
3.1



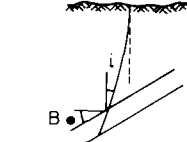
3.2



3.3



4. WELL DEVIATED IN SAME DIRECTION AS THE DIP OF THE BED

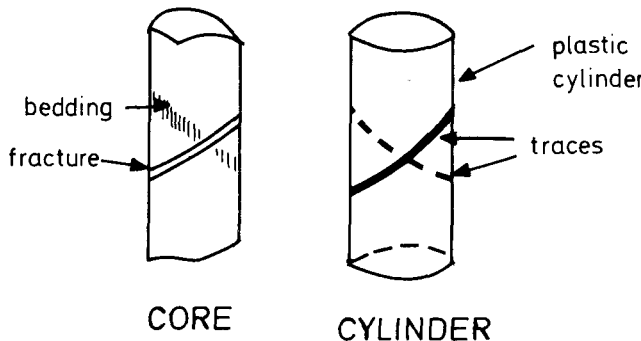


Taking into consideration the relationship between fracture orientation and core orientation, the following<sup>1</sup> may be stated:

- a. the absolute orientation of fractures is obtained only if the cores have been oriented in-situ;
- b. the cores not oriented in-situ must later be oriented through correlation between traces of bedding, dipmeter and hole deviation data;
- c. if the deviation of the hole exceeds 10° from the vertical, the cores taken from a horizontal, thin bedded rock can be oriented from the elliptical traces remaining on the cores.

With regard to fracture orientation in space of a given core, the following procedure was indicated by Stearn<sup>1</sup>:

- a. the core is inserted in a plastic cylinder;
- b. the traces of bedding and fracture planes are traced (by the observer) on the cylinder surface (figure 2.18);
- c. the cylinder is oriented as it was in-situ based on hole deviation, strike and dip bedding through a special device which is able to orient and measure the core vs. fracture orientation relationship.

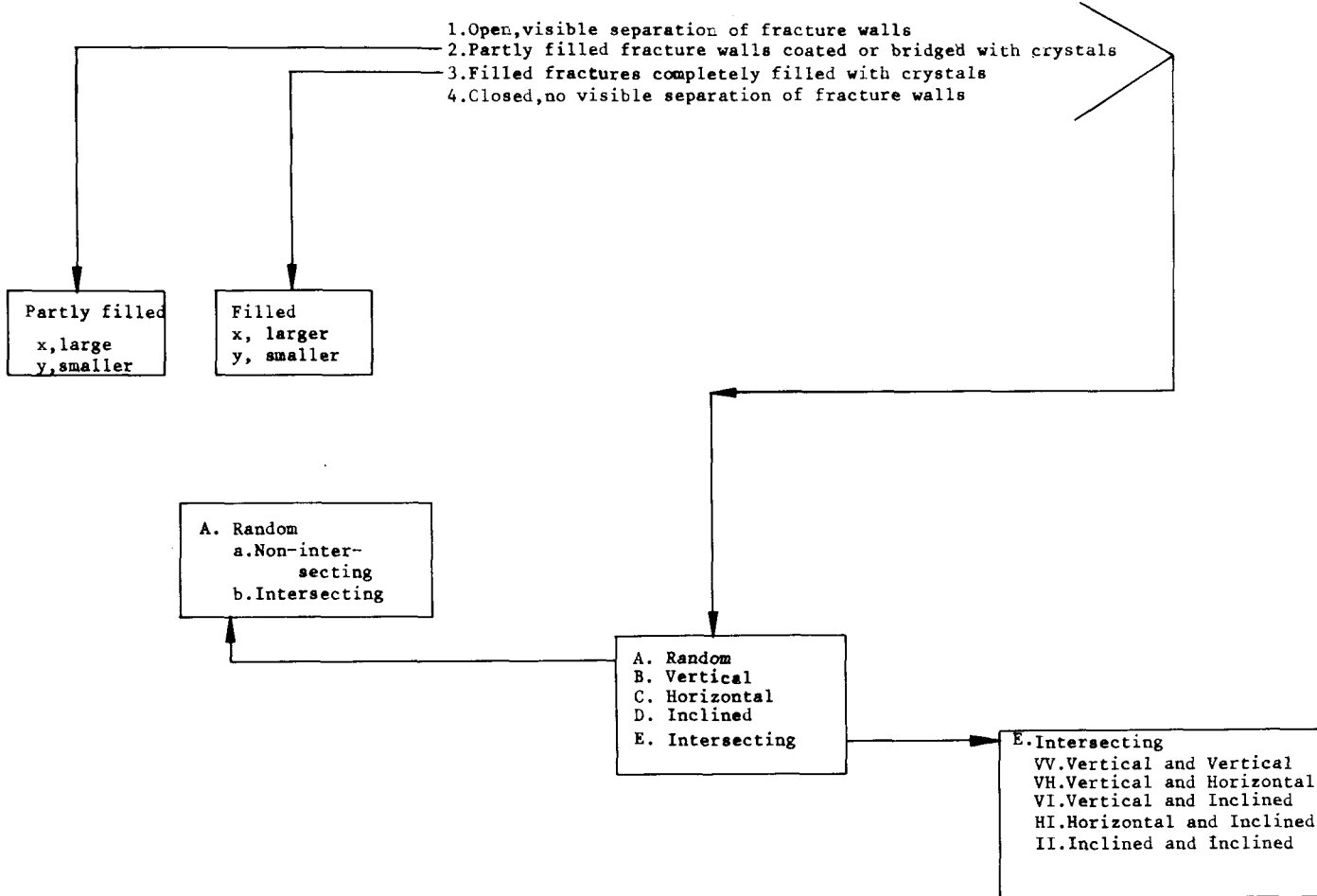


2.18 – Plastic cylinder for cores where fractures and bedding have to be traced

After the orientation of each single fracture has been established, a privileged direction could be evaluated for the totality of fractures through frequency curves and stereographic diagrams.

#### d. Nature of fracture

Each single fracture has to be examined and described in detail in order for it to be classified by comparison with other fractures. The fracture morphology (open, partially open, filled, closed, etc.) has to be combined with fracture size (large, small) and orientation. The oriented fractures have to be examined by their single orientation (vertical, horizontal, inclined) and by their intersection with other planes.



Classification of fractures in cores may be further elaborated as in table 2.4 (Waldschmidt)<sup>7</sup>.

Table 2.4

CLASSIFICATION OF FRACTURES IN CORES			
	TYPE	ORIENTATION Note: B, C, & D - Single or parallel fractures	MINERAL GRAINS IN FILLING LARGER OR SMALLER THAN IN MATRIX
1 OPEN	A Random	a Non-intersecting	
		b Intersecting	
	B Vertical		
	C Horizontal		
	D Inclined		
	E Intersecting	VV Vert. & Vert.	
		VH Vert. & Horiz.	
		VI Vert. & Inc.	
		HI Horiz. & Inc.	
		II Inc. & Inc.	
2 PARTLY FILLED	A Random	a Non-intersecting	x Larger y Smaller
		b Intersecting	x Larger y Smaller
	B Vertical		x Larger y Smaller
	C Horizontal		x Larger y Smaller
	D Inclined		x Larger y Smaller
	E Intersecting	VV Vert. & Vert.	x Larger y Smaller
		VH Vert. & Horiz.	x Larger y Smaller
		VI Vert. & Inc.	x Larger y Smaller
		HI Horiz. & Inc.	x Larger y Smaller
		II Inc. & Inc.	x Larger y Smaller
3 FILLED	A Random	a Non-intersecting	x Larger y Smaller
		b Intersecting	x Larger y Smaller
	B Vertical		x Larger y Smaller
	C Horizontal		x Larger y Smaller
	D Inclined		x Larger y Smaller
	E Intersecting	VV Vert. & Vert.	x Larger y Smaller
		VH Vert. & Horiz.	x Larger y Smaller
		VI Vert. & Inc.	x Larger y Smaller
		HI Horiz. & Inc.	x Larger y Smaller
		II Inc. & Inc.	x Larger y Smaller
4 CLOSED	A Random	a Non-intersecting	
		b Intersecting	
	B Vertical		
	C Horizontal		
	D Inclined		
	E Intersecting	VV Vert. & Vert.	
		VH Vert. & Horiz.	
		VI Vert. & Inc.	
		HI Horiz. & Inc.	
		II Inc. & Inc.	

### 2.3.2.2. Multi-fracture parameters

#### a. Evaluation of fracture density

In thin sections the width of the opening and length of the fractures are simultaneously measured so that the fracture density can be evaluated using equation 2.3,

$$A_{fD} = \frac{\text{number of fractures} \times \text{length (in thin section)}}{\text{area thin section}}$$

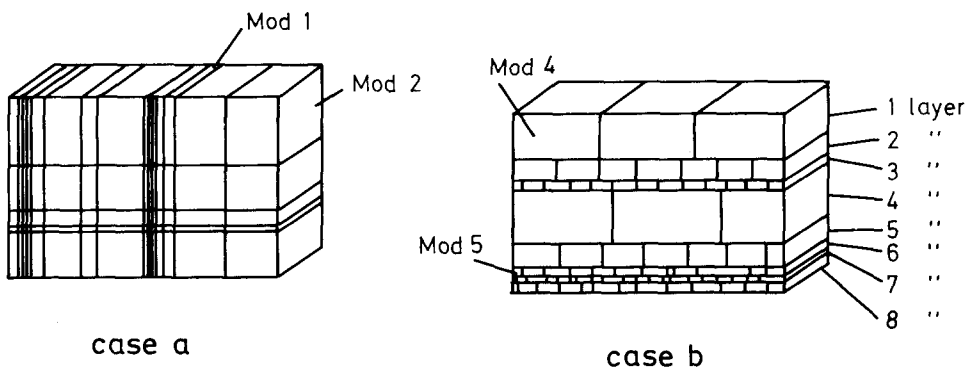
For a random distribution (equation 2.12) the following average relationship will occur,

$$V_{fD} = \frac{\pi}{2} A_{fD} \quad (2.22)$$

The linear fracture density is obtained from the intersection of fractures along a vertical line. The procedure follows the indications described in paragraph 2.2.3.3.

#### b. Evaluation of fracture intensity

The uniformity or non-uniformity of fracturing (similar to that shown in figure 2.19) may be evaluated by the fracture intensity in a multi-layer reservoir. In case *a* the total number of fractures remains the same in all layers independent of layer thickness and location, while in case *b* another fracture density is observed in each of the eight layers.



2.19 – Two idealized rocks: a) equal number of fractures in all layers b) different number of fractures in each layer

The equation in this case remains the same as in equation 2.17, and is expressed by,

$$FINT = \frac{FF}{THF} = \frac{n_f}{\sum n_i h_i}$$

where  $n_f$ ,  $n_i$  and  $h_i$  are the number of fractures, number of layers and thickness of intervals. In this case, the various degrees of fracture intensity can be interpreted from a Log FF vs. Log THF diagram (figure 2.20).

The diagonals show the relationship of FINT (fracture intensity) to vary from 100/1 to 1/100, and the interpretation<sup>3</sup> of various straight lines is as follows:

1. horizontal straight line *A* shows that, independent of the increment of thickness, the fracture frequency remains the same. This corresponds to a fracturing limit over which the formation can not be fractured (Fig. 2.19 case a);
2. vertical straight line *B* shows a formation formed by constant thickness layers where the fracture frequency increases as a result of layer location versus stress distribution. The increments may correspond to the increasingly stressed zones (near the faults, top of folding zone, etc.);
3. diagonal *C* shows that in certain rocks the fractures increase substantially if the thickness increases slightly;
4. diagonal *D* inversely shows for other rocks a slight increase in fracture intensity for substantial increase of layer thickness;
5. diagonal *E* shows an increase in fracture intensity in case of a reduction in pay frequency. This represents a highly unusual case.

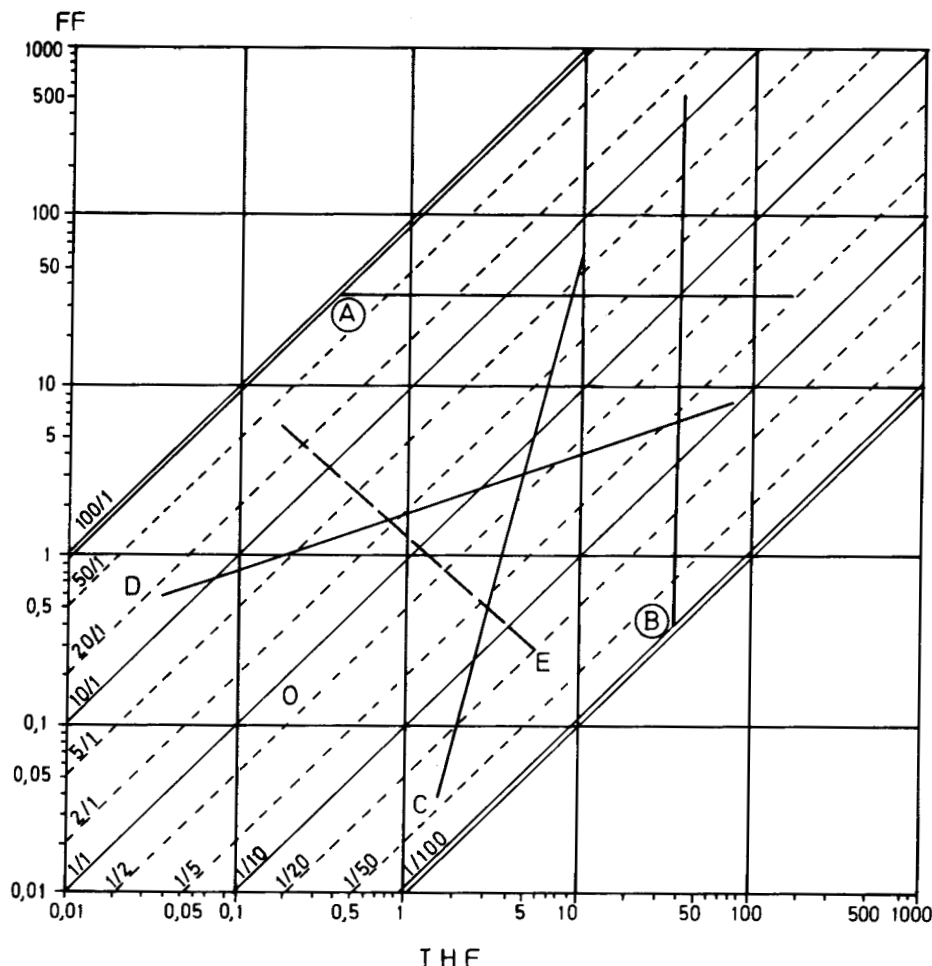
c. Evaluation of matrix block unit

In a reservoir (as shown in an idealized simplification in figure 2.19) the various fracture distributions and layer heights will delineate matrix block units of various sizes. These block units (figure 2.19), indicated as Mod. 1, 2, 4 and 5, are similar to cases 1, 2, 4 and 5 discussed in table 2.1.

For a reservoir as shown in figure 2.19, where only vertical fractures exist and where the layers are horizontal, the parameter FF represents the fracture frequency resulting from the intersection of a horizontal bedding plane with vertical fractures. This parameter defines the matrix blocks as *large* or *thin*. The parameter THF represents the thickness frequency which results from the intersection of a vertical plane with horizontal bedding planes, and defines the height of the block as *tall* or *short*.

The shape and magnitude of these blocks can be examined by use of the FF vs. THF diagram (figure 2.21). The cube is on the diagonal, starting from origin 0, if both scales have the same basic value. For constant values of FF the increase in THF represents the increase in the thickness frequency, which corresponds to the increase in the block base and reduction in the block height (blocks will become flatter). Inversely, if the thickness frequency remains constant but the fracture frequency FF increases, the blocks will become more elongated, reducing their base, and also will tend to take the shape of a thin column or a pencil.

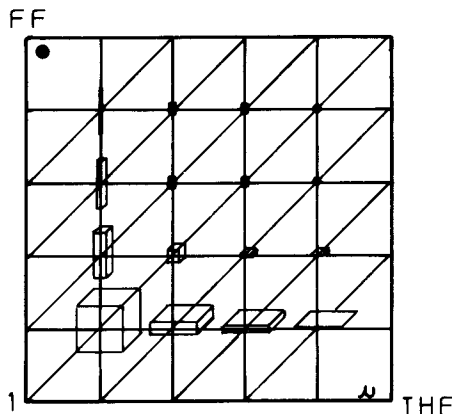
The shape/size relationship of an idealized block unit, related to the single layer pay and fracture density, may show large variations between vertically and horizontally



2.20 – Fracture intensity for various cases of fracturing (Ruhland<sup>3</sup>)

elongated block elements. The idealization of a block unit is developed under the following procedure:

1. Each single matrix block extension is *laterally* delineated by fracture density (assuming the fractures are subvertical) and *vertically* by the height of the layer (between the top and bottom of each).
2. From the average layer gross pay  $e$  and fracture frequency FF, the block shape and size will result from a well analysis.
3. Since the average thickness frequency THF is considered to be equivalent to the reciprocal value of the average pay  $\bar{e}$ , *and average height a the reciprocal of FF*, the block shape vs. height can be obtained from the relationship  $e$  vs.  $a$ .



2.21 – Fracture intensity and unitarian blocks (Ruhland<sup>3</sup>)

**Example:**

Four cores of various length have been extracted during the drilling of a fractured reservoir and each core provided the following data: number  $n_i$  of layers (beds); total number  $n_f$  of fractures; length of each core. Based on these data the fractures frequency FF and thickness THF are estimated. (Columns 2 and 3, Table 2.5.) In the Table 2.5 is shown the evaluation of each block size and the FINT values, based on frequency of fractures and beds.

Core	FF (1/m)	THF (1/m)	FINT (4)=(2):(3)	$\tilde{a}$ (meters) (5)= $\frac{1}{(2)}$	$\tilde{e}$ (meters) (6)= $\frac{1}{(3)}$
(1)	(2)	(3)	(4)=(2):(3)	(5)= $\frac{1}{(2)}$	(6)= $\frac{1}{(3)}$
1	1,13	1,13	1,00	0,884	0,884
2	5,83	1,44	4,08	0,171	0,694
3	2,59	0,65	3,98	0,386	1,53
4	0,312	1,33	0,312	3,20	0,75

The results obtained for fracture frequency (column 2) and thickness frequency (column 3) are introduced in figure 2.22. These results will permit of evaluating the type of block. As observed, only one block will be a cube where  $FINT = 1$  since in core 1  $FF = THF = 34$ . It may be assumed (hav-

ing estimated the fracture intensity) that the cores indicate the following types of matrix blocks:

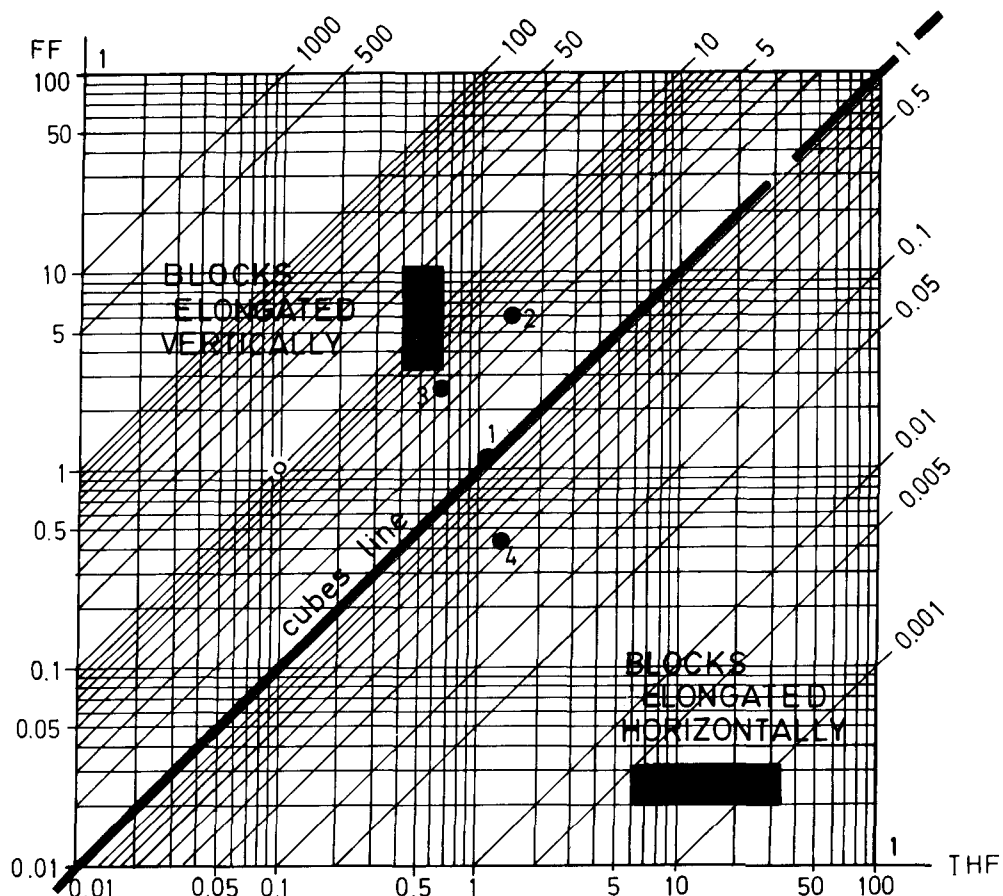
FINT >1 – the matrix block is elongated vertically (cores, 2,3)



FINT = 1 – the matrix block is a cube (core 1)

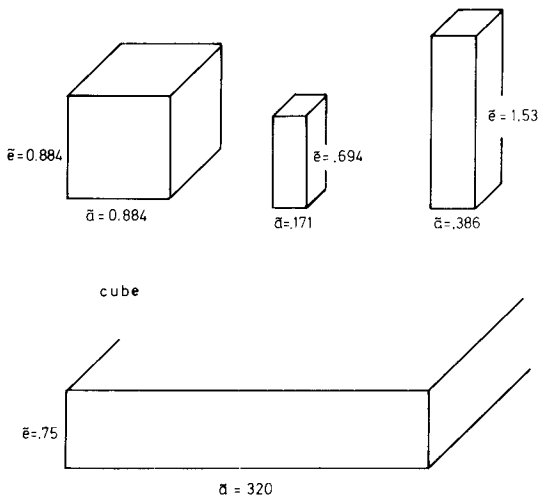


FINT <1 – the matrix block is elongated horizontally (core 4)



2.22 – Fracture intensity diagram for the example results

The shapes of the block units for each of the four cores are drawn in figure 2.23.



2.23 – Block units of the four cores idealized as parallelepipeds

#### 2.4. PROCESSING OF DATA

After the basic data has been obtained from the cores, the first step is to tabulate the gathered information through various criteria. In order to get a better understanding of the relationship between the various parameters and certain trends, different graphic representations are used.

##### 2.4.1. *Tabulation and classification of data*

###### 2.4.1.1 Table format

There are many ways to tabulate coring results, but only two are proposed as more convenient. The first model (table A) illustrates, over the total depth of the well, all recorded data for stylolites and fractures. Fracture qualities (open, closed, filled), dip angle and lithology are considered. In addition, the testing interval and the ratio between matrix permeability and testing permeability are recorded. The second model (table B) is more detailed since the fractures can be divided into macrofractures and microfractures. The results of fracture intensity have been added to the data in order to better understand the shape of the matrix blocks.

Table A

Table B

DEPTH METERS	LITHOLOGY	CORE	DIP	AZIMUTH	N-NORMAL Joints	N-VERSE StyloLites	NUMBER/M	NUMBER/M	NUMBER/M	FRACTURE & JOINTS					FRACTURE INTENSITY M/M
										OPENING MM	FILLED MM	FILLED BY: C-CALCITE; A-ANHYDRITE S-SHALF ; O-OIL	FRACTURE DIP NUMBER OF FRACTURES		
										0 - 5cm 0 20 40 60	5 - 10cm 0 20 40 60	10 - 30 0 20 40 60	> 30 0 20 40 60		

#### **2.4.1.2. Classification and tabulation**

In general, the rough data obtained from core examination are presented (see tables A and B) as a function of depth. However, for further detailed analysis new classification criteria should be used, and then only a portion of the parameters are selected and reinterpreted. When the reservoir is formed by large pay and if important lithological variations are present, the results are generally examined through lithological features, such as:

- a. rock hardness
- b. presence or absence of shale
- c. presence or absence of chert
- d. occurrence of mineral or fossil traces
- e. orientation of the bedding planes.

Rock hardness, which results from examination of the core, is related to the following criteria:

- a. soft (can be scratched by a finger nail)
- b. soft-medium
- c. medium (can be scratched by a plastic triangle)
- d. medium-hard
- e. hard (can be scratched by using a steel knife blade)
- f. hard-very hard
- g. very hard (can be scratched by using a sharp point of a steel probe)

The presence or absence of shale is associated with:

- a. lenses or bands
- b. argillaceous material
- c. high shaliness from turbidite conditions

#### **2.4.2. Representation of data**

The information obtained from core examination (to which may be added the results obtained from indirect measurements) must be processed through statistic diagrams or pure geometric representations. The following are the data which are mainly processed: fracture width, size, nature, orientation, distribution, block unit, density and intensity.

The criteria through which various results are examined are depth, lithology, pay magnitude, etc.

The representative models are of two types:

- a. *statistic models*, which include the histograms and statistic stereograms. In the histograms the single parameter values (eventually selected through certain criteria) indicate, by use of the frequency curve, the most probable average value. For stereograms mainly used for fracture orientation parameters (strike, dip angle,

- etc.), the preferential directions of the fractures are evidenced;
- b. *geometrical models* mainly use the stereographic projection especially in the case of matrix block units. Polar stereograms and various schematic representations are particularly useful in the identification of the preferential trends of certain parameters, and also help in the description of properties through simplified schemes for large groups of fractures.

#### 2.4.2.1. Statistic representation

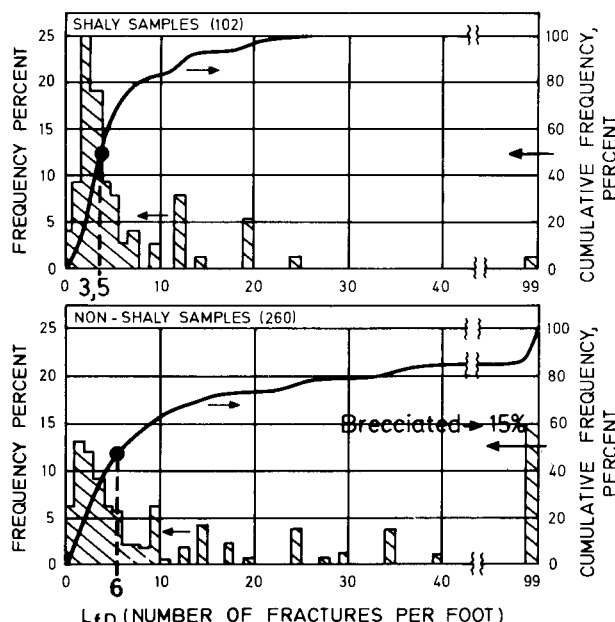
##### a. Histograms

As mentioned, histograms are used for evaluating the most frequent range of variations of a given parameter. The data are generally collected in relation to a given criterion, such as lithology, pay interval, number of cores, types of fractures, etc. Histograms are applied to almost all parameters which define single fractures or multi-fractures.

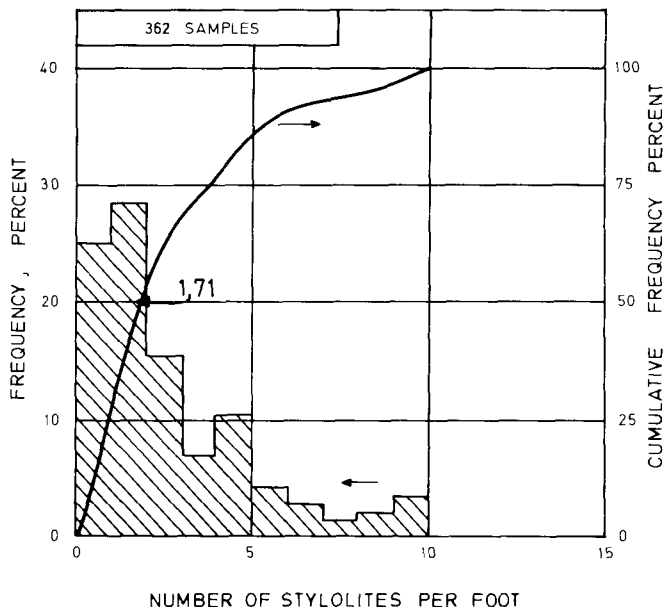
From the frequency curve and cumulative frequency curve the range of average values of a given parameter is obtained by a conventional procedure.

##### Example 1:

Fracture density was examined on 362 samples and the results obtained were separated into two groups through lithological criteria: shaly samples (102), non-shaly samples (260). For the two categories of samples, frequency and cumulative frequency vs. linear fracture density (fractures/foot) have been presented in figure 2.24.



2.24 – Frequency curve of linear fracture density, for shaly and non-shaly samples (example)



2.25 – Frequency curve of linear stylolite density (example)

As observed for the 50% cumulative frequency, the average value of the linear fracture density is 6 fractures/foot in non-shaly samples compared with 3.5 fractures/foot in shaly samples. In addition, it is also observed that breccia (over 100 fractures/foot) develops in non-shaly samples (15% frequency).

#### Example 2:

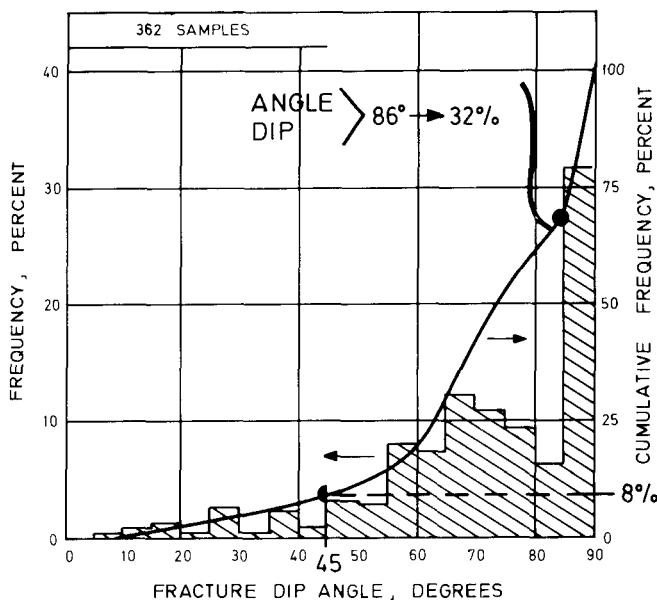
Similar procedures may be used for finding stylolite density. For 362 cores examined the average number of stylolites/foot was found to be 1.71 (figure 2.25).

#### Example 3:

By using the histograms for the same cores for other parameters, such as fracture dip angle (degrees), it is possible to appreciate the general trend of the fracture dip around the well bore. In the example given (figure 2.26), it is observed that only 8% of the fractures have an angle below 45°, but 32% of the fractures dip more than 86%. The average dip angle remains 75°. It is evident that a preferential subvertical orientation of fractures is predominant inside the reservoir.

#### b. Stereograms

Statistic stereograms generally use a circle in order to define the spatial position of the fractures. In addition, frequency is measured on the radius, which is divided into units by concentric circles.

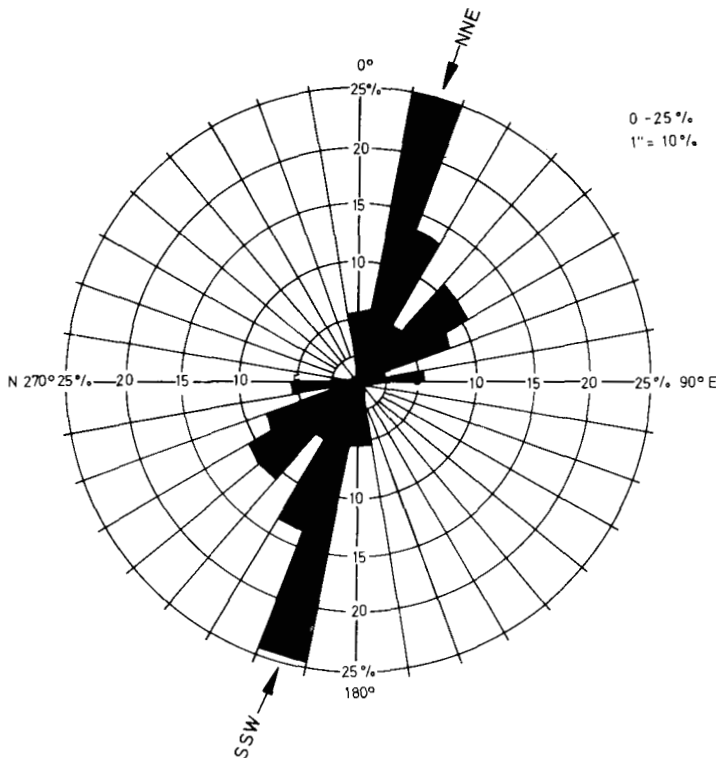


2.26 – Frequency curve of fracture dip angle (example)

#### Example 4:

The fracture strike orientation has been determined on the same 362 cores, and the results have been projected on stereograms. The strike direction was projected along the radius, and the frequency magnitude was expressed by concentric circles in each direction. The variations of the circles were between 1–25% (figure 2.27). The stereogram shown as an example indicates the strike fracturing direction preferentially oriented along NNE-SSW direction. A similar representation is used for orientation parameters, such as dip angle, azimuth angle, etc., or for nature of fracture, such as open, filled, partially filled. This last representation shows the relationship between fracture orientation and fracture characteristics. The same procedure is used for stylolites.

If a preferential orientation of the fractures or stylolites results from the stereogram, this may be used for further interpretation of the past geological events such as, for example, the relationship between the orientation of principal stresses and the generated fractures or the stylolites. It is also interesting to examine the fracturing direction of closed fractures and to compare it with the preferential direction of open fractures. The difference between these two orientations may indicate a direction of the fluid flow, containing the fracture-filling material.



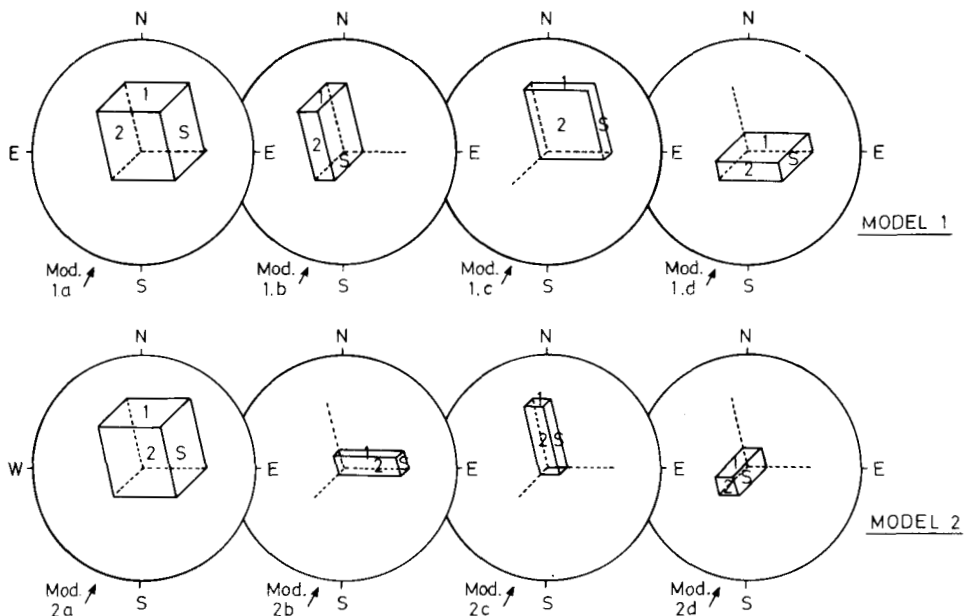
2.27 – Fracture strike projected in a statistic stereogram (example)

#### 2.4.2.2. Geometrical representation<sup>3</sup>

##### a. Stereograms

In this case, a stereographic projection is mainly used for the understanding of the geometric interrelationship of the results and observations of various measurements.

1. Block unit stereogram (spatial stereogram). A stereographic projection of the matrix block unit could represent the orientations of layer (S) and the fracture surfaces (1,2). In addition, elongation of the block and its spatial direction is satisfactorily represented (figure 2.28). In the example given by Ruhland<sup>3</sup> in figure 2.28, the projection is done only in the upper hemisphere. The layer (S) is oriented N 0°, 60°E, and the fracture plane 1 (N74;66°NW) and 2(N136; 40W). The unitarian block is shown as a cube, reduced to a flat block in Model 1, cases b, c and d, and to a column-style block in Model 2, cases b, c and d (figure 2.28).
2. Orientation vs. single fracture parameter stereogram. Stereograms are successfully used when a certain single fracture parameter is examined in association with



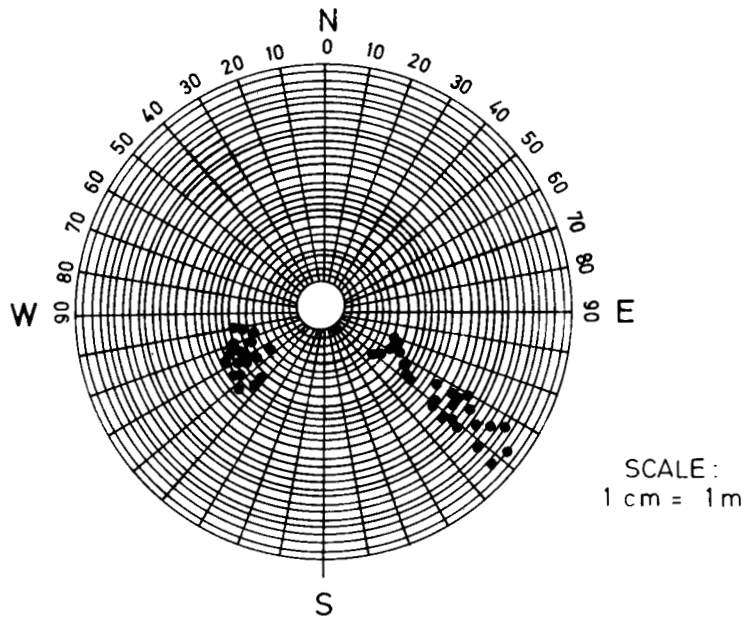
2.28 – Stereographic projection of a block unit

the fracture orientation. Parameters, such as fracture density and fracture size are very interesting if associated with the fracture orientation. If, for example, in addition to the fracture orientation, the circles indicate the fracture length (size), the fractures will be larger in the SE-NW direction (figure 2.29) than in the SW-NE direction. If these results are associated to lithological features, such as rock hardness, shaliness, bed pay, etc., a better understanding of fracturing differentiation may be reached.

3. Polar stereogram. This is a stereographic spatial projection whereby the planes are represented through the points tangential to the plane to the hemisphere. Similarly as in figure 2.28, the layer and fracturing planes have the same orientation [S(NO,60°E), 1(N74,60°NW), 2(N136,40°W)], and will be represented by the tangent points  $a$ ,  $b$ , and  $c$  as in figure 2.30 a. From the intersection of the three planes, the intersection line inside the hemisphere will result as  $\alpha$ ,  $\beta$ ,  $\gamma$  (figure 2.30 b). This representation is called a cyclograph stereogram.
4. Complex stereogram. In the literature<sup>3</sup> and in geological studies, various stereograms are proposed for fracturing and stylolite analysis in association with tectonic events.

#### Example:

In stereogram figure 2.31a, the layers (S) and longitudinal fractures (L) are presented as large circles. Transverse fractures (T) and their orientation in relation to the folding axis are indicated.

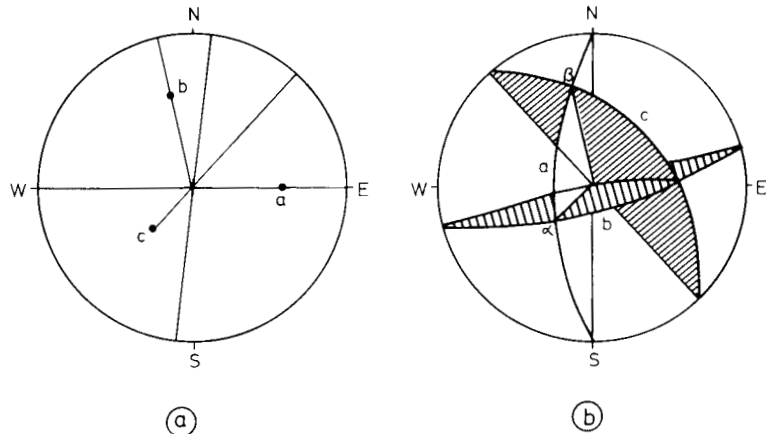


2.29 – Orientation vs. fracture length stereogram (courtesy of Ruhland<sup>3</sup>)

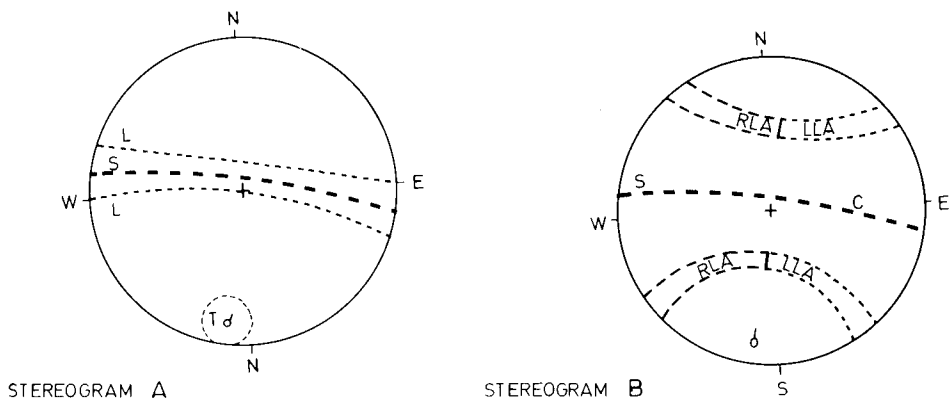
In figure 2.31b right lateral and left lateral fractures are shown as alternatives to longitudinal fractures.

b. Schematic representation (symbols)

Any kind of symbol could simplify the representation of the results, either inside a stereogram or in any other graphic geometric representation.



2.30 – Polar (a) and cyclograph (b) stereogram (courtesy of Ruhland<sup>3</sup>)

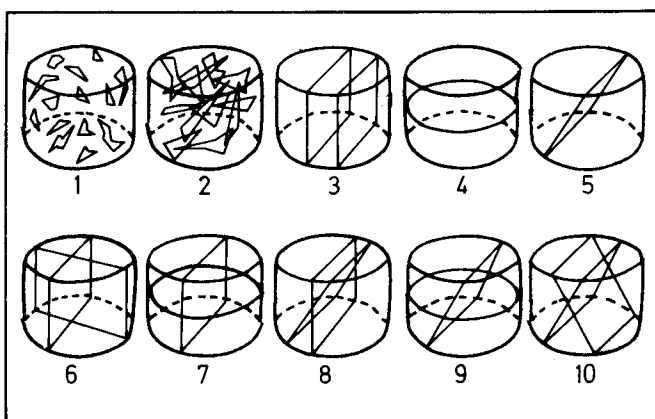


LEGEND

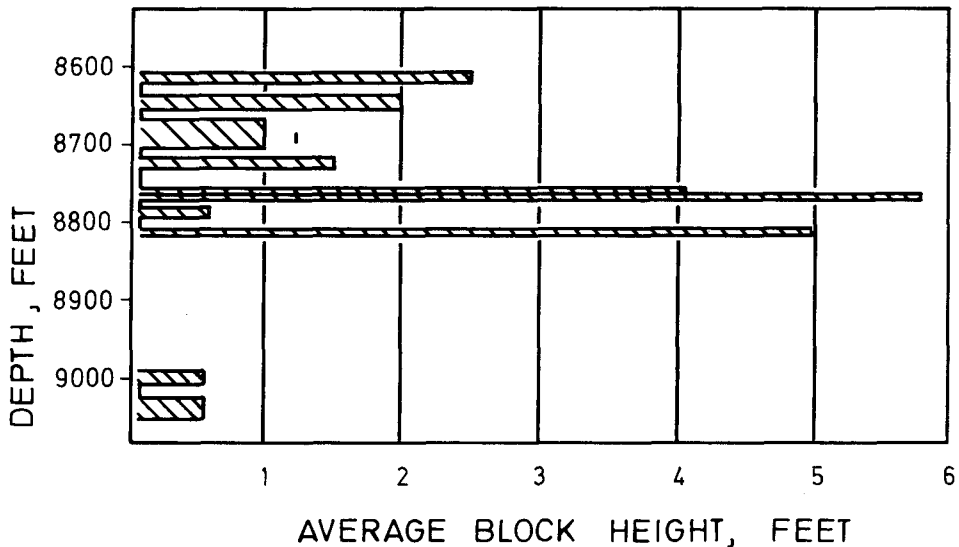
AXIAL ORIENTATION & L- LONGITUDINAL FRACTURE DISTRIBUTION  
C LAYER DISTRIBUTION RLA -RIGHT LATERAL " " "  
LLA -LEFT " " " "

2.31 – Complex stereograms, type A and B (courtesy of Ruhland<sup>3</sup>)

1. Fracture orientation in association with fractures in cores, based on Waldschmidt's<sup>7</sup> classification, is shown in figure 2.32. Fracture orientation includes all cases from simple horizontal, inclined, vertical to random as well as all kinds of combinations.
  2. Variations of fracturing parameters vs. depth. This procedure is mainly of interest for average values of different parameters along various zones. An example of



2.32 – Schematization of fracture orientation: 1) random 2) random – intersecting 3) vertical  
 4) horizontal 5) dipping 6) intersecting, vertical – vertical 7) intersecting, vertical – horizontal  
 8) intersecting, vertical – inclined 9) intersecting, horizontal – inclined 10) intersecting, inclined  
 – inclined (courtesy of Waldschmidt<sup>7</sup>)



2.33 – Average block height, vs. depth (example)

block height evaluated at various depths at each interval is given (figure 2.33). Through this representation it becomes possible to later evaluate the average block height per interval, per zone or throughout the reservoir.

- Frequency schematization. The shape of the block unit is a result of pay and fracture frequency. Considering the following frequencies,

interval  $L = 1/F$  – reciprocal layer thickness frequency

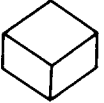
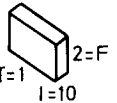
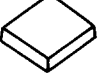
interval  $X = 1/Lo$  – reciprocal longitudinal ( $Lo$ ) fracture frequency

interval  $Y = 1/T$  – reciprocal transversal ( $T$ ) fracture frequency

and assuming that the variations of pay are between 0.1m and 1m, and the variations of longitudinal ( $L$ ) and transverse ( $T$ ) number of fractures are between 1 and 10, a number of geometrical block shapes will result (figure 2.34). The block unit will consist of either cubes or parallelepipeds<sup>3</sup>.

Example: Considering the respective pay, longitudinal fractures and transverse frequencies equal to  $F = 2(1/m)$ ;  $L = 10(1/m)$ , a block results of dimensions  $h = 0.5m$ ;  $X = 0.1m$  and  $Y = 1 m$ . (See Fig. 2.34, second column, third row). This representation of  $F$ ,  $L$ ,  $T$  or  $h$ ,  $x$ ,  $z$  may be used in a stereogram similar to that of fig. 2.28.

- Cross-section containing fracture traces. Fracture traces may be obtained by projecting fractures on a horizontal or vertical section (figure 2.35). The traces

LAYERS PAY		Longitudinal (L) and transversal (T) fractures				
PAY	F= 1/h	X	L=1	L=10	L=1	L=10
h		Y	T= 1	T=1	T=10	T=10
1 m	Z 1					
						
	10					

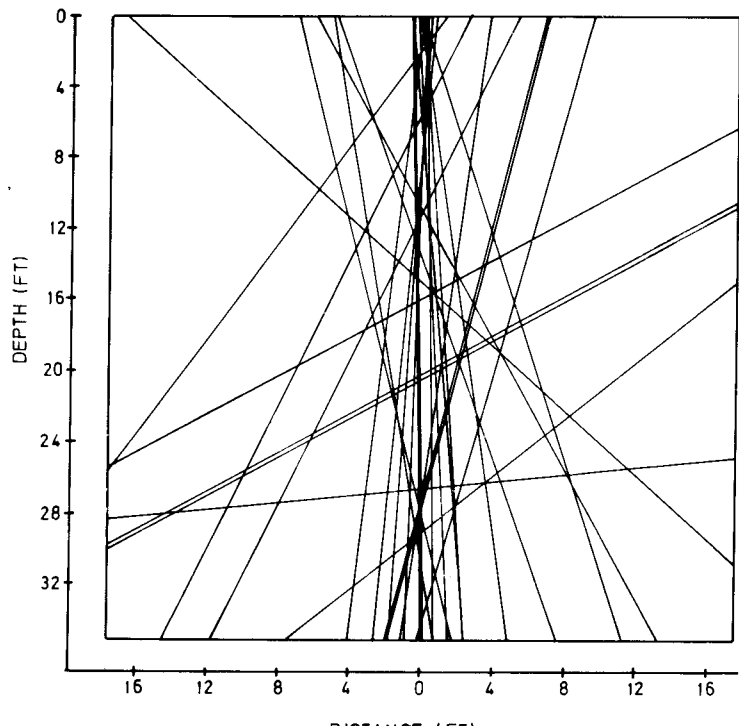
2.34 – Frequency of layers of fractures (F) vs. longitudinal (L) and transverse (T) fracture frequency (courtesy of Ruhland<sup>3</sup>)

obtained from the large zone (32 feet in the example shown) will be further used for the evaluation of the average block size. The height will result from the vertical section if rotated around its vertical axis.

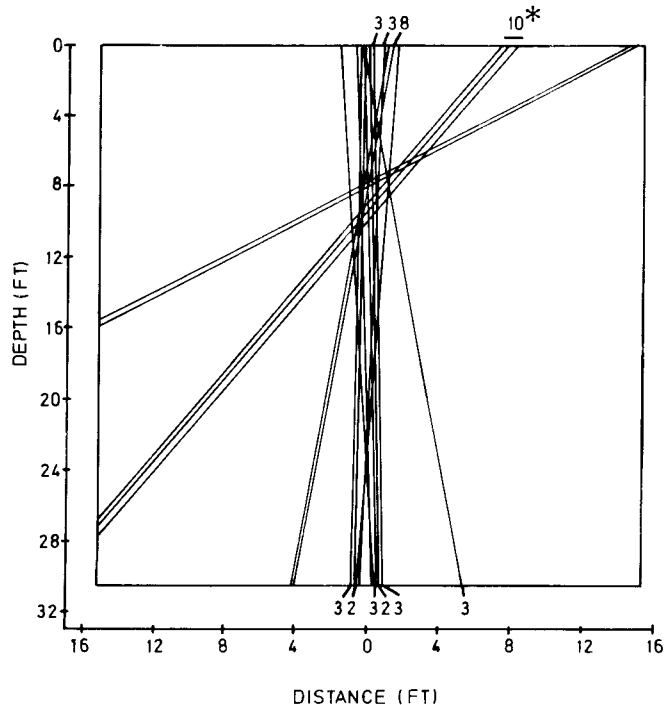
## 2.5 APPLICATION OF FRACTURING STUDIES

A number of regional studies have been carried out in various structures where tectonic movements developed significant stresses which have generated various fracture systems. The examination of fracturing has further permitted the interpretation of the relationship between stress and fracture network.

Examples of such type of work are studies performed by Grenier<sup>8</sup> in the Jura of southwest Germany, studies on fractures of limestones covering the diapiric structure<sup>9</sup> in São Mamede et Pragosa (Portugal), and studies of fracture blocks in the Eschau reservoir.<sup>10</sup>



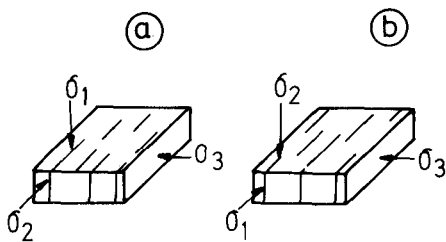
a



b

\*Number indicates total  
amount of parallel fractures  
within bracketed area.

2.35 – Fractures traced on cross sections: a) vertical cross section b) horizontal cross section



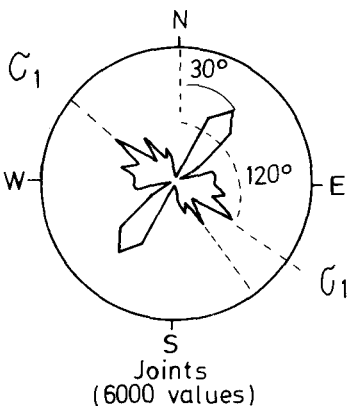
2.36 – Possible stress system for a given joint system (courtesy of Grenier<sup>8</sup>)

### 2.5.1. Tectonophysical study in southern Germany

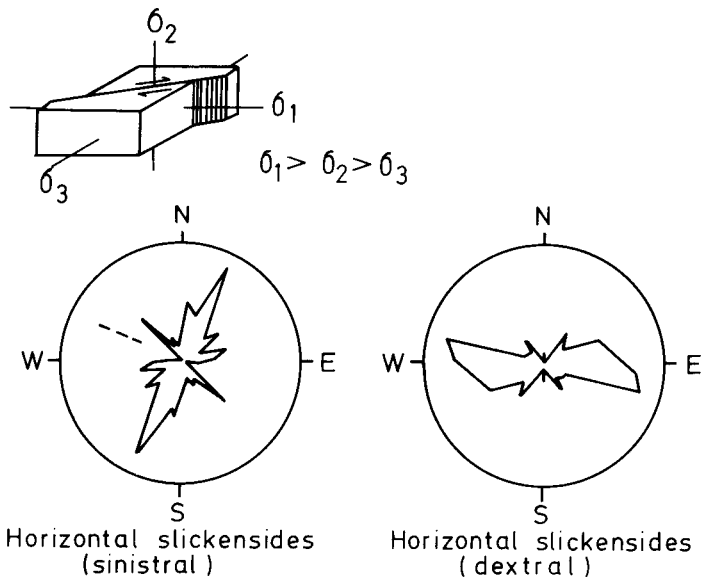
Based on in-situ measurements carried out in the Jura deposits of southern Germany, a series of interesting correlations has been obtained by Grenier<sup>8</sup>. From the examination of joint direction, two possible interpretations for stress distribution systems appear to be possible:  $\sigma_1$  acting vertically (figure 2.36a) and  $\sigma_1$  acting horizontally (figure 2.36b).

The solution to the problem is given by strike data shown in figure 2.37, where it is illustrated that the difference between the maximum strike ( $30^\circ$ ) and the subsidiary direction ( $120^\circ$ ) is  $90^\circ$ . This corresponds to the most common regional direction of jointing where the tectonic stresses have the same pattern. This is also reconfirmed by the overburden conditions which were never thick enough to create any significant vertical stress.

Another important indication is the strike-slip fault. In the presence of high lateral stresses it is possible to deduce the direction of the last movement if there are slickensides on the fault plane. The acute angle between two planes of a pair of conjugate shear fractures indicates that the fractures are bisected (figure 2.38) by the highest compression stress and thus, it is possible to calculate the angle of internal friction of the rock.



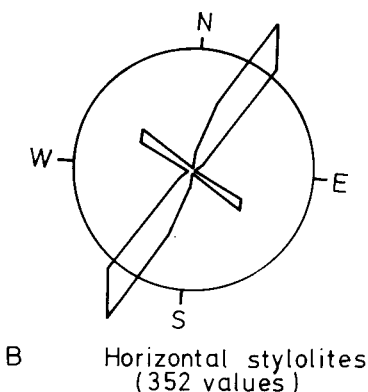
2.37 – Strike stereogram (courtesy of Grenier<sup>8</sup>)



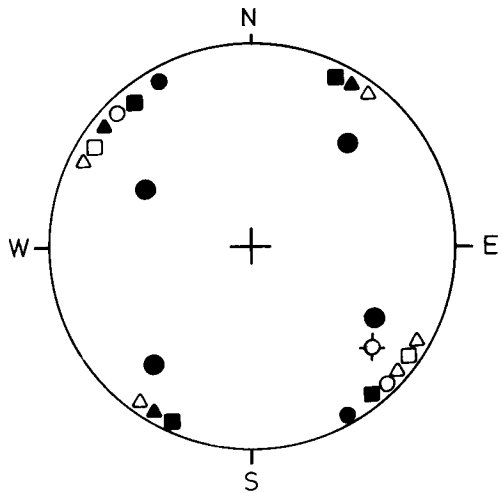
2.38 – Compression stress and in presence of slickensides

From the combination of sinistral and dextral slickensides, the maximum stress  $\sigma_1$ , oriented around  $160^\circ$  to  $170^\circ$  will result.

The fact that the stylolites in figure 2.36 have the same distribution as in figure 2.39 shows that a genetic relationship exists between the horizontal stylolites and the joints. Grenier<sup>8</sup> presents a stereographic projection (figure 2.40) of structural data and stress directions. A series of structural features cannot be attributed to the present stress field since the actual pattern of joints, faults and horizontal stylolites indicates a change in  $\sigma_1$  from  $130^\circ$  to  $30^\circ$ . This suggests that the tectonic pattern is related to a series of stress phases which have been superimposed on the structures throughout the region.



2.39 – Stylolite stereogram (courtesy of Grenier<sup>8</sup>)



- $\delta_1$  - direction (locality Strassberg)
- ◊  $\delta_1$  - direction (locality Onstmettingen)
- $\delta_1$  - direction from focal mechanisms of earthquakes
- Horizontal slickensides (sinistral)
- Horizontal slickensides (dextral)
- ▲ Horizontal stylolites
- △ Joints
- Normal faults

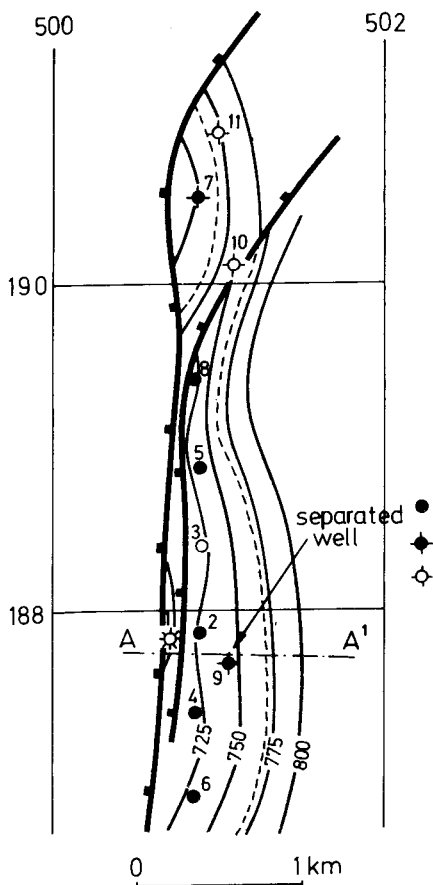
2.40 -- Stereogram for results obtained (courtesy of Grenier<sup>8</sup>)

### 2.5.2. Evaluation of matrix block units

A representative estimation of the shape and dimensions of the average matrix block units is very important when considering dynamic aspects of a fractured reservoir. There is a considerable difference in the recovery behaviour of oil saturating small blocks and oil saturating large blocks (discussion in chapter 9). Various methods for the evaluation have been discussed, and several methods have been proposed<sup>10,11</sup>.

Ghez's<sup>10</sup> study proposes to use subsurface information for further statistical computation of the distribution law of matrix block volume.

The fractured reservoir is treated as a group of matrix blocks limited by discontinuities (fracture networks). In order to avoid the complexity of block geometry, the following is assumed: 1) the fissures are simulated to the continuous planes, and 2) the fractured reservoir is represented by a certain number of networks 3) the distance between fractures of the same plane is reported by a frequency law.



2.41 – Map of Eischau reservoir (courtesy of Grenier<sup>8</sup>)

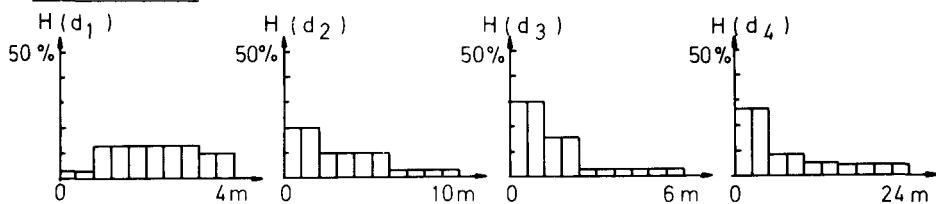
Simulated blocks will result from the intersection of all networks of all fracturing planes.

An application was made by Ghez<sup>10</sup> in a study on the Eischau reservoir, which is a simple monocline limited in the west side by a double normal fault (figure 2.41). The well data have been examined for wells 3, 5, 8 (near the fault) and 9 (far from the fault). Based on azimuth angle histograms and on interval (distance between fractures) histograms (figure 2.42), it was possible to calculate the block volumes.

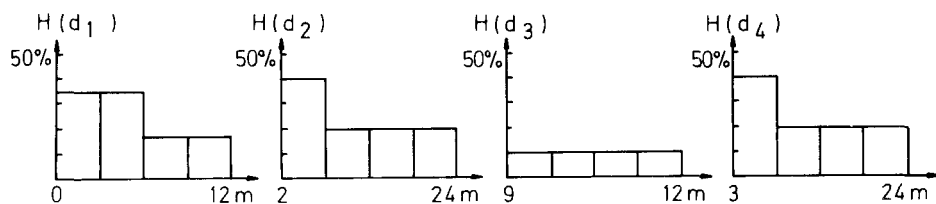
For  $p$  values of volumes  $V_1, V_2, \dots, V_p$  the average and variance are:

$$\bar{V} = \frac{1}{p} \sum_{i=1}^p V_i$$

ESCHAU 3-5-8



ESCHAU 9



2.42 – Fracture interval histogram (courtesy of Ghez<sup>10</sup>)

$$S^2 = \frac{1}{p-1} \sum_{i=1}^p (V_i - \bar{V})^2$$

In the wells near the fault (figure 2.43) 93% of the blocks are below  $0.60\text{m}^3$ , representing 58% of reservoir volume; 7% have a block volume between  $0.60$  and  $1.50\text{m}^3$  which corresponds to 42% of the total reservoir, therefore:

$$\bar{V} = 0.19 \text{ m}^3$$

$$\bar{S} = 0.29 \text{ m}^3$$

In the zone far from the fault (represented by well 9), 91% of the blocks have a volume below  $16\text{m}^3$ , therefore:

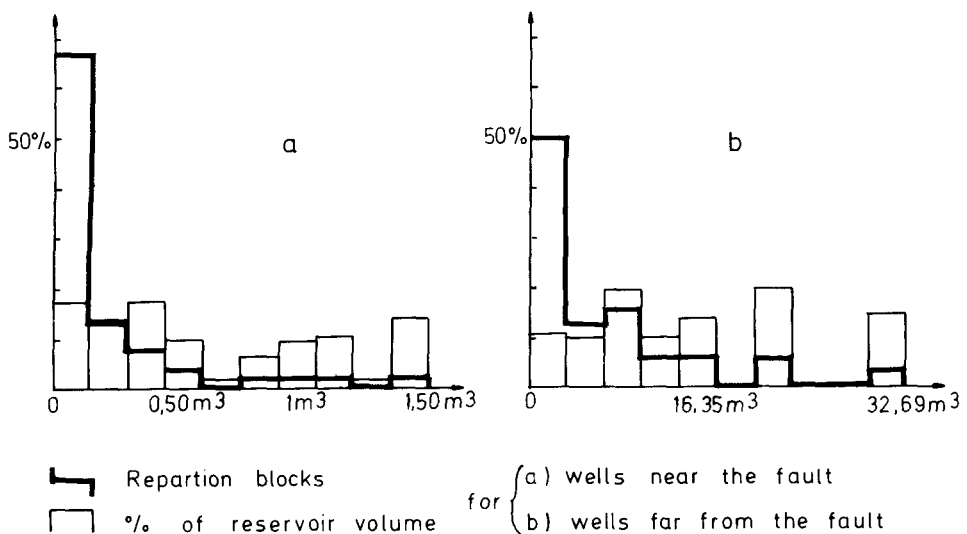
$$\bar{V} = 6.7 \text{ m}^3$$

$$\bar{S} = 7.4 \text{ m}^3$$

In this way is demonstrated how structural conditions cause the occurrence of larger blocks at some distance away from the faulted zone, and smaller blocks close to it.

Conrad's<sup>11</sup> method of evaluation of a natural fracture network consists in creating, *a priori*, a plausible fracture distribution model, in checking its validity by a series of measurements, and at the same time in estimating the parameters included in the model.

The theoretical basis of the project is related to the theory of random functions and mathematical morphology. The measurements are experimentally accessible with a Texture Analyzer. Such a model was approached initially with arbitrary parameters, thus enabling the accuracy of the operating method to be checked in relation



2.43 – Block distributions: a) wells near fault b) wells far from fault (courtesy of Ghez<sup>10</sup>)

to the estimation of the different parameters. Then the geometric dimensions concerning the matrix blocks defined by fractures could be calculated along with, if possible, an estimate of the accuracy of the result, i.e. a variance.

The fracture network with the estimated parameters may be simulated so that the model could be visually compared with reality.

### 2.5.3. Iranian structure studied through outcropping

In large zones of overthrusting, such as in the Zagros mountains of Iran (figure 2.44) where large faulted areas have allowed a detailed examination of the structural and all fracture characteristics, complex studies have been carried out. The Asmari formation in the southwest of Iran is one of the more prominent structures where the outcrops still contain well exposed fracture systems. The outcrops are represented by well exposed limestones where fracturing in carbonate can be examined locally and/or regionally in beds of various thicknesses.

McQuillan<sup>12</sup>, in his study has examined three structures: Kuh-e Asmari, Kuh-e Pahn and Kuh-e Pabdeh-Gurpi which, for simplification purposes, will be abbreviated as Kuh 1; Kuh-2; and Kuh 3. The observation stations have been spaced at 200 m – 300 m along the traverses. The orientation and density of fractures has been presented together with a fracture description.

Since the study developed by McQuillan<sup>12</sup> may be used as a model, the methodology, correlations and types of diagrams are discussed below as an example.



2.44 – Example of folding of Zagros mountains

### 2.5.3.1. Data correlation

In order to examine the relationship between fracture density and local or regional features, the following procedures have been used:

- a. Structural cross-sections – these have been drawn in order to establish the relationship between fracture and structure curvature, where curvature expresses the rate of variation of dip angle or of strike azimuth.
- b. Bedding units – the relationship between fracture density and bed thickness is established by using various ranges of bed thickness.
- c. Structural realms – the relationship between fracture density and structural settings, such as plunges (NW and SE) central axial realm, etc., were examined.
- d. Polar diagrams – ten-degree azimuth classes vs. six rows containing various bedding thickness ranges have been presented as in table 2.6. Given for each class are the average fracture density, number of observations and the percentage of total.
- e. Fracture density and distribution mapping – these maps present polar diagrams vs. fracture numbers and percentages of frequency.
- f. Graphs and histograms – graphs plot the average density over all azimuth classes against bedding thickness.

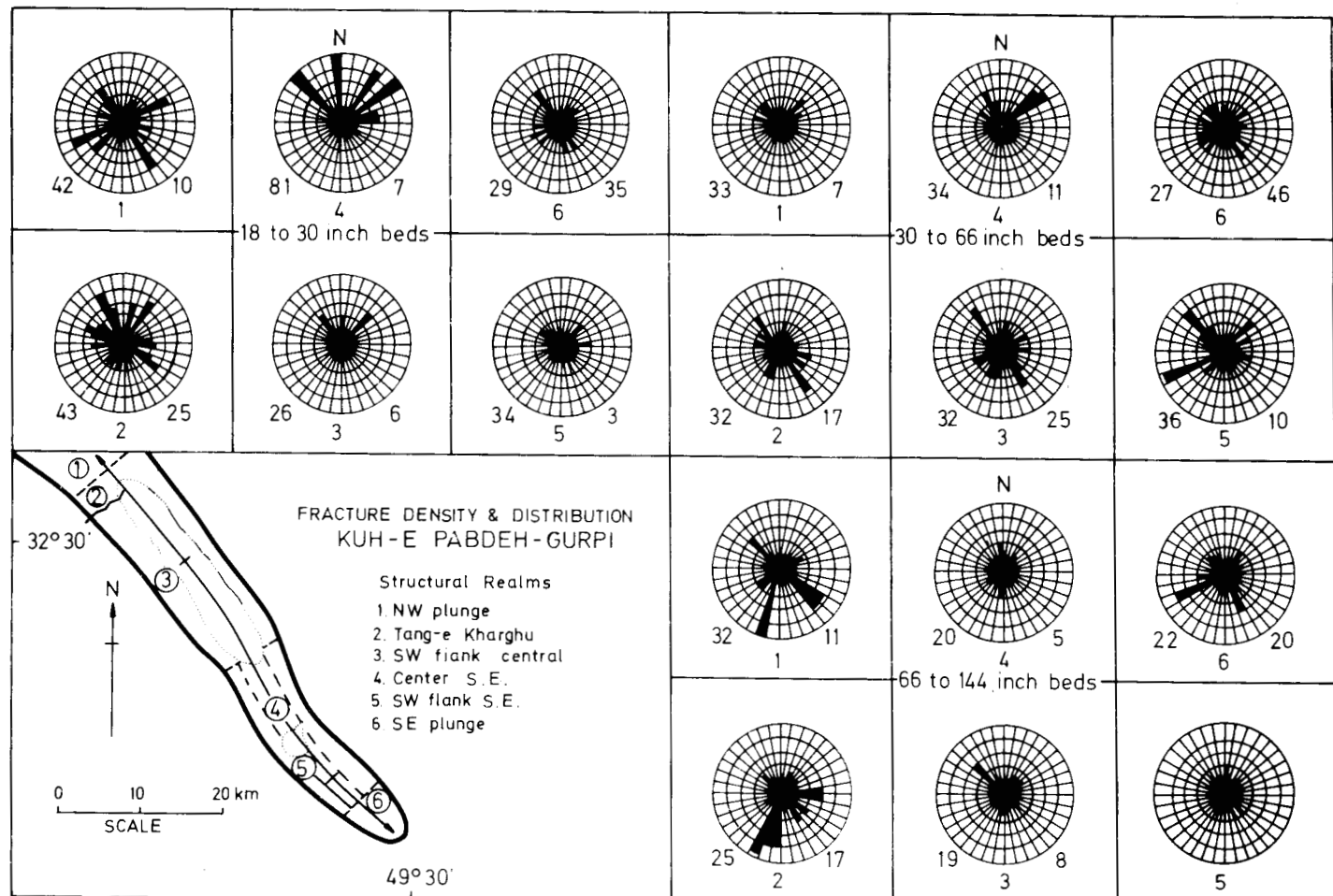
All three individual structures have been studied by McQuillan, but only the Kuh-e Pabdeh Gurpi, denominated Kuh 3, will be analyzed below.

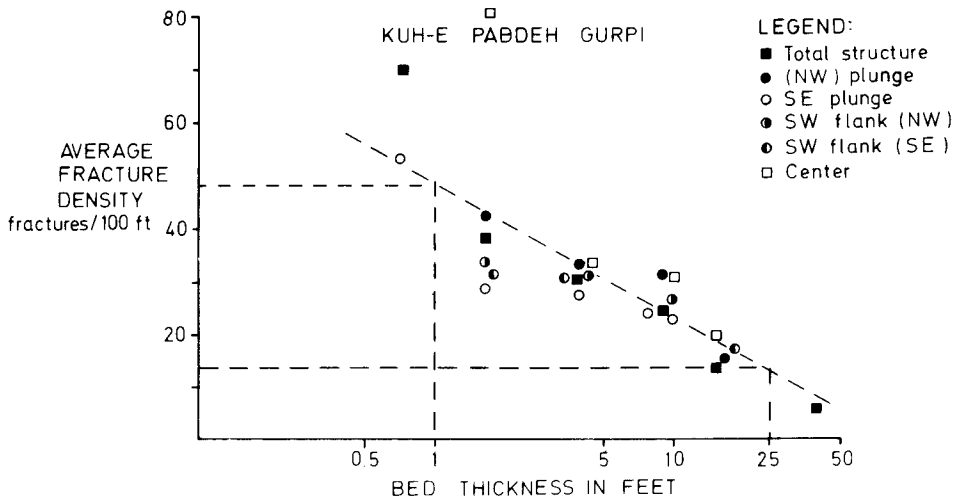
The Kuh 3 anticline is large, 24km × 8km, with flanks dipping gently except for the northern folding flank which changes abruptly. The axis shows a sinuous trace towards the south, and the Asmari limestone is breached, exposing Pabdeh and Gurpi formations. Data from 197 stations along nine fracture traverses have been used for further correlations. The indications from these data are that fracturing in the bedding classes range from the amount of 45 to 365. For each of the six realms examined and each bedding interval, the results obtained are recorded in figure 2.45. The fracture azimuth spread in all directions is obvious, which means that the fractures are related to entire structures. In azimuth classes 7 and 15, however, a preferred orientation is observed.

Another interesting relationship between average fracture density and bed thickness (figure 2.46) compares the reduction of fracture density with the increasing bed thickness. A trend in fracture variation, parallel or normal to the regional strike, or associated with the major fault system was not observed. A uniform distribution of fracture density over azimuth classes was observed; for a given thickness the fracture density seems constant. From the polar diagrams a preference is observed in classes 3 to 15 and 14 to 15, which may suggest the influence of late Tertiary folding. The

**Table 2.6**  
Observations of fracture density on Kuh 3.

## Totals for all Azimuth Classes

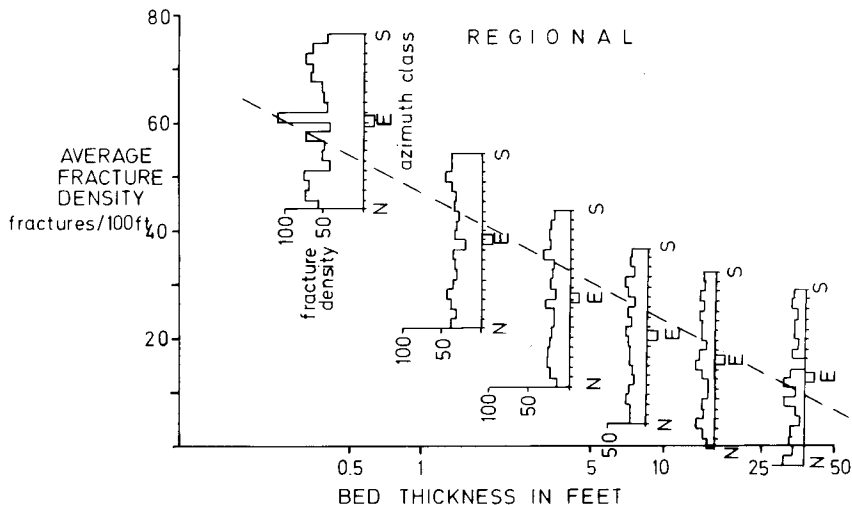
2.45 – Fracture density and distribution of Kuh-3 (courtesy of McQuillan<sup>12</sup>)



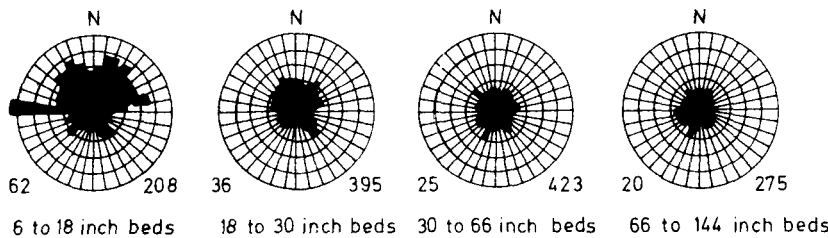
2.46 – Fracture density vs. thickness variation of Kuh (courtesy of McQuillan<sup>12</sup>)

constant fracture density for a given bed thickness suggests that the blocks may be calculated by an over simplification of pay-fracture density ratio. From figure 2.46 it can be observed that for 1 foot and 25 feet thicknesses, the layers have a fracture density varying from 48/100 feet to 16/100 feet.

Regional interpretation; from McQuillan's<sup>12</sup> study, where all data from the six structural realms have been cumulated, the following results have been obtained:



2.47 – Regional fracture density vs. thickness for various azimuth classes indicating fracture frequency (courtesy McQuillan<sup>12</sup>)



2.48 – Regional results from stereographic diagrams showing fracture density and distribution (courtesy of McQuillan<sup>(12)</sup>)

1. It is not definite that all fractures of Asmari limestone have a tectonic origin.
2. The small blocks and high number of fractures are typical in the case of a reduction in thickness if these parameters depend only on structural position.

A regional relationship is presented in figures 2.47 and 2.48 in connection with the cross-sections indicated on the map in figure 2,45, which shows a relationship between fracture density and orientation versus bed thickness.

## SYMBOLS

### Latin letters

A	– areal
a	– cube length
B	– angle
b	– fracture width
$\bar{b}$	– average fracture width
e	– fracture interval
FF	– fracture frequency
FINT	– fracture intensity
n	– thickness
i	– angle
L	– linear, length
Lo	– longitudinal fractures
m	– number of fracture systems
n	– number of fractures
P	– values referring to volumes
S	– surface
$\bar{S}$	– average surface
T	– transverse fractures
THF	– thickness frequency
V	– volumetric, volumes
$\bar{V}$	– average volume
x	– longitudinal fracture interval
y	– transverse fracture interval

### Greek letters:

$\alpha$	- angle
$\delta$	- angle
$\omega$	- angle

### Subscripts:

$B$	- bulk
$c$	- closed
$f$	- fracture
$f_D$	- fracture density
$o$	- open
$T$	- total

## REFERENCES

1. Stearns, D.W. and Friedman, M., 1972. Reservoirs in fractured rock. Am. Assoc. Petroleum Geologists. Reprint Series No. 21.
2. Leroy, G., 1976. Cours de Géologie de Production. Inst. Français du Pétrole. Ref. 24, 429.
3. Ruhland, R., 1973. Méthode d'étude de la fracturation naturelle des roches, associée à divers modèles structuraux. Geol. Soc. Bull., 26, 2-3, p 91-113. Strasbourg.
4. Romm, E.S., 1966. Fluid flow in fractured rocks. Nedra, Moscow.
5. Reiss, L. H., 1966. Reservoir engineering en milieu fissuré. French Institute of Petroleum.
7. Waldschmidt, W.A., Fitzgerald, P.E. and Lunsiorf, 1956.  
Classification of porosity and fractures in reservoir rocks. Bull., Am. Assoc. Petroleum Geologists. V. 40, No. 8.
8. Grenier, g., 1975. In-situ stress measurements in southwest Germany. Tectonophysics, Elsevier, Amsterdam.
9. Grunersen, P., Hirlemann, G., Janot, P., Lillié, F. and Ruhland, M., 1973. Fracturation of limestone overlaying the diapiric salt domes of São Mamede and Pragosa. Geol. Soc. Bull., p 187-217.
10. Ghez, P. and Janot, P., 1974. Statistical calculation of a matrix block volume in a fractured reservoir. Revue of French Institute of Petroleum, Paris. p 375-387.
11. Conrad, F. and Jaquin, C., 1973. Representation of a bidimensional fracture network for a probabilistic model to estimate matrix block magnitude. Revue of French Institute of Petroleum, Paris. p 843-890.
12. McQuillan, H., 1973. Small-scale fracture density in Asmari Formation of southwest Iran. Am Assoc. Petroleum Geologists. v. 57, No. 12, p 2367-2385.

This Page Intentionally Left Blank

# CHAPTER 3

## FRACTURED RESERVOIRS, CASE HISTORIES\*

In this chapter a number of well-documented and long-producing oil and gas fields are chosen to illustrate the importance and significance of natural fractures in reservoirs of different lithologies and trapping mechanisms. Accordingly, the chapter is divided into four parts describing fractured carbonate reservoirs, fractured silt/sand reservoirs, fractured shale reservoirs, and finally fractured basement reservoirs.

In the first part examples are taken from the Ain Zalah and Kirkuk fields in Iraq, and the Dukhan field in Qatar. Each provides an excellent example of the different effects on production of various types of *fracture poro-perm systems* within broadly similar litho-facies.

A fourth review looks at southwest Iran where an entire belt of oilfields, comprising what was one of the worlds most prolific oil producing regions, owe their existence to fracture systems developed in the Tertiary Asmari Formation.

The final examples of fractured carbonate reservoirs are taken from the Gela and Ragusa fields of southeast Sicily.

In the second, third and fourth sections an attempt is made to emphasize how widely fractured reservoirs occur. Several fields are chosen for their suitability as examples of prolific oil and gas production from zones which would otherwise be thought of as <<tight>> lithology or ineffectually structured.

### 3.1. FRACTURED CARBONATE RESERVOIRS

#### 3.1.1. General

Many well described examples of fractured carbonate reservoirs exist in the world today; J.E. Smith<sup>1</sup> reported the joint Mara-LaPaz fields of Venezuela to have a combined production in 1951 of 250.000 barrels of oil per day from the Cretaceous Colongollo Formations, where matrix porosity does not exceed 3% and permeability is normally only 0.1md. Production was, in this case, the result of fracture permeability. Braunstein, reporting on the Selma

---

\*By D. Nicklin

fractured chalk reservoir of the Gilbertown field in Alabama<sup>2</sup>, found that fracture porosity existed as a secondary trap for oil migrating from the older Eutaw sands. This zone of porosity, however, was only to be found close to a fault plain on its downthrown side. Step-out drilling away from the fault encountered sound, unfractured chalk which was totally dry.

In Mexico<sup>3,4</sup> the Tamaulipas limestone is so variably fractured that wells as closely spaced as 200 feet may have completely different production characteristics. Dry holes may be drilled adjacent to producers of rates up to 30,000 barrels per day of high gravity oil. Both in the Tamaulipas and Cretaceous Reforma reservoirs, enormous production is obtained from fractures and caverns.

In the Beaver River field<sup>5</sup> on the border of the Yukon and British Columbia territories of Canada, Davidson and Snowdon described what turned out to be an unhappy production experience with a substantial loss of reserves due in part to vertical fracture permeability. The field was once thought to be British Columbia's largest gas field, with recoverable reserves estimated at more than 1 TcH, but despite initial production rates of over 200 MM cf/D from six wells, rapidly increasing water influx caused a dramatic decrease in production in only five years to 3 MM cf/D, leading to the ultimate closure of the field in 1978. This resulted from a combination of the following factors. Firstly, the reservoir formation, made up of a thick sequence of highly altered middle Devonian dolomites, was a two porosity system consisting of a very low matrix porosity and a secondary fracture-vug porosity resulting from moderate to severe folding. This gave rise to high horizontal and vertical permeabilities. The matrix porosity probably amounted to 2% or less, whereas the secondary porosity varied from 0–6% or more. Secondly, the depletion mechanism was controlled by water influx which was not (as first thought) the result of water coning. Instead, the rapid influx was attributed to a steeply dipping permeable aquifer which, in combination with the high vertical permeability and small matrix pore volume, led to the trapping of high pressure gas in the dead-end fractures and vugs in the matrix as the water rapidly moved up the structure via the long reaching fracture systems.

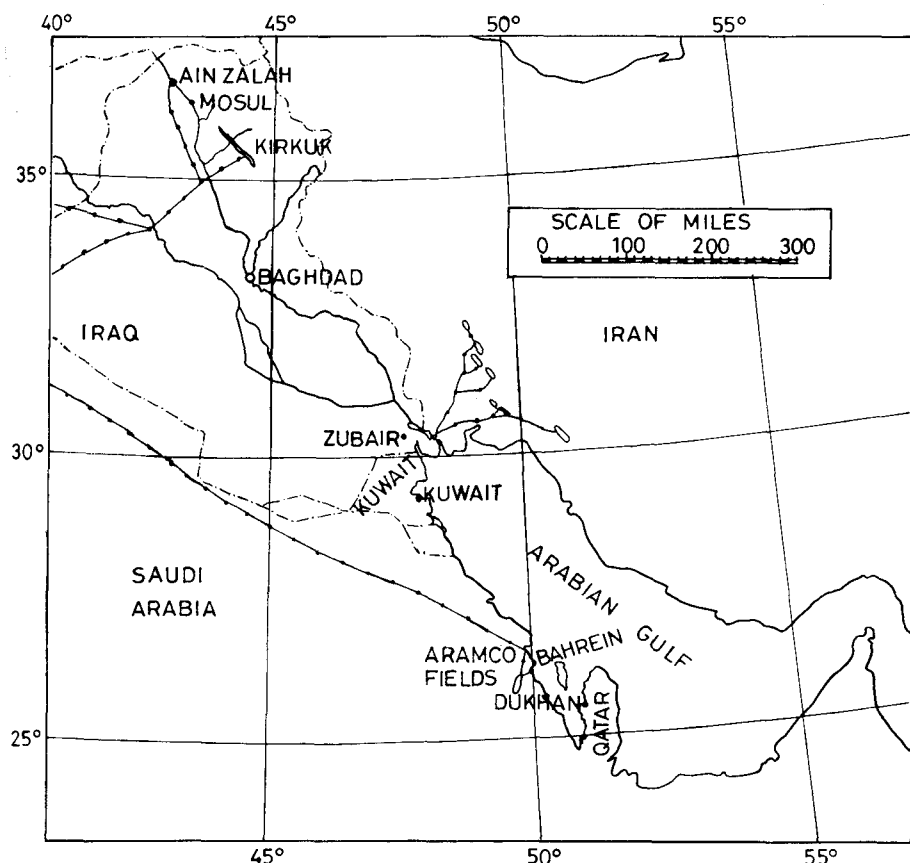
The effects of fracturing on production are not so disastrous by far, as is indicated by the following examples.

### *3.1.2. Ain Zalah field, Iraq<sup>6</sup>*

This oilfield exists today only as a result of a complex fracture system which provides both the porosity and permeability essential for oil production. The country rocks are otherwise low in porosity and entirely without permeability.

The field is located some 60 miles northwest of Mosul in northern Iraq (figure 3.1) on a surface anticline 12 miles long and 3 miles wide (figure 3.2).

Although the field was first discovered in 1939, development did not follow until 1947, and full production (27,000 barrels of oil per day) was not reached before 1952.

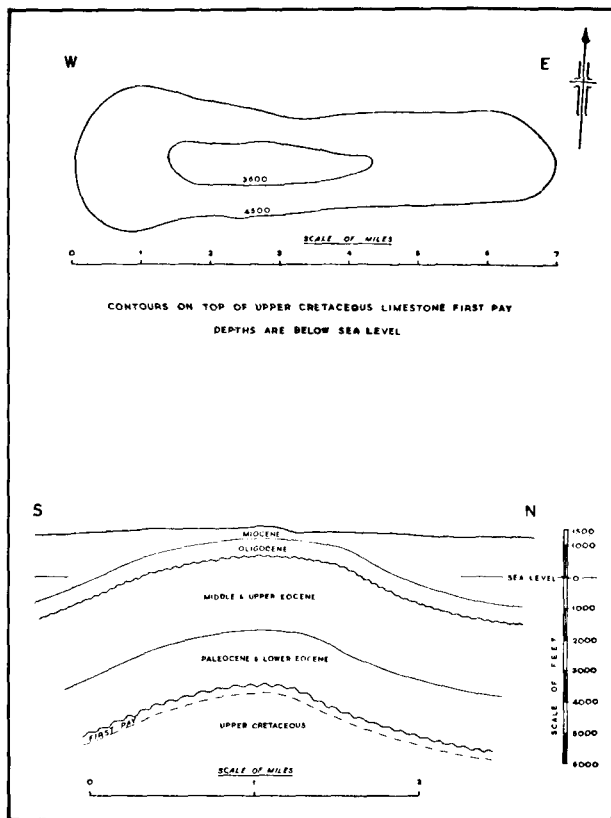


3.1 – General map of the Middle East showing the position of the Ain Zalah, Kirkuk and Dukhan reservoirs. (Daniel 1954.)

Prior to 1951 total production was obtained from 13 wells drilled into fractured marly limestones of upper Cretaceous age, named the *First Pay Reservoir*. Deeper drilling between 1949 and 1950 proved a lower reservoir in porous and fractured limestones of lower-middle Cretaceous age, then named the *Second Pay Reservoir*, separated from the first by approximately 600m of seemingly impermeable strata. Detailed testing, however, immediately indicated a connection between these previously assumed separate reservoirs, an explanation for which was found in the presence of rare, fine, feeder fissures.

A typical well section (figure 3.3.) illustrates the lithology and stratigraphy of the two pay zones and their relation to both over and underlying strata. The Ain Zalah oil most certainly originated in the middle Cretaceous and/or Jurassic horizons, but did not migrate to the higher reservoirs until after the fracturing had taken place.

Although both pay zones are essentially fractured reservoirs, the Second Pay Reser-



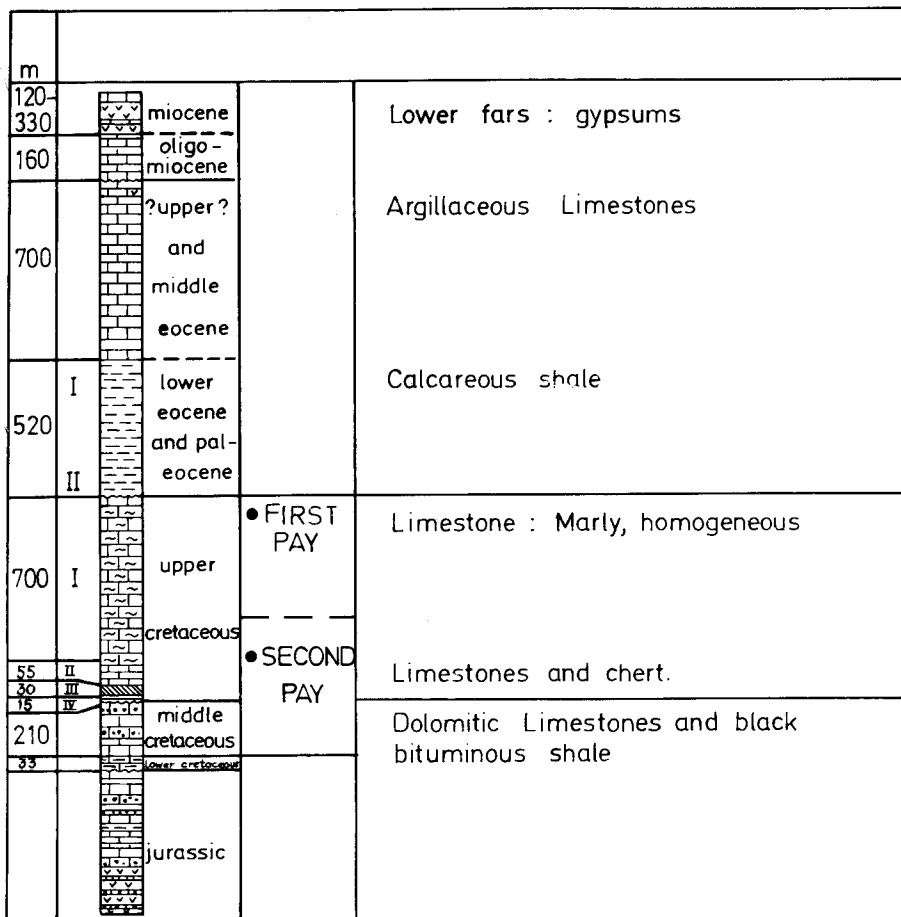
3.2 – Structural map and cross-section of the Ain Zalah Field. (Daniel 1954.)

voir is much thicker than the First Pay Reservoir, comprising a more heterogeneous lithology and a greater diversity of fractures. Despite the complexity of the fracture networks, three main types have been recognized. In their relative order of importance for oil production they are:

1. **Fracture networks filled or partially filled with calcite (found only below the base Paleocene unconformity)** and, although apparently multi-directional, they comprise three classes:
  - a. those at  $30^{\circ}$ – $35^{\circ}$  to the long axis of a core,
  - b. those vertical or near vertical, and
  - c. those at  $65^{\circ}$ – $70^{\circ}$  to the long axis of a core.

The density of these fractures varies between 6–12 per foot (brecciating the rock in places), and their width varies from 0.1–1.8 mm.

2. Fractures filled or partially filled with calcite and silica (found mainly in the Second Pay Reservoir), evidencing multiphased mineralization.



3.3 – Typical well section, Ain Zalah, N. Iraq.

3. Open fractures/joints (found in both pay reservoirs), generally several sets at different dip and strike angles and varying in width from 0.1–0.2mm.

In addition to recognizing these types, drilling has further shown that both the total amount of fractures of Types 1 and 2 and the number of fracture phases increase with age, whereas Type 3 is more or less evenly distributed throughout the column.

The origin of these fractures is explained by two phases of structural deformation which has selectively shattered the more brittle strata. The earliest period occurred between the upper Cretaceous and the early Paleocene when the First Pay Reservoir was gently uplifted and exposed to sub-aerial erosion. The highest frequency of mineralized fractures (Types 1 and 2) is found in those areas of maximum Cretaceous–Paleocene uplift. A later period

of uplift occurred between the upper Eocene and basal Miocene; but this was mild and the rocks remained relatively undisturbed. The latest and most significant movements which uplifted the present day anticline occurred between the Miocene and the Pliocene, and are believed to have caused the third type, or open joints.

In Ain Zalah the porosity of the unfractured rock matrix may vary between 0–11%, but the permeability is too small to record. Production, therefore, depends entirely on the fracture networks, a fact which is confirmed by drilling operations. Where equivalent unfractured rocks are encountered, experimental data<sup>2</sup> has established that a single fracture 1mm in width can produce at the rate of 7.000–10.000 barrels of oil per day.

### *3.1.3. Kirkuk field, Iraq<sup>6</sup>*

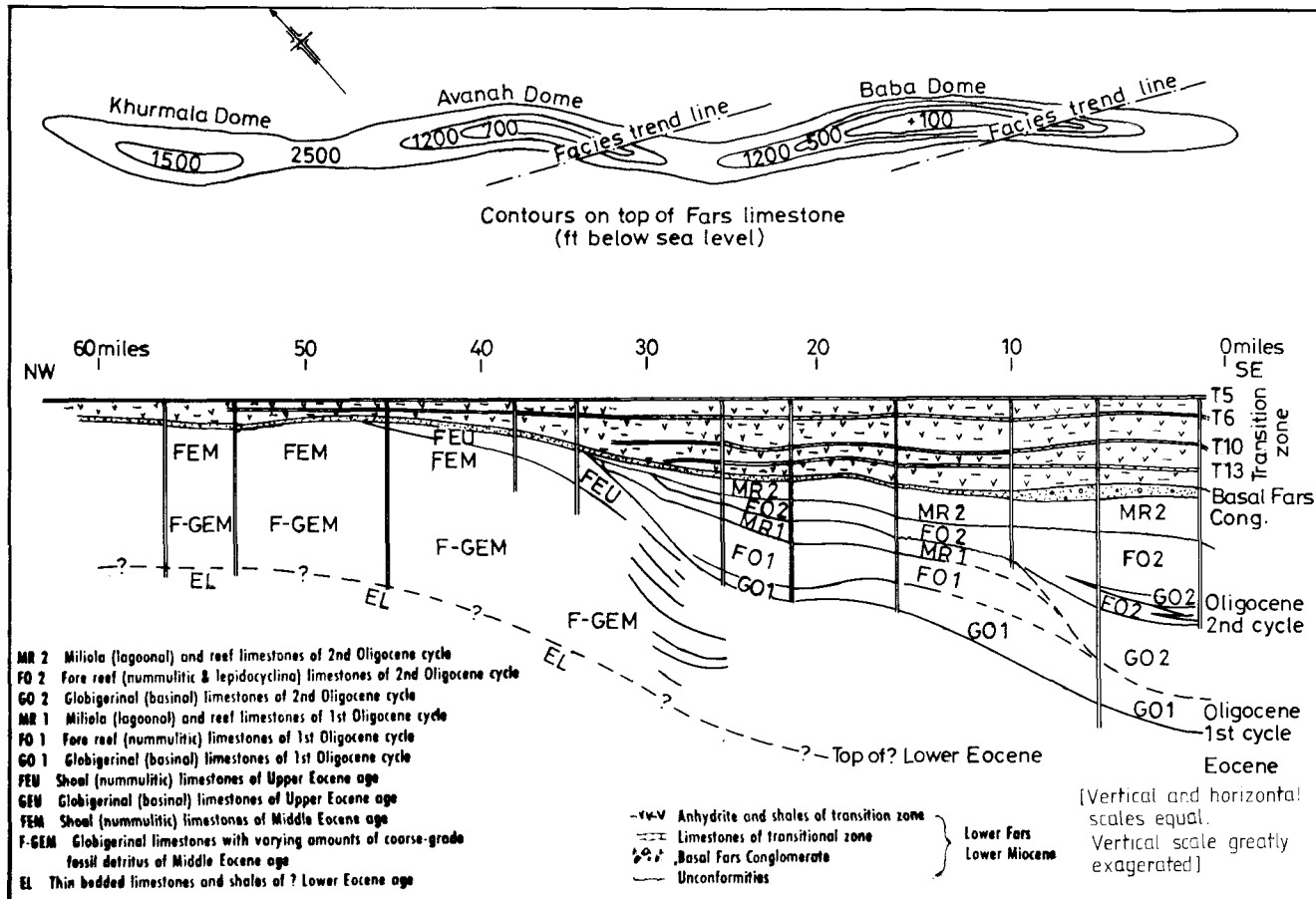
This field occupies a stratigraphically complex area comprising multiple facies developments of a complicated diagenetic history. Abundant and variable porosity and permeability exist which, although primarily lithology dependent, are enormously enhanced by the development of intensive faults, fractures and joints, this combination of uncommonly high porosity and permeability gives rise to enormously high and continuous production.

The field lies 122 miles north of Baghdad (figure 3.1), occupying a large, sinuous anticlinal structure approximately 2–3 miles (3.2–4.8 km) wide and 63 miles (100 km) long. Figure 3.4 illustrates the structural and stratigraphic configuration of the three domes which comprise the structure: Khurmala, Avanah and Baba.

The discovery well was drilled in 1927, and by 1939 a total of 54 wells outlined the field. By 1954, 111 wells had been drilled, out of which 48 were plugged and abandoned, 46 were producers, with 17 observation wells, 2 gas and 15 water wells.

Figure 3.5 illustrates a typical reservoir section with the stratigraphy and lithology; the maximum reservoir thickness is generally taken as approximately 1,000 feet comprising six main facies types:

1. *Transition zone limestone*. These are normally too thin and variable to be included in the gross reservoir, though free communication with the main reservoir exists via fractures.
2. *The Basal Fars conglomerate*. These are normally non-porous and impermeable, but produce where fractured.
3. *Back-reef and reef limestone facies*. These are highly fossiliferous, but completely cemented. Blue clays of the Lower Fars now infill cavities and fissures in the upper part of these beds, sealing any possible porosity. With recrystallization, minor matrix porosity occurs, but production is only possible where the rock is cut by fractures penetrating deeper, more saturated formations.



3.4 – Stratigraphic diagram along the axis of the Kirkuk structure with structure map showing the three domes. (Daniel 1954.)

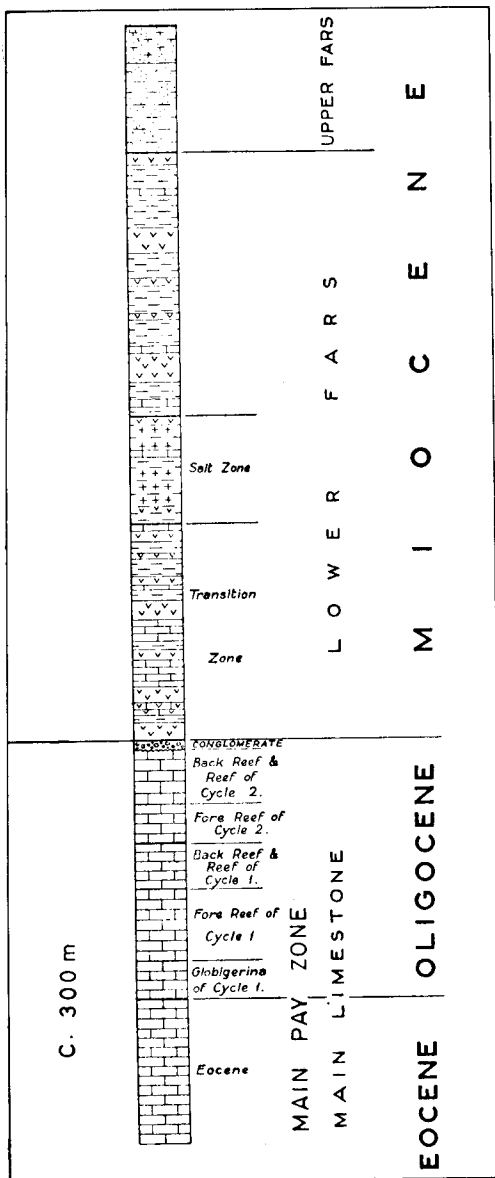
4. *Fore-reef and shoal facies.* These are the best reservoirs, with large volumes of apparently unaltered rock with high porosity and rich in oil; where selective recrystallization has taken place, porosity varies from vugular to intergranular, with wide ranging differences in size and permeability.
5. *Globigerinal limestones.* These are thinly bedded basinal facies with much less porosity; good production only exists along open, closely spaced bedding planes.
6. *Globigerinal limestones with coarse grade fossils.* These may have frequent heavy oil saturation due to selective recrystallization and/or the presence of fore-reef talus.

Most of the oil in the Kirkuk field is contained in fabric selective porosity; non-fabric selective porosity or macrovoids comprising fissures, large vugs, fractures and caverns account for only minor amounts. Permeability and production, however, are almost entirely along these channels, a fact which was indicated quite early in the history of the field, both by large losses of drilling fluids, poor core recovery (less than 30%), and the early discovery through production testing of very free communication throughout the entire reservoir. Relatively little, however, is known about the history and nature of these macro-voids. A broad five-fold classification describes the various types:

- a. True faults; indicated by slickensiding, brecciation, and missing sections between wells. Normally post-transition zone age with throws up to 650 feet. Very little is known of their true strike and/or hade.
- b. Tension tear fissures; confined to the upper parts of the main limestone along a hinge-zone between the steep flanks of the structure and its relatively flat top. They are thought to be younger than the transition zone.

Table 3.1.

<i>Stratigraphic Position</i>	<i>Number of Feet of Well Depth per Observed Joint</i>		
	<i>K.30</i>	<i>K.19</i>	<i>Average</i>
MR 2	11.1	5.2	8.0
FO 2	5.0	6.7	5.7
MR 1	3.4	—	
FO 1	3.2	4.6	4.0
GO 1 and Eocene	—	Steep angle 3.0 Flat angle 1.5 Total 1.0	



3.5 – Typical well section, Kirkuk, N. Iraq. (Daniel 1954.)

- c. Vertical caverns; normally found in the back-reef facies, resulting from pre-Lower Fars karst erosion, now clay filled, but probably once the routeways for meteoric waters percolating down into the underlying fore-reef facies.
- d. Horizontal caverns; found mainly in the fore-reef facies.
- e. Jointing; the smallest but most abundant and important of all the fractures. The average frequency of joints for each of the reservoir strata is given in table 3.1.

The flatter crestal areas of the structure have a preponderance of high angle joints; the steeper flanking beds have more medium angle joints. Average widths approximate 0.2 and 0.1mm and may extend vertically in cores for over 1.0m. Their faces are dependent on the rock type but, in general, the harder, porcellanous and fine grained rocks have the smoothest faces. These joint patterns are amplified, particularly in the globigerinal facies where additional passageways are provided by the low-angle bedding planes. Productivity in these beds depends entirely on the size of the matrix blocks (normally 3' X 1½' X ½').

f. *Stylolites*; generally rare and not of great significance.

Although these various macro-voids may be related to separate origins, the formation of the production-significant faults and joints is attributed to the end-Miocene uplift of the present structure. Prior to this uplift, oil existed but was restricted to a number of largely stratigraphic traps with a far inferior permeability. Although these were filled with oil migrating from the syncline to the southwest, considerable leakage probably occurred due to the paleogeography and lack of effective seal. With the rapid folding and fracturing a new phase of migration into the newly formed anticline occurred. Furthermore, new oil migrating along the deep-rooted faults mixed with old oil, setting up convection currents which upset the hydrostatic gradients and destroyed any remnants of previous fluid stratification.

Production in the Kirkuk wells today can be as large as 30,000 barrels of oil per day for a bottom hole differential pressure of only three or four psi, and communication throughout the field is so free that equal pressure changes are instantaneously recorded throughout most of the field whenever flow adjustments are made.

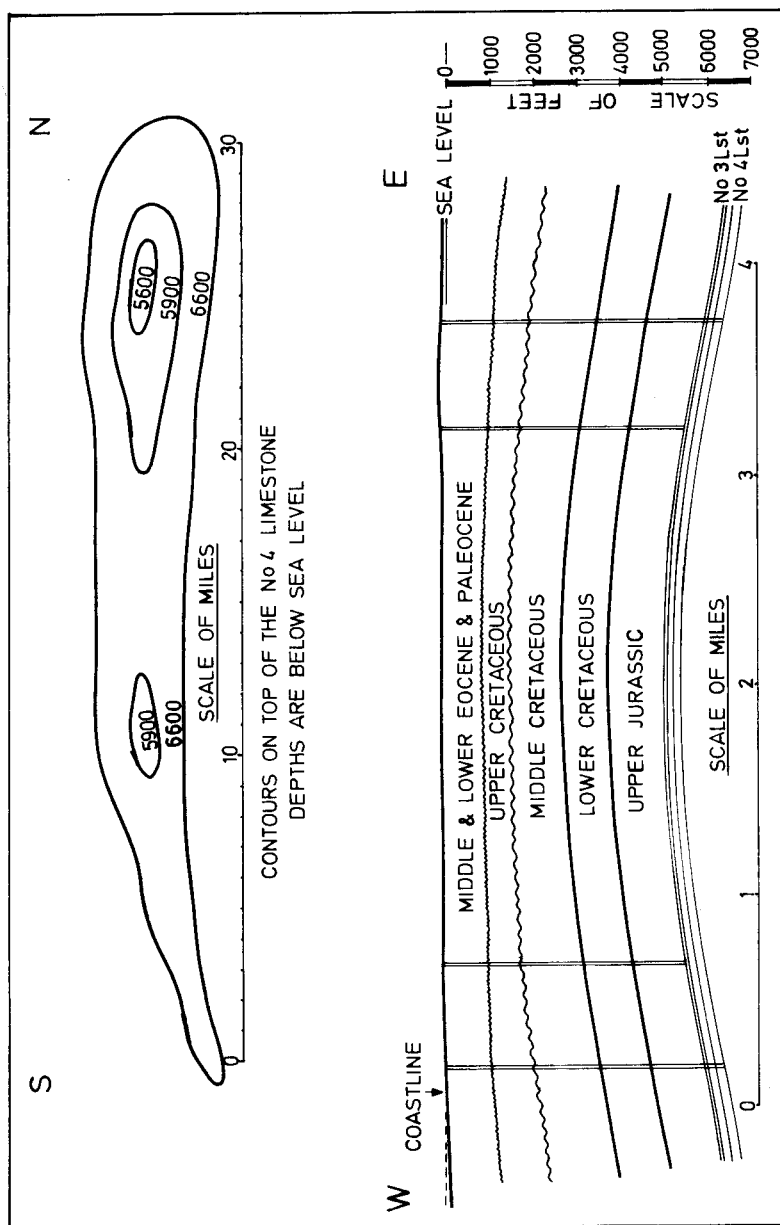
### *3.1.4. Dukhan field, Qatar<sup>6</sup>*

In the Dukhan field, however, fracturing plays a much lesser role than in the first two examples. In this case, the limestones which comprise the reservoir are moderately to highly porous and permeable, with a limited number of joints effecting only minor vertical drainage and almost no lateral movement.

The field occupies a low symmetrical anticline, 31 miles (49.6km) long by approximately 3 miles (4.8km) wide (figure 3.6), situated on the western side of the Qatar peninsula.

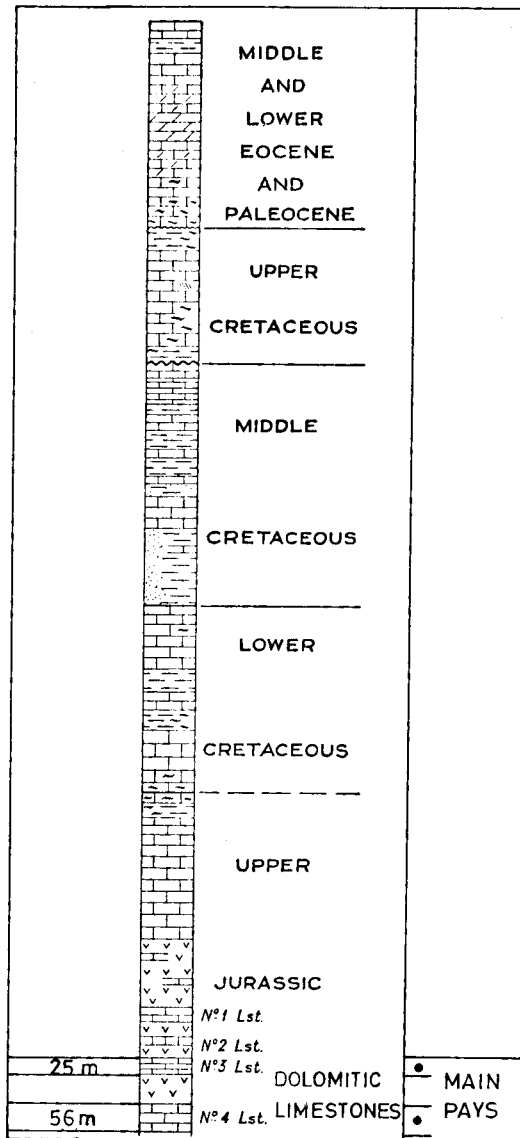
Although it is a gentle structure with flank dips of only 10°, it appears to have grown slowly (originating as early as Jurassic time) with oil migration and entrapment taking place in the later Cretaceous.

A discovery of oil was made in the first well on the structure in 1938–1939, following which, operations were suspended for the duration of the war. Between 1947–1953, 27 wells were drilled, including 3 water observation wells and 1 gas



3.6 – Structural section and map of the Dukhan field, Qatar. (Daniel 1954.)

observation. Figure 3.7 illustrates a typical well section together with the lithology, stratigraphy and pay intervals: the No. 3 and No. 4 upper Jurassic limestones. These are separated, without any vertical communication, by 63 feet (19.2m) of impermeable unfractured anhydrite and each reservoir has quite different properties. In



3.7 – Typical well section: Dukhan field, Qatar. (Daniel 1954.)

both pays the average core recovery has exceeded 95%, with the result that a great deal is known about each pay interval.

The *No. 3 limestone*, both under and overlain by anhydrite, has a more or less constant thickness of 84 feet (25.5m) over a very wide area, and is subdivided into three units comprising various limestones and/or dolomites. Porosity averages 16%,

with permeabilities of 30 mD parallel to the bedding and 15 mD perpendicular to it. Notably in the finer textured beds a clearly defined joint system is observed, cutting the rock at right angles to the bedding and parallel to the strike. Joints have an average frequency of 1 per 9 feet (2.7m) of core, and joint openness is estimated as 0.1mm.

In contrast, the *No. 4 limestone* averages 185 feet (56.4m) thick, is subdivided into seven parts, and underlain by fine grained, dense, pale grey limestones. It has an average porosity of 21% with permeabilities of 75 mD parallel to the bedding and 40 mD perpendicular to it. Jointing similar to that of the No. 3 limestone is also recorded, though a higher frequency of 1 joint per 4.5 feet (1.3m) is recorded.

The origin of the joints is attributed to an early stage in the tectonism which gave rise to the anticline (possibly before the oil accumulation). This was mild, however, resulting in correspondingly narrow openings, while less brittle rocks, such as the anhydrite seals, simply yielded to the flexure without rupture. Their significance in the two reservoirs is not fully understood, and they may have different effects in each reservoir.

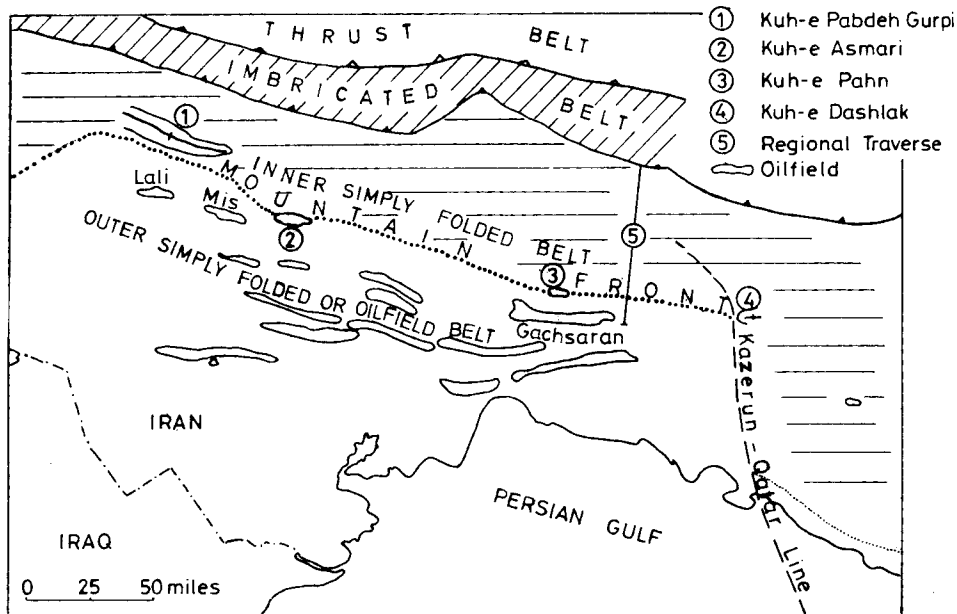
In the No. 3 limestones 75–80% of the oil comes from the lowermost 20 feet (6.0m), initially casting doubt on the drainability of the upper 65 feet (19.8m). Testing, however, proved that pressure remained constant throughout the interval and that top to bottom drainage could be expected, probably as a result of vertical passage via the joints. Horizontal flow, however, proved far less amenable.

In the No. 4 limestone, however, less is known of the effect of the joints. That they assist flow is obvious, but where the joints are no wider than the matrix porosity and permeability (common in the No. 4 limestones), their role may be insignificant. In fact, a harmful effect is suggested since they extend downwards into the underlying limestones, providing routeways for coning waters.

Dukhan may, therefore, be described as a field in which fractures play only a nominal role. The formation is moderate in the first two examples. Efficient drainage of Dukhan, therefore, requires a fairly close spacing of wells, which contrasts significantly with Kirkuk and Ain Zalah.

In Ain Zalah the reservoir has extremely low matrix porosity and permeability, but has prolific production due entirely to the presence of dense and extensive vertical fracture systems, along which oil has migrated from deeper, older horizons. Fracturing is so extensive, in fact, that it has been suggested that two or three correctly placed wells could effectively drain the entire field.

In Kirkuk, however, the lithology is characterized by intervals with extremely high matrix porosity and permeability in addition to that resulting from the extensive fracture systems. Consequently, this field yields enormous production from wells with a two mile wide spacing, and it is again suggested that the communication throughout the field is so free that relatively few wells would eventually drain the entire structure.

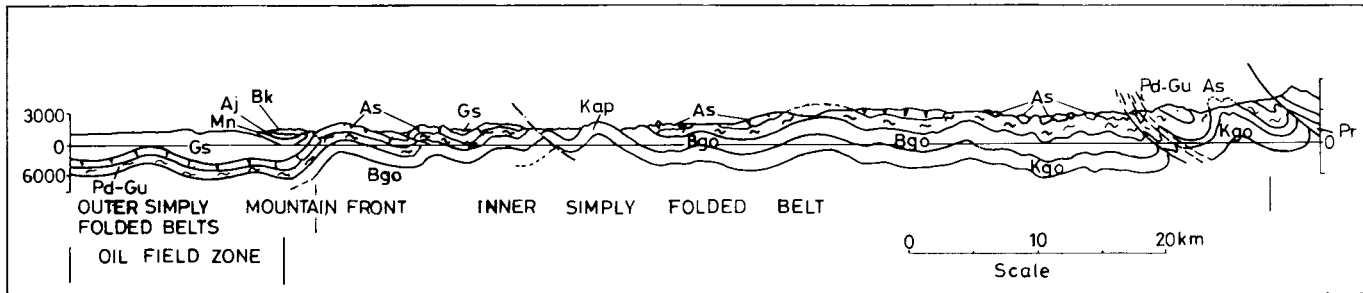


3.8 – Oilfields along the south west, simply folded belt of the Zagros Mountains. (McQuillan 1973.)

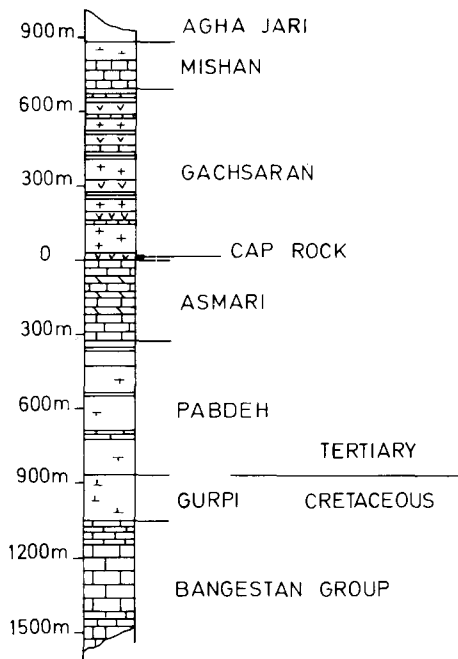
### 3.1.5. Southwest Iran, The Asmari Formation<sup>7,8</sup>

The greatest percentage of Iranian oil reserves occurs in a number of fields lying along the southwest flank of the Zagros Mountain chain (figures 3.8 and 3.9), occupying a belt of gently folded en-echelon anticlines running parallel to the main mountains. From early Paleozoic to late Miocene time this area has been the site of a stable shelf with more or less uninterrupted marine sedimentation. Consequently, a considerable accumulation of sediments exists, comprising mainly limestones, shales and marls. During the Triassic, a tectonic event divided Iran along a line which was later to become the Zagros Thrust Zone. To the southwest of this the marine trough continued, but to the northeast there was uplift and considerable folding, resulting in several long periods of sub-aerial erosion and large unconformities at several horizons within the Tertiary and Mesozoic record.

The marine sedimentation of the southwest trough, meanwhile, remained undisturbed. It was not until the violent uplift of the Zagros mountains in the late Tertiary that this continuous marine deposition was ended. The onset of tectonism brought a change in sedimentary environment, evidenced by the Miocene/Pliocene accumulation of interbedded evaporites, sandstones, siltstones and marls. Shortly thereafter, as the intensity of folding increased, this southwest basin was uplifted and gently folded into the undulating anticlines and synclines seen today. This combination of



3.9 – Cross-section through the south west Zagros Mountains, relating the oilfield belt to the main foldes areas. Formations are indicated as: Bk = Baktyari Formation, Aj = Agha Jari Formation, Mn = Mishan Formations, Gs = Gachsaran, As = Asmari Formation, Pd-Gu = Pabdeh and Gurpi Formations, Bgp = Gangestan Group, Kgp = Khami Group, Tr = Triassic, Pz = Paleozoic. (McQuillan 1973.)



3.10 – Generalized lithology above and below the Asmari limestone to the south west of the Zagros mountains. (Schlumberger.)

circumstances brought into existence a fortunate configuration of thick reservoir rocks, abundant source beds, excellent cap rocks, and large anticlines, and has given rise to one of the worlds most significant oil producing areas.

The main reservoirs of southwest Iran occur in the extensively fractured carbonate rocks of the Tertiary Asmari Formation, with other accumulations in older Cretaceous horizons within the Bangestan Group. The Asmari is of Oligocene/Miocene age, comprising some 300–370m of locally dolomitic, shallow water, neritic limestones which (apart from some sandstones) developed in the southwest of the basin and with a fairly uniform lithology over wide areas (figure 3.10). This unconformably overlies marls and marly limestones of the Pabdeh Formation, and is capped by the conformable anhydrites and limestones of the Gachsaran Formation. The primary porosity ranges from 5–25%, with a very low matrix permeability seldom exceeding 2 mD. This would, at first glance, appear to preclude the Asmari as reservoir potential; however, the Asmari is so extensively fractured that permeabilities may commonly exceed 5 darcys.

McQuillan<sup>4</sup>has examined these fractures in great detail in several well exposed areas within the gently folding belt of the Zagros mountain front. He identified two major and two minor sets of fractures, which are showing a more or less constant fracture density, regardless of structural setting, wherever beds were of similar

thickness and lithology; furthermore, he discovered that density would only vary as an inverse logarithmic function of bed thickness. Fracture orientation was found to be widely varied, with only a slight preference for the regional trends related to the late Tertiary folding and uplift of the Zagros mountains. His conclusion was that the generally accepted tectonic theory for the origin of the fractures should be rejected, and that they could be explained, instead, as features occurring soon after deposition of the sediments (Cook<sup>4</sup>), probably resulting from shock waves. Fracture orientation was thereby explained by the morphology of the depositional surface and the physical properties of the beds, with the later Tertiary folding exploiting only the appropriately orientated sets.

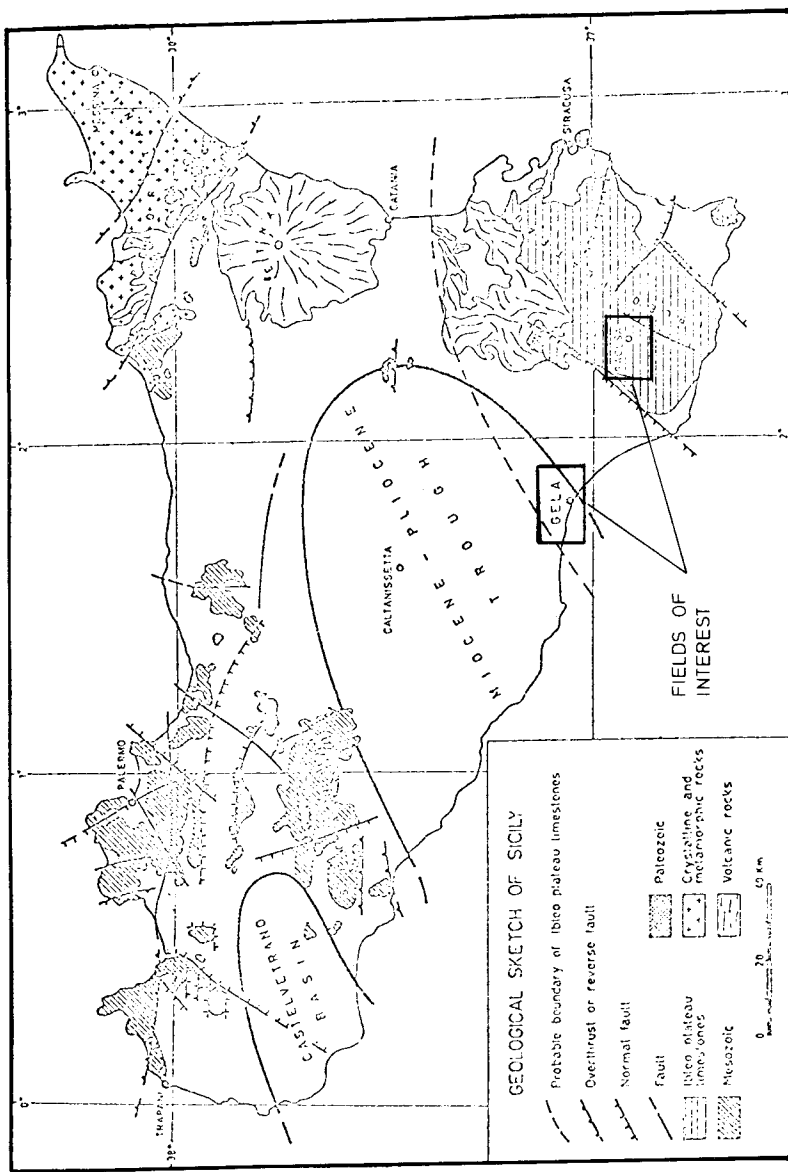
Whatever their origin, they alone explain the unusually high production of the Asmari reservoir, their frequency and dimension defining the major production zones. These networks have divided the limestone into variously sized blocks from whose primary porosity, hydro-carbons are readily transferred to the free-flowing fracture-formed conduits, which are apparently of far reaching communication in both depth and lateral extent. Both the initial migration of the oil, its emplacement, and latterly, its extraction, owe their origins to the fracturing of the Asmari limestone.

### *3.1.6. Gela and Ragusa Fields, Sicily<sup>9,10</sup>*

In contrast to the ease with which the large Middle Eastern reservoirs were discovered, it was only after nearly a century of fruitless exploration that the next two examples were discovered. The two fields, Gela and Ragusa, both lie in south-eastern Sicily (figure 3.11), the former on the depressed western margin of the Ibleic Plateau, and the latter in the area around the town of Ragusa.

In Gela field is situated on a Mesozoic anticline in which several secondary highs are mapped, presumably representing reef growths. The first well on this structure was drilled in 1955 with the primary objective of Triassic dolomites at around 3,000m depth. The main pay was as predicted by seismic survey of the area, with approximately 160m of brecciated and fractured dolomites, between 3,200 and 3,400m. These were overlain by the upper and/or middle Triassic black shales, which consist of interbedded layers of black or grey variegated clays which form the cap rock (fig. 3.12). Thin dolomitic limestones with abundant vugs and fractures form a number of secondary pools above the main reservoir.

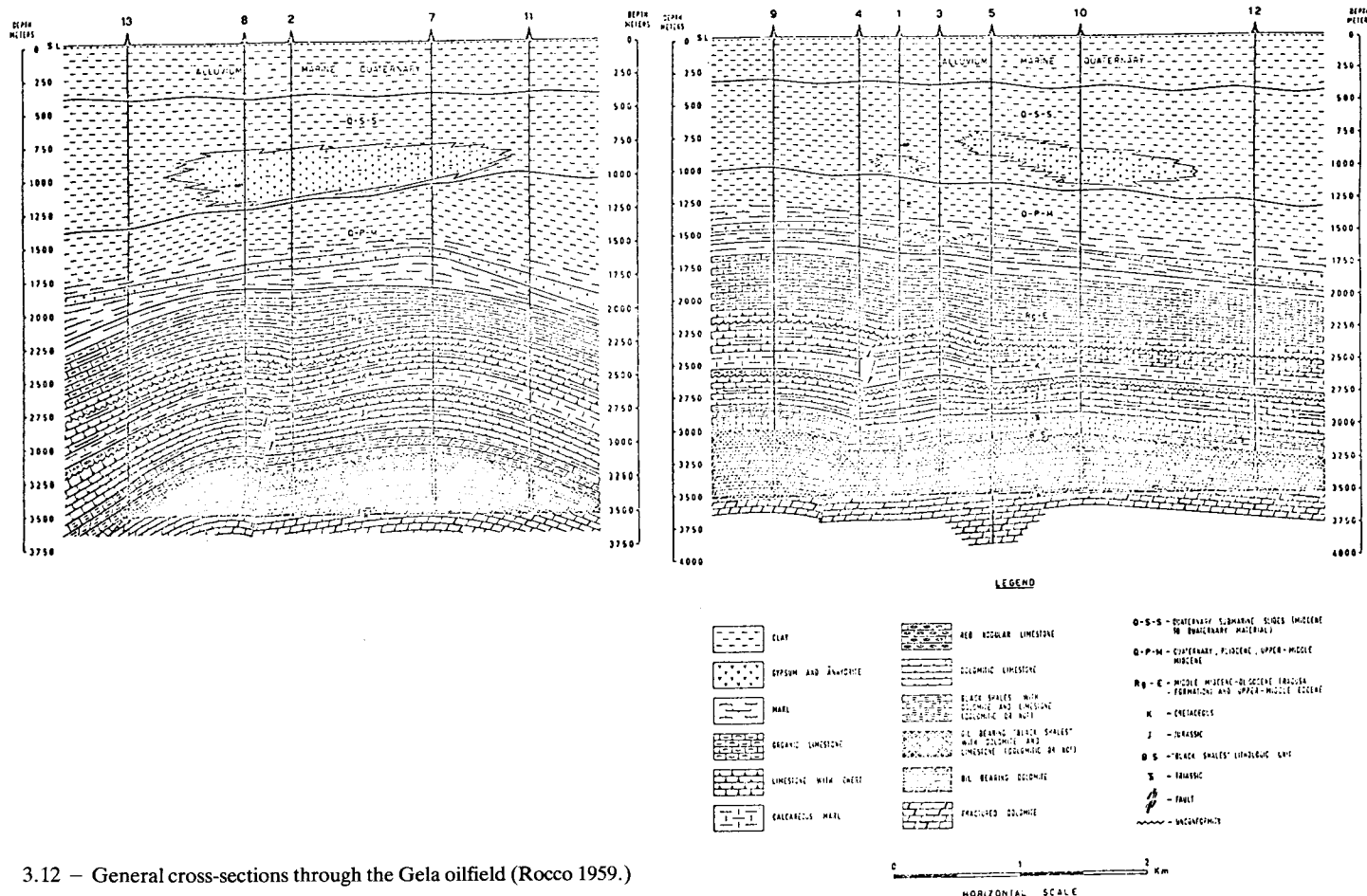
The porosity and permeability within these reservoirs are governed by fractures. Porosity may range between 3–5% with permeabilities of up to 10 darcys. By comparison, the matrix permeability may only be between 0.01–0.1md. Brecciation often occurs where dense networks of fine fractures interconnect with long-reaching feeders, enabling flow rates of up to 1,000 barrels of oil per day, despite high viscosity-low gravity oil of 7.3° API. The origin of these fractures is ascribed to



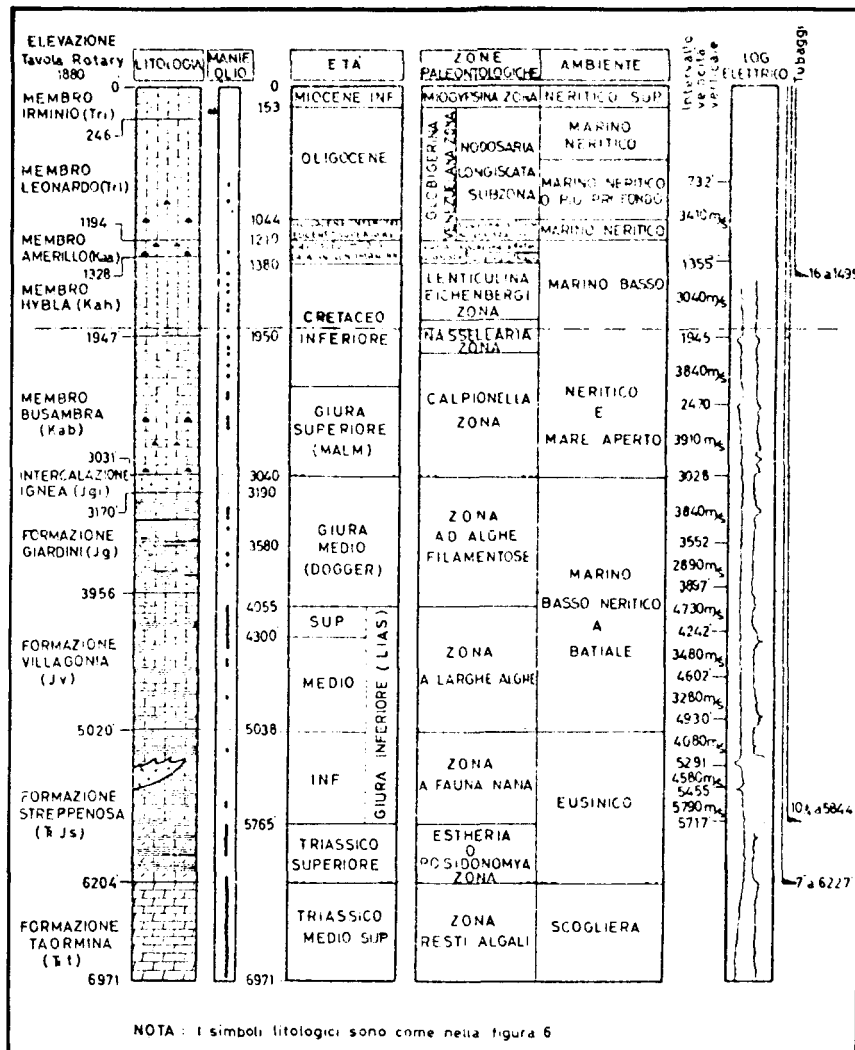
3.11 – Map of Sicily showing Gela and Ragusa Fields. (Rocco 1959.)

tectonic uplift of the area towards the end of the Cretaceous period followed by a gradual subsidence from Eocene to Pliocene.

By contrast, the Ragusa field lies within the central part of a *horst* block extending for some 30km in a north-northeast, south-southwest direction and bounded on each side by normal faults.



3.12 – General cross-sections through the Gela oilfield (Rocco 1959.)



3.13 – Typical well section in the Ragusa oilfield (Kafka and Kirkbride<sup>11</sup> 1959).

The first well in this structure was drilled in 1953, penetrating some 750 feet of productive dolomite of the middle Triassic, Taormina dolomite formation. This is overlain by an upper Triassic/lower Jurassic cap-rock called the Streppenosa shales (figure 3.13).

The production controlling fractures, in this case, result from the repeated uplift of the Ragusa structure during major tectonic phases in the upper Jurassic, upper Eocene and late Miocene, each phase of which has been related to the growth of deep seated igneous intrusions. Permeabilities exceeding 1 darcy have been experienced in this field.

### **3.2 FRACTURED SILT/SAND RESERVOIRS**

#### **3.2.1. General**

From the preceding examples it becomes apparent that the variety of ways in which fractures have effect is very high. Each reservoir must be considered separately for its own particular problems, each one being a near-unique research problem; but fracturing may exist in all types of lithology, and the following examples illustrate similarly significant effects in sandstones, siltstones and shales.

Many fractured sandstone reservoirs are documented within the North American continent, and the Altamont trend of the Utah Unita Basin<sup>11</sup>, is one such example.

Production, in this case, is obtained from fine grained Tertiary sandstones, carbonates and calcareous shales, all of which have low matrix porosities and permeabilities.

The reservoir sands have porosity ranges from 3–7% with permeabilities of less than 0.01 md, and yet production yields initial flows in excess of 1,000 barrels of oil per day from an optimum well spacing of 640 acres.

#### **3.2.2. Spraberry Trend, Midland Basin, West Texas**

A second, significant example is the Spraberry Trend of the Midland Basin in West Texas. It is claimed by some<sup>12</sup> that the Spraberry reservoir is unique. Shales constitute 87% of the reservoir column and there are virtually no typical structural traps; and yet in a single month this reservoir produces 2,744,156 barrels of oil from 1,558 wells, most of which was the result of natural fractures.

This phenomenon exists in the Spraberry Formation where a so-called *fairway*, occupying a low homoclinal, extends north-southwards for 150 miles with a width of some 50–70 miles at an average depth of 6,800 feet (2,070 m).

Exploration interest in this area arose in the early forties, and following an unsuccessful exploration well in 1944 the first discovery well was completed in early 1949, with a production of 319 barrels of oil per day. This was closely followed by a number of wells on various license holdings in the area, each producing from thin, apparently *tight* sandstones. An exploration rush followed, and by May 1, 1952, 1,630 producing wells had been completed, outlining a productive area known as the fourcounty area, which covered parts of the Midland, Glasscock, Upton and Reagen counties (figure 3.14). The stratigraphy of the Spraberry is shown in table 3.2 and a typical well section is given in figure 3.15.

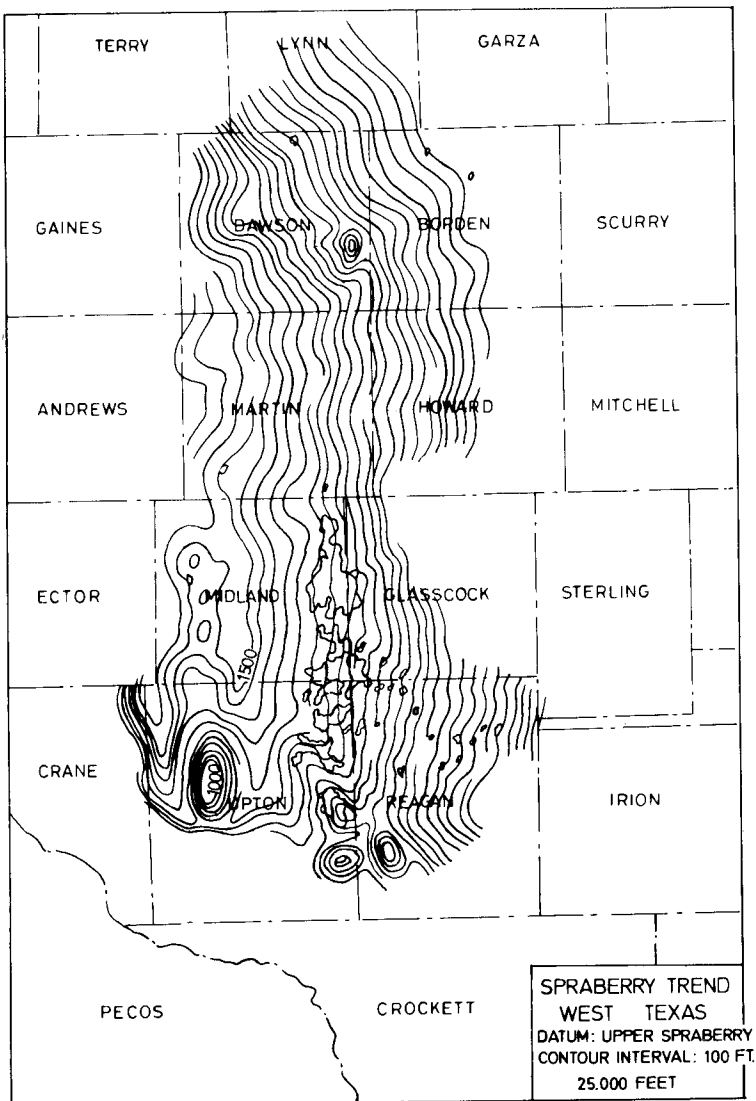
Table 3.2 Spraberry stratigraphy

Stratigraphy	Depth	Lithology
Quaternary		
Cretaceous	488 m (1600 feet)	Sandstone and red-beds
Triassic		
<i>Upper Permian</i>		
Ochon series		red beds + halite + polyhaline + andrite
<i>Middle Permian</i>		
↓		
~ Guadelupe Series	518 m (1700 feet)	interbedded dolomites and clastics
~ Upper Leonard Series (cleastock group)	915 m (3000 feet)	interbedded dolomites <b>black shale and sandstone</b>
~ Lower Leonard Series (Spraberry Formation)		

Typically, the Spraberry Formation comprises approximately 100 m (305 feet) of various black, carbonaceous shales or silty shales, siltstones or silty sandstones, and occasional thin limestones or dolomites, the total of which has been subdivided into the following three units:

1. *Upper Spraberry*; comprising 13.7m (45 feet) of massively bedded siltstones, 1m limestone and 83.8m (275 feet) of black shales.
2. *Middle Spraberry*; comprising 8.0m (26 feet) of thinly bedded siltstones, 0.3m limestone and 102m (334 feet) of black shale and silty shale.
3. *Lower Spraberry*; comprising 18.2m (60 feet) of thinly bedded siltstones, becoming more massively bedded towards the base, and 74m (242 feet) of black shale and silty-shale.

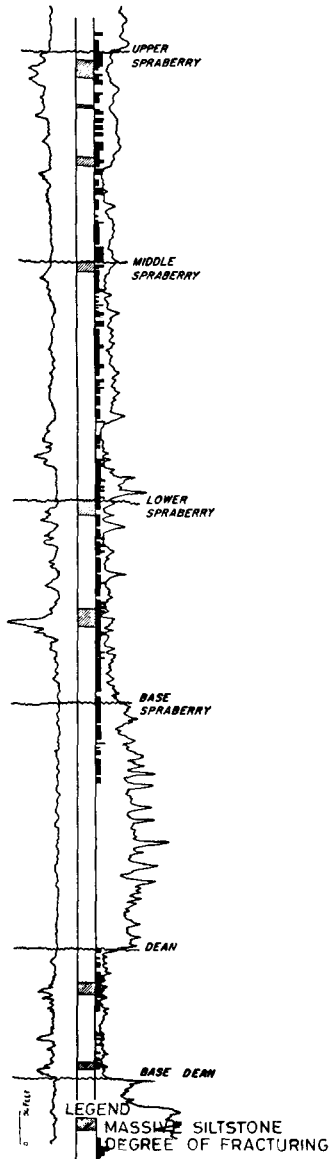
Regionally, these sediments and their equivalents were deposited in an open marine environment stretching over the entire Midland Basin. However, the predominance of euxinic facies within the four county area clearly indicates a subenvironment in which toxic bottom conditions prevailed. Attempting to understand the distribution of the oil in this context, the early workers in this area related the siltstones to a *shoreline* trend. As well coverage increased and the true extent of the facies became apparent, this philosophy was rejected and the productive area was eventually defined as an anomalously triangular area which could not be related to any such



3.14 – General map: Spraberry Trend, West Texas. (Wilkinson 1952).

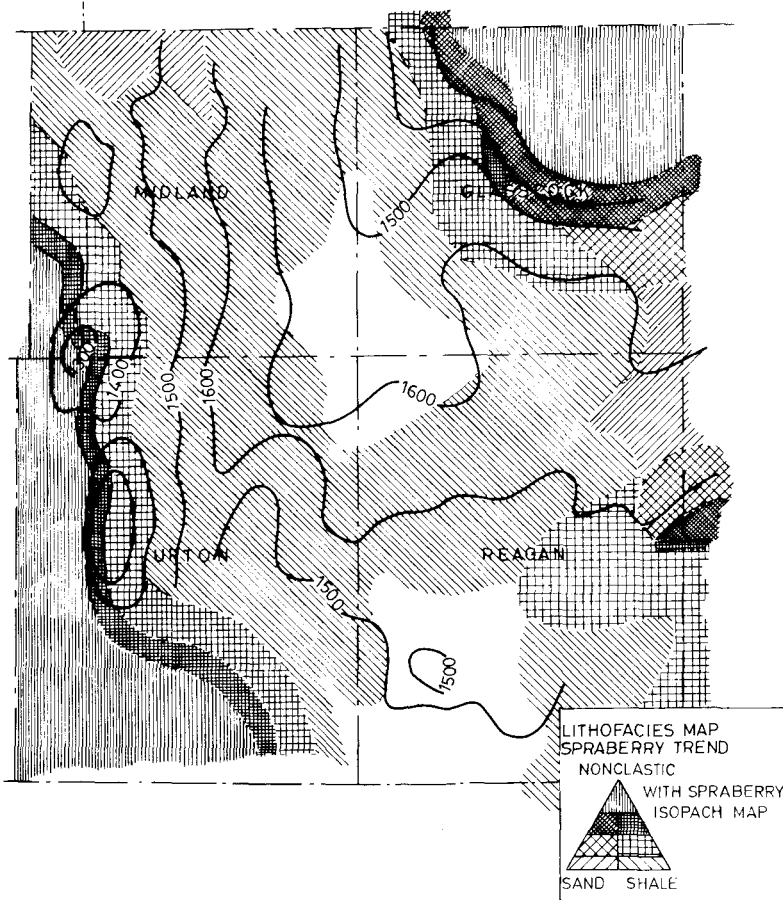
trends. Figure 3.16 is a map which illustrates one of the many techniques applied during efforts to reconstruct the original facies distribution and environments of deposition. *The conclusion of these studies was that the presence of oil was largely independent of structure or lithology.*

Fractures were considered as a reservoir mechanism after considerable experience of production in the area and the detailed examination of numerous cores, many of which were oriented for the determination of fracture trends.



3.15 – Typical well section: Spraberry Trend. (Wilkinson 1952.)

A variety of high pressure injection techniques, including water imbibition and pressure pulsing, have been used to force-fracture the formations along pre-existing lines of weakness. These methods have given enhanced oil production and emphasized the significance of natural fractures in production. After considerable studies of cores, Wilkinson reported a set of five arbitrary indices that could be given to the observed fractures:



3.16 – Lithofacies map, Four-County area, with Spraberry isopach contours. (Wilkinson 1952.)

- Latent or incipient fractures.
- Single vertical or oblique fractures, discontinuous for a relatively short distance.
- Single vertical fractures, extending the entire length of lithologic unit.
- Single vertical fractures parallel with each other.
- Vertical fractures parallel, intersected by oblique or vertical cross fractures.

The most common type of fracture with the greatest continuous vertical extent is found in the black shales and varved, sandy shales. Oblique fracturing is most common in the silts. It has been proposed that the differences in distribution of fracture types is a function of the lithology in which they occur, but it has also been considered that some may be artificial as the result of stress relief during drilling.

That the fractures are open is evidenced by both mineralization of the fracture plains and infill by lost circulation materials, and this pore space has been measured

in places by micrometer gauge with overall average for a single vertical fracture being estimated at 0.002 inches. Within the siltstone country rock, porosity has been measured in the main reservoir as 8% with permeability at 0.50md; but since 87% of the Spraberry rocks are shale, retort tests were carried out with positive results to prove the presence of hydrocarbons in capillary and sub-capillary porosity and permeability in the shales. On consideration of this data it becomes apparent that, although the siltstone forms the main reservoir, the shale itself also has reservoir capacity and that the fractures act as *feeder lines* to conduct the oil to the well-bore.

The origin of these fractures was attributed to two forces:

- a. non-directional reduction in volume, and
- b. regional tensions created by basinward subsidence.

Although each of these acted independently, both are a function of the basin development. In the first case, laboratory experiments showed that shrinkage resulting from compaction and lithification of shale led to randomly oriented lines of weakness or *latent fracturing*. In the second case, oriented cores from several wells indicate a major fracture trend in a general N.25°E direction with a more poorly developed trend at right angles. These are further confirmed by production potential maps and production testing results, all of which roughly coincide with macro-structural trends mapped throughout the region. Consequently, the second process is felt to be due to stretching of the sedimentary cover during both initial basin subsidence and, latterly, renewed uplift.

Whatever the origin of these fractures, their significance in the development of this field is inescapable. The Spraberry reservoir covers an enormous area, with some 488,000 acres expected to be proven commercial within the *four-county area* alone, and many marginal outlying areas planned for future development. Yet there are no typical folded structural traps or lithology which could normally be considered reservoir potential.

Although the greatest percentage of production is from fractured silts and sandstones, some attention is also focused on the possibility of shales as a reservoir. From this example we move further now to the consideration of shales alone as reservoirs.

### 3.3 FRACTURED SHALE RESERVOIRS

#### 3.3.1. General

Oil and gas have been produced in significant quantities from fractured shale reservoirs since the early 1900's, usually from organic-rich, bituminous, *black shales* which are common source rocks for many conventional reservoirs.

These organic facies may be deposited in several different environments, from restricted marine basins to non-marine delta plains, and are fairly common through-

hout the world. Production from the shales themselves is usually low, but gross reserves are high and production habit depends entirely upon the nature of the fracture permeability.

Many examples are found within the North American continent, particularly in the Devonian-Mississippian black shales. Along the western margin of the Appalachian Basin<sup>13</sup> gas reserves have been estimated at 460 quadrillion scf. The Cottageville field in northern West Virginia<sup>14</sup> has produced oil and gas for over 25 years from some 90 wells, amounting to an estimated production of 15 billion scf. In southwestern West Virginia<sup>15</sup> approximately 3,000 wells have been drilled in fractured shales, with an estimated ultimate recovery of 1 trillion scf. of gas; and good oil production was obtained from the Mancos shale<sup>16</sup> in the fractured Rangely anticline in Rio Blanco County, Colorado. Significant examples of fractured shale reservoirs in California are well documented by Regan (1953)<sup>17</sup> and by Hunter and Young in the Big Sandy gas field of eastern Kentucky (1953)<sup>18</sup>.

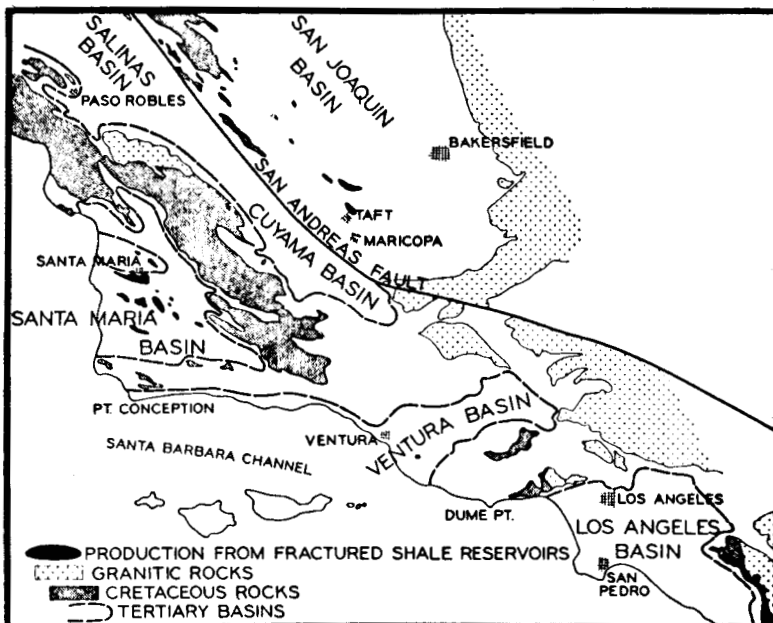
### *3.3.2. Californian fractured shale reservoirs<sup>17</sup>*

By 1953, 93% of some 290,000,000 barrels of generally heavy crude oil had been extracted from upper Miocene fractured chert and siliceous shale reservoirs within the Santa Maria Basin of western California; the remaining 7% having been produced from similar reservoirs within the southwest of the San Joaquin Basin (figures 3.17, 18 and 20).

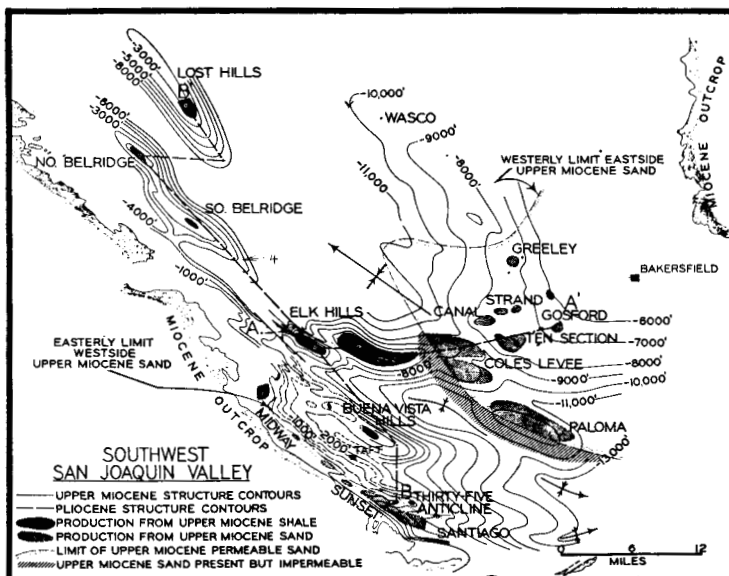
Between 1902 and 1953 several hundred wells had been drilled in these two basins and a number of common characteristics proved in each:

1. The production is from fractured zones within rocks which are also regarded as the source for most Californian oil.
2. Oil can be found in various kinds of structural traps.
3. Production rates increase in the more cherty areas, but are limited to those areas with a Pliocene cap-rock and varies markedly with the variations in fractures.
4. Fractures vary in nature and origin between the two basins.
5. Zones are easily overlooked without lengthy production tests.
6. Drilling habits are similar in potentially productive zones, including slow drilling rates, poor core recovery and loss of drilling fluids.
7. Oil shows while drilling are poor and are usually limited to oil in fractures seen in core fragments or oily drill fluids or cuttings.

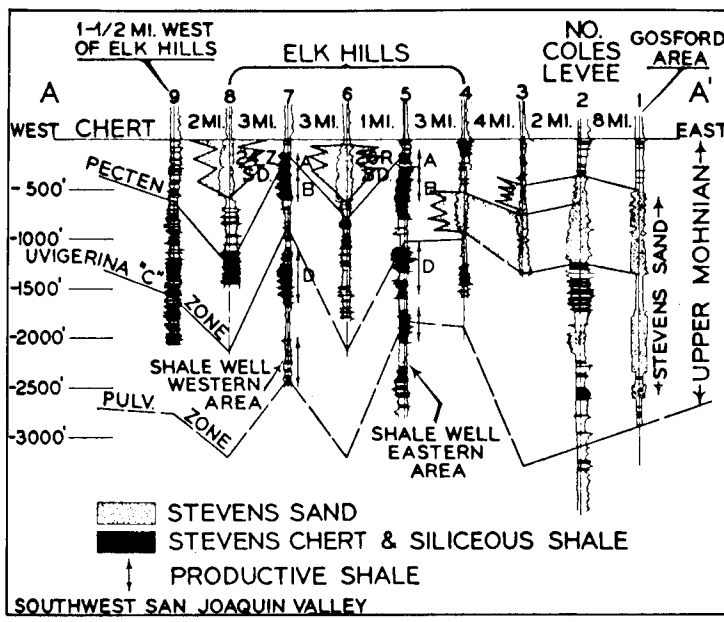
In the *San Joaquin Valley* accumulations are found in six anticlines: the 35 anticline of the Sunset field, Elk Hills, Buena Vista Hills, South Belridge, North Belridge, and Lost Hills (figure 3.18), the reservoirs contained in the Stevens sand and Stevens chert and siliceous shale formations of the upper Mohnian. Figure 3.19 illustrates how the cherts are developed as basinal equivalents of the marginal sands, and the



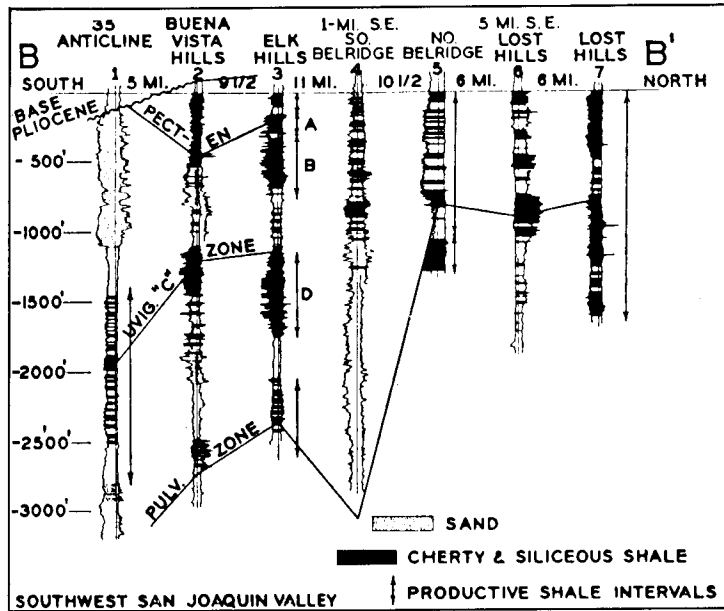
3.17 – Map of California showing the San Joaquin and Santa Maria Basins (Reagen 1953).



3.18 – Map of south west San Joaquin Valley, California. (Reagen 1953.)



SECTION A - A'



SECTION B - B'

3.19 – Sections through the San Joaquin Valley, taken from figure 3.19. (Reagen 1953.)

best production comes from the central part of the basin, the Elk Hills, to the west of the Elk Hills and Belridge area where the most siliceous and cherty shales are best developed. Fracturing in these brittle units appears to be better developed as the result of mechanical forces during the folding, with favourable effects on production as a result. Within the Elk Hills field, approximately 90 wells have been completed on 80 acre spacing, with initial production ranging up to 2,000 barrels per day of 35 °API oil.

In the Santa Maria district (figure 3.20) oil lies within fractured zones of the upper Miocene Monterey Formation, accumulating in combinations of anticlinal, stratigraphic and fault traps. The fractured zones occur in chert, cherty shale, calcareous shale and platy, siliceous and porcellanous shale, with most of the oil occurring in the fractured chert. The distribution of these lithofacies is apparently related to definite environments of deposition, the fracturing in this case, being the result of shrinkage during chemical changes in the history of the rock rather than folding. Correspondingly, the fractures have been found to be extremely variable locally, with significant effects on well production. In general, however, high permeabilities are indicated for most of the fields by high initial production rates of between 2,500 and 10,000 barrels per day of heavy, high viscosity oil. An estimated maximum permeability of 35 darcys with averages of 10 to 15 darcys have been obtained empirically for the chert zone in the Santa Maria field. A well developed chert zone in this field may ultimately recover 20,000–40,000 barrels an acre (100–150 barrels per acre foot), which may be as high as 30% of the total oil in place.

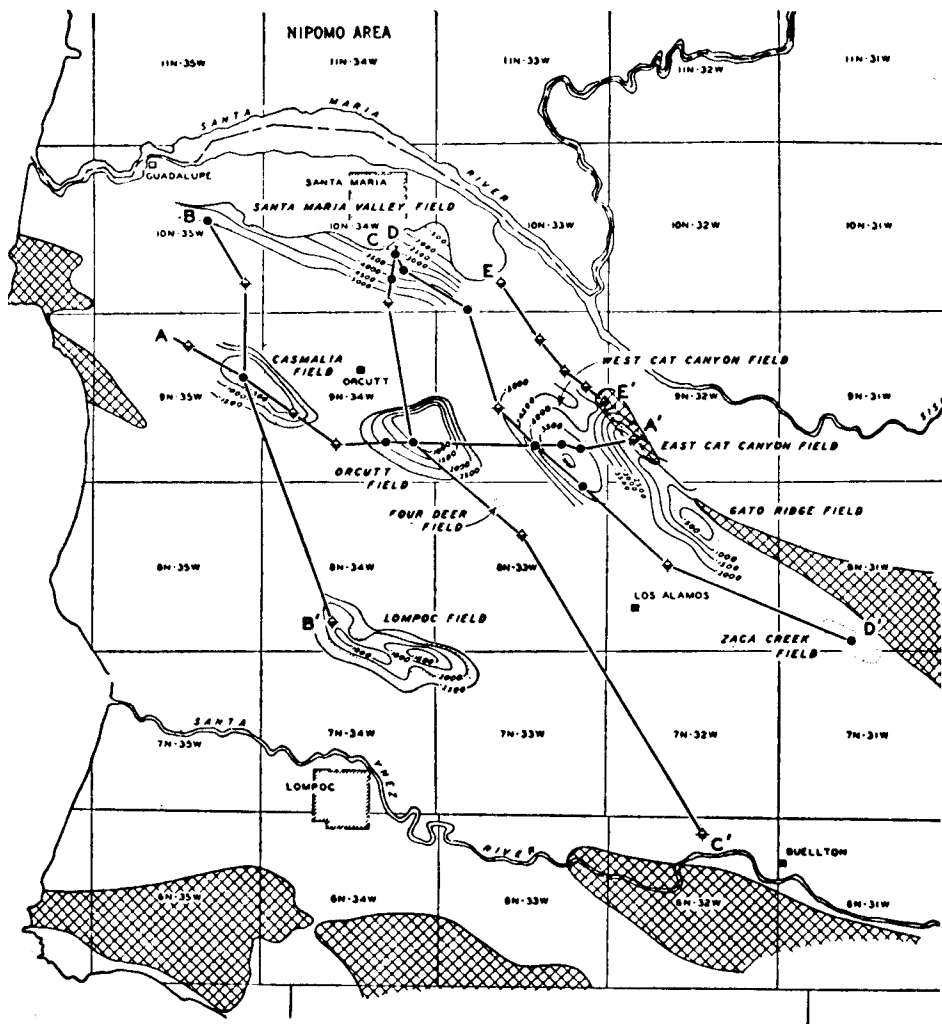
### *3.3.3. Big Sandy gas field, eastern Kentucky<sup>18</sup>*

Following its discovery in 1914 commercial gas production from the upper Devonian bituminous shales of eastern Kentucky has existed since 1929, with more than 3,800 wells drilled up until 1953. Total volume of gas produced by 1953 amounted to some 1 trillion, 250 billion cubic feet, with reserves estimated at that time to be 1 trillion, 400 billion cubic feet, 80% of which is produced from the Devonian shales.

Although poor sample recovery due to cable tool drilling initially led to some confusion as to the exact nature of the porosity and permeability within the reservoir formations, it was concluded by Hunter and Young that the gas occurs within two systems:

- a. a minor one consisting of thinly interbedded silts and sands within the shales, and
- b. a major system provided by joints, fractures and bedding planes, contributing most of the commercial reserves.

This conclusion is largely borne out by production experience. Pressure decline appears to be constant over a wide area, and on the occasions of field shut-in, a fairly



#### INDEX MAP

##### SANTA MARIA VALLEY DISTRICT

SHOWING

CONTOURS ON BASE OF PLIOCENE



AREAS IN WHICH MONTEREY IS ABSENT



OIL FIELDS

3.20 – Santa Maria Valley District. (Reagan 1953.)

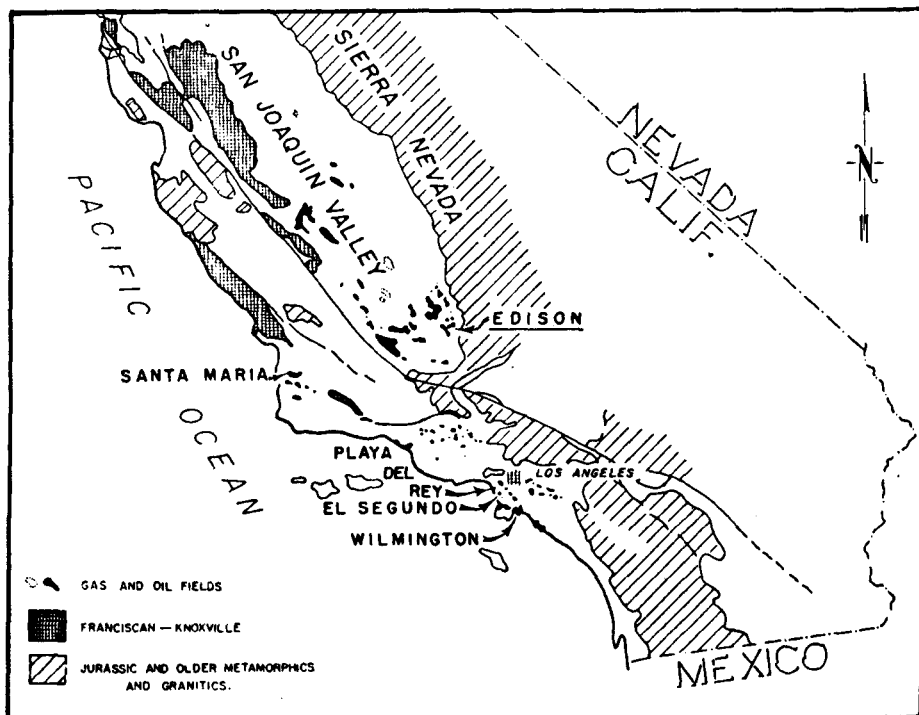
uniform pressure recovery has been registered. Furthermore, field production has required the routine use of explosive charges in order to develop flow from the shales.

### 3.4 FRACTURED «BASEMENT» RESERVOIRS

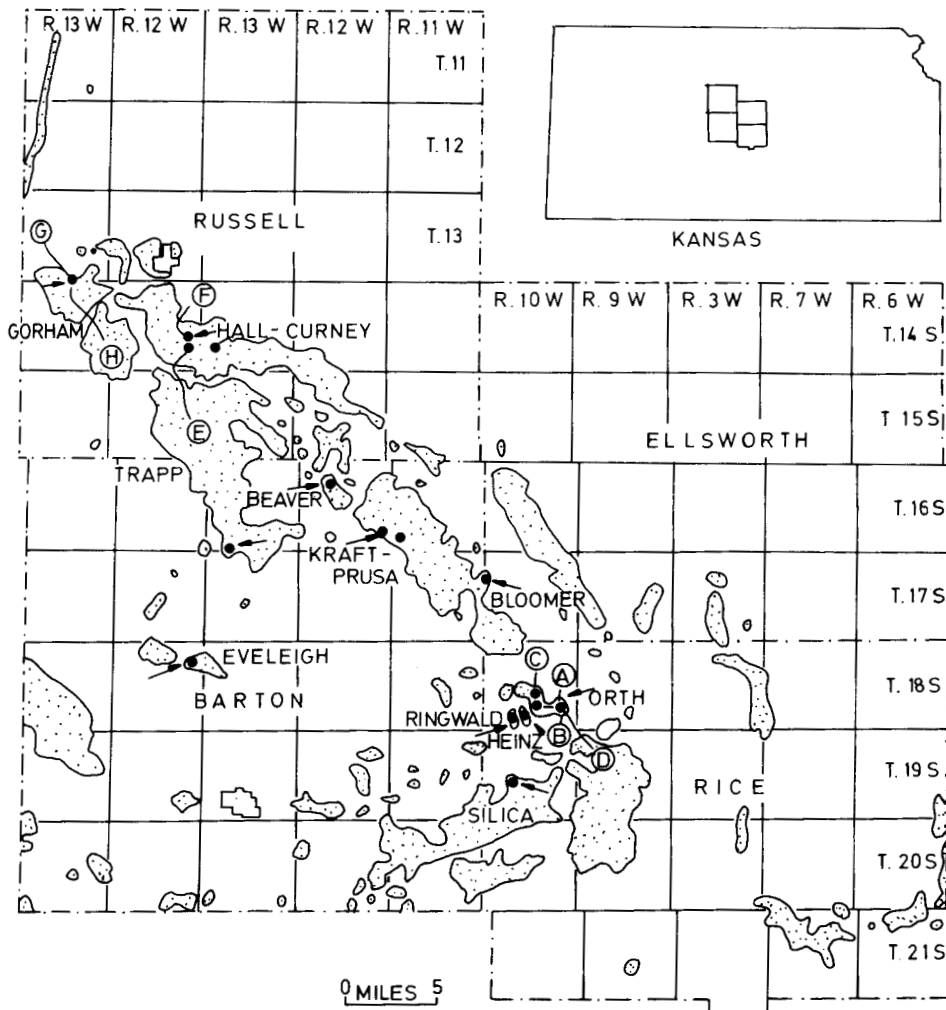
An important feature of fractured reservoirs is that they need not be confined to the soft rocks which are normally associated with oil exploration. The term «basement» refers to these rocks in which natural matrix porosity and permeability do not exist; this includes igneous and metamorphic rocks.

In the event of oil or gas production from these, it may be stated that storage and transmission of hydrocarbons is the result of a fractured environment. Examples of such fields are not uncommon. Smith<sup>1</sup> described production of 3,900 barrels of oil per day from one well in the La Paz-Mara field of Venezuela, which he concluded to have originated in fractured igneous and metamorphic basement rocks at a depth of 8,884 feet (2.710m). The fields went on to produce 80,000 barrels of oil per day from 29 wells.

Eggleson<sup>19</sup> and later McNaughton<sup>20</sup>, both described a number of fields and processes involved in accumulation of oil in basement reservoirs in California. The discovery of these fields was significant in that they were the first examples of hydrocarbons in basement rocks, which at the time (1948) was viewed with considerable suspicion by the geological experts. Figure 3.21 illustrates the positions of



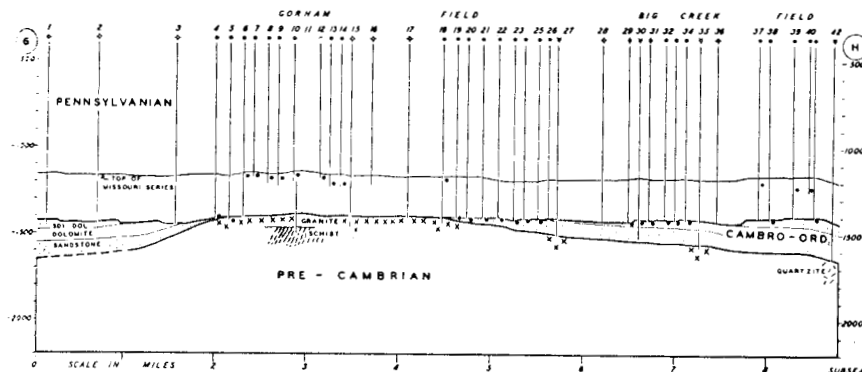
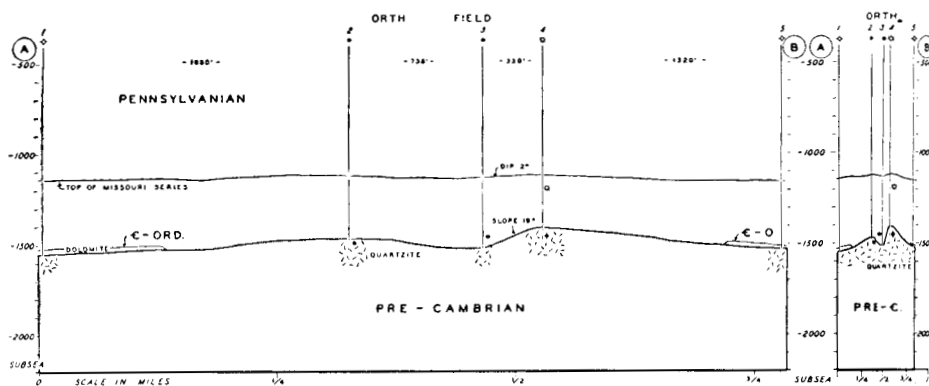
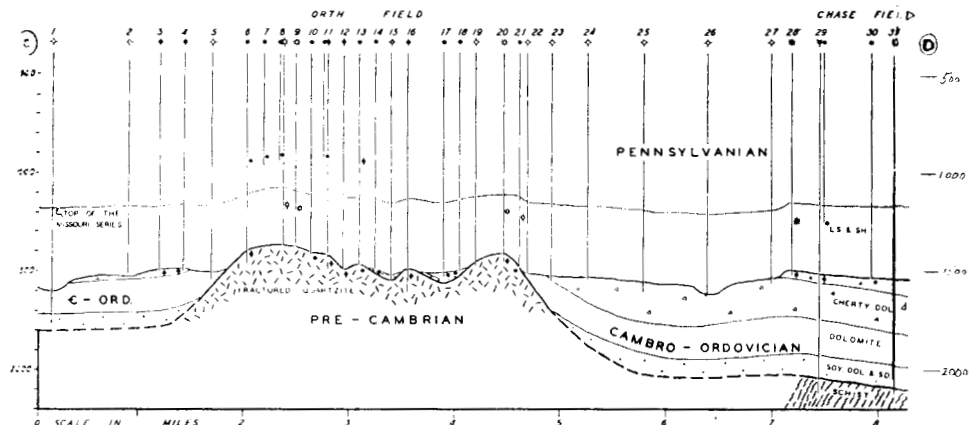
3.21 – Map of Southern California showing locations of fields producing oil from fractured metamorphic rocks. (D.A. McNaughton 1953.)



3.22 – Map of central Kansas showing location of fractured reservoirs in basement rocks. (Walters 1953.)

these fields, which include Edison, Santa Maria Valley, Wilminton, El Segundo and Playa del Rey fields. Some 15,000 barrels of oil per day were being produced from these reservoirs in 1948.

McNaughton in particular went on to stress the importance of these discoveries, and criticized geologists for not examining the phenomena adequately, stating that all of these fields were discovered by accident. He offered an alternative explanation to the widely accepted upwards migration of oil from lower down land source beds, indicating that, instead, rock volume reduction and the associated fracture systems could set up inverse pressure gradients from the sedimentary cover to the underlying



3.23 – Comparative cross-sections through fractured basement reservoirs in central Kansas. (Walters 1953.)

**basement rocks which would effectively suck-in the hydrocarbons to the basement.** This he felt might, as a hypothesis, add a further dimension to exploration in areas where known basement rocks were accessible.

Walters<sup>21</sup> described production of over a million barrels of oil from fractured Pre-Cambrian quartzite basement rocks in sixteen wells in the Orth field of Rice County, Kansas. He also described similar reservoirs in the nearby Kraft Prusa, Beaver, Bloomer, Eveleigh, Trapp, Ringwald, Heinz and Silica fields. Fractured granites are also recorded as reservoirs in the Hall-Gurney and Gorham fields of Russel County. Figure 3.22 illustrates the locations of these fields, and figure 3.23 compares the various structures of the reservoirs.

Of these fields Walters estimated that some 50 wells were producing from the Pre-Cambrian quartzites, and his conclusions that the reservoir mechanism related to fracturing was based on the following observations:

- a. The erratic occurrence of hydrocarbons throughout the area.
- b. Lack of matrix porosity in structurally high basement rocks.
- c. Lack of visible porosity in well cuttings.
- d. Lack of oil staining on cuttings.
- e. Dramatically increased production after artificial fracturing.

Furthermore, no oil shows were found where the basement rocks were structurally low. The only cases of shows were confined to *apex* areas of buried Pre-Cambrian *hills*, on the flanks of which oil bearing beds were found. It was also common for oil to occur in the overlying anticlinal Pennsylvanian *draped* limestones.

From these observations fracture porosity was assumed and migration was thus considered to have taken place from the flanks, along the pre-Pennsylvanian unconformity, into both the basement and unconformably outlying beds.

In view of a proven recovery of 78,000 barrels per well in the Orth field alone, Walters concludes that, where suitable conditions exist, fractured basement rocks, however seemingly unattractive, may form significant exploration objectives.

## BIBLIOGRAPHY

1. Smith, J.E., 1951. «The Cretaceous limestone producing areas of the Mara and Maracaibo district, Venezuela». Proc. Third World Petrol Cong. Sec 56–71.
2. Braunstein, J., 1953. «Fracture-controlled production in Gilbertown Field, Alabama». Bull. Am. Assoc. Petrol. Geol. Vol 37 No. 2, 245–249.
3. Muir, J.M., 1934. «Limestone reservoir rocks in the Mexican oilfields». Problems of petroleum geology, Am. Assoc. of Pet. Geol. 382.
4. Delgado, O.R. and Loreto, E.G., 1975. «Reforma's Cretaceous reservoirs: An engineering challenge». Petroleum Engineer. 56–66.
5. Davidson, D.A. and Snowdon, D.M., 1978. «Beaver River Middle Devonian Carbonate: Performance review of a high-relief, fractured gas reservoir with water influx». J. of Petroleum Technology 1672–1678.

6. Daniel, E.J., 1954. «Fractured reservoirs of Middle East». Bull. Am. Assoc. Petrol Geol. Vol 38 No. 5, 774–815.
7. Afshar, A., Eshghi, M. and Odouli, K.. «Geological history and stratigraphy of Iran». Schlumberger Symposium Document.
8. McQuillan, H., 1973. «Small-scale fracture density in Asmari Formation of southwest Iran and its relation to bed thickness and structural setting». Bull. Am. Assoc. Petrol. Geol. Vol 57, No. 12, 2367–2385.
9. Rocco, T., 1959. «Gela in Sicily, an unusual oilfield». Proc. Fifth World Petrol. Congress
10. Kafka, F.T. and Kirkbride, R.K., 1959. «History, discovery and development of Ragusa field». Proc. Fifth World Petrol. Congress.
11. Baker, D.A. and Lucas, P.T., 1972. «Strat. Trap. production may cover 280 plus square miles». World Oil. 65–68.
12. Wilkinson, W.M., 1953. «Fracturing in Spraberry Reservoir, West Texas». Bull. Am. Assoc. Petrol. Geol. Vol. 37, No. 2, 250–265.
13. Provo, L.J., 1976. «Upper Devonian black shale -- Worldwide distribution and what it means». Proc. of the Seventh Appalachian Pet. Geol. Symp.
14. Martin, P. and Nuckols, E.B., 1976. «Geology and oil and gas occurrence in Devonian shales: Northern West Virginia». Proc. of the Seventh Appalachian Pet. Geol. Symp.
15. Bagnal, W.d. and Ryan, W.M., 1976. «The geology reserves and production characteristics of the Devonian shales in south western West Virginia». Proc. of the Seventh Apopalachian Pet. Geol. Symp.
16. Peterson, V.E., 1955. «Fracture production from Mancos shales, Rangely field, Rio Blanco County, Colo». Bull. Am. Assoc. Petrol Geol. Vol 39, 532.
18. Hunter, C.D. and Young, D.M., 1953. «Relationship of natural gas occurrence and production in eastern Kentucky (Big Sandy Gas Field) to joints and fractures in Devonian bituminous shale». Bull. Am. Assoc. Petrol. Geol. Vol 37, No. 2, 282–299.
19. Eggleston, W.S., 1948. «Summary of oil production from fractured rock reservoirs in California». Bull. Am. Assoc. Petrol Geol. Vol 2, 1352–1355.
20. McNaughton, D.A., 1953. «Dilatency in migration and accumulation of oil in metamorphic rocks». Bull. Am. Assoc. Petrol. Geol. Vol 37, 217–231.
21. Walters, R.F., 1953. «Oil production from fractured Pre-Cambrian basement rocks in central Kansas». Bull. Am. Assoc. Petrol Geol. Vol 37, 300–313.

# CHAPTER 4

## PHYSICAL PROPERTIES OF ROCKS

### 4.1. INTRODUCTION

The physical properties of rocks and fluids have been studied extensively in the last three, four decades and the results have been published in papers, books and manuals. It may be stated that in order to examine and discuss the flow of fluid in porous rock, the greatest attention was given to the evaluation of properties, such as permeability, porosity, saturation in fluids, etc. Special physical characteristics of rocks (capillary pressure, relative permeability, etc.) have been developed simultaneously with the fluid behaviour (through the relationship pressure-volume-temperature) by use of a PVT analysis. All these results are generally used as basic data for any reservoir engineering study of a conventional reservoir.

Since the object of this chapter is to examine rock characteristics in a non-conventional reservoir (specifically in a fractured reservoir), only some of the parameters have been taken into consideration. Thus the rock properties, such as permeability and porosity, will be discussed as properties of fractures or of the fracture-matrix system. But matrix porosity and matrix permeabilities will not be discussed, since both represent classic properties of a conventional reservoir.

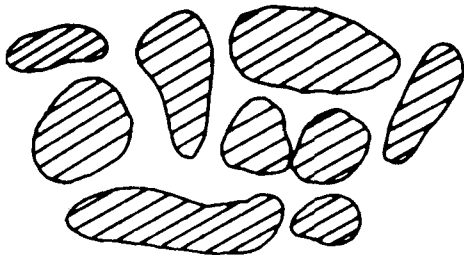
A review is presented concerning the compressibility of the fracture-matrix system and the fluid saturating the system, since together these are involved in the *storage capacity* of the transient flow.

Particular attention has been given to the properties of capillary pressure and the consequences for a matrix block saturated with fluid «A» while the surrounded fractures are saturated by a different fluid «B». These specific properties form the basis of fluid displacement mechanisms in any fractured reservoir.

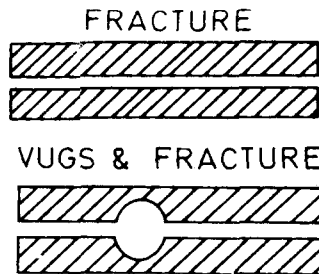
Relative permeability, which remains a very complex problem, has been discussed by analogy with various conventional reservoirs.

### 4.2. POROSITY

Fractured reservoir rocks are made up of two porosity systems; one intergranular (figure 4.1) formed by void spaces between the grains of the rock, and a second formed by void spaces of fractures and vugs (figure 4.2). The first type is called



4.1 – Consolidated grain void space (matrix).



4.2 – Simplified representation  
of vugs and fracture void space.

primary porosity and is typical of sandstone or limestone. The second type is called *secondary porosity* or, when referring to only vugs or fractures, *vugular porosity/fracture porosity*.

Secondary porosity is generally found in compact, brittle rock of relatively low intergranular porosity, such as compact limestones, shales, shaly sandstones, siltstones, schists, etc. Secondary porosity is normally caused by rock fracturing, jointing and dissolution by circulating water.

Often secondary porosity is reduced with time by becoming partially filled with minerals younger than those of which the matrix is composed. These minerals are the result of dissolution and precipitation. In carbonate rocks, such as limestones and dolomites, the solution channels and the vugs are formed during weathering or burial in the sedimentary basin. A certain vertical preferential orientation of fractures or joints, occurring in large structures formed by limestones, dolomites, siltstones, etc., may be the result of tectonic or overburden stresses which reduce rock cohesion as described in Chapter 1.

#### 4.2.1. Definition of double porosity

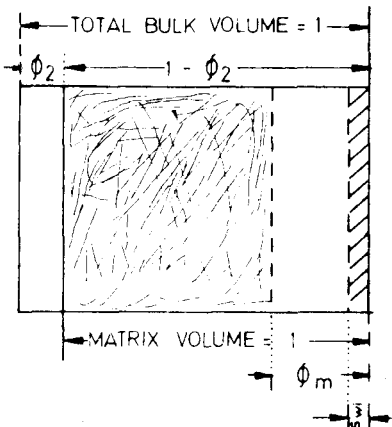
In a fractured reservoir the total porosity ( $\Phi_t$ ) is the result of the simple addition of the primary and secondary porosities,

$$\Phi_t = \Phi_1 + \Phi_2 \quad (4.1)$$

This *total porosity* is equivalent to the static definition of *rock storage* or *total void space*.

From a large number of laboratory measurements on various types of rocks, the *fracture porosity* was considerably less than the *matrix porosity*. The two porosities are expressed by the conventional definitions,

$$\left. \begin{aligned} \Phi_1 &= \text{matrix void volume/total bulk volume} \\ \Phi_2 &= \text{fracture void volume/total bulk volume} \end{aligned} \right\} \quad (4.2)$$



4.3 – Schematization of double-porosity.

and are relative to the total bulk volume (matrix + fractures)

In the correlation of the matrix porosity ( $\Phi_m$ ) and the fracture porosity ( $\Phi_f$ ), the fact that the matrix porosity refers only to the matrix bulk may be taken into consideration<sup>1</sup>,

$$\Phi_m = \frac{\text{volume voids of the matrix}}{\text{matrix bulk volume}}$$

while the fracture porosity,

$$\Phi_f \approx \Phi_f \quad (4.3)$$

In this case the primary porosity, as a function of matrix porosity, is expressed by,

$$\Phi_p = (1 - \Phi_f) \Phi_m \quad (4.4)$$

and the effective primary porosity, containing the oil phase, is,

$$\Phi_{p,\text{eff}} = (1 - \Phi_f) \Phi_m (1 - S_{wi}) \quad (4.4')$$

The porosity is presented schematically in figure 4.3, where the unit of bulk is scaled in the upper part and the matrix bulk unit is scaled in the lower part. Within the matrix porosity ( $\Phi_m$ ), one part is saturated with water and one part with oil, and each is expressed as a percentage of matrix bulk unit.

Double porosity also plays an important role in dynamic evaluations where, in place of rock storage, the term *storage capacity* is used. This parameter is expressed by the combined parameters  $\bar{\Phi} \bar{C}$ , which show the total expansion and/or compression capacity of the fluid and rock void volume.

#### 4.2.2. Qualitative description of secondary porosity

Based on empirical criteria, the carbonates containing vugs caused by dissolution or fossiliferous rocks are divided into various categories as suggested by Waldschmitt<sup>2</sup>:

- a. Non-vuggy – without true vugs.
- b. Vuggy, no filling – rocks that have no crystal lining in vugs. Matrix forms walls of vugs.
- c. Vuggy, partly filled – vugs coated, wholly or partly, by minerals the same as, or different from, those comprising the matrix. Minerals forming linings are usually younger than those of matrix.
- d. Vuggy, filled – vugs completely filled by minerals the same as, or different from, those of matrix. Minerals filling vugs are usually younger than those composing matrix.
- e. Fossiliferous — rocks containing fusulines or other fossils with small cells. This group is divided further on basis of intercrystalline porosity of matrix, such as good, fair, etc., on nature of fossil shells:
  - Where shells of fossils are not broken and are composed of carbonate grains finer than those in matrix.
  - Where shells of fossils are broken but «healed» with carbonate crystals larger than those composing walls of shells.
  - Where shells of fossils have been destroyed by recrystallization of their original carbonate.

For all categories of vugs an index of qualitative characteristics concerning the size, density and degree of filling may be included as follows:

<i>For all groups (Porosity)</i>	<i>For groups a, b, c Vug size</i>	<i>Number of vugs</i>	<i>For groups a, b, c, d, e</i>
VG – Very good	VL – Very large (greater than 10mm)	A – Abundant	O – Open
G – Good	L – Large (4mm – 10mm)	M – Moderate	PF – Partly filled
F – Fair	M – Medium (1mm – 4mm)	F – Few	F – Filled
P – Poor	S – Small (1mm or less)		C – Closed
VP – Very poor			

A similar description for fractures and fissures was also suggested by Waldschmitt in table 2.4 of Chapter 2.

#### 4.2.3. Quantitative evaluation of $\Phi_f$

In general, evaluation of total porosity by an indirect procedure (logging) or even by a direct procedure (core analysis) does not present any particular difficulties; but it is rather difficult to distinguish the primary porosity from the secondary porosity.

##### 4.2.3.1. Empirical evaluation of $\Phi_f$

Secondary porosity values will display substantially different response values in the case of vugs or fractures. Different results are also expected when the fractures are of one or another type. The most important fracture subdivision related to fracture porosity concerns two categories – *macrofracture* and *microfractures*.

As discussed in Chapter 1, macrofractures are extended fractures with wide openings which develop through various layers; while microfractures (or fissures) are fractures with narrow openings and limited extent, often limited to a single layer.

Depending on type of rock and state of stress, either the macrofractures or the microfractures will be more predominant. The most probable secondary porosity ranges are:

- a. Macrofracture network      –  $\Phi_f = .01 - .5\%$
- b. Isolated fissures            –  $\Phi_f = .001 - .01\%$
- c. Fissure network            –  $\Phi_f = .01 - 2\%$
- d. Vugs (in Karstic rock)    –  $\Phi_f = .1 - 3\%$

The maximum secondary porosity based on the magnitude of total porosity is also given by various empirical correlations from which the following can be inferred:

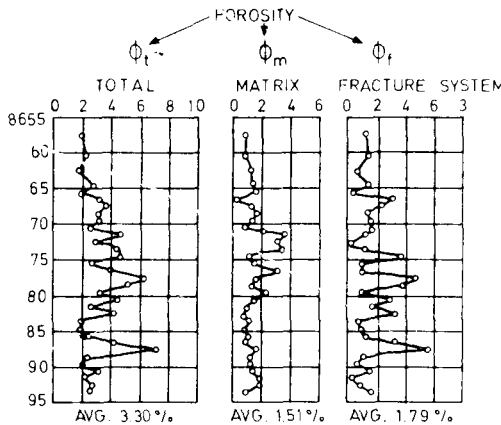
$$\Phi_{f\max} < 0.1\Phi_t \text{ when } \Phi_t < 10\%$$

$$\Phi_{f\max} < .04\Phi_t \text{ when } \Phi_t > 10\%$$

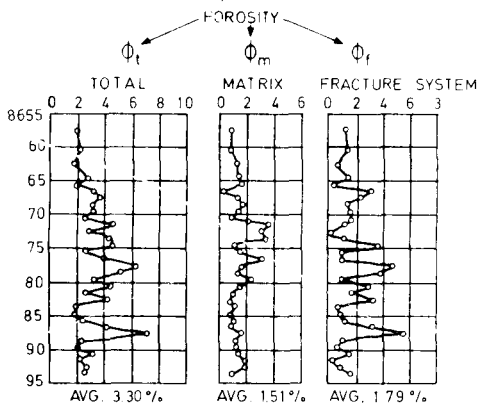
From the point of view of *rock storage*, the accuracy of the evaluation of  $\Phi_f$  is of very limited importance, since it is generally negligible when compared with the matrix porosity. But from the point of view of *storage capacity*, especially in relation to the transient flow problem, the accuracy of  $\Phi_f$  may play an important role. It is important to evaluate the  $\Phi_f$  value only when  $\Phi_t$  is very small ( $\Phi_t < 5\%$ ).

#### 4.2.3.2. $\Phi_f$ from core analysis

The evaluation of the total porosity ( $\Phi_t$ ) of a fractured rock using conventional procedures does not present any problems, especially if the fracture porosity is negligible compared to the matrix porosity ( $\Phi_f \ll \Phi_m$ ).



4.4 – Porosities  $\Phi_t$ ,  $\Phi_m$  and  $\Phi_f$  vs. depth  
(Atkinson<sup>3</sup>, courtesy AIME).



4.5 –  $\Phi_m$  vs.  $\Phi_t$  and  $\Phi_f$  vs.  $\Phi_t$  relationship  
(Atkinson<sup>3</sup>, courtesy AIME).

The following procedure was used by Atkinson<sup>3</sup> in his study of the Ellenburger reservoir of West Texas:

- two to four adjacent cores, while still frozen, were submerged in toluol in a Dean-Stark water extractor, modified for the purpose;
- the extracted water was measured after 24 hours;
- the cores were dried and then weighed under high vacuum before being saturated with water, and the bulk volume was measured.

This procedure determines the water saturation for the adjacent core sections, while the total corrected porosity ( $\Phi_t$ ) is estimated for the individual samples. The results from the core specimens (without vugs and fractures) represent matrix porosity.

The information obtained on the Ellenburger<sup>3</sup> cores reveals an average total porosity  $\Phi_t = 3.3\%$ . The variation of  $\Phi_t$  vs. depth is similar to fracture porosity  $\Phi_f$  vs. depth, while the  $\Phi_m$  variation does not show any correlation with  $\Phi_t$  (figure 4.4.) Similar observations are shown in the diagrams in figure 4.5 where a linear relationship between  $\Phi_t$  and  $\Phi_f$  is evident, while no correlation is possible between  $\Phi_t$  and  $\Phi_m$ .

#### 4.2.3.3. $\Phi_f$ vs. fracture opening b and $A_{fD}$

If the average fracture opening and the volumetric fracture density are obtained from core examination, the value  $\Phi_b$  is directly obtained.

As discussed in Chapter 2, the volumetric fracture density is expressed by,

$$V_{fD} = \frac{\frac{1}{2}S}{V_B}$$

where the value S represents the contact area between fractures and bulk volume unit. Therefore, in order to express the volume of pores, the surface must be multiplied by the opening width b:

$$\Phi_f = \frac{\text{vol voids}}{\text{vol bulk}} = \frac{\frac{1}{2}Sb}{V_B} = V_{fD} \times b \quad (4.5)$$

In the case of irregular fracture openings, an average value  $\bar{b}$  must be introduced.

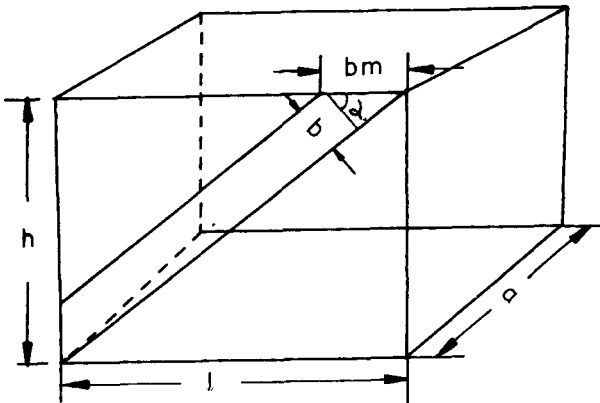
**Example .** If the average value shown in Chapter 2 for  $V_{fD}$  and b are  $V_{fD} = 40 \text{ m}^2/\text{m}^3$  and  $b \approx .08\text{mm}$  respectively, the fracture porosity will be,

$$\Phi_f = .8 \times 10^{-3} \text{ cm} \times 0.4 \frac{1}{\text{cm}} = 3.2 \times 10^{-3} = .32\%$$

#### 4.2.3.4. $\Phi_f$ from thin section analysis

In the case of fracture porosity evaluation by injection of fluid into pores, the behaviour is similar to the injection of fluid into large intergranular pores, when in reality the fluid is injected into the void spaces of the fracture. This is understandable in highly porous rock, where the errors in measuring the total porosity of the rock by conventional methods are in the same order of magnitude as fracture porosity. The uncertainty of the evaluation increases when the sample is so small that it does not exceed the distance between the two adjacent fractures. Therefore, the use of thin section measurements is a very favourable method, especially if a sufficient number of thin sections are available. Referring back to the areal fracture density parameter discussed in Chapter 2, the evaluation of the fracture porosity will be expressed by,

$$\Phi_f = \frac{V_{void}}{V_{bulk}} = \frac{\text{Vol fracture}}{\text{Vol bulk}} = \frac{\text{Fracture area} \times \text{opening}}{\text{Vol bulk}}$$



4.6 – Fracture in a block, simple schematization.

In a simplified case presented in figure 4.6, it is observed that there is a difference between real opening  $b$  and measured opening  $b_m$  in a horizontal thin section:

$$\Phi_f = \frac{b_m \times \cos\alpha \times a \times h / \cos\alpha}{Lah} = \frac{b_m}{L} = \frac{b_m \times a}{S}$$

For  $n$  fractures parallel to each other (belonging to a fracture system):

$$\Phi_f = \frac{n \times b_m \times a}{S} = b_m \times A_{fD} = b_m \frac{l_T}{S} \quad (4.6)$$

where  $a$  is the extension of the single fracture and  $l_T$  the total length of the fractures.

In general, in each section the value of  $b_m$  and  $l_T$  will be evaluated as well as the thin section surface. For  $n$  thin sections examined the average value is,

$$\Phi_f = \bar{\Phi}_f = \frac{\sum_{i=1}^n b_{m,i} \times l_{T,i}}{\sum_{i=1}^n S_i} \quad (4.7)$$

A more accurate value of the porosity will result from a larger number of thin sections randomly oriented.

#### 4.2.3.5. $\Phi_f$ from structural geological data

It was mentioned in equation 1.19 in Chapter 1 that a relationship between fracture porosity and structural characteristics has been elaborated by Murray<sup>4</sup>. The relationship associates the bed thickness and the structural curvature to the porosity

under the hypothesis that during structural folding, fractures normal to the bedding may result. The approximate value of the porosity value is then

$$\Phi_f = H \left( \frac{d^2z}{dx^2} \right) \quad (4.8)$$

where  $H$  is the bed thickness and  $d^2z/dx^2$  the structure curvature (second derivative of the structure profile). Based on data obtained in Sanish Pool<sup>4</sup> (example discussed in Chapter 1), where the highest reservoir curvature is in the range of  $0.5 \times 10^{-5}$  to  $10^{-5}$  l/ft and  $H = 20$  ft, the porosity is,

$$\Phi_{\min} = 20 \times 0.5 \times 10^{-5} = 0.1\%$$

$$\Phi_{\max} = 20 \times 10^{-5} = 0.2\%$$

#### 4.2.3.6. The evaluation of $\Phi_f$ from triaxial core testing<sup>5</sup>

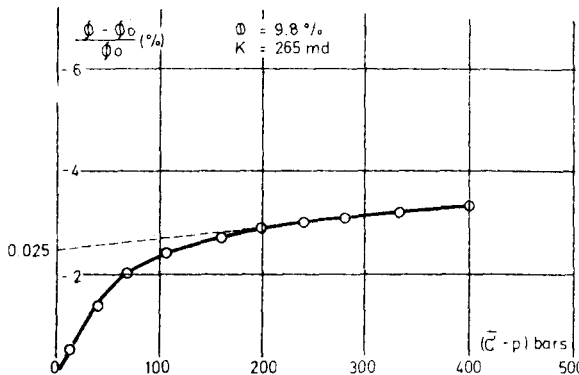
As discussed in Chapter 1, the reservoir rock is subjected to the overburden pressure due to the overlying rocks and to the pore pressure  $P$  caused by fluid saturating the pores. The environmental conditions (depth, temperature), as well as geological events (faulting, folding), influence the magnitude of stress  $\bar{\sigma}$  acting on the reservoir rock. Since the pore pressure  $P$  will decrease during reservoir depletion, a modification in net overburden  $\bar{\sigma} - P$  is expected.

In order to simulate the reservoir conditions, a triaxial laboratory test is generally performed recording the porosity value vs. net overburden pressure<sup>5</sup>. The results obtained are expressed as a relative reduction in porosity  $(\Phi - \Phi_0)/\Phi_0$  vs.  $(\bar{\sigma} - P)$ . In general, the results show an important variation of the relative porosity at low  $(\bar{\sigma} - P)$  values. At high values of the net overburden very small variations of relative porosity are observed (figure 4.7).

Considering that the latest part of the curve represents the zone where the variation of the relative porosity refers to the fracture pores, it is possible to evaluate fracture porosity by extrapolating the straight line at  $\bar{\sigma} - P = 0$ .

In figure 4.7 where a sample of Courtenay rock has been examined<sup>5</sup> ( $\Phi_0 = 9.8\%$ ;  $K = 265$  mD) the fracture porosity is resulting from the extrapolated value  $\Phi - \Phi_0 / \Phi_0 = 0.025$ , where  $\Phi_f = \Phi - \Phi_0$  and thus,

$$\Phi_f = .025 \times .098 = .245\%$$



4.7 - Variation of  $(\Phi - \Phi_0) / \Phi_0$  vs.  $\sigma - P$  (Abgrall<sup>s</sup>, courtesy IFP).

### 4.3. PERMEABILITY

The basics of permeability established in the case of a conventional reservoir remain valid in the case of a fractured reservoir. But in the presence of two systems (matrix and fractures), permeability may be redefined as *matrix* permeability, *fracture* permeability and *system* (fracture-matrix) permeability.

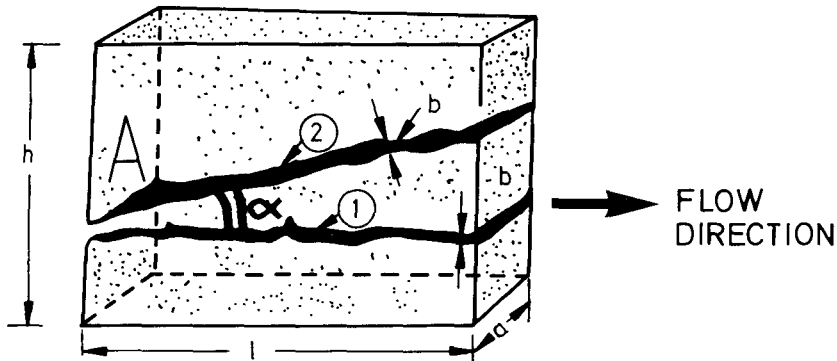
This redefinition of permeability may create some confusion especially concerning fracture permeability, which may be interpreted either as single fracture permeability or as fracture network permeability, or sometimes as fracture permeability of fracture-bulk volume. Therefore, the various expressions of permeability will be examined and discussed in detail.

#### 4.3.1. Intrinsic fracture permeability, $K_{ff}$

The intrinsic fracture permeability is associated to the conductivity measured during the flow of fluid through a *single fracture* or through a fracture network, independent of the surrounding rock (matrix). It is, in fact, the conductivity of a single channel (fracture) or of a group of channels (fracture network). In this case the *flow cross section* is represented *only* by the fracture void areas (excluding the surrounding matrix area). In a simplified case of a block, where the fracture is parallel to the flow direction (figure 4.8, fracture 1 is parallel to the horizontal flow direction), the flow rate through the fracture is given by,

$$q_f = a \times b \times \frac{b^2}{12\mu} \cdot \frac{\Delta P}{\Delta l} = a \cdot \frac{b^3}{12\mu} \cdot \frac{\Delta P}{l} \quad (4.9)$$

If the single fracture forms an angle with the flow direction (figure 4.8, fracture 2), the cross-section ( $a \times b$ ) will remain unchanged, but the fracture will be projected on the flow direction:



4.8 – Matrix block containing a single fracture. Fracture 1( $\alpha=0$ ). Fracture 2( $\alpha\neq0$ ).

$$q_f = ab \times \frac{b^2 \cos^2 \alpha}{12 \mu} \times \frac{\Delta P}{l} \quad (4.10)$$

On the other hand, based on the Darcy concept, if limited to the entire cross flow section,  $A = a \times b$ , the rate is expressed by,

$$q = A \frac{K_{ff}}{\mu} \times \frac{\Delta P}{\Delta l} = ab \times \frac{K_{ff}}{\mu} \times \frac{\Delta P}{l} \quad (4.11)$$

The further comparison of equation 4.11 with 4.10 will lead to,

$$K_{ff} = \frac{b^2}{12} \cos^2 \alpha \quad (4.12)$$

#### OBSERVATION

For a *fracture system* having  $n$  fractures of similar orientation (as defined in Chapter 2, the fracture system is formed by parallel groups of fractures), the intrinsic permeability is expressed by,

$$K_{ff} = \frac{\cos^2 \alpha}{12} \left[ \sum_i^n b_i^2 \right] \quad (4.13)$$

For a fracture network formed by fracture systems  $\alpha, \beta$ , each with its own orientation, the intrinsic permeability<sup>6</sup> is,

$$K_{ff} = \frac{1}{12} \left[ \cos^2 \alpha \sum_i^{n_\alpha} b_{\alpha i}^2 + \cos^2 \beta \sum_i^{n_\beta} b_{\beta i}^2 + \dots \right]$$

#### 4.3.2. Conventional fracture permeability, $K_f$

The *intrinsic fracture permeability*, as discussed above, disregards the rock bulk volume associated to the *single fracture* or to the group of fractures; on the contrary, in the *conventional fracture permeability* (based on the classic Darcy definition) the fracture and the associated rock bulk form a hydrodynamic unit. This means that the flow cross section, if referring to figure 4.8, is not expressed by section  $A = ab$ , but instead by,

$$A_B = ah \quad (4.14)$$

and therefore,

$$q = A_B \frac{K_f}{\mu} \times \frac{\Delta P}{l} = ah \times \frac{K_f}{\mu} \times \frac{\Delta P}{l} \quad (4.15)$$

If equations 4.15 and 4.9 are compared, and the result then applied to equation 4.12, the following expression will be obtained,

$$K_f = K_{ff} \frac{ab}{ah} = K_{ff} \frac{b}{h} = \frac{b^3}{12h} \quad (4.16)$$

#### 4.3.3. Permeability of fracture-matrix system

The permeability of a fracture-matrix system may be represented by the simple addition of the permeabilities of matrix  $K_m$  and fractures  $K_f$ ,

$$K_t = K_m + K_f \quad (4.17)$$

If equation 4.17 refers to the block described in figure 4.8 where the specific permeabilities of matrix and fracture were discussed, it is evident that the total permeability will depend on flow direction. Any change in direction of flow will change the value of  $K_f$ , since  $K_f$  depends on the relationship between fracture and flow directions.

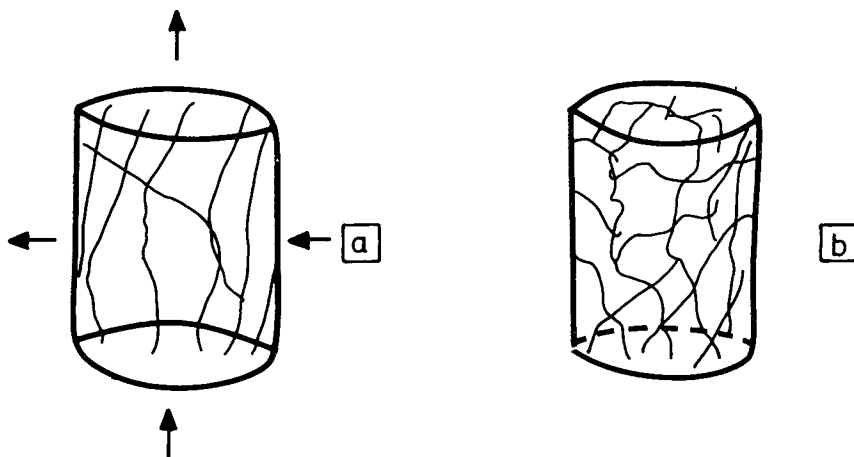
##### 4.3.3.1. Permeability from cores

By using conventional cylindrical cores and a conventional permeameter the permeability, based on Darcy's equation, is expressed by,

$$K_t = \frac{Q\mu l}{A \times \Delta P} \quad (4.18)$$

through which is obtained the total permeability of the system, and not the single permeabilities of matrix and fractures. In addition, fracture orientation vs. flow direction is essential in the evaluation of the value of  $K_t$ . If the permeability of the core shown in figure 4.9a is determined (for a vertical and horizontal flow), the resulting permeabilities will be completely different since a preferential vertical direction of fractures exists in the core. On the other hand, if the fractures show a random orientation (figure 4.9b), the value  $K_t$  from equation 4.18 represents an effective characteristic of the entire fracture-matrix system, independent of the direction of flow. This last case is less probable.

*NOTE:* It is generally difficult to obtain representative values of the three terms of permeability –  $K_t$ ,  $K_f$ ,  $K_m$  in a fractured reservoir. Under certain idealized conditions the core (shown in figure 4.9a), measurements from vertical and horizontal flow may result in  $K_{t,v} = K_m + K_f$  and  $K_{t,h} = K_m$ , respectively.



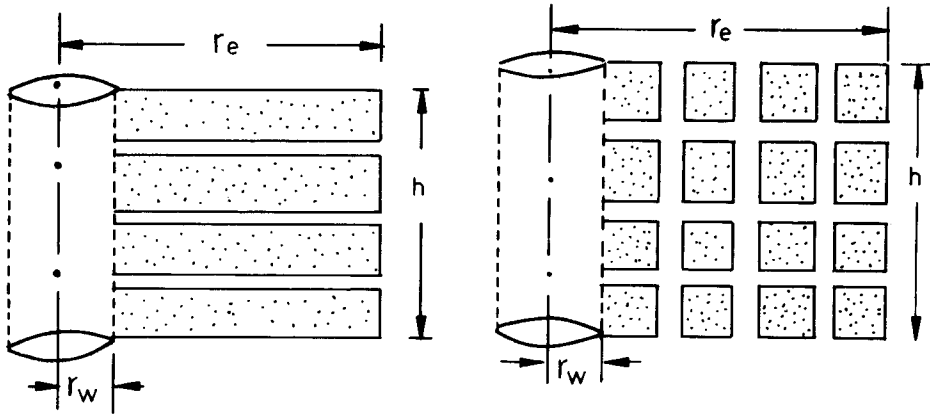
4.9 – Cylindrical core: a) oriented fractures, b) random orientation of fractures

#### 4.3.3.2. Permeability from well testing

In the case of a steady-state radial-symmetrical flow of a fluid towards a well, the permeability is obtained from the classic equation,

$$K_t = \frac{Q\mu [\ln r_e/r_w + S]}{2\pi h \Delta P} \quad (4.19)$$

The total permeability  $K_t$  (obtained from equation 4.19) vs. single permeabilities  $K_m$  and  $K_f$  will depend mainly on the reservoir model chosen. In other words, the idealization of the fracture-matrix system through a certain model will further



a) Kazemi, model

b) Warren - Root model

4.10 — Radial flow towards a well: a) Kazemi model, b) Warren-Root model.

determine the relationship between  $K_t$  and  $K_m$ ,  $K_f$ . The following idealized models, used currently in the literature are presented in figure 4.10:

- Kazemi model<sup>7</sup> – formed by alternate horizontal layers of matrix and fractures as shown in figure 4.10a.
- Warren-Root model<sup>1</sup> – formed by a number of matrix blocks (cubes) intersected by an orthogonal network of fractures as shown in figure 4.10b.

In the Kazemi model the flow through the layers (in parallel) of different permeabilities will be, in fact, related to the equation,

$$K_t = K_m + K_f = K_m + K_{ff} \frac{n \times b}{h}$$

In the Warren-Root model the steady-state fluid mechanism is quite different. The matrix blocks permanently feed the fractures and the fluid flows towards the wellbore only through the fracture network. Therefore, through equation 4.19, the fracture permeability is obtained:

$$K_t = K_f$$

*Conclusion:* from well testing under steady-state conditions the single permeability of the matrix can be estimated by the Kazemi or Warren-Root models. In the case of the Kazemi model, when  $K_m \ll K_f$ , the permeability resulting from equation 4.19 may lead to the approximation  $K_t \approx K_f$ . In case of the Warren-Root model,

since the matrix is considered not to be involved at all in the flowing process in steady-state conditions,  $K_t = K_f$  (equation 4.19). The only way to evaluate indirectly the  $K_m$  value is during transient flow periods (this technique is developed in detail in Chapter 7).

#### 4.3.4. Permeability in simplified models

As discussed above, the evaluation of fracture permeability through laboratory tests and well testing data is independent of any knowledge concerning fracture parameters (opening, orientation, distribution, etc.). An equivalent geometric model using the permeability obtained from test data can be obtained by simulating the fracture characteristics and their geometry through either a *single fracture* or a *multi-fracture* model. This procedure allows the transformation of results obtained from well testing or core analysis in what is called an idealized fractured reservoir model.

##### 4.3.4.1. In the case of a single fracture

If the single fracture is similar to fracture 1 of the model represented in figure 4.8, the porosity may be expressed by,

$$\Phi_f = \frac{a \times L \times b}{a \times L \times h} = \frac{b}{h} \quad (4.20)$$

which, combined with equation 4.16, will give,

$$K_f = \frac{b^3}{12h} = \frac{b^2}{12} \Phi_f = K_{ff} \times \Phi_f \quad (4.21)$$

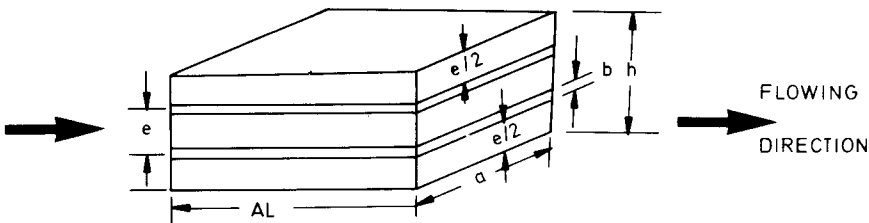
The porosity and fracture opening associated with permeability will be derived from equation 4.21:

$$\Phi_f = \frac{b}{h} = \frac{12K_f}{b^2}$$

$$b = \sqrt[3]{12hK_f} = \sqrt{12K_f / \Phi_f}$$

##### 4.3.4.2. In the case of a multi-fracture

The multi-fracture model is formed by parallel slices of matrix which regularly alternate with fracture intervals and thus the flow is considered parallel to the fractures. This idealization will permit the simulation of field results through a more simplified flow model.



4.11 – Multi-fracture layer. Fractures and layers in parallel.

The flow of a fluid through  $n$  fractures as in figure 4.11 can be expressed by,

$$q_f = n \times \text{fracture cross flow} \times \text{velocity} \quad (4.24)$$

or

$$q_f = n \times ab \times \frac{K_{ff}}{\mu} \times \frac{\Delta P}{\Delta L} = na \frac{b^3}{12\mu} \times \frac{\Delta P}{\Delta l} \quad (4.25)$$

The flow through  $n$  fractures, based on Darcy's law, is expressed by

$$q_f = S \frac{K_f}{\mu} \times \frac{\Delta P}{\Delta l} = ah \times \frac{K_f}{\mu} \times \frac{\Delta P}{\Delta l} \quad (4.26)$$

which disregards any idealization since the flow conductivity is expressed by  $K_f$  and the flowing area is considered the entire cross flow section,  $S = ab$ . In continuation, the analogy between equations 4.25 and 4.26 will lead to,

$$K_f = \frac{nab^3}{12S} = A_{fD} \times \frac{b^3}{12} = \Phi_f b^2 / 12 \quad (4.27)$$

or

$$K_f = \frac{nab^3}{12ah} = L_{fD} \frac{b^3}{12} = A_{fD} b K_{ff} \quad (4.27')$$

since (as discussed in Chapter 2) the areal and linear fracture densities are, respectively,

$$A_{fD} = \frac{n \times a}{S} = \frac{l_T}{S} = \frac{n \times a}{h \times a} = \frac{n}{h} = L_{fD}$$

and

$$\Phi_f = \frac{nab}{S} = \frac{nab}{ah} = A_{fD} \times b$$

Other relationships between permeability, porosity, fracture density and average fracture opening, may be expressed by:

$$\left. \begin{aligned} \Phi_f &= \frac{nab \times 1}{S \times L} = \frac{nab}{S} = \frac{nab}{ah} = \frac{nb}{h} = A_{fD} \times b = L_{fD} \times b \\ K_f &= \Phi_f \frac{b^2}{12} = K_{ff} \times b \times A_{fD} = K_{ff} \times b \times L_{fD} \\ b &= \sqrt[3]{12 K_f / \Phi_f} = \sqrt[3]{12 K_f / A_{fD}} = \sqrt[3]{12 K_f / L_{fD}} \\ \Phi_f &= \frac{12 K_f}{b^2} = \sqrt[3]{12 K_f A_{fD}^2} \end{aligned} \right\} (4.28)$$

*Note.* In the case of random distributions of fractures in the rock matrix, the fracture density distribution must be corrected with  $\pi/2$  and, thus, the porosity  $\Phi_f$  can be expressed by,

$$\Phi_f = \sqrt[3]{12 K_f (\pi/2)^2 \times V_{fD}^2} = \sqrt[3]{29,6 K_f A_{fD}^2} \quad (4.28')$$

The linear fracture density could also be expressed as the reciprocal value of *fracture interval* (Chapter 2), so that,

$$L_{fD} = 1/e \quad (4.29)$$

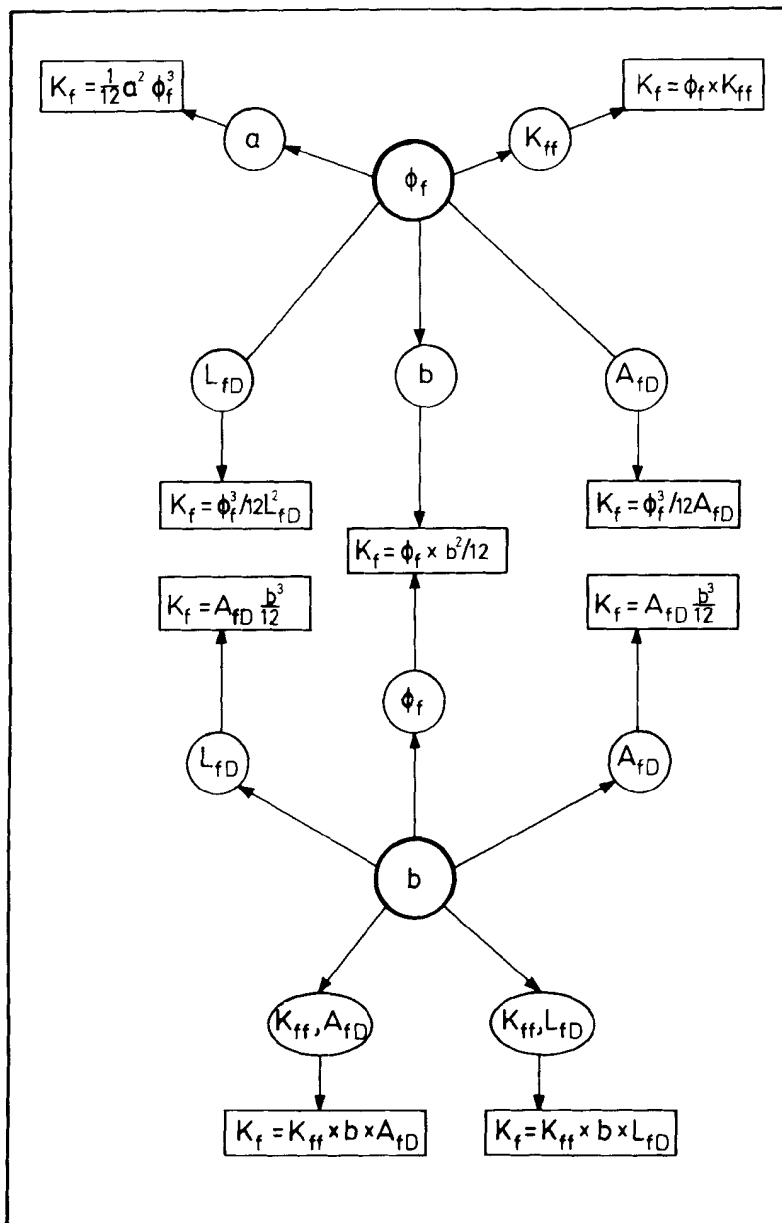
where  $e$  is also often called block height (Fig. 4.11).

*Note.* A resumé of permeability as a function of various parameters of a fractured reservoir system is given in schematic table 4.1.

#### 4.3.5. Permeability evaluated through permeameter measurements

The correct evaluation of fracture permeability is substantially more significant than that of fracture porosity. In fact, the errors in fracture porosity when compared with the total porosity magnitude are negligible and will never influence the hydrocarbon pore space or what is otherwise called the *total storage capacity*. Permeability errors on the other hand may substantially modify the well productivity index, especially in tight formations, and therefore a representative value is of extraordinary importance. Unfortunately, the permeability obtained by using conventional permeameters is completely inadequate since permeability depends largely on fracture orientation vs. flowing direction. If the fracture does not have a random

Table 4.1



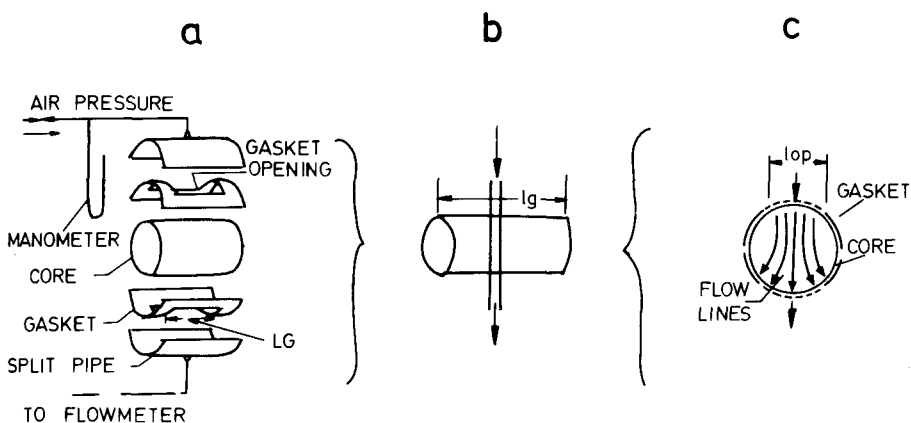
orientation distribution (figure 4.9b) but a preferential orientation (figure 4.9a), the permeability evaluation procedure must be modified.

#### 4.3.5.1. Permeability from cores

In direct measurements of permeability on cores, it is difficult to estimate the conditions in which the cores were oriented in the reservoir. The lack of such information reduces the value of measured permeability, especially in the case of a strong preferential orientation of fractures in the reservoir. Therefore, the conventional permeameter has been substituted by an improved permeameter elaborated by Kelton<sup>9</sup>.

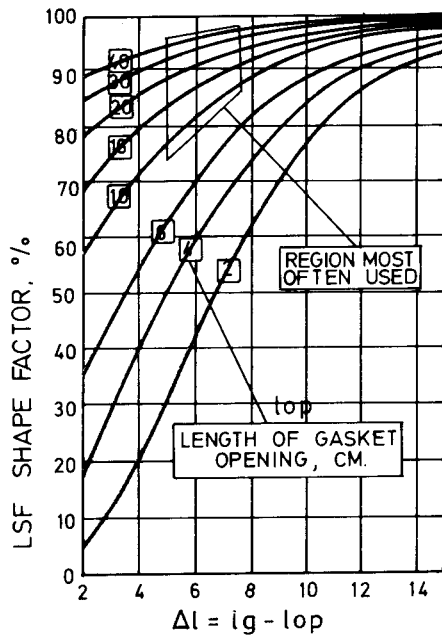
#### 4.3.5.2. The Kelton permeameter

The objectives of Kelton's technique are to limit the developing of additional fractures by mechanical manipulation of the core, and to approach the flowing conditions to those which may exist in the reservoir.

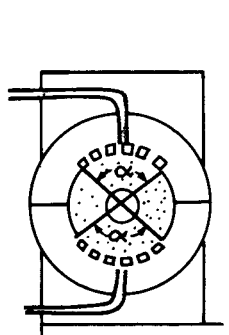


4.12 – Kelton permeameter: a) detail of flowmeter, b) permeameter general view, c) cross-section of flow (Kelton<sup>9</sup>, courtesy AIME).

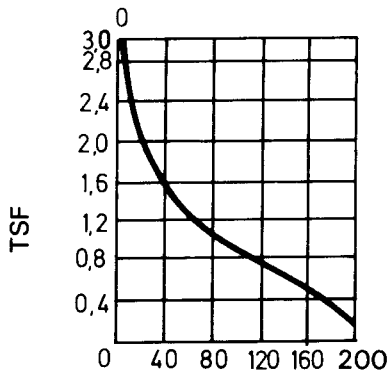
The equipment is made up of a core holder, which has the opposite sides covered by two rectangular rubber gaskets with openings that extend over one fourth of the core circumference (figure 4.12). The components of the permeameter (left side), the flow-through core (center) and the flow lines on a transversal cross-section (right side) are shown in figure 4.12a, b and c. An essential characteristic of this permeameter is the change in flowing direction. In a conventional permeameter the flow is along the core axis, while in the Kelton permeameter the flow is only through a part



4.13 – Longitudinal shape factor diagram (Kelton<sup>o</sup>, courtesy AIME).



(a)



(b)

4.14 – Transversal shape factor: a) entrance and exit angle in transversal section, b) TSF vs. angle  $\alpha$  (Kelton<sup>o</sup>, courtesy AIME).

of the lateral cylindrical surface. The direction of flow is transverse if referring to the cylinder axis of the core.

- a. *Type of permeability:* the evaluation is performed in two stages by a special orientation of the core when it is mounted in the core holder. In the *first stage* the core is oriented so that the flow crosses the direction of the principal sample fracture. The permeability obtained is called  $K_{max}$  (figure 4.12 c)

In the *second stage* the core is turned  $90^\circ$  in the same core holder and the permeability measured in the new conditions is called  $K_{90^\circ}$ .

- b. *Basic equation;* The permeability in the case of Kelton's permeameter is obtained by the equation,

$$K = \frac{Q}{\Delta P} \times \frac{\mu}{l_{g,eff}} \quad (4.30)$$

where the  $l_{g,eff}$  is an equivalent gasket length, which takes into consideration the shape factor due to special geometry of flow lines. Adjusting the gasket length (equal to the core length) with two shape factors, longitudinal (LSF) and transversal (TSF), the effective length becomes,

$$l_{g,eff} = l_g \times LSF \times TSF \quad (4.30')$$

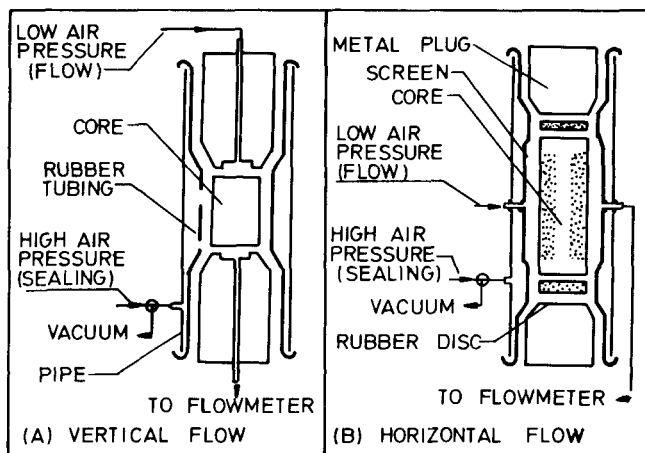
- c. *Correction factors;* There are two correction factors, LSF and TSF, which have been elaborated by Kelton<sup>9</sup>. The LSF is expressed as a function of non-flowed core length  $\Delta l = l_g - l_{op}$ , where  $l_g$  and  $l_{op}$  are respectively the gasket and open gasket lengths. The results are shown in figure 4.13. Thus LSF corrects the end effects of the core where the gasket is not opened.

The TSF is associated with the shape of the flow line in a transversal cross-section, and is a function of the entrance opening angle  $\alpha$  (figure 4.14a). The relationship TSF vs.  $\alpha$  is shown in figure 4.14b.

- d. *Equipment improvement;* An improvement in Kelton's technique was obtained by use of the Hasler type permeameter which may be used for vertical and horizontal flow. Fig. 4.15

This modification, despite excellent sealing conditions, is not as successful unless adequate cores are available. It is suggested that the length exceeds the diameter, since adjustment to the great variety of sample diameters limits the validity of the core holder.

- e. *Conclusion:* If the cores are not long enough the uncertainty of the resulting permeability will increase. The results improve for large core diameters through Kelton's method, even though the values of permeability may remain uncertain.



4.15 – Hassler type permeameter (Kelton®, courtesy AIME).

#### 4.3.5.2. Comment concerning use of permeameter

For evaluating fracture permeability conventional methods have proved to be inadequate. Results obtained from the Kelton permeameter, however, have been quite successful; nevertheless a number of difficulties remain, independently of the method used. Among these the most important are:

- Core length;* If fracture density is low, the length of the rock sample could be between two adjacent fractures and, in this case, the permeability represents only the matrix.
- Fracture orientation;* Fracture orientation vs. flowing direction substantially changes results. If the laboratory results have to be used later to simulate the flowing direction in a reservoir, then the problem does not have any solution. The radial flow towards a well will have very little in common with the linear flow examined in the laboratory by use of the permeameter. This explains why the permeability obtained from well testing often results tens to hundred times higher than the permeability obtained in the laboratory.

A relationship between lab data and prediction of reservoir behaviour is practically impossible, since the cores are seldom oriented during coring.

- Reservoir pressure conditions;* Additional difficulties may arise when making laboratory measurements in the absence of pore pressure and overburden pressure. In this case the fracture openings are reduced as a result of bulk rock expansion. This will reduce the lab permeability by comparison with reservoir permeability.

#### 4.3.6. Permeability from thin sections (micro-sections)

The use of thin sections for the evaluation of permeability gives the impression of being a very satisfactory analytical procedure; but the successful use of these results is very dependent on additional information concerning fracture orientation and fracture density. However, the procedure may help in the understanding of the relationship between permeability and spatial distribution of the fracture network.

##### 4.3.6.1. Analytical procedure

By using a micro-section analysis the evaluation of permeability is associated to the measuring of fracture openings and density.

The following results are based on equations 4.28 and 4.12:

$$K_f = K_{ff} \times b \times A_{fD} = \frac{b^2}{12} \times b \times A_{fD} = \frac{b^3}{12} A_{fD} \quad (4.31)$$

and when substituting  $A_{fD} = \Phi_f/b$ ,

$$K_f = \frac{1}{12} b^2 \Phi_f \quad (4.32)$$

These equations show that it is sufficient to measure the fracture opening  $b_m$  (measured opening) the number of fractures and their lengths ( $l_t = \sum l_{fi}$ ) in order to directly evaluate the permeability (if all fractures have one orientation).

In case of a random distribution of fracture orientation in a thin section, fracture permeability will be expressed by<sup>8</sup>,

$$K_f = C_1 \times \left( \frac{2}{\pi} \frac{b_m}{b} \right)^2 \times \frac{b_m \times l_t}{S} = C_1 \frac{4}{\pi^2} \times \frac{b_m^3 l_t}{S} = C_2 \frac{b_m^3 \times l_t}{S} \quad (4.33)$$

where  $S$  is the area of the micro-section and  $C_1$  and  $C_2$  are constants, depending on the orientation of the fracture system (table below). For  $n$  thin sections of surface  $S$ , where various fracture systems coexist, the resulting permeability will be,

$$K_f = C_2 \frac{\sum_{i=1}^n b_{m,i}^3 \times l_{ti}}{\sum_{i=1}^n S_i} \quad (4.34)$$

<i>Fracture system</i>	$C_1$	$C_2$ (in K Darcy)
1. Horizontal single fracture system	1	$3.42 \times 10^6$
2. Vertical, mutually perpendicular fracture system	1/2	$1.71 \times 10^6$
3. Mutually perpendicular system	2/3	$2.28 \times 10^6$
4. Random fracturing	1/1	$1.71 \times 10^6$

*Calculation example:*

For two perpendicular fractures having the dimensions  $b_1 = 20\mu$ ;  $b_2 = 35\mu$ ;  $l_1 = 6\text{mm}$ ;  $l_2 = 5\text{mm}$  and  $S = 0,2 \text{ cm}^2$ , it results,

$$K_f = 2,28 \times 10^6 \quad \frac{(20 \times 10^{-4})^3 \times .6 + (35 \times 10^{-4})^3 \times 0.5}{0.2} = 299 \text{ mD}$$

#### 4.3.6.2. Empirical evaluation procedure

The empirical method is based on qualitative observations of thin sections as a result of visual appreciation of type of porosity, shape of canals, and communication, etc. The essential observations in micro-sections concern type of rock, porosity, pore size and shape, which are then elaborated quantitatively by use of the Teodorovici<sup>10</sup> method (further improved by Aschenberger<sup>11</sup>). This method proposes the evaluation of permeability by using the empirical equation,

$$K = A \times B \times C \times D \quad (4.35)$$

where parameters A, B, C and D are functions of various basic rock characteristics.

A – is a function of type of rock (table 4.2)

B – is a function of porosity (table 4.3)

C – is a function of pore size (table 4.4)

D – is a function of pore shape (table 4.5)

Parameter A (table 4.2) presents a large range of variations between 2 and 64. Among various categories of rocks, category II was found to be the best.

Parameter B (table 4.3) is practically in the same range as matrix porosity. As observed, the reduction in permeability is associated with rock tightness (lower permeability for more compact rock).

Parameter C (table 4.4) is associated with pore size, taking into consideration the

**TABLE 4.2** EMPIRICAL COEFFICIENT A FOR PORE-SPACE TYPE

PORE SPACE TYPE	Characteristic of Subtype (As Seen in Thin Sections)	Empirical Coefficient A	DESCRIPTION
I	With very narrow conveying canals (avg. diameter $\approx 0.01$ mm), usually not visible in thin section under the petrographic microscope using normal range of magnification	2	PORE SPACE WITH CONVEYING CANALS
	With rare relatively wide canals (avg. diameter $\approx 0.02$ mm.) visible in thin sections	4	
	With few relatively wide canals, visible in thin section	8	
	With many relatively wide canals, visible in thin section, or with few wide canals (avg. diameter $\geq 0.04$ mm.)	16	
II	With abundant wide canals or few to many very wide conveying canals	32	PORE SPACE STRUCTURE WITH OR WITHOUT VUGS
	With poor porosity, the pores being relatively homogeneous in size and distribution	8	
	With good porosity and (or) porosity ranging from poor to good: pores being of different size pores being vuggy and irregular in outline	16–32 32–64	
III	With very poor porosity inside the conveying canals	6	INTERGRANULAR PORES
	With poor porosity inside the conveying canals	12	
	Conveying canals finely porous	24	
IV	With interconnected pore space between rhombohedral grains	10	PORE SPACE OF VARIOUS SHAPE
	With interconnected pore space between subangular-subrounded grains	26	
	With interconnected pore space between rounded to well rounded grains	30	

presence of vugs. The impact of this parameter on permeability is small compared with parameter A.

Parameter D (table 4.5) is associated with pore shape. It has the smallest influence of all four parameters on the magnitude of permeability. Aschenberger<sup>11</sup> mentions that a relatively acceptable correlation was found between measured permeability in carbonate rock and the results obtained from the Teodorovici method. The deviations observed were in the average range of 12–15%.

Permeability magnitude related to conveying canals during analysis of thin sections has shown the following values:

- |  |                               |                            |
|--|-------------------------------|----------------------------|
| ~ conveying canals                         | $-\Phi \approx 0.01\text{mm}$ | $K = 2 - 16\text{mD}$      |
| ~ pore intercommunication                  | $-\Phi \approx 0.02\text{mm}$ | $K = 30 - 75\text{mD}$     |
| ~ large number of canals                   | $-\Phi \approx 0.03\text{mm}$ | $K = 600 - 800\text{ mD}$  |
| ~ abundance of wide interconnecting canals | $-\Phi \approx 0.04\text{mm}$ | $K = 1200 - 1300\text{mD}$ |

### EMPIRICAL COEFFICIENT C FOR PORE SIZE

<i>Effective porosity</i>		
<i>Descriptive Term</i>	<i>Limits in Per Cent</i>	<i>Empirical Coefficient B</i>
Very porous	>25	25–30
Porous	15–25	17
Moderately porous	10–15	10
Pores abundant	5–10	2–5
Pores present	2–5	0.5–1.0
Some pores present	<2	0

Table 4.3

### EMPIRICAL COEFFICIENT C FOR PORE SIZE

<i>Descriptive Term</i>	<i>Maximum Size of Pore (mm.)</i>	<i>Empirical Coefficient C</i>
Large vugs	>2.00	16
Medium to large vugs	0.50–2.00	4
Medium pores	0.25–1.00	2
Fine to medium pores	0.10–0.50	1
Very fine to fine pores	0.05–0.25	0.5
Very fine pores	0.01–0.10	0.25
Pinpoint to very fine pores	<0.10 and in part <0.01	0.125
Mostly pinpoint porosity	<0.03 and in part <0.01	0.0625

Table 4.4

### EMPIRICAL COEFFICIENT D FOR PORE SHAPE

<i>Descriptive Term</i>	<i>Empirical Coefficient D</i>
More or less isometric pores	1
Elongate pores	2
Very elongate pores or pores arranged in bands with emanating conveying canals	4

Table 4.5

#### 4.3.7. Permeability from structural geological data

The relationship between structural geology and fractured rock properties (porosity and permeability) was discussed in Chapter 1.

Permeability may be calculated by analogy with the conventional flow in porous media, as was shown in equation 1.23, section 1.5, Chapter 1. An easier and more direct way is to express permeability in association with porosity through one of the equations indicated in table 4.1.

It follows from the equation,

$$K_f = \frac{1}{12 A_{fD}^2} \Phi_f^3 \quad (4.36)$$

that permeability is a function of porosity and fracture density. Considering the porosity to be expressed by,

$$\Phi_f = \frac{1}{2} H \frac{d^2 z}{dx^2} \quad (4.37)$$

as illustrated in Chapter 1 (equation 1.19), and,

$$A_{fD} = \frac{H}{S} \quad (4.38)$$

the result is,

$$K_f = \frac{1}{12} \times \frac{S^2}{H^2} \times \frac{1}{8} \left( H \frac{d^2 z}{dx^2} \right)^3 \quad (4.39)$$

Since fracture width  $b$  is a variable (figure 4.16) as a result of structural folding (a linear variation  $b = aH$ ), permeability has to be considered as an average equivalent of half of what results from equation 4.39,

$$K_f \approx \frac{1}{48} \frac{S^2}{H} \left( H \frac{d^2 z}{dx^2} \right)^3 \quad (4.40)$$

or,

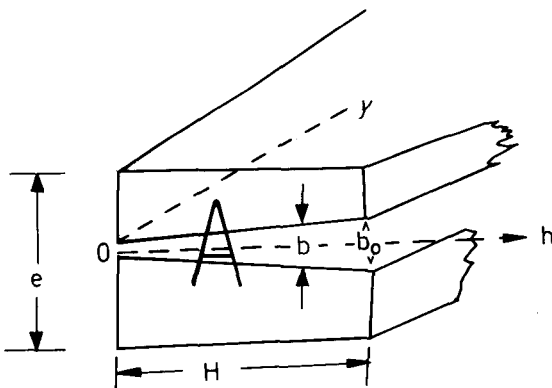
$$K_f \approx 0.02e^2 \left( H \frac{d^2 z}{dx^2} \right)^3 \quad (4.41)$$

where  $K_f(\text{cm}^2)$ ,  $e(\text{cm})$  and  $H$  with  $d^2 z/dx^2$  are the same units.

If  $K(\text{mD})$  and  $e$  are in cm, then,

$$K_f(\text{mD}) = 0.2 \times 10^{10} \times e^2 \times \left[ H \frac{d^2 z}{dx^2} \right]^3 \quad (4.41')$$

*Note:* The simplified assumptions concerning the types of fractures and their shapes restrict the validity of the results (equation 4.41) to some very limited cases. However, the order of magnitude of the result can be used for comparison with other values of fracture permeability obtained through other procedures.



4.16 – Cross-section through fracture.

#### EXAMPLE:

In a reservoir of pay  $H = 20$  feet and curvature  $d^2z/dx^2 = 10 \times 10^{-5}$  feet $^{-1}$  the distance between two adjacent fractures  $e = 10$  cm, the permeability is,

$$K_f(\text{mD}) = 0.2 \times 10^{10} \times 100 [20 \times 10^{-4}]^3 = 1600 \text{ mD}$$

For another zone of lower pay  $H = 10$  feet and small curvature  $d^2z/dx^2 = 10^{-5}$  feet $^{-1}$  and the same distance  $e = 10$  cm, the permeability is,

$$K_f(\text{mD}) = 0.2 \times 10^{10} \times 100 [10 \times 10^{-5}]^3 = 0.2 \text{ mD}$$

From the calculation example the importance of the structure curvature on well location is evident. The reduced curvature and pay reduces fracture permeability to matrix permeability, while large curvature and pay improve the productivity index considerably.

#### 4.3.8. Permeability vs. overburden pressure

A similar study to that which examined the variation of porosity with the net overburden pressure was carried out for the variation of permeability resulting from a change in the net overburden pressure<sup>5</sup>.

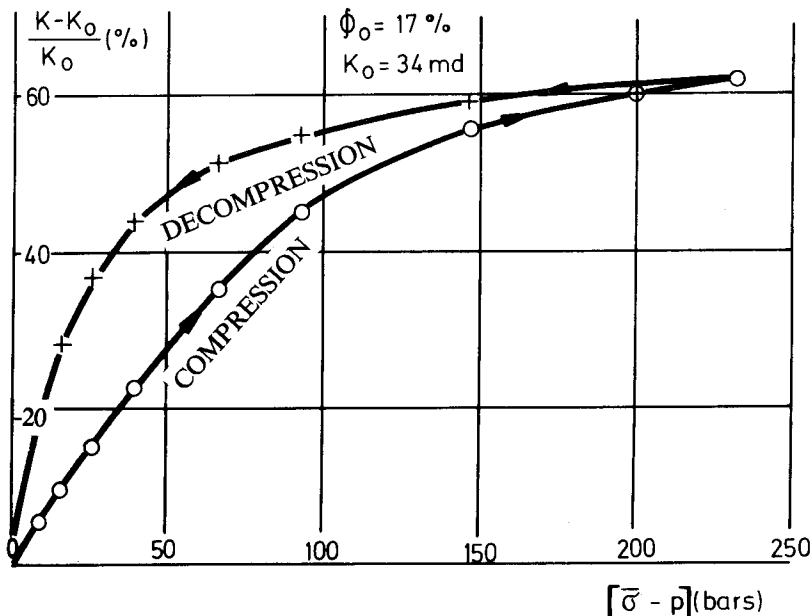
Compression and decompression of the rock in the triaxial cell are equivalent to the variation  $\bar{\sigma} - P$ , where  $\bar{\sigma}$  is the overburden pressure and  $P$  the pore pressure. The experiments were performed on intergranular limestone and fractured limestone in elastic and elasto-plastic states of deformation.

#### 4.3.8.1. Intergranular limestone core

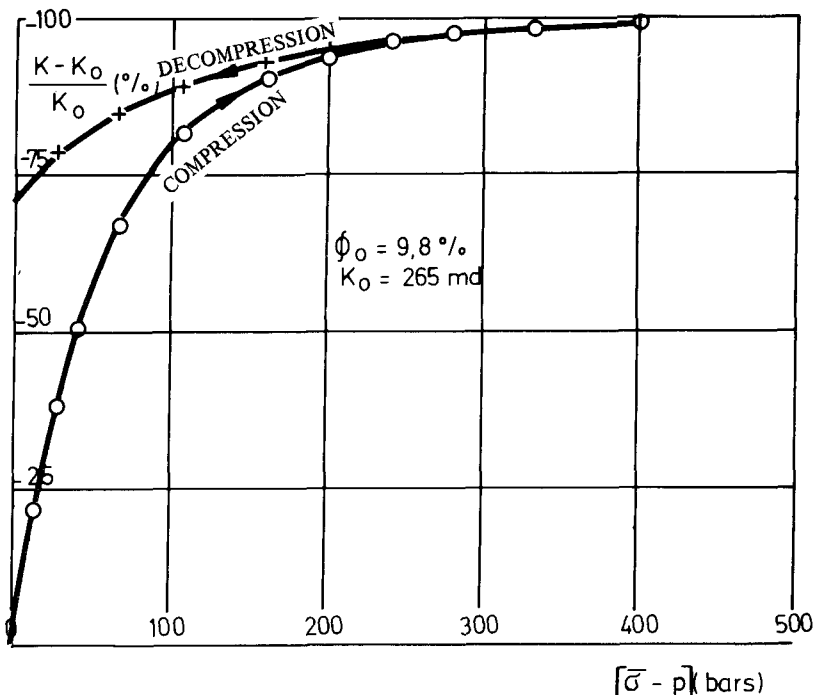
A limestone of  $\Phi = 17\%$  and  $K_o = 34\text{mD}$  showed a linear reduction of permeability (up to 100 bars) during compression, then a small parabolic decrease (up to 230 bars), and later during decompression a hysteresis is observed, since permeability remains permanently smaller than the respective value while the sample was in compression. But rock permeability returns to its original permeability when  $\bar{\sigma} - P \rightarrow 0$ , (figure 4.17).

#### 4.3.8.2. Fractured limestone core

A Courtenay fractured limestone<sup>5</sup> of  $\Phi = 9.8\%$  and  $K_o = 265\text{mD}$  was tested in compression. After a rapid linear reduction (to 100 bars) in permeability a slow parabolic reduction was observed (to 400 bars) where the permeability is practically zero [ $(K - K_o)/K_o = 100\%$ ]. In decompression the deformations are permanent and permeability will no longer be equal to the initial value, but only 25% of the original value (figure 4.18).



4.17 –  $(K - K_o)/K_o$  vs  $(\bar{\sigma} - p)$  at temperature 20 °C for Chailly limestone (Paris Basin) (Abgrall<sup>5</sup>, courtesy IFP).



4.18 –  $(K - K_0) / K_0$  vs  $(\bar{\sigma} - p)$  of fractured Courtenay limestone (Paris Basin) (Abgrall<sup>s</sup>, courtesy IFP).

#### 4.4. DISCUSSION CONCERNING BASIC PARAMETERS ( $K$ , $\Phi$ , $S_{wi}$ )

By the *routine analysis of basic rock parameters* in a conventional reservoir, is understood the evaluation in laboratory conditions of the permeability, porosity, and saturation (in the laboratory). In the case of a double porosity reservoir the evaluation of the three parameters,  $K$ ,  $\Phi$ , and  $S_{wi}$ , is more complex and loses the aspect of pure *routine analysis*.

In addition, if the data obtained in the laboratory (especially that concerning  $\Phi_f$ ,  $K_f$ , and  $S_{wi}$ ) are compared with the field data, the results are often different. The reservoir information together with lab data are used more and more to simulate a simplified geometrical model<sup>1,6,7,12,13</sup> of a fractured reservoir. The objective is to correlate the parameters, such as  $\Phi$ ,  $K$ , and  $S_{wi}$  with an idealized matrix-fracture system represented by a matrix block shape, fracture network geometry, fracture opening, fracture density, etc. Before the correlations between idealized models and field/lab data are discussed, the correlations of the basic parameters will first be examined.

#### *4.4.1. Fluid saturation in a fractured reservoir*

In a fractured reservoir, the matrix fluid saturation is a problem similar to that of a conventional reservoir. The evaluation of saturation is obtained by the same procedure through logs (indirectly) or in the laboratory by direct measurements.

The low value of the secondary porosity (fracture network, vugs) compared with the primary porosity, does not influence saturation in hydrocarbons per unit of volume. In any case, saturation in fractures could be considered 100% with the fluids of respective zones (water in water zone, oil in oil zone, etc.). But the problem of fluid saturation in a fractured reservoir must be examined in the frame of a double porosity system. In this case the relationship between matrix saturation vs. fracture saturation is evidenced by a series of peculiarities.

##### **4.4.1.1. Transition zones are absent in a fractured reservoir**

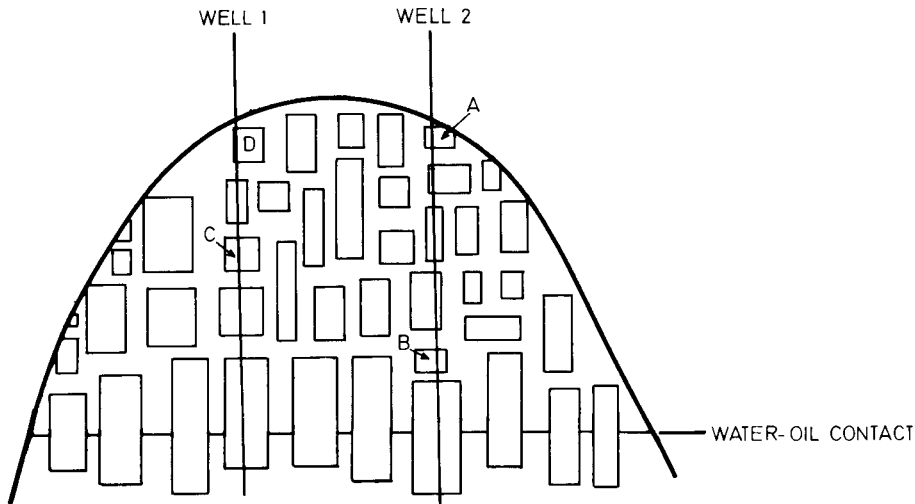
Explanation of the paradoxical aspect of the above statement is simple when compared with the concept of a conventional reservoir. Zonation in a fractured reservoir is determined by fluid distribution in the fracture network. Since the capillary forces in the fracture network are negligible if compared with gravitational forces, the two-fluid contact (water-oil, gas-oil, water-gas) will be represented by a very distinct horizontal plane (figure 4.19).

Consequently, a water-oil contact or gas-oil contact in a fracture system will delimit over the entire reservoir the water zone from the oil zone and the oil zone from the gas zone.

##### **4.4.1.2. High water saturation zones are unrelated to water-oil contact**

If rock fracturing in a fractured reservoir took place prior to hydrocarbon migration, it is possible to find inside the hydrocarbon zone variations in water saturation which are independent of the water table and transition zone. In order to show the paradoxical aspect of water saturation vs. depth, an example will be given, based on the simplified fractured reservoir shown in figure 4.19. Porosity of the matrix is assumed constant, but the average matrix block height varies as a result of the fracturing process. The high saturation in water is found in the small blocks A, B, C, and D. Any correlation of water-oil contact as an effect of the transition zone is worthless, since the blocks are far from the transition zone. The explanation is simple. During the migration phase the capillary threshold forces opposing the entering of a non-wetting phase (oil), could not be overrun by small gravity forces generated by the small block height.

$$H_{c,TH} > h_{BLOCK} \times \Delta\gamma$$



4.19 – Fractured reservoir formed by various sized matrix blocks.

For all other blocks of wells 1 and 2 with heights greater than those of blocks A, B, C, and D, gravity forces are higher than capillary forces and the matrix blocks are saturated with hydrocarbons.

It may be concluded that the magnitude of capillary threshold pressure, the matrix block height and fracture density play an essential role in saturation distribution of a fractured reservoir (further discussions on the physical aspects of the problem are given in this chapter, section 4.6, and also in Chapters 9 and 10).

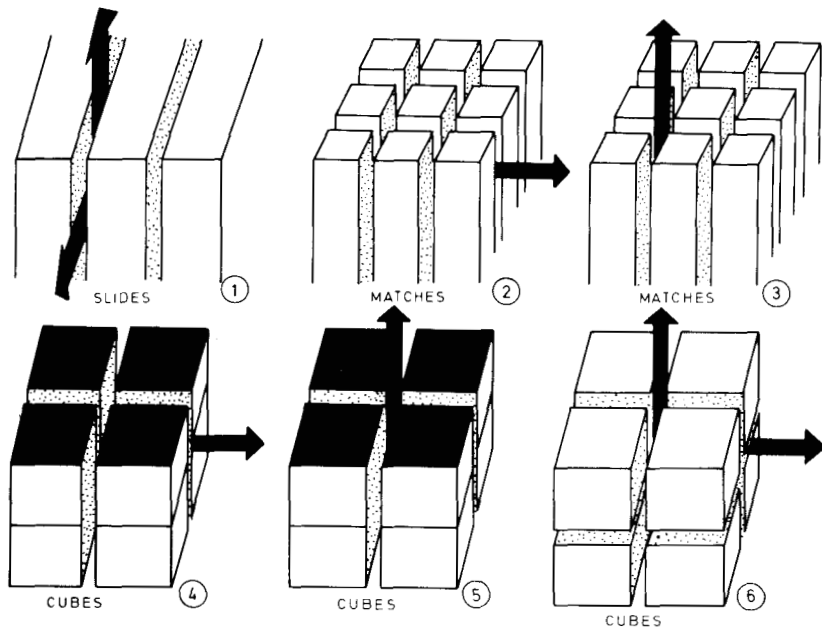
#### 4.4.2. Relationship of permeability vs. porosity

The relationship between permeability and porosity in a fractured reservoir is different from the permeability and porosity relationship in a conventional reservoir since it refers to both primary and secondary properties.

In general, the problem of intergranular primary porosity will lead to the relationship  $\Phi$  vs.  $K$ , which is similar to that of a conventional reservoir; but for the fracture network the relationship may require some different approaches.

##### 4.4.2.1. $\Phi_f$ vs. $K_f$ in a fracture network

The problem can be examined through a simplified geometrical model which may be further correlated with specific reservoir flowing problems or through the results obtained from well testing.



4.20 – Simplified geometrical matrix blocks (Reiss<sup>13</sup>).

#### a. $\Phi_f$ vs. $K_f$ in models with simplified geometry

The complex fracture-matrix structure could be reduced to matrix blocks of simple geometry (parallelepiped, cubes, sphere, etc.) separated by uniform spaced intervals which represent fracture voids. Various block geometries, such as those shown in figure 4.20 (which are named *slides*, *matches* and *cubes* in agreement with their shape<sup>13</sup>) can be considered. The size and shape of the blocks depend on fracture density and type of fracture. For example, if the horizontal fracture density is equal to the vertical fracture density, the matrix block approaches cube shape. If the vertical fracture density prevails over the horizontal fracture density, the blocks will be elongated parallelepiped, and if vice-versa, the blocks will be flat parallelepiped (as discussed in Chapter 2, section 2.3.2).

For the models presented in figure 4.20, the basic parameters, porosity  $\Phi_f$  and fracture density  $A_{fD}$ , are presented in table 4.6. Permeability  $K_f$  is expressed as a function of porosity block dimension  $a$ , or fracture opening  $b$  through dimensional and dimensionless equations.

*Example:* Basic equations of Model 5; In the case of Model 5 the basic equations to be evaluated are,

TABLE 4.6 PARAMETER OF SIMPLIFIED MODELS

MODEL		DIMENSIONLESS EQUATIONS				DIMENSIONAL EQUATIONS			
Nº	TYPE	A <sub>fD</sub>	Φ <sub>f</sub>	k <sub>f</sub> (Φ <sub>f</sub> ,a)	k <sub>f</sub> (Φ <sub>f</sub> ,b)	A <sub>fD</sub> cm <sup>-1</sup>	Φ <sub>f</sub> %	k <sub>f</sub> (Φ <sub>f</sub> ,a) darcy	k <sub>f</sub> (Φ <sub>f</sub> ,b) darcy
1	SLIDES	$\frac{1}{a}$	$\frac{b}{a}$	$\frac{1}{12}a^2\Phi_f^3$	$\frac{1}{12}b^2\Phi_f$	$\frac{1}{a}$	$\frac{1}{100}\frac{b}{a}$	$8,33 a^2\Phi_f^3$	$8,33 \times 10^{-4} b^2\Phi_f$
2	MATCHES	$\frac{1}{a}$	$\frac{2b}{a}$	$\frac{1}{96}a^2\Phi_f^3$	$\frac{1}{24}b^2\Phi_f$	$\frac{1}{a}$	$\frac{1}{100}\frac{2b}{a}$	$1,04 a^2\Phi_f^3$	$4,16 \times 10^{-4} b^2\Phi_f$
3	MATCHES	$\frac{2}{a}$	$\frac{2b}{a}$	$\frac{1}{48}a^2\Phi_f^3$	$\frac{1}{12}b^2\Phi_f$	$\frac{2}{a}$	$\frac{1}{100}\frac{2b}{a}$	$2,08 a^2\Phi_f^3$	$8,33 \times 10^{-4} b^2\Phi_f$
4	CUBES	$\frac{1}{a}$	$\frac{2b}{a}$	$\frac{1}{96}a^2\Phi_f^3$	$\frac{1}{12}b^2\Phi_f$	$\frac{1}{a}$	$\frac{1}{100}\frac{2b}{a}$	$1,04 a^2\Phi_f^3$	$4,16 \times 10^{-4} b^2\Phi_f$
5		$\frac{2}{a}$	$\frac{2b}{a}$	$\frac{1}{48}a^2\Phi_f^3$	$\frac{1}{12}b^2\Phi_f$	$\frac{2}{a}$	$\frac{1}{100}\frac{2b}{a}$	$2,08 a^2\Phi_f^3$	$8,33 \times 10^{-4} b^2\Phi_f$
6		$\frac{2}{a}$	$\frac{3b}{a}$	$\frac{1}{162}a^2\Phi_f^3$	$\frac{1}{18}b^2\Phi_f$	$\frac{2}{a}$	$\frac{1}{100}\frac{3b}{a}$	$0,62 a^2\Phi_f^3$	$5,55 \times 10^{-4} b^2\Phi_f$

UNITS : K (Darcy) , a (cm) ; b (microns) ; Φ<sub>f</sub> (percent units)

### ● Areal fracture density

$$A_{fD} = \frac{n \times l}{\text{surface}} = \frac{2a}{a^2} = \frac{2}{a}$$

### ● Volumetric fracture density and linear fracture density

$$V_{fD} = 6a^2/a^3 ; L_{fD} = \frac{n}{l} = \frac{2}{a}$$

### ● Permeability as a function of opening will result through equation 4.28.

$$K_f = \Phi_f \times \frac{b^2}{12} ; \Phi_f = \frac{2b}{a}$$

$$K_f = \Phi_f \times \frac{(\Phi_f a/2)^2}{12} = \frac{1}{48} a^2 \Phi_f^3$$

and in dimensional units, K(Darcy), a(cm), b(microns) and  $\Phi_f$ (fraction), give,

$$K_f = 2.08 \times a^2 \Phi_f^3$$

$$K_f = 8.33 \times 10^{-4} b^2 \Phi_f$$

b.  $\Phi_f$  vs.  $K_f$  for fracture-matrix alternately in parallel

The equations already discussed for single and multi-fracture systems are:

- single fracture system

$$\Phi_f = \frac{12}{b^2} K_f \quad (4.22)$$

- multi-fracture system

$$\Phi_f = \sqrt[3]{12 K_f A_{fD}^2} \quad (4.28)$$

- multi-fracture random distribution

$$\Phi_f = \sqrt[3]{29.6 K_f A_{fD}^2} \quad (4.28')$$

c.  $\Phi_f$  vs.  $K_f$  from well testing data

A correlation may be established between equation 4.28' and the value  $K_f$  obtained from oil well testing data under steady-state flowing conditions,

$$K_f = PI \frac{B\mu \ln re/rw}{2\pi h} \quad (4.42)$$

The result<sup>14</sup> will then be for an oil well

$$\Phi_f = \frac{1}{577,9} \left[ PI \frac{B_o \mu_o \log re/rw}{h} A_{fD}^2 \right]^{1/3} \quad (4.43)$$

$$\Phi_f(\text{fraction}) ; \text{PI} (\text{m}^3/\text{day/at}) ; \mu (\text{cP}) ; h (\text{meter}), A_{fD} (\text{1/cm}).$$

For gas wells in a fractured reservoir, porosity as a function of well deliverability will result as,

$$\Phi_f = \frac{1}{458} \left[ D_G \frac{(273+T) \times Z \times \mu \log r_e/r_w}{(273+T_0) h} A_{fD}^2 \right]^{1/3} \quad (4.43')$$

where temperature T (°C), and well gas deliverability  $D_G = q/\Delta(P^2)$  [ $\text{m}^3/\text{D/at}^2$ ]

If the reservoir is anisotropic a correction has to be introduced so that,

$$\Phi_{f,\text{aniz}} = \Phi_f \times J_A \quad (4.44)$$

where the correction factor,

$$J_A = \left[ \left( \frac{K_{11}}{K_{22}} \right)^2 + \left( \frac{K_{22}}{K_{11}} \right)^2 \right]^{1/3} \quad (4.44')$$

if two orthogonal directions, 11 and 22, are considered.

#### d. Calculation example

From well testing in a fractured reservoir the following data have been obtained:

Stabilized rate,  $Q = 1880 \text{ STCM/D}$  and stabilized pressure, in the formation  $\Delta P = 4.7 \text{ at}$ . Also known are: oil viscosity  $\mu_o = 1.5 \text{ cP}$ , oil volume factor  $B_o = 1.2$ , formation thickness  $h = 100 \text{ m}$ , fracture areal density  $A_{fD} = 3/\text{meter}$ , drainage radius  $r_e = 2000 \text{ m}$ , and well radius  $r_w = 10 \text{ cm}$ .

#### *Random distribution of fractures*

Permeability  $K_f$  from equation 4.42 results as,

$$K_f = \text{PI} \frac{B_o \mu_o \log^{2000/0.1}}{6.28 h} = \frac{1880}{4.7} \times \frac{1.2 \times 1.5 \log^{2000/0.1}}{6.28 \times 10^4} \times \frac{1}{0.0864} = 0.57 \text{ D}$$

Porosity in the case of a random distribution of fractures is given by,

$$\Phi_f = \frac{1}{577,9} \left[ \frac{1880}{4,7} \times \frac{1,2 \times 1,5 \times \log 2000/0,1}{100} - 0,03^2 \right]^{1/3} = 5,2 \times 10^{-4} = 0,052\%$$

*Simulated fractured reservoir by an idealized model*

If the results obtained are transformed in a fractured reservoir idealized such as model 4, table 4.6, from  $K_f$  and  $\Phi_f$  the result will be,

$$b = \sqrt{\frac{K_f}{4,16 \times 10^{-4}}} \frac{1}{\Phi_f} = \sqrt{\frac{0,57 \times 10^4}{4,16 \times 0,052}} = 162 \mu$$

$$a = \sqrt{\frac{K_f}{1,04 \Phi_f^3}} = \sqrt{\frac{0,57}{1,04 \times 0,052^3}} = 62,4 \text{ cm}$$

The new fracture density is,

$$A_{fD}' = \frac{1}{a} = \frac{1}{62,4} = 0,0162 \left( \frac{1}{\text{cm}} \right)$$

As observed  $\Phi_f$  is the same through equation,

$$\Phi_f = \frac{2b}{100a} = \frac{2 \times 162}{100 \times 62,4} = 0,052\%$$

By a similar procedure, if the reservoir data simulates a reservoir such as model 6, the result is,

$$b = \sqrt{\frac{K_f}{\Phi_f} \times \frac{10^4}{5,55}} = \sqrt{\frac{0,57}{0,052} \times \frac{10^4}{5,55}} = 140 \mu$$

$$a = \sqrt{\frac{K_f}{\Phi_f^3} \times \frac{1}{0,62}} = \sqrt{\frac{0,57}{0,052^3} \times \frac{1}{0,62}} = 80,8 \text{ cm}$$

The new fracture density is,

$$A_{fD} = \frac{2}{a} = \frac{2}{80,8} = 0,0248$$

Checking  $\Phi_f$  through parameters a and b, the result is,

$$\Phi_f = 0.03 \left| \frac{b}{a} \right| = 0.052\%$$

### *Matrix permeability $K_m$*

From a steady-state flow test, fracture permeability  $K_f$  results from the productivity index (PI)<sub>f</sub> of the fracture network. The problems which may arise are: whether or not the matrix has the capacity to feed the fracture network, and what order of magnitude should the permeability of the matrix have in order to assure this rate?

Referring to the same calculation example, according to the type of flow mechanism, the result is:

- Monophase simple expansion; If the blocks are the same as in case 6 (Table 4.6), the rate may be expressed by,

$$Q_{1 \text{ Block}} = 12a \times \frac{K_m}{\mu} \Delta P$$

and therefore,

$$(PI)_{1 \text{ Block}} = 12a \frac{K_m}{\mu}$$

The number of blocks being,

$$n = \frac{V_{\text{Bulk}}}{V_{1 \text{ Block}}} = \frac{h \times RA \text{ (reservoir surface)}}{a^3} = \frac{RA \times h}{a^3}$$

the result is,

$$(PI)_{\text{global}} = n \times (PI)_{1 \text{ Block}} = 12 \frac{RA \times h}{a^2} \times \frac{K_m}{\mu}$$

or,

$$K_m = (PI)_{\text{global}} a^2 \mu / 12 RA \times h$$

As may be observed in the case of a monophase simple expansion, a very low matrix permeability is capable of assuring a high productivity index without any difficulties at all. For a block of  $a \times 0.8m$ , and a drainage radius of 500m it results that a permeability of 0.005mD is sufficient for a productivity index of  $100 \text{ m}^3/\text{day}/\text{at}$  if  $\mu_o = 1.017 \text{ CP}$ ,  $h = a = 80 \text{ cm}$

$$K(D) = \frac{100}{0.0864} \times \frac{0.8 \times 1.017}{12 \times \pi \times 500^2} \times \frac{1}{80} = 5 \times 10^{-6} \text{ Darcy}$$

#### *Gravitational flow*

As discussed in Chapters 9 and 10 gravitational flow only gives the expression of rate and not the productivity index. Initial gravitational flow (water imbibition) for a single block instantaneously immersed in water, is expressed by the equation,

$$Q_{g, 1 \text{ Block}} = A^2 \frac{K_m}{B_o \mu_o} \Delta\gamma$$

If it is considered  $\Delta\gamma = (\gamma_w - \gamma_o) = 0.2 \times 10^{-3} \text{ Kg/cm}^3$ ;  $a = 0.8 \text{ m}$ ;  $B_o = 1.2$ ;  $\mu_o = 1.5 \text{ C.P.}$

$$Q_{g, 1 \text{ Block}} = [0.8 \times 10^2]^2 \times \frac{K_m}{1.2 \times 1.5} \times 0.2 \times 10^{-3} \times 0.0864 = 0.061 K_m(D)$$

For each row of blocks the surface corresponding to a radius of 2000m is

$$RA_{1, \text{row}} = \pi \times (2 \times 10^3)^2 = 12.56 \times 10^6 \text{ m}^2$$

and thus, the number of blocks,

$$n = 12.56 \times 10^6 / 0.64 = 19.62 \times 10^6 \text{ blocks}$$

gives the rate in  $\text{m}^3/\text{day}$ ,

$$Q_{g, 1 \text{ row}} = Q_{g, 1 \text{ block}} \times n = 0.061 \times 19.62 \times 10^6 K_m = 1.2 \times 10^6 K_m(D)$$

Rates over  $1000 \text{ STM}^3/\text{D}$  or over  $10000 \text{ STM}^3/\text{D}$  will result if the first row of blocks is totally invaded by water and if permeability is in first case higher than  $10 \text{ mD}$  and in second case higher than  $100 \text{ mD}$ . If ten rows are invaded by water the same rates will result for matrix permeabilities of respectively only  $1 \text{ mD}$  in first case and  $10 \text{ mD}$  in the second case.

Even if in gravitational conditions, the problems are different from those in mono-phase simple expansion, it is necessary to remember that a small matrix permeability becomes very productive if the flow takes place in a fractured reservoir, as a result of double-porosity flowing mechanism.

#### 4.4.2.2. $\Phi_m$ vs. $K_m$ in matrix

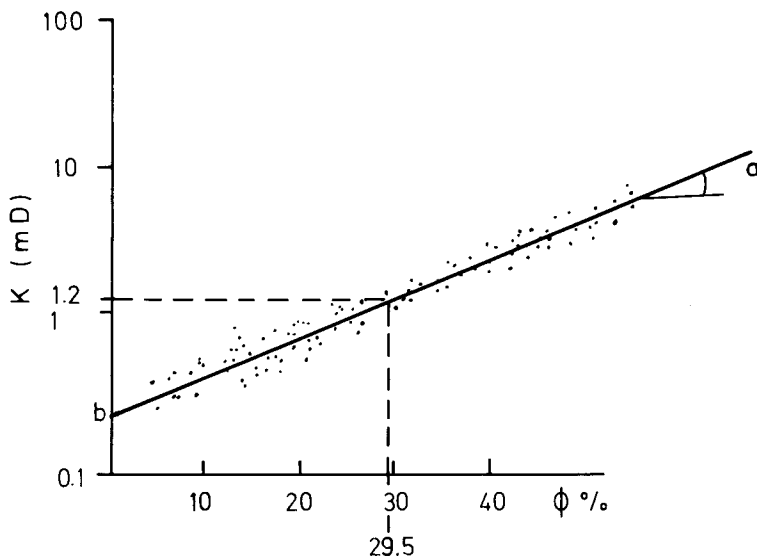
The relationship between porosity  $\Phi_m$  and permeability  $K_m$  for the matrix rock follows the classic equation,

$$K_m = e^{a\Phi_m + b} \quad (4.44)$$

or

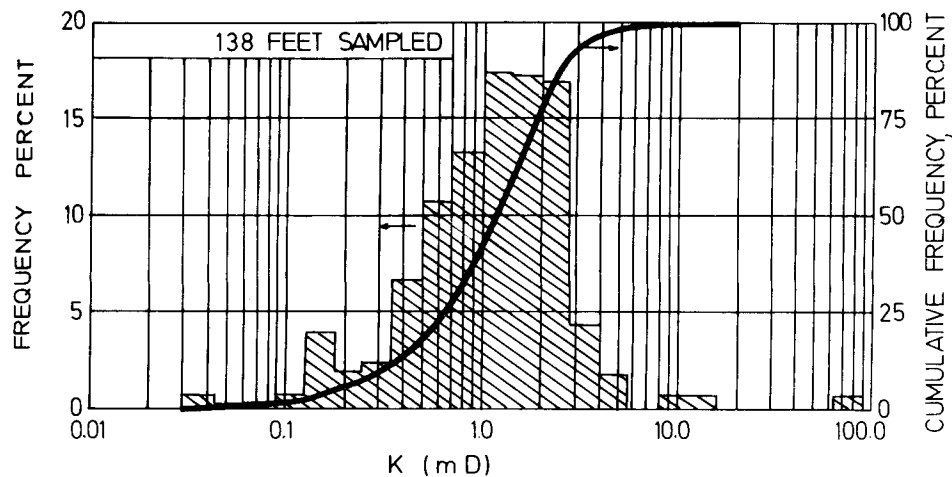
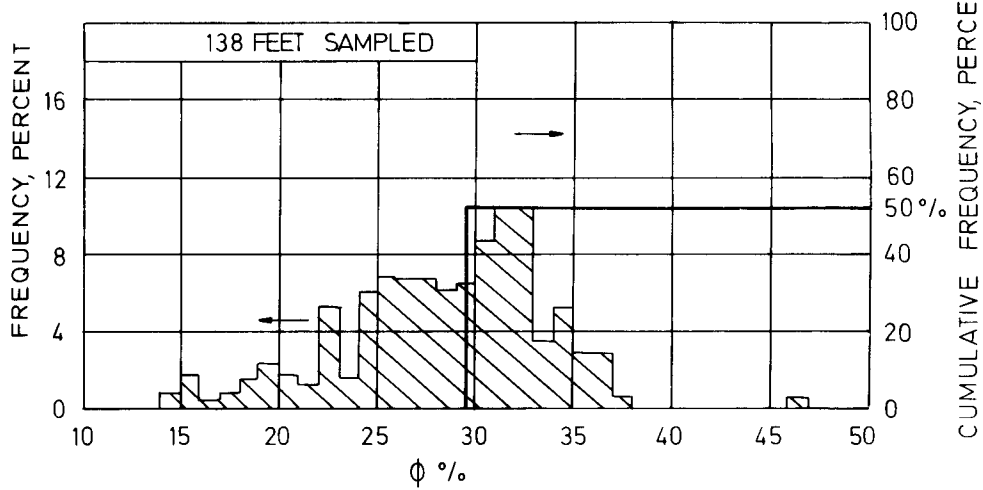
$$\log K_m = a\Phi_m + b \quad (4.45)$$

The experimental results of core analysis are introduced in a semilog diagram (figure 4.21) and a straight line (as in equation 4.44) is obtained.



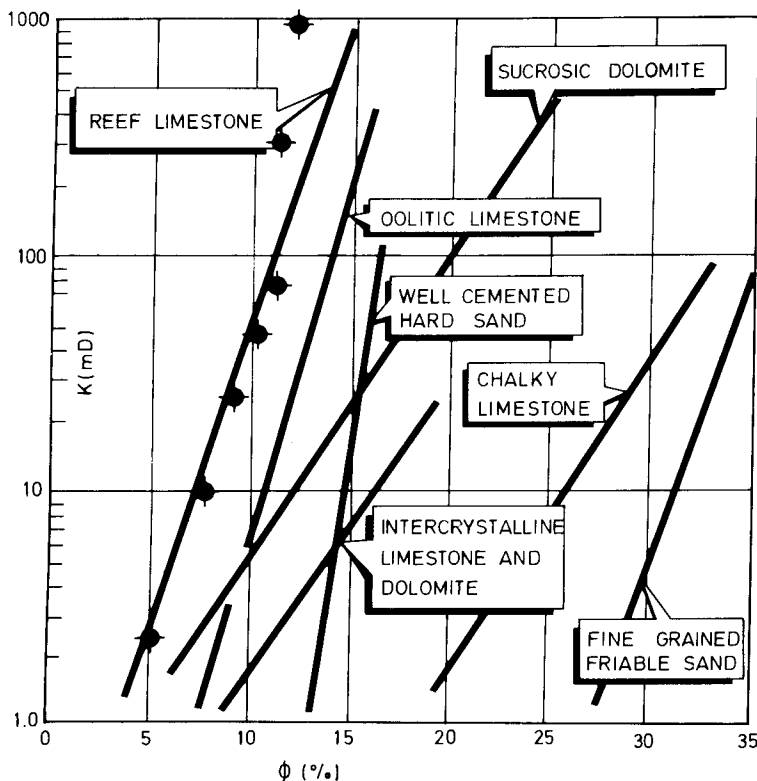
4.21 –  $K$  vs.  $\Phi$  from core data.

In order to calibrate the straight line the average permeability and average porosity are often found separately from *histograms* (as in figure 4.22a and b in the example shown  $\Phi_m = 29.5\%$  corresponds to  $K_m = 1.2 \text{ mD}$ ).

**a****b**

4.22 – Histograms: a) permeability case, b) porosity case.

In the absence of data from core analysis, various empirical correlations are given in the literature. The correlation shown in figure 4.2.3 gives the variation  $\Phi_m$  vs.  $K_m$  for various types of rocks (limestone, dolomite, sandstone, etc.)



4.23 – K vs.  $\Phi$  relationship for various rock types.

There are also various empirical analytical correlations ( $\Phi_m$  vs.  $K_m$ ) among which the Trebin<sup>8</sup> relationship is associated to the range of porosity,

$$\Phi_m < 12\% \quad K_m = 2 \times e^{-0.316 \Phi}$$

$$\Phi_m > 12\% \quad K_m = 4.94\Phi^2 - 7.63$$

In general, the low porosity equation is closer to the results from cores, and if compared with the results in figure 4.23 it matches well with the straight line of the reef limestone.

#### a. Statistical procedure<sup>15</sup>

An interesting feature of the previous equation 4.19 may be expressed by stating that a given matrix porosity  $\Phi_m$  corresponds to a given permeability  $K_m$  at all values of

$$X^* = \frac{\Phi_m - \bar{\Phi}}{\sigma_{\Phi}} \quad (4.46)$$

through the equation

$$\log K_m = (\Phi_m - \bar{\Phi}) - \frac{\sigma_k}{\sigma_{\Phi}} + \log \bar{K} = a\Phi_m + b \quad (4.47)$$

where

$\bar{\Phi}$  ~ arithmetic means (average porosity)

$\Phi_{SD}$  ~ porosity at a given standard deviation above  $\Phi_m$

$$\sigma_{\Phi} = |\Phi_{SD} - \bar{\Phi}| \quad (4.48)$$

$$\sigma_k = |\log K_{SD} - \log \bar{K}| \quad (4.49)$$

$$a = -\log(1 - V_k) / \Phi_m \quad (4.50)$$

$$b = -a\bar{\Phi} + \log \bar{K} \quad (4.51)$$

$$V_{\Phi} = \frac{\bar{\Phi} - \Phi_{84,1}}{\bar{\Phi}} = \frac{\sigma_{\Phi}}{\bar{\Phi}} \quad (4.52)$$

$$V_k = \frac{\bar{K} - K_{84,1}}{\bar{K}} \quad (4.53)$$

Based on statistical evaluation of  $\Phi_m$  and  $K_m$  data, through normal and log-normal definitions, the values  $\sigma_k$ ,  $\sigma_{\Phi}$ ,  $\bar{K}$ ,  $\bar{\Phi}$  are known and equation 4.45 can be defined (Whitson<sup>15</sup>).

### b. Example<sup>15</sup>

If the following data are known:

$\bar{\Phi} = 0.2$  – from porosity data obtained through log analysis (as average value).

$\Phi_{84,1} = 0.13$  – from normal probability plot of porosity data at standard deviation 84.1%.

$\bar{K} = 100$  mD (geometric) average resulted from DST interpretation.

$V_k = 0.7$  permeability variation by Dykstra-Parson obtained from an analogical formation.

The relationship  $K$  vs.  $\Phi$  will be obtained through the following procedure:  
It results in this case from equation 4.53 that:

$$K_{84,1} = (1 - V_k) \bar{K} = (1 - 0.7) 100 \text{ mD} = 30 \text{ mD}$$

and from equation 4.48 and 4.49

$$\sigma_\Phi = |\Phi_{84,1} - \Phi| = |0.13 - 0.2| = 0.07$$

$$\sigma_k = |\log K_{84,1} - \log \bar{K}| = |\log 30 - \log 100| = 0.523$$

In continuation from 4.52 and 4.53

$$V_\Phi = \frac{\sigma_\Phi}{\Phi} = \frac{0.07}{0.2} = 0.35$$

$$V_k = \frac{\bar{K} - K_{84,1}}{K} = \frac{100 - 30}{100} = 0.7$$

from which

$$a = -\frac{\log(1 - V_k)}{\Phi V_\Phi} = -\frac{\log(1 - 0.7)}{0.2 \times 0.35} = 7.47$$

$$b = -a \bar{\Phi} + \log \bar{K} = -(7.47)(0.2) + \log 100 = 0.506$$

The matrix permeability ( $K_m$ ) vs. porosity ( $\Phi_m$ ) relationship based on equation 4.47 becomes

$$\log K_m = (\Phi_m - 0.2) \frac{0.523}{0.070} + \log 100$$

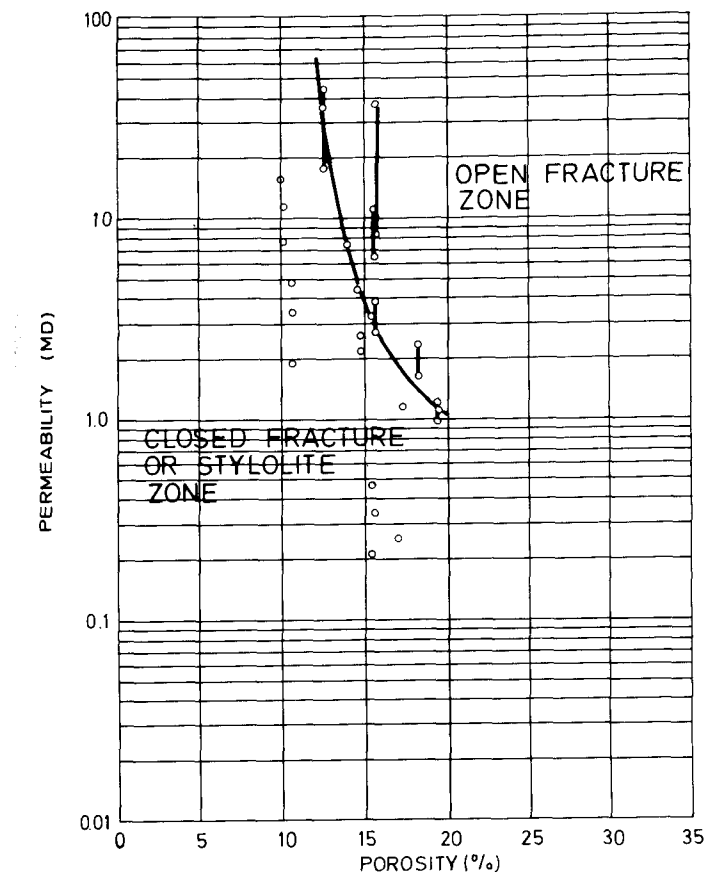
or

$$\log K_m = 7.47 \Phi_m + 0.506$$

#### 4.4.2.3. $\Phi$ vs. $K$ in a fracture-matrix system

##### a. Correlation by using conventional core analysis

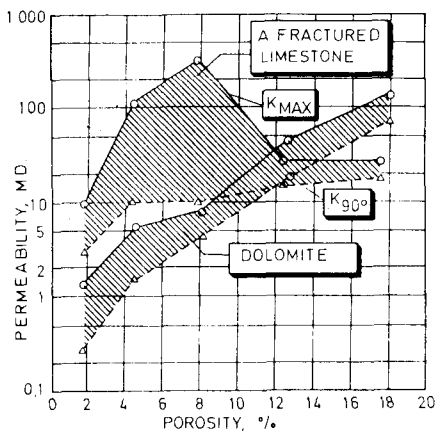
If the samples examined in the laboratory are not only a compacted rock matrix, but also contain fractures, the relationship between porosity and permeability will change. The data obtained from the analysis of samples will be dispersed as in figure



4.24 – K vs.  $\Phi$  in fractured cores.

4.24 (not as in figure 4.21). It was observed that in the range of larger porosities, the permeabilities measured by conventional procedures showed larger variations.

From the example shown in figure 4.24, it is observed that if  $\Phi = 16.2\%$ , the permeability  $K$  varies from 2 to 40mD. From the experimental data, it is possible to draw a curve which represents the relationship  $\Phi_m$  vs.  $K_m$ . Above this curve the parameters obtained are influenced by the presence of open fractures, and below this curve the data obtained represent the matrix, including closed fractures and stylolites.



4.25 –  $\Phi$  vs.  $K_{\max}$  and  $K_{90^\circ}$  for dolomite and limestone (Kelton<sup>9</sup>, courtesy AIME).

### b. Correlation by using the Kelton permeameter

If permeability is measured through Kelton procedure, the relationship  $\Phi$  vs.  $K$  must include both values  $K_{\max}$  and  $K_{90^\circ}$ . If the results obtained from the Ellenburger formation of the Fullerton Field (table 4.7) are introduced in a diagram  $\Phi$  vs.  $\log K$  as in figure 4.25, they show that:

- For a fractured limestone in a low porosity range (between 2–4%) the  $K_{\max}$  value increases considerably compared with  $K_{90^\circ}$ . But for high porosity range (over 12%), the ratio  $K_{\max}/K_{90^\circ}$  becomes constant.
- For dolomites, independent of the porosity range, the linear relationship  $\Phi = \ln K_{\max}$  is parallel to  $\Phi = \ln K_{90^\circ}$ .

TABLE 4.7. Ellenburger formation, Fullerton Field  
Variation  $\Phi - K_{\max}$  and  $\Phi - K_{90^\circ}$

Porosity Range	%	0–3	3–6		6–10	10–15	>15
Permeability mD		<0.1	>0.1	<0.1	>0.1		
Number Samples	12	75	8	88	94	105	99
Porosity (% Bulk)	1.57	1.89	4.34	4.36	7.82	12.43	17.53
Oil (% Pore)	0.9	4.5	8.6	7.5	12.7	16.7	19.9
Water (% Pore)	85.1	73.9	59.7	55.0	42.4	30.5	29.7
Gas (% Pore)	14.0	21.6	31.7	37.5	44.9	52.8	50.4
$K_{\max}$ (md)	0.04	11	0.05	133	335	28	28
Range	0.00	0.13	0.00-	0.11-	0.08-	0.00-	3.01-
	0.10	228	0.08	9.680	27.400	334	793
$K_{90^\circ}$ , md	0.03	3.33	0.02	11	10	16	18

#### 4.4.3. Data and examples of basic parameters

From the literature, the order of magnitude of parameters, such as  $\Phi_m$ ,  $\Phi_f$ ,  $K_{max}$ ,  $K_{90^\circ}$ , etc., are presented in tables 4.8 to 4.13. The data concern Iranian and USA fields<sup>16 17</sup>.

##### 4.4.3.1. Ellenburger formation of Fullerton Field

From 300 to 500 samples of fractured limestone and nonfractured dolomite, the porosity, saturation and permeability are given in table 4.8.

TABLE 4.8. Formation parameters of the Ellenburger Formation, Fullerton Field<sup>9</sup>.

Formation:	$\Phi_m$ Porosity % Bulk	Water		Oil		$K_{max}$ , md Aver. Range	$K_{90^\circ}$ Aver. Range
		% Bulk	% Pore	% Bulk	% Pore		
Low-porosity fractured formation	2.38	1.41	60	0.39	16	96	1-5060
Fractured limestone	9.05	4.14	46	1.12	12	106	0-27400
Non-fractured dolomite	8.72	3.65	42	1.31	15	42	0-970
						19	0-857

Another classification in four groups of cores is shown as a relationship between matrix characteristics and whole core data (table 4.9). The rest of the data includes saturation,  $K_{max}$  and  $K_{90^\circ}$ , and porosity values.

TABLE 4.9. Matrix vs. whole core data.  
Ellenburger, Fullerton Field<sup>9</sup>

Group	1	2	3	4
Gas, % bulk	0.08	0.91	0.63	3.72
Oil, % bulk	0.06	0.06	0.88	1.84
Water, % bulk	2.07	1.65	1.66	3.27
% pore	94	63	52	39
Matrix porosity, % bulk	1.98	1.58	2.56	7.92
% total pore	90	60	81	94
Total porosity, % bulk	2.21	2.62	3.17	8.40
$K_{max}$ , md	10	409	23	94
$K_{90^\circ}$ , md	0.6	1.2	10	38
Matrix K, md	0.3	0.2	0.3	3.7

There is also a classification through sample descriptions associated to the content of hydrocarbons, which is described qualitatively and quantitatively in four groups (table 4.10).

TABLE 4.10. Classification of data from Ellenburger, Fullerton Field<sup>9</sup>

Group	Gas content	Oil content	Sample description
Group 1	low 0–0.29% bulk	low 0–0.4% bulk	dense & few fractures
Group 2	intermediate 0.4–1.52% bulk	low 0–0.16% bulk	large fractures and open vugs
Group 3	intermediate 0.06–0.89% bulk	intermediate 0.17–2.10%	intergranular porosities developed
Group 4	high gas 1.43–5.63% bulk	high oil bulk 1.05–2.40% bulk	intergranular & fractures

#### 4.4.3.2. Iranian field data

The general qualitative evaluation of Iranian fields is presented for matrix characteristics  $\Phi_m$ ,  $K_m$  and  $S_{wi}$ , (table 4.11).

Table 4.11. Iranian fields qualitative evaluation<sup>10</sup>

Type of Rock	$\Phi_m$ (%)	$K_m$ (mD)	$S_{wi}$ (%)
Good	>8%	>>1	25
Poor	5–8%	0.1–1	25–50
Dense	<5%	<0.1	>50

In the specific case of the Gachsaran field core data, a more detailed qualitative classification will result (table 4.12).

TABLE 4.12. Gachsaran field data

$\Phi_m$ Porosity Range %	$K_m$ Permeability Range, md	$S_{wi}$ Water Content %	Qualitative description
12–18	4–100	10–15	Good productive rock
8–17	0.5–10	15–30	Good permeability
8–15	0.5– 5	15–30	Low content in water
8–10	0.5– 2	20–30	
8–12	0.1–0.5	30–40	Poor productive rock
13–16	0.1	25–30	
8–12	0.05	40–60	Very low permeability
6– 8	0.2	30–50	
5– 8	0.3	30–50	Rather high sat. in water
4– 8	1.0	25–50	
5– 8	–	60–80	Dense, unproductive rock
3– 8	–	70–100	No permeability
0– 4	–	100	High water saturation

The average porosities of large Iranian fields<sup>16</sup> are shown in table 4.13.

TABLE 4.13. Porosity of Iranian fields.

Field	Average Porosity Percent
Agha Jori	14
Ahwaz	12 (F.L.S.) 25 (S.S.)
Bibi Hakimeh	10
Cyrus	24
Darius Kharg	14
Gachsaran	11
Haft Kel	16
Karanj	10
Lali	7
Mashjid-i-Sulalman	11-0
Naft-e-Shah	
Naft Safid	14
Pazanan	12

The qualitative appreciation of the calcarenites based on Iranian field data<sup>17</sup> is given in table 4.14.

TABLE 4.14. Qualitative evaluation of calcarenite reservoir rock.

Qualitative values	GOOD		MEDIUM		MEDIUM-LOW		POOR		VERY POOR	
	$\Phi(\%)$	$K(mD)$	$\Phi(\%)$	$K(mD)$	$\Phi(\%)$	$K(mD)$	$\Phi(\%)$	$K(mD)$	$\Phi(\%)$	$K(mD)$
Calcarene medium-grained	15-17		11-15		6-11		0.5-6		<0.5	
Calcarene fine-grained	18-20		14-18		8-14		2-8		<2	
Calcisiltite, <3.3 coarse-grained	22-24	500- 1000	17-22	10-20	10-17	10-100	3-10	1-10	<3.3	<1
Calcisiltite fine-grained	<1		21-27		12-21		4-12		<3.6	
	27-29									

#### 4.4.4. Variation of $\Phi$ and $K$ with reservoir pressure decline

As discussed in Chapter 1, the difference between overburden pressure  $\bar{\sigma}$  and pore pressure  $p$  called net overburden pressure, increases during reservoir depletion since reservoir pressure  $p$  declines.

The increasing net overburden pressure and its consequences on fractured reservoir permeability and porosity has been examined in a series of experimental works<sup>5 18 19</sup>. The behaviour of the whole bulk (matrix + fracture) was examined through triaxial cell tests<sup>5 19</sup>. For better experimental conditions a Hassler type core holder was used, and the compressive loading was simulated by compressing oil through the annulus space<sup>18</sup> (figure 4.26).

The following has been deduced from the experimental results:

- Fracture permeability is very much reduced with the increase of the confining pressure, which is equivalent to the increasing net overburden pressure.
- Total rock permeability  $K_t$ , as defined in equation 4.17, is expressed by the summation of the two permeabilities,  $K_m$  and  $K_f$ :

$$K_t = K_f + K_m$$

but fracture permeability compared with matrix permeability is very sensitive to the modification of the effective pressure  $P_e = \bar{\sigma} - p$ . The following equation was proposed,

$$\frac{K_f}{K_{fi}} = \left[ \frac{\log P_e - 4.602}{\log P_{ei} - 4.602} \right]^3 \quad (4.54)$$

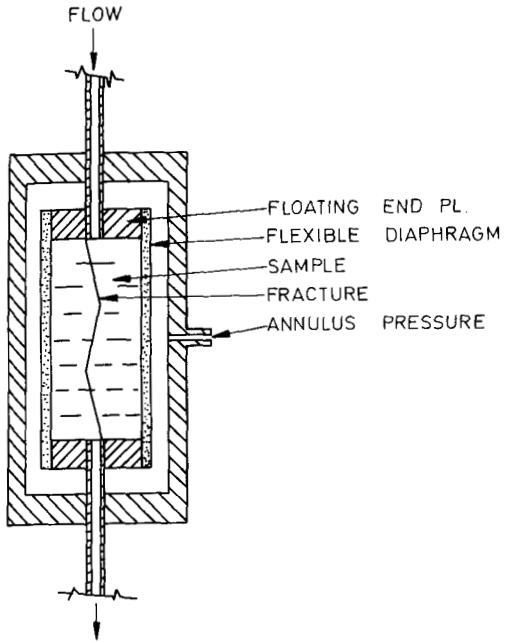
where fracture permeability and fracture porosity are related by the equation,

$$\frac{K_f}{K_{fi}} = \left[ \frac{\Phi_f}{\Phi_{fi}} \right]^3 \quad (4.55)$$

A nomogram<sup>18</sup> was elaborated for net overburden pressure up to 20,000 psi (figure 4.27), which directly gives the ratio  $K/K_i$  and  $\Phi/\Phi_i$ . A straight line is drawn between the initial net overburden pressure and the pole. All values  $K/K_i$  and  $\Phi/\Phi_i$  will be obtained for the new net overburden pressure through the traced straight line.

**CALCULATION EXAMPLE:** In a fractured reservoir the following data are known: — total permeability  $K_t = 25 \text{ mD}$ ; matrix permeability  $K_m = 3 \text{ mD}$ ; initial fracture porosity  $\Phi_{fi} = 0.3\%$ ; overburden pressure 10,000 psi; initial pore pressure  $p = 7000 \text{ psi}$ .

It is required to find the variation of  $K_f$  and  $\Phi_f$  versus reservoir pressure decline.



4.26 – Permeameter for evaluation of  $K$  vs.  $\bar{\sigma}-p$  (Jones<sup>18</sup>, courtesy AIME).

**SOLUTION:** By using the equations 4.54 and 4.55 during depletion of the reservoir, the result will be obtained through,

$$K_f = 22 \times \left[ \frac{\log (\bar{\sigma}-p) - 4.6}{\log 3000 - 4.6} \right]^3 = 22 \times \left[ \frac{\log (\bar{\sigma}-p) - 4.6}{-1.12} \right]^3 = 22 \times 0.516$$

$$K_f = 11.35 \text{ mD}$$

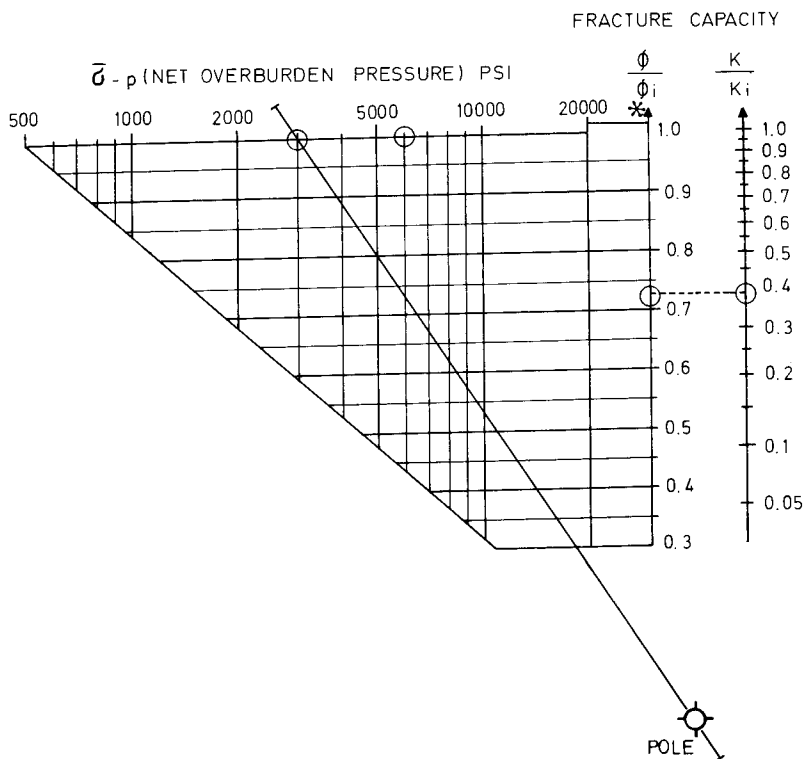
$$\Phi_f = 0.3 \times \left( \frac{K_f}{22} \right)^{1/3} = 0.107 (K_f)^{1/3} = 0.107 (11.35)^{1/3} = 0.238$$

From figure 4.27 the new permeabilities and porosities will result the same. For example, the  $\bar{\sigma}-p = 10,000 - 7000 = 3000$  psi is connected with the pole of figure 4.27. For the new value  $P = 5000$  psi, the result is  $\bar{\sigma}-P = 5000$  psi, and through the straight line the result is,

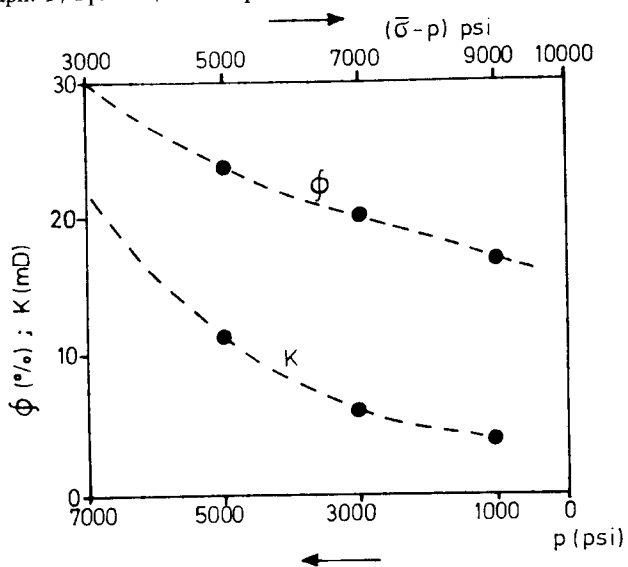
$$\Phi_f / \Phi_{fi} \approx 0.8 \text{ and } K_f / K_{fi} \approx 0.516$$

$$\Phi_f = 0.8 \times 0.3 \approx 0.24\% \quad K_f \approx 0.516 \times 22 = 11.35 \text{ mD}$$

The variation of porosity  $\Phi_f$  and permeability  $K_f$ , vs. reservoir pressure is shown in figure 4.28.



4.27 – Nomograph:  $\Phi/\Phi_i$  and  $K/K_i$  vs  $\bar{\sigma}-p$ .



4.28 – Calculated result from nomograph Fig. 4.27.

TABLE 4.15

P (psi)	$\bar{\sigma} - P$ psi	$K_f$ (mD)	$K_t$ (mD)	$\Phi_f$ %
7000	3000	22,00	25,00	.30
5000	5000	11,35	14,36	.24
3000	7000	6,68	9,68	20
1000	9000	4,18	7,18	17

#### 4.5. COMPRESSIBILITY IN A FRACTURED ROCK

In a fractured reservoir, compressibility of a rock system plays an important role, especially if there is a great contrast between the two porosities of matrix and fractures ( $\Phi_f \ll \Phi_m$ ). The role of compressibility is essential in the interpretation of the transient pressure behaviour resulting from well testing. In this case, compressibility associated to the double porosity system is expressed by the *storage capacity* parameter which extensively controls pressure behaviour.

Compressibility is, in general, defined as the change  $\Delta V$  per unit of volume  $V$  for an applied pressure  $\Delta P$ :

$$C = -\frac{1}{V} \frac{\Delta V}{\Delta P} \quad (4.57)$$

According to volume  $V$  to which it may refer, compressibility may represent a property of a certain rock volume submitted to compression, such as a bulk volume ( $V_B$ ), or only to the pore ( $V_p$ ) or fluid volume ( $V_f$ ).

The change in volume due to the variation of effective net pressure  $P_{eff}$  is the result of a change, either in overburden stress  $\bar{\sigma}$  (while the pore pressure  $P$  remains constant) or a change in pore pressure  $P$  (while the overburden pressure  $\bar{\sigma}$  remains constant). The usual case during reservoir production history is given by a change in pore pressure,

$$P_{eff} = \bar{\sigma} - P$$

as the result of a reservoir depletion.

The relationship between compressibility and the fracture-matrix system has to be examined in detail.

#### 4.5.1. Rock compressibility

##### 4.5.1.1. Conventional reservoir

The compressibility of rock in a conventional reservoir refers to bulk, rock and pore volume,

$$\left. \begin{aligned} V_B &= V_r + V_p \\ V_p &= V_B \times \Phi \end{aligned} \right\} \quad (4.57)$$

and is expressed through a basic definition<sup>20</sup>,

$$\left. \begin{aligned} - \text{ Bulk compressibility } C_B &= \frac{1}{V_B} \cdot (dV_B/dP)_{\sigma=\text{constant}} \\ - \text{ Matrix compressibility } C_r &= \frac{1}{V_r} \cdot (dV_r/dP)_{\sigma=\text{constant}} \\ - \text{ Pore compressibility } C_p &= \frac{1}{V_p} \cdot (dV_p/dP)_{\sigma=\text{constant}} \end{aligned} \right\} \quad (4.58)$$

Based on equations 4.57 and 4.58,

$$\frac{dV_p}{V_p} \approx \frac{1}{\Phi} \times \frac{dV_B}{V_B} \quad (4.59)$$

$$C_p = \frac{1}{\Phi} C_B \quad (4.60)$$

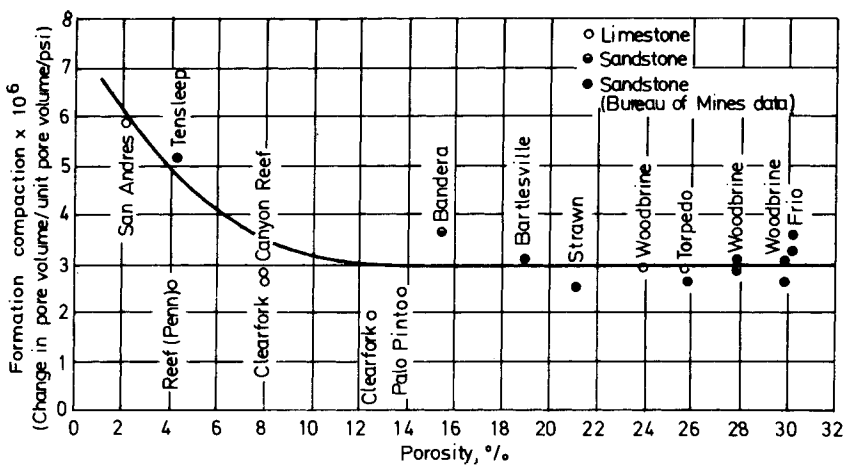
$$C_r = \frac{1}{1-\Phi} C_B \quad (4.60')$$

$$C_p = \frac{1-\Phi}{\Phi} C_r \quad (4.60'')$$

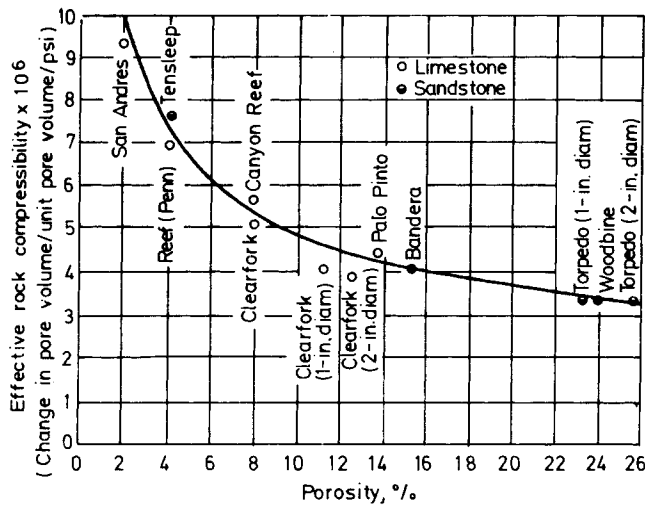
The experimental results<sup>21</sup> obtained from various formations are presented as the relationships between pore compressibility and porosity (figure 4.29) and rock compressibility and porosity (figure 4.30).

In the absence of horizontal compaction there will be no deformation and, thus, the effective compressibility of reservoir rock, when the reservoir is depleted, can be expressed by,

$$\frac{1}{V_p} \times \frac{dV_p}{dp} \approx \frac{1}{2} \frac{C_B}{\Phi} = \frac{1}{2} C_p \quad (4.61)$$



4.29 – Formation compaction vs. porosity (Hall<sup>25</sup>, courtesy AIME).



4.30 – Effective rock compressibility vs. porosity (Hall<sup>25</sup>, courtesy AIME).

#### 4.5.1.2. Fractured reservoir

In the case of a fractured reservoir in addition to primary porosity of matrix ( $m$ ), it is necessary to take into consideration the secondary porosity of fractures ( $f$ ), caverns ( $c$ ), and vugs ( $v$ ). Rock compressibility is then expressed by,

$$C_r = C_m + \Phi_c C_c + \Phi_f C_f + \Phi_v C_v$$

Some simplifications obtained from the experimental results allow the following statements:

- compressibility of vugs and caverns may be approximated

$$C_v \approx 3C_m$$

- Secondary porosity compressibility in carbonates (psp) can be expressed by,

$$C_{psp} \approx \left[ \left( \frac{\Phi_{fr}}{\Phi_{ts}} \times \frac{1350}{\sigma - P} \right) - 0.09 \right] \times 10^{-4} \quad (4.62)$$

where  $\Phi_{ts}$  is total secondary porosity (fraction). In equation 4.62 the pressure and compressibilities are given in  $\text{Kg/cm}^2$ . The variation of the fracture porosity ratio  $\Phi_{fr}/\Phi_{ts}$  (expressed as a fraction of total secondary porosity) vs. secondary pore compressibility  $C_{ps}$  is shown in figure 4.31.

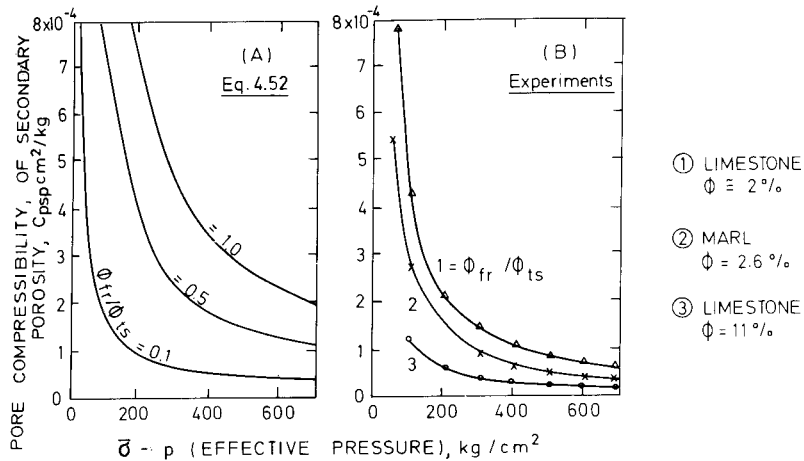
In figure 4.31A the results of equation 4.62 for various ratios  $\Phi_{fr}/\Phi_{ts}$  are presented. In figure 4.31B experimental data for three types of rocks, low porosity limestone ( $\Phi = 2\%$ ), marl ( $\Phi = 2.6\%$ ) and high porosity limestone ( $\Phi = 11\%$ ), are presented.

The experimental trend confirms the theoretical approach, figure 4.31 B.

#### 4.5.2. Fluid compressibility

The compressibility of the fluids saturating the pores, if evaluated at isothermal conditions, for each of the three phases, oil, water and gas, will give, respectively,

$$C_o = - \frac{1}{V_o} \times \frac{dV_o}{dp} = - \frac{1}{B_o} \frac{dB_o}{dP}$$



4.31 – Pore compressibility vs. effective pressure ( $\bar{\sigma} - p$ ) in the case of fractured cavernous limestone: A theoretical relationship, B experimental relationship.

$$\left. \begin{aligned} C_w &= -\frac{1}{V_w} \times \frac{dV_w}{dP} = -\frac{1}{B_w} \quad \frac{dB_w}{dP} \\ C_g &= -\frac{1}{V_g} \times \frac{dV_g}{dP} = -\frac{1}{B_g} \quad \frac{dB_g}{dP} \end{aligned} \right\} \quad (4.63)$$

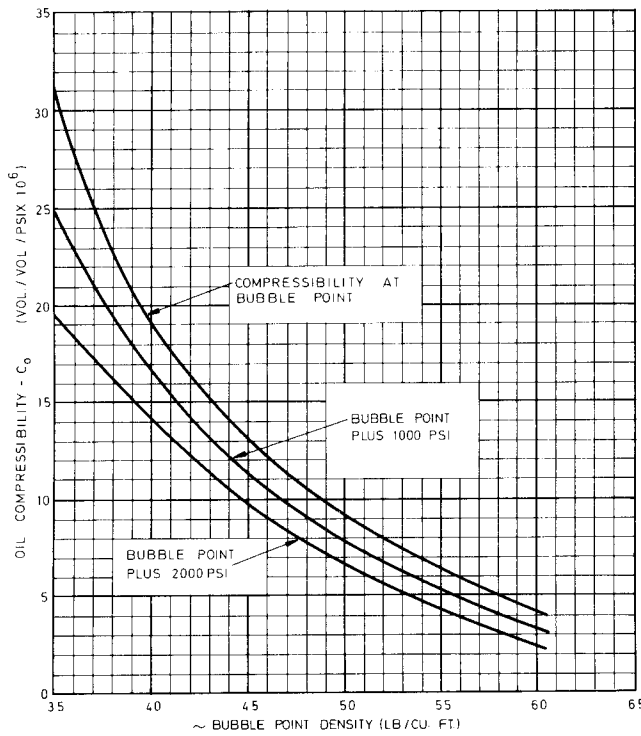
Oil compressibility,  $C_o$ , is obtained from the relationship  $B_o$  vs.  $P$  when  $P > P_b$ . An approximated relationship is given in figure 4.32 between bubble point density value and oil compressibility for various undersaturated oils where various overpressures ( $P_i - P_b$ ) are taken into consideration.

The equation which fits the curve is the following

$$C_o = \left[ \exp \frac{\varrho_{ob} + [0.004347(P - P_b) - 79.1]}{7.141 \times (10^{-4})(P - P_b) - 12.938} \right] \times 10^{-6} \quad (4.64)$$

Another equation which represents a more complex correlation (Vasquez<sup>15</sup>) is,

$$C_o = (-1433 + 5R_{sb} + 17.2T - 1180\gamma_g + 12.61\text{API})(10^{-5})/P \quad (4.64')$$



4.32 – Oil compressibility ( $P > P_B$ ) vs. density at  $P_B$ .

In addition, an approximate compressibility for fluids and rocks is given in the diagram in figure 4.33. The data concerns an average oil of 30°API and a free gas of gravity 0.75.

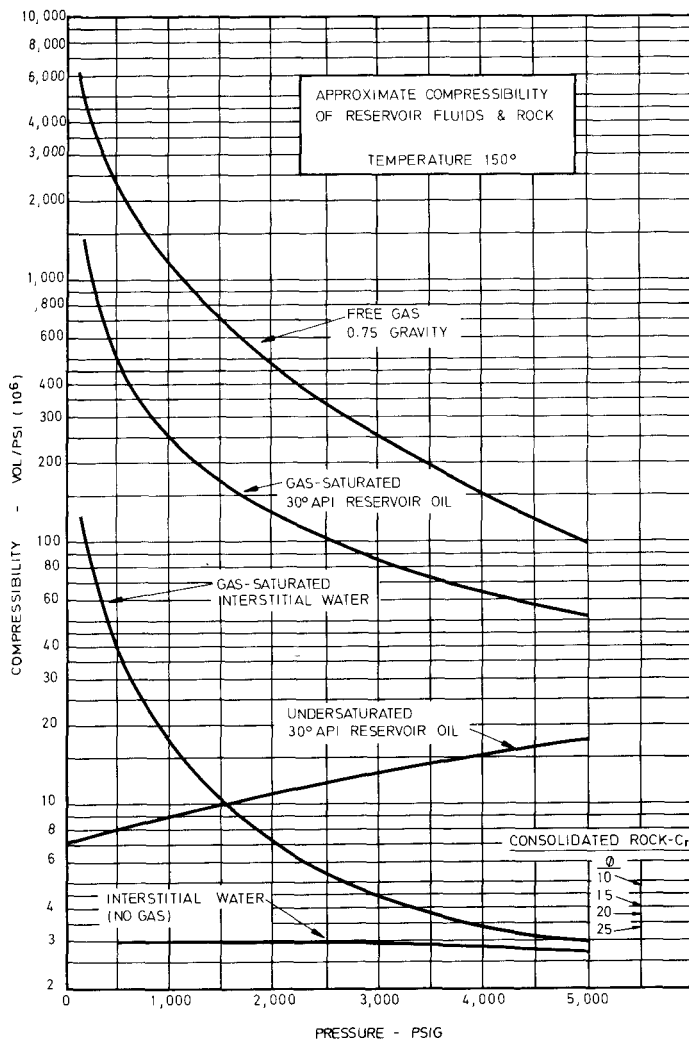
#### 4.5.3. Total compressibility (rock and fluid)

Total compressibility of the system, including the rocks and fluids which saturate the pores, may be written as the sum of all terms contained in a porosity unit,

$$C_T = S_o C_o + S_w C_w + S_g C_g + C_p \quad (4.65)$$

##### 4.5.3.1. Effective compressibility in a conventional reservoir

Total compressibility when referring to only one phase becomes effective compressibility for the given phase. For example, the effective compressibility for oil is expressed by,



4.33 – Rock and reservoir fluid compressibility vs. pressure.

$$C_{e,o} = C_o$$

or if combined with equation 4.65, the result is,

$$C_{e,o} = C_o + \frac{S_w C_w + S_g C_g + C_p}{S_o} \quad (4.66)$$

or if  $S_o = S_{oi} = 1 - S_{wi}$  and  $S_g = 0$ ,

$$C_{e,o} = C_o + \frac{S_w C_w + C_p}{1 - S_{wi}} \quad (4.67)$$

or,

$$C_{e,o} = C_o + \frac{S_w C_w}{1 - S_{wi}} + C_f \frac{1 - \Phi}{\Phi} \cdot \frac{1}{1 - S_{wi}} \quad (4.68)$$

By analogy, in a gas reservoir,

$$C_{e,g} = C_g + \frac{C_w S_w + C_p}{1 - S_{wi}} \quad (4.69)$$

but often, since  $C_g \gg C_w$  and  $C_g \gg C_p$ , the equation 4.59 may be reduced to,

$$C_{eg} \approx C_g \approx Z/p \quad (4.70)$$

#### 4.5.3.2. Effective compressibility in a fractured reservoir

In the case of a double porosity reservoir, oil saturation ( $S_o = 1 - S_{wi}$ ) in the matrix is related to the magnitude of interstitial water saturation, while in the fracture network ( $S_o = 1$ ) since the interstitial saturation in water is zero.

$$\left. \begin{array}{l} S_{oif} \approx 1 \\ S_{wif} \approx 0 \\ S_{oim} = 1 - S_{wim} \end{array} \right\} \quad (4.71)$$

In this case,

$$\begin{aligned} C_{eo} \approx C_o + C_w & \frac{\Phi_m S_{wm}}{\Phi_m (1 - S_{wim}) + \Phi_f} + C_{pm} \frac{\Phi_m}{\Phi_m (1 - S_{wim}) + \Phi_f} \\ & + C_{pf} \frac{\Phi_f}{\Phi_m (1 - S_{wim}) + \Phi_f} \end{aligned} \quad (4.72)$$

where all compressibilities may be approximated from figure 4.33, since the fracture porosity is very small,

$$\Phi_f \ll \Phi_m$$

$$C_p = C_{pm} + C_{pf} \quad (4.73)$$

and thus, equation 4.72 becomes,

$$C_{eo} \cong C_o + C_w \cdot \frac{S_{wm}}{1 - S_{wim}} + C_p \cdot \frac{1}{1 - S_{wim}} \quad (4.74)$$

if the matrix is very tight,

$$S_{wm} = S_{wi} = 1$$

equation 4.72 becomes,

$$C_{eo} = C_o + C_w \cdot \frac{\Phi_m}{\Phi_f} + C_{pm} \cdot \frac{\Phi_m}{\Phi_f} + C_{pf} \quad (4.75)$$

In a double porosity system the total storage capacity is defined by,

$$\Phi C = \Phi_1 C_1 + \Phi_2 C_2 \quad (4.76)$$

where  $\Phi_1$  and  $\Phi_2$  are expressed by equations 4.3 and 4.4<sup>1</sup>,

$$\Phi_1 = (1 - \Phi_2) \Phi_m (1 - S_{wi}) \quad (4.77)$$

$$\Phi_2 \cong \Phi_f$$

and respective compressibilities from equation 4.74 are,

$$\left. \begin{aligned} C_1 &\cong C_o + \frac{C_w S_{wi} + C_p}{1 - S_{wi}} \\ C_2 &\cong C_o \end{aligned} \right\} \quad (4.71)$$

#### 4.5.3.3. Fracture volume compressibility

Fracture compressibility according to calculations (Jones<sup>18</sup>), is an order of magnitude greater than pore volume compressibility. This results from the relationship

$$\frac{\Phi}{\Phi_i} = \frac{\log(P_{eff}/P_h)}{\log(P_{eff}/P_h)_i} \quad (4.79)$$

where  $P_{eff}$  refers to net confining pressure ( $\bar{\sigma} - P$ ) and where  $P_h$  is defined<sup>18</sup> as *the apparent healing pressure* expressed by the intercept of the pressure axes at  $\Phi/\Phi_i = 0$ . If it is assumed that bulk changes are insignificant, fracture compressibility is expressed by the relationship between the rate of change of fracture porosity and pressure variation.

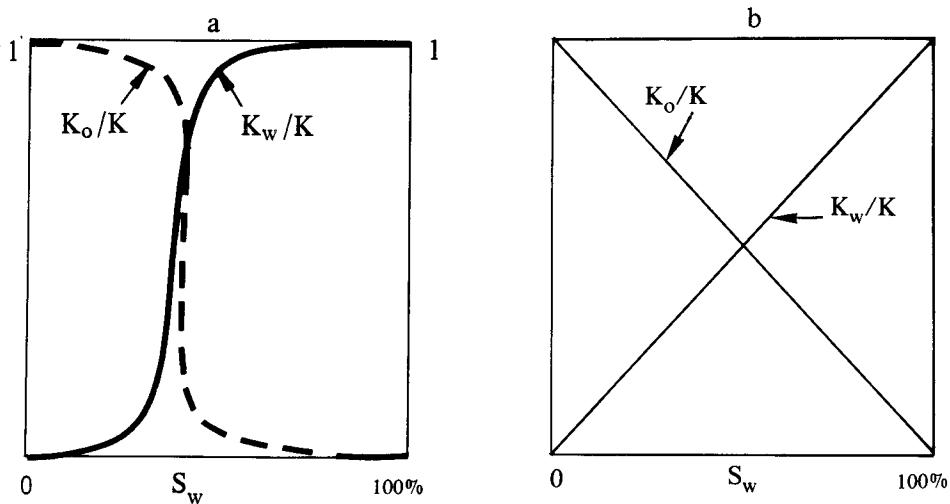
$$C_f = \frac{1}{\frac{\Phi_f}{\Phi_{fi}}} \frac{d(\Phi_f/\Phi_{fi})}{dP_{eff}} = \frac{0.4343}{P_{eff} \log \frac{P_{eff}}{P_h}} \quad (4.80)$$

In an example given by Jones<sup>18</sup>, it is mentioned that fracture carbonate compressibility (at 10,000 feet) is estimated at initial pressure  $C_f = 96 \times 10^{-6}$  (1/psi) and the state of final depletion of the reservoir  $C_f = 72 \times 10^{-6}$  (1/psi). The compressibility of the matrix pores will usually vary between  $2 \times 10^{-6}$  (psi<sup>-1</sup>) and  $15 \times 10^{-6}$  (psi<sup>-1</sup>) as a result of fluids withdrawing from the reservoir.

#### 4.6. RELATIVE PERMEABILITY IN A FRACTURED RESERVOIR

Relative permeabilities in a conventional reservoir are obtained from special core analysis. In a fractured reservoir, evaluation of relative permeability curves is complicated because of the nature of the double porosity system, where the fracturing plane between two matrix units develops a discontinuity in the multi-phase flowing process. In the literature the relative permeability of a specifically fractured reservoir is seldom examined, but the influence of heterogeneity within a porous media on relative permeability was studied in detail.

Since the behaviour of relative permeability vs. heterogeneity may be used as a basic approach of a fractured reservoir, it is interesting to examine the influence of flooding rate, core length, and wettability on the laboratory results in a heterogeneous reservoir (Huppner<sup>22</sup>, Bradner<sup>23</sup>, Erlich<sup>24</sup>). Evaluation of relative permeability in heterogeneous rocks through water-flooding presents the risk of inaccuracy if an earlier water breakthrough has taken place. This means that the results become uninterpretable if the water breakthrough through fractures or vugs is ahead of the main advancing front in the matrix. The fracture-matrix relative permeability curve



4.34 – Anomalously shaped relative permeability curve. a) fractures not along core axis; b) fractures along core axis.

in this case will resemble an anomalously shaped curve (figure 4.34) as a result of a piston-like displacement in some fractures (the largest), but not in the fracture-matrix system.

#### 4.6.1. Review of some basic concepts

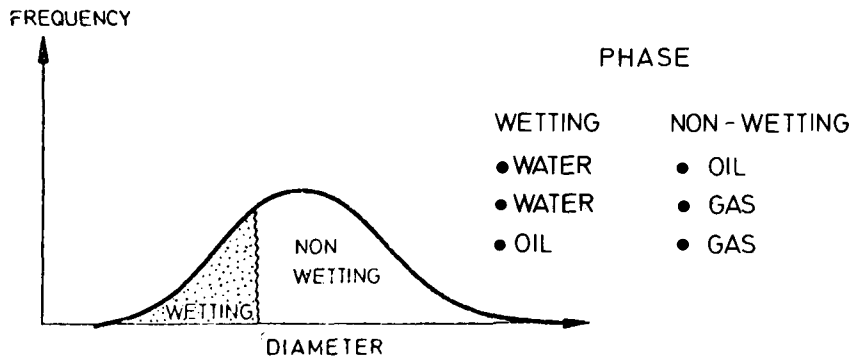
Relative permeability is basically associated with intergranular pores and, therefore, before approaching the more complicated aspects of a double porosity rock, a review of some basic concepts and principles is necessary.

In an intergranular system, the fluid arrangement in pores is controlled by the capillary forces and, therefore, saturation in fluids will depend on the relationship between the wetting and non-wetting phases of all fluids which fill the pores.

The wetting phase will occupy the smaller pores and the non-wetting phase will occupy the larger pores as a result of the relationship between fluid saturation and pore size distribution. Thus, relative permeability curves will be influenced by the pore frequency curve as well as by the saturation history (since the flowing process may develop during drainage or imbibition conditions).

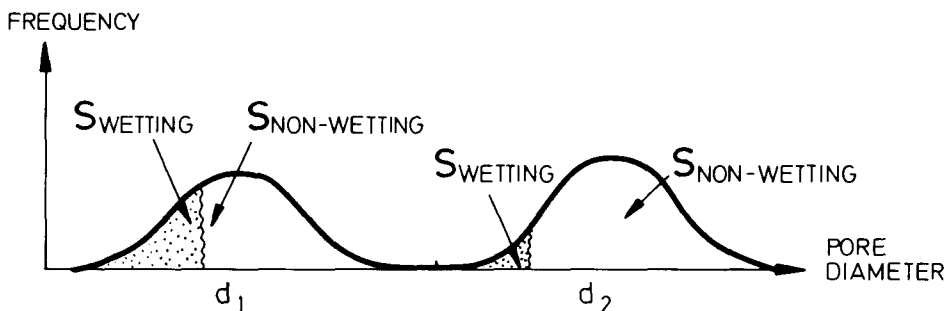
##### 4.6.1.1. Relative K vs. pore frequency distribution

If a pore size frequency curve is available, distribution of the wetting and non-wetting phases will be as shown in figure 4.35 where the wetting phase fills small pores and the non-wetting phase fills the large pores. Thus, saturation in the



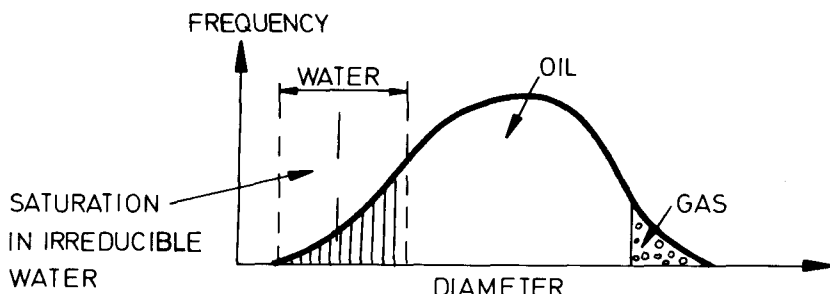
4.35 – Pore size frequency curve and fluid saturation

irreducible wetting phase will depend on the average pore size. Saturation in irreducible water will be greater in small pores than in large pores (as shown in figure 4.36 where  $d_1 < d_2$ ).



4.36 – Influence of average pore size on saturation magnitude

If all three phases, water, oil and gas, coexist simultaneously in the reservoir, their distribution will follow the same pattern. According to the degree of wettability, water will fill the smallest pores and gas the largest pores, leaving the intermediate pores for oil (figure 4.37).



4.37 – Three-phase saturation distribution.

If the three phases do coexist, the relative permeability of each phase will be influenced by the saturation of the other phases<sup>25</sup> in the following ways:

- a.  $K_{rw}$  will only depend on mobile water,  $S_w - S_{wi}$ , but remains independent of oil and gas saturation.
- b.  $K_{rg}$  will only depend on gas saturation,  $S_g$ , but is independent of oil and water saturation.
- c.  $K_{ro}$  depends on oil saturation, but is also *indirectly dependent on the range of pore size* in which there is oil saturation.  $K_{ro}$  will be larger if, for example,  $S_w = 0.45$  and  $S_g = 0.05$ , than if  $S_{wi} = .30$  and  $S_g = .20$ , because at the same saturation in oil  $S_o = 0.5$  in the second case oil will be located in smaller pores while in first case the oil will be located in larger pores.

#### 4.6.1.2. Normalization of relative permeability curves

Normalization of relative permeability curves is related to saturation in mobile phases. In various saturation cases the relative saturation of a phase is expressed by  $S_{phase}$  which may be  $S_w$ ,  $S_o$ ,  $S_g$ .

If the reference is to pores where mobile phases are contained

$$S_{phase}^* = \frac{S_{phase}}{1 - S_{wi} - S_{oR}}$$

and if it refers to all pores excluding those containing interstitial water

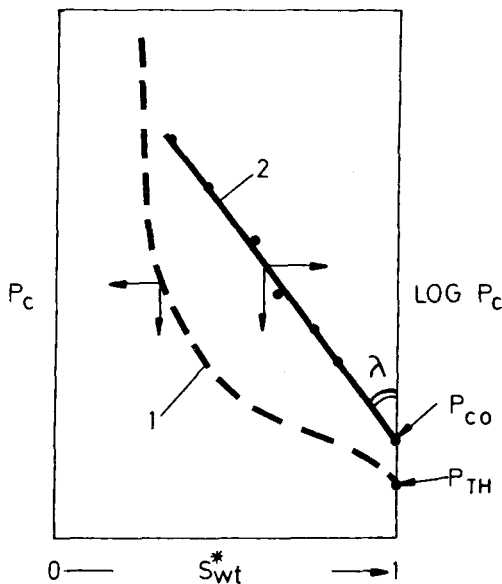
$$S_{phase}^* = \frac{S_{phase}}{1 - S_{wi}}$$

The permeabilities are expressed as fractions of critical permeability obtained from relative permeability curves at  $S_{wi}$  or  $S_{or}$ .

$$K_{ro} = K_o / K \Big|_{S = S_{wi}} \quad K_{rw} = K_w / K \Big|_{S = S_{or}}$$

#### 4.6.1.3. Role of pore size distribution

As a result of saturation normalization of relative permeability curves, the straight dependence of relative permeability on pore size distribution becomes more clear, in addition to its dependence on wettability and saturation history<sup>25 26</sup>. Pore size distribution may be fully described by a drainage capillary pressure curve vs. satura-



4.38 – Variation of  $P_c$  vs.  $S_{wt}$ , note:  $S_{wt}^* = (S_w - S_{wi})/(1 - S_{wi})$ .

tion. The frequency curve (figure 4.37) may generate a *drainage capillary pressure curve* such as curve 1 in figure 4.38, and the pressure will be expressed by,

$$\log P_c = \log P_{co} - \frac{1}{\lambda} \log S_{wt}^* \quad (4.81)$$

or,

$$S_{wt}^* = 1/(P_c/P_{co})^\lambda \quad (4.82)$$

If the straight line 2 (Fig. 4.38) expressing equation 4.81 is extrapolated at  $S_{wt} = 100\%$ , the value  $P_{co}$  is often the same as threshold pressure  $P_{TH}$ . In such a capillary pressure curve the small  $\lambda$  values indicate a very large distribution of pore size, while very large  $\lambda$  values indicate uniformity of pore size. A correlation between pore size, frequency distribution, capillary pressure curve and distribution index  $\lambda$  is described in table 4.16. The average pore size mainly influences the  $P_{co}$  magnitude, but the pore size distribution is strongly associated to the  $\lambda$  value.

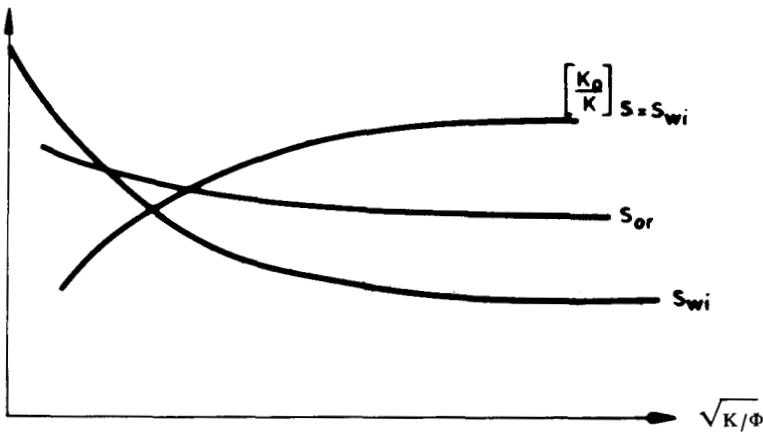
Table 4.16 Relationship of  $\lambda$  versus pore size range distribution, pore distribution and capillary pressure curve.

PORE SIZE RANGE DISTRIBUTION	FREQUENCY DISTRIBUTION	CAPILLARY PRESSURE CURVE	$\lambda$
VERY WIDE	$f$	$P_c$	0.5
WIDE	$f$	$P_c$	2
MEDIUM RANGE	$f$	$P_c$	4
UNIFORM	$f$	$P_c$	$\infty$

#### 4.6.2. Evaluation of relative permeability in homogeneous rocks

##### 4.6.2.1. Introduction

From the relative permeability results obtained in the laboratory on a large number of relatively homogeneous cores, it is possible to establish some correlations for the basic critical parameters. A classic relationship is the variation of  $S_{wi}$ ,  $S_{or}$ ,  $K_o/K|_{S_w=S_{wi}}$  and  $K_w/K|_{S_o} = S_{oR}$ , with the ratio  $\sqrt{K/\Phi}$  (figure 4.39).



4.39 – Critical values of relative permeability curves as a function of  $\sqrt{K/\Phi}$ .

If sufficient data are not available the relative permeability curves can be elaborated by use of analytical relationships in which a parameter  $\lambda$  has to be chosen in agreement with pore size distribution. The wetting and non-wetting phases and the saturation history also need to be defined. The procedure developed for homogeneous porous media<sup>26 27</sup> gives very representative results. The problem becomes more complicated if it is necessary to take in account the heterogeneity of the porous media.

The use of standard methods is generally unsuccessful when cores have typical heterogeneous characteristics. The standard procedure may eventually be improved by the examination of the relationship between recovery and pressure response<sup>28</sup>. Laboratory testing conditions (rate of flooding, wettability and core length<sup>22</sup>) must also be accurately examined.

In the case of a vertical flooding test of a heterogeneous core<sup>23</sup>, the results may be unreliable if the sample length is substantially smaller than the capillary height.

#### 4.6.2.2 Procedure for analitical data elaboration

In a homogeneous rock the main element which influences relative permeability is the saturation history. In other words, it is necessary to refer to the type of flowing process (drainage or imbibition) which took place during the change in saturation.

##### a. Drainage case

###### ● 2 phases

$$K_{rw} = (S_{wt}^*) \frac{2+3\lambda}{\lambda} \quad (4.83)$$

$$K_{rnw} = (1-S_{wt}^*)^2 [1 - (S_{wt}^*) \frac{2+\lambda}{\lambda}] \quad (4.83')$$

where  $K_{rnw}$  is the relative permeability of the non-wetting phase and  $K_{rw}$  is the relative permeability of the wetting phase.

• 3 phases

For the mobile water phase.

$$K_{rw} = \left( \frac{S_w - S_{wi}}{1 - S_{wi}} \right)^{\frac{2+3\lambda}{\lambda}} = (S_w^*)^{\frac{2+3\lambda}{\lambda}} \quad (4.84)$$

NOTE: If the water is immobile,  $S_w = S_{wi}$

(4.84')

For the oil phase,

$$K_{ro} = K_r^o \left( \frac{S_o}{1 - S_{wi}} \right)^2 \left[ \left( \frac{S_o + S_w - S_{wi}}{1 - S_{wi}} \right)^{\frac{2+\lambda}{\lambda}} - \left( \frac{S_w - S_{wi}}{1 - S_{wi}} \right)^{\frac{2+\lambda}{\lambda}} \right]$$

where  $K_r^o$  is the non-wetting permeability at residual wetting saturation.

For the gas phase

$$K_{rg} = K_r^o \left( \frac{S_g + S_m - S_l}{S_m - S_{wi}} \right)^2 \left[ 1 - \left( \frac{S_o + S_w - S_{wi}}{1 - S_{wi}} \right)^{\frac{2+\lambda}{\lambda}} \right] \quad (4.84)$$

where

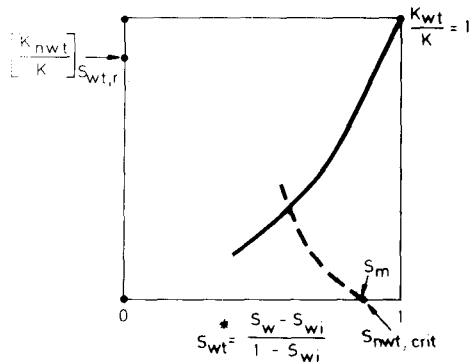
$$S_m = 1 - S_g, \text{ critical}$$

In the case of a two phase flow, the wetting phase is normalized for  $S_{wt} = 100\%$ , and therefore, permeability of the maximum wetting phase will remain equal to the absolute permeability. The maximum relative permeability in the non-wetting phase is obtained for  $1 - S_{wt,r}^*$ .

At the residual wetting saturation  $S_{wt,r}$ , the non-wetting phase permeability is expressed<sup>25</sup> by,

$$K_r^o = \left[ \frac{K_{nwt}}{K} \right]_{S = S_{wt,r}} = 1.08 - 1.11 S_{wt,r} - 0.73 (S_{wt,r})^2$$

The movement of the non-wetting phase begins at the *critical saturation* of this phase ( $S_{cnwt}$ ). This value, different from  $S_{wt} = 1$  or from  $S_{nwt} = 0$ , represents a critical value indicated as  $S_m$  (figure 4.40).



4.40 – Pore size distribution influence on  $P_C$  vs.  $S_w$  and on  $S_{ro}$  and  $P_{TH}$ .

### b. Imbibition case

During a drainage displacement process the capillary forces oppose (together with viscous forces) the displacement of the wetting phase by a non-wetting phase. Contrary to this, during the imbibition process the capillary forces assist the wetting phase in the displacement of a non-wetting phase.

The problem of calculating a non-wetting phase saturation was examined by Naar-Henderson<sup>29</sup> and Land<sup>30</sup>. They concluded that the main difficulty is the elaboration of a representative relationship between the non-wetting phase saturation and the amount of trapped phase. Land<sup>30</sup> established a relationship between the initial gas saturation and the residual gas saturation, expressed by,

$$\left. \begin{array}{l} S_{gi}^* = S_{gi}/(1-S_{wi}) \\ S_{gr}^* = S_{gr}/(1-S_{wi}) \end{array} \right\} \quad (4.86)$$

This general equation

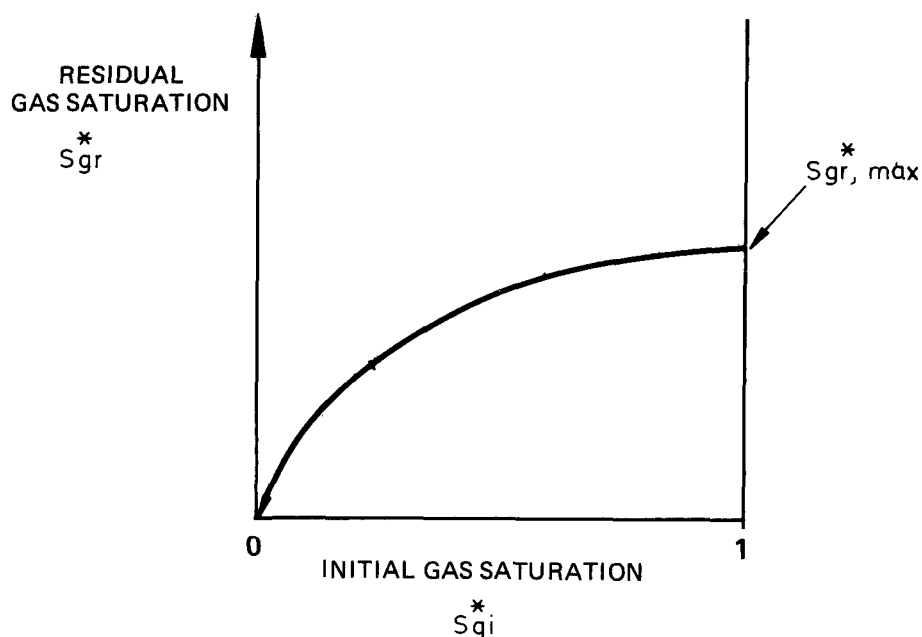
$$\frac{1}{S_{gr}^*} - \frac{1}{S_{gi}^*} = C \quad (4.87)$$

where  $C$  is the trapping gas constant (figure 4.41), will if  $S_{gi} = 1$ , correspond to  $S_{gr} = S_{gr,max}^*$  and thus,

$$C = \left\{ \frac{1}{S_{gr,max}^*} - 1 \right\} \quad (4.88)$$

where  $S_{gr,max}^*$  represents the effective residual gas saturation at the end of an imbibition process in a porous media.

Values of  $C$  for various formations have been estimated and published in the literature (Whitson<sup>15</sup>). The best data are those obtained through data-fitting (Land<sup>30</sup>) as shown in Table 4.17.



4.41 – Initial  $S_{gi}^*$  vs. residual  $S_{gr}$  saturation in gas (Standing<sup>25</sup>).

Table 4.17 Values of Trapping Constant for Various Rock Types

Formation	$S_{wi}$	$\lambda$ .	$\Phi$	C
Chalk	0.152	0.464	0.350	1.98
Abo	0.200	0.769	0.130	0.597
Lansing K.C.	0.121	0.644	0.251	0.387
Smackover (TX)	0.045	0.458	0.311	1.603
Smackover (MISS)	0.210	0.632	0.137	0.739
Alendum	0.020	10.00*	0.450	4.617 (1.800)**
Berea	0.190	$\infty^*$	0.230	1.273 (0.800)**
Torpedo	--		0.230	1.273

\* Determined by curve-fitting drainage R.P. data

\*\* Determined by curve-fitting imbibition R.P. data, the first values being determined experimentally

The first five listed formations are carbonate reservoirs and the last three formations are highly homogenous sandstone with ideal properties. From observed data in case of lack of better information, C may be approximated between 1.5–2.

c. Water-gas relative permeability

The basic equation of the relative permeability for gas in a porous media, when there is no oil, but only a water phase, is expressed by,

$$K_{rg \text{ imb}} = \left[ \frac{(S_m - 1)}{(S_m - S_{wi})} + S_{gF}^* \frac{(1 - S_{wi})}{(S_m - S_{wi})} \right]^2 \times \left[ 1 - (1 - S_{gF}^*) \frac{2+\lambda}{\lambda} \right] \quad (4.89)$$

where  $S_{gF}$  is the *free* gas saturation.

$$S_{gF}^* = \left[ \frac{1}{2} (S_g^* - S_{gr}^*) + \sqrt{(S_g^* - S_{gr}^*)^2 + \frac{4}{c} (S_g^* - S_{gr})} \right] \quad (4.90)$$

and where

$$S_g^* = \frac{S}{1 - S_{wt}} ; \quad S_{gr}^* = \frac{S_{gr}}{1 - S_{wi}} ; \quad S_{gi}^* = \frac{S_{gi}}{1 - S_{wi}}$$

C is the same rock constant representing the trapping gas.

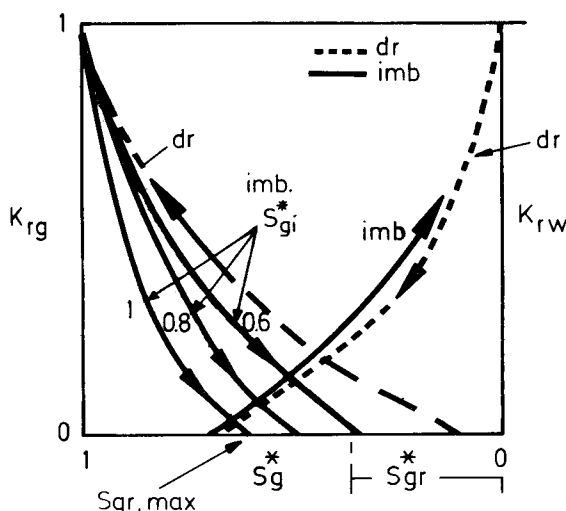
For the same 2 phase system, the relative permeability for water will be similar to that of drainage displacement,

$$K_{rw} = (1 - S_g^*)^{(2+3\lambda)/\lambda} = S_w^* \quad (4.91)$$

#### 4.6.2.3. Observations

When comparing the behaviour of the relative permeability curves under imbibition and drainage conditions, the results are as follows:

- a. At  $S_g^* = 0$ , when water starts to imbibe the pore and displace the gas phase or when gas starts to drain the water, the relative permeability  $K_{rw}$  of the wetting phase is the same.
- b. Even if  $S_g^* > 0$ , the difference between the two relative permeabilities  $K_{rw}|_{imb}$  and  $K_{rw}|_{dr}$  is very small (figure 4.42).
- c. On the contrary, the relative permeability of the non-wetting phase reveals quite a different behaviour. The relative permeability  $K_{rg}$  is substantially higher in the drainage case than in the imbibition case, where the increasing saturation  $S_g^*$  develops a substantial reduction in gas relative permeability and a larger residual gas saturation,  $S_{gr}^*$ .
- d. The imbibition limit curve of  $K_{rg}$  varies between  $S_{gi}^* = 1$  and  $S_{gi}^* = 0$ . In the first case, when  $S_{gi}^* = 1$ , the  $S_{gr}^* = S_{gr,max}$  and the  $K_{rg}$  will be the lowest relative gas permeability. On the contrary, when  $S_{gi}^* = 0$ , the result will be  $S_{gr}^* = 0$  as shown in figure 4.41 and  $C = \infty$  from equation 4.87. In this last case the relative permeability of gas in imbibition conditions will be the same as that obtained in drainage (Figure 4.42).



4.42 – Drainage and imbibition relative curves, influenced by initial gas saturation  $S_{gi}^*$  (Standing<sup>25</sup>).

#### 4.6.3. Evaluation of relative permeability in heterogeneous rock

The heterogeneity problem in rock was for a long time limited to the reservoir having a directional variation of permeability and its consequences on field behaviour. Later the reservoir heterogeneity was examined in relation to relative permeability<sup>31</sup>. Among the various heterogeneities of a reservoir the most significant are the

layered formation where the flow may be normal or parallel to the bedding, or double porosity systems, such as the combinations matrix-fracture, vugs-matrix or vugs-fracture-matrix.

#### 4.6.3.1. Relative permeability of a layered formation

The layered formation is one of the most common heterogeneities, especially in the case of sandstones. Layering may be visualized as a rock composed of alternate layers of fine and coarse material forming a number of layers of different thicknesses and permeabilities. The flow direction may be assumed to run either parallel to the bedding planes (flow in parallel) or across the bedding planes (flow in series). The relationship between the layers characteristics and the flow direction will influence evaluation of relative permeability.

An approach to the solution of the calculation of *relative permeability for an oil-gas system* in the case of a multi-layered formation was given by Corey<sup>31</sup>.

##### a. Theoretical approach

The evaluation of relative permeability was made through the following equations.

- capillary pressure desaturation curve approximated by the equation,

$$1/P_c^2 = B S_{oe}^* \quad (4.92)$$

where B is a constant and  $S_{oe}^*$  is the effective saturation in oil (percentage of pore volume effective for flow).

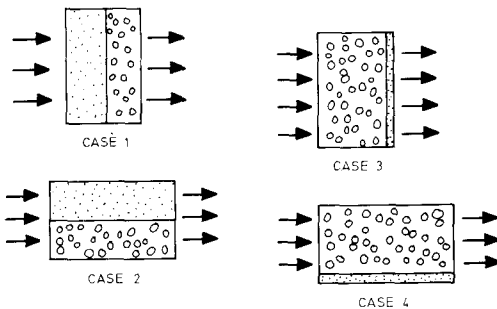
- relative permeabilities expressed as a function of saturation are,

$$\left. \begin{array}{l} K_{ro} = S_o^{*4} \\ K_{rg} = (1 - S_o^*)^2 [1 - (S_o^*)^2] \\ S_o^* = \frac{S_o^* - S_{or}^*}{1 - S_{or}^*} \end{array} \right\} \quad (4.93)$$

##### b. Calculation example

Based on equations 4.92 and 4.93 a calculation was made<sup>31</sup> for a reservoir rock formed by two different layers in capillary equilibrium. The following parameters are known: residual oil saturation  $S_{or}=20\%$ , absolute permeabilities of the two layers are  $K=100mD$  and  $K=10mD$ , and the constant  $B=10$  (equation 4.92). The flowing direction, combined with heterogeneous layering, will lead to various flowing arrangements. If the flow is parallel to the bedding, the layer arrangement is considered to be *in parallel*, and if the flow is normal to the bedding, the layer

arrangement is considered to be *in series*. Based on this type of arrangement (figure 4.43) the permeability of the system was computed for four cases as in table 4.18.



4.43 – Arrangement of layers in series and parallel. (Cases 1, 2, 3, 4 described in Table 4.17).

The relative permeabilities for these composite cores have been calculated by using equations 4.92 and 4.93. Cases 1 and 2 are formed by 50–50% composition of two layers, while cases 3 and 4 are formed by 90–10% volumetric composition. The computed relative permeabilities have shown a very interesting behaviour of  $S_{gcr}$ , as well as the role of flow vs. bedding and volume distribution. The results of cases 1 and 2 are presented in figure 4.44a, and the results of cases 3 and 4 are presented in figure 4.44b.

Table 4.18. Composite permeability cases

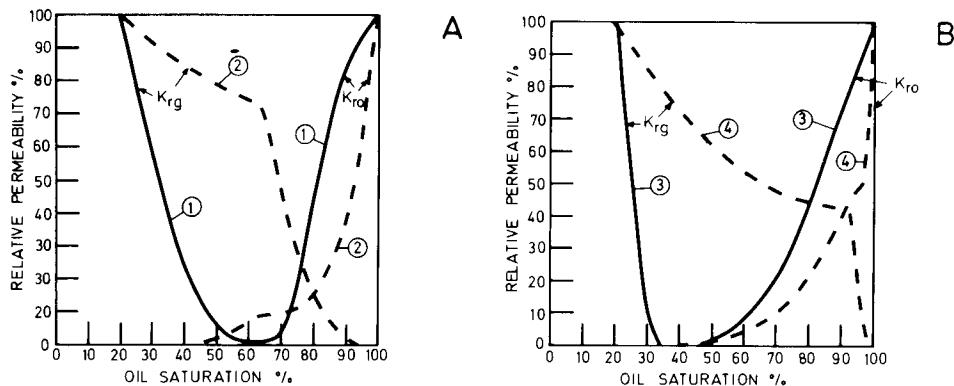
Case	Volume distribution Layer 1      Layer 2 $K_1=100\text{mD}$ $K_2=10\text{mD}$		Flow vs. Bedding	Arrangement Type	System permeability (mD)
1	50%	50%	normal	series	$\bar{K}=2K_1K_2/(K_1+K_2)=18,2$
2	50%	50%	parallel	parallel	$\bar{K}=(K_1+K_2)/2=55,0$
3	90%	10%	normal	series	$\bar{K}=10K_1K_2/(9K_2+K_1)=52,6$
4	10%	90%	parallel	parallel	$\bar{K}=(K_1+9K_2)/10=19,0$

The conclusions are as follows:

- Critical saturation in gas in the case of a series arrangement is substantially high (35% – case 1, 65% – case 3) when compared with a parallel arrangement where these values are very small (6% – case 2, 1% – case 4).
- Apparently the most favourable gas-oil relative permeability will be that presented in case 3, where the coarse component is 10%. It may be concluded that for a gas-oil flowing process, the ideal is a heterogeneous formation in series having a thin layer of low permeability and a thick layer of high permeability.

– The discontinuity of the  $K_{rg}$  curve in both cases of a parallel layer arrangement is the result of the saturation at which the low permeable layer starts to overcome its critical gas saturation. The inflection is at  $S_g=35\%$  in case 2 (distribution 50–50%) and only at  $S_g=8\%$  in case 4 (flow dominated by low permeable layer).

– The decline of  $K_{ro}$  with the increasing gas saturation is substantially more severe in a parallel arrangement (cases 2,4) than in a series arrangement of layers (cases 1, 3). The worst  $K_{ro}$  decline is in case 4 where, in the parallel arrangement, the low permeability layer is volumetrically predominant.

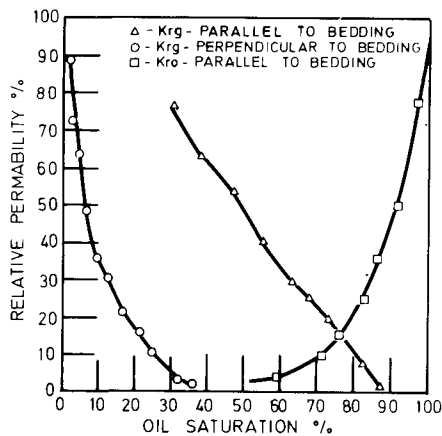


4.44 – Calculated relative permeability based on Table 4.18.

A-layer distribution 50%-50%; B-layer distribution 90%-10% (Corey<sup>31</sup>, courtesy AIME).

### c. Experimental results

Measurements on sandstone cores in both flowing conditions parallel and normal to the bedding, have given  $K_{rg}$  and  $K_{ro}$  curves as in figure 4.45. In a parallel arrangement, the critical gas saturation is very small compared with a series arrangement. The relative permeability curve of oil is less influenced by the formation heterogeneity.



4.45 – Relative permeability  
(Corey<sup>31</sup>, courtesy AIME).

d. Other verifications

The effect of several core heterogeneities on waterflood was examined through computed and experimental investigations by Hupp<sup>22</sup>. The cases examined are described below:

TABLE 4.19

CASE	Layer Number	Layer-permeability Ratio	Wetting Conditions
1	2	1	water wet
2	20	1	water wet
3	2	10/1	water wet
4	20	10/1	water wet

The results have shown the following:

- In cases 1 and 2 a lack of sensitivity concerning flooding rate, core length and oil-water viscosity was observed.
- An important sensitivity to the 'wettability, flooding rate and core length was observed in cases 3 and 4.
- In the case of 20 layers, capillary crossflow helps drainage of a tight formation, while in the case of 2 layers this effect is not observed.
- Better results have been obtained by sectioning the core into six parts (case 3) and then rotating the alternate layers 180°; but less spectacular results have been obtained in case 4.

#### 4.6.3.2. Relative permeability of vuggy and fractured rocks

In carbonate rocks where a secondary vuggy type porosity has been developed in addition to the intergranular porosity, the conventional measurements are questionable if the secondary porosity is significant and uniformly distributed.

##### a. Relative permeability of water-oil in vuggy rocks (lab experiments)

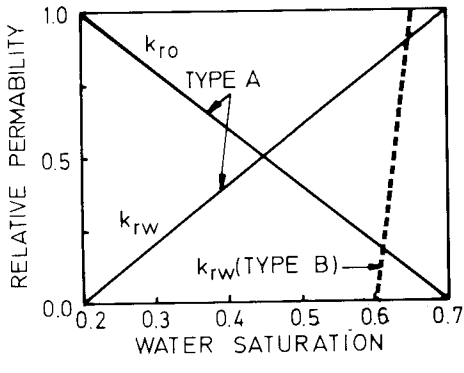
The relative permeability behaviour of water-oil has been examined in the laboratory<sup>22</sup> on vuggy glass-bead packs and qualitative characteristics have been obtained. At high rates the water flushes oil out of the matrix entirely, but at low rates where capillary pressure becomes significant, oil is trapped in the vugs. From the results obtained the presence of two types of curves has been considered:

- Type A, where both relative permeability curves show a linear variation with water saturation (figure 4.46). It was observed that water sometimes flows along the bottom of vugs which still contains oil.
- Type B, includes the result of the advance of the water-oil front through the vugs until the oil is totally removed. The relative permeability of water in rock will vary from zero when oil is still in the vug, to 1 when oil is displaced (figure 4.46).

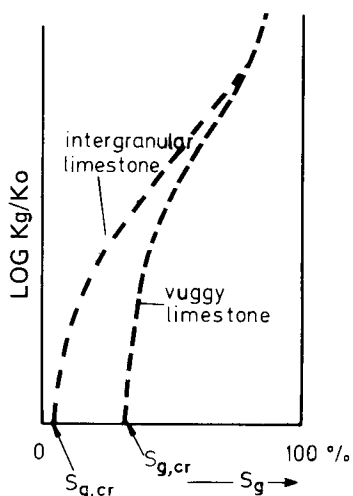
Simulation of relative permeability and laboratory tests have been examined by Archer<sup>32</sup> on vuggy carbonate rocks. The results showed a substantial difference between core data in the laboratory and simulator where the piston-like displacement was accepted as in a conventional reservoir.

b. Relative permeability of gas-oil in vuggy limestone (lab experiments).

From the experiments developed by Abgrall and Iffly<sup>33</sup>, the critical gas saturation may become very high especially if the pressure decline rate is small. The gas phase develops in vugs without moving from the vugs until a large part of the oil leaves them. This is explained by the fact that liberated gas in vugs can not displace oil in the matrix which surrounds the vugs as a result of capillary forces which oppose it. Only later when the elevated saturation in free gas develops in the matrix will the vug-matrix system be described by only one relationship –  $Kg/Ko$  vs.  $Sg$ . The behaviour of the relative permeability curve is shown in figure 4.47. This figure illustrates the difference between the same intergranular matrix with and without vugs.

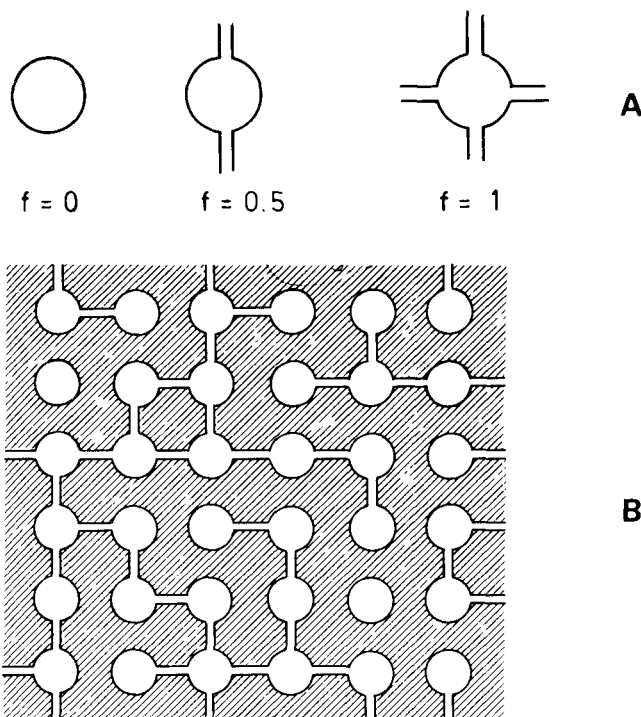


4.46 – Vug relative permeability  
(Hupp<sup>22</sup>, courtesy AIME).



4.47 – Relative permeability curves

At a low pressure decline rate  $\Delta P/\Delta t$  it is necessary to substitute the intergranular relative permeability curve of a limestone with the specific  $Kg/Ko$  for vuggy limestone.

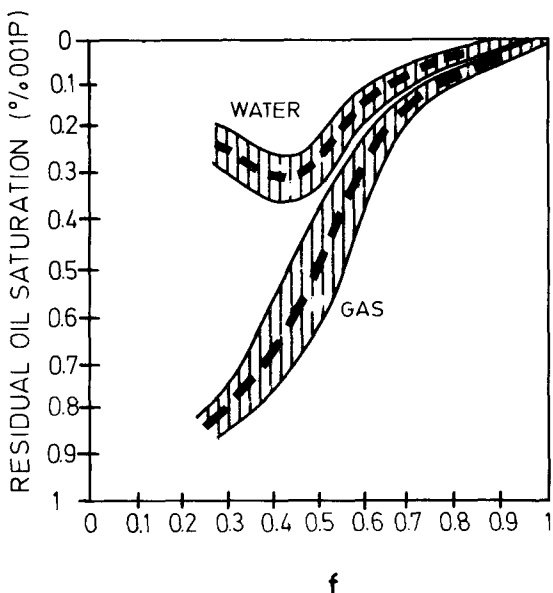


4.48 – Fracture-vug model. A – Type of network and probability factor  $f$ . B – Matrix and fracture-vug, case  $f=0.5$ . (Erlich<sup>24</sup>, courtesy AIME).

### c. Relative permeability in vuggy fractured rock (theoretical approach).

The relative permeability of fractures and vugs forming the secondary porosity of an intergranular limestone was examined through a simplified model developed by Erlich<sup>24</sup>. The model includes isolated vugs inside the matrix, and vugs connected with fractures in one or two directions (figure 4.48A). The interconnection of vug-fracture is expressed by a probabilistic factor  $f$ , indicating the degree of fracture-vug connection. The variation of  $f$  from 0 to 1 is illustrated in figure 4.48A. An example of a fracture-vug network superimposed on a matrix with a fracture probability factor of  $f=0.5$  is drawn in figure 4.48B. Residual oil saturation was evaluated in the Erlich model<sup>24</sup> on a  $12 \times 12$  array by a random process according to the intercommunication probability. In this case there are 312 possible fracture locations. If some fractures are filled with oil and some with water, a displacement process can be simulated. For water and gas displacement, both residual oil saturations are given in figure 4.49 as a function of parameter  $f$ . The simulated outputs have been compared with core data and the matching was satisfactory with the exception of cores with a large secondary porosity, where in case of an immiscible displacement, a substantially higher residual oil saturation was obtained. Using such models in a fracture-matrix block unit

as a *pseudo-function* it is possible to build a better approach for evaluation of displacement behaviour.



4.49 – Residual oil saturation vs.  $f$  factor in a given model (Erlich<sup>24</sup>, courtesy AIME).

d. Relative permeability of fracture-matrix system (theoretical approach).

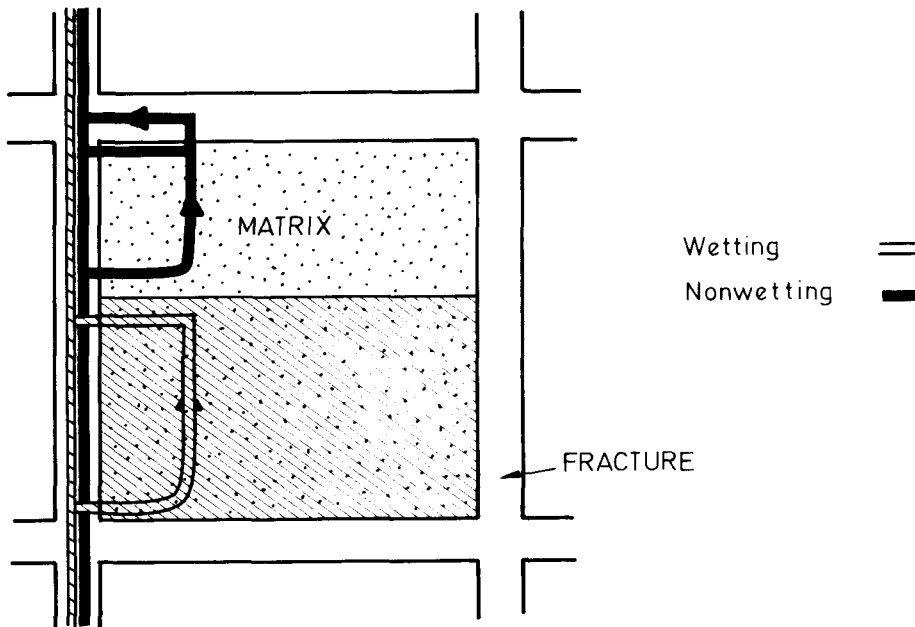
The relative permeability of a fracture-matrix system or a fracture-fissure-matrix system can be examined by use of the core results obtained in the laboratory by conventional methods. This procedure is more successful if a preferential direction of fractures was observed. The approaches may be acquired by using the methods already discussed for heterogeneous rock (layered composite rock<sup>24</sup>, vugs and fractures<sup>31</sup>), in order to build a *pseudo-relative permeability curve*.

● . A relative permeability concept was developed by Braester<sup>34</sup>. The basic principles are:

- In a fractured reservoir, with pressure gradients not negligible if compared to those occurring during imbibition, a certain fracture-matrix fluid exchange will take place.

- The wetting and non-wetting phase from fractures is circulating from the fractures in the matrix and back in the fractures, in the zones saturated with respective water and oil phases (Fig. 4.50).

- Through such a model the relative permeability becomes a function of saturation degree of fractures and porous medium.
- The process is considered as a continuous flow in both zones, matrix block and fractures.



4.50 – Schematization of flowing process between matrix and fractures of wetting and non-wetting phase (Braester<sup>34</sup>, courtesy AIME).

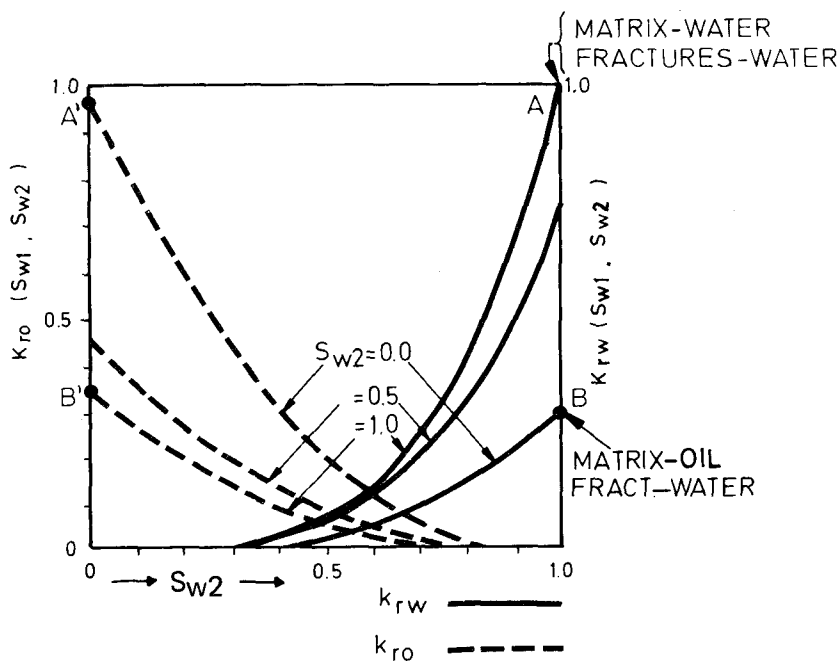
A schematic representation of the relative permeability curve is given in Fig. 4.51 where, based on assumption of continuity of flow in blocks and fractures, it results that:

- The shape of the two relative permeability curves  $K_{ro}$ ,  $K_{rw}$  will vary as a function of fracture water saturation ( $S_{w2}$ ) as shown in Fig. 4.51, where index 1 and 2 refer to matrix and fractures.
- The relationships between two permeabilities are respectively

$$K_{ro} = \left[ \frac{K_2}{K} + \left(1 - \frac{K_2}{K}\right) (1-S_{w1})^2 \cdot (1-S_{w1})^2 \right] (1-S_{w2})^2 (1-S_{w2}). \quad (4.94)$$

$$K_{rw} = \left[ \frac{K_2}{K} + \left(1 - \frac{K_2}{K}\right) S_{w2}^4 \right] \cdot S_{w2}^4 \quad (4.95)$$

which are similar to the Corey equations.



4.51 — Relative permeability of a matrix-fracture reservoir unit. (Braester<sup>34</sup>, courtesy AIME).

— As observed from the curves of Fig. 4.51 it results that:

IF			RESULTS		REMARKS
S <sub>w1</sub>	S <sub>w2</sub>	S <sub>o</sub>	K <sub>rw</sub>	K <sub>ro</sub>	
1	1	0	K <sub>rw</sub> = 1 (point A)	—	K <sub>rw</sub> = K <sub>rw</sub> max
0	1	1	K <sub>rw</sub> << 1 (point B)	—	K <sub>rw</sub> = K <sub>rw</sub> min
0.5	1	0.5	K <sub>rw</sub> average	—	
0	0	1	—	K <sub>ro</sub> = 1	K <sub>rw</sub> = K <sub>ro</sub> min
1	0	0	—	K <sub>ro</sub> << 1	K <sub>ro</sub> = K <sub>ro</sub> min
0.5	0	0.5	—	K <sub>ro</sub> average	

— This may be interpreted as follows:

Point A. This corresponds to a matrix saturation S<sub>w1</sub>=1 and fracture saturation S<sub>w2</sub>=1. No oil in matrix and fractures, K<sub>rw</sub>=1.

Point B. This case corresponds to S<sub>w1</sub>=0 and S<sub>w2</sub>=1 which means matrix saturated with oil S<sub>o1</sub> = 1 and fractures saturated with water.

The permeability values are thus,

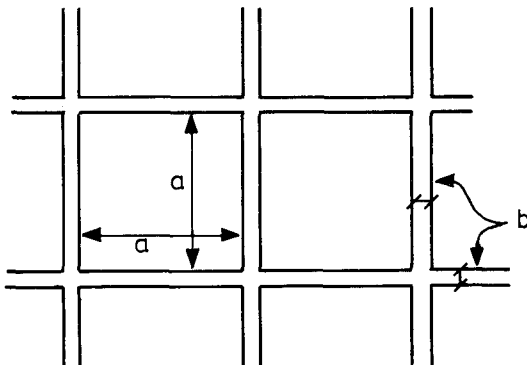
$$K_{rw}|_A = K \text{ (absolute permeability)} ; K_{rw}|_B = \frac{K_e}{K}$$

Application<sup>35</sup>. In case of an idealized fracture-matrix system idealized by cubic blocks the value of permeability is given by

$$K_{rw|B} = \frac{K_e}{K} \text{ for } S_{w1}=0, S_{w2}=1$$

where from figure 4.20 and Table 4.6 (for model 6) it results

$$K_e = K_f = \frac{1}{18} b^2 \Phi_f = \frac{1}{18} b^2 \frac{3b}{a} = \frac{1}{6} \frac{b^3}{a}$$



4.52 – Cubic model section through fracture-matrix. (Torsæter<sup>35</sup>, Courtesy SINTEF.)

Since the fracture-matrix (reservoir) permeability is given by

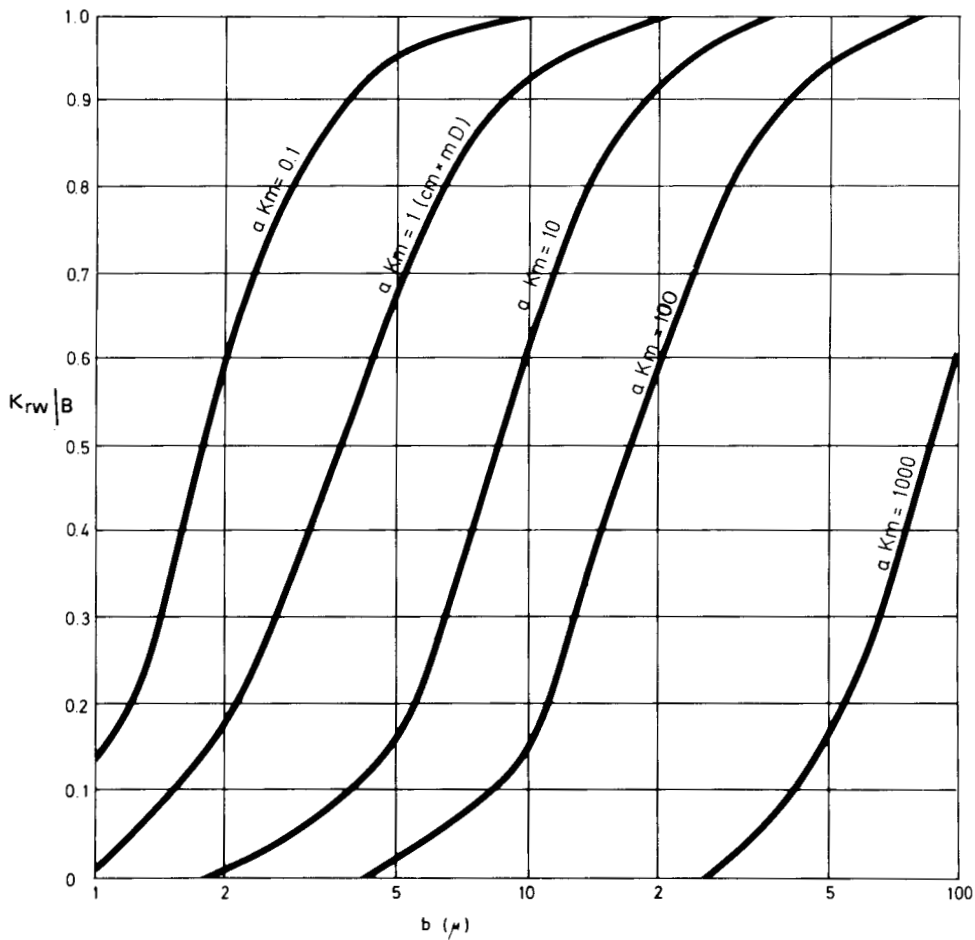
$$K = K_1 + K_2 = K_{matrix} + \frac{1}{6} \frac{b^3}{a}$$

then

$$K_{rw|B} = \frac{b^3/6a}{K_m + b^3/6a} = \frac{1}{1 + 6K_m a/b^3} \quad (4.96)$$

corresponding to point B of saturation  $S_{w1} = 0, S_{w2} = 1$ .

For a generalization of this model and based on reservoir data as fracture width from 1 to 100  $\mu$  and  $K_m \times a$  between 1 to  $10^3$  ( $mD \times cm$ ), the variation of  $K_{rw|B}$  values was obtained (Fig. 4.53). As observed in case of a given value of matrix permeability and block dimension, any reduction in fracture width considerably reduces the values of point B. In other words the relative permeability of water is working in large fractures but reduces its impact in very thin fractures.



4.53 – Variation  $K_{rw}|_B$  vs. width  $b(\mu)$  for various values  $a \times K_m (\text{cm} \times \text{mD})$  in case of an idealized cubic matrix reservoir.

EXAMPLE: for a block height of 100cm and permeability of matrix 1mD, a fracture width of 10  $\mu$  is reduces the  $K_{rw}|_B$  to only 0.16

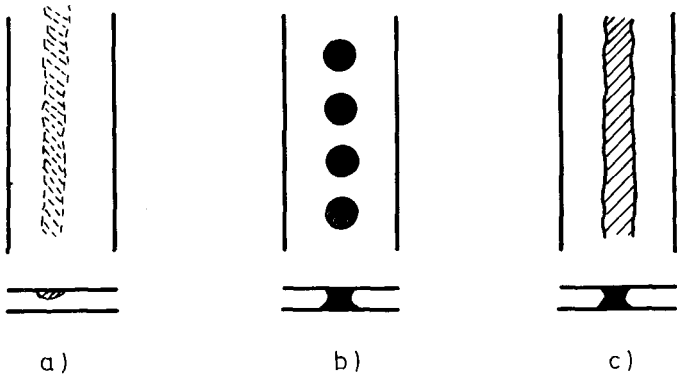
The value  $K_{rw}|_B$  remains the same for the idealized models 3, 4, 5 (Table 4.6) reducing to  $K_{rw}|_B = b^3/12.a$ , only for models 1 and 2.

#### e. Relative permeability of fracture network (without matrix role).

The evaluation of relative permeability in a fracture network has to be treated in a different way from a flow in porous media since the hydraulic radius of the fractures is considerably larger than pore radius of a conventional intergranular rock. In general it may be stated that the flow of two phases

in a fractured medium has to be related to the flow conditions and physical parameters fluids and rock.

The *flow conditions* are illustrated in Fig. 4.54, where: the *trickle flow* (a) permits the wetting phase bubble to adhere to only one wall; the *bubble flow* (b), where the bubbles adhere to both fracture walls, as result of buoyancy effect; *string flow* (c) the fluid is present as a continuous string and the wetting phase adheres to fracture walls.



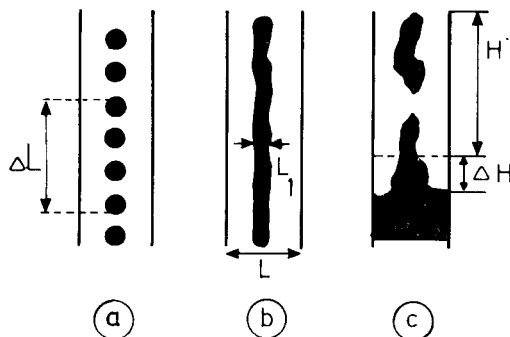
4.54 – Flow regimes in fractures: a) Trickle flow, b) Bubble flow and c) String flow (Torsæter<sup>35</sup>, courtesy SINTEF).

The *physical parameters* of fluids and rock which influence the flow in a fractured medium are: density, viscosity, interfacial tension, wetting properties, fracture width, fracture walls roughness and their dip. A first approach to two-phase flow relative permeability was carried out through a simplified model (Romm<sup>8</sup>) formed by 10 to 20 parallel fractures. The saturation was measured by electrical resistance and the permeability evaluated from the rates of flow of both fluids, water and kerosene. The results obtained show the same linear trend  $K_f$  vs. saturation as was obtained in diagram fig. 4.46. The result has to be considered of limited value since the behaviour of two-phase flow in fractures can not be reduced to the single fracture results. Fracture interconnection may completely modify the flow characteristics.

Other experiments carried out by du Prey<sup>36</sup> were performed in two plexiglass plate models where the fluid was injected in one and more holes. The relative permeability was obtained from rates  $Q_o$  and  $Q_w$  through theoretical equations:

$$\left. \begin{aligned} K_{ro} &= \frac{12 Q_o \mu_o L_f}{a b^3 \Delta P_o} \\ K_{rw} &= \frac{12 Q_w \mu_w L_f}{a b^3 \Delta P_w} \end{aligned} \right\} \quad (4.97)$$

Since the pressure  $\Delta P_o$  and  $\Delta P_w$  can not be measured if both fluids are moving, this problem may be circumvented by keeping one phase immobile and leaving the other the possibility to move as effect of fluid segregation. In this case, in the place of pressure drop, the gravity force  $\Delta\gamma \times g \times \sin\alpha$  will act. The saturation is given under various conditions of flow by measuring the time or length during the experimental phase (Fig. 4.55).



4.55 – Saturation measurements in fracture during segregation: a) drops, b) string, c) segregated water (Torsæter<sup>35</sup>, courtesy SINTEF).

- Bubble regime (through time measured  $t_m$ ) as shown in Fig. 4.55a.

$$S = \frac{V_o}{V_o + V_m} = \frac{q \times t_m}{\Delta l}$$

- String regime (figure 4.55b)

$$S = \frac{l_1}{l}$$

- Water segregation from oil (fig. 4.55c)

$$S = \frac{\Delta H}{\Delta H + H}$$

Two-phase flow experiments have also been carried out by Merill<sup>37</sup> in parallel glass plates where discrete slugs of brine and hydrocarbon were injected. Based on a theoretical analysis and experimental results, Merill recommended a relationship between total pressure gradient  $\Delta P/\Delta L_1$  and phase pressure gradient  $\Delta P/L_f$ ,

$$\frac{\Delta P}{L} = \frac{12 \mu_w}{b^2} (V_{sw} + V_{so} \frac{\mu_o}{\mu_w}) + \frac{\Delta P_i}{L_f} \quad (4.98)$$

from where the relative permeability for phase i (oil or water) becomes

$$K_{r,i}^{(i)} = \frac{12 Q_i \mu_i}{ab^3 [12 \mu_w (Q_w + Q_o \mu_o / \mu_w) / ab^3 + \Delta P_i / L_f]} \quad (4.99)$$

The two-phase flow process in the fracture network still needs to be studied in order to find an answer to a number of problems such as:

- Could the concept of relative permeability be extended to the fracture network?
- If drops of a non-wetting phase come from the matrix in the fracture wetting phase which surrounds the matrix, what are the flowing conditions of these drops? What may be the relationship between fracture opening and minimum dragging force to move those drops? What is the behaviour of those drops in horizontal fractures when compared with vertical fractures?

The whole material balance in a fractured reservoir greatly depends on the exchange of fluids in matrix-fracture system, and therefore, new concepts are expected from future research, in this area.

#### 4.7. CAPILLARY PRESSURE CURVE

In a fractured reservoir the capillary pressure curve plays a much more important role than in a conventional reservoir. Capillary forces in fractured reservoirs are an extremely important component of the driving mechanism, while the dynamic role of the capillary forces in a conventional reservoir is more limited. In a fractured reservoir capillary forces may contribute to the displacement process inside the imbibition process, or may oppose it in the drainage displacement process. The capillary pressure curve is reviewed in this section, and new concepts are discussed.

#### 4.7.1. Review of conventional capillary pressure

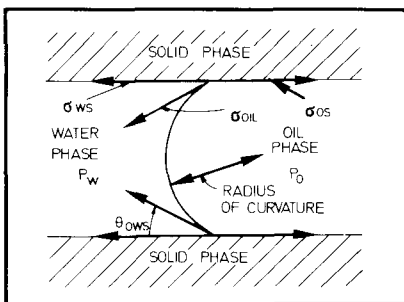
##### 4.7.1.1. Capillary forces

Two or more immiscible fluids (phases) coexisting in a porous medium (consisting of small pores) are generally comingled. The configuration of the total fluid-fluid interfacial area can be quite accurately described by two equations derived from the hydrostatic basic principles<sup>38,39</sup>. For example, if the two fluids are oil and water (Fig. 4.56), the equations will be:

$$P_o - P_w = \sigma_{ow} J_{ow} \quad (4.100)$$

$$\sigma_{os} = \sigma_{os} + \sigma_{ow} \cos \theta_{ows} \quad (4.101)$$

Equation 4.100 is the classic Laplace equation, and 4.101 is the Young equation. Equation 4.100, through a thermodynamic relationship, can be related to parameter  $\sigma$  by using a function of pressure and temperature, while angle  $\theta$  is essential for defining the wettability properties of the system, oil-water vs. reservoir rock.



4.56 – Hydrostatic equilibrium – two liquid phases in contact with a solid phase (Melrose<sup>39</sup>, Courtesy JCPT).

The description of the fluid-fluid interface within a porous solid by using equations 4.100 and 4.101 is relatively difficult, mainly due to the expression of the curvature of the fluid-fluid interface. The mean curvature expression  $J$  includes terms which involve a second-order non-linear differential equation, for which a general solution in terms of known functions is not available.

The condition for stability in equation 4.101 must be expressed as the derivative of curve  $J$  with respect to fractional volume  $S$  in order to check if the inequality  $dJ/dS < 0$ . An intuitive thermodynamic approach suggests that the appropriate condition for a configurational stability may be expressed by,

$$\left. \begin{array}{l} dJ_w/dS_w < 0 \text{ for } \theta < 40^\circ \\ dJ_o/dS_o < 0 \text{ for } \theta > 140^\circ \end{array} \right\} \quad (4.102)$$

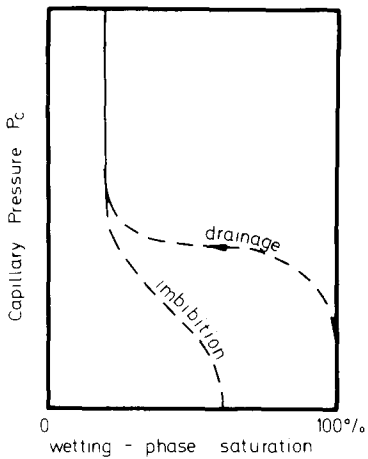
#### 4.7.1.2. Capillary pressure curves<sup>40, 41, 42, 43</sup>

If a reservoir rock is fully saturated by a wetting phase (having a value of  $\theta \cong 0$ ), the displacement of this phase by a non-wetting phase will be related to the capillary pressure magnitude and to the corresponding *decrease of the wetting-phase saturation*. This displacement is called *drainage displacement* and the relationship between capillary pressure and saturation is known as the *drainage capillary pressure curve* (figure 4.57).

Imbibition capillary pressure develops when reservoir rock is saturated with a non-wetting phase which must be displaced by a wetting phase. For a conventional pore distribution the imbibition capillary pressure is approximately half of the order of magnitude of the drainage pressure and, therefore, the curve will show a considerable hysteresis between *drainage* and *imbibition* displacement of the same rock (figure 4.57).

An essential characteristic of both curves (drainage and imbibition) for two slightly compressible fluids (oil and water) is the minimum saturation of the wetting phase.

The *residual* wetting phase in *drainage* conditions is reached asymptotically as the capillary pressure increases to infinity. The minimum saturation of the wetting phase for a typical unconsolidated rock is presented as pendular rings or as individually isolated segments of water surrounding the contact points of adjacent particles. This leads in the case of water as wetting-phase to a straight association between

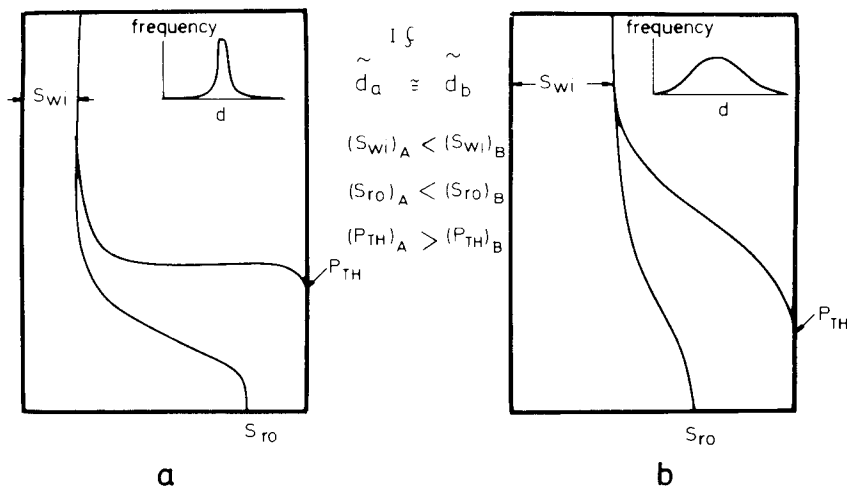


4.57 – Drainage and imbibition capillary pressure curve.

$S_{wi}$  and pore size distribution. The uniform distribution (narrow) of a sample shows a value of  $S_{wi}$  similar to those given in figure 4.58a; but if pore size distribution is wide (figure 4.58b) for a sample which has the same average diameter ( $\bar{d}_A = \bar{d}_B$ ), a higher  $S_{wi}$  will result on the capillary pressure curve. The difference is due to increased pore heterogeneity, which is equivalent to the presence of a larger percentage of small pores.

The shape of the *drainage capillary* curve reflects the homogeneity of the pore size. If over a large water saturation interval the  $P_c$  remains constant (figure 4.58a), this proves the homogeneity of pore dimension and vice-versa, the variation  $P_c$  vs. saturation (figure 4.58b) proves the heterogeneity of pore dimension.

On the other hand, only *imbibition* curves show the existence of a particular saturation in the non-wetting phase saturation (in the case of water-oil,  $S_{ro}$ ). This residual saturation occurs during the imbibition displacement when the trapped *non-wetting phase* fills individual pores or small clusters of neighboring pores. This trapping is a result of the partial interruption of communication among various pores and, therefore, some pores are bypassed during imbibition displacement. It seems physically evident that there are greater chances of bypassing more pores if there is a



4.58 – Capillary pressure curve if average pore diameters  $d_2=d_1$ . a) uniform pores; b) wide pore dispersion.

broader pore size distribution where the variations of pore dimensions reduce pore inter-communication. Therefore, a larger residual non-wetting phase saturation will occur during imbibition displacement if pore distribution is similar to the case shown in figure 4.58b.

#### 4.7.1.3. Experimental procedure

The experimental procedure must be associated to the specific conditions which have developed, or may develop in the reservoir<sup>41, 42, 43</sup>

During the migration period either gas or oil (both non-wetting phases) will have to displace the water (wetting phase). This is a typical drainage process which governs the migration of both conventional and fractured reservoirs.

If advancement of the aquifer displaces the oil during reservoir exploitation, this displacement corresponds to an imbibition process; and vice-versa, if advancement of the gas-cap displaces the oil this corresponds to a drainage process.

All these processes are extremely important in a fractured reservoir where each matrix block, saturated with one fluid, is surrounded by fractures which are saturated with a different fluid. The entire exchange of fluids between matrix and fracture is essentially dependent on capillary pressure expressed by the capillary pressure curve. These forces assist displacement in the imbibition process, and oppose displacement in the drainage process.

##### a. Drainage experiments

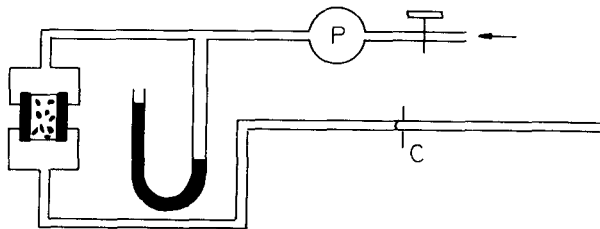
In one way or another, all experiments make use of injection under pressure of a non-wetting phase in a core saturated with a wetting phase. The objective of this injection is to displace the wetting phase from the intergranular pores.

##### ● Injection of fluids

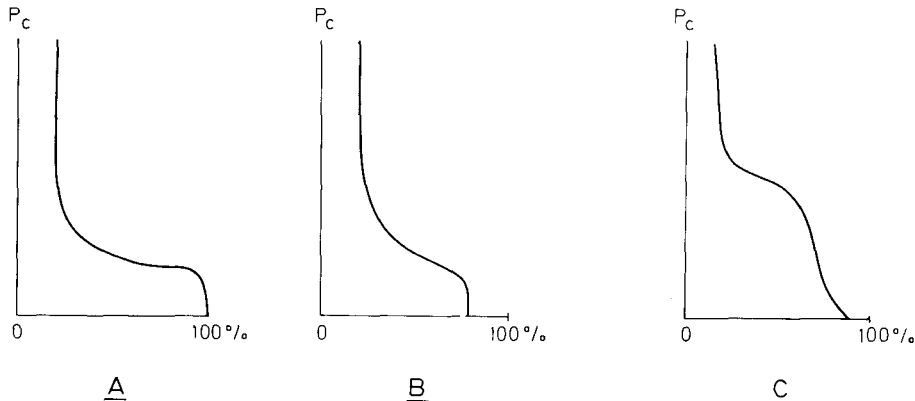
Gas is introduced (in the upper part of the core) into a water-saturated core (a cylinder with impermeable walls) at various pressures (P), displacing the water whose volume is measured by the indicator (C), as shown in figure 4.59. The displacement of indicator C will begin only after the injection pressure overcomes the *threshold* pressure  $P_{TH}$ . This will then reveal the relationship between the minimum injection pressure and capillary resistance in the wetting phase displacement. The threshold pressure is, in general, very near to the minimum pressure necessary to overcome the pressure in correspondence to the radius of the smallest pore entrance. This minimum pressure is called *throat pressure*.

An analog procedure is that of mercury injection by using a high-pressure liquid pump. The relationship between pressure and injected volume describes the capillary pressure curve and pore frequency simultaneously.

The results shown in figure 4.60 may be considered representative of various types of intergranular rock. The first case is a classic homogeneous rock (figure 4.60a). Figure 4.60b illustrates the presence of macropores or a few open fractures, and figure 4.60c illustrates two matrix type units or the presence of fissures in the matrix.



4.59 — Schematic equipment for pressure vs. saturation.



4.60 — Pore size distribution and its influence on  $P_c$  vs  $S_w$  relationship.

### ● Other methods

Other methods, such as *restored state*, *vaporization* and *centrifuge* should also be considered valuable methods. Details of the different procedures and comparison of these procedures are discussed in references 40, 41, 42 and 43.

The use of a centrifuge is still one of the most reliable methods available for the evaluation of the capillary pressure curve. The reason this method is most advantageous is because it permits a rapid evaluation of the variations in saturation of the wetting and non-wetting phases, as well as the role of gravity forces and capillary forces.

The centrifuge method uses a sample of a given length  $h$  and cross-section  $a$  saturated with water (density  $\gamma_w$ ) introduced into a cell containing oil (density  $\gamma_o$ ). The difference in the pressure working on the sample will be expressed by,

$$\Delta P = A \times \Delta \gamma \times h \times n^2 \quad (4.103)$$

where  $\Delta P$  is the pressure difference at the terminal face, if the core is not too long, and the average pressure will result as  $P_m = \Delta P/2$ .

### b. Evaluation methods

A rapid evaluation of various methods, along with their uses and advantages, is presented below:

Method	To be used for	Disadvantages
Hg injection	rapid and accurate data	not valid for shaly sands
Restored state	shaly sands	time too long (tens of days)
Evaporation	rapid evaluation of $S_{wi}$	
Centrifuge	when high pressure is requested	

### ● Conversion of data

The relationship between reservoir (R) and laboratory model (M) is obtained through

$$P_{c,R} = \frac{\sigma_R \times \cos\theta_R}{\sigma_m \times \cos\theta_m} \times P_{c,m}$$

For example, if the experiment is performed in the laboratory for mercury-air, the capillary pressure resulting for water/oil in reservoir conditions would be expressed as,

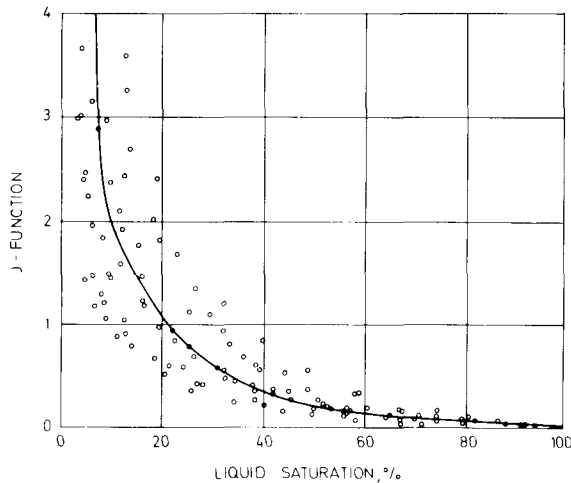
$$\frac{P_c, Hg/air}{P_c, water/oil} = \frac{480}{72} = 6.57$$

► The basic parameters to be used for the transformation of laboratory data to field data and vice-versa, are given in the table below:

System	$\theta$ Contact Angle (grades)	Cos $\Theta$	$\sigma$ Interfacial Tension (dynes/cm)	$\sigma \cos \Theta$
<i>Laboratory</i>				
Air-water	0	1.0	72	72
Oil-water	30	0.866	48	42
Air-mercury	140	0.765	480	367
Air-oil	0	1.0	24	24
<i>Reservoir</i>				
Water-oil	30	0.866	30	26
Water-gas	0	1.0	50*	50

\*Pressure and temperature dependent. Reasonable value to depth of 5000 feet.

Experience has often shown that in the case of limestone the ratio is only 5.8, and for sandstone 7.5.



4.61 – Leverett capillary function.

#### c. Capillary pressure normalization

In order to normalize various capillary pressure curves obtained in the laboratory as a generalized dimensionless relationship, the Leverett<sup>40</sup> procedure is used. The dimensionless function

$$J(S_w) = P_c / \sigma \cos\theta (K/\Phi)^{1/2} \quad (4.104)$$

which (as stated by Leverett<sup>40</sup>) is related to pores characteristics by permeability ( $K$ ) and porosity ( $\Phi$ ). The results obtained from various capillary pressure tests on various cores (of given  $\Phi$  and  $K$ ) produced a generalized dimensionless curve  $J(S_w)$  vs.  $S_w$  (figure 4.61).

#### d. Capillary drainage and imbibition curve

The capillary pressure curve depends essentially on type of displacement, drainage or imbibition (figure 4.61).

In the case of a *drainage* displacement, capillary forces *oppose the entrance* of a non-wetting phase into the matrix, while in an *imbibition* displacement capillary forces act as a *driving force* in displacing a non-wetting phase from the matrix.

In a fractured reservoir the relationship between fluid saturating the matrix block and fluid saturating the fracture will determine (during production process) if a drainage or imbibition process takes place. This relationship may be simplified as follows:

MATRIX	FRACTURE	TYPE OF DISPLACEMENT
Oil	Water	Imbibition
Oil	Gas	Drainage
Water	Oil or gas	Drainage
Gas	Water or oil	Imbibition

#### 4.7.2. Composite capillary imbibition curve

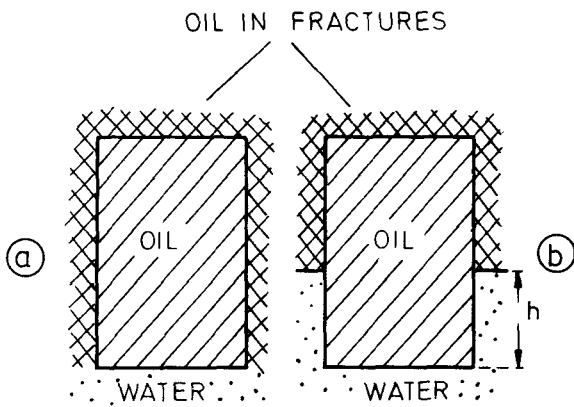
Imbibition in a fractured reservoir will take place whenever the wetting-phase in the fractures displaces the non-wetting phase (oil) saturating the matrix block. According to the relationship between fluids coexisting in matrix and fracture, the displacement process will be controlled by gravity or capillary forces. A simplified scheme is shown in Fig. 4.62: in case *a* the capillary forces imbibing the matrix displace the oil; in case *b* the difference in level *h* will generate a displacement through gravity effect. Since the pores where gravity forces are working preferentially are *larger* and the pores where preferentially capillary forces are working are smaller, the *composite imbibition curve* will take care of both forces working during imbibition. The first step should be to examine displacement conditions of the two matrix blocks saturated with oil (figure 4.62). If the water-oil contact is at the lower face (figure 4.62a) of the matrix block, the forces displacing the oil are the capillary forces. If the water-oil contact is above the bottom of the matrix block (figure 4.62b), the difference in the specific weights between the water in fractures and the oil in matrix generates a gravitational force  $h \times \Delta\gamma = P_G$ , acting as driving force for the displacement of oil from the matrix block. In this case (figure 4.62b) capillary forces, in addition to gravitational forces, act as a second driving force for the displacement of oil.

As mentioned, the presence of gravity forces is related to the existence of a level difference between water-oil contacts in fractures and in matrix. If the water oil contact is higher in the fractures than in the matrix, the gravitational forces are expressed by (figure 4.62b).

$$P_G = h \times \Delta\gamma \quad (4.105)$$

the capillary forces relate to an average capillary height  $h_c$  and are expressed by

$$P_c = h_c \times \Delta\gamma \quad (4.106)$$



4.62 – Type of displacement from matrix block: a) Displacement under capillary forces; b) Displacement under capillary and gravity forces.

where the average capillary height depends on the radius  $r_c$ , avg, of the average pore size, which establishes a proportionality

$$h_c \approx \frac{1}{r_c, \text{avg}} \quad (4.107)$$

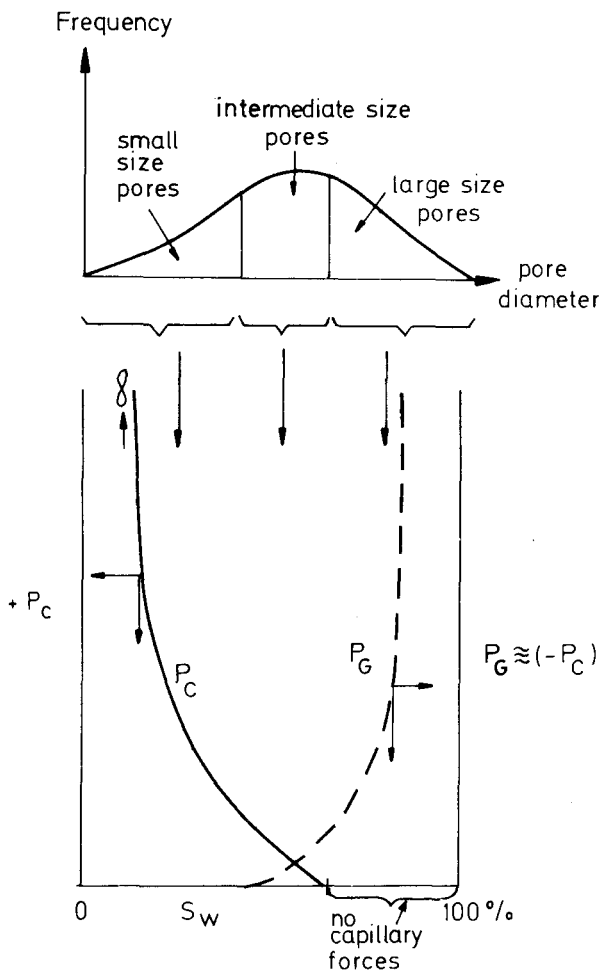
#### 4.7.2.1. Magnitude of $P_c$ and $P_G$

Capillary forces will be large if pore size is small while gravity forces will increase as the height of the matrix block increases. As a result the gravity forces will govern the imbibition in the case of high blocks and large pore size, while capillary forces will govern the imbibition in the case of small matrix blocks and reduced pore size.

For example, considering a fractured reservoir with an average pore diameter of  $4\mu$  (microns) in which oil is displaced by water capillary imbibition one may compare the capillary and gravity forces of one block with a height of  $h_{BL} = 0.3$  m and with another of height  $h_{BL} = 20$  m.

$$h_c = \frac{P_c}{\Delta\gamma} = \frac{1}{\Delta\gamma} \cdot \frac{\sigma \cos\theta}{2r} = \frac{1}{0.2 \times 10^{-3}} \cdot \frac{42 \times 10^{-6}}{4 \times 10^{-4}} = 525 \text{ cm} = 5.25 \text{ m}$$

Comparing capillary height  $h_c = 5.25$  m with the block heights  $h_{BL} = 0.3$  m and  $h_{BL} = 20$  m, it results that in the first case the capillary pressure dominates the displacing process and in the second case the gravitational forces.

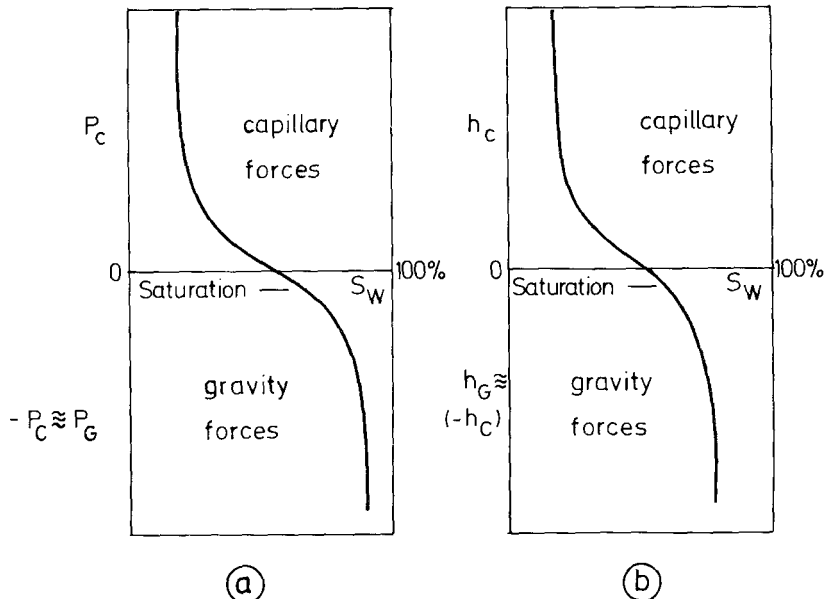


4.63 – Influence of pore size distribution on  $P_c$  vs  $S_w$  and on  $P_G$  vs  $S_w$

#### 4.7.2.2. Magnitude of pores displaced by $P_c$ and $P_G$

In reconsidering the relationship between the frequency curve and pore diameter (figure 4.63) it is clear that small and very small pores are associated with capillary forces of various magnitudes. If pore size increases from small to intermediate, their magnitude will directly influence the  $P_c$  curve, which decreases from infinite to zero (figure 4.63). But a number of pores (intermediate and large) between  $P_c = 0$  and  $S_w = 100\%$  may not show any capillary force (figure 4.63) and thus the displacement will be related to gravitational forces.

As capillary forces vs. saturation in water ( $P_c - S_w$  curves) shows the role of capillary forces in displacing oil by water, the gravitational forces role as predominant force or single force may be expressed by a similar curve  $P_G - S_w$  as in figure 4.63.



4.64 – Composite curves: a) Pressure vs.  $S_w$ ; b) height vs.  $S_w$ .

The gravity forces which may be predominant forces of displacement in intermediate and large pores are limited in the displacement of oil by the interpenetration of small pores and large pores, which leads to the blockage of oil in the area of contrasting pore size. Thus the relationship  $P_G - S_w$  is dependent on pore size distribution and pore intercommunication.

#### 4.7.2.3. Composite imbibition curve approach

Due to the fact that the relationship  $P_G$  vs. saturation may be considered similar to a capillary curve, it is permissible to write  $P_G$  equivalent to a negative  $P_c$  where the negative sign of  $P_c$  is a conventional sign, since during imbibition both forces may displace the matrix fluid in the same direction. The composite curve is thus presented as in figure 4.64, either as pressure (figure 4.64a) or height ( $h_G$  or  $h_c$ , figure 4.64b).

In figure 4.64b for a given block height  $h$ , both  $\Delta S_w$  values, above zero line for capillary forces and below zero line for gravitational forces, will result. The values  $\Delta S_{WG}$  and  $\Delta S_{WC}$  represent total recoveries of oil obtainable from the matrix in a very long time if the block height is known and if the matrix block was completely invaded by water.

#### 4.7.2.4. Capillary curve vs. matrix block

In a conventional reservoir the capillary pressure curve controls fluid distribution through the reservoir; therefore, the transition zone will come between the water-oil contact and the oil zone which, in the case of important capillary forces (tight formation), may be very thick. In a fractured reservoir this situation is completely different as discussed in section 4.4.1.1.

The discontinuity of the matrix caused by the fracture network cutting the *continuum* of the matrix bulk into small individual matrix blocks, explains why the water table is only related to the fracture network. In addition, since the fractures are large channels with negligible capillary forces, the transition zone disappears in a fractured reservoir, and water-oil contact becomes a horizontal plane. On the other hand, capillary and gravitational forces (through the capillary pressure curve and gravitational curve) control the static and dynamic equilibrium of each matrix block. The basic element which relates individual block behaviour to reservoir behaviour is the water-oil contact in fractures and is called *water table level*. These water-oil contacts in fractures, together with the oil-water contacts inside the matrix, the last corresponding to *displacement front level*, are essential reference planes for the evaluation of the driving mechanism of capillary and gravity forces. An analogical situation will take place in the case of a gas-cap for both gas-oil contacts in fractures and matrix blocks, where the first is called *gas-cap table* and the second *gas displacement front*.

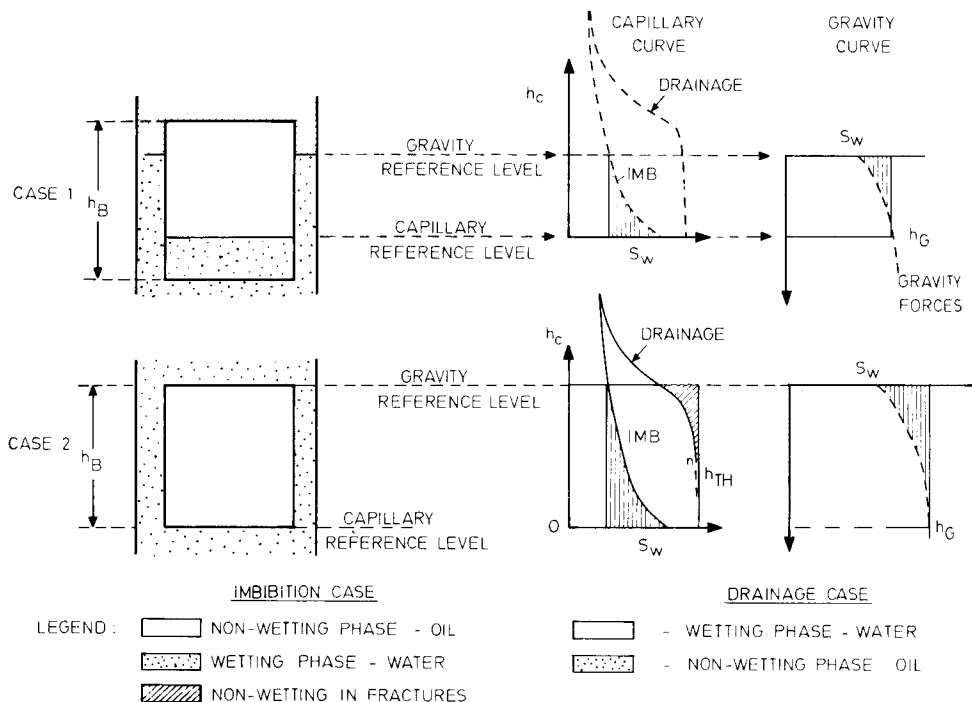
EXAMPLE: Considering a block height  $h_B$ , as is graphically described in figure 4.65, a procedure through which (at any stage) a correlation between the driving forces and fluid equilibrium may be established can be developed.

Case 1; As observed, the water-oil contact advanced during displacement in matrix and fractures, so that the water-oil level in fractures is above the bottom level in matrix. In this case the reference level of capillary forces should be related to the water-oil level of the matrix. A dotted line represents capillary forces in the imbibition capillary curve. The gravity forces, in this case, refer to the fracture water-oil contact, and therefore, the height of the gravity forces will be limited to the water-oil contact in the matrix.

In the same case 1, when a wetting phase is in the matrix and non-wetting phase in fractures, the same procedure will be followed on the drainage capillary pressure curve. As observed, capillary forces are higher on the drainage curve than gravity forces, which explains why it is impossible to displace water with oil in fractures under existing conditions of equilibrium. Capillary forces, which are larger than gravity forces, oppose the entrance of oil into the block.

Case 2; The oil-saturated block is immersed in water so that the reference for capillary forces is at water-oil contact in the matrix (bottom face of block), and the reference for gravity forces is at the higher level of the block (top face). Capillary and gravity efficiencies are represented by dotted zones which indicate the magnitude of total recovery expected from gravity and capillary forces.

In the case that water saturates the matrix a drainage process will take place. By using the drainage curve (the oil-non-wetting phase displaces water-wetting phase), the threshold height  $h_{TH}$ , being somewhat lower than block height, a partial imbibition of oil becomes possible in the block (hatched area).



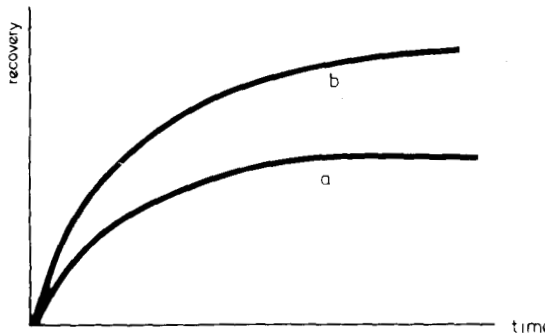
4.65 – Schematic description of reference levels in fractures and matrix during imbibition displacement.

#### 4.7.2.5. Recovery by imbibition vs. time

The displacement process of a matrix block saturated with oil implies a relationship *recovery vs. time* which may be considered as basic data in the reservoir engineering of a fractured reservoir. This relationship is often presented as in diagram Fig. 4.66 in dimensional or dimensionless time.

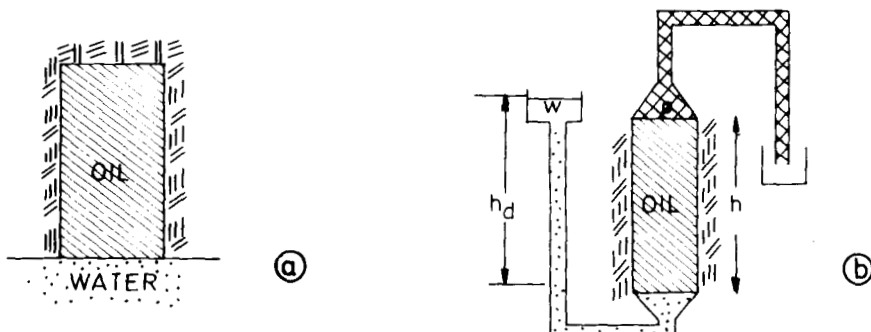
The curve is obtained by direct measurements in the laboratory or through the mathematical simulation of a displacement process. A detailed discussion is given in chap. 9 and the simulation is discussed in chap. 11.

The results are very much influenced by rock homogeneity, reservoir lithology, fluid nature, surface contact between rock and fluids, fluid viscosity, mobility factor, etc.



4.66 – Recovery vs. time for cases a and b of Fig. 4.67.

In order that laboratory experiments may be useful for a correct interpretation of field behaviour, it will be necessary to simulate the same role played in the field by capillary and gravity forces under laboratory conditions. Conventional experiments such as those shown in cases a and b in Fig. 4.67 give different results. In case a the fluid displacement will be the result of only capillary imbibition forces, while in case b gravity and capillary forces are working together during the displacement process. The result of recovery vs. time will be quite different, as observed in Fig. 4.66, (Iffly<sup>44</sup>).



4.67 – Water imbibing oil: a) capillary forces, b) gravity and capillary forces.

Due to the fact that the cores are small and often the simulation of gravity forces in the laboratory requires long samples, the conventional analyses are substituted by centrifugal experiments (KYTE<sup>45</sup>). The centrifuge, similar to that shown in Fig. 4.68, has a length  $H$ , and is introduced into a core holder saturated with brine. Based on the rotation of the centrifuge, it may be considered that the gravity potential is given by

$$dG = \omega^2 \Delta \rho (R + h) dh \quad (4.108)$$

which integrated along the sample length gives

$$\bar{G} = \omega^2 \Delta \rho (Rh + h^2/2) \quad (4.109)$$

The volume-weighted gravitational potential will then be

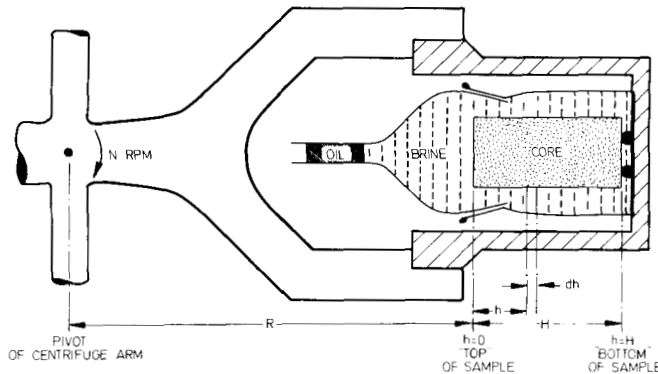
$$\bar{G} = \frac{1}{H} \int_0^H \Phi dh = \omega^2 \Delta \varrho \left( \frac{3RH + H^2}{6} \right) \quad (4.110)$$

If the capillary pressure is expressed by equation 4.104,

$$P_c = (\sigma f(\theta) / \sqrt{K/\Phi}) J(S_w)$$

the ratio gravity capillary will give

$$\frac{\bar{G}}{P_c} = \frac{\omega^2 \Delta \varrho (3RH + H^2)/6}{(\sigma f(\theta) / \sqrt{K/\Phi}) J(S_w)} \quad (4.111)$$



4.68 – Scheme of centrifuge displacement (Kyte<sup>15</sup>, courtesy AIME).

or as centrifugal speed

$$\omega = \sqrt{\frac{\bar{G} (\sigma f(\theta) / \sqrt{K/\Phi}) J(S_w)}{P_c \Delta \varrho (3RH + H^2)/6}} \quad (4.112)$$

where

$$N = \frac{60}{2\pi} \omega \quad (4.113)$$

If the tests are carried out on small samples (small H) the preponderance of gravity forces may be obtained by using a high centrifugal speed (discussed in Chap. 9).

## SYMBOLS

### Latin letters

#### Section 4.2.

$a$	– extension
$A$	– area
$b$	– fracture width
$K$	– permeability
$L$	– length, linear
$n$	– indefinite number
$s$	– section, surface
$V$	– volume
$Z$	– length variable
$x$	– length variable
$\Phi$	– porosity

#### Subscripts:

$1$	– primary porosity
$2$	– secondary porosity
$B$	– bulk
$D$	– density
$eff$	– effective
$f$	– fracture
$fD$	– fracture density
$i$	– indefinite number
$m$	– matrix
$min$	– minimum
$max$	– maximum
$t$	– total

#### Section 4.3.

$a$	– extension
$A$	– constant depending on rock type
$A$	– area
$A_{fD}$	– area fracture density
$b$	– fracture width
$B$	– porosity constant
$C$	– pore size constant
$C_1, C_2$	– constants
$D$	– pore shape constant
$e$	– interval
$h$	– net pay
$H$	– gross pay
$K$	– permeability
$LSF$	– longitudinal shape factor
$m$	– matrix

$n$	– number of fractures
$p$	– pressure
$q$	– unit of rate
$Q$	– rate
$r$	– radius
$S$	– skin
$TSF$	– transversal shape factor
$V_{fD}$	– volumetric fracture density
$y$	– variable
$\alpha$	– angle between fracture and flow direction
$\Phi_f$	– fracture porosity
$\mu$	– viscosity

#### Subscripts:

$f$	– fracture
$ff$	– single fracture
$fD$	– fracture density
$g$	– gasket
$g, eff$	– gasket, effective
$i$	– indefinite number
$m$	– matrix
$o, g$	– opening, gasket
$w$	– water

#### Section 4.4.

$A$	– area
$A^1$	– constant
$b$	– fracture width
$B$	– constant
$B_o$	– oil volume factor
$B_g$	– gas volume factor
$D_G$	– gas deliverability
$h$	– net pay
$H$	– pay
$J.A$	– correction anisotropy factor
$K$	– permeability
$n$	– number of blocks
$p$	– pressure
$PI$	– productivity index
$Q$	– rate
$RA$	– reservoir area
$r$	– radius
$\Phi$	– porosity
$\mu$	– viscosity
$\sigma$	– overburden stress

*Subscripts:*

B	– volume factor
Block	
Bulk	
e	– external boundary
f	– fracture
fi	– fracture original
fD	– fracture density
global	
g	– gas
m	– matrix
o	– oil
row	– row of matrix blocks
w	– well boundary

*Section 4.5.*

B	– volume factor
C	– compressibility
P	– pressure
S	– saturation
V	– volume
$\Phi$	– porosity
$\sigma$	– overburden stress

*Subscripts:*

1	– primary
2	– secondary
B	– bulk
c	– cavern
e,g	– effective gas
e,o	– effective oil
eff	– effective
f	– fracture
fr	– fracture
g	– gas
h	– hailing apparent pressure
i	– initial
k	– overburden or net confining
o	– oil
oif	– original oil in fracture
oim	– original oil in matrix
p	– pore
pf	– porosity fracture
pm	– porosity matrix
psp	– carbonate secondary porosity
r	– rock
T	– total

ts	– total secondary
w	– water
wi	– water irreducible
wif	– water irreducible in fractures

*Section 4.6.*

d	– pore diameter
K	– permeability
$K_r^o$	– permeability of non-wetting phase at wetting phase residual saturation
P	– pressure
S	– saturation
$S^*$	– relative saturation
$\lambda$	– pore uniformity coefficient
$\Phi$	– porosity

*Subscripts:*

b	– fracture width
c	– capillary
co	– capillary oil
dr	– drainage
g	– gas
gc	– gas capillary
g, cr	– gas critic
gf	– gas in fractures
gi	– gas initial
gr	– gas residual
imb	– imbibition
nwt	– non-wetting
m	– complement to critical saturation
m	– maximum
o	– oil
r	– relative
ro	– relative oil
rg	– relative gas
w	– water
wt	– wetting
wi	– irreducible water
1, 2	– matrix fractures

*Section 4.7.*

A	– section
G	– gravity force
H	– height
J(sw)	– Leverett function
J	– curvature
K	– permeability

n	- number of rotations
N	- number of rotations per minute
P	- pressure
R	- capillary radius
S	- saturation
$\Phi$	- porosity
Z	- ordinate
$\gamma$	- specific weight
$\sigma$	- interfacial tension
$\theta$	- interfacial angle
$\Delta$	- difference
$\omega$	- rotational speed

*Subscripts:*

air	
c,r	- capillary reservoir
c,l	- capillary laboratory
dr	- drainage
G	- gravity
g	- gas
Hg	- mercury
imb	- imbibition
m	- model
o	- oil
ow	- oil-water
ows	- oil-water contact
R	- reservoir
w	- water

## REFERENCES,

1. Warren, J.W. and Root, P.J., 1963. The behaviour of naturally fractured reservoirs. Soc. of Petroleum Engineers Journal Vol. 3, No. 3, p. 245.
2. Walschmidt, W.A., Fitzgerald, P.E. and Lunsdorf, 1956. Classification of porosity and fractures in reservoir rocks. Bull. Am. Assoc. of Petroleum Geologists, Vol. 40, No. 8, May.
3. Atkinson, B. and Johnston, D., 1948. Core analysis of fractured dolomite in the Permian Basin. AIME, Petr. Techn. TP 2432.
4. Murray, G.H., 1977. Quantitative fracture study, Sanish Pool, McKenzie County, North Dakota. Am. Assoc. of Petroleum Geologists, reprint series No. 21.
5. Abgrall, E., 1971. Porous media behaviour versus temperature and compression variation. French Institute of Petroleum Revue (IFP), pp. 571-584, July-Aug.
6. Parsons, R.W., 1966. Permeability of idealized fractured rock. Soc. of Petroleum Engineers Journal, pp. 126-136, June.

7. Kazemi, H., 1969. Pressure transient analysis of naturally fractured reservoir with uniform fracture distribution. Soc. of Petroleum Engineers Journal, pp. 451-426, Dec.
8. Romm, E.S., 1966. Fluid flow in fractured rocks. Nedra, Moscow.
9. Kelton, F.C., 1950. Analysis of fractured limestone dolomite. AIME, Petroleum Transactions, Vol. 189.
10. Teodorovich, G.I., 1943. Structure of the pore space of carbonate oil reservoir rocks and their permeability as illustrated by the Paleozoic reservoir of Bash-Kirya. Doklady Academy Nauk USSR, Vol. 39, No. 6, pp. 231-234.
11. Aschenbrenner, B.C., Chilingar, G.V. and Teodorovich, G.I., 1960. Method for determining permeability from pore-space characteristics of carbonate rocks. Bull. Am. Assoc. of Petroleum Geologists, Vol. 44, pp. 1421-1444.
12. Barenblatt, G.I. and Zheltov, Y.P. Fundamental equation of filtration of homogeneous liquids in fissured rocks. Academy of Sciences, USSR, pp. 522-526.
13. Reiss, L.H., 1976. Reservoir engineering in fractured reservoirs. French Institute of Petroleum.
14. Khanin, A.A., 1969. Oil and gas reservoir rocks and their study. Izd. Nedra, Moscow, pp. 366.
15. Whitson, C. 1980. Rock & Fluid physical correlations for Petroleum Engineers NTH, University of Trondheim.
16. Saidi, A., Martin, R.E., 1966. Application of reservoir engineering in the development of Iranian reservoirs. The Bulletin of the Iranian Petroleum Institute, No. 24, Sept.
17. Chilingar, G.E., Mannon, R. and Rieke, H.H., 1976. Oil and gas production from carbonate rocks. Elsevier.
18. Jones, F.G., 1975. A laboratory study of the effects of confining pressure of fracture flow and storage capacity in carbonate rocks. Journal of Petroleum Technology, pp. 21-29, Jan.
19. Van Golf-Racht, T.D. and Henking, E., 2972. A new forecast method applied to Rostam fractured reservoir. Preprint No. 3720, European SPE Meeting, Amsterdam.
20. Geertsma, J., 1957. The effect of fluid pressure decline on volumetric changes in porous rocks. Trans. AIME, Vol. 210, pp. 331-340.
21. Hall, H.N., 1953. Compressibility of reservoir rock. Trans. AIME, Vol. 198, pp. 309-311.
22. Huppner, J.D., 1970. Numerical investigations of the effects of core heterogeneities on waterflood relative permeabilities. Soc. of Petroleum Engineers Journal, pp. 381-392, Dec.
23. Brandner, C.F. and Slatboom, R.A., 1975. Vertical immiscible displacement experiments in a non-homogeneous flow cell. Canadian Journal of Petroleum Technology, pp. 25-33, Jan.-March.
24. Erlich, E., 1971. Relative permeability characterisits of vugular cores. Paper SPE 3553, Fall Meeting SPE, New Orleans.
25. Standing, M.b., 1974. Relative permeability relationships. Lectures given at Trondheim University.
26. Burdine, N.T., 1953. Relative permeability calculations from pore size distribution data. Trans. AIME, 198, pp. 71-78.
27. Brooks, R.H. and Corey, A.T., 1965. Hydraulic properties of porous media. Hydrology Papers, Colorado State University, No. 3, March.
28. Sigmund, P.M. and McCaffery, F.G., 1971. An improved unsteady-state procedure for determining the relative permeability characteristics of a heterogeneous porous media.
29. Naar, J. and Henderson, J.R., 1961. An imbibition model. Soc. of Petroleum Engineers Journal, pp. 61-70, June.
30. Land, C.S., 1971. Calculation of imbibition relative permeability for two-phase and three-phase flow. Trans. AIME 251, II, pp. 419.
31. Corey, A.T. and Rathjens, C.H., 1956. Effect of stratification on relative permeability. Trans. AIME, 207, 358.
32. Archer, J.S. and Wong, S.W., 1973. Use of a reservoir simulator to interpret laboratory waterflood data. Soc. of Petroleum Engineers Journal, pp. 343-347, Dec.

33. Abgrall, A. and Iffly, R., 1973. Physical study for the flow by expansion of dissolved gas. Revue of French Petroleum Institute, pp. 667-692, Sept.-Oct.
34. Braester, C., 1972. Simultaneous flow of immiscible liquids through porous fissured media. Journal of Petroleum Technology, pp. 297-303, Aug.
35. Torsæter, S. 1980. Flow of immiscible fluids in fractured porous media. Sintef Report. Trondheim, STF 28 A 80.005.
36. Lefebvre du Prey, E., Verre, R., 1973. Polyphasic flow in fissures study, Report of French Institute of Petroleum. Ref. 20950, January 1973.
37. Merill Lavaun, S. Jr., 1973. Two phase flow in fractures. Dissertation presented at Univ. of Denver.
38. Melrose, J.C., 1970. Interfacial phenomena as related to oil recovery mechanism. The Canadian Journal of Chemical Engineering, Vol. 48, pp. 638-644, Dec.
39. Melrose, J.C., Brandner, C.F., 1974. Role of capillary forces in determining microscopical displacement efficiency for oil recovery by water flooding. The Journal of Canadian Petroleum Technology, pp. 54-62, Oct-Dec.
40. Leverett, M.C., 1941. Capillary behaviour in porous solids. Trans. AIME, Vol. 142, 151.
41. Leverett, M.C., Lewis, W.B. and True, M.E., 1942. Dimensional model studies of oil field behaviour. Trans. AIME, Vol. 142, 175.
42. Purcell, W.R., 1950. Interpretation of capillary pressure data. Trans. AIME, Vol. 189, pp. 369-371.
43. Rose, W. and Bruce, W.A., 1949. Evaluation of capillary character in petroleum reservoir rock. Trans. AIME, Vol. 186, pp. 127-142.
44. Iffly, R., Rousselet, D. and Veunewlen, J.L., 1974. Etude fondamentale de l'imbibition dans un réservoir fissuré. French Institute of Petroleum Revue, pp. 217-239.
45. Kyte, J.R., 1970. A centrifuge method to predict matrix-block recovery in fractured reservoirs. Soc. of Petr. Engineers, June, pp. 164-170.

This Page Intentionally Left Blank

# CHAPTER 5

## LOGGING VS. FRACTURE EVALUATION

### 5.1 INTRODUCTION

In the last two decades (1960–1980), great efforts have been made in order to make fracture detection easier and to estimate their density through well logging. However, the qualitative and quantitative evaluation of fractures was found to be much more complicated than first expected. This is due to the technical difficulties involved in the identification of fractures, especially when trying to give an accurate description of the fracture system in contact with the wellbore.

This chapter attempts to summarize the available logging tools which can be used individually or combined for detecting natural fractures, and also to explain the present possibilities of fracture interpretation with the available techniques.

Since no log *sees* a fracture as such (except the recent borehole televiewer), any attempt to detect fractures will require a rather large number of logs. Generally, the various techniques are based on the fact that in a homogeneous formation with constant hole size, a fractured zone will produce an anomaly in the normal sensor response. If the fracture is open, the anomaly is sizable; but if it is sealed, the anomaly is negligible.

Logging is generally sensitive to the presence of a high permeability path (formed by fractures) in a low permeability medium (formed by matrix). This sensitivity will cover the logging response of a fracture, or of what may be called joint, vug, cavern, crack, etc.

In general, the location of high permeability zones is obtained from log responses, unusually high drilling rates, and loss of drilling fluids. Often the log response can locate the high specific productivity index in wells after stimulation, very poor core recovery, and significant increase of hole size.

The effect of fractures on the single tool response is discussed in the first part of this chapter, the combined technique for the identification of fractures is developed and reviewed in the second part, and the interpretation and methods of analysis of fracture detection logs are discussed in the last part.

Where fracture detection depends on the presence of higher permeability zones (compared to that of the matrix), then fracture detection by logging will be limited to only open fractures or those which are partially filled. However, logging of natural fractured reservoirs will never distinguish natural fractures from induced ones, the

detection of small cracks induced during drilling is of very great importance if connected to the natural fracture system.

Logging will mainly examine the *fractured zone* around the wellbore where fractures are more often vertical and subvertical than horizontal<sup>1</sup>. Particular attention, however, must be given to fractures of limited length which may result from stylolites or thin shale strings.

## 5.2 LITHOLOGY LOGS

Lithology logs are defined as those logs normally used to differentiate between shales and non-shales. Included in this category are the spontaneous-potential (SP) and gamma ray logs.

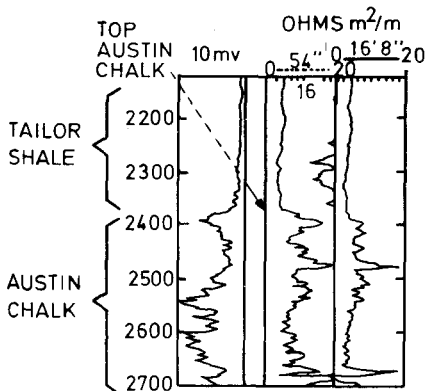
### 5.2.1 Spontaneous-potential (SP) log

The spontaneous-potential or SP log is a recording versus depth of the difference in electrical potential of a movable electrode in the borehole and the fixed potential of a similar electrode at the surface.

In front of the shales the readings of the SP curve are usually fairly constant and tend to follow a straight line (shale base line); while in the case of permeable formations, the SP curve shows variations from the shale base line. In the case of a natural fractured reservoir the curve may indicate an anomaly which could be associated with the fractured zone. An example of these variations (taken from the Austin limestones<sup>2</sup>) is given in figure 5.1. The interpretation in this case is that each pip should correspond to an SP response as a result of the mud filtrate in the fractures. Nevertheless, negative SP responses have been recorded for a number of very tight matrixes, and the spontaneous-potential provides only limited validity for the identification of fractures, since the filling material in fractures (such as pyrite) may often influence the SP response. This tool was found inadequate for the identification of fractures in limestones.

### 5.2.2. Gamma Ray log

The gamma ray log detects and evaluates radioactive mineral deposits, and in sedimentary formations it is an excellent indicator for the content of shale due to the radioactive elements concentrated in clays and shales. Increased shaliness in fractures or radioactive crystals (such as uranium) deposited on the fracture opening during water circulation, may increase the radioactivity and give a higher gamma ray response. Such a response may be added to other indications and, thus, will help detect fractures.



5.1 – Conventional SP log obtained on Austin chalk (Pirson<sup>1</sup>, Courtesy World oil).

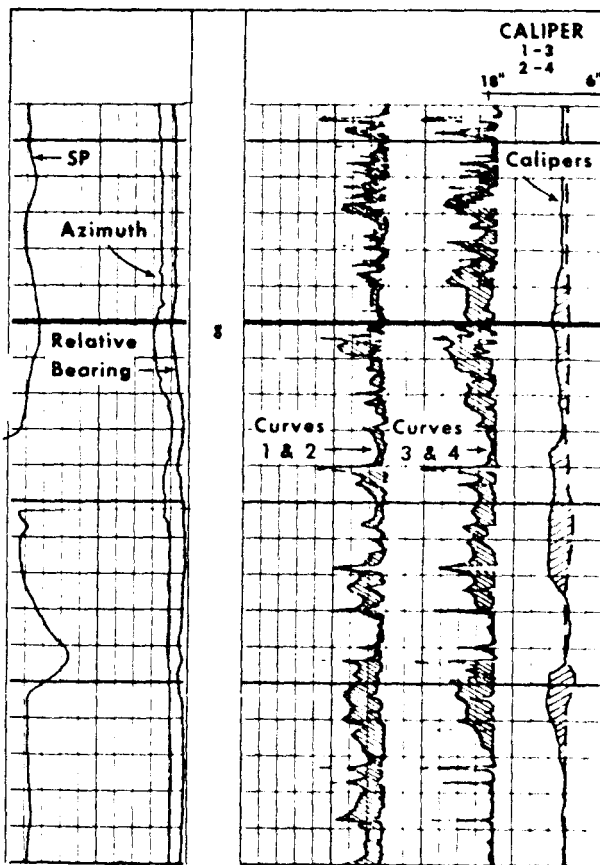
### 5.3. CALIPER LOGS

The caliper log is a measurement of the borehole diameter. During the drilling operation, the mud in the borehole is usually conditioned so that the hydrostatic pressure of the mud column is greater than the pressure of the formations. The differential pressure forces mud filtrate into the permeable formations, and the solid particles of the mud are deposited on the borehole wall where they form a mud cake.

Fractured zones will usually show up on the caliper log as a reduction in hole size (which is probably due to thick mud cake), mainly if *lost circulation material* is used.

The opposite case could be a hole size elongation, most likely caused by the breaking of the formation during drilling and the fall of various sized blocks, especially if they are between fractures parallel to the wellbore hole. This can often be seen on a four-arm, two-diameter caliper log (figure 5.2). Opposite arms 1 and 3 provide a caliper along one diameter, and arms 2 and 4 provide a caliper along another diameter perpendicular to the first. At the right of figure 5.2 the fractured separation between the two caliper curves indicates an out-of-round hole which could be due to fractures<sup>2</sup>.

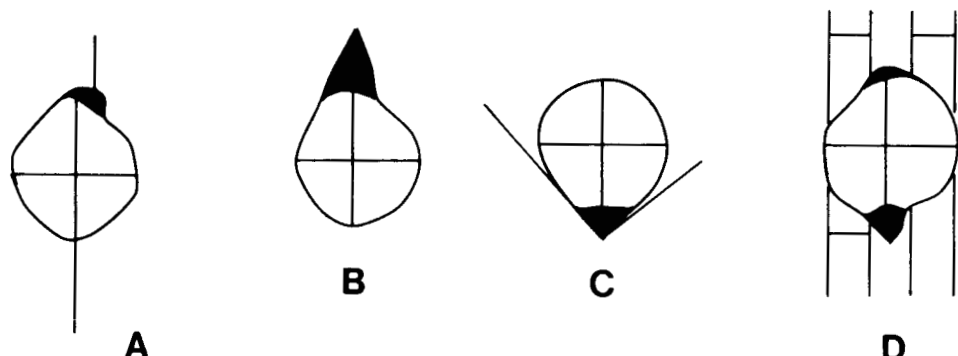
Elongated boreholes in the fractured zone are shown by the cross-sections A, B, C and D in figure 5.3; but it should be pointed out that not all non-circular holes (elliptical shape) are caused by fractures<sup>3</sup>, and the elongation of the deformed hole cannot be correlated with the dip azimuth or with the lithology. A relationship, however, may sometimes develop between fracture orientation and hole ellipticity.



5.2 – Out of round borehole (indicated by double caliper curve) which indicates vertical fracturing (Beck<sup>2</sup>, Courtesy SPLWA).

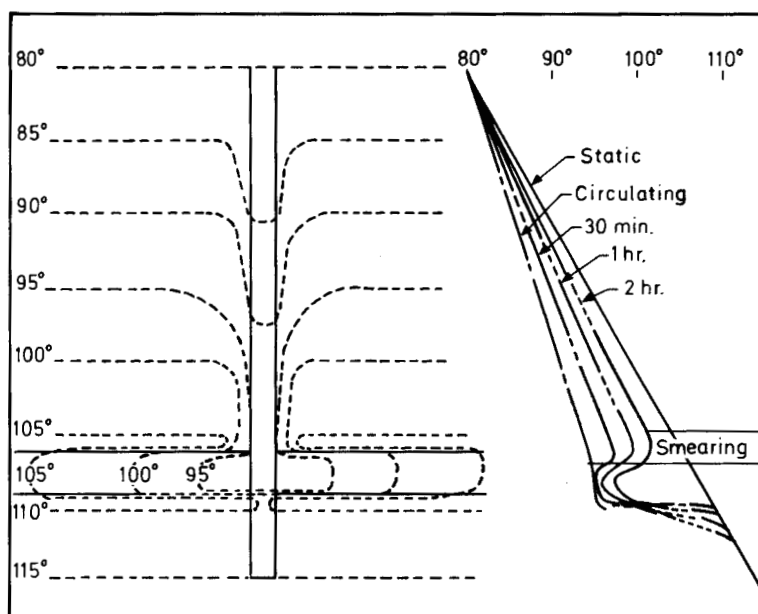
#### 5.4. TEMPERATURE LOGS

The circulation of cooler mud in a wellbore reduces the temperature gradient throughout the well depth, but considerably more so in front of the permeable formation. The reduction in temperature depends on formation thermal conductivity, difference in temperature between mud and formation, and also on mud invasion and mud loss. It is evident that the presence of fractures, which increases mud loss (invasion), will cause a modification of the temperature gradient in the fractured zone during mud circulation, or later in time when mud circulation has stopped. But fractures can only be detected if the thermometers have a sufficiently high sensitivity and a relatively limited inertia effect. In this case, the local change in temperature vs. time will be accurately recorded. The classic behaviour of the temperature log after

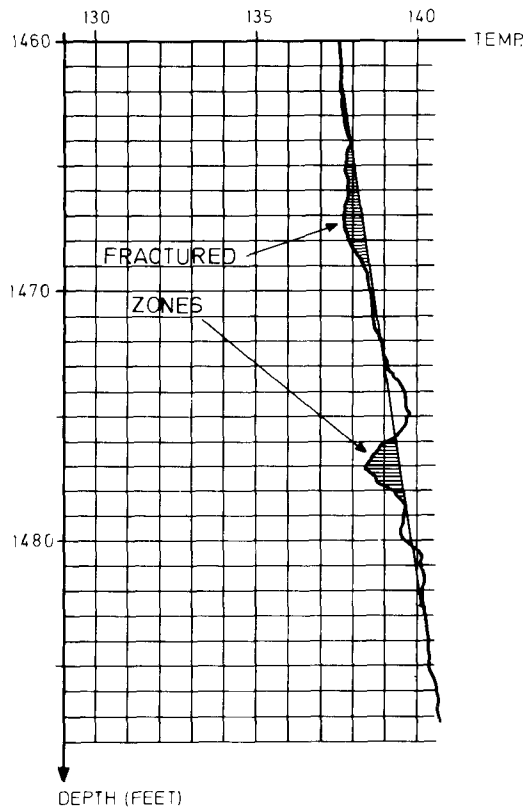


5.3 – Elongated holes due to broken rocks as a result of the presence of fractures: A – Single fracture intersection, B – Borehole intersecting vugs, C – Intersecting fractures, D – Intersecting fracture network (Courtesy Schlumberger).

circulation of a cold fluid, is shown in figure 5.4. The lowest temperature is obtained during mud circulation, and after the circulation is interrupted, the temperature will increase continuously until the static temperature is reached. Return to the initial temperature is slower in the case of increasing mud losses, and therefore, in the presence of fractures temperature restabilization is expected to take a longer amount of time. Anomalies created by fractures indicate the fractured zone<sup>3</sup> (fig. 5.5).



5.4 – Schematic temperature log after circulation of cold mud (Courtesy Schlumberger).



5.5 – Temperature anomalies in fractured zone (Suau<sup>4</sup>, Courtesy SPLWA).

However, because of the misinterpretation of temperature logs, the results obtained from these logs should only be considered as a qualitative indication of the presence of fractures.

Temperature logs might be more successful in the case of an open hole gas producing well. The kick of the temperature curve indicating a low temperature is a classic example of the identification of fractures in a wellbore. Examples from the Utica shale of the lowlands of Quebec have been discussed<sup>4</sup>.

## 5.5. RESISTIVITY LOGS

### 5.5.1. Classification

The resistivity tools are classified into different categories as a function of the investigated zone around the wellbore and also as a function of the devices used for measuring resistivity. Based on the investigated zone, there are two main categories:

- a. the deep investigation devices for measuring the true resistivity of the formation;
- b. the shallow investigation devices for measuring the resistivity of the invaded zone ( $R_{x0}$ ), close to the tool.

Based on the type of device used, there are also two main categories:

- a. the *electrode devices* where the measured resistivity is the sum of the resistivities *in series* of the zones positioned around the wellbore. In the case of *shallow* devices the zones are: the drilling mud ( $R_m$ ), mud cake ( $R_{mc}$ ), and the flushed and invaded zones ( $R_i$ ), respectively, as distance away from the tool increases. The *deep* investigation devices examine the same zones plus the undisturbed formation resistivity ( $R_t$ ). The apparent resistivity of the formation measured by the deep investigation device can be expressed mathematically as:

$$R_a = G_m R_m + G_i R_i + G_t R_t \quad (5.1)$$

- where  $G$  represents the integrated geometric factors for each region;
- b. the *induction devices*, by which the current loops are induced in the above regions, and flow *in parallel* around the tool. For this arrangement of resistivities the apparent resistivity recorded by the deep investigation tool can be expressed mathematically as:

$$\frac{1}{R_a} = \frac{G_m}{R_m} + \frac{G_i}{R_i} + \frac{G_t}{R_t} \quad (5.2)$$

The possible combinations of resistivity tools used for fracture identification can now be understood in the light of the above discussion.

### 5.5.2. Resistivity vs. measurement conditions

Measurement of resistivity depends on the geometric fracture characteristics and the fluid which fills the fractures, and is influenced by fracture direction (vertical or horizontal), size and length, as well as by the type of fluid which saturates the fractures (water, mud filtrate, hydrocarbons).

#### 5.5.2.1. Fracture direction

If the fracture network is predominantly formed by *vertical fractures* and a small number of horizontal fractures the *induction log* will not be able to detect them. This is explained by the fact that the induced current in the formation tends to flow in horizontal loops around the wellbore and, therefore, the vertical fractures contain-

ning a conductive fluid will represent a negligible portion of the loop path of the current; thus the induction log response will practically ignore the presence of vertical fractures. On the other hand, a horizontal fracture filled with water indicates an important conductive anomaly.

#### 5.5.2.2. Fracture fluid

If the fractures are filled by water the current lines will tend to be short-circuited, thus causing a decrease in resistivity. In tight formations, however, resistivity in fractures having the same orientation will apparently increase. Resistivity increases with the increase of depth of investigation, especially in a hydrocarbon-bearing formation.

#### 5.5.3. Role of short and long normal

If the fractures and matrix are considered to be connected in parallel the equations (proposed by Pirson<sup>1</sup>) respectively, are,

$$\text{Short normal: } 1/R_{fi} = \nu \Phi_t/R_{mf} + (1 - \alpha) \Phi_t/R_{bo} \quad (5.3)$$

$$\text{Long normal: } 1/R_{fo} = \nu \Phi_t/R_w + (1 - \alpha) \Phi_t/R_{bo} \quad (5.4)$$

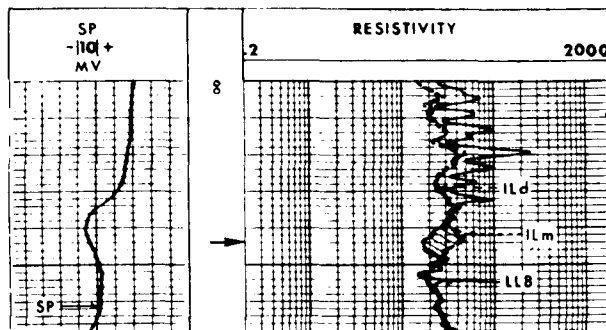
where  $R_{fi}$  and  $R_{fo}$  are the short and long normal (induction) resistivities, respectively, while  $R_{mf}$ ,  $R_w$  and  $R_b$  are the resistivities of mud filtrate, water and rock matrix saturated with 100% water.

If a microresistivity tool is used (equation 5.3) the formation examined will represent a small volume of rock around the wellbore, and occasionally there is the risk of missing fractures. If the fractures are involved in the measurements the zone will indicate an increase in conductivity as a result of a larger local porosity and total saturation in water (caused by the total displacement of hydrocarbons). The anomaly is also associated to the substantial reduction of the cementation factor<sup>4</sup> (below 2, usually around 1.4).

#### 5.5.4. Discussion of combined tools

##### 5.5.4.1. Induction-laterolog

If the two tools are run together, the results can be used for what Beck<sup>2</sup> termed the *first quick-look method*. The fractures may be detected if the LL8 response is combined with the medium-deep investigating induction log. The LL8 is a vertically



5.6 – Fracture response (at level of arrow) of dual-induction laterolog (Beck<sup>2</sup>, Courtesy SPLWA).

focused, short-spaced resistivity which can detect vertical fractures if they are saturated with mud filtrate (of relatively low resistivity). The mud resistivity will be substantially lower than that of the induction log response.

The response of the induction log curves will disregard the presence of fractures, and the difference between the two responses may aid in the detection of fractures (figure 5.6).

However, the success of this method depends on a series of factors, such as fracture characteristics (dimensions, lateral extension), drilling fluid resistivity, lithology, borehole shape and size, etc. Therefore, it is necessary to compare the response with the results obtained from other logs in order to come to a conclusion on the presence of fractures.

#### 5.5.4.2. Dual laterlog-Rxo

The combined effects of the curves DLL-Rxo (suggested by Suau<sup>4</sup>) is very indicative if the fractures are saturated with hydrocarbons far from the wellbore (figure 5.7).

As observed, the presence of fractures is already indicated by the difference between LLD and LLs which, in addition, is accentuated by the Rxo response. The DLL, if successful, may help in the evaluation of fracture porosity, expressed as a fraction of non-porous bulk. In fact, the expression  $v\Phi_t$  which relates the total porosity to the coefficient  $\gamma$ , as elaborated by Aguilera<sup>56</sup>, represents the fracture and solid rock which form the bulk unit (as in figure 5.8):

$$V_m + V_f + V_r = V_B = 1 \quad (5.5)$$

The porosities  $\Phi_m$  and  $\Phi_f$  form the total porosity:

$$\Phi_m + \Phi_f = \Phi_t \quad (5.6)$$

and, therefore:

$$v = \frac{\Phi_t - \Phi_m}{\Phi_t(1 - \Phi_m)} = \frac{\Phi_f}{\Phi_t(\Phi_f + \bar{V}_r)} \approx \frac{\Phi_f}{\Phi_t \bar{V}_r} \quad (5.7)$$

since

$$V_r = 1 - \Phi_f - \Phi_m$$

In order to evaluate the expression  $v\Phi$ , Aguilera recommends the simultaneous solution of equations 5.3 and 5.4. This may be achieved by using the results obtained from DLL-Rxo.

In the Malosa field carbonate (Italy) the dual laterolog  $-R_{x0}$  proved to be a powerful detector of fractures<sup>7</sup>. The deep and shallow laterolog gave the ratio  $LL_d/LL_s \approx 2$ , while  $R_{x0}$  was close to  $R_{x0} = R_m/\Phi^{1.6}$ . This last relationship reconfirmed Suau's<sup>4</sup> observation that the cementation factor in the presence of fractures decreases to values below 2 and is generally around 1.4.

## 5.6. DIPMETER LOGS

The dipmeter log is basically the tool which evaluates the dip angle and dip direction of a bedding plane which intersects the wellbore. By analogy, the dipmeter passing in front of a fracture is expected to indicate its presence by an increasing in conductivity, if compared with matrix conductivity (non-fractured zone). The recordings of the four radial pads positioned with an angular interval of  $90^\circ$  resemble four microresistivity curves. If the tool is rotated in the borehole with uniform speed, the dipmeter response may describe all types of fractures from vertical to horizontal.

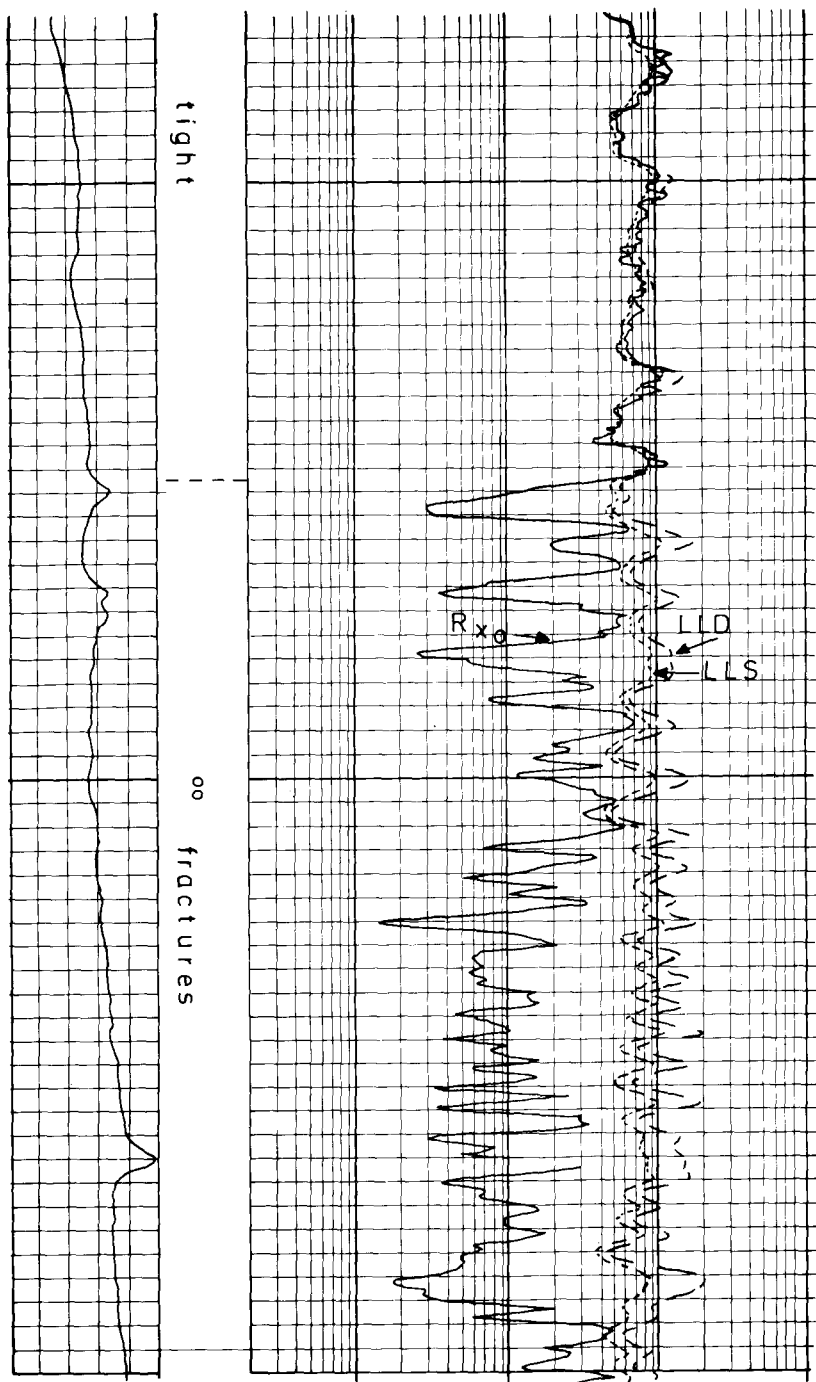
Simultaneously with resistivity, the azimuth measurements are obtained by the azimuth recording of electrode 1. The azimuth of electrodes 2, 3 and 4 will represent the respective east, south and west by adding increments of  $90^\circ$  ( $180^\circ$  and  $270^\circ$ ), as shown in figure 5.9.

### 5.6.1. Idealized cases

Two ideal cases have been examined using the dipmeter for a limestone with a single vertical and horizontal fracture system.

#### 5.6.1.1. Single vertical fractures

In the case of a *single vertical fracture system* (figure 5.10A), due to the rotation of the tool, a time interval between the responses of the four-pad dipmeter is observed,



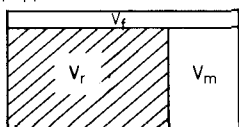
5.7 – Fracture detection in a tight formation through DLL-RXO (Suau<sup>4</sup>, Courtesy SPLWA).

$$V_m + V_f + V_r = V_B = 1$$

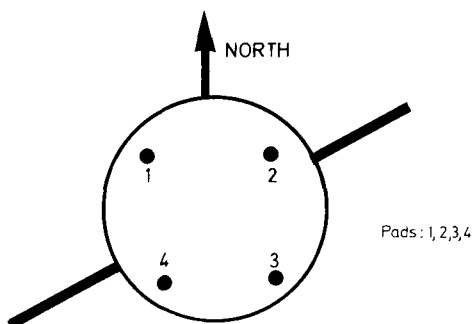
$$\phi_m = \frac{V_m}{V_B} ; \phi_f = \frac{V_f}{V_B}$$

$$V_r = 1 - \phi_m - \phi_f \approx 1 - \phi_m \text{ since } \phi_m \gg \phi_f$$

$$\phi_t = \phi_m + \phi_f$$



5.8 – Schematization of rock volumes

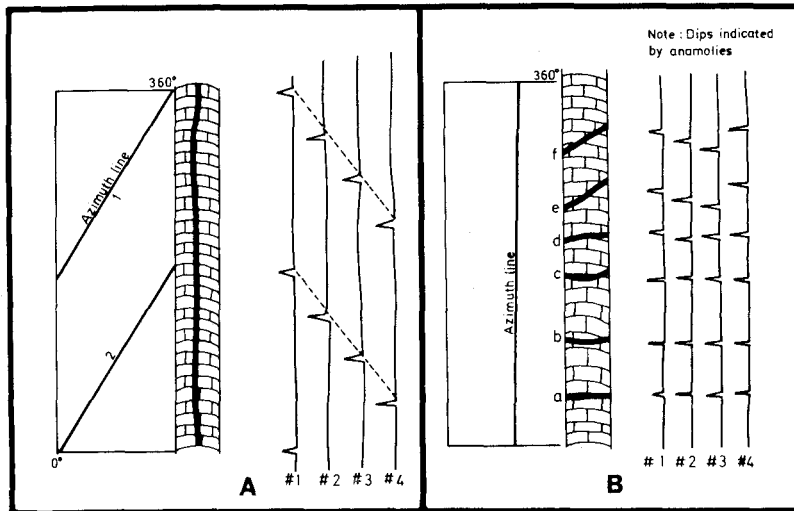


5.9 – Top view: fracture, borehole and dipmeter electrodes.

which depends on the rotation speed. The consecutive signals during each complete rotation form parallel lines, and the equal distances between anomalies confirm the single vertical fracture. The azimuth lines 1 and 2 correspond to a complete rotation ( $360^\circ$ ) of the tool on the azimuth diagram, and therefore, the position of the fracture could be evaluated and its orientation referred to the north direction. The single vertical fracture will show this anomaly on a single curve (1) which jumps to a new curve (2) when the tool rotates (left side of figure 5.10A). If another vertical fracture coexists, another azimuth line parallel to lines 1 and 2 will represent the second fracture.

#### 5.6.1.2. Horizontal fracture system

In the case of a *horizontal fracture system*, such as *a*, *b*, *c* and *d* of figure 5.10B, the four-pad response indicates a short anomaly on all four curves, since the four electrodes simultaneously pass in front of the fractures. A delay is observed in the sub-horizontal (slightly dipping) fractures *e* and *f* (figure 5.10B). When the fractures



5.10 – Dipmeter response for idealized case: A – Single vertical fracture, B – Horizontal fractures (Courtesy<sup>7</sup>, Schlumberger).

are perpendicular to the hole the azimuth line will be a continuous vertical line, since each fracture is recorded as a point. In addition, the fracture plane may appear to have an apparent dip.

#### 5.6.1.3. Dendritic fracture system

In the case of a dendritic fracture system, the azimuth electrode is represented by a continuous line, while the four-pad response varies for each electrode (figure 5.11).

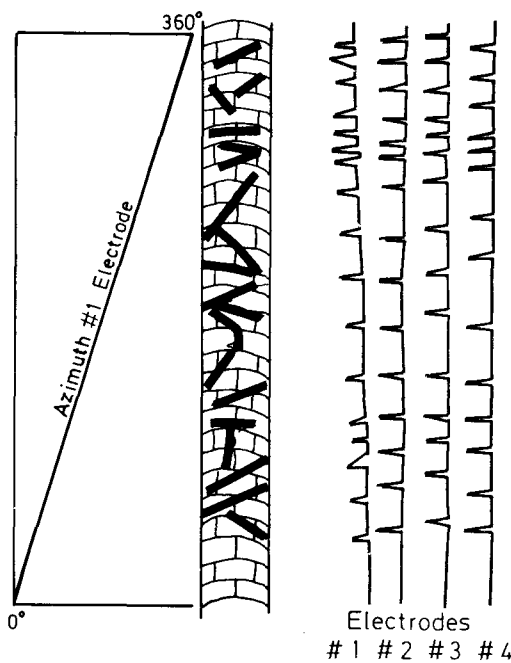
#### 5.6.2. Tools and applications

The FIL log (fracture identification log) is an improved tool which is highly efficient in the detection of fractures. The efficiency of the tool is due to superimposing the response of a *couple of electrodes*.

The most usual couple is formed by two-curve pairs resulting from the superposition of the responses of electrode couple 1 and 2 and couple 3 and 4.

A more complex format is the four-curve pairs display, resulting from the superposition of the responses of electrodes 1 and 2; 3 and 4; 2 and 3; 4 and 1.

To get more information about fractures and their characteristics the following combinations are used: the conventional four path dipmeter curves and two or four-curve pairs display.



5.11 – Idealized dendritic fracture system and its dipmeter response (Ref. 3).

Example: From the FIL log obtained in the Austin chalk (Frio County) shown in figure 5.12, the four-curve and two-curve overlays (stacked) are presented on the same diagram. The advantage of these recordings is that they make it possible to differentiate between the vertical fractures and the bedding planes. As observed in figure 5.12, the permeable bedding planes are very thin and their correlation is excellent over the four pads. The vertical fractures are observed only on one or two pads.

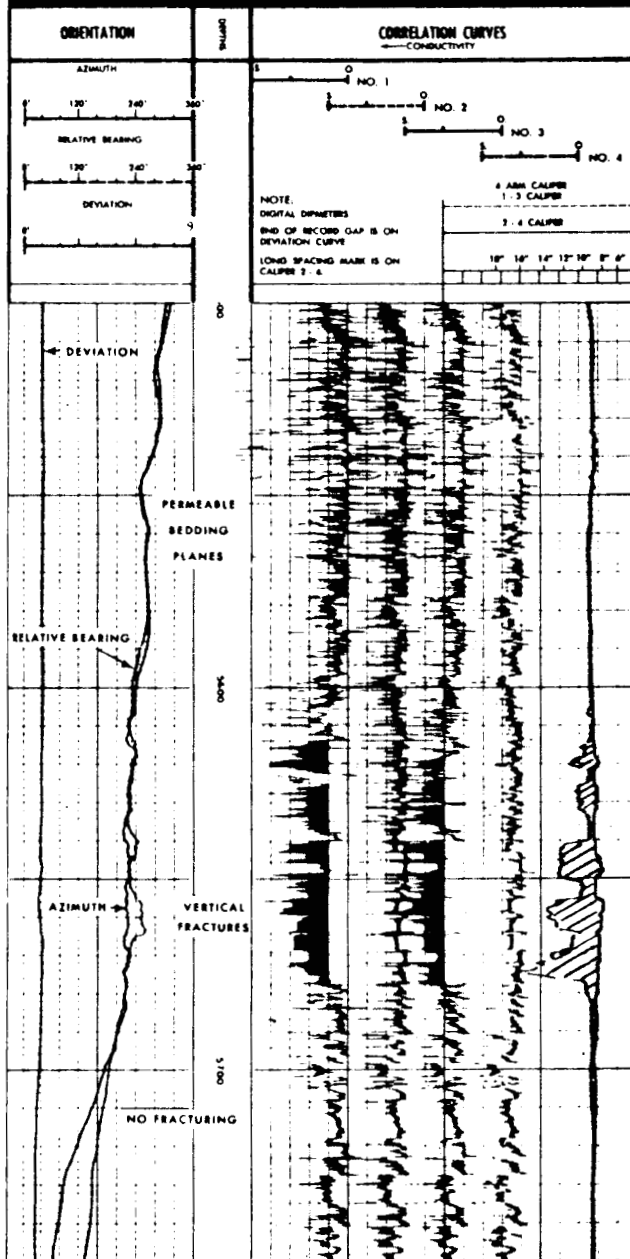
On the same Austin chalk formation in South Texas<sup>3</sup>, vertical fracture detection was evaluated through a dual two-curve overlay (figure 5.13) where the separation inside each couple of curves gives a qualitative evaluation of the fractures.

Since the two-curve overlay is due to separation of the two pads by a 90° angle, the anomaly will result as the difference between the records of the two adjacent pads. A larger variation between two curves corresponds to a larger degree of fracturing.

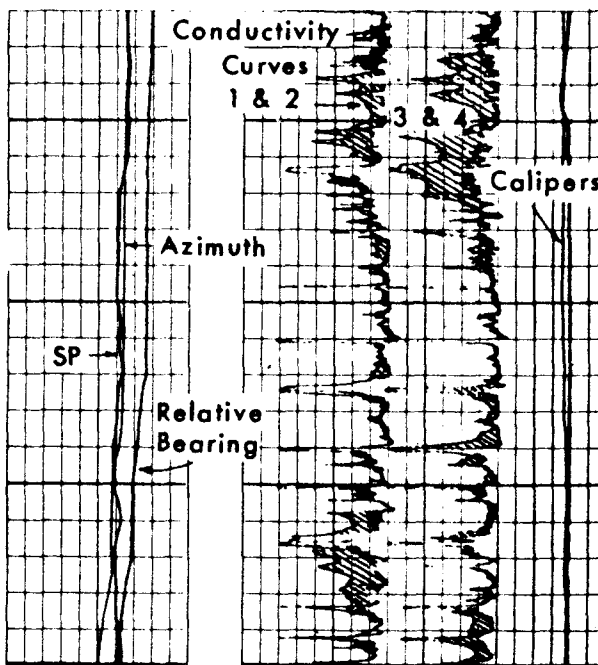
Experience has shown that the logging results satisfactorily match the core results; however, if there are a large number of microfractures present, the matching results are far less satisfactory. Because it is difficult to find similar conditions to those of the Austin chalk (low dip, vertical fractures not cemented, and low deviation), the results are not always as encouraging. If a number of anomalies are caused by well logging runs, a repetition of runs over the fractured zone and on a non-fractured zone is recommended (to be used as a reference).

Schlumberger

# FRACTURE IDENTIFICATION LOG



5.12 – FIL-4-curve presentation in Austin chalk (Beck<sup>2</sup>, Courtesy SPLWA).



5.13 – Vertical fracture identified by two-curve underlay. Curve separation proportional to fracturing magnitude (Beck<sup>2</sup>, Courtesy SPLWA).

If the response obtained by using a different orientation of the tool reveals a repetition of the anomalies, the uncertainties concerning fracture detection are much fewer. In addition, since the electrodes can not detect all fractures from one run, multiple runs with different azimuths will increase the detection of fractures around the wellbore.

It is generally recommended to devote more attention to large anomalies (except if fractures are almost normal to the borehole axis), and to be particularly cautious in interpreting the results if the pad-borehole contact is lost.

### 5.7. POROSITY LOGS

The porosity logging devices – density, neutron and sonic – are considered to be capable tools for the detection of fractures, and also for the evaluation of secondary porosity. In the evaluation of the secondary porosity, the density and neutron logs (which have responses greatly related to the lithological characteristics) may be less efficient than the sonic log.

In any case, the evaluation of secondary porosity must be evaluated as the difference between the total porosity and the matrix porosity which, in principle, can

be measured through logs. Considering a double-porosity model where matrix and fracture are connected in parallel, Aguilera<sup>8</sup> proposes the following equation which controls the relationship between the total porosity and the matrix porosity:

$$\Phi_t^{-m} = 1 / [ \nu \Phi_t + (1 - \nu) / \Phi_b^{-m_b} ] \quad (5.8)$$

The total porosity  $\Phi$  and the matrix porosity  $\Phi_b$  are related through the fracture-matrix system exponent  $m$  and the matrix exponent  $m_b$ , as well as the porosity ratio discussed in equation 5.7.

### 5.7.1. Density log

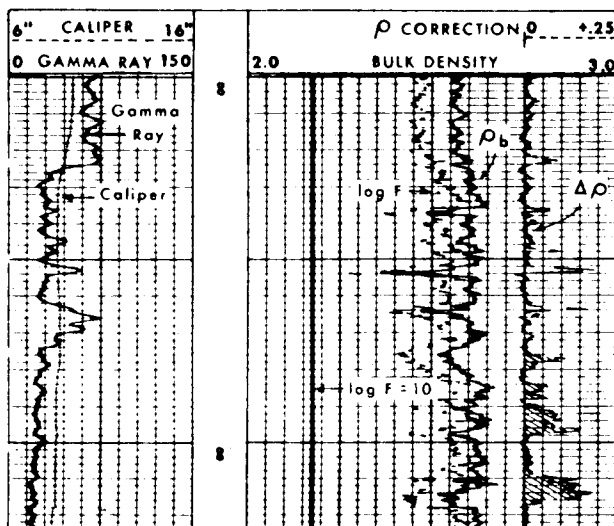
The bulk density of the lithological column through which the well is drilled can be presented as a continuous recording by using a density log tool. A gamma ray beam is transmitted from a source mounted in the tool and a counting system detects any change in the intensity caused by a given rock. The response will depend on changes in the formation bulk density, therefore, a higher density will reveal a lower level of gamma radiation intensity. In other words, since low porosity rocks give low count rates, the fractures may give higher porosity indications for this portion of the borehole which is in front of the detector. In practice, there are a great number of difficulties because the tool is unidirectional and can not rotate, therefore, there is a risk that fractures will only be detected on one side of the borehole.

Beck<sup>2</sup> considers the correction curve  $\Delta\rho$  on the FDC (compensate density) log to be a *quick-look* method. In fact, since the Delta-Rho was designed to compensate the density log for rough holes and mud cake, it can also be used for fracture detection. The Delta-Rho curve will show an anomaly when the tool is moved in front of the fractures (figure 5.14). The main disadvantage of the tool is that some fractures may be missing during fracture detection, but the basic advantage is that porosity is recorded, which may be used for further calculation.

In the example presented in figure 5.14 it is observed that the out-of-roundness of the borehole from the caliper curve may be helpful in the location of fractures.

### 5.7.2. Neutron logs

Basically, for the same observations mentioned above, the neutron log will measure the total porosity. As in the previous case the same difficulties in fracture identification are due to the unidirectional orientation and lack of rotation of the tool. Since the neutron device responds primarily to the amount of hydrogen present in the formation (as a result of energy less occurring when the neutron strikes a nucleus of hydrogen), in the presence of an open fracture, an anomaly indi-



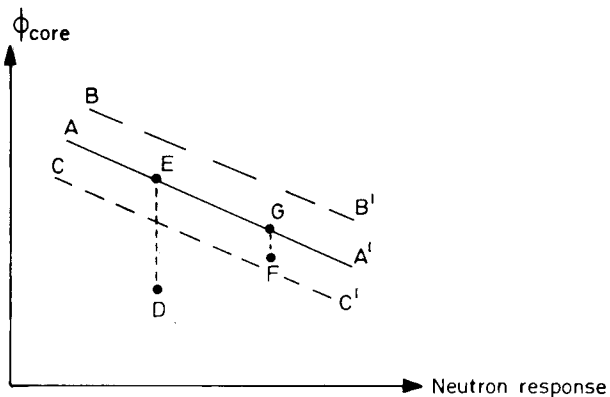
5.14 – Compensated formation density log. Fracture indicated through  $\rho_b$  (Beck<sup>2</sup>, Courtesy SPLWA).

cating higher porosity can be expected. The neutron log can be a useful tool for locating dense carbonates, since carbonates give a high count rate.

In his discussion on porosity evaluation, Prickett<sup>9</sup> gives the relationship between the total porosity obtained from cores and the neutron response. If the segment AA' represents this relationship (figure 5.15), the points D and F may be the response of the fractured zones, and thus, DE and FG would be the measurements to be used for fracture porosity. Actually, two additional straight lines will limit the scatter resulting from the uncertainty in the measurements (figure 5.15) and, therefore, only segment ED will be used for the evaluation of fracture porosity<sup>9</sup> while the results EF will be included in the matrix zone. This procedure, if used for field data, provides a discriminating criterion by elaborating the limit curves BB' and CC' as a function of standard deviation. A test was carried out on a Mississippi formation which showed<sup>9</sup> that the distance between AA' and respective BB' and CC' was equivalent to  $1.5\sigma$  ( $\sigma$  is standard deviation)<sup>9</sup>.

### 5.7.3. Sonic log

The sonic log is one of the more suitable measurements to be used for fracture detection. Even though the research efforts in this field were considerable, the results obtained have been less successful than expected; but in the opinion of logging specialists, the conviction persists that a better use of acoustic wave propagation vs. fractures remains the base of fracture detection.

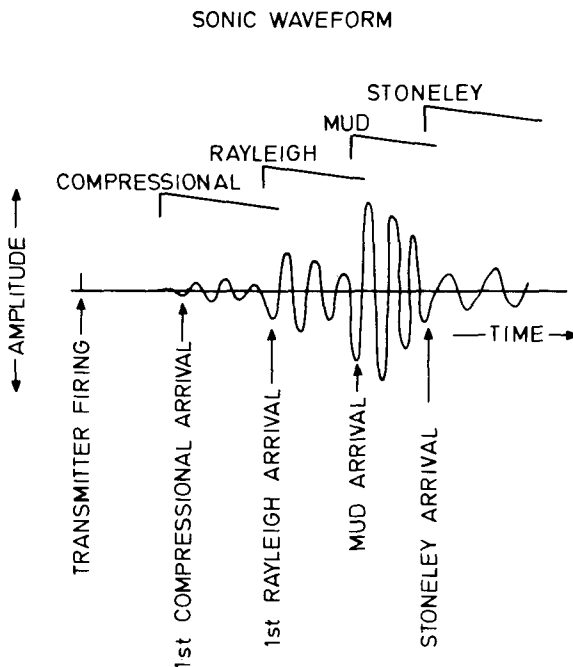


5.15 – Core porosity vs. neutron response (idealized case, Ref. 9).

The main advantages of the sonic log are: 1) the tool based on mechanical properties is less sensitive to the anomalies of the borehole than other tools, and 2) it gives an exceptionally correct response in dense rock.

Before the discussion of the interpretation of sonic logging, the sonic wave amplitude vs. time (resulting from the operation of a single transmitter) is shown in an idealized picture in figure 5.16. In order of arrival there are four types of waves: compressional, shear , mud and Stoneley<sup>10</sup>. The characteristics of these waves are related to wave travel velocity between the transmitter and the formation along the borewall and back to the receiver. The velocities for each type of wave are shown below.

Type of Wave	TRAVEL VELOCITY		
	Transmitter-formation	Along borewall	Back to receiver
1. Compressional wave (P wave)	Pressure wave	Compressional wave	Pressure wave
2. Shear (Rayleigh) wave (S wave)	Pressure wave	Shear wave	Pressure wave
3. Mud wave (M wave)	Compressional wave velocity		
4. Stoneley wave (low velocity wave)	Smaller than compressional wave velocity		



5.16 – Schematization of sonic waves.

#### 5.7.3.1. Fracture identification by sonic wave

##### a. Ideal case (horizontal fractures)

In the case of horizontal fractures normal to a vertical well, and the sonic tool with transmitter (T) and receiver (R) below and above the fractures, the various waves will behave differently<sup>10</sup> in front of the fractures (figure 5.17).

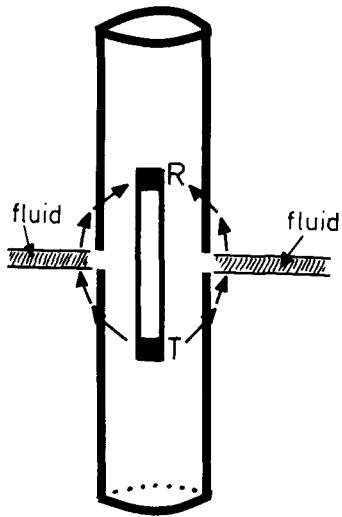
The compressional wave passing through solid/fluid interfaces will be reflected at the interfaces, reducing its amplitude.

If the shear wave falls upon the fracture, a complete absence of the transmitted amplitude may be expected.

##### b. Real case (dipping fractures)

In the case of dipping fractures there are two different approaches, the theoretical and experimental approaches.

In the theoretical approach the compressional and shear waves will be influenced by the fracture dip, therefore, the transmission loss under certain conditions may become very significant. In the theoretical calculation an infinitely thin lubricated fracture in an infinite medium was chosen, and the reduction in transmission was examined. The transmission was expressed as a coefficient with reference to plane compressional and plane shear waves. The results are shown in the diagram in figure 5.18 have been presented in table 5.1 below.



5.17 – Idealized horizontal fractures when sonic log is used.

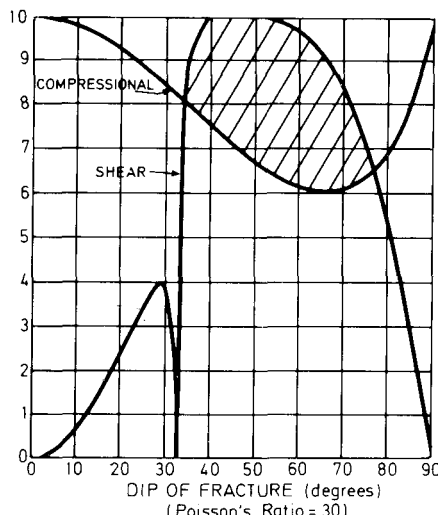
Table 5.1

Type of wave	Dip angle	0 – 33°	33° – 78°	78° – 90°
Shear wave	$0 \rightarrow 0.4$	$\approx 1$	$1 \rightarrow 0$	
Compressional wave	$1 \rightarrow 0.8$	$\approx 0.6$	$0.6 \rightarrow 1$	

The attenuation is expressed as a fraction which sometimes shows the attenuation in the intermediate zone of the compressional wave, or the attenuation of the shear wave at the extremes. This may help in recognizing the types of fractures: vertical, horizontal and intermediate.

In the experimental approach the attenuation of the compressional and shear-velocity arrival has been examined in the laboratory, and the results obtained reconfirmed the trend obtained in figure 5.18. The results (table 5.2) indicate the following<sup>10</sup>:

1. since the dip angle is not clear, all fractures over 60° are considered to correspond in practice to *vertical* fractures, and all from 0 – 30° are considered to correspond to horizontal and sub-vertical fractures;
2. if the compressional amplitude vs. shear-velocity amplitude is examined, the



TRANSMISSION THROUGH AN INCLINED THIN FRACTURE

5.18 – Calculated relationship of transmission coefficient vs. fracture dip for compressional and shear waves (Morris<sup>10</sup>, Courtesy JPT).

Hypothesis: infinite lubricated fracture in an infinite medium.

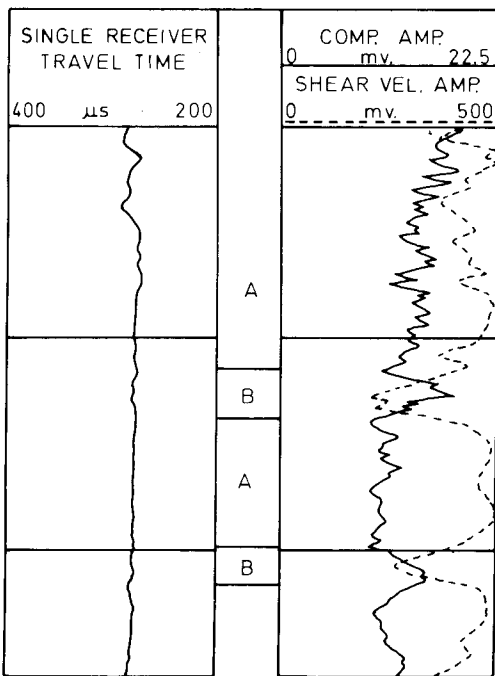
result is: increasing compression and reducing shear indicates horizontal fractures, increasing shear and reducing compressional indicates vertical fractures.

With this approach the two different types of fractures can be identified.

Table 5.2.  
Attenuation by fracture in models (Morris<sup>9</sup>)

Fracture dip	0°	45°	60°	90°
Compressional Arrival Attenuation (db)	0	4.5	8	0
Shear-Velocity Arrival Attenuation (db)	> 12	8	2	–
Fracture type	Horiz.		Vertical	

Field examples. Morris<sup>9</sup> presented an interesting example of the interpretation of signal arrival vs. fracture orientation in two simplified field cases:



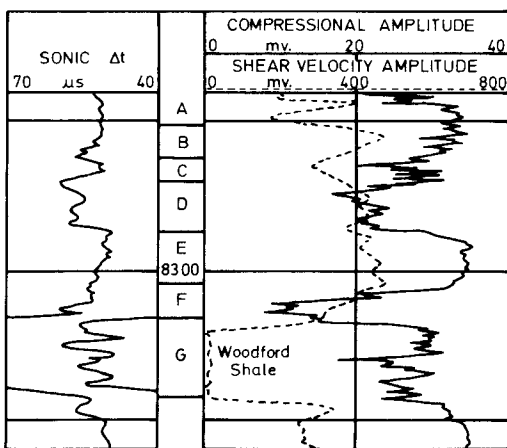
5.19 – Interpretation of compressional and shear-velocity amplitude records in a Mississippi limestone.  
Zone A: Predominant vertical fractures; Zone B: Predominant horizontal fractures (Morris<sup>10</sup>,  
Courtesy JPT).

1. Case 1; in a Mississippi limestone the shear and compressional velocity amplitude have been recorded as in figure 5.19. The single receiver travel time curve is uniform, therefore, the variation of the two amplitude curves is due to the type of fracture. Zone A, where shear velocity remains unchanged and compressional is attenuated, corresponds to vertical fractures. Zone B, on the contrary, corresponds to the high compressional amplitude and reduction in shear velocity as an effect of horizontal fractures. Laboratory results obtained from core testing supported this interpretation.
2. Case 2; in the same Mississippi limestone it can be observed from the logging shown in figure 5.20 (left track) from the sonic transit time of the compressional arrival, that there are thick beds with little velocity contrast in each bed. The changes in amplitude of compressional arrival and shear velocity indicate the type of fracture in the interval. (table 5.2) The interval G (indicated as Woodward shale) clearly indicates the transit time as a change in lithology T.

Table 5.3

Discussion of figure 5.20 results (Morris<sup>9</sup>).

Interval	Fracture Orientation	Amplitudes	
		Shear	Compressional
A	horizontal (H)	low	high
B	few scattered H and V	high	high
C	H and V	low	low
D	vertical (V)	high	low
E	none	high	high
F	many vertical	low	very low



5.20 – Interpretation of compressional and shear-velocity amplitude records in a formation with large variations in fracture orientation (Morris<sup>10</sup>, Courtesy JPT).

### c. Sonic amplitude influenced by other factors.

Other factors which may influence the compressional and shear-velocity amplitude are tool centralizing in the borehole, hole size, mud properties, borehole rugosity, bed boundaries, velocity range, etc. The attenuation or any modification of the amplitude may influence the interpretation of the response and, therefore, fracture detection.

The tool eccentricity as well as hole ellipticity will substantially reduce the amplitude of the compressional-arrival. It was observed that a 50% reduction in amplitude may cause an eccentricity of 1/4 inch.

The mud effect becomes significant especially when the gas is present as bubbles, then the attenuation of the signal also becomes significant.

The change in lithology affects both compressional and shear-velocity arrivals across the mud formation interface. Transmission across a thin bed, such as a shale stringer, will influence the amplitude as a result of the interference of the reflection of two interfaces; this will, therefore, depend on the thickness of the bed.

The conclusion is that amplitude logs are valuable tools for fractured zones. But if these logs are used alone, fracture detection remains uncertain. A more recent procedure is to present the acoustic wave data as a variable density or a variable intensity display.

#### d. Variable intensity log

This log procedure offers a panoramic view of the sonic waveform, which can give a better identification of the fractured zone.

Basically the formation response is presented as a continuous recording of time interval  $\Delta t$  vs. depth (where  $\Delta t$  represents the time after the initiation of the acoustic pulse). The aspect of a recording is similar to that shown in figure 5.21, where the waves and the first arrival of various wave categories, such as compression, Rayleigh and mud waves are clearly marked.

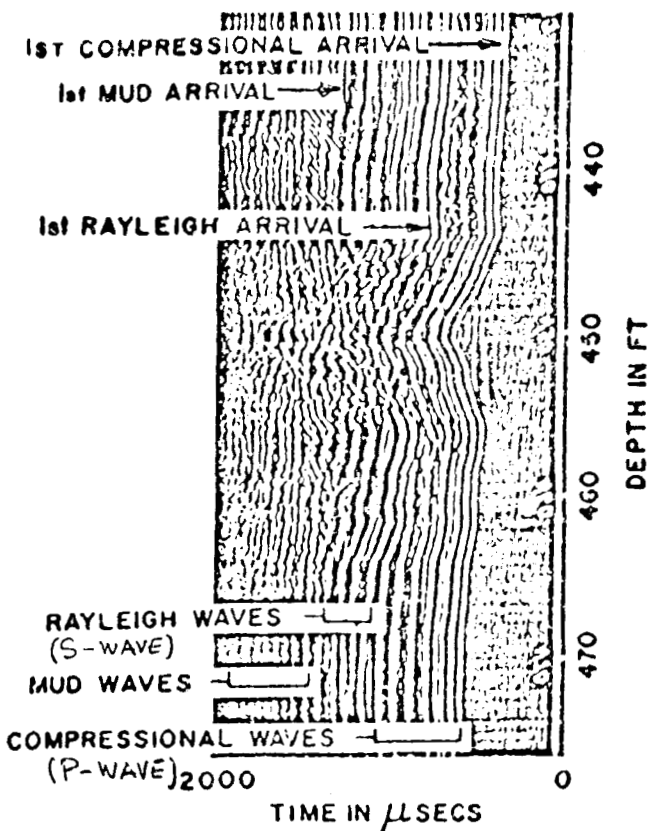
The log is influenced by various conditions of the formation which express different amplitudes through shadowing variations. The changes in a positive amplitude correspond to darker areas, whereas, changes in a negative amplitude correspond to lighter areas. Through these shadow variations, amplitude changes of wave trains will indicate the qualitative changes in the formation characteristics. Zero amplitude will be recorded as halfway between black and white. In the case of a zone of constant porosity, which is unfractured and lithologically uniform, the display gives the impression of banding. On the contrary, if the fracture intervals are met by the tool, impressive breaks occur and diagonal patterns criss-cross the display. The diagonal patterns are called *chevron-patterns*. They are the result of the reflection of a large proportion of the wave energy which, travelling back to the receiver, is superimposed on the normal pattern. When the logging tool approaches the fracture, the reflected compressional energy creates a diagonal disturbance of slope  $2/V_c$  across the normal pattern ( $V_c$  being the compressional velocity in the formation).

#### e. Fracture examination

Since fractures are very thin the transit time is independent of their presence and, therefore, the first step is the examination of chevron patterns independent of transit time. The patterns which show changes in lithology or influence of hole non-uniformity can be eliminated.

The second step is to examine the pattern of a fracture interval. Based on figure 5.18, types of fractures could be examined through the results obtained from the

## VARIABLE DENSITY DISPLAY



5.21 – Sonic waves and 1st arrival wave in variable density display.

P-curve (compressional) and S-curve (shear-velocity), as shown in figure 5.22 and discussed in table 5.4. The fractures could be divided into two categories, sub-horizontal (including the dip angle of fractures from  $0 - 35^\circ$ ) and sub-vertical (including all fractures from  $35^\circ - 80^\circ$ ).

The example given in figure 5.22 shows the presence of a fracture (at approximately 85 feet) which has an image reflected at 91,5 feet.

Table 5.4

TYPE OF FRACTURE		Sub-horizontal	Sub-vertical
DIP ANGLE		$0^\circ - 35^\circ$	$35^\circ - 80^\circ$
energy transmitted across the fracture	compression	integral	weak
	shear	weak	integral
Reflected pattern	compression	no	totally
	shear	totally	no
Arrival of the Variable Density display	compression	not reduced	reduced
	shear	reduced	not reduced
TYPE of CURVE	P-curve	weak	strong
	S-curve	strong	weak

#### 5.7.4. Secondary porosity

If the sonic log is combined with the density or neutron log the responses obtained may improve the evaluation of the secondary porosity in certain cases. In this method it is assumed that the sonic log result is independent of fractures and vugs, being a function only of the matrix porosity and giving an undisturbed  $\Delta t$ . On the other hand, the density or neutron log gives the total porosity and, therefore, the secondary porosity can result as the difference,

$$\Phi_f = \Phi_{ND} - \Phi_{\Delta t}$$

The problem is the same as discussed previously; the secondary porosity is so small compared with  $\Phi_{ND}$  and  $\Phi_{\Delta t}$ , that  $\Phi_f$  values may be of the same order of magnitude as the errors of  $\Phi_{ND}$  and  $\Phi_{\Delta t}$ . In addition successful evaluation will always depend on variations in shaliness, lithology and irregularity of hole roundness.

#### 5.7.5. Role of lithoporosity cross plot

For complex lithologies the lithoporosity cross plot technique was introduced, which makes it possible to simultaneously handle neutron, density and sonic data. The M and N parameters are obtained from these logs as porosity-independent values,

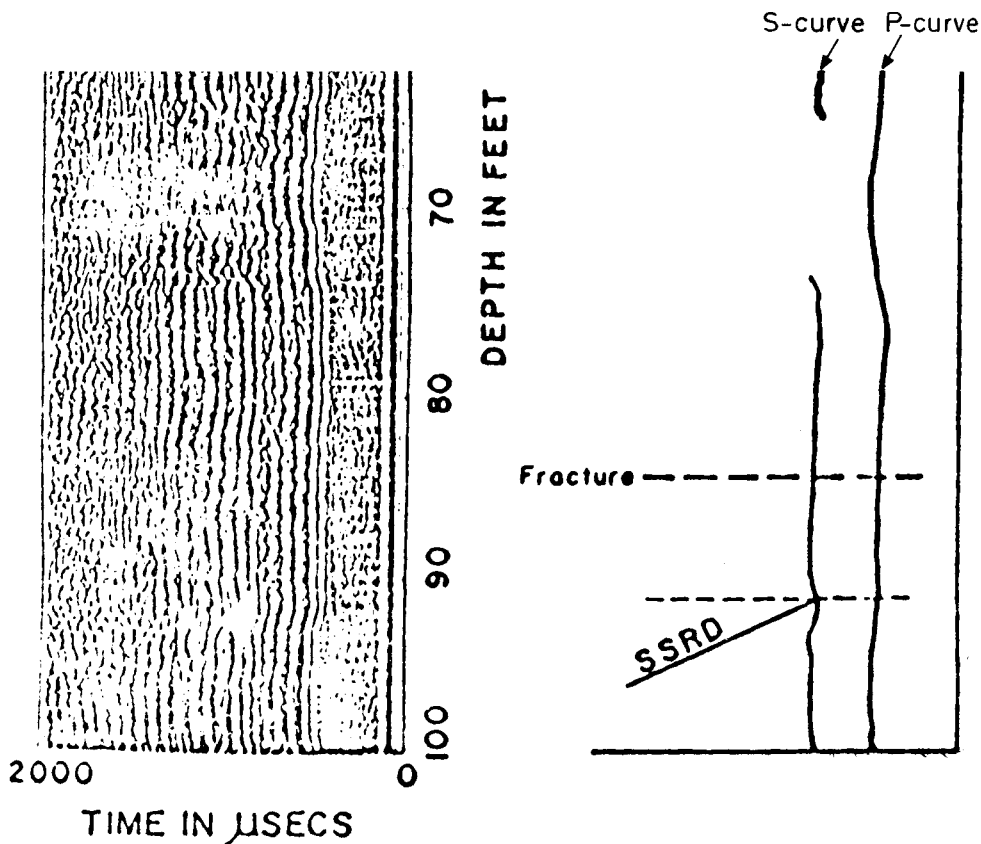
$$M = \frac{\Delta t_f - \Delta t}{\varrho_b - \varrho_f} \quad (5.9)$$

$$N = \frac{(\Phi_n)_f - \Phi_n}{\varrho_b - \varrho_f} \quad (5.10)$$

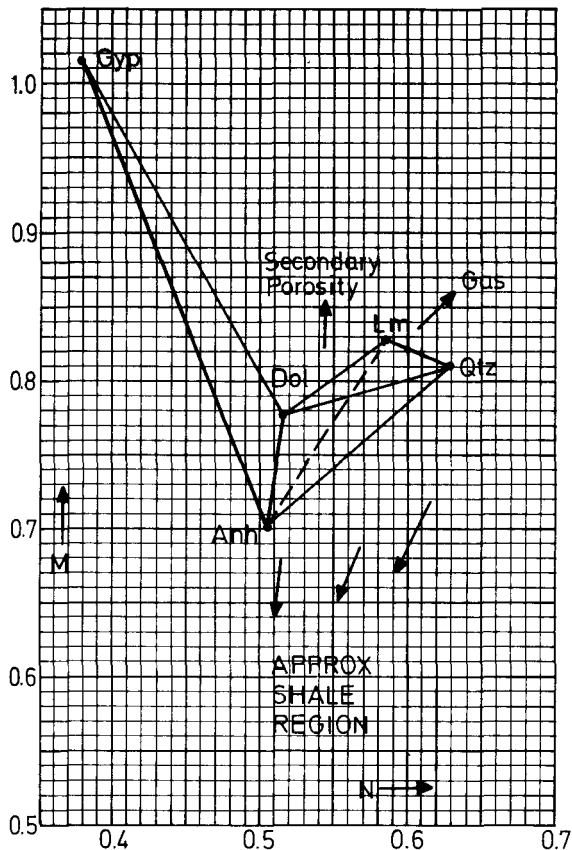
In the cross plot M vs. N (figure 5.23) each pure mineral inside the diagram is represented independently of porosity. For a more complex lithology, the percentages of the various minerals existing in the formation give the values M and N (figure 5.23):

If it is assumed that the sonic log is only associated with the matrix porosity, it is logical to assume that the value N will not be influenced by the secondary porosity.

On the contrary, the value M is dependent of the secondary porosity, increasing when the secondary porosity increases. Therefore, the litho-porosity diagram may be a tool for finding the secondary porosity which, on the M-N diagram, is located above the dolomite-limestone line.



5.22 – Example of fracture identification through variable density display.



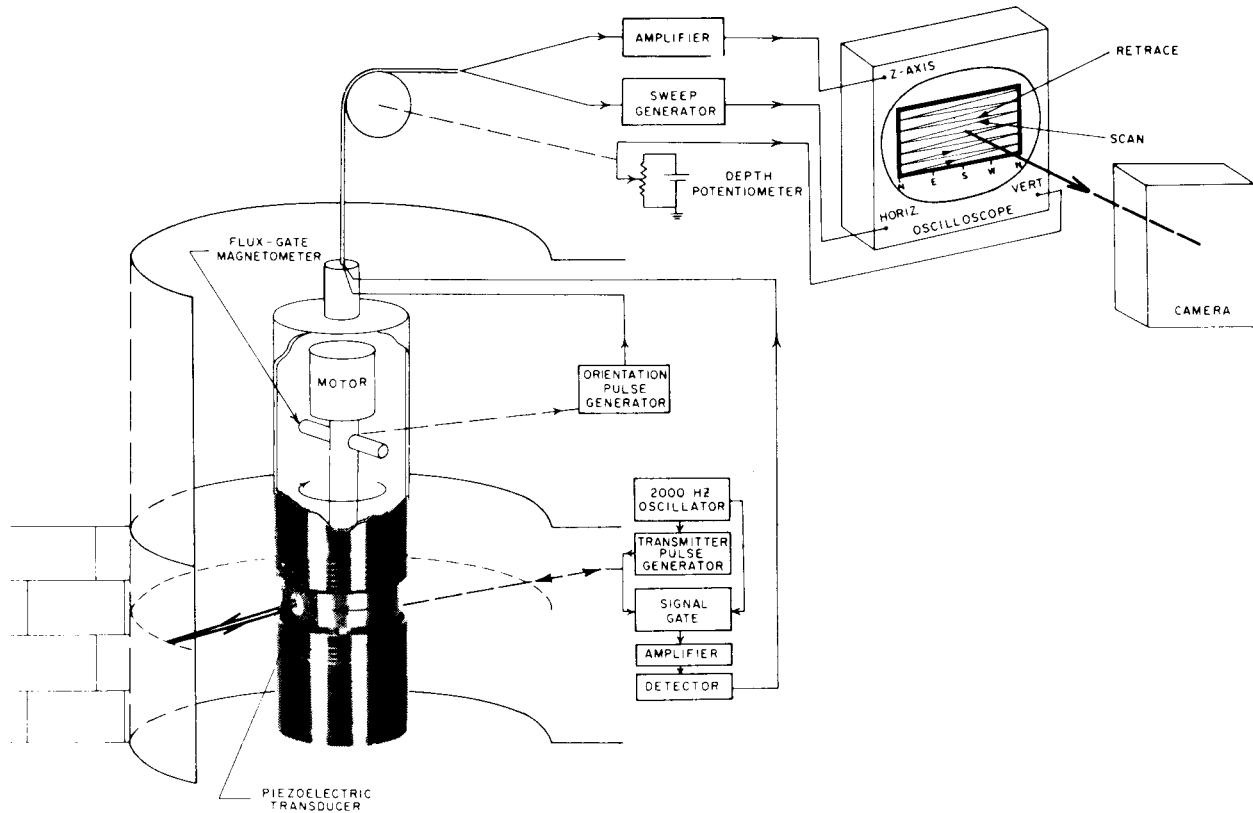
5.23 – Lithoporosity cross plot.

### 5.8. BOREHOLE TELEVIEWER

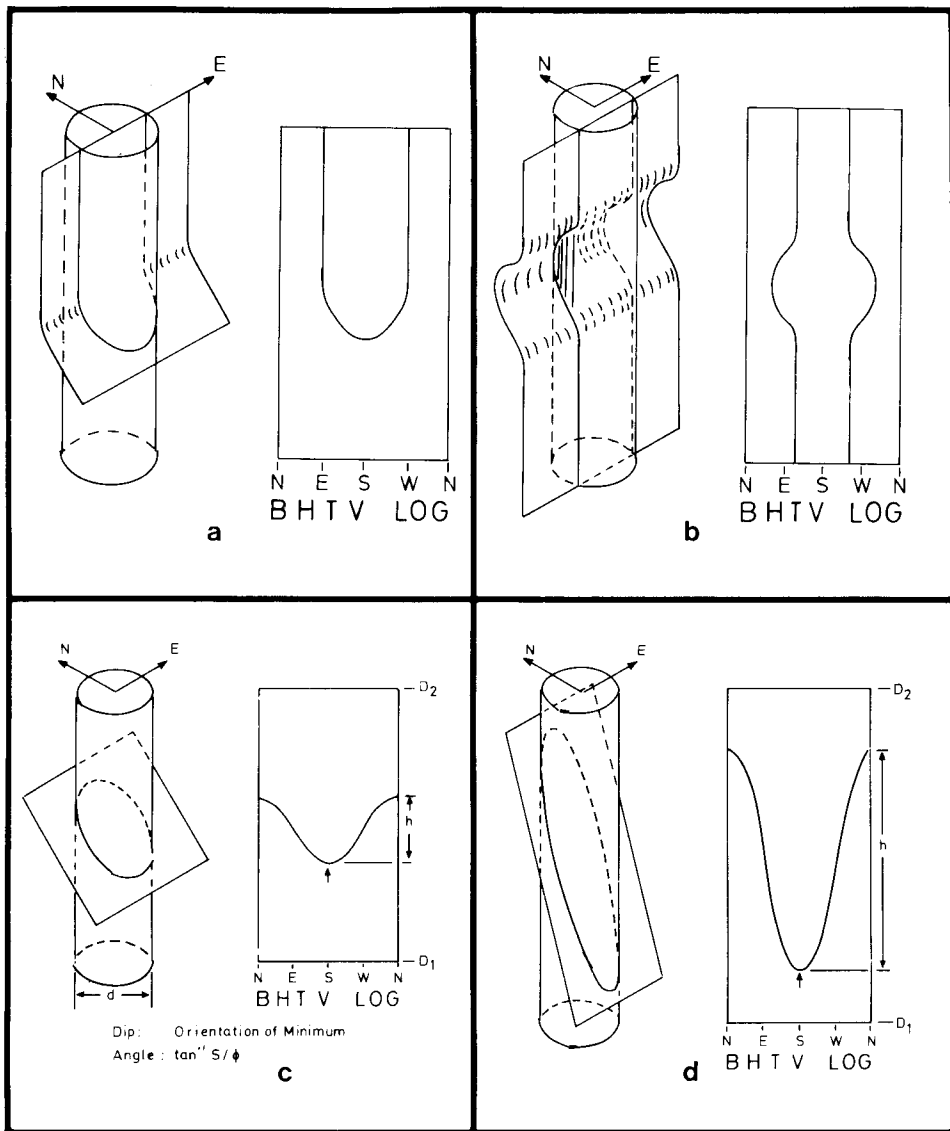
The borehole televiewer (BHTV) is the first and only tool which detects and evaluates fractures by direct measurement.<sup>12</sup> Although this breakthrough in technology has its limitations, it still remains as a very valuable tool if combined with core data, and even if it is a partial substitute for continuous well coring. Logging, however, requires that the borehole is filled with a homogeneous gas-free liquid, such as fresh water, salted brine, crude oil or drilling mud.

The fundamental parts of the tool (figure 5.24) are:

- a source of acoustic energy and a flux-gate magnetometer which are mounted in the tool;
- a motor which rotates the transducer and magnetometer at three revolutions per second, with the possibility of transmitting signals to the surface.



5.24 – Borehole televiewer, logging unit



5.25 – Isometric representation: fracture intersecting borehole and BHTV log. A – vertical fracture, B – mirror behaviour, C – borehole moderate dip angle, D – borehole at steep dip angle (Zemanek<sup>11</sup>, Courtesy JPT).

The tool is moved vertically and rotates during logging, assuring that the sonic log responds simultaneously with reference to the north pulse at any instant.

The changes in the uniformity of the borehole walls, such as fracture vugs, pits, etc., are reflected as changes in picture intensity. The results obtained from logging

are presented in a plane as a flat image, where the vertical scale corresponds to the well depth and the horizontal scale corresponds to the azimuth of the borehole wall.

The intersection of a fracture with the borehole and the resulting BHTV logging due to the intersection is illustrated in figure 5.25a. As observed on the right side of all examples of figure 5.25, the vertical depth scale is associated with the azimuth of the borehole. The vertical fracture in the upper part is presented as two lines oriented in east (E) and west (W) directions. The lower part of the diagram shows the zone where fractures disappear.

In another case the vertical fracture presents a series of irregularities (figure 5.25b). The advantage of the mirror image is that it allows the differentiation between effective fractures and artificial scratches. In the case of intersection with a moderate dip and steep dip angle bedding, the BHTV log is presented as in Figures 5.25c and d.

Figure 5.26 illustrates a log made in an artificially fractured West Texas Spraberry well, filled with crude oil. The large dark spots are probably hole enlargements caused by chipping or sloughing of the formation. The continuous dark line, which becomes apparent at approximately 7,045 feet and disappears into the hole enlargement at 7,072 feet, is interpreted as a stimulated natural fracture or an induced fracture that intersects the wellbore over this interval. The fracture cuts the hole approximately in an east-west direction. The gross behaviour of the fracture pattern around a south orientation line, as well as the slight irregularities on each side of the fracture at 7,062 feet, are examples of the *mirror effect*.

Changes in lithology and porosity may be obtained as changes in BHTV log intensity occur. The vertical resolution being very small, thin beds and changes in lithology are observed in a very clear way. In figure 5.27 an interbedded limestone is shown where the BHTV records are combined with the acoustic travel time, caliper and gamma ray logs. The contrasting of light and dark shows the variations between limestone and shale.

## 5.9. DISCUSSION

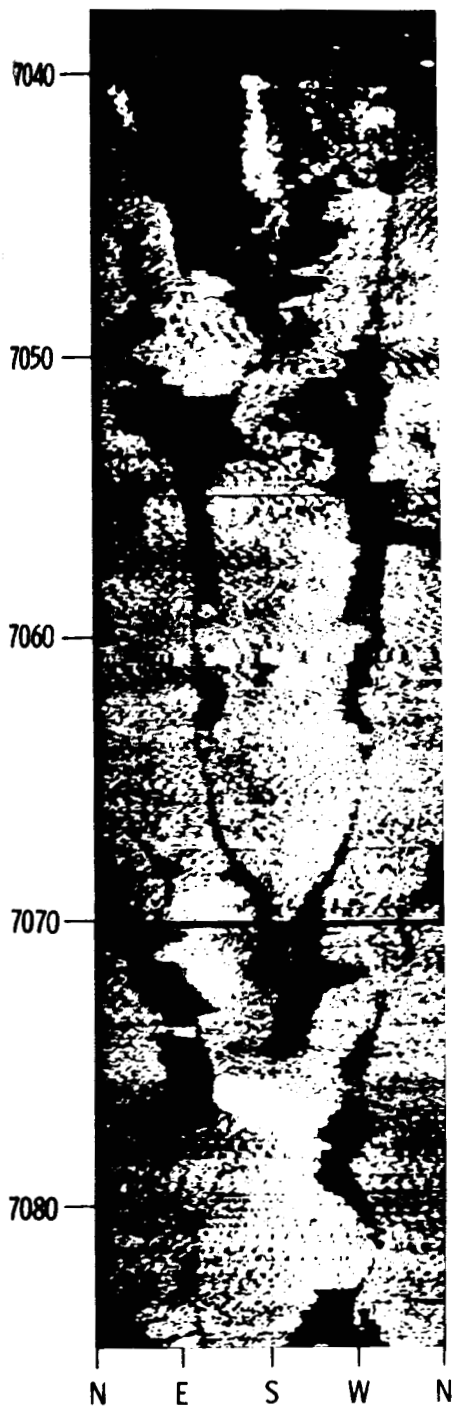
### 5.9.1. Logging programs

Any fracture detection project requires a number of logs and specific combinations of logs and priorities.

In a fractured zone the first logging must be the temperature log. This priority of the temperature log is valid in the case of intermediate logging, also in hole reconditioning during logging, and even in the case of a specific series of logs. The temperature log will be able to obtain (in front of the fractures) the  $\Delta T$  cycle skipping, which may be used as a first indication.

From various log responses (in front of the fractures), such as:

- a. large  $\Delta q \sim$  secondary porosity



5.26 – BHTV log of induced fracture in Spraberry formation of West Texas (Zemenek<sup>11</sup>, Courtesy JPT).

- b. neutron porosity increase ~ change in  $F - \Phi$  relationship
- c. low readings on Rxo tools ~ FIL departure
- d. caliper change ~ VDL chevron patterns
- e. substantial differences between laterolog-induction log ~ low HDT readings, the following program of logs (excluding the temperature log, which is first) will result:
  - a. DLL-Rxo-CAL
  - b. FDC/CNL/GR/CAL
  - c. BHC/GR/CAL
  - d. BHC/VDL/CAL
  - e. long spacing sonic/VDL, 10' spacing
  - f. HDT
  - g. FIL
  - h. and a second and final temperature log.

#### *5.9.2. Logging results vs. other information*

The logging procedure for the detection or evaluation of fractures is compared with the results obtained through other techniques.

##### **5.9.2.1. Core porosity vs. log porosity**

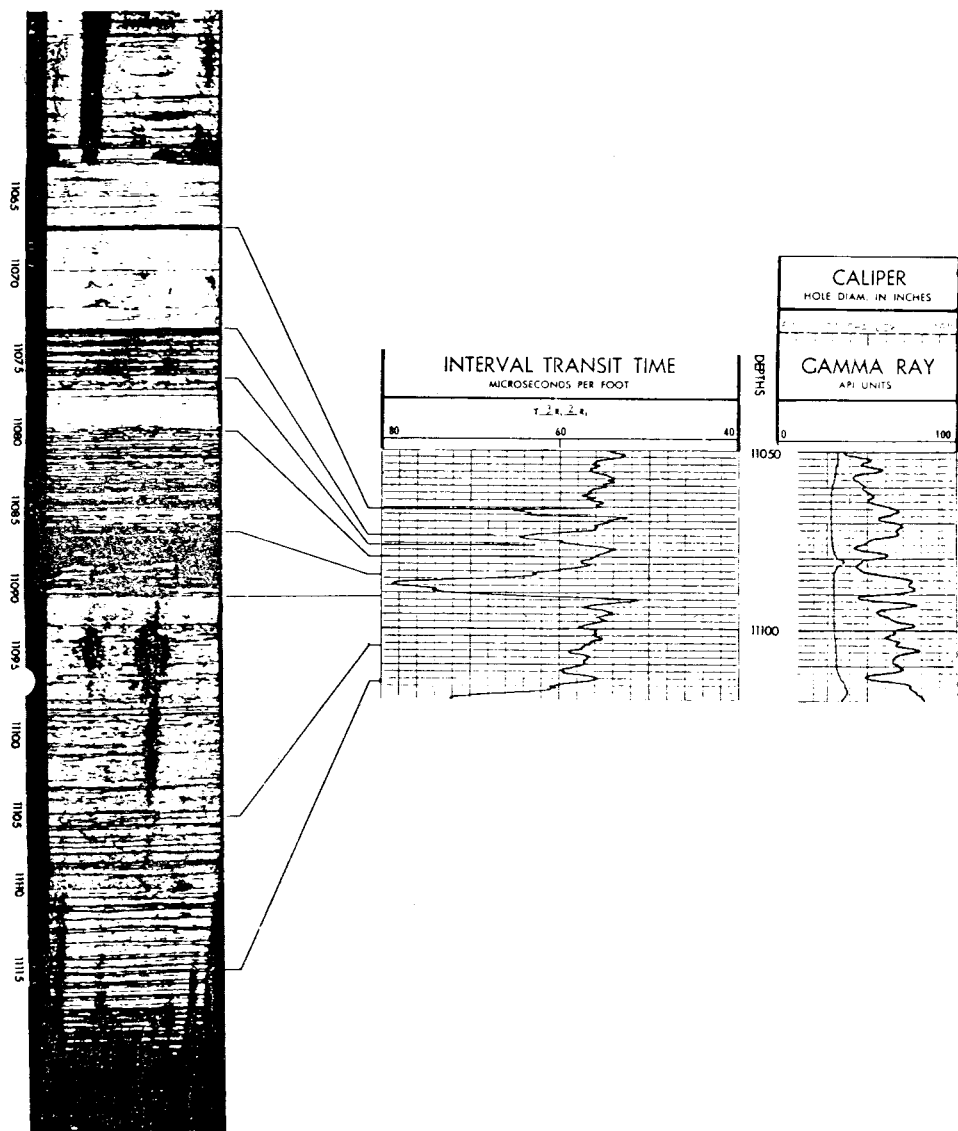
The neutron log response together with core results permits the elaboration of a calibration relationship which is extremely helpful in the evaluation of fractured reservoir zones.

##### **5.9.2.2. Impression packer**

A direct method of borehole inspection involves the use of inflatable formation packers equipped with semi-curved rubber. The packers are inflated opposite the interval of interest and the rubber conforms to the surface of the borehole. The packers remain in place for approximately twelve hours. After deflation of the packers the rubber retains the shape of the borehole. This technique could provide various information concerning density of fractures, apparent fracture dip, number of fracture sets, and the relative orientation of fracture sets.

##### **5.9.2.3. Formation testing**

From pressure draw-down, build-up and interference testing, the fractured formation can be described and the results may be compared with the logging information. This is discussed in detail in chapter 7.



5.27 – BHTV log correlated with other log for lithology evaluation.

#### 5.9.2.4. Flowmeter

A continuous flow profile vs. depth provides the most accurate confirmation of fracture location. The continuous flowmeter, which is a centralized spinner-type velocimeter, can be used for such a survey. It is most effective in single-phase flow conditions in wells with high production rates and/or small diameter casings.

## 5.10. QUANTITATIVE INTERPRETATION

### 5.10.1. Interpretation approach

After the identification of the fractured zones by use of the various logging tools the last objective is the quantitative evaluation of the logs. Such an analysis seems to be a complex one. It may be simplified by considering the rocks to be composed of two separate units, the matrix with intergranular porosity, and the fracture network. The intergranular porosity is assumed to be constant over any given zone; hence, the variations in the total porosity are attributed to changes in the volumes represented by the fracture system.

To determine the amount of water saturation in the fracture system it is necessary to know the total water saturation, the water saturation of the intergranular porosity, and the fraction of the total pore volume represented by each. A method proposed by Hilchie<sup>13</sup> for determining the water cut produced from multiple porosity reservoirs, is one of the most practical. The following is the proposed relationship:

$$S_{wt} = vS_{wg} + (1 - v)S_{wb}$$

$S_{wt}$  — the total water saturation calculated by a modified Archie equation, assuming it applies to heterogeneous reservoirs.

$$S_{wt} = \left( \frac{F_t R_w}{R_A} \right)^{1/n}$$
$$v = \frac{\Phi_T - \Phi}{\Phi}$$

$$S_{wb} = \left( \frac{F_b R_w}{R_{Ab}} \right)^{1/n}$$

Fluid flow in multiple porosity formations is assumed to be primarily through the fracture network and, thus, the relative permeability of the rock to the fluids is directly proportional to the fluid saturation in the fracture network.

The interpretation approach can be summarized as follows:

#### a. Determination of $R_w$

Water resistivity is determined by the usual quantitative methods employing the SP and is verified by formation water analysis when available.

#### b. Determination of porosity

Total porosity is obtained in the zone being interpreted. The acoustic, density, and neutron devices or combinations of these tools are the more reliable ones. The matrix porosity is obtained in a zone of reduced porosity and high resistivity.

### c. Resistivity determination

The resistivities measured in multiple porosity formations are usually high valued (greater than  $200 \Omega m$ ) and change rapidly from section to section of the formation. The laterolog or equivalent is the desirable tool to use because of its ability to measure resistivities accurately over a wide zone and with a minimum of effects from bed thickness.

The true resistivity must be obtained in the zone of interest. The matrix resistivity is assumed to be the highest resistivity in the immediate zone of interest or below, if there is any evidence of a change in fluid saturation condition in the formation. If no reasonable matrix resistivity is available, a good estimation in high resistivity zones (based on experience) is 1–5 times  $R_t$ , and in low resistivity zones is 10–100 times  $R_t$ .

#### 5.10.2. Applications

In the Canadian Big Lake well (D-2 NISKO) the interval examined was 4,420 – 4,450 feet (figure 5.28).

Reservoir conditions:  $T_f = 114^\circ F$ ;  $R_m$  at  $T_f = 1.13$ ;  $R_{mf} = 0.95$ ;  $\Phi_{mc} = 1.7$

$R_w$  evaluation:  $SSP = -76mV$ ;  $R_{mf}/R_{we} = 84$ ;  $R_{we} = 0.0113$ ;  $R_w = 0.03$ ; water analysis  $R_w = 0.048 \text{ ohm} \times \text{meters}$ .

$\Phi_t$  evaluation: cores,  $\Phi_t = 5.15\%$ ; neutron,  $\Phi_t = 5.85\%$ ; short normal,  $\Phi_t = 5.85\%$  value used,  $\Phi_t \approx 5\%$ .

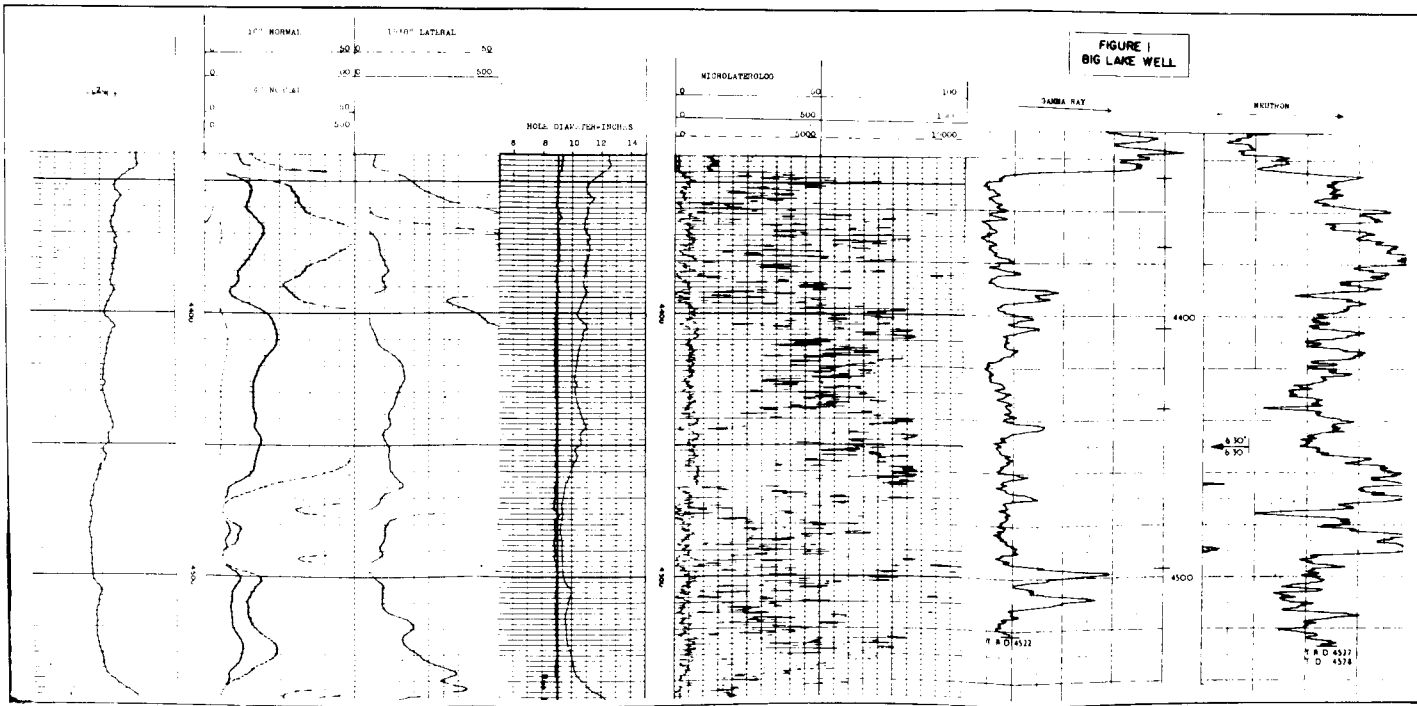
$\Phi_b$  evaluation: neutron,  $\Phi_b = 2\%$ ; microlaterolog,  $\Phi_b = 2\%$ ; value used,  $\Phi_b = 2\%$ .

the result is,

$$v = 0.6$$

#### General Conclusions:

1. The logging interpretation may help in identification of the fracture, and in a qualitative evaluation rather than a quantitative evaluation.
2. The double porosity system can be evaluated in low porosity rocks ( $\Phi_t < 10\%$ ) rather than in high porosity zones.
3. In very low porosity zones ( $\Phi_t < 6\%$ ) there are many chances to evaluate the correct fracture porosity .
4. Since in large porosity formations the fracture porosity is negligible as storage



5.28 – Big Lake Well.

capacity, but is important in low porosity zones, the fact that quantitative evaluation is possible only in tight formations, justifies the logging operations.

5. In large porosity formations only the identification of fractures without their evaluation is really important. Therefore no further development of the logging tool for quantitative evaluation of porosity is justified in these cases.

## SYMBOLS

$b$	— bulk
$F_t$	— formation resistivity factor (fracture and matrix)
$G_m$	— integrated geometric factor of the region
$m$	— exponent of fracture-matrix system
$m_b$	— exponent of matrix
$M$	— porosity independent parameter
$n$	— saturation exponent
$N$	— porosity independent parameter
$R_A$	— true resistivity
$R_a$	— apparent resistivity
$R_{Ab}$	— true resistivity of matrix
$R_b$	— matrix ( $S_w = 1$ ) resistivity
$R_{fi}$	— short normal resistivity
$R_{fo}$	— long normal resistivity
$R_i$	— invaded matrix resistivity
$R_m$	— mud resistivity
$R_{mc}$	— mud cake resistivity
$R_{mf}$	— mud filtrate resistivity
$R_t$	— undisturbed formation resistivity
$R_T$	— total resistivity
$R_w$	— formation water resistivity
$S_{wb}$	— water saturation in the intergranular pores of matrix (Archie)
$S_{wf}$	— water saturated fractures
$S_{wT}$	— total saturation calculated by a modified Archie equation for a heterogeneous reservoir
$\Delta_{tt}$	— transit time
$\Delta_{tf}$	— fracture transit time
$V_B$	— bulk volume
$V_f$	— fracture volume
$V_m$	— matrix volume
$V_r$	— rock volume (fraction)
$V_C$	— compressional velocity in formation

## Greek letters

$\Phi$	— porosity
$\Phi_b$	— matrix porosity

$\Phi_m$	— matrix porosity
$\Phi_f$	— fracture porosity
$\Phi_t$	— total porosity
$v$	— fracture volume, as fraction of rock
$\Phi_{ND}$	— neutron density porosity
$\Phi_{\Delta t}$	— sonic porosity
$\varrho_b$	— formation density
$\varrho_f$	— fracture density

## REFERENCES

1. Pirson, S.J., 1967. How to map fracture development from well logs. *World Oil*. p 106-114, March.
2. Beck, J., Schultz, A. and Fitzgerald, D., 1977. Reservoir evaluation of fractured cretaceous carbonates in South Texas. *SPWLA Logging Symposium Transactions*, Paper M.
3. Schlumberger, internal manual, 1978. A review of fracture detection techniques with open holes.
4. Suau, J.J. and Gartner, J., 1978. Fracture detection from logs. *SPWLA*.
5. Aguilera, R. and Van Poolen, K.H., 1978. How to evaluate naturally fractured reservoirs from various well logs. *Oil and Gas Journal*, Dec.
6. Aguilera, R., 1976. Analysis of naturally fractured reservoirs from conventional well logs. *Journal of Petroleum Technology*, July, p. 764.
7. Suau, J. and Roccabianca, R., 1979, et al. Evaluation of very low-porosity carbonates. Preprint.
8. Aguilera, R. and Van Poolen, K.H., 1979. How to evaluate naturally fractured reservoirs from various logs. *Oil and Gas Journal*, Jan. 8.
9. Pickett, R.G. and Reynolds, B.E., 1969. Evaluation of fractured reservoirs. *SPEJ*, March.
10. Morris, R.L., Grine, D.R. and Arkfeld, T.E., 1964. The use of compressional and shear acoustic amplitudes for the location of fractures. *Journal of Petroleum Technology*, June.
11. Knopff, L., 1957, et al. 2nd Report, seismic scattering project. Institute of Geophysics. UCLA, Ch. 12, April.
12. Zemanek, J. and Caldwell, R.L., 1969, et al. The borehole televiewer, a new logging concept for fracture location and other types of borehole inspection. *Journal of Petroleum Technology*, June, p. 762.
13. Hilchie, D.W., 1959. A quantitative study of electrical log interpretation in fractures and vuggy reservoirs. Master thesis, University of Texas, Aug.

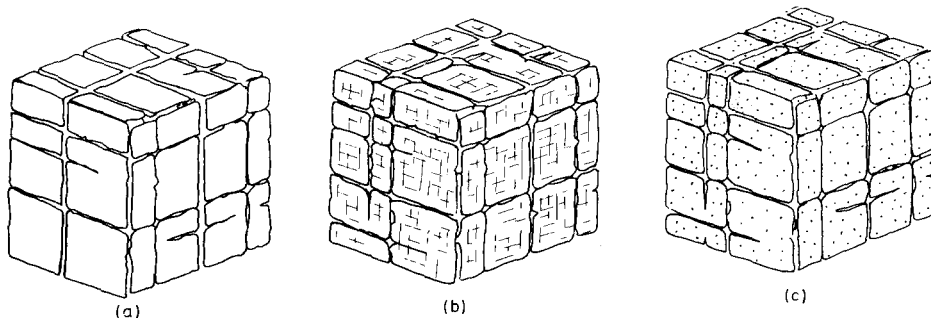
## **SECOND PART**

This Page Intentionally Left Blank

# Well dynamics: flow of homogeneous fluids toward a well

In a non-conventional fractured reservoir two types of reservoirs may be distinguished: (1) fractured reservoirs of single porosity and (2) fractured reservoirs of double porosity (figure 6.1). Both reservoirs are constituted of a network of fractures surrounding blocks, but what differentiates the two types of reservoirs is the porosity of the blocks. In the first case the blocks are practically impervious while in the second case the porosity is quite significant. The porosity considerably increases the storage capacity of the formation and, therefore, fractured reservoirs of double porosity are those of greater interest.

In a single porosity fractured reservoir having a developed network of fractures the equations of flow can be formulated through the continuum approach, i.e. replacing the actual discontinuum of fractures and blocks with a continuum of equivalent properties. The substitution is made by attributing to every reservoir point the properties of the surrounding representative sample of the reservoir including fractures and blocks. In this way porosity and permeability are defined at each reservoir point, and the equations of flow can be formulated by partial differential equations. In the case of a reservoir of double porosity, two overlapping continuums, one corresponding to the medium of the fractures and one corresponding to the medium of blocks, are considered. In such a case two values of porosities and permeabilities are attributed to each point, e.g. fracture porosity and block porosity.



6.1 – Sample of fractured reservoir Single porosity. (a) double porosity due to a system of microfissures and joints in the blocks (b), and double porosity due to granular porosity of the blocks.

In a reservoir of single porosity, disregarding the scale of a representative reservoir sample, the impervious blocks play the role of the solid grains of a conventional reservoir while the fracture porosity plays the role of the intergranular voids. As one may expect the equations describing the flow through fractured reservoirs of single porosity are the same as those used in conventional reservoirs; thus, there is no essential difference between the behaviour of fractured reservoirs of single porosity and conventional reservoirs. The equations of flow and behaviour description of the reservoir of double porosity are different and more complex.

Chapter 6 of this book discusses in detail the basic law of flow in a non-porous fractured rock, and in particular laws governing the flow of fluids through the fractures towards a well. Chapter 7 develops the law of flow in a double-porosity reservoir together with a critical discussion of the flowing equations actually available. Special attention is given to the flow towards a well. Procedures for the interpretation of physical parameters pressure vs. time are also discussed in detail. In chap 8 various specific problems of well behaviour resulting from interference or in-situ transient flow for reservoir characteristics evaluation are discussed in detail. In addition the possibility is examined of using for a natural fractured reservoir the procedure developed for induced fractures in porous media.

# CHAPTER 6

## FLOW OF FLUIDS TOWARDS A WELL IN NON-POROUS FRACTURED ROCK

In a non-porous fractured reservoir or a reservoir of single porosity the flow takes place only through the network of fractures. Due to the analogy between a fractured formation of single porosity and intergranular voids, one may postulate directly that the same equations govern both systems, e.g. in the range of laminar flow through the fractures the equation of motion is represented by Darcy's law. For flow through a fractured network Darcy's law can also be obtained from conceptual models (Irmay<sup>1</sup>, Romm<sup>2</sup>, Snow<sup>3</sup>). The starting point in this derivation is the equation of flow through an individual fracture. The flow problem examined in a non-porous fractured reservoir is also valid for double porosity systems as a result of the specific flow conditions in a fractured reservoir under steady-state conditions. The steady-state flow conditions are, in fact, the result of a permanent fluid mass transfer from the matrix to the fracture network, and a simultaneous movement of an equivalent of fluid mass towards the wellbore. The fluid flow through a double porous system under steady-state conditions is physically identical to the flow through a non-porous fractured rock.

### 6.1. LAW OF HOMOGENEOUS LIQUIDS

#### 6.1.1. Flow of homogeneous liquids through an individual fracture

The simplest model of flow through an individual fracture is the flow through the narrow space between two parallel plates (figure 6.2).

Laminar flow is governed by the Napier-Stokes equation:

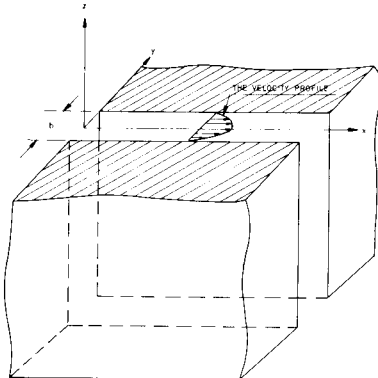
$$\rho \frac{\partial \vec{V}_f}{\partial t} + g (\vec{V}_f \nabla) \vec{V}_f = -\nabla \psi + \mu \nabla^2 \vec{V}_f \quad (6.1)$$

where  $\vec{V}_f$  is fracture velocity,  $\psi$  is potential,  $p$  is pressure,  $g$  is acceleration of gravity,  $\rho$  is density, and  $z$  is vertical coordinate (positive upward).

Assuming the case of small Reynolds number, the inertial term  $(\vec{V}_f \cdot \nabla) \vec{V}_f$  is sufficiently small compared with the viscous term  $\mu \nabla^2 \vec{V}_f$  to be neglected. In this case

the steady-state flow of an incompressible fluid may be expressed by equation 6.1 reduced to

$$-\nabla\psi + \mu\nabla^2\bar{V}_f = 0 \quad (6.2)$$



6.2 – Sketch for flow through an individual fracture plane.

The equation of conservation of mass in incompressible flow is:

$$\operatorname{div} \bar{V}_f = 0 \quad (6.3)$$

In the narrow space between the plates the flow is essentially two-dimensional in the (x,z) plane. In the y direction the velocity changes from zero at the walls (non-slip conditions) to a maximum at the center of the plane. The rate of variation of velocity in x and z directions is low, therefore, the following simplifications are appropriate:

$$\partial V_{fx}/\partial x = 0; \partial V_{fy}/\partial y = 0; \partial V_{fz}/\partial z = 0$$

and equation 6.2. may be written along the directions x,y,z, as follows:

$$\left. \begin{aligned} -\partial\psi/\partial x + \mu\partial^2 V_{fx}/\partial y^2 &= 0 \\ -\partial\psi/\partial y &= 0 \\ -\partial\psi/\partial z + \mu\partial^2 V_{fz}/\partial z^2 &= 0 \end{aligned} \right\} \quad (6.4)$$

The second equation of 6.4 shows that a function of y does not exist and the other two equations can be easily integrated under the appropriate boundary conditions  $y = \pm b/2$  ( $b$  is distance between the plates) where  $v_{fx} = v_{fz} = 0$ . The velocity components  $v_{fz}$  and  $v_{fy}$  then result as:

$$V_x = -(1/2\mu)(b^2/4 - y^2) \partial\psi/\partial x$$

$$V_z = -(1/2\mu)(b^2/4 - y^2) \partial\psi/\partial z \quad (6.5)$$

Being interested in the mean velocities when equation 6.5 is averaged over the section of flow, the following is obtained:

$$\langle V_{fx} \rangle = \frac{1}{a} \int_{-a/2}^{a/2} V_x dy = -(b^2/12\mu) \frac{\partial\psi}{\partial x} \quad (6.6)$$

$$\langle V_{fy} \rangle = \frac{1}{a} \int_{-a/2}^{+a/2} V_z dy = -(b^2/12\mu) \frac{\partial\psi}{\partial z}$$

or

$$\langle \vec{V}_f \rangle = -(b^2/12\mu) \nabla\psi \quad (6.7)$$

Equation 6.7 is the equation of flow between parallel planes simulating the flow through an individual fracture. The equation is similar to Darcy's law with an intrinsic permeability of the fracture  $K_{ff} = b^2/12$ , as discussed in section 4.2.1 of chapter 4.

### 6.1.2. Flow through a network of fractures

Romm<sup>2</sup> has developed a conceptual model leading to the equation of motion (Darcy's law) through a network of fractures.

#### 6.1.2.1. Vectorial evaluation: velocity and permeability

In a fractured formation constituted of pervious fractures and impervious blocks, the flux is given by:

$$\vec{u}_i = b_i f_i \vec{V}_{fi} \quad (6.8)$$

where  $v_{fi}$  is the velocity in the  $i$ -th direction of a fracture,  $b_i$  is the fracture width and  $f_i$  is the linear fracture density, i.e. the number of fractures per unit length ( $f = L_{fD}$  as discussed in chap. 2)

The velocity vector in the  $i$ -th direction (equation 6.7) is:

$$\vec{V}_{fi} = -(b_i^2/12\mu) (\nabla\psi \cdot \vec{m}_i) \vec{m}_i \quad (6.9)$$

with  $\vec{m}_i$  as the unit vector in the  $i$ -th direction.

Combining equations 6.8 and 6.9 the result obtained is:

$$\vec{u}_i = -b_i^3 (f_i / 12\mu) (\nabla \psi \cdot \vec{m}_i) \vec{m}_i \quad (6.10)$$

The total rate of flow is the sum of the partial rates  $u_i$  in the  $n$  individual fractures:

$$\vec{u} = -(1/12\mu) \sum_{i=1}^n b_i^3 f_i (\nabla \psi \cdot \vec{m}_i) \vec{m}_i \quad (6.11)$$

When the gradient  $\nabla \psi$  is split into two components, one in the direction of the fracture plane and the other in the normal direction (with  $\vec{n}_i$  as unit vector) the result is:

$$\nabla \psi = (\nabla \psi \cdot \vec{m}_i) \vec{m}_i + (\nabla \psi \cdot \vec{n}_i) \vec{n}_i \quad (6.12)$$

Substitution of equation 6.12 in 6.11 yields:

$$\begin{aligned} \vec{U} &= -(1/12\mu) \sum_{i=1}^n b_i^3 f_i [\nabla \psi - (\nabla \psi \cdot \vec{n}_i) \vec{n}_i] = \\ &= -(1/12\mu) \sum_{i=1}^n b_i^3 f_i [\bar{\bar{I}} - (\vec{n}_i \vec{n}_i)] \nabla \psi \end{aligned} \quad (6.13)$$

where  $\bar{\bar{I}}$  is the unit tensor.

Equation 6.13 can also be written as:

$$\vec{V} = -\frac{\bar{\bar{K}}}{\mu} \nabla \psi \quad (6.14)$$

which is identical to Darcy's law for a conventional granular porous formation. From equations 6.13 and 6.14 it may be written

$$\bar{\bar{K}}_f = (1/12) \sum_{i=1}^n b_i^3 f_i \left[ \bar{\bar{I}} - (\vec{n}_i \vec{n}_i) \right] \quad (6.15)$$

expressed as a symmetric tensor of the second order: The anisotropic permeability

$\bar{\bar{K}}$  based on the above conceptual model, is expressed by equation 6.15 which may be written in a matrix form as,

$$\bar{\bar{K}}_f = \begin{vmatrix} \sum_{i=1}^n b_i^3 f_i (1 - \alpha_{1i}^2) - \sum_{i=1}^n b_i^3 f_i \alpha_{1i} \alpha_{2i} & \sum_{i=1}^n b_i^3 g_i (1 - \alpha_{2i}^2) \\ - \sum_{i=1}^n b_i^3 f_i \alpha_{1i} \alpha_{2i} & - \sum_{i=1}^n b_i^3 f_i (1 - \alpha_{2i}^2) - \sum_{i=1}^n b_i^3 f_i \alpha_{1i} \alpha_{3i} \\ - \sum_{i=1}^n b_i^3 f_i \alpha_{3i} \alpha_{1i} & - \sum_{i=1}^n b_i^3 f_i \alpha_{3i} \alpha_{2i} \sum_{i=1}^n b_i^3 f_i (1 - \alpha_{3i}^2) \end{vmatrix}$$

where  $\alpha_{1i}$ ,  $\alpha_{2i}$  and  $\alpha_{3i}$  are the direction cosines of the  $n_i$  vectors with the axes  $x_1$ ,  $x_2$  and  $x_3$  respectively, of a cartesian system of coordinates.

With respect to a coordinate system  $(x_1, x_2, x_3)$  coinciding with the principal direction of anisotropy, we obtain:

$$\bar{\bar{K}}_f = \begin{vmatrix} \sum_{i=1}^n b_i^3 f_i (1 - \alpha'_{1i}^2) & 0 & 0 \\ 0 & \sum_{i=1}^n b_i^3 f_i (1 - \alpha'_{2i}^2) & 0 \\ 0 & 0 & \sum_{i=1}^n b_i^3 f_i (1 - \alpha'_{3i}^2) \end{vmatrix} \quad (6.17)$$

where  $\alpha'_{1i}$ ,  $\alpha'_{2i}$  and  $\alpha'_{3i}$  are the direction cosines of the  $\vec{n}_i$  vectors with the axes  $x'_1$ ,  $x'_2$  and  $x'_3$ , respectively.

For an isotropic system of fractures we obtain:

$$\sum_{i=1}^n b_i^3 f_i (1 - \alpha'_{1i}^2) = \sum_{i=1}^n b_i^3 f_i (1 - \alpha'_{2i}^2) = \sum_{i=1}^n b_i^3 f_i (1 - \alpha'_{3i}^2) \quad (6.18)$$

If a random fracture distribution is assumed with equiprobable distribution,  $1 - \alpha'_{ni}^2$  independent of  $b_i^3 f_i$  and sufficiently high  $i$  values so that all  $\alpha'_{ni}$  ( $n = 1, 2, 3$ ) be equally probable, the mathematical expectation of  $(1 - \alpha'_{ni}^2)$  is:

$$1 - \frac{2}{\pi} \int_0^{\pi/2} \cos^2 x_{ni} dx_{ni} = \frac{1}{2} \quad (6.19)$$

and

$$\sum_{i=1}^n b_i^3 f_i (1 - \alpha'_{ni}) = \frac{1}{2} \sum_{i=1}^n b_i^3 f_i \quad (6.20)$$

In such a case the fracture permeability tensor will have the form:

$$\bar{\bar{K}}_f = \frac{1}{24} \sum_{i=1}^n b_i^3 f_i \bar{\bar{I}} \quad (6.21)$$

The basic difference between the intrinsic fracture permeability ( $K_{ff}$ ) and the formation permeability ( $K_f$ ), often called Darcy's permeability and resulting from well testing, was discussed in chap. 2. The intrinsic permeability refers to the individual fracture width and therefore may be very big, while the formation permeability measured as result of the flux through the cross flow surface (including therefore the impervious blocks) shows moderate values. As an example, in the case of a fractured formation having a linear fracture density of one fracture per meter and a fracture width of 0.1 mm, the intrinsic permeability of the individual fracture ( $k_{ff} = b^2/12$ ) is approximately 1000 Darcies, while the permeability  $K_f$  of the fractured formation (equation 6.21) is only 42 mD.

$$K_{ff} = \frac{(10^{-2})^2}{12} (\text{cm}^2) = 8,33 \times 10^{-6} (\text{cm}^2) = 833 \text{D} \cong 1000 \text{D}$$

$$K_f = \frac{1}{24} (10^{-2})^3 \frac{1}{100} = 4,2 \times 10^{-10} \text{ cm}^2 = 42 \text{ mD}$$

In the case of flow of hydrocarbons a minimum value for the irreducible water is the water layer absorbed along the fracture walls. The order of magnitude of this layer is 1 to 2 microns. Therefore, the minimum fracture width allowing flow of a non-wetting fluid has to be of an order of magnitude of 2 to 4 microns.

#### 6.1.2.2. Case of unidimensional flow

The calculation of permeability is based on the continuity of the flow through the fractured formation equivalent to a constant rate ( $q_f = \text{constant}$ ):

$$V = q_f/A_s = V_f A_f / A_s \quad (6.22)$$

where  $V$  is Darcy's velocity,  $V_f$  is effective velocity in fractures,  $A_f$  is fracture cross-section, and  $A$  is formation cross-section.

If  $n$  fractures of width  $b$  and length  $l$  form a non-porous fractured reservoir, the Darcy velocity is expressed through equations 6.7 and 6.11 as:

$$V = \left( \frac{nbl}{A_s} \frac{b^2}{12\mu} \right) \frac{d\psi}{dx} \quad (6.23)$$

in which,

$$K_f = \frac{nb^3l}{12A_s} \quad (6.24)$$

can be identified with the permeability of the fractured formation. This equation (6.24) can also be written as:

$$K_f = A_{fD} \frac{b^3}{12} = K_{ff} \times b \times A_{fD} \quad (6.25)$$

where  $A_{fD} = \frac{n \times 1}{A_s}$  represents the areal fracture density (discussed in chapter 4, equations 4.28 and table 4.1).

### 6.1.3. Turbulence in fractures

#### 6.1.3.1. Turbulent flow through analogy with flow in pipes

The occurrence of turbulent flow is related to the Reynolds number defined as:

$$Re = \frac{VD\rho}{\mu} = \frac{VD}{v} \quad (6.26)$$

where V is velocity in the pipe, D is characteristic length of conduit,  $\rho$  is density,  $\mu$  is dynamic viscosity, and v is kinematic viscosity.

The characteristic length for pipes is the diameter D. Defining the hydraulic radius as the ratio between area of flow and the pipe wetted perimeter, the equation obtained for the flow through pipes  $R_h = D/4$  when substituted for equation 6.26 is:

$$Re = \frac{4R_h V}{v} \quad (6.27)$$

For flow through parallel plates the hydraulic radius equals  $b/2$ , and with the definition of the Reynolds number through the hydraulic radius (equation 6.27) the result is:

$$Re = \frac{2bV}{v} = \frac{\rho V^2 b}{\mu} \quad (6.28)$$

Considering a one-dimensional flow in a S-direction, the relationship between the velocity and potential gradient as expressed by equation 6.7 is:

$$\frac{\partial \psi}{\partial S} = \frac{12\mu}{b^2} V_s \quad (6.29)$$

This same equation when expressed through the Reynolds number becomes:

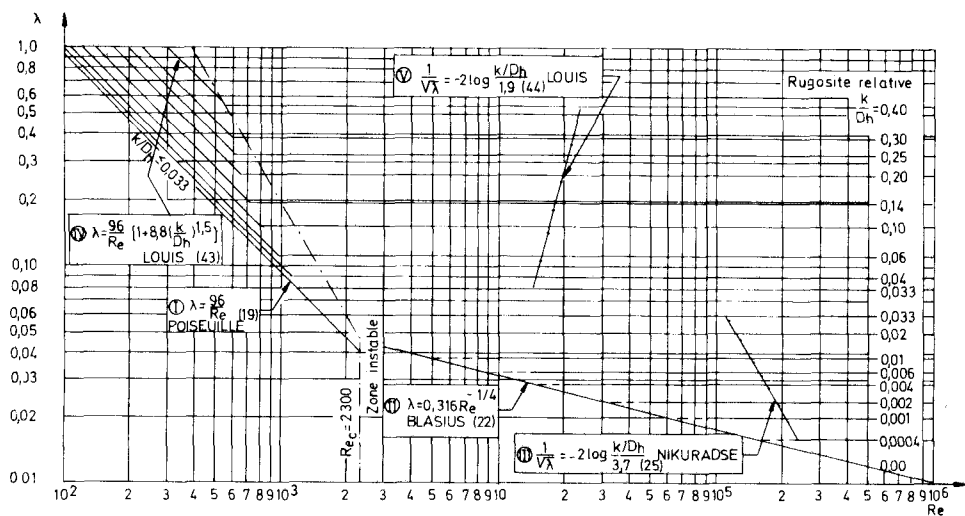
$$-\frac{1}{\rho g} \frac{\partial \psi}{\partial S} = \frac{96}{Re} \frac{1}{D} \frac{V^2}{2g} = f(Re) \frac{1}{D} \frac{V^2}{2g} \quad (6.30)$$

The velocity V represents the effective velocity in the flowing section and if applied to a fracture will be equivalent to  $V_f$  (effective filtration velocity in fractures) while f is defined as a friction factor. It is well known that a similar expression is obtained for laminar flow through pipes with a friction factor of  $64/Re$  instead of  $96/Re$  in the present case. As for transition from laminar to turbulent flow in pipes the same value of  $Re = 2300$  was found experimentally for flow through parallel plates.

In turbulent flow the pressure loss is a function of the roughness of the conduit, and equation 6.31 is generalized to include also turbulent flow with a friction factor function of both Reynolds number and roughness as:

$$-\frac{1}{\rho g} \frac{\partial \psi}{\partial S} = f(Re, \varepsilon) \frac{1}{D} \frac{V^2}{2g} \quad (6.31)$$

Values of the friction factor in the region of turbulent flow were determined experimentally (Lomize<sup>4,5</sup>, Huit<sup>6</sup>, Louis<sup>7</sup>). Louis' diagram (figure 6.3), plotted in a similar way as Moody's<sup>8</sup> diagram for pipes, is a synthesis of the experimental results obtained by different investigators.



6.3 – The friction factor (f) as a function of the Reynolds number (Re) for flow through fractures (Louis<sup>7</sup>).

a. Empirical equations found through experiments

In experiments on single fractures with smooth walls it was found<sup>2</sup> that the relationship  $\lambda - Re$  in laminar flow is expressed by the classic equations:

$$\lambda = \frac{6}{Re} \quad (6.32)$$

$$V = \frac{b^2}{12\mu} \frac{dp}{dx}$$

and for turbulent flow,

$$V = 4.7 \left[ b^5 \left( \frac{dp}{dx} \right)^4 / \mu \rho^3 \right]^{1/7} \quad (6.33)$$

$$\lambda = 0.056 / Re^{1/4} \quad (6.34)$$

From experimental data the transition between laminar and turbulent flow in a single fracture was found to be between 550 and 770 or an average critical number:

$$Re_{critic} \approx 600$$

b. Influence of roughness

The walls of a natural fracture will always show a certain degree of roughness, therefore, an additional pressure drop may develop as a result of the degree of roughness of the fracture walls. This roughness is related to the ratio  $\varepsilon = \frac{e^*}{b}$  (where  $e^*$  is the average height of roughness and  $b$  the width of the fracture opening). The empirical equation for velocity is:

$$V = \frac{b^2}{12\mu} \frac{1}{1 + 6(e^*/b)^{1.5}} \frac{dp}{dx} \quad (6.35)$$

and the empirical equation for  $\lambda$  is:

$$\lambda = \frac{6}{Re} [1 + 6(e^*/b)^{1.5}] \quad (6.36)$$

Experiments on naturally fractured reservoirs provided the following information:

- If fracture walls are covered by consolidated grains then  $\lambda \cong 40/\text{Re}$  which corresponds to equation 6.36 in the case of  $e^*/b = 1$ .

• The critical relative roughness in a fractured reservoir is  $\varepsilon \cong 0.065$ , but the majority of natural fractures have shown values of  $\varepsilon < 0.065$ . In general, the measured  $\varepsilon$  values are between 0.002 and 0.01 which justifies the use of the equations 6.33 and 6.34. In order to solve a flow problem through this approach it is necessary to know the fracture geometry and its equivalent roughness. Since these parameters are beyond the scope of a reservoir engineer, the above results obtained through experiments from individual fractures are more limited to academic interest rather than general engineering methodology.

#### 6.1.3.2. Turbulent flow by analogy with known flow in porous media

At the present time nothing in the published literature provides any general procedure for the study of flow in either a single fracture or a fracture system or network, without detailed information of fracture size, shape, distribution, etc. However, an analogy between the flow through a fracture network and the flow through a conventional porous media seems possible in certain limits. Based on equations 6.2 and 6.14 of a porous medium it is possible to write:

$$\bar{V}_f = -\frac{K_f}{\mu} \text{grad } P \quad (6.37)$$

for the classic Darcy's flow. In case of turbulence the additional pressure drop is expressed as follows:

$$\text{grad } P = \frac{\mu}{K_f} \bar{V}_f + \beta \rho \left| \bar{V}_f \right| \bar{V}_f \quad (6.38)$$

Furthermore, in the case of a unidimensional flow, equation 6.38 is written as follows:

$$\frac{dp}{dl} = \frac{\mu}{K_f} V_f + \beta \rho V_f^2 \quad (6.39)$$

The right hand terms of equation 6.39 represent viscous and inertial forces. If velocity  $\bar{V}$  is low, the second right-hand term is negligible and the flow is governed by viscous forces, but if the flow rate grows, the inertial term increases and begins to dominate the flow process. If the inertial forces are negligible the law of flow is reduced to the classic Darcy's law and its validity limit may be indicated by a critical value expressed by Reynolds dimensionless number as follows:

$$Re = \left( \beta \rho V_f \frac{K_f}{\mu} \right) \quad (6.40)$$

where  $\beta$  is a coefficient of inertial<sup>10</sup> flow resistance, often called the velocity coefficient<sup>11</sup> or turbulence factor<sup>12</sup>.

#### a. Flowing equation

In a fractured network, as in a porous media, a pressure drop can also be expected to be expressed as:

$$\Delta P = AQ + BQ^2 \quad (6.41)$$

This corresponds to a *linear flow* for low rates when  $BQ^2 \ll AQ$ , and to *turbulent flow* for high rates when  $BQ^2 \gg AQ$ . Both A and B constants in these cases depend on flow geometry and the physical properties of rock and fluids. Thus, the difference in approach between a conventional reservoir and a fracture network is based on the similitude between the parameters of the fracture system ( $K_f$ ,  $K_{ff}$ ,  $\Phi_f$ ,  $b$ ,  $n$ ,  $A_{FD}$ ) and the parameters of a conventional reservoir ( $K$ ,  $\Phi$ ,  $h$ ). Such relationships for various simplified geometrically arranged networks of fractures are given in tables 4.1 and 4.6.

- Parameter A expresses the *linear proportionality between the rate and pressure drop* and is associated to *geometrical flow characteristics and flow resistance parameters*.

The geometrical characteristics are influenced by the length and extension of the fracture network inside the flowing cross-section. The parameters of resistance to a flowing process are represented by the ratio between permeability and viscosity,  $K_f/\mu$  or  $b^2/\mu$  if the fracture permeability  $K_f$  is expressed by fracture width  $b$ .

If the fracture network is reduced to a simplified geometrical model,  $K_f$  and  $b$  will be associated to the fracture porosity  $\Phi_f$ , and if the flow is linear or radial, it is necessary that A take into consideration the flowing geometry.

•• Parameter B represents the *non-linear relationship* between rate Q and pressure drop  $\Delta P$ . From the analysis of this parameter developed in various experimental and theoretical work<sup>10,12</sup>, it was found that B depends less on flowing geometry and more on physical characteristics of fluid (viscosity  $\mu$ , mass  $\rho$ ) and rock (porosity  $\Phi$  and permeability K). The relationship B vs.  $\Phi$  and K depends on the turbulence factor  $\beta$ . Among the various relationships it may be mentioned that the most recent ones published in literature<sup>11,12</sup> are the following:

$$\beta (1/\text{ft}) = 4.16 \times 10^{10} / K^{1.34} \text{ (mD)} \quad (6.42)$$

and,

$$\beta (1/\text{ft}) = 2.20 \times 10^{10} / K^{1.19} \text{ (mD)} \quad (6.43)$$

In both equations the role of porosity is disregarded. If porosity is taken into consideration the  $\beta$  is given by<sup>11</sup>:

$$\beta \text{ (1/ft)} = 2.2 \times 10^9 / [\text{K} \times \Phi (\text{mD} \times \text{fraction})]^{1.085} \quad (6.44)$$

The validity of these equations is questionable since the experimental results were obtained for large porosities and small permeabilities, while in a fracture network it is more the case of very small porosities and very large permeabilities. However, as orientative relationships these equations may be carefully used for checking permeabilities. In general, equations 6.42 and 6.43 are more recommendable for single fracture modelling, and equation 6.44 for multi-fracture modelling.

#### b. Reynolds number

For the delimitation of laminar and turbulent flow the use of equation 6.28 is perfectly valid for flow in single fractures, with a critical number of around  $\text{Re}_{cr} \cong 600$ . If a fractured reservoir is treated by analogy with flow in a porous media, the most general equation is the same as expressed in equation 6.40 as a function of the following parameters:

$$\text{Re} = f\left(\beta, \rho, v, \frac{k}{\mu}\right)$$

The equations which indicate the Reynolds number have been obtained through experimental work. The equation published in 1953 by Scelkacev<sup>13</sup>, which takes into consideration the role of porosity, is as follows:

$$\text{Re} = \frac{10}{\Phi^{2.3}} \frac{V \sqrt{K}}{\mu} \rho \quad (6.45)$$

where  $V$ (cm/sec),  $K$ (cm<sup>2</sup>),  $\rho$ (dyne sec<sup>2</sup>/cm<sup>4</sup>),  $\mu$ (dyne sec/cm<sup>2</sup>) and  $\Phi$  (fraction). The critical value of the Reynolds number in this case is:

$$\text{Re}_{cr} \cong 1$$

A more recent equation elaborated by Geertsma<sup>10</sup> indicates the Reynolds parameter as:

$$\text{Re} = \frac{5 \times 10^{-3}}{\Phi^{5.5}} \cdot \frac{V \sqrt{K}}{\mu} \rho \quad (6.46)$$

and the critical Reynolds number as:

$$\frac{\rho V \sqrt{K}}{\mu \Phi^{5.5}} = 20 \quad (6.47)$$

In the case of a complex fracture network, when testing data is available it is possible to evaluate the *critical rate* and *critical velocity* when the relationship Q vs.  $\Delta P$  is no longer linear. The critical velocity is calculated from the critical rate, and the value of permeability is obtained through equation 6.47 (see example).

## 6.2. STEADY-STATE FLOW OF HOMOGENEOUS LIQUIDS THROUGH A FRACTURE NETWORK TOWARDS A WELL

From field experience very high rates (up to 30 000–50 000 barrels per day) are obtained from fractured reservoirs wells under a very limited pressure drop. The magnitude of rates or productivity index is directly associated to the presence or absence of fractures, to their dimensions and distribution. The production testing data under a stabilized condition of flow, if correctly processed, make it possible to evaluate the characteristics of the fractured network.

In order to simplify the complexity of fracture networks, models based on their regular geometry have been proposed. All the models are ideally formed by a group of uniform matrix blocks separated from each other by fractures which develop a small friction resistance to the fluid flow compared with the friction resistance of a porous medium. If the matrix blocks are so tight that the movable fluid is located only in the fracture network, the flow towards the well will be governed by the laws of flow through a non-porous fractured rock. But a similar flow condition takes place even if the porosity of the matrix is high and it contains movable fluids when the flowing process is stabilized and when matrix fluid *rate* (feeding the fractures) becomes quasi-steady state.

Consequently, the following basic statement can be made: In a double porosity system, when the flow is stabilized, the flow process towards a well is actually a flow only through the fracture network, whereas the flow from each matrix block is reduced to a steady-state supply of fluid to the surrounding fractures.

### 6.2.1. Modelling of a fracture network

The fracture-matrix block is generally simulated by simplified geometrical schemes. The most classic ones are formed by alternate block and fractured layers, or by an orthogonal system of matrix blocks similar to the models indicated in Part 1, chapter 4, table 4.6.

### 6.2.1.1. Idealization through orthogonal matrix blocks

A simple idealized picture of a fractured reservoir considers an orthogonal system of continuous, uniform fractures to be oriented in such a way that each fracture is positioned towards one of the principal axes of a cartesian system of coordinates. When the fractures are uniformly spaced and of uniform width along each direction, this corresponds to an isotropic system; but if along each axis a change in width is introduced, this will simulate the proper degree of anisotropy. The model so idealized could be defined by the block dimensions, their orientation and their distribution. As a result of the observations obtained from cores and outcrops and from dynamic observations obtained from well tests, data such as permeability and porosity of matrix and fractures and other characteristics can be evaluated. Correlations can be further developed in order to build various simplified models for the fracture network.

#### a. Equivalent length of orthogonal blocks

If the block has the dimensions as shown in figure 6.4, such that  $x = a_x$ ;  $y = a_y$ ; and  $z = a_z$ , an equivalent length can be calculated from the surface-volume ratio for the number  $n$  of sets of fractures. If  $n = 1, 2, 3$ , the result is:

$$l = \frac{3a_x \cdot a_y \cdot a_z}{a_x \cdot a_y + a_x a_z + a_y a_z} \dots \text{for } n = 3$$

$$l = \frac{2a_x \cdot a_y}{a_x + a_y} \dots \text{for } n = 2 \quad (6.48)$$

$$l = a_x \dots \text{for } n = 1$$

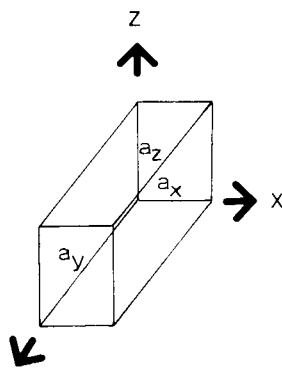


Fig. 6.4

6.4 – Orthogonal block with fracture planes oriented in a xoyz axis system.

#### b. Equivalent porosity in an idealized model.

If the block is surrounded by fractures having an opening width  $b$ , then only the

width  $b/2$  is associated with the respective block as in figure 6.5. Therefore, the porosity of an orthogonal block is:

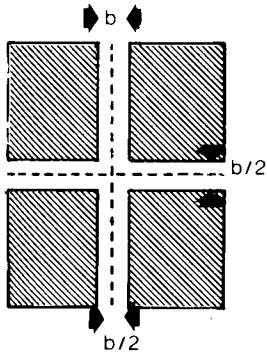
$$\Phi_f = \frac{V_f}{V_B} = \frac{b_x}{a_x} + \frac{b_y}{a_y} + \frac{b_z}{a_z} \quad (6.49)$$

and if  $b_x = b_y = b_z = b$ :

$$\Phi_f = b \left[ \frac{1}{a_x} + \frac{1}{a_y} + \frac{1}{a_z} \right] = \frac{b}{1} \quad (6.50)$$

If  $a_x = a_y = a_z = a$  (in the case of a cube), the porosity is reduced to:

$$\Phi_f = 3b/a \quad (6.51)$$



### 6.5 – Cross-section through adjacent matrix blocks.

#### c. Fracture permeability $K_f$ in an idealized model

As discussed in chapter 4, section 4.2, in the case of a single fracture of width  $b$  and extension 1, the rate is expressed by the product between cross-flow-section  $S$  and velocity  $v$  as follows:

$$q = S \times V = b \times 1 \times \frac{b^2}{12\mu} \frac{\Delta P}{L} \quad (6.52)$$

which when compared with the Darcy equation:

$$q = b \times 1 \times \frac{K_{ff}}{\mu} \frac{\Delta P}{L} \quad (6.53)$$

indicates that the relationship between permeability and fracture flow resistance is:

$$K_{ff} = b^2/12 \quad (6.54)$$

which represents the intrinsic permeability of the fracture. For a fracture system (a fracture system was defined in chapter 2 as a group of fractures in parallel) the rate is given by:

$$q = S \times V = n \times b \times 1 \times \frac{b^2}{12\mu} \frac{\Delta P}{L} \quad (6.55)$$

which, when compared with Darcy's equation:

$$q = S \frac{K_f}{\mu} \frac{\Delta P}{\Delta L} \quad (6.56)$$

gives the following equivalent permeability (as already discussed in equation 4.27 and based on the definition of equation 2.3 in chapter 2):

$$SK_f = n \times b \times 1 \times \frac{b^2}{12} \quad (6.57)$$

or

$$K_f = \frac{nb \times 1}{S} \frac{b^2}{12} = A_{fD} \times \frac{b^3}{12} = \Phi_f \frac{b^2}{12} \quad (6.58)$$

since  $\Phi_f = n \times b \times 1/S$ .

Other relationships for this simple analogical modelling are shown in table 4.1 of chapter 4.

#### 6.2.1.2. Basic parameters of simplified models.

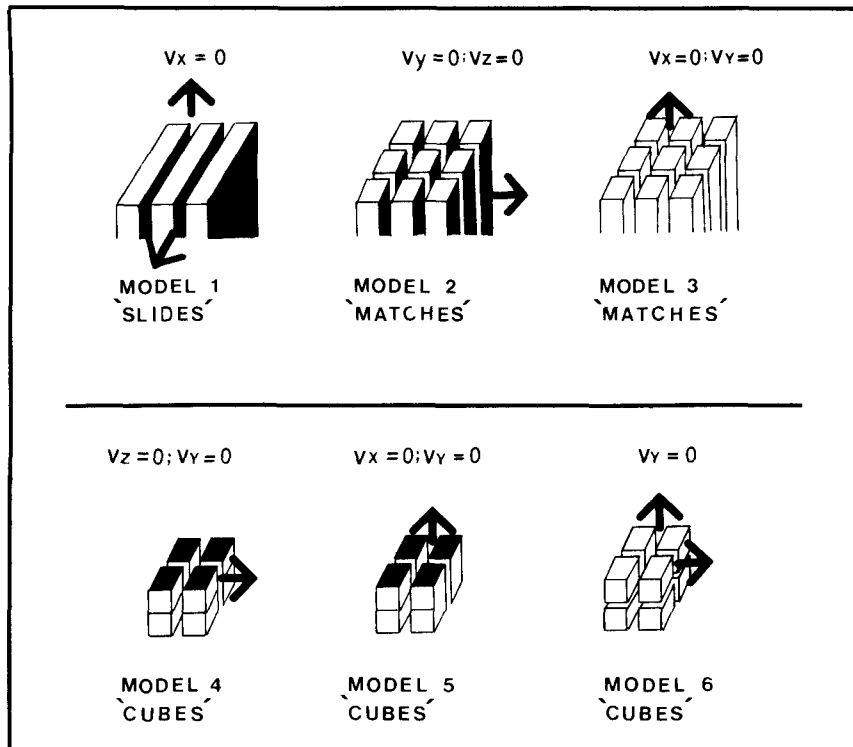
The basic models<sup>14</sup> are the same as shown in figure 4.20 of chapter 4, and the basic relationships remain the same as illustrated in table 4.6. The direct relationships are established between fracture width  $b$ , fracture interval  $a$ , fracture permeability  $K_f$  and fracture porosity  $\Phi_f$ .

If the data are obtained from well testing, the permeability  $K_f$  can be determined from the test results. Since the parameter  $A_{fD}$  is often determined by coring or logging analysis, the porosity  $\Phi_f$  and fracture width  $b$  may be determined by use of the equations given in table 6.1. The models and flowing direction are given in figure 6.6.

For example, a fracture width of 0.1mm in the case of a 1.00 m cube will give, from equations shown in tables 4.6 and 6.1, the following values of porosity and permeability for the model type 6:

$$\Phi_f = 3b/a = 3 \times 10^{-4}/1 = 0.03\%$$

$$K_f = b^2 \Phi_f / 18 = (10^{-2})^2 \times 3 \times 10^{-4} / 18 = 0.17 \times 10^{-8} \text{ cm}^2 = 170 \text{ mD}$$



### 6.6 – Basic idealized models and flowing directions.

Table 6.1. BASIC PARAMETERS OF SIMPLIFIED MODELS

Model type	Velocity	$A_{fD}$	$\Phi_f$	$\Phi_f$	a	b
1. Slides	$V_x = 0$	$1/a$	$b/a$	$(12 K_f A_{fD}^2)^{-3/3}$	$1/A_{fD}$	$(12 K_f/\Phi_f)^{0.5}$
2. Matches	$V_y = 0; V_z = 0$	$1/a$	$2b/a$	$(96 K_f A_{fD}^2)^{-3/3}$	$1/A_{fD}$	$(24 K_f/\Phi_f)^{0.5}$
3. Matches	$V_x = 0; V_y = 0$	$2/a$	$2b/a$	$(48 K_f A_{fD}^2)^{-3/3}$	$2/A_{fD}$	$(12 K_f/\Phi_f)^{0.5}$
4. Cubes	$V_z = 0; V_y = 0$	$1/a$	$2b/a$	$(96 K_f A_{fD}^2)^{-3/3}$	$1/A_{fD}$	$(12 K_f/\Phi_f)^{0.5}$
5. Cubes	$V_x = V_y = 0$	$2/a$	$2b/a$	$(48 K_f A_{fD}^2)^{-3/3}$	$2/A_{fD}$	$(12 K_f/\Phi_f)^{0.5}$
6. Cubes	$V_y = 0$	$2/a$	$3b/a$	$(162 K_f A_{fD}^2)^{-3/3}$	$2/A_{fD}$	$(18 K_f/\Phi_f)^{0.5}$

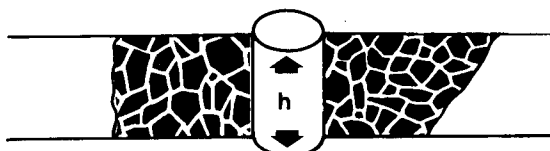
Such simplified models as proposed by Reiss<sup>14</sup> may lead to a greatly underestimated porosity when this is evaluated from permeability calculated through well testing data. For example, in case of a directional flow through a network of fractures with variable widths, the equivalent permeability for fractures connected in series is given by the harmonic mean, strongly influenced by the fracture of the smallest width. Consequently, porosity which will be calculated from this value is, in fact, uncorrelated with the true porosity. Using such a correlation the fracture storage capacity will be underestimated.

### 6.2.2. Modelling of a radial symmetrical flow

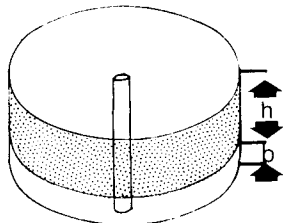
The idealized model used for flow towards a well assumes a radial symmetrical flow between the external boundary formed by the lateral surface of a cylinder and the wellbore formed by the lateral surface of a coaxial cylinder.

#### 6.2.2.1. Type of models

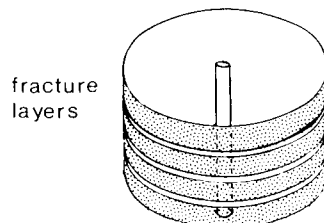
- a. The Baker model.<sup>15</sup> In this model the real fracture formed by impervious matrix blocks separated by a fracture network (fig. 6.7) is represented by a single matrix block and a single fracture (fig. 6.8). The equivalence between the model and real reservoir is given by simulating the same conductivity in both model and real reservoir.
- b. The Kazemi model<sup>16</sup>; This model reduces the fracture network (figure 6.7) to a set of uniformly spaced horizontal matrix layers, where the set of fractures are equivalent to spaces between cylindrical slices of matrix (figure 6.9).



6.7 – Radial symmetrical flow through a fracture network similar to a porous media.

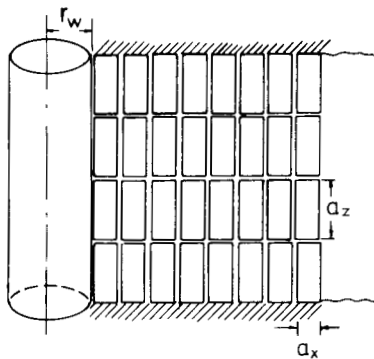


6.8 – Single fracture for the simulation of a radial symmetrical flow through fracture network



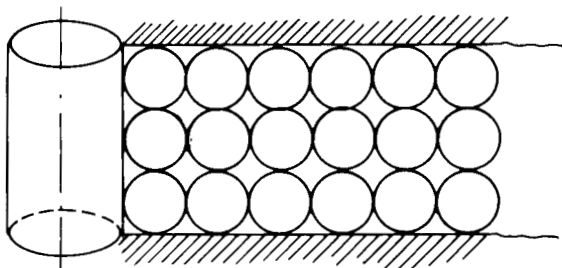
6.9 – Parallel multi-fracture system for the simulation of a radial symmetrical flow through fracture network (Kazemi model)

- c. The Warren-Root model<sup>17</sup>; The fractures in this case form a continuous and uniform network oriented in such a way as to be parallel to the principal direction of permeability (figure 6.10). The fractures are assumed to be of constant width. In the case of an isotropic network or a variation in a given direction, the anisotropy must be simulated. The fracture spacing associated to fracture density is directly related to the fracture permeability and porosity. The section shown in figure 6.10 illustrates a model where the blocks may be parallelepipeds if  $a_x \neq a_z$  or cubes if  $a_x = a_z$ .



6.10 – Multi-block system for the simulation of a radial symmetrical flow through fracture network (Warren-Root model).

- d. The De Swaan model<sup>18</sup>; This model is similar to the Warren-Root model, but instead of matrix blocks shaped as parallelepipeds, the block units are shaped as spheres. The spheres are superimposed in a regular orthogonal distribution. The fracture volume is represented by the spherical interspace (figure 6.11) which is further correlated with porosity values.



6.11 – Multi-sphere blocks having an orthogonal arrangement for the simulation of a radial symmetrical flow through fracture network (De Swaan model).

### 6.2.2. Basic equations of flow

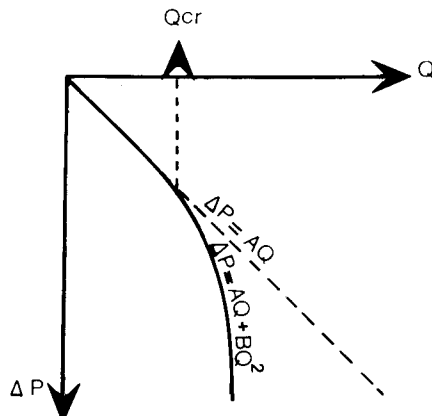
The flow through a fracture network towards a well when fractures are not distributed in a regular pattern (figure 6.7) may be assumed similar to the flow in a po-

rous medium. The fracture network formed by interconnecting channels has a certain porosity representing its storage capacity and a certain permeability equivalent to its flow conductivity.

Low porosity and high permeability, by analogy with a porous medium or flow in channels, will demonstrate a linear relationship  $Q - \Delta P$  at low rates of flow and a nonlinear relationship when the rates of flow are considerably increased. This classic general equation will maintain its validity:

$$\Delta P = AQ + BQ^2 \quad (6.41)$$

The diagram of  $Q$ - vs.  $\Delta P$  (figure 6.12) in this case shows that laminar flow  $\Delta P = AQ$  is valid until a critical rate value  $Q_{cr}$  is reached. If the rates continue to increase beyond a certain transition zone, the second right-hand term of equation 6.41 becomes predominant and the flow is almost completely controlled by a turbulent flow law expressed by  $\Delta P = BQ^2$ .



6.12 – Production steady-state curve  $Q$  vs.  $\Delta P$ , of a radial symmetric flow.

#### 6.2.2.2. Evaluation of basic parameters of an idealized fractured reservoir

If it is assumed that a fracture network has a certain permeability  $K_f$  and porosity  $\Phi_f$ , based on the following equation:

$$\text{grad } P = \frac{\mu}{K_f} V + \rho\beta V^2 \quad (6.38)$$

and on equation 6.41, the result is:

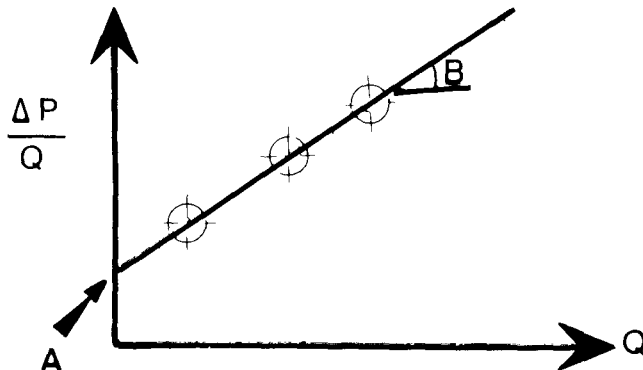
$$A = \frac{\mu_o B_o}{2\pi K_f h} \left( \ln r_e/r_w + \sum S \right) \quad (6.59)$$

$$B = \beta \frac{\rho B_o}{4\pi^2 h^2} \left[ \frac{1}{r_w} - \frac{1}{r_e} \right] \quad (6.60)$$

If from well testing operations rates  $Q$  and pressure drop  $\Delta P$  are recorded under steady-state flowing conditions, the values  $A$  and  $B$  may be obtained from equation 6.41 if this is rewritten in the following form

$$\frac{\Delta P}{Q} = A + BQ \quad (6.61)$$

and then represented graphically as in figure 6.13. The straight line obtained will directly give value  $A$  as the ordinate at  $Q = 0$  and  $B$  as the slope of the straight line.



6.13 – The relationship  $\Delta P/Q$  vs.  $Q$ , of a radial symmetric flow.

a. Evaluation of  $K_f$

From parameter  $A$  it is possible to evaluate the permeability if the skin effect  $\sum S$  is not taken into consideration.  $K_f$  may be expressed as follows:

$$K_f = \frac{\mu_o B_o \ln r_e / r_w}{6.28 h} \cdot \frac{1}{A} \quad (6.62)$$

b. Evaluation of  $\Phi_f = f(A)$

If the fracture density ( $A_{fD} = L_{fD}$ ) is known, the porosity  $\Phi_f$  could be expressed as a function of the productivity index  $PI = \frac{1}{A}$  based on equation 6.59 and of the equation given for various simplified models in the fifth column of Table 6.1. A discussion was developed in chapter 4, section 4.6 for this correlation:

$$\Phi_f = \sqrt[3]{PI \frac{B_o \mu_o \ln r_e / r_w}{2\pi h} A_{fD}^2 \cdot \delta} \quad (6.63)$$

where  $PI$  ( $\text{cm}^3/\Delta/\text{at}$ );  $\mu_o$  ( $\text{cP}$ );  $h$  ( $\text{cm}$ );  $A_{fD}$  ( $1/\text{cm}$ );  $\Phi_f$  (%);  $\delta$  ( $1/\text{cm}^2$ )

For the models discussed in figure 6.6 the values  $A_{fD}$  and  $\delta$  are indicated below:

TABLE 6.2

Model	1	2	3	4	5	6
$A_{fD} (1/cm)$	1/a	1/a	2/a	1/a	2/a	2/a
$\delta (1/cm^2)$	0.12	0.96	0.48	0.96	0.48	1.62

c. Turbulence factor  $\beta$

From equation 6.40 and B acquired from figure 6.13, the turbulence factor  $\beta$  is obtained directly. If equations 6.42, 6.43 and 6.44 are valid, then it is possible to cross-check the permeability  $K_f$ .

d. Fracture width b

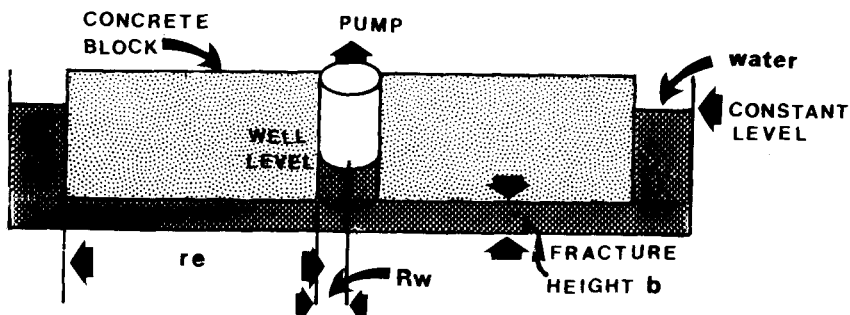
For the idealized model chosen, the fracture width b may be estimated from table 6.1. (last column)

### 6.2.3. Practical application of modelling

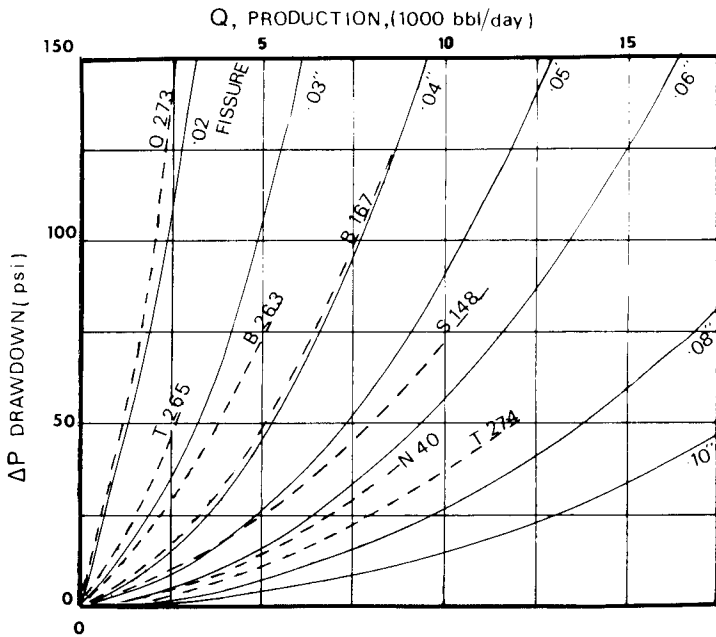
#### 6.2.3.1 Single fracture modelling (Baker's model)

##### a. Experimental procedure.

The objective of Baker's experiments was to evaluate the relationship  $Q$  vs.  $\Delta P$  in the case of a radial symmetrical flow through a single fracture. The model used by Baker<sup>15</sup> (figure 6.14) is built from a concrete base on which a circular concrete block 10 feet in diameter could be raised in order to increase fracture size. The central well of radius  $r_w = 3''$  is connected to a centrifugal pump and produces (through a single fracture) water from a basin where the water is kept at a constant level. The rates examined varied between 1000 and 22 000 barrels of oil per day for fractures with widths varying from .05 to .4 inches. A continuous recording of pressure drop and rates under stabilized conditions of flow has given the results presented in figure 6.15.



6.14 – Baker's experimental model.



6.15 – Results of Baker's model, Q vs.  $\Delta P$  for various fracture widths.

The analytical expression obtained by Baker may be reduced to the parameters:

$$A = \frac{6\mu B_o}{\pi b^3} \ln \frac{r_e}{r_w} \quad (6.64)$$

and

$$B \cong \frac{\rho B_o}{4\pi^2 b^2 r_w} \left[ \frac{1}{1.66 r_w} - \frac{\xi}{b} + \frac{1}{2r_w} \right] \quad (6.65)$$

which are similar to equations 6.59 and 6.60.

Baker also expressed a relationship between permeability  $K_f$  of a conventional reservoir and fracture width  $b$  in association with formation pay  $h$ . The relationship is written as follows:

$$h(\text{feet}) = 4.52 \times 10^9 \frac{b^3(\text{inches})}{K(\text{mD})} \quad (6.66)$$

For a fracture width of  $b = 0.1$  mm and  $K_f = 100$  mD, an equivalent pay  $h = 2.75$  feet results if Baker's model is used.

#### b. Baker's experimental results.

From the results obtained through Baker's model (figure 6.15) it is observed that the

relationship  $Q$  vs.  $\Delta P$  is linear at small rates and becomes non-linear with the increasing of the production rate  $Q$ . The linear relationship, as expected, is maintained even for high  $Q$  values when fracture width  $b$  is larger. The conventional porous medium solution has been verified by Baker's experiments and the results are given hereunder as a calculation example.

### c. Experimental results vs. theoretical approach.

The  $Q$  and  $\Delta P$  obtained (from Baker's experiment) for  $b = 0.4''$  (figure 6.15) have been used for this verification.

1. The recorded data  $Q$  vs.  $\Delta P$  from figure 6.15 are expressed as  $\Delta P/Q$  vs.  $Q$  as in figure 6.16.

2. Based on the equation,

$$\frac{\Delta P}{Q} = A + BQ$$

it will directly result from diagram figure 6.15 that:

$$A = 1.50 \times 10^{-3} \text{ Psi/Bbl/day} = 5.53 \times 10^{-5} \text{ at/cm}^3/\text{sec}$$

$$B = 1.46 \times 10^{-6} \text{ psi/(Bbl/day)}^2 = 2.92 \times 10^{-8} \text{ at}/(\text{cm}^3/\text{sec})^2$$

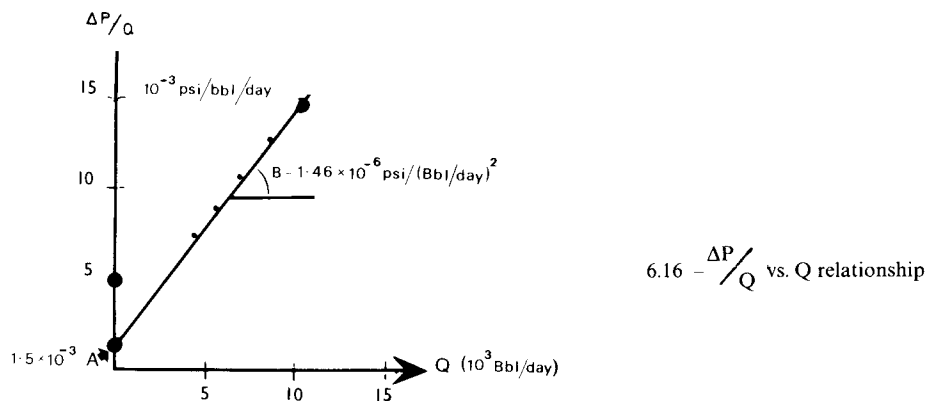
3. Parameter A. Experimental vs. theoretical matching. Based on equation 6.59,

$$A = \frac{B_o \mu_o}{2\pi k h} \ln r_e/r_w \pm \sum S$$

which in case of a fracture of width  $b$ , where  $K_{ff} = b^2/12$  and  $h = b$  it results

$$A = 6 \frac{\mu_o B_o}{\pi b^3} \ln \frac{r_e}{r_w} \pm \sum S$$

This shows the direct relationship between Baker's equation and a conventional porous medium.



Neglecting the skin effect  $\sum S$  and based on Baker's experimental data,  $b = 0.4''$ ,  $r_w = 3''$ ,  $r_e = 5'$ ;  $\mu_w \cong 1$ ,  $B_w = 1$ , the result is:

$$A = 6 \frac{\mu_w B_w}{\pi b^3} \ln \frac{r_e}{r_w} = 6 \frac{10^{-2}(\text{Poise})}{\pi \times 0.101^3 (\text{cm}^3)} \ln \frac{1.524}{0.0762}$$

$$A \cong 55 \frac{\text{dyne/cm}^2}{\text{cm}^3/\text{sec}} \cong 1.5 \times 10^{-3} \text{ psi/Bbl/day}$$

The same value was obtained from experimental results in figure 6.16, which shows an excellent matching between theoretical and experimental values.

4. Parameter B. Experimental vs. theoretical matching. Referring to equation 6.60 where  $h_f = b$ ,

$$B = \beta \frac{\rho B_w}{4\pi^2 b^2} \left[ \frac{1}{r_w} - \frac{1}{r_e} \right]$$

the parameters are  $r_w = 3''$ ,  $h = b = 0.4''$ ,  $B_w = 1$ ,  $\gamma_w = 1 \text{ gr/cm}^3$ ,  $r_e = 5'$ ,

$$B = \beta \frac{10^{-5} [\text{kg s}^2/\text{cm}^4]}{4 \times 3.14^2 \times 0.101^2 (\text{cm}^2)} \left[ \frac{1}{7.62} - \frac{1}{152.4} \right]$$

$$B \left[ \frac{\text{kg/cm}^2}{(\text{cm}^3/\text{sec})^2} \right] \cong \beta (1/\text{cm}) \times 3.10 \times 10^{-7}$$

The turbulence factor may be directly calculated from equations 6.42 and 6.43 and the results averaged. Since both equations are functions of permeability, this parameter (K) will be calculated from equation 6.54:

$$K_{ff} (\text{mD}) = 10^{11} \frac{b^2 (\text{cm})}{12} = 10^{11} \frac{0.101^2}{12} = 8.5 \times 10^7 \text{ mD}$$

and further

$$\text{Eq. 6.42} \rightarrow \beta_1 (1/\text{ft}) = \frac{4.16 \times 10^{10}}{K_{ff}^{1.34} (\text{mD})} = \frac{4.16 \times 10^{10}}{(8.5 \times 10^7)^{1.34}} = .985 \left( \frac{1}{\text{ft}} \right) = 3.24 \times 10^{-2} (1/\text{cm})$$

$$\text{Eq. 6.4.3} \rightarrow \beta_2 (1/\text{ft}) = \frac{2.2 \times 10^{10}}{K_{ff}^{1.19} (\text{mD})} = \frac{2.2 \times 10^{10}}{(8.5 \times 10^7)^{1.19}} = 8.06 \left( \frac{1}{\text{ft}} \right) = .265 (1/\text{cm})$$

In continuation the values B will result

$$B_1 = 3.1 \times 10^{-7} \times 3.24 \times 10^{-2} = 10^{-8} \text{ (kg/cm}^2\text{)/(cm}^3\text{/sec)}^2$$

$$B_2 = 3.1 \times 10^{-7} \times 0.265 = 8.2 \times 10^{-8} \text{ (kg/cm}^2\text{)/(cm}^3\text{/sec)}^2$$

$$\bar{B} = (B_1 + B_2)/2 = 4.6 \times 10^{-8} \text{ (kg/cm}^2\text{)/(cm}^3\text{/sec)}^2$$

If the average theoretical value  $B = 4.6 \times 10^{-8}$  is compared with the experimental  $B = 3.1 \times 10^{-8}$ , it may be stated that a good match results between theoretical and experimental data.

##### 5. Critical Reynolds number

The critical Reynolds number expressed by equation 6.28 is a function of the critical velocity  $V_{cr}$ :

$$Re_{cr} = \frac{\rho V_{cr} \times 2b}{\mu}$$

If  $\rho_w = 1$  (dyne  $\times$  sec $^2$ /cm $^4$ ),  $b = 0.101$  (cm) and  $\mu_w = 10^{-2}$  (Poise) the result is:

$$Re_{cr} = 20V_{cr} \text{ (cm/sec)}$$

The critical velocity is calculated from the maximal linear rate  $Q_{MAX,I}$  divided by the well lateral surface  $2\pi r_w b$ .

Since,  $Q_{MAX,I}$ , based on Fig. 6.16 indicates

$$Q_{MAX,I} \cong \frac{A}{B} = \frac{5.697 \times 10^{-5}}{3.1 \times 10^{-8}} \cong 1837 \text{ cm}^3/\text{sec}$$

which corresponds to  $Q \cong 1000$  Bbl/day in Fig. 6.15.

The velocity will then result

$$V_{cr} = \frac{Q_{MAX,I}}{2\pi r_w b} = \frac{1837}{6.28 \times 7.62 \times 0.101} = 30 \text{ cm/sec}$$

and therefore,

$$Re_{cr} = 20 V_{cr} = 20 \times 30 = 600$$

##### Conclusion

The matching of theoretical and experimental results concerning parameters A, B and the critical Reynolds number confirms the proposal that the conven-

tional equation of flow in a porous medium can be used to solve the problems of radial flow through a single fracture.

#### Observation

The above problem was limited to the radial flow through a fracture, disregarding the matrix thickness. The results are thus limited to intrinsic permeability  $K_{ff}$  and fracture width  $b = h$ .

In case the problem is examined in the light of fracture porosity  $\Phi_f$ , the permeability  $K_f$  may be related to the total pay  $h$  of fracture & matrix.

Based on equation 6.58

$$K_f = A_{fD} b^3 / 12 = \Phi_f b^2 / 12 = b^3 / 12h$$

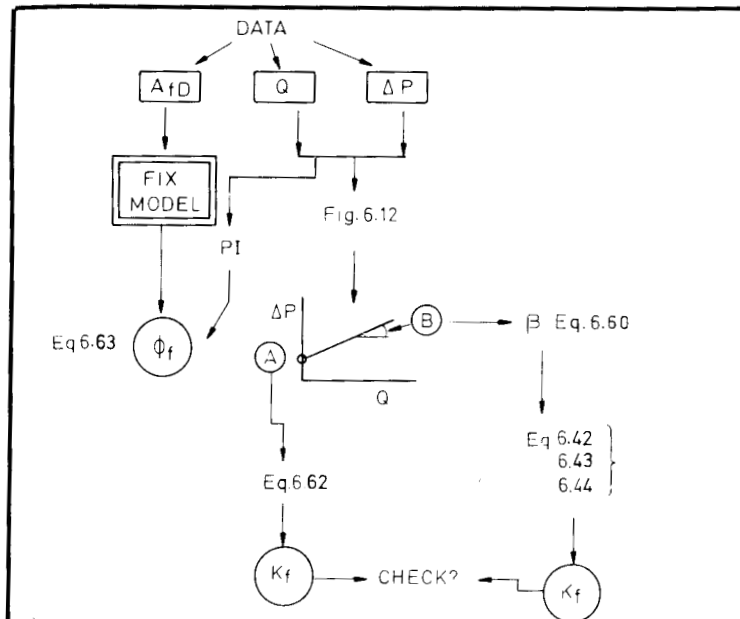
which is similar to equation 6.66.

If in the present case the fracture density  $A_{fD} = 1/m$  is considered equivalent to  $h = 1m$ , it will result that

$$K_f = \frac{0.101^3}{12 \times 100} \cong 8.5 \times 10^{-7} \text{ cm}^2 = 85D$$

#### 6.2.3.2. Fracture network modelling

The problem of an irregular fracture network may be solved by direct analogy with the porous medium, or by empirical equations resulting from field experiments.



6.17 – Calculation flow chart.

a. General procedure

The procedure is based on reservoir testing data  $Q$  vs.  $\Delta P$  obtained from various stabilized rates and on fractured density  $A_{fD}$ , resulting through fracturing studies or assumed for an idealized model. The flow chart presented in figure 6.17 shows the way of evaluating the PI and  $\beta$  through parameters A and B of a diagram such as figure 6.12. The permeability  $K_f$  obtained from A through equation 6.62 is checked with permeability  $K_f$  obtained from parameter B, through equations 6.42, 6.43, 6.44. There results from this calculation a porosity  $\Phi_f$  and a permeability  $K_f$  which for a given idealized model (Figure 6.6) will indicate that the values  $A_{fD}$ , a and b. (Table 6.1) The fracture network is therefore defined through an idealized simplified model.

b. Calculation example: PROBLEM NO. 1,

A well is tested under steady-state conditions recording various rates  $Q$  (STBD) and pressure drop  $\Delta P = P_e - P_w$  (psi), as shown in the table hereunder:

Recorded Data			Calculated
Measure	$Q$ (STBD)	$\Delta P$ (PSI)	$\Delta P/Q$ (PSI/STBD)
1	3360	17.8	$5.3 \times 10^{-3}$
2	7080	58.7	$8.3 \times 10^{-3}$
3	8920	87.4	$9.8 \times 10^{-3}$
4	10 660	123.0	$11.6 \times 10^{-3}$

The following additional data are available:

oil viscosity  $\mu_o = 0.7$  cP      Total pay  $h = 160$  m

oil volume factor  $B_o = 1.32$    Well radius  $r_w = 10$  cm

oil gravity  $\rho_o = 0.8$    External boundary radius  $r_e = 500$  m

Estimate the reservoir permeability, porosity and fracture width assuming first the Kazemi model and then Warren-Root model, knowing that  $a = 1/L_{fD} = 100$  cm.

Solution

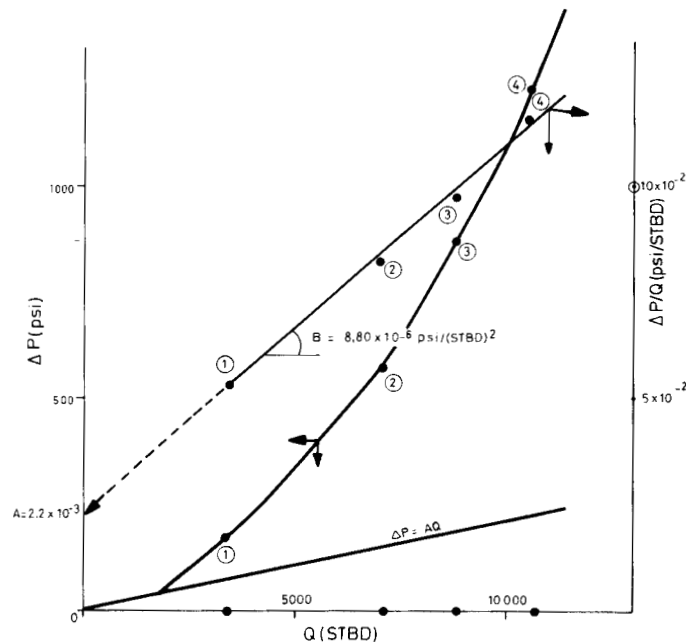
b.1 Evaluation of basic relationship

Based on testing data a diagram is obtained such as in figure 6.18 which represents the recorded  $\Delta P$  vs.  $Q$  and the calculated  $\Delta P/Q$  vs. relationships. From the extrapolation of  $\Delta P/Q$  vs.  $Q$  the following ordinate will result:

$$A = \frac{1}{PI} = 2.20 \times 10^{-2} \left( \frac{\text{psi}}{\text{STBD}} \right) \cong 8.16 \times 10^{-4} \left( \text{at/cm}^3/\text{sec} \right)$$

and from the straight line slope the result is:

$$B = 8.80 \times 10^{-6} \text{ psi}/(\text{STBD})^2 = 1.77 \times 10^{-7} \text{ at}/(\text{cm}^3/\text{sec})^2$$



6.18 – Results obtained from flowmeter recordings.

### •• Productivity index (linear flow)

Based on definition of A as reciprocal value of productivity index in the absence of turbulence

$$PI = \frac{1}{A} = 1/8.16 \times 10^{-4} \cong 1200 (\text{cm}^3/\text{s}/\text{at}) = 45,6 \text{ Bbl/day}/\text{psi}$$

### •• Equation of flow

Based on A, B and equation 6.41 the general equation of flow is:

$$\Delta P (\text{psi}) = 2.23 \times 10^{-3} Q(\text{STBD}) + 8.80 \times 10^{-7} Q^2(\text{STBD})^2$$

•• Evaluation of permeability

By using equation 6.55:

$$K_f = \frac{\mu_o B_o \ln r_e/r_w}{6.28 \times h \times A} = \frac{0.7 \times 1.32 \times \ln 5000}{6.28 \times 1.6 \times 10^4 \times 8.36 \times 10^{-4}} \cong 93.7 \text{ m.D.}$$

•• Evaluation of turbulence factor  $\beta$

Using the conventional reservoir expression of B (equation 6.60), the following equation is calculated:

$$\beta = \frac{4\pi^2 h^2 r_w B}{\rho_o B_o}$$

or

$$\beta = \frac{4 \times 3.14^2 \times 1.6^2 \times (10^4)^2 \times 10 \times 1.77 \times 10^{-7}}{0.8 \times 10^{-6} (\text{kg sec}^2/\text{cm}^4) \times 1.3} \cong 1.75 \times 10^{10} (1/\text{cm}) = \\ 5.32 \times 10^{11} (1/\text{feet})$$

b.2 Kazemi<sup>16</sup> model case

Based on the model described in figure 6.9, the relationship among various parameters corresponds to case 1 in figure 6.6 and tables 4.6 (chapter 4) and 6.1.

•• Porosity

From table 6.1:

$$\Phi_f = (12K_f A_{fD}^2)^{3/3} = (12 \times 0.0937 \times 10^{-8} (\text{cm}^2) \times 10^{-4} (1/\text{cm}^2))^{0.333} \\ = 1.04 \times 10^{-4} = 0.0104 \%$$

A similar result is obtained from equation 6.56 where PI = 12,100 (cm<sup>3</sup>/sec/at) a = 1/L<sub>fD</sub> = 100 (cm), δ = 0.12 (table 6.2).

•• Permeability K<sub>f</sub> – function of β and Φ<sub>f</sub>

From equation 6.40 the following is calculated:

$$K_f (\text{mD}) = \frac{1}{\Phi_f (\text{fact})} \times \left[ 2.2 \times 10^9 / \beta (1/\text{ft}) \right]^{1/1.085} = \frac{1}{1.04 \times 10^{-4}} \left[ \frac{2.2 \times 10^9}{5.32 \times 10^{11}} \right]^{1/1.085} \\ K_f = 61 \text{ mD.}$$

There is a negligible difference between K<sub>fB</sub> obtained from parameter B and K<sub>fA</sub> obtained from parameter A. If K<sub>fB</sub> is different from K<sub>fA</sub> this might indicate the influence of skin effect, as a result of neglecting  $\sum S$  in equation 6.59.

•• Intrinsic permeability  $K_f$  – function of  $K_f$  and  $\Phi_f$

From equation 6.49 the following is calculated:

$$K_{ff} = K_f / \Phi_f = 0.0937 / 1.04 \times 10^{-4} = 900 \text{ (Darcy)}$$

•• Fracture width b

From table 6.1, model 1, and using  $K_f$  obtained from parameter A

$$b = (12k_f/\Phi_f)^{0.5} = (12 \times 0.0937 \times 10^{-8})^{0.5} = 1.04 \times 10^{-2} \text{ cm}$$

•• Reynolds number

The limit of linear flow is observed for the rate of  $Q \geq 2000 \text{ STB/D} = 3680 \text{ cm}^3/\text{sec}$ . The critical velocity in a single fracture at well radius  $r_w$  will result as:

$$V_{er} = \frac{Q_{cr} \times B_o}{6.28 \times r_w \times n \times b} = \frac{3680 \times 1.32}{6.28 \times 10 \times 160} = 46.5 \text{ cm/sec}$$

$$\text{where } n = h \times L_{fD} = 16000 \text{ (cm)} \times 10^{-2} \text{ (1/cm)} = 160$$

From equation 6.28:

$$Re_{cr} = \frac{\rho \times 2 \times b \times V_{crit}}{\mu} = \frac{0.8 \times 2 \times 0.0224 \times 46,5}{0.7 \times 10^{-2}} = 238$$

Warren-Root<sup>17</sup> model

•• Porosity

From table 6.1, case 6:

$$\Phi_f = (162 K_f A_{fD}^2)^{0.33} = \left( 162 \times 0.0937 \times 10^{-8} (\text{cm}^2) \times 4 \times 10^{-4} \text{ (1/cm}^2) \right)^{0.33}$$

since,  $A_{fD}^2 = \left(\frac{2}{a}\right)^2$ ;  $\Phi_f = 3.92 \times 10^{-4} = 0.0392\%$

From equation 6.63 and table 6.2

$$\Phi_f = \left( PI \frac{\mu_o B_o \ln r_e/r_w}{2\pi h} A_{fD}^2 \times \delta \right)^{0.33}$$

will result

$$\Phi_f = \left( 1200 \times \frac{0.7 \times 1.32 \times 8.51}{6.28 \times 16000} \times \frac{4}{10^4} \times 1.62 \right)^{0.33} = 3.92 \times 10^{-2} \%$$

•• Intrinsic permeability  $K_{ff}$

From equation 6.54:

$$K_{ff} = K_f/\Phi_f = 0.0937/3.92 \times 10^{-4} = 239 \text{ Darcy}$$

•• Fracture width b

From table 6.1, model 6:

$$b = (18 K_f/\Phi_f)^{0.5} = (18 \times 0.0937 \times 10^{-8}/3.92 \times 10^{-4})^{0.5}$$

$$b = 6.54 \times 10^{-3} \text{ cm}$$

#### 6.2.3.3. Use of empirical equation

Based on well testing experience<sup>13</sup> in the Iranian fields the basic law of flow expressed by,

$$\Delta P = AQ + BQ^2 \quad (6.37)$$

is valid.

The constants A and B are expressed by:

$$A \left( \frac{\text{psi}/\text{ft}^3/\text{day}}{} \right) = 0.00715 \frac{\mu_o \text{ (poise)} \times B_o}{b_A^3 \text{ (inch)}} \log r_e/r_o \quad (6.67)$$

and

$$B \left( \frac{\text{psi}/(\text{ft}^3/\text{day})^2}{\text{ }} \right) = 0.015 \frac{\rho B_o^2}{r_w^2 b_B} \left( 1 + \frac{0.083}{b_B} \right) \quad (6.68)$$

where  $\rho$  (gr  $\times$  sec<sup>2</sup>/cm<sup>4</sup>);  $r_w$  (inch);  $b_B$  (inch).

The limit of linear flow is, at radius  $r_o$ , expressed by:

$$r_o = 0.045 \frac{\rho Q B_o}{\mu}$$

where  $r_o$  (inches),  $\rho$  (gr  $\times$  sec<sup>2</sup>/cm<sup>4</sup>);  $\mu$  (poise).

The calculation procedure remains the same: the use of Baker model, the estimation from production data of parameters A and B, and then evaluation of the equivalent fracture width  $b_A$  and  $b_B$  through the equations 6.67 and 6.68. In fact, these equations are basically equivalent to the equations 6.64, 6.65 from Baker's example, which were discussed in the application developed in calculation example No. 1.

It has been shown empirically<sup>19</sup> that the skin effect of pressure may be evaluated with good approximation from:

$$\Delta P_{\text{Skin}} \cong 2 B Q^2 \quad (6.69)$$

This equation (6.69) may not be valid if the well testing evaluation is performed as usual after the well stimulation. From field experience<sup>19</sup> it is also assumed that the linear pressure drop  $\Delta P = A Q$  takes place mainly in a zone of larger radius than  $r_o = 10$  m.

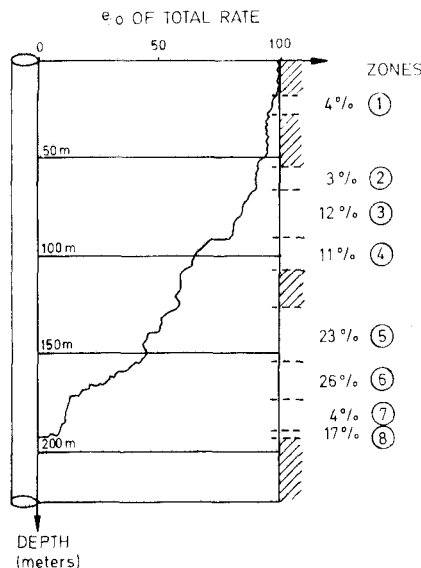
#### 6.2.3.4. Water and gas coning evaluation.<sup>19, 20, 21</sup>

The problem of coning was examined by Muskat<sup>21</sup> in a conventional reservoir formed by intergranular pores, where the flow is governed by Darcy's law.

The general consideration concerning the formation and development of coning will remain valid for a fractured reservoir, but the flowing conditions must be reviewed through specific conditions which govern the flow in fractures. The basic equations are almost the same, independent of the fact that the vertical fissures may or may not be present throughout the water or gas levels, so long as the continuity of the fracture network is developed over the oil and water zones, or oil and gas cap zones.

##### a. Simplified approach.

From Iranian fractured reservoir experience<sup>17</sup> it is evident that the flow towards a well takes place through a fracture network and not just through one fracture. The flow meter, if run into an open hole, indicates the fracture distribution to be similar to that shown in figure 6.19 where zones of high fluid entry rates (zones 4,6) and reduced fluid entry zones (zones 1, 2, 7) exist.

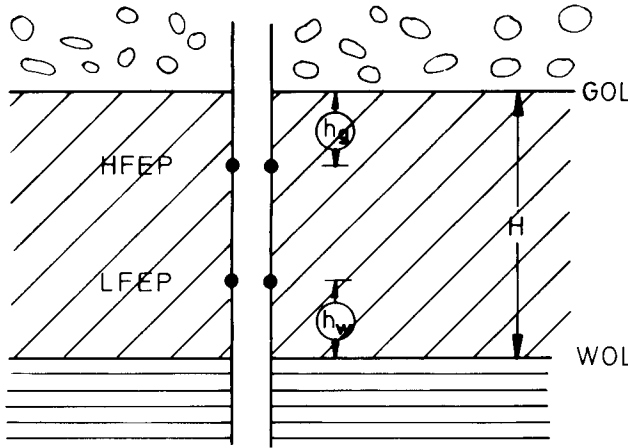


6.19. – Flow meter results.

The fractured zone, either in an open hole or in a completed and perforated well, will have a certain producing pay delimited by two upper and lower boundaries (figure 6.20):

- HFEP: the highest fluid entry point
- LFEP: the lowest fluid entry point

The relationship between HFEP and LFEP and respective gas-oil and water-oil contacts in the fracture network (GOL and WOL) is indicated by the height  $h_g$  and  $h_w$  (figure 6.20) equivalent to the gas coning and water coning heights respectively.



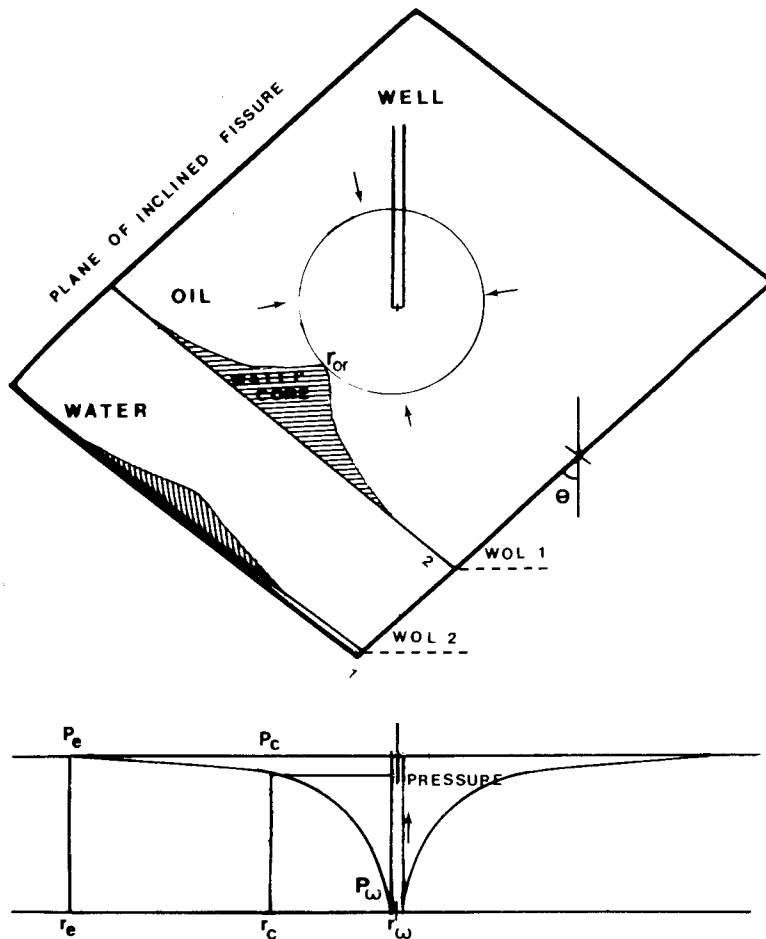
6.20 – Sketch of water-oil and gas-oil contacts vs. LFEP and HFEP.

If the behaviour of the fracture network is assumed to be similar to a conventional intergranular porous medium, the distribution of pressure will follow a logarithmic variation and, therefore, a critical zone of radius  $r_{cr}$  will result around the wellbore (as shown in figure 6.21).

Applying Muskat's equation to various WOL positions (figure 6.21) at critical radius  $r_{cr}$  the coning will start rising when,

$$\left[ \frac{dp}{dr} \right]_{r=r_{cr}} > \left( G_w - G_o \right) \times \cos \theta \quad (6.70)$$

Based on the above considerations and the type of flow (laminar or turbulent), Birks<sup>19</sup> defined two types of water coning: *critical coning* and *safe coning* in relation to the order of magnitude of parameters A and B of equation 6.41.



6.21 – Water coning, function of movable water-oil contact position.

*Critical coning* refers to the *lowest fluid entry point* (LFEP) defined in relation to the pressure drop in the absence of the turbulence effect ( $B = 0$ ), and is expressed by:

$$(LFEP)_{CRITIC} = h_{w, cr} = \frac{AQ}{(G_w - G_o) 2.303 \log \frac{r_e}{r_o}} \quad (6.71)$$

which may be approximated (if  $r_e/r_w \geq 1000$ ) with,

$$h_{w, cr} \cong \frac{AQ}{6.9 (G_w - G_o)} \quad (6.71')$$

where  $G_w$  and  $G_o$  are the respective water and oil gradients.

This equation includes Birks' assumption that the linear flow will remain limited to the zone between the external boundary and radius  $r_o \cong 10$  feet.

*Safe coning* refers to flowing conditions where, for high flow rates, the pressure drop around the wellbore increases very much and a turbulence pressure drop is developed. By using the same considerations mentioned above the following will result:

$$(LFEP)_{SAFE} = h_{w, safe} \cong \frac{AQ + BQ^2}{6.9 (G_w - G_o)} \quad (6.72)$$

In order to produce high rates in thin pay reservoirs it is necessary to increase the pressure drop, and consequently turbulent flow might occur. It could be stated that, in general, equation 6.71' is valid for large pay and equation 6.72 for thin pay.

From Iranian field experience<sup>19, 20</sup> a series of principles concerning the calculation of water coning have been established:

- The effective drainage radius to be used in calculations is  $r_e \cong 1000$  feet.
- If total pay  $200' < h < 1000'$  the critical coning theory is used (equation 6.71'), where pressure drop may be expressed by,

$$\Delta P = AQ$$

- If total pay  $h < 200'$  the *safe coning* conditions have to be used (equation 6.72), where pressure drop is expressed by,

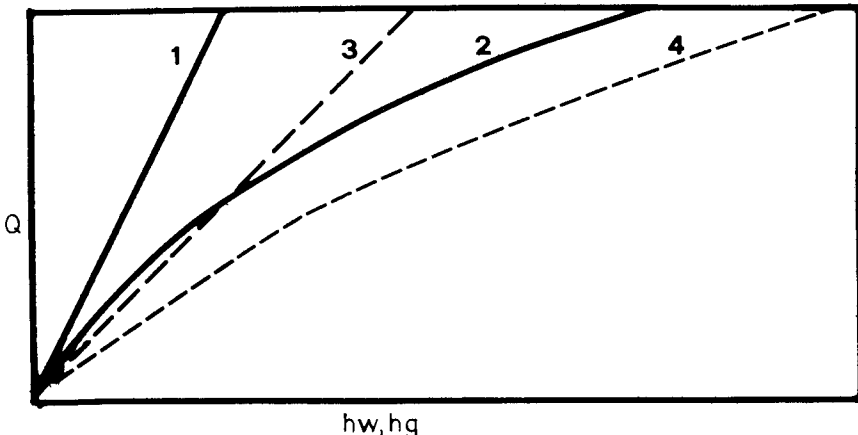
$$\Delta P = AQ + BQ^2$$

In order to design the well completion in the case of an oil zone bounded by a gas cap and an aquifer, it is necessary to use equations 6.71' and 6.72 simultaneously in order to evaluate the relationship  $h_w$  vs.  $Q$  as shown in figure 6.22.

Gas coning will have a similar expression as equations 6.71' and 6.72, the only difference being that the gradient will be related to oil and gas gradients  $G_o, G_g$ . The critical and safe heights  $h_g$  may be expressed as,

$$(HFEP)_{CRITIC} = h_{g, cr} = \frac{AQ}{6.9 \times (G_o - G_g)} \quad (6.73)$$

$$(HFEP)_{SAFE} = h_{g, safe} = \frac{AQ + BQ^2}{6.9 (G_o - G_g)} \quad (6.74)$$



6.22 – Critical and safe height vs.  $Q$ : 1)  $h_{g, cr}$ ; 2)  $h_{w, cr}$ ; 3)  $h_{g, safe}$ ; 4)  $h_{w, safe}$ .

#### Observations

- Equation 6.70 indicates the correlation between fluid gradients and structural slope (figure 6.21) through the expression of angle  $\theta$ . If the fractures between WOL and LFEP or GOL and HFEP are vertical (figure 6.20) then  $\cos \theta = 1$ . But if vertical fractures are absent or cut by horizontal fractures and/or interrupted by stylolites,  $\cos \theta$  decreases to very small values, permitting higher pressure gradients, equivalent to high water-free rates or high rates with reduced coning risk.
- Due to the difference between gas-water gradient and water-oil gradient,

$$G_w - G_g \gg G_w - G_o$$

the allowable gas coning rate is higher than the water coning rate. This may be observed also in figure 6.22 where, for the same pressure drop  $\Delta P$  higher values for both heights  $h_{w,cr}$  and  $h_{w,safe}$  are required (straight line 1 compared with straight line 3, and curve 2 compared with curve 4 in figure 6.22).

- By the advancement of WOL and GOL the critical and safe rates decline as a result of the reduction of  $h_w$  and  $h_g$ . It, therefore, becomes possible to predict the relationship between fluid withdrawal, WOL and GOL advancement, and the maximum well rate produced without coning risk, versus time.

#### b. Calculation example: PROBLEM No. 2.

Using the modified data of PROBLEM No. 1, the well will be perforated as in Figure 6.20 on intervals of 30 m, so that HFEP = 50 m and LFEP = 80 m (see Fig. 6.20).

The following are required:

- The relationships  $h_{cr}$  and  $h_{safe}$  vs.  $Q$  (for gas and water coning risk evaluation.)
- Data based on given in table 6.2 (columns 1,2,3) concerning the water table and gas-oil contact advancement in time (obtained from material balance calculation) to evaluate the maximum rate vs. time.
- Additional data: Initial well rate 20 000 STBD; Reservoir fluid densities are,  $\rho_w = 1.05$ ;  $\rho_o = 0.8$ ;  $\rho_g = 0.25$ .

### 1. Basic equation

Solution

The basic data obtained from problem 1 (same A, modified B)  $A = 8.16 \times 10^{-4}$  (at/cm<sup>3</sup>/sec) and  $B = 1.77 \times 10^{-8}$  at/(cm<sup>3</sup>/sec)<sup>2</sup> are introduced in water coning and gas coning equations 6.71, 6.72 and 6.74 under both conditions (safe and critical).

The critical heights result as shown hereunder:

$$h_{w, cr} \text{ (meter)} = \frac{AQ}{6.9(\gamma_w - \gamma_o)} = \frac{8.16 \times 10^{-4} Q \text{ (cm}^3/\text{sec)}}{6.9 \times 0.25 \times 10^{-3} \text{ at/cm}} \cong 2.60 \times 10^{-3} Q(\text{STBD})$$

$$h_{w, safe} \text{ (meter)} = \frac{AQ + BQ^2}{6.9(\gamma_w - \gamma_o)} = \frac{8.16 \times 10^{-4} Q + 1.77 \times 10^{-8} Q^2 \text{ (cm}^3/\text{sec})^2}{6.9 \times 0.25 \times 10^{-3} \text{ (at/cm)}} \cong \\ 2.6 \times 10^{-3} Q(\text{STBD}) + 3.05 \times 10^{-8} Q^2(\text{STBD})^2$$

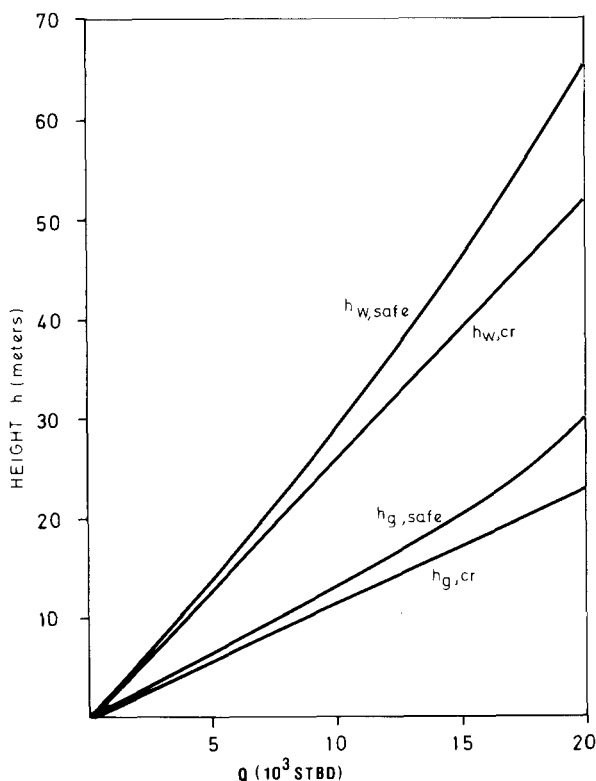
$$h_{g, cr} \text{ (meter)} = \frac{AQ}{6.9(\gamma_o - \gamma_g)} = \frac{8.16 \times 10^{-4} Q \text{ (cm}^3/\text{sec)}}{6.9 \times 0.55 \times 10^{-3}} \cong 1.18 \times 10^{-3} Q(\text{STBD})$$

$$h_{g, safe} \text{ (meter)} = \frac{AQ + BQ^2}{6.9(\gamma_o - \gamma_g)} = \frac{8.16 \times 10^{-4} Q + 1.77 \times 10^{-8} Q^2 \text{ (cm}^3/\text{sec})^2}{6.9 \times 0.55 \times 10^{-3}} \cong \\ 1.18 \times 10^{-3} Q(\text{STBD}) + 1.38 \times 10^{-8} Q^2(\text{STBD})^2$$

The results are plotted in figure 6.23 as relationship  $Q$  vs.  $h$  where the variations of  $h_w$  and  $h_g$  required in critical and safe conditions of water coning may be observed.

Table 6.2

Given data			Available height		water coning	gas coning	Final Q safe
Year	$H_w$	$H_g$	LFEP - $h_w$	HFEP - $h_g$	$Q_{safe}$	$Q_{safe}$	limited by
	(m)	(m)	(m)	(m)	STBD	STBD	STBD
1	6	4	74	46	20 000	20 000	20 000 no limit
2	10	8	70	42	20 000	20 000	20 000 »
3	14	10	66	40	20 000	20 000	20 000 »
4	20	16	60	34	18 600	20 000	18 600 $W_{coning}$
5	23	20	57	30	17 500	20 000	17 500 »
6	28	24	52	26	16 600	18 260	16 600 »
7	33	28	47	22	15 300	15 300	15 300 »
8	38	30	42	20	13 600	14 800	13 600 »
9	40	32	40	17	12 500	12 000	12 000 gas coning
10	42	38	38	12	12 000	10 000	10 000 »



6.23 – Rate Q vs. safe and critical heights.

## 2. Well rate vs. time

Based on data of columns 1, 2, 3 the advancement in time of water table  $H_w$  and gas-oil contact  $H_g$  (Tab. 6.2) is known. The available pay will result as,

$h_w = LFEP - H_w$ , for water coning (column 4, Table 6.2).

and  $h_g = HFEP - H_g$  for gas coning (column 5, Table 6.2).

Based on available height  $h_w$  and  $h_g$  the maximum safe rates without danger of water-coning (column 6) and gas-coning (column 7) will result from Fig. 6.23. The power rate value (column 8) represents the safe rate vs. time in a project calculation (Table 6.2).

Example: At 5th year,  $H_w = 23$  m and  $H_g = 20$  m. It results that available height for water coning is 57 m and for gas coning 30 m. From Fig. 6.23 it results that for water-coning  $Q_{safe} = 17,500$  STBD and for gas-coning  $Q_{safe} = 20,000$  STBD. The lower rate will be the safe rate in order to prevent coning flow.

## 6.3 FLOW OF GAS IN FRACTURED RESERVOIR

### 6.3.1. Basic concepts and experimental results

The flow of gas through fractures is of particular interest since many gas reservoirs belong to the category of naturally fractured reservoirs.

The problem has been examined through a rigorous mathematical solution and the results obtained show that the behaviour of the flow in a fracture is essentially dependent on critical condition between the entry and exit pressures of the fracture.

Table 6.3 LIQUID VS. GAS, BASIC EQUATIONS OF FLOW

LIQUID FLOW	No. Equat.	GAS FLOW	No. Equat.	OBSERVATIONS
$v = (b^2/12\mu) \frac{dp}{dx}$	6.32	$v = b^2 \left( \frac{R_o T}{M \rho} \right) \frac{dp}{dx}$	6.75	
$q = (b^3/12\mu) \frac{dp}{dx}$	(6.32')	$q = \left( b^3/12\mu \right) \left( \frac{R_o T}{M \rho} \right) \frac{dp}{dx}$	6.75'	{ Laminar flow
$\lambda = 6/Re$	(6.32'')	$\lambda = 6/Re$	6.76	
$Re = \rho b V / 2\mu$		$Re = \frac{q_o P_o M}{2R_o T \mu}$	6.77	
$\lambda = (b/\rho V^2) \frac{dp}{dx}$		$\lambda = \frac{b^3 R_o T}{\rho M q^2} \frac{dp}{dx}$	6.78	{ Flowing parameters
$v = 4,7 \left[ b^5 \left( \frac{dp}{dx} \right) / \mu \rho^3 \right]^{1/7}$	6.33'	$v = 4,7 \left[ \frac{b^2}{\mu} \left( \frac{2R_o T}{M \rho} \right)^3 \left( \frac{dp}{dx} \right)^4 \right]^{1/7}$	6.79	
$q = 4,76 \left[ b^5 \left( \frac{dp}{dx} \right)^4 / \mu \rho^3 \right]^{1/7}$	6.33'	$q = 4,76 \left[ \frac{b^2}{\mu} \left( 2R_o T / \mu \rho \right) \left( \frac{dp}{dx} \right)^4 \right]^{1/7}$	6.79'	{ turbulent flow
$\lambda = 0,056/Re^{1/4}$	6.34	$\lambda = 0,056/Re^{1/4}$	6.80	

Another approach for solving the gas flow through a fracture was the analogy with liquid flow. The results obtained from experiments on liquid flow have been extended to the specific characteristics of gas such as compressibility and density.

The equation obtained in section 6.1 for basic parameters of liquid flow under laminar or turbulent conditions have been reviewed in the case of gas as shown in Table 6.3.

The equations 6.32, 6.33, 6.34 have been modified through the gas density expressed as a function of average pressure

$$\bar{P} = \frac{P_1 + P_2}{2}$$

where  $P_1$  and  $P_2$  are respectively the entry and exit pressure in a fracture.

The basic equation expressing the liquid flow in Table 6.3 for laminar and turbulent flow as well as Reynolds expression are translated in gas flow equations through density expression

$$\rho = \frac{p_o M}{R_o T}$$

and by using the rate as function of unit extension of fracture

$$q = b \times l \times v$$

The experiments for evaluation of the validity of these equations have been carried out on special models, by varying the rates, as well as the fractures' opening, length and width.

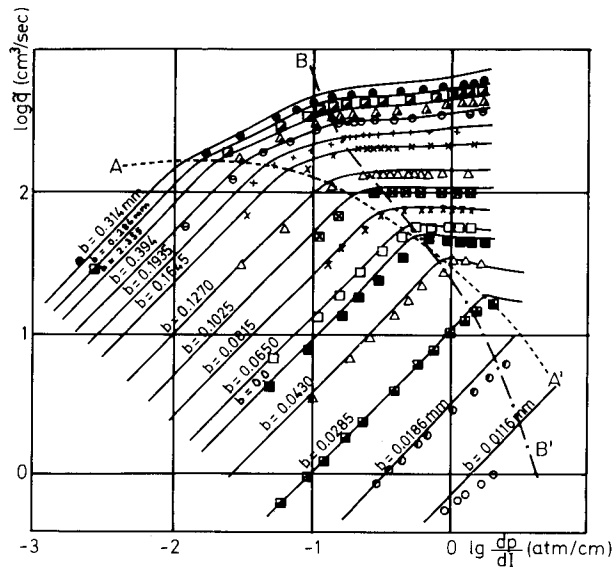
Initially the experiments were concluded on large fracture openings, varying between 0.45 – 6 mm, and a constant length of 10 cm. The gas used was nitrogen at an average temperature of 20°C; the characteristics were:

$$\rho = 1.125 \times 10^{-5} \text{ gr/cm}^3; \mu_{20^\circ\text{C}} = 1.75 \times 10^{-4} \text{ gr/cm} \times \text{sec}; M = 28.02 \text{ gr/mol};$$

At a further stage the same model has been used for narrow fractures varying between 0.011 and 0.031 mm. The pressure measurements have been accurately recorded and the results presented in Fig. 6.24 and 6.25. The two log-log diagrams show the variation of rate vs. pressure gradient ( $dp/dx$ ) and  $\lambda$  versus  $Re$ . In both cases an average rate value was used, by referring the rate measured at entry point of fractures  $q_{P_1}$  to the fracture section,

$$\tilde{q} = q_{P_1}/b \sqrt{\frac{R_o T_o}{M}}$$

The pressure gradient is expressed by  $\Delta P/L = (P_1 - P_2)L = (P_1 - P_2)/L$  as a difference between entry and exit point of a single fracture.



6.24 – Relationship rate ( $q$ ) vs. pressure gradient ( $dp/dx$ ) in the case of gas flowing through thin fractures ( $0.0116 < b < 0.314 \text{ mm}$ ).

In fig. 6.24 the straight-lines having a slope of  $45^\circ$  in the log-log scale represent the linear relationship between  $q$  and pressure gradient  $dp/dx$  as result of laminar flow. The limit of these straight-lines is indicated by the line  $A-A'$ , and in this interval the pressure drop or rate has to be calculated by using the equations 6.75 and 6.75' (Table 6.3).

A certain transition is noted for larger values of opening  $b$ , for rates between  $200-300 \text{ cm}^3/\text{sec}$ . At the end of transition zone the pressure gradients are increasing considerably for small increments of rate as may be observed in Fig. 6.24. The line  $B-B'$  represents the critical pressure which is related to maximum exit velocity from the fracture.

In Fig. 6.25 the expression  $\lambda$  vs.  $Re$  based on equations 6.77 and 6.78 is represented. It is interesting to note that during the laminar flowing condition of gas, the same basic relation obtained for liquid flow fractures is maintained,

$$\lambda = 6/Re \quad (6.76)$$

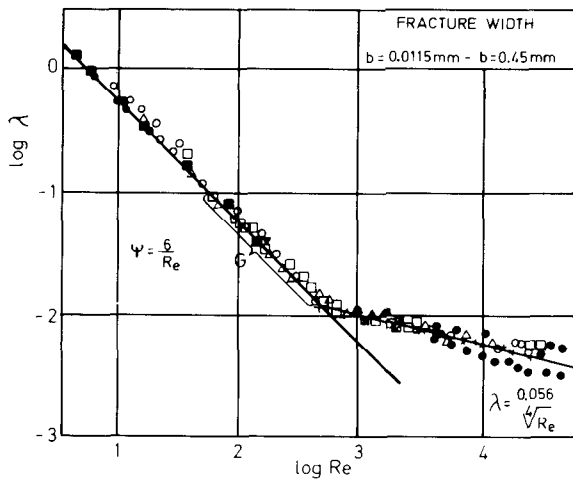
The requirements also indicate that the critical Reynolds number for gas glow may be approximated (fig. 6.25) in the range of

$$Re_{cr} \cong 1000$$

The experiments have also demonstrated that in turbulent flow of gas through a fracture ( $Re > 1000$ ) the Blasius  $\lambda$ - $Re$  relationship may be applied in the form

$$\lambda = 0.56/Re^{0.25} \quad (6.80)$$

where  $\lambda$  and  $Re$  are expressed by equations 6.77 and 6.78 (Table 6.3)



6.25 – Relationship  $\lambda - R_e$  in case of gas flowing through medium and thin fractures.

### 6.3.2. Radial symmetrical flow of gas toward a well

Based on the experimental results discussed in section 6.31 for the flow of gas in a single fracture, in which the results obtained for liquid flow may be extended to the gas case, the solution through a porous medium approach may be acceptable for a fracture network. Taking into consideration the results obtained in case of gas flow toward a well through a porous medium and introducing the specific characteristics of a fractured reservoir, an approximate procedure may be elaborated, as is presented hereunder.

- The basic relation between pressure drop and rate under turbulence and laminar flow may be expressed in a general form as

$$\Delta(P^2) = AQ + BQ^2 \quad (6.81)$$

which by analogy with a conventional reservoir is represented by:

$$\begin{aligned}\Delta(P^2) &= .135 \frac{Q \mu_g Z T}{k h} [\ln r_e/r_w + \sum S] + \\ &+ 3.163 \times 10^{-19} \frac{\beta G Z T Q^2}{h_{eff}^2} \left( \frac{1}{r_w} - \frac{1}{r_e} \right)\end{aligned}\quad (6.82)$$

where  $Q$  ( $\text{Nm}^3/\text{day}$ ),  $P$  (atm),  $K$  ( $\text{mD}$ ),  $h$  (m),  $T$  ( $^\circ\text{K}$ )  $\beta$  ( $1/\text{m}$ ) and  $r$  (m).

- The calculation procedure is similar to that followed in a conventional reservoir when the gas is flowing toward a well:
- Based on steady-state recorded data  $Q$ ,  $P_{wf}$ ,  $P_s$  the equation of flow

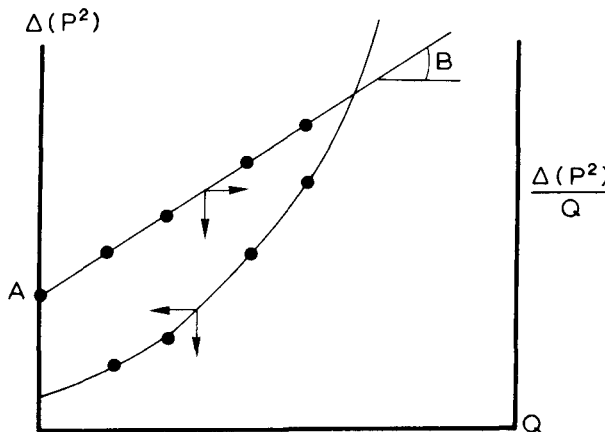
$\Delta(P^2)/Q$  vs.  $Q$  is

$$\frac{\Delta(P^2)}{Q} = A + BQ \quad (6.83)$$

By representing the straight-line  $\Delta(P^2)/Q$  vs.  $Q$  as in Figure 6.26, it is possible to evaluate,

value  $A$  – at  $Q = 0$

value  $B$  – as slope  $\Delta[\Delta(P^2)/Q]/\Delta Q$



6.26 – Basic relationship  $Q$  vs.  $\Delta(P^2)$  and  $Q$  vs.  $\Delta(P^2)/Q$  in the case of gas flowing through a fracture network.

• The evaluation of  $k_f$  may be obtained through the equation

$$A = 0.135 \frac{\mu_g ZT}{K_f h} \left[ \ln \frac{r_e}{r_w} + \sum S \right] \quad (6.84)$$

where all parameters are known, including  $\sum S$  which is obtained from the transient pressure interpretation.

Indirectly from parameter B, through the turbulence factor  $\beta$  resulting from the equation.

$$B = 3.169 \times 10^{19} \frac{\beta GZT}{h_{eff}^2} \frac{1}{r_w} \quad (6.85)$$

and further from equations 6.42, 6.43 and/or 6.44.

#### Observations

- The above method is a simple *extension of* the conventional gas reservoir to the fractured reservoir and may be valid *only* if the fracture density is high and the distribution of fractures relatively uniform.
- In the case of an open hole well, it is normal to use equation 6.85 for the total pay  $h$ , but in the case of a partially opened or partially penetrated well, it is necessary to introduce a corrected value  $h_{eff}$  instead of total pay  $h$ . This correction is essential since term B must include in one way or another the effect of the geometrical skin.
- In term A, equation 6.84 is very important if  $\sum S$  is to be accurately evaluated from the transient pressure vs. time relationship. Often due to well acidizing which takes place before starting the well testing, a negative skin value may be expected.

#### Calculation Example: PROBLEM No. 3

Through testing under steady-state conditions of a gas well in a fractured reservoir, the following relationship between rate  $Q$  and well pressure  $P_w$  (columns 1 and 2) was determined:

$Q$ (Nm <sup>3</sup> /day)	$P_w$ (atm) (1)	$P_w^2$ (atm <sup>2</sup> ) (3)	$\Delta(P^2)$ (atm <sup>2</sup> ) (4)	$\Delta(P^2)/Q$ (atm <sup>2</sup> /Nm <sup>3</sup> /day) (5)
260 000	209,2	43 784	316	$1.215 \times 10^{-3}$
480 000	208,10	43 337	763	$1.589 \times 10^{-3}$
860 000	205,50	42 225	1874	$2.180 \times 10^{-3}$
130 000	199,30	39 720	4380	$3.224 \times 10^{-3}$

- Static reservoir pressure:  $P_s = 210$  at
- Total pay of the open hole well:  $h = 190$  m
- Viscosity:  $\mu_g = 0.0178$  (c.P); Temp:  $T = 333^\circ\text{K}$
- Skin effect  $\sum S = +6,8$  was obtained from transient pressure analysis.

Requirements:

1. Basic equation of flow
2. Since the fracture density is  $L_{fd} = 2/\text{m}$ , to evaluate the characteristics of the reservoir in the case of a cubic idealized block model (Type model 6 in Fig. 6.6 and table 6.1).

Solution

### 1. Flow equation of flow

Based on  $P_w^2$  (column 3) and on static pressure  $P_s^2$  the pressure drop  $\Delta(P^2)$  is obtained in column 4. The characteristic curve  $Q - \Delta(P^2)$  indicates the presence of a linear flow at low rates and of a turbulent flow at high rates (figure 6.27).

Based on equation 6.81 the ratio  $\Delta(P^2)/Q$  (column 5) is expressed as a function of rate  $Q$  (figure 6.27). The results are:

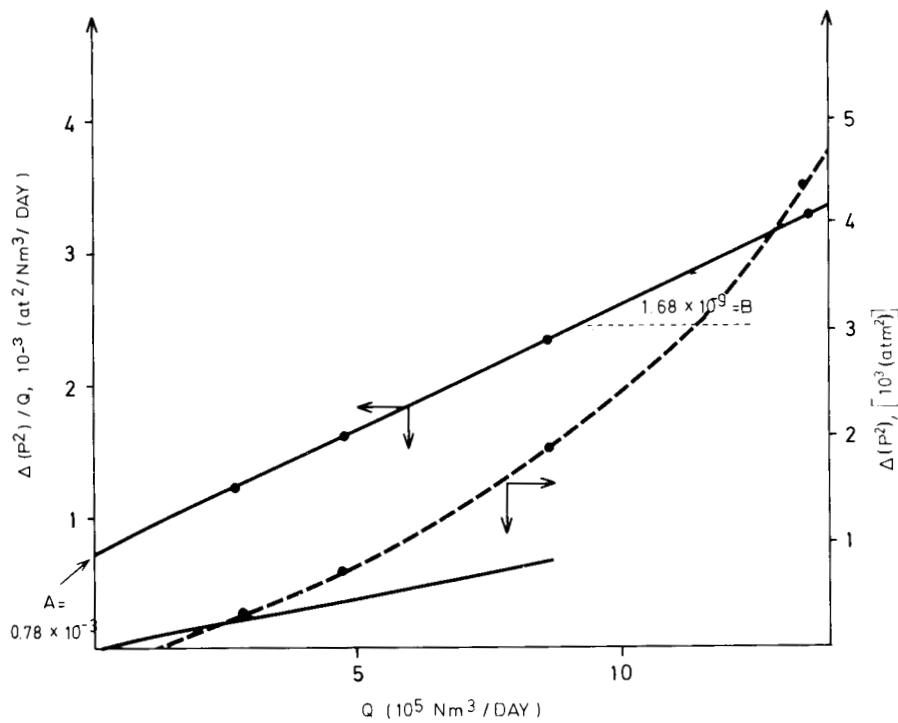
$A = 7.84 \times 10^{-4} (\text{at}^2/\text{Nm}^3/\text{day})^2$  as a result of extrapolation of the straight-line at well rate  $Q = 0$ ,

$B = 1.68 \times 10^{-9} (\text{at}^2/\text{Nm}^3/\text{day})^2$  (figure 6.27), expressing the slope of the straight-line. The equation of flow based on equation 6.81, may be thus expressed as

$$\Delta(P^2) = AQ + BQ^2$$

or

$$\Delta(P^2) = 7.84 \times 10^{-4}Q + 1.68 \times 10^{-9}Q^2$$



6.27 -  $Q$  vs.  $\Delta(P^2)$  and  $Q$  vs.  $\Delta(P^2)/Q$ .

## 2. Reservoir description

In order to describe the reservoir, the first parameter to evaluate is the fracture permeability  $K_f$  obtained from equation 6.84.

$$K_f \text{ (mD)} = 0.135 \frac{1}{A} \frac{\mu_g Z T}{h} \left[ \ln \frac{r_e}{r_w} + \sum S \right]$$

which depends on the gas deliverability index

$$DI = Q/\Delta(p^2) = \frac{1}{A}$$

Taking into consideration also the role of skin effect the result will be

$$K_f \text{ (mD)} = 0.135 \frac{1}{7.84 \times 10^{-4} \text{ (at/m}^3\text{/day)}} \frac{0.0178 \text{ (CP)} \times 0.86 \times 333 \text{ (K)}}{190 \text{ (m)}} \left[ \ln \frac{10^5}{10} + 6.8 \right]$$

$$K_f = 154 \text{ mD} = 0.154 \text{ D}$$

- Porosity  $\Phi_f$  for an idealized model such as No. 6 of table 6.1 and figure 6.6 will be expressed by

$$\Phi_f = \left( 162 K_f \times A_{fD}^2 \right)^{0.33} = \left[ 162 \times 154 \times 10^{-11} \times \left( \frac{1}{50} \right)^2 \right]^{0.333} = 4.64 \times 10^{-4}$$

$$\Phi_f = 0.0464 \%$$

- Intrinsic permeability  $K_{ff}$  will thus result

$$K_{ff} = K_f / \Phi_f = 0.154 / 4.64 \times 10^{-4} = 331 \text{ D}$$

- Fracture width  $b$  of the same idealized model given by the expression

$$b = (18 K_f / \Phi_f)^{0.5} = (18 \times 154 \times 10^{-11} / 4.64 \times 10^{-4})^{0.5}$$

$$b = 0.77 \times 10^{-2} \text{ cm} = 77 \mu$$

- Turbulence factor  $\beta$  (from equation 6.85):

$$\beta = \frac{B \times h^2 \times r_w}{3,169 \times 10^{-19} \times G \times Z \times T}$$

$$\beta \left( \frac{1}{\text{m}} \right) = \frac{1.68 \times 10^{-9} \times 190^2 \times 0.10}{3,169 \times 10^{-19} \times 0.58 \times 0.86 \times 333} = 1.14 \times 10^{11} \left( \frac{1}{\text{m}} \right) =$$

$$0.35 \times 10^{11} \left( \frac{1}{\text{ft}} \right)$$

- Permeability  $K_f$  from turbulence parameter  $B$ , by using the parameters  $\beta$  and  $\Phi_f$ , from equation 6.44 will be

$$K_f (\text{mD}) = \frac{1}{\Phi_f (\text{fraction})} \times \left[ \frac{2.2 \times 10^9}{\beta (1/\text{ft})} \right]^{1/1.085} =$$

$$\frac{1}{4.64 \times 10^{-4}} \left[ \frac{2.2 \times 10^9}{0.35 \times 10^{11}} \right]^{1/1.085} = 168 \text{ mD}$$

As observed, there is a small difference between the permeability obtained from laminar flow conditions and that obtained from turbulence flow. The value obtained through laminar flow parameter  $A$  is generally considered more representative, since  $B$  is dependent on the type of idealized model assumed and on the limited validity of the relationship  $\beta$  vs.  $K$ .

## 6.4. TRANSIENT FLOW IN A NON-POROUS FRACTURE NETWORK

In the case of a reservoir formed by a tight impervious matrix block and a large network of fractures the reservoir has to be considered essentially as a single porosity medium. In case of a developed fracture network throughout the reservoir, the flow toward a well has the same transient behaviour as a conventional reservoir. This concept represents the basis on which Warren and Root<sup>17</sup> have approached the analysis of transient flow toward a well (described in detail in chapt. 7).

### 6.4.1. General solution of the problem

If the procedure remains the same as in a conventional intergranular medium, the basic interpretation is related to pressure vs. time relationship

$$\Delta P = m \times \log \frac{\Delta t}{(t_o + \Delta t)} \dots \dots \dots \text{«build-up»}$$

$$\Delta P = m \times \log \Delta t \dots \dots \dots \text{«draw-down»}$$

The evaluation of slope  $m$  (Fig. 6.28) will give for the case of build-up, an indication of the parameter  $K_f h$  through the equation

$$k_f h = \frac{q_o \mu_o B_o}{2\pi} \cdot \frac{1}{m} \quad (6.86)$$

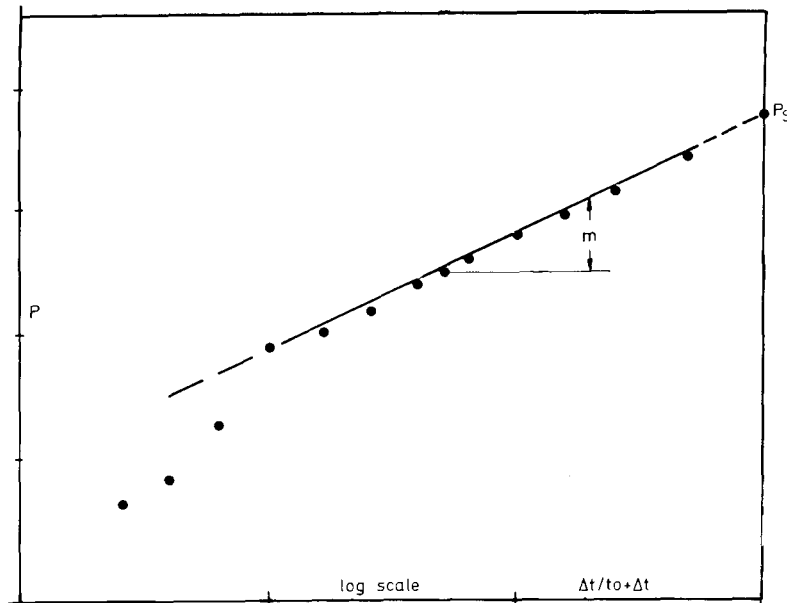
If the understanding of fracture density and orientation permits a correct estimation of  $h$ , the value of  $k_f$  may be really representative. It has to be observed that in case of an open-hole well, after cleaning-up and acidizing, there are more chances of estimating correctly the effective pay  $h$ , than in a completed well. This is the result of fracture plugging around the wellbore during cementation and in continuation of partial communication between fractures and wellbore, as result of perforations which are not contacting all fractures.

Observations.

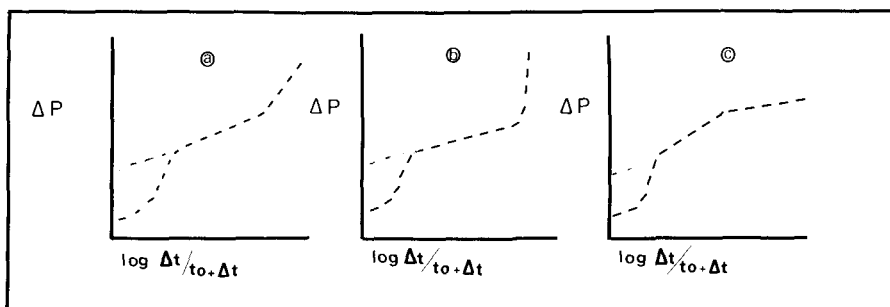
The high value of permeability in a fractured network will be associated to small pressure drop and therefore will require very accurate pressure readings. Since the pressure drop often is in the range of units of psi, the slope could not be representatively interpreted if conventional pressure recorders are not substituted for by special pressure gauges.

The varying behaviour of the relationship pressure vs. time has to be interpreted in direct connection with the fractured network characteristics. If the build-up pressure curves are similar to those in Fig. 6.29, the following comments and interpretation may be made:

- In all cases (a, b, c) the skin effect is positive. In general this result is the consequence of a cased wellbore, where part of the fractures have been plugged during cementation and where later stimulation has been unsuccessful. There is also the risk of perforations which are not contacting the fracture whereby the fracture intercommunication around the wellbore is very much reduced.



6.28 –  $P$  vs.  $\log \Delta t/t_0 + \Delta t$  in a fractured reservoir.



6.29 – Various build-up pressure curves.

- On the other hand, the skin effect is expected to be negative in the absence of casing (open hole wells) and especially if the well stimulation was successful.

Examining case *a*, the change of slope has limited chances of being the result of faulting or a depositional variation as in a conventional reservoir. This situation may be more the result of a reduction of horizontal fractures and of an increasing density in vertical or sub-vertical fractures. The limiting case *b* represents a total reduction of horizontal fractures and therefore a limited drainage radius around the wellbore.

Case *c*, on the contrary, may correspond to a favourable development of a fracture network which was reduced around the wellbore either by original fracturing conditions or as a consequence of well-completion operations. If in case *c* the cleaning and acidizing becomes effective, the higher slope of the initial stage may decrease in time, approaching a smaller slope similar to that obtained at a later stage. This may be interpreted as a reopening of the fracture network around the wellbore.

#### 6.4.2. Evaluation of storage capacity $\Phi_f C_f$

The storage capacity is a term which will represent the compressibility or expansion capacity of the fracture network filled with fluid. This parameter is obtainable only through interference tests (see chapter 8) where the distance and time between two wells being known, a direct evaluation of  $\Phi_f C_f$  results from the piezoconductivity parameter<sup>21,22</sup>:

$$\alpha \equiv \frac{K_f}{\Phi_f C_{fe} \mu} \quad (6.87)$$

A further evaluation of porosity  $\Phi_f$  is related to a correct evaluation of  $C_f$  for which it is necessary to reexamine the basic considerations developed in chapter 4.

The term  $C_{fe}$  of equation 6.87 is associated to the fluid contained in pores of a fracture network if expressed as in section 4.5.3.2.

$$C_{fe} = C_{eo} = C_o + C_w \frac{\Phi_m}{\Phi_f} + C_{pm} \frac{\Phi_m}{\Phi_f} + C_{pf} \quad (6.88)$$

If the matrix is very tight, neglecting the second and third term of right-hand equation 6.88, then

$$C_{fe} = C_o + C_{pf} \quad (6.89)$$

Since  $C_{pf}$  may take important values compared with  $C_o$  it is necessary to evaluate it accurately.

It must also be observed that porosity and permeability of a fracture depend on pore pressure variation which may modify in time the piezoconductivity factor (equation 6.87). In fact the single fracture porosity and permeability are expressed by

$$\Phi_f = A_{fD} b_{oi} (1 - C_f \Delta P)$$

$$K_f = A_{fD} \frac{b_{oi}^3}{12} (1 - C_f \Delta P)^3$$

which indicates a continuous reduction of both parameters during the reservoir life.

## SYMBOLS

### Latin letters

A	- reciprocal PI laminar flow
$A_s$	- cross flow section
a	- block height
B	- index in turbulent flow
$B_o$	- formation volume factor
C	- constant
$f = L_{fD}$	- fracture density (linear)
G	- gas gravity
$G_g G_o, G_w$	- pressure gradient (of gas, oil water)
GOL	- gas-oil limit
g	- gravity acceleration
LFEP	- lowest flowing entry point
h	- pay
HFEP	- highest flowing entry point
K	- permeability
l	- fracture extension
n	- number of fractures
P	- pressure
Q, q	- flow rate
r	- radius
$R_e$	- Reynolds
S	- skin effect
WOL	- water oil limit
x, y, z	- coordinates

### Greek letters:

$\alpha$	- piezoresistivity factor
$\beta$	- turbulence factor
$\gamma$	- density
$\Delta$	- difference
$\epsilon$	- permeability ratio
$\theta$	- angle
$\lambda$	- friction factor
$\psi$	- potential
$\Phi_f$	- porosity of fractures
$\mu$	- viscosity
$\rho$	- specific mass

### Subscripts:

B	- bulk
cr	- critical
e	- external
f	- fracture
fD	- fracture density
g	- gas
max	- maximum
o	- oil
safe	
w	- wellbore
x, y	- direction of coordinate

### REFERENCES

1. Irmay, 1964. Theoretical models of flow through porous media. RILEM Symp. on the Transfer of Water in Porous Media, Paris, April.
2. Romm, E.S., 1966. Fluid flow in fractured rocks. Nedra, Moscow.
3. Snow, D.T., 1965. A parallel model of fractured permeable media. Ph.D. thesis, Berkely, 330 p.
4. Lomize, G.M., 1947. Flow through fissures. Acad. of Sci. RSS Arm. in Russian.
5. Lomize, G.M., 1951. Flow through fissured rocks. Gpsenergoizdat in Russian.
6. Huit, J.K. 1956. Fluid flow in simulated fractures. AIChE Jour., Vol 2, p 259.
7. Louis, C., 1968. Etude des écoulements d'eau dans les roches fissurées et de leurs influence sur la stabilité des massifs rocheux. Bull. de la Direction des Etudes et Recherches, Series A, No. 3, p. 5–132.
8. Moody, L.F 1944. Friction factors for the Pipe Flow Trans. ASME, vol 66, 1944.
9. Forcheimer, 1901. Wasserbewegung durch Boden. ZUDI, Vol. 45, p 1781.
10. Geertsma, J., 1974. Estimating coefficient of inertial resistance in fluid flow through porous media. Jour. Petrol. Tech., Oct., p 445.
11. Firoozabadi, A. and Katz D.L., 1979. An analysis of high-velocity gas flow through porous media. Jour. Petrol. Tech., February, p 211.
12. Katz, D.L. and Coats, K.H., 1965. Underground storage of fluids. Ulrich Book, Inc. An Arbor, Michigan.
13. Scelkacev, V.N., and Lapuk, B.B., 1953. Underground hydraulics. Technical Editions, Budapest.
14. Reiss, L.H., 1976. Reservoir engineering of fractured reservoir. French Institute of Petroleum, Paris.
15. Baker, W.J., 1955. Flow in fissured reservoir. Proceeding Fourth World Petroleum Congress, Section II/E. p 379–393.
16. Kazemi, H., 1969. Pressure transient analysis of naturally fractured reservoir with uniform fracture distribution. Soc. Pet. Eng. J., p 451–458.
17. Warren, J.E. and Root, P.J., 1963. The behaviour of naturally fractured reservoir. Soc. Pet. Eng. J., p 245–255.
18. DeSwaan, H., 1975. Analytical solution for the determination of naturally fractured reservoir parameters by well testing. SPE Ventura meeting, California.
19. Birks, J., 1963. Coning theory and its use in predicting allowable producing rates of wells in a fissured limestone reservoir. Iranian Petroleum Institute, Bull. 12 & 13, p 470.
20. Saidi, A.M. and Martin, R.E., 1965. Application of reservoir engineering in the development of Iranian reservoirs. Paper presented to the E.C.A.F.E. Symposium of Petroleum, Tokyo, No. 10–20.
21. Muskat, M. 1937. Homogeneous flow in porous media. McGraw Hill, New York.
22. Ofstad, D.R., 1976, Research project B5020: Fractures reservoir behaviour. Univ. of Trondheim.

This Page Intentionally Left Blank

## CHAPTER 7

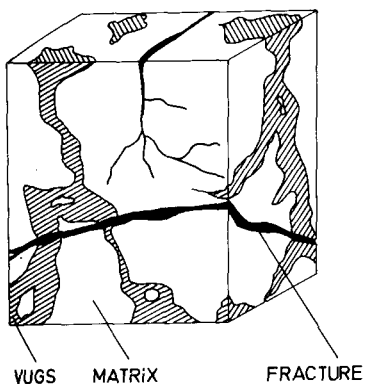
### FLOW TOWARDS A WELL IN FRACTURED ROCK OF DOUBLE POROSITY

The conventional reservoir formed by intergranular porosity is studied under the simplified assumption that the reservoir is homogeneous and the basic physical properties, such as porosity and permeability, are always associated with a trend.

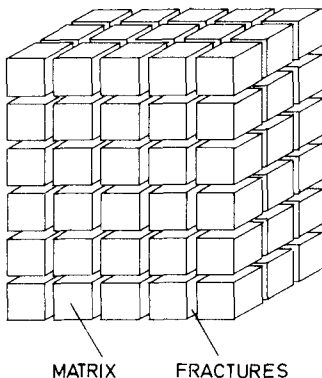
In a *non-conventional reservoir* (naturally fractured reservoir) there are discrepancies and discontinuities throughout the whole reservoir as the result of two distinct porosity systems in the same formation (figure 7.1). The *matrix region* containing finer pores and having a high storage capacity, but a low flowing capability, is interconnected with the *fractured network region*, which has a low storage capacity but a high flowing capacity. In such a system different reservoir engineering techniques from those used in a conventional intergranular reservoir are required, and in a number of papers<sup>1,2,3,4,5</sup> various procedures have been elaborated based on simplified models. The aim of these papers is to evaluate the flow characteristics under special conditions of increasing heterogeneity. By successful use of one or more of the proposed models, more information may be expected from the interpretation of in-situ recorded data. This information includes an estimation of the porosity and permeability of both regions and under certain conditions, an evaluation of the fracture distribution and frequency, etc.

The Warren-Root model is discussed most in this chapter, but the models proposed by Odeh<sup>2</sup>, Pollard<sup>2</sup>, Kazemi<sup>4</sup>, De Swaan<sup>5</sup> and Najurieta<sup>6</sup> have also been examined.

The *Warren-Root model* presents the fractured reservoir as an idealized system formed by identical rectangular parallelepipeds separated by an orthogonal network of fractures (figure 7.2). The flow towards the wellbore is considered to take place in the fractured network, while the matrix continuously feeds the system of fractures under quasi-steady flow conditions.



7.1 – Real fractured reservoir rock  
(Warren and Root<sup>1</sup>, Courtesy AIME).



7.2 – Idealised fractured reservoir: Warren-Root model. (Warren and Root<sup>1</sup>, Courtesy AIME).

Under transient conditions, a pressure response function has been developed as a function of two new dimensionless parameters  $\lambda$  and  $\omega$ . These parameters characterize the relationship between the two regions of different porosities.

$\lambda$  is a function of the interflow between the two regions, and  $\omega$  expresses the relative storage capacity of the two regions. The results of this model when processed by the conventional semilog plot of the pressure variation vs. log time (for pressure drawdown and build-up cases) reveal the presence of two parallel straight lines instead of one, as is usually obtained in a conventional reservoir.

The *early* and *later* parallel straight line separation depends on the relative storage capacity of the fracture  $\omega$ , while the transient period of the pressure from the *early* to the *later* straight line will be a function of the interflow coefficient  $\lambda$ . The slope of the two parallel straight lines is a direct function of the flowing capacity of the fracture network independent of granular porosity (as described in chapter 6). The Warren-Root model offers a detailed understanding of the flowing mechanism of the naturally fractured reservoir and based on this consideration, a comprehensive description of the model is carried out in this chapter.

The basic assumptions of the *Odeh model*<sup>2</sup> are similar to the Warren-Root model, the only difference being his redefinition of the two porosities. From the examination of the basic data of a fractured reservoir Odeh concluded that the storage capacities of the two systems (fracture and matrix) are generally so similar that the transient behaviour will terminate by approaching *conventional reservoir* behaviour. Thus, in further discussion the Odeh model will be included in what will be usually called *conventional reservoir* model.

The *Pollard model*<sup>3</sup> estimates that the pressure behaviour in transient conditions is the result of the interaction of three regions which develop in the fractured reservoir. The first region is formed by the fractured network around the wellbore, the second by the entire fractured network of the reservoir (far from the wellbore), and the third by the matrix which feeds the fracture.

The last two regions represent a similar fracture-matrix system as already mentioned, but the pressure drawdown initially involves the wellbore's surrounding fractures, then the fractured network throughout the reservoir, and only in the third stage will the pressure drawdown be associated with the matrix pressure drop. After the depressed matrix starts to feed the fractures the flowing process will become quasi-steady state very rapidly. The pressure drop in the wellbore (as the result of successive events) will be represented by a series of time exponential terms.

A special elaboration of the logarithmic pressure drop vs. time will permit an evaluation of the fracture and matrix volume. The model though it does not take into consideration the radial flowing geometry, and reduces the problem to a simple expansion process, gives acceptable results in some cases. The extension of the Pollard model to the evaluation of various other parameters through analogy with conventional reservoirs is sometimes successful, but could often result in considerable errors.

The *Kazemi model*<sup>4</sup> approximates the naturally fractured reservoir by a layered system composed of thin but highly conductive layers, representing the fractures, alternating with thicker, low conductive, high storage capacity layers representing the matrix. By use of the numerical integration of well pressure variation vs. time, this model gave results which proved a satisfactory matching with those obtained by the Warren-Root model for cases of uniform fracture distribution where high storage capacity of matrix contrasted with high interflow capacity.

The *De Swaan*<sup>5</sup> model describes the unsteady-state flow by assuming regular geometrical matrix blocks as infinite slabs and spherical blocks. The model was further developed by *Najurieta*<sup>6</sup> for the interpretation of well testing data obtained during pressure drawdown and shut-in, or during well interference tests.

## 7.1. BASIC EQUATIONS OF FLOW

The equations of flow for fractured reservoirs of double porosity were formulated by Barenblatt et al., through the continuum approach. According to Barenblatt<sup>7</sup> the two media, fracture network and block, are considered to be an overlapping *continuum*, whereby the flow and medium parameters are defined at each mathematical point.

The equations of motion and of conservation of mass are written independently for each medium, and transfer of liquid between the two media is taken into consideration by a source/sink function in the equations of conservation of mass.

### 7.1.1. The Barenblatt<sup>7</sup> approach

#### 7.1.1.1. Barenblatt's equations of flow

Assuming a homogeneous isotropic reservoir and flow in both media (fractures and

blocks) to be in the range of validity of Darcy's law, the equations of motion in horizontal flow are as follows:

$$\begin{aligned}\vec{u}_1 &= -\frac{K_1}{\mu} \operatorname{grad} P_1 \\ \vec{u}_2 &= -\frac{K_2}{\mu} \operatorname{grad} P_2\end{aligned}\quad (7.1)$$

where  $\vec{u}$  is flux,  $K$  is permeability,  $\mu$  is dynamic viscosity and  $p$  is pressure. Subscripts 1 and 2 denote the medium of matrix blocks and fractures, respectively.

The equations of conservation of mass are:

$$\begin{aligned}\frac{\partial(\Phi_1 \rho)}{\partial t} + \operatorname{div}(\rho \vec{u}_1) + u^* &= 0 \\ \frac{\partial(\Phi_2 \rho)}{\partial t} + \operatorname{div}(\rho \vec{u}_2) + u^* &= 0\end{aligned}\quad (7.2)$$

where  $\Phi$  is porosity,  $\rho$  is density of fluid, and  $u^*$  (rate of mass flow per unit volume) represents the transfer of fluid between blocks and fractures.

The source function  $u^*$  derived by Barenblatt from dimension analysis considerations is:

$$u^* = \frac{\rho S K_1}{\mu} (P_1 - P_2) \quad (7.3)$$

where  $S$  is a characteristic coefficient of the fractured rock proportional to the specific surface of the block. Equation 7.3 implies a quasi-steady state flow from block to fracture. This assumption was discussed by Kazemi<sup>4</sup> who concluded that in the range of values of the parameters of interest, a quasi-steady state is reached relatively quickly and, therefore, this assumption is reasonable.

The liquid is considered slightly compressible and thus the relationship between density and pressure is expressed by:

$$\rho \cong \rho_0 [1 + C p] \quad (7.4)$$

where  $C$  is the coefficient of compressibility of the fluid and subscript zero denotes standard conditions.

The change in porosity of each medium is considered to be the result of changes in liquid pressure  $p_1$  and  $p_2$  in both media and of compressibility values:

$$\begin{aligned} d\Phi_1 &= \alpha_1 dp_1 - \alpha_* dp_2 \\ d\Phi_2 &= \alpha_2 dp_2 - \alpha_{**} dp_1 \end{aligned} \quad (7.5)$$

By combining equations 7.1 through 7.5 the following are obtained:

$$\left. \begin{aligned} \frac{K_1}{\mu} \text{lap } p_1 &= \Phi_1 C_1 \frac{\partial p_1}{\partial t} - \alpha_* \frac{\partial p_2}{\partial t} + \frac{SK_1}{\mu} (p_1 - p_2) \\ \frac{K_2}{\mu} \text{lap } p_2 &= \Phi_2 C_2 \frac{\partial p_2}{\partial t} = \alpha_{**} \frac{\partial p_1}{\partial t} \frac{SK_1}{\mu} (p_1 - p_2) \end{aligned} \right\} \quad (7.6)$$

where

$$\begin{aligned} \Phi_1 C_1 &= \alpha_1 + \Phi_1 \beta \\ \Phi_2 C_2 &= \alpha_2 + \Phi_2 \beta \end{aligned} \quad (7.7)$$

Equation 7.6 represents the equations of flow through fractured media of double porosity as formulated by Barenblatt.

#### 7.1.1.2. Solutions to Barenblatt's equations

Barenblatt et al<sup>7</sup> considered the flow through a fractured formation which has negligible fracture compressibility and negligible block permeability. The secondary effect of liquid pressure on porosities  $\Phi_1 C$  and  $\Phi_2 C$  in equation 7.5 is also negligible. In such a case the equations 7.6 are reduced to:

$$\left. \begin{aligned} \Phi_1 C_1 \frac{\partial p_1}{\partial t} - \frac{SK_1}{\mu} (P_1 - P_2) &= 0 \\ \frac{K_2}{\mu} \text{lap } p_2 + \frac{SK_1}{\mu} (P_1 - P_2) &= 0 \end{aligned} \right\} \quad (7.8)$$

Elimination of  $p_1$  from equation 7.8 yields:

$$\frac{\partial p_2}{\partial t} - \frac{K_2}{SK_1} \frac{\partial}{\partial t} (\text{lap } p_2) - \frac{K_2}{\mu \Phi_1 C_1} \text{lap } p_2 = 0 \quad (7.9)$$

or

$$\Phi_1 C_1 \frac{\partial p_2}{\partial t} + \text{div} \left( -\frac{K_2}{\mu} \text{grad } p_2 - \Phi_1 C_1 \frac{K_2}{SK_1} \frac{\partial}{\partial t} (\text{grad } p_2) \right) = 0 \quad (7.10)$$

Equation 7.10 can be regarded as an equation of conservation of mass through a formation with equivalent porosity and compressibility, equal in fact, to those of the matrix blocks, and an equivalent flux:

$$\bar{u} = -\frac{K_2}{\mu} \text{grad } P_2 - \frac{\Phi_1 C_1 K_2}{SK_1} \frac{\partial}{\partial t} (\text{grad } P_2) \quad (7.11)$$

A solution of interest in reservoir engineering (presented by Barenblatt<sup>7</sup>) is one corresponding to a production at constant rate from a well located in an infinite reservoir which pressure initially is constant and equal to  $P_o$ .

In a radial system of coordinates, equation 7.10 is written as:

$$\frac{\partial P_2}{\partial t} - \frac{K_2}{SK_1} \frac{\partial}{\partial t} \left[ \frac{1}{r} \frac{\partial}{\partial r} \left( r \frac{\partial P_2}{\partial r} \right) \right] - \frac{K_2}{\mu \Phi_1 C_1} \left[ \frac{1}{r} \frac{\partial}{\partial r} \left( r \frac{\partial P_2}{\partial r} \right) \right] = 0 \quad (7.12)$$

and the initial and boundary conditions are expressed by:

$$\left. \begin{aligned} P_2(r, 0) &= P_o \\ r = 0: q &= -2\pi h \left[ \frac{K_2}{\mu} \left( r \frac{\partial P_2}{\partial r} \right) + \frac{\mu \Phi_1 C_1 K_2}{SK_1} \frac{\partial}{\partial t} \left( r \frac{\partial P_2}{\partial r} \right) \right] = \text{const} \\ r \rightarrow \infty: P &= P_c \end{aligned} \right\} \quad (7.13)$$

where  $h$  is the thickness of the formation.

The solution obtained by the Laplace transformation is:

$$p(r, t) = p_c + \frac{q\mu}{2\pi K_2 h} \int_0^\infty \frac{J_0(vr)}{v} \left\{ 1 - \exp \left[ -\frac{v^2 K_2}{\mu \Phi_1 C_1} / \left( 1 + \frac{v^2 K_2}{SK_1} \right) \right] \right\} dv \quad (7.14)$$

where  $J_0$  is the Bessel function of first kind and order zero.

### 7.1.2. Warren and Root<sup>1</sup> approach

Warren and Root<sup>1</sup> present a more comprehensive solution to the same problem. They take into account fracture compressibility, but neglect the flow through the blocks. The corresponding equations for radial flow, as follows from equation 7.6, are:

$$\left. \begin{aligned} \Phi_1 C_1 \frac{\partial p_1}{\partial t} + \frac{SK_1}{\mu} (p_1 - p_2) &= 0 \\ \Phi_2 C_2 \frac{\partial p_2}{\partial t} - \frac{K_2}{\mu} \left[ \frac{1}{r} \frac{\partial}{\partial r} \left( r \frac{\partial p_2}{\partial r} \right) \right] + \frac{SK_1}{\mu} (p_1 - p_2) &= 0 \end{aligned} \right\} \quad (7.15)$$

### 7.1.2.1. Pressure drawdown in an infinite boundary.

The initial and boundary conditions considered are:

$$\left. \begin{array}{l} t = 0; \quad p_1(r,0) = p_2(r,0) = p_o \\ r = r_w; \quad q = -2\pi r_w \frac{K_2}{\mu} \frac{\partial p_2}{\partial r}, \text{ when } t > 0 \\ r \rightarrow \infty; \quad p_1 = p_2 = 0, \text{ when } t \geq 0 \end{array} \right\} \quad (7.16)$$

Warren and Root<sup>1</sup> define the following dimensionless parameters and express the equations in 7.15 and the conditions in 7.16 in a dimensionless form:

$$\left. \begin{array}{l} P_D = (2\pi K_2 h / q\mu) [P_o - p(r,t)] \\ r_D = r/r_w \\ t_D = K_2 t / [(C_1 \Phi_1 + C_2 \Phi_2) \mu r_w^2] \\ \lambda = \alpha K_1 r_w^2 / K_2 \\ \omega = \Phi_2 C_2 / (\Phi_1 C_1 + \Phi_2 C_2) \end{array} \right\} \quad (7.17)$$

Equations 7.16 and 7.15 combined with the boundary conditions in equation 7.16 will give:

$$\left. \begin{array}{l} \frac{1}{r_D} \frac{\partial}{\partial r_D} \left( r_D \frac{\partial P_{2D}}{\partial r_D} \right) - \omega \frac{\partial P_{2D}}{\partial t_D} - (1 - \omega) \frac{\partial P_{1D}}{\partial t_D} = 0 \\ (1 - \omega) \frac{\partial P_{1D}}{\partial t_D} - \lambda (P_{2D} - P_{1D}) = 0 \end{array} \right\} \quad (7.18)$$

with

$$\left. \begin{array}{l} t_D = 0 \quad P_{1D} = P_{2D} = 0 \\ r_D = 1 \quad \partial P_{2D} / \partial r_D = -1; \text{ when } t_D > 0 \\ r \rightarrow \infty \quad P_{1D} = P_{2D} = 0; \text{ when } t \geq 0 \end{array} \right\} \quad (7.19)$$

The solution obtained by the Laplace transformation is:

$$P_{2D}(r_D, t_D) = L^{-1} \left[ \frac{K_o(r_D \sqrt{S f(S)})}{S \sqrt{S f(S)} K_1(\sqrt{S f(S)})} \right] \quad (7.20)$$

where  $L^{-1}$  denotes the Laplace inverse transformation operator:

$$f(S) = \frac{\omega(1-\omega)S + \lambda}{(1-\omega)S + \lambda} \quad (7.21)$$

and  $K_0$  and  $K_1$  are modified Bessel functions of the second kind of order zero and one, respectively.

The inversion of equation 7.20 cannot be obtained analytically in a general case. However, an asymptotic solution for low  $sf(s)$  values can be obtained by considering only the first terms of the ascending series of the Bessel functions, i.e.:

$$K_0(\sqrt{S f(S)}) = -\gamma - \ln\left(\frac{r_D}{2}\sqrt{S f(S)}\right) \quad (7.22)$$

$$K_1(\sqrt{S f(S)}) = \frac{1}{\sqrt{S f(S)}} \quad (7.23)$$

where  $\gamma = 0.5772$  is Euler's number.

Such an approximation restricts the solution to only  $\sqrt{S f(S)}$  values if less than 0.01, corresponding in general to time values  $t_D > 100$  or more accurately  $t_D > 100 \omega$  for  $\lambda \ll 1$  and  $t_D > 100\lambda - 1/\lambda$  for  $\omega \ll 1$ .

With equation 7.20 the inverse transformation of equation 7.21 is:

$$P_{2D}(1, t_D) = \frac{1}{2} \left[ 0.80908 + \ln t_D + Ei\left(-\frac{\lambda t_D}{\omega(1-\omega)}\right) - Ei\left(-\frac{\lambda t_D}{1-\omega}\right) \right] \quad (7.24)$$

where  $Ei$  denotes the exponential integral function defined by:

$$Ei(-x) = - \int_x^{\infty} \frac{e^{-u}}{u} du \quad (7.25)$$

#### a. Discussion on graphical representations.

The solution given by equation 7.24 is represented in a graphical dimensionless form in figures 7.3 and 7.4, for some particular values of the parameters  $\lambda$  and  $\omega$ , characterizing the properties of the naturally fractured formation.

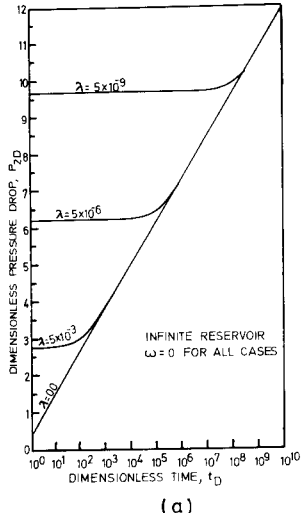
The presence of three regions of different behaviours to the solution represented in figure 7.4 in the  $(p, \log t)$ -plane, can be distinguished:

The first region corresponds (figure 7.4.b) to the early stages of production, during which the liquid is produced mainly from the fracture system. In this region, corresponding to small argument values of the Ei function, one may approximate:

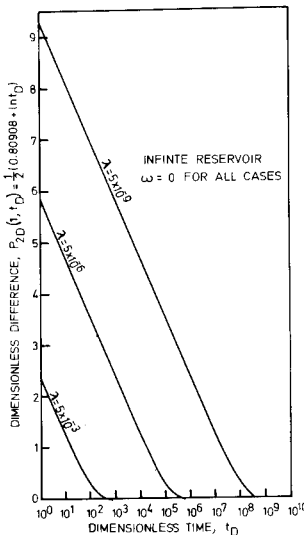
$Ei(-x) = -\gamma - \ln x$  in equation 7.24 and obtain:

$$P_{2D} = \frac{1}{2} \left( 0.80908 + \ln t_D + \ln \frac{1}{\omega} \right) \quad (7.27)$$

i.e., a straight line in the  $(p, \log t)$  – plane.

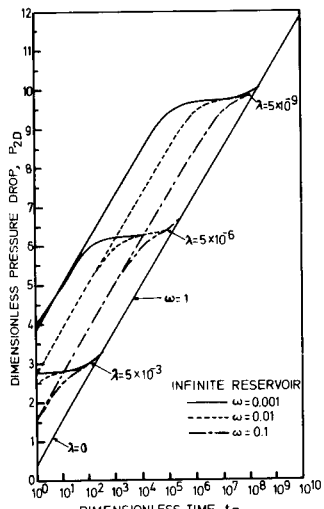


(a)

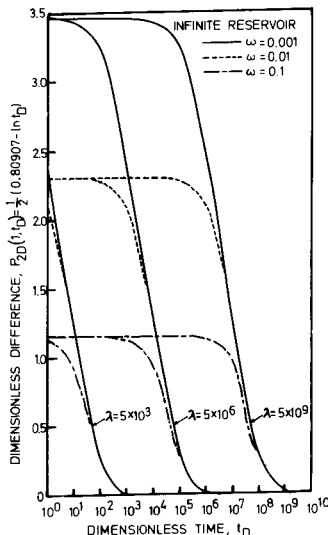


(b)

7.3 – Warren and Root<sup>1</sup> solution (equation 6.24) for an infinite reservoir  $w = 0$  and some particular values of  $\lambda$ . (Courtesy AIME).



(a)



(b)

7.4 – Warren and Root<sup>1</sup> solution (equation 7.24) for an infinite reservoir and some particular values of the parameters  $\omega$  and  $\lambda$ . (Courtesy AIME).

If the storage capacity of the fracture system is negligible, i.e.,  $\omega = 0$ , the beginning of production is characterized by a *jump* in pressure reflecting the lack of fluid capacity in the fractures (figure 7.3a).

The *second region* corresponds to a *transition stage*, during which the pressure vs. time in the fractures remains approximately constant. This corresponds to the early stages of supply of liquid from the matrix blocks into the fracture system. The occurrence and duration of this transition region is dependent on both parameters  $\omega$  and  $\lambda$ .

The *third region*-corresponds to large time values when a *quasi-steady state* flow is reached and the whole reservoir produces as an equivalent homogeneous one. Since permeability of the blocks is low and negligible in comparison to the permeability of the fracture system, the production of the *equivalent homogeneous reservoir* equals the permeability of the fractures, and the reservoir behaviour is similar to that discussed in chapter 6.

#### b. Analytical observations.

At large time values both Ei functions in equation 7.24 tend to be zero, and thus the following is obtained:

$$P_D = \frac{1}{2} (0.80908 + \ln t_D) = \frac{1}{2} \ln 2.25 t_D = 1.15 \log 2.25 t_D \quad (7.28)$$

i.e., a straight line *parallel* to that of the early stages of production and *vertically displaced* by  $\ln \sqrt{1/\omega}$ . The slope of both lines is  $-1.15/\text{cycle}$ .

Figures 7.3b and 7.4b present the deviation from the asymptotic behaviour i.e.:

$$\Delta_D = P_{2D}(1, t_D) - \frac{1}{2} (0.80908 + \ln t_D) = \text{Ei}\left(-\frac{\lambda t_D}{\omega(1-\omega)}\right) - \text{Ei}\left(-\frac{\lambda t_D}{1-\omega}\right) \quad (7.29)$$

The difference *curves* in equation 7.29 intercept the  $\Delta_D$ -axis at:

$$\Delta_{1D} = \ln \sqrt{1/\omega} \quad (7.30)$$

The intercept of the tangent to the difference curve through the inflection point at  $t_D = 1$  is:

$$\Delta_{2D} = [-\gamma - \ln \lambda/(1-\omega)]/2 \quad (7.31)$$

With  $\Delta_{1D}$  and  $\Delta_{2D}$  as known values resulting from a production test, the parameters  $\omega$  and  $\lambda$  (characterizing the fracture formation of double porosity) can be determined.

### 7.1.2.2. Build-up pressure curve in an infinite boundary

A build-up pressure equation may be directly obtained by superposition of the solutions of equation 6.24 as follows:

$$\Delta P_{2D} = \frac{1}{2} \left\{ \ln \frac{t_D + \Delta t_D}{\Delta t_D} + Ei \left[ -\frac{\lambda(t_D + \Delta t_D)}{\omega(1-\omega)} \right] - Ei \left[ -\frac{\lambda \Delta t_D}{\omega(1-\omega)} \right] \right. \\ \left. - Ei \left[ -\frac{\lambda(t_D + \Delta t_n)}{1-\omega} \right] + Ei \left[ -\frac{\lambda \Delta t_D}{1-\omega} \right] \right\} \quad (7.32)$$

where  $t_D$  is the dimensionless production time and  $\Delta t_D$  is the dimensionless shut-in time.

For large values of the production time the Ei function containing the parameter  $t_D$  will tend more rapidly to zero, and thus the asymptotic solution of equation 7.32 is reduced to,

$$\Delta P_{2D} = \frac{1}{2} \left\{ \ln \frac{t_D + \Delta t_D}{\Delta t_D} - Ei \left[ -\frac{\lambda \Delta t_D}{\omega(1-\omega)} \right] + Ei \left[ -\frac{\lambda \Delta t_D}{1-\omega} \right] \right\} \quad (7.33)$$

#### a. Discussion on graphical representation.

Equations 7.32 and 7.33 are subject to the same limitations as equation 7.24, i.e.,  $\Delta t_D > 100\omega$  for  $\lambda \ll 1$  or  $\Delta t_D > 100\lambda - 1/\lambda$  for  $\omega \ll 1$  and  $\lambda t_D > 3$ .

Equation 7.33 is of similar form as equation 7.24, and therefore the behaviour of the solution is similar. Figure 7.5 presents some typical build-up curves for a constant  $\lambda$  value and different  $\omega$  values. The same three regions of different behaviour as for drawdown may be observed during build-up:

- At early stages of build-up the solution is represented by a straight line corresponding to replenishment of fluid into the fractures.
- During the second stage the straight line is followed by a quasi-constant pressure vs. time representing the massive transfer of fluid from fractures into the blocks.
- During the third phase, the whole reservoir behaves as a homogeneous one, and its behaviour is again a straight line, displaced but parallel with respect to the initial one.

A similar analysis as developed for drawdown leads to the same values of the vertical displacement between the two straight lines in the  $P_{D2}$  vs.  $\ln \Delta t / (t_D + \Delta t_D)$  plane, as for build-up, i.e.  $\ln \sqrt{1/\omega^2}$ .

The intercept of the tangent through the inflection point, to the difference curve to the asymptotic behaviour, expressed by

$$\Delta = P_{2D} - \ln \Delta t_D / (t_D + \Delta t_D) \text{ vs. } \ln \Delta t_D / (t_D + \Delta t_D)$$

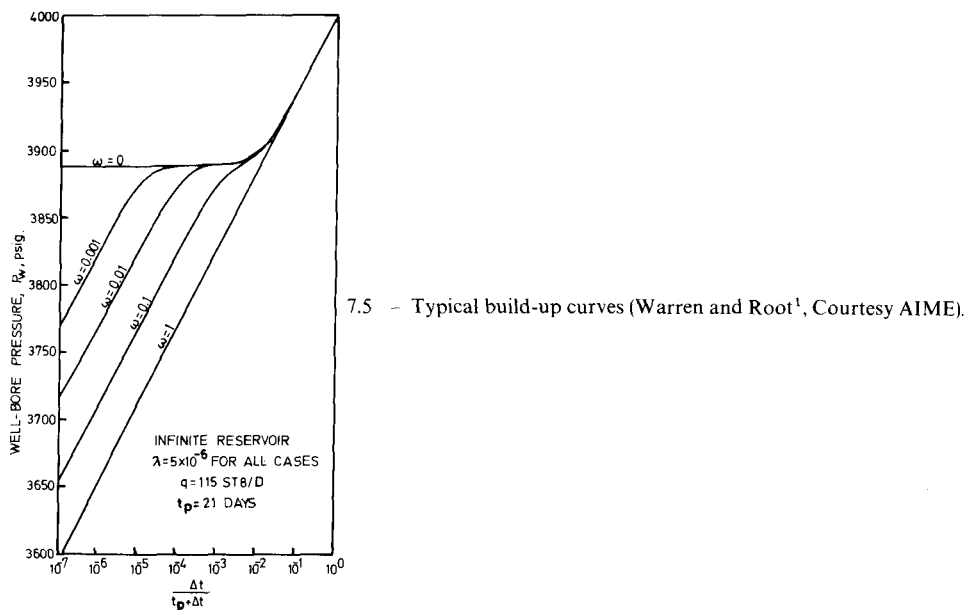
is obtained for initial time of build-up when  $\Delta t = 0$ , or

$$\ln \Delta t (t_D + \Delta t_D) = \Delta$$

The result is the same as for drawdown, i.e.

$$\Delta = \left[ -\gamma - \ln \lambda / (1 - \omega) \right] / 2$$

Therefore, the parameters  $\lambda$  and  $\omega$  can be determined in a similar way by using drawdown or build-up test results.



### b. Analytical observations

As follows from the definition of the dimensionless parameters  $\omega$  and  $\lambda$  (equation 7.17),  $\omega$  represents the ratio between the storage capacity of the fracture network and the total storage capacity of the formation, while fluid transfer capacity  $\lambda$  is proportional to the ratio between the permeability of the fracture and the of the blocks. From the examination of  $\lambda$  and  $\omega$  under various conditions it results:

- Small  $\omega$  values (equation 7.17) indicate a small storage capacity of fractures and a good storage capacity of the blocks, and the behaviour of the solution is represented in figure 7.4 and 7.5 by a large plateau of quasi-constant pressure in the transition between the early stages of production and the asymptotic behaviour.

- Based on equation 7.17, small  $\lambda$  values mean that for a constant value of the specific surface coefficient  $\alpha$ , a large contrast between fracture and matrix block permeabilities exists. On the other hand, for a constant ratio  $K_1/K_2$ , small values of  $\lambda$  indicate small specific surfaces of the blocks i.e. large size of the blocks.
- An analysis of a build-up test enables the determination of  $\omega$  and of the coefficients  $\Phi_1 C_1$  and  $\Phi_2 C_2$  separately while  $\lambda$  is determined as a whole value. To obtain more data information on the constituent parameters involved in the  $\lambda$  coefficient additional evaluations are necessary. For example, if the permeability of the blocks can be determined by laboratory tests then the product  $k_1$  can be calculated.
- It must be pointed out that the Warren and Root solution to Barenblatt's equations does not assume some regular shape of the blocks or some regular fracture pattern as is sometimes mentioned in the literature as a weak point of the result. The only requirement, as follows from Barenblatt's *continuum approach*, is that mean properties could be defined for a sample surrounding the considered mathematical point.
- In the special case when  $K_1$  was not evaluated in the laboratory but its value is desired, it will be necessary to calculate the value  $\alpha$  through some model of block disposition, as for example, a fractured formation of uniformly spaced fractures and different fracture widths (Warren and Root<sup>1</sup> model). For such a model the equation is written as follows:

$$\alpha = 4n(n + 2)/L^2 \quad (7.34)$$

where  $n$  is the number of normal sets of fractures ( $n = 1, 2, 3$ ) and  $L$  is a characteristic dimension of the block corresponding to:

$L = a$	for $n = 1$
$L = 2ab/(a + b)$	for $n = 2$
$L = 3abc/(ab + bc + ca)$	for $n = 3$

(7.35)

where  $a$ ,  $b$ , and  $c$  are the lengths of the block faces.

#### 7.1.2.3. Finite boundary cases

##### a. Pressure drawdown

Warren and Root<sup>1</sup> also present a solution for a finite reservoir. In this case the third equation of the set (7.16) is replaced by the condition of no flux through the impervious boundary, which is:

$$r_D = R_D; \quad \frac{\partial P_{2D}}{\partial r_D} = 0; \quad t_D > 0 \quad (7.36)$$

where  $R_D$  is the dimensionless radius of the reservoir. The corresponding solution is:

$$P_{2D}(1, t_D) = \left( \frac{2}{R_D^2 - 1} \right) \left\{ \frac{1}{4} t_D + \frac{(1-\omega)^2}{\lambda} \left[ 1 - \exp \left( -\lambda t_D / \omega (1-\omega) \right) \right] - \left[ (3R_D^4 - 4R_D^4 \ln R_D - 2R_D^2 - 1)/4 (R^2 - 1)^2 \right] \right\} \quad (7.37)$$

or for large values of  $R_D$  and  $t_D$  the solution is:

$$P_{2D} = \frac{2}{R^2} \left\{ t_D + \frac{(1-\omega)^2}{\lambda} \left[ 1 - \exp \left( -\lambda t_D / \omega (1-\omega) \right) - (0.75 - \ln R_D) \right] \right\} \quad (7.38)$$

The solution is limited to  $t_D > 100\omega R^2$  for  $\lambda \ll 1$  or  $t_D > 100 R^2 - 1/\lambda$  for  $\omega \ll 1$ .

The present solution indicates the following:

- The pressure moves asymptotically to a linear function of the dimensionless time  $t_D$  with a slope  $(R_D^2 - 1)/2$  and an intercept approximately equal to  $[\ln R_D - 0.75 + 2(1-\omega)^2/\lambda R_D^2]$ .
- The logarithm of the deviation from the asymptote is also a linear function of  $t_D$  with a slope of  $-\lambda/2.3\omega(1-\omega)$  cycles, and an intercept at  $r = 0$  equal to  $\log [2(1-\omega)^2/\lambda(R_D^2 - 1)]$ .
- The analysis of a production test enables the determination of  $\omega$ ,  $\lambda$  and  $R_D$ .

#### b. Pressure build-up.

An equation for build-up is obtained by superposition of the solution (6.66) and is as follows:

$$P_{2D} = \frac{2}{R^2} \left\{ \Delta t_D + \frac{(1-\omega)^2}{\lambda} [1 - \exp(-\lambda t_D / \omega (1-\omega))] \right\} \quad (7.39)$$

This solution is limited to  $\Delta t_D > 100 \omega R^2$  for  $\lambda \ll 1$  or  $\Delta t_D > 100 R^2 - 1/\lambda$  for  $\omega \ll 1$  and also for  $\lambda \Delta t_D > 5\omega$ .

#### 7.1.3. Other models and solutions

##### 7.1.3.1. Odeh's<sup>3</sup> model and solution

Odeh<sup>3</sup> calculated an equation of flow under the same assumptions as Barenblatt but with a slightly different definition of the parameters of the fractured formation.

A solution for radial flow through an infinite reservoir, under the same boundary and initial conditions as considered by Warren and Root<sup>1</sup> leads to a solution similar to equation 7.24. Odeh pretends that the first straight line and the transient period was never observed. To support his conclusion Odeh chose some particular values of the argument of the Ei functions, which lead to them quickly disappearing. Then he concluded that all fractured reservoirs behave as homogeneous ones.

Warren and Root discussing Odeh's solution calculated the relationships between the fractured rock parameters as defined by Odeh and the parameters appearing in equation 7.24. With these relationships Odeh's equation becomes identical to equation 7.24.

Warren and Root also present some field tests in which the appearance of the first straight line in the  $(p, \log t)$ -plane and the transition to homogeneous behaviour is evident.

One may conclude that the Warren and Root solution describes the general behaviour of fractured reservoirs, while the cases considered by Odeh are exceptions.

#### 7.1.3.2. The Kazemi<sup>4</sup> solution

Kazemi and al.<sup>4</sup> have solved Barenblatt's equations under the same assumptions as Warren and Root. They considered a zero radius of well and obtain by using the same technique as Warren and Root the following:

$$P_{2D} = L^{-1} \left[ \frac{K_c(V_D \sqrt{Sf(S)})}{S} \right] \quad (7.40)$$

where  $f(S)$  is defined by equation 7.23.

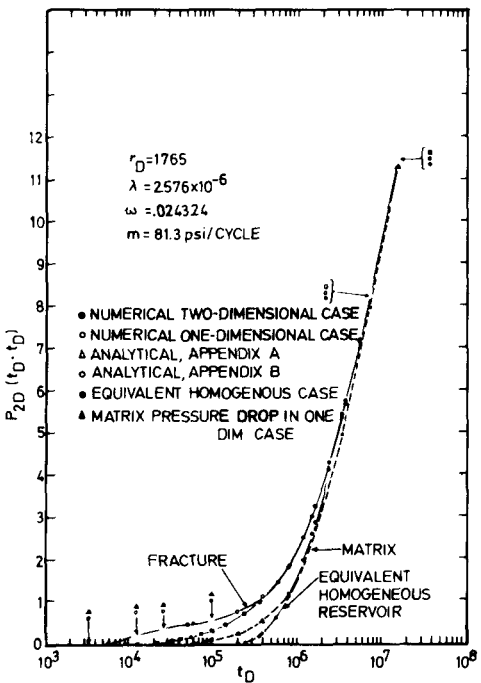
The approximation of the Bessel function  $K_c$  by the first terms of the ascending series (equation 7.23) enables the inverse transformation of equation 7.40, and also a solution can be obtained as a function of radius, suitable for interpretation of interference tests. The equation is expressed as:

$$P_{2D}(r_D, t_D) = \frac{1}{2} \left[ 0.80908 + \ln(t_D/r_D^2) + Ei\left(-\frac{\lambda t_D}{\omega(1-\omega)}\right) - Ei\left(-\frac{\lambda t_D}{1-\omega}\right) \right] \quad (7.41)$$

The solution is considered as a good approximation for  $t_D > 100r_D^2$ .

Results of the computations for particular values of  $r_D$ ,  $\omega$  and  $\lambda$  are presented in figure 7.6 and are compared with those obtained by a finite-difference numerical method.

Homogeneous reservoir behaviour occurs very rapidly in the observation well, and therefore the interpretation and calculation of the parameters of the fractured reservoir is difficult.



7.6 – An interference drawdown as obtained by equation 7.41 and comparison with numerical solution  
(Kazemi, Seth and Thomas<sup>4</sup>, Courtesy AIME).

#### 7.1.3.3. De Swaan's<sup>5</sup> model and solution

De Swaan<sup>5</sup>, as Barenblatt, also considered the equation of conservation of mass through the fractures with a source term representing the transfer of liquid from the blocks as:

$$\Phi_f C \frac{\partial \Delta P_f}{\partial t} - \frac{K_f \partial^2 \Delta P_f}{\mu \partial r^2} + u^*(\Delta P_f, t) = 0 \quad (7.42)$$

where  $\Delta p_f = p_{if} - p_i$  and  $p_{if}$  is the initial pressure of the reservoir.

The outflow from the block into the fracture of variable pressure is considered to be a convolution expressed as:

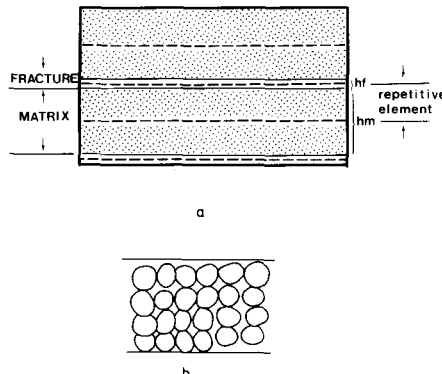
$$u^*(\Delta P_f, t) = - \frac{2}{A_m h_f} \int_0^t \frac{\partial \Delta P_f}{\partial t} q^{1*}(t - t_o) dt \quad (7.43)$$

where  $q^{1*}$  is the outflow across the block boundaries due to a unit-step drop in pressure ( $\Delta p_f$ ), and  $A_m$  is the area of the matrix blocks:

$$q^{1*} = - \frac{K_m}{\mu} A_m \operatorname{grad}(\Delta P_m^1) \quad (7.44)$$

For blocks of regular, simple geometries the pressure drop  $p_m^1$  and the outflow through the block can be calculated and equation 7.42 can be solved.

Two simple geometries of the blocks were considered: slabs (layered reservoir) and spheres (figure 7.7). For these geometries the solutions are analogous to those encountered in heat conduction problems.



7.7 – Slabs and spheres, matrix model<sup>5</sup>. (De Swaan<sup>5</sup>, Courtesy AIME).

For slabs the unit-pressure increment of the boundary is:

$$\Delta P_m(z, t) = 1 \frac{4}{\pi} \sum_{n=0}^{\infty} \frac{(-1)^n}{2n+1} e^{-\eta_m(2n+1)^2 \pi^2 t/h_m^2} \quad (7.45)$$

and for spheres the unit-pressure increment of the boundary is:

$$\Delta P_m(r, t) = 1 + \frac{2r_m}{\pi r} \sum_{n=1}^{\infty} \frac{(-1)^n}{n} e^{-\eta_m n^2 \pi^2 t / r_m} \sin \frac{n\pi r}{\eta_m} \quad (7.46)$$

De Swaan<sup>5</sup> considered only the asymptotic solutions of equations 7.45 and 7.46, which is similar to Barenblatt's quasi-steady state assumption.

A solution to equation 7.42 is presented for boundary and initial conditions corresponding to production at a constant rate from an infinite reservoir initially at a constant pressure  $p_{if}$ , i.e.:

$$\left. \begin{array}{ll} t = 0 & \Delta P_f = 0 \\ r = r_w & \frac{\partial(\Delta P_r)}{\partial r} = \frac{q\mu}{2\pi r_w h_f k_f} \\ r \rightarrow \infty & \Delta P_f = 0 \end{array} \right\} \quad (7.47)$$

where  $h_f$  is the thickness of the fracture, and  $k_f$  is the permeability of the individual fracture.

Block and fracture compressibility are assumed equal. De Swaan<sup>5</sup> considered only the asymptotic solutions corresponding to the *early stages* of production and to homogeneous behaviour. At the early stages of production, during which time flow takes place only in the fractures, the source term (equation 7.42) in the fractures, the source term in equation 7.42 is negligible and the equation is reduced to the classic one for flow through conventional homogeneous reservoirs. The solution to this equation under the conditions presented in equation 7.47 is:

$$\Delta P_f = \frac{q\mu}{4\pi h_f k_f} Ei\left(-\frac{r_w^2}{4\eta_f t}\right) \quad (7.48)$$

where  $\eta_f (= k_f/\Phi_f \mu c)$  is the diffusivity of the fracture medium.

For small arguments of the exponential integral function ( $r_w/4\eta_f t < 0.01$ ) one may approximate equation 7.48 by:

$$\Delta P_f = \frac{q\mu}{4\pi h_f k_f} \ln\left(\frac{4\eta_f t}{1.78 r_w^2}\right) \quad (7.49)$$

Then during the early stages of production the pressure decline is a linear function of the logarithm of time.

When liquid is produced from the fracture and the pressure is lowered, liquid from the blocks flows into the fractures. The outflow through the area  $A_m$  of the blocks is assumed to be distributed over half of the fracture where its approximate value is  $A_m h_f / 2$ .

By solving equation 7.42 with the asymptotic values of the equations 7.43 and 7.44, De Swaan obtained a solution similar to that in equation 7.49 but with a modified diffusivity.

For the slab model:

$$\eta_{sl} = 1 / \left( \frac{1}{\eta_f} + \frac{k_m}{k_f} \frac{h_m}{h_f} \frac{1}{\eta_m} \right) \quad (7.50)$$

and for the sphere model:

$$\eta_{sp} = 1 / \left( \frac{1}{\eta_f} + \frac{2}{3} \frac{k_m}{k_f} \frac{r_{sp}}{h_f} \frac{1}{\eta_m} \right) \quad (7.51)$$

where  $r_{sp}$  is the radius of sphere and  $\eta_m$  is matrix diffusivity. Thus, at large time values the relationship between pressure and logarithm of time is again linear.

In the  $p$  vs.  $\log t$ -plane the solution at early stages of production and at large time values is represented by two parallel lines as already obtained by Warren and Root<sup>1</sup>.

De Swaan's<sup>5</sup> solution does not add further information to the behaviour of naturally fractured reservoirs, and *only represents a part* of Warren and Root's<sup>1</sup> solution without any particular advantages in simplicity.

As discussed and proven by Kazemi<sup>4</sup>, quasi-steady state flow from blocks to fractures is reached very rapidly and a source function proportional to pressure difference in the block fracture is suitable. Therefore, it is difficult to see the advantage of derivation of the source function by using a regular geometrical shape of the block over Barenblatt's source function.

#### 7.1.3.4. Najurieta's<sup>6</sup> solution

Najurieta<sup>6</sup> considered the entire expression of equations 7.45 and 7.46 and obtained a solution which is also valid for the transient flow period.

Applying the Laplace transformation to equation 7.42 with a source as the resulting from equation 7.45 or 7.46, Najurieta obtained:

$$\Delta P_f = \frac{\mu q}{2\pi r_w K_2 h_2} L^{-1} \left[ \frac{\sqrt{\eta(s)} K_0 \left( r_w \sqrt{\frac{s}{\eta(s)}} \right)}{S^{3/2} K_1 \left( r_w \sqrt{\frac{s}{\eta(s)}} \right)} \right] \quad (7.52)$$

where  $\eta$  depends on the considered model of blocks.

For spheres:

$$\frac{1}{\eta(s)} = \frac{1}{\eta_2} + \frac{4k_1}{K_2 h_2 h_1 s} \left[ \frac{h_1}{2} \sqrt{\frac{s}{\eta_1}} \coth \left( \frac{h_1}{2} \sqrt{\frac{s}{\eta_1}} \right) - 1 \right] \quad (7.53)$$

and for slabs:

$$\frac{1}{\eta(s)} = \frac{1}{\eta_2} + \frac{2k_1}{k_2 h_2 \sqrt{s \eta_1}} \tanh \left( \frac{h_1}{2} \sqrt{\frac{s}{\eta_1}} \right) \quad (7.54)$$

As observed Najurieta's general solution (equation 7.52) is similar to Warren and Root's solution but with a different definition of  $\eta(s)$  resulting from the different definition of parameters.

A solution to equation 7.52 obtained by an approximate inverse Laplace transformation (Sharpey's method) is:

$$\Delta P_2 = \frac{q\mu}{4\pi k_2 h_2} Ei\left(-\frac{r^2}{4\eta t}\right) \quad (7.55)$$

where  $\eta$  is the function of time also dependent on the considered model of a fractured reservoir.

For slabs:

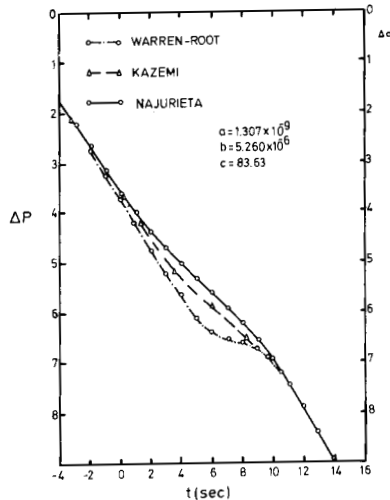
$$\eta = \frac{K_2 h_2}{\mu \left( \Phi_2 C_2 h_2 + \Phi_1 C_1 h_1 \sqrt{\frac{t}{\alpha}} \tanh \sqrt{\frac{\alpha}{t}} \right)} \quad (7.56)$$

for spheres:

$$\eta = \frac{K_2 h_2}{\mu \left[ \Phi_2 C_2 h_2 + \Phi_1 C_1 h_1 \left( \sqrt{\frac{t}{\alpha}} \coth \sqrt{\frac{\alpha}{t}} - \frac{t}{\alpha} \right) \right]} \quad (7.57)$$

where  $\alpha = h_1^2 / 4\gamma \eta_1$  and  $\gamma$  is Euler's constant.

This solution is compared with the Warren-Root and Kazemi solution in figure 7.8.



7.8 – A comparison between Najurieta's solution and those of Warren and Root, and Kazemi. (Najurieta<sup>6</sup> 1976).

#### 7.1.4. Special model – the Pollard model

The Pollard theory<sup>3</sup> was developed through the evaluation of the acid treatment in fractured limestone reservoirs.

In this approach the flow result from the simultaneous expansion of fluid saturating the pores of both units, matrix and fractures. This may be expressed as:

$$C_f \Phi_f \frac{\partial P_f}{\partial t} = \alpha (P_m - P_f) \quad (7.58)$$

$$C_m \Phi_m \frac{\partial P_m}{\partial t} = C_f \Phi_f \frac{\partial P_f}{\partial t} \quad (7.59)$$

from which the differential equation results as:

$$\frac{d^2 P_m}{dt^2} + A \frac{dP_m}{dt} = 0 \quad (7.60)$$

where:

$$A = \frac{C_f V_f + C_m V_m}{C_f V_f C_m V_m} \alpha \quad (7.61)$$

If equation 7.61 is integrated for the following boundary conditions:

- at the initial stage  $t = 0$ ,  $P_{fi} = P_{m,i}$
- at a later stage ( $t > 0$ ), the material balance of fluid expansion may indicate

$$V_f C_f (P_{fi} - P_s) = V_m C_m (P_s - P_{m,i}); \quad (7.62)$$

- at a very late stage  $t = \infty$ ,

$$P_f = P_s$$

the general solution is expressed by pressure drop related to time

$$\Delta P = \text{constant } e^{-\text{constant } \Delta t} \quad (7.63)$$

which is equivalent to a linear relationship between  $\log \Delta P$  and  $\Delta t$ .

The flowing process, in conditions of pressure drawdown or in conditions of pressure build-up after shut-in, is viewed as a process taking place in three zones as shown schematically in figure 7.9.

- a. The *first zone* is the fractured network zone around the wellbore which *first* reacts to well changes as variation of production rate, or starting of production or shut-in.
- b. The *second zone* which reacts in a *second stage* is the fractured network of the entire reservoir.
- c. The *third zone* is the matrix zone which, due to pressure drawdown or build-up, will act at a *later stage*. The matrix pressure will start either to build-up in case of well shut-in, or to decline in case of starting the well production.

If the pressure refers to the reservoir static pressure  $P_s$  and well pressure  $P_w$ , three

pressure differences will result:

- $\Delta P_1$  – pressure difference between static pressure  $P_s$  and matrix pressure  $P_m$ .
- $\Delta P_2$  – pressure difference between matrix pressure  $P_m$  and fractured network throughout the reservoir pressure  $P_f$ .
- $\Delta P_3$  – pressure difference between fractures around the wellbore pressure  $P_{wf}$ , and fracture network pressure,  $P_f$ .

Based on this model the total pressure drop  $\Delta P_t$  will be expressed by:

$$\Delta P_t = \Delta P_1 + \Delta P_2 + \Delta P_3 \quad (7.64)$$

or,

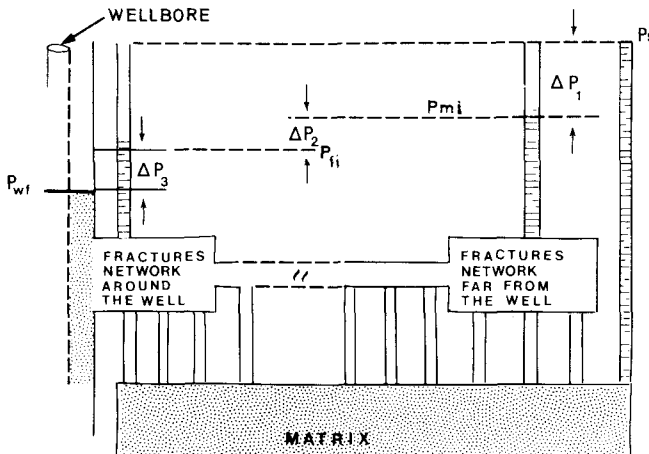
$$\Delta P_t = P_s - P_{wf} = C_p e^{-m_1 \Delta t} + D_p e^{-m_2 \Delta t} + E_p e^{-m_3 \Delta t} \quad (7.65)$$

or,

$$\Delta P_1 = C_p e^{-m_1 \Delta t} \quad (7.67)$$

$$\Delta P_2 = D_p e^{-m_2 \Delta t} \quad (7.67)$$

$$\Delta P_3 = E_p e^{-m_3 \Delta t} = (P_s - P_{wi} - C_p - D_p) e^{-m_3 \Delta t} \quad (7.68)$$



7.9 – Schematic description of Pollard model.

Pollard<sup>3</sup> and Pirson<sup>8</sup> derived the additional relationships for the evaluation of fine voids (matrix) and coarse voids (fractured network), based on *global balances* throughout the whole reservoir.

As *global balances* throughout the whole reservoir, these equations must include average pressure values. It is hard to understand how these *global balances* lead to the pressure build-up behaviour at the well, nevertheless equation 7.63 of Pollard is similar to the Warren-Root model in case of build-up in a finite reservoir (simplified equation 7.39).

In general, it is difficult to believe that Pollard build-up curves represent the true behaviour of a fractured reservoir. It is however not easy to make an analysis of the factors which can deform the results and lead to a build-up relationship as in equation 7.68. Warren and Root<sup>1</sup>, referring to Pollard's method, stated that «there is a finite probability that the use of  $\log(p_s - p_w)$  vs. time could result in a complete description of a reservoir solely on the basis of after production», and also «it is probable that any decaying function can be approximated by a series of exponential terms over an interval of graduate change».

## 7.2. DISCUSSION OF THE WARREN AND ROOT<sup>1</sup> MODEL

Since Warren and Root's model actually represents the best approach for a transient flowing process in a fractured reservoir, a discussion of dimensional and dimensionless parameters in relation to physical implications becomes necessary. Based on a detailed analysis it will also become possible to develop the methodology for the interpretation of transient pressure data.

### 7.2.1. Basic dimensional equation

Transient flowing pressure ( $P_{wf}$ ) based on dimensionless parameters  $\lambda$ ,  $\omega$ ,  $t_D$ , and with reference to static pressure  $P_i$ , is expressed by the following equations for the four basic cases associated with infinite and finite reservoir, drawdown and build-up pressure:

Drawdown pressure ( $R = \infty$ , infinite reservoir)

$$P_{wf} = P_i - m' \left\{ \log t_D + .351 + .435 \operatorname{Ei} \left[ -\frac{\lambda t_D}{\omega(1-\omega)} \right] - .435 \operatorname{Ei} \left[ -\frac{\lambda t_D}{1-\omega} \right] \right\} \quad (7.69)$$

Drawdown pressure ( $R = R_o$ , finite reservoir)

$$P_{wf} \cong P_i - \frac{1.74 m'}{R_o^2} \left\{ t_D + \frac{(1-\omega)^2}{\lambda} \left[ 1 - \exp \left( -\frac{\lambda t_D}{\omega(1-\omega)} \right) \right] - .87 m' (\ln R_o - .75) \right\} \quad (7.70)$$

Build-up pressure ( $R = \infty$ , infinite reservoir)

$$P_{wf} = P_i - m' \left\{ \log \frac{t_{DP} + \Delta t_D}{\Delta t_D} - .435 \operatorname{Ei} \left( -\lambda \Delta t_D / \omega (1-\omega) \right) + .435 \operatorname{Ei} \left( -\frac{\lambda \Delta t}{(1-\omega)} \right) \right\} \quad (7.71)$$

Build-up pressure ( $R = Ro$ , finite reservoir)

$$P_{wf} = P_i - \frac{1.74 m'}{R_o^2} \left[ t_{DP} + \frac{(1-\omega)^2}{\lambda} \exp(-\lambda \Delta t_D / \omega (1-\omega)) \right] \quad (7.72)$$

where

$$\Delta P_D (1, t_D) = P_{i,D} - P_{2D} = (P_i - P_w)/m = \Delta P_w/m \quad (7.73)$$

$$m' = \frac{2.3}{2} m = 1.15 \frac{q \mu B}{2\pi K_2 h} \quad (7.73)$$

The approximated solution obtained for drawdown in equations 7.69 and 7.70 are valid only if:

$t_D > 100$ , or

$t_D > 100 \omega$  for  $\lambda \ll 1$ , or  $t_D > 100 - \frac{1}{\lambda}$  for  $\omega \ll 1 \rightarrow \text{Case } R = \infty$

$t_D > 100 \omega R^2$  for  $\lambda \ll 1$ , or  $t_D > 100 R^2 - 1/\lambda$  for  $\omega \ll 1 \rightarrow \text{Case } R \neq \infty$

The approximated solutions obtained for build-up in equations 7.71 and 7.72 are only valid if:

$$t_{DP} \geq 3/\lambda \quad \text{or} \quad t_p \geq 3/\theta\lambda$$

or if,

$$\lambda \ll 1 \rightarrow \Delta t_{D, min} = 100\omega \text{ or } \Delta t_{min} = 100 \frac{\omega}{\theta}$$

$$\omega \ll 1 \rightarrow \Delta t_{D, min} = 100 - \frac{1}{\lambda} \text{ or } \Delta t_{min} = \frac{100 - 1/\lambda}{\theta}$$

Equations 7.69, 7.70, 7.71 and 7.72 are modified versions of equations 7.24, 7.37, 7.33 and 7.39.

### 7.2.2. Basic dimensionless parameters

- a. Parameter  $\omega$ ; representing the *dimensionless storage capacity* of the fractured network can be expressed as a fraction of the total storage capacity as follows:

$$\omega = \frac{\Phi_2 C_2}{\Phi_1 C_1 + \Phi_2 C_2} = \frac{1}{1 + \frac{\Phi_1 C_1}{\Phi_2 C_2}} = \frac{1}{1 + \text{SCR}} \quad (7.74)$$

where SCR is the storage capacity ratio.

It is evident that:

- if  $\Phi_2 C_2 \gg \Phi_1 C_1$ ,  $\text{SCR} \rightarrow 0$  and  $\omega \rightarrow 1$ , which corresponds to a *non-porous* fractured reservoir (discussed in chapter 6).
- if  $\Phi_1 C_1 \gg \Phi_2 C_2$ ,  $\text{SCR} \rightarrow \infty$  and  $\omega \rightarrow 0$ , which corresponds to a conventional intergranular porous reservoir.
- Between values 0 and 1, the parameter  $\omega$  indicates a reservoir with double porosity.

- b. Parameter  $\lambda$ ; represents the *dimensionless interporosity flowing capacity* depending on the permeability ratio  $K_1/K_2$  of two domains and of contact surface per unit of volume of rock:

$$\lambda = \alpha \times \frac{K_1}{K_2} \times R_w^2 \quad (7.75)$$

For a given  $\alpha$  it is evident that:

- if  $K_1 \cong K_2$ , the flowing process will become similar to that of a single porosity reservoir.
- if  $K_1 \ll K_2$ , the flowing process will behave similarly to that of a double porosity system.

On the other hand if  $K_1/K_2$  is constant and:

- if  $\alpha$  is high  $\rightarrow$  large contact surface – smaller matrix blocks – high fracture density.
- if  $\alpha$  is low  $\rightarrow$  reduced contact surface – large matrix blocks – low fracture density.

- c. Parameters  $\lambda$  and  $\omega$ ; in examining the Warren and Root model for various reservoirs it was observed that this model works satisfactorily in the case of a big contrast between matrix and fractures controlled by the dimensionless parameters  $\lambda$  and  $\omega$ . The values of these parameters, based on various evaluations, would have to be of the following order of magnitude:

- when  
 $10^{-3} < \lambda < 10^{-9}$

this corresponds to small  $\alpha \cong$  large blocks, small  $K_1 \cong$  tight matrix and high  $K_2 \cong$  large fracture width.

- when

$$10^{-2} < \omega < 10^{-4}$$

this corresponds to  $\Phi_1 C_1 \gg \Phi_2 C_2$  and often to  $\Phi_1 \gg \Phi_2$ .

On the other hand if the dimensionless parameters approach the limits of validity:

$$\omega \rightarrow 0 \quad \lambda \rightarrow 0$$

$$\omega \rightarrow 1 \quad \lambda \rightarrow \infty$$

a series of physical data is evidenced, such as: porosity, permeability, fracturing density and block size. Some limit cases also show that a double porosity system might be reduced to a single porosity case 1, 3, 5, 6 presented in Table 7.1.

The detailed analysis indicates that certain fractured reservoirs will behave as conventional single porosity reservoirs when certain physical parameters approach limit values. But if the contrasting characteristics of the double porosity system are evident (as in cases 2, 7 and 8), the basic data might be evaluated through the Warren and Root model.

d. Parameter  $t_D$ ; represents the dimensionless time:

$$t_D = \theta t = \frac{a'}{r_w^2} t = \frac{K_2}{(\Phi_1 C_1 + \Phi_2 C_2) \mu r_w^2} t \quad (7.76)$$

where  $a' = K_2 / (\Phi_1 C_1 + \Phi_2 C_2)$   $\mu$  is a *complex piezo-conductivity factor* since it includes both storage capacity of matrix and fractures but only fracture permeability.

e. Parameters  $\lambda$ ,  $\omega$ ,  $t_D$ ; and their influence on Ei functions are shown in table 7.2 for various values of  $\omega$ ,  $\lambda$ ,  $t_D$ . The Ei functions indicate, for various limit values of parameters  $\omega$ ,  $\lambda$  and  $t_D$ , either a logarithmic approximation or a tendency of Ei and exp functions towards zero. These limits are used in interpretation of equations 7.69, 7.70, 7.71 and table 7.2.

### 7.2.3. Pressure drawdown behaviour in the case $R = \infty$

#### 7.2.3.1. Equations governing pressure drawdown

The more general equation expressing pressure drawdown based on equations 7.73 and 7.69 is written as a summation of Ei ( $-z$ ) functions, as follows:

$$\Delta P_D = \frac{1}{2} \left[ -\text{Ei}\left(-\frac{1}{4t_D}\right) + \text{Ei}\left(-\frac{\lambda}{\omega(1-\omega)} t_D\right) - \text{Ei}\left(-\frac{\lambda}{1-\omega} t_D\right) \right] \quad (7.77)$$

Table 7.1

ANALYSIS OF PARAMETERS  $\omega$  AND  $\lambda$ 

Table 7.1

Parameter	Case	If Magnitude	Due to Reservoir parameter	Storage capacity $\omega$		Interporosity Flow $\lambda$	Fracturing Density	Block Dimension	Porosity System		OBSERVATIONS	
				Fracture	Matrix				SINGLE	DOUBLE	System	type of reservoir
$\omega$	1	$\omega \approx 0$	$\frac{\text{if}}{\phi_2 C_2 = 0}$	zero	large	—	Practical zero	—	YES	—	only Matrix	single porosity (conventional)
	2	$\omega \rightarrow 0$	$\frac{\text{if}}{\phi_1 C_1 \gg \phi_2 C_2}$	small	large	—	low	big	—	YES Matrix predominant	Matrix and fractures	(fractured) double porosity
	3	$\omega \rightarrow 1$	$\frac{\text{if}}{\phi_2 C_2 \gg \phi_1 C_1}$	large	small	—	high	very small	YES fractures	—	only fractures	single porosity (semi-convent.)
$\lambda$	4	$\lambda = 0$	<u>case</u> $K_1 \approx 0$	—	—	small	—	—	YES fractures	—	..	..
	5		<u>case</u> $\alpha \approx 0$	—	—	small	Practical zero	very big	YES Matrix	—	only Matrix	single porosity (conventional)
	6	$\lambda \rightarrow \infty$	<u>if</u> $\alpha \rightarrow \infty$ <u>if</u> $K_1 \gg K_2$	—	—	very high	very high	very	YES	—	only fractures	single porosity (semi-convent.)
	7	$0 < \lambda < 1$	$\alpha K_1 \ll K_2$ $\alpha$ small	—	—	high	average	average	—	YES	—	(fractured reservoir) double porosity
$\lambda, \omega$	8	$0 < \lambda < 0.01$ $0 < \omega < 0.1$	$K_2 \gg K_1$ $\phi_1 C_1 \gg \phi_2 C_2$	normal	normal	normal	average	average	—	YES	Matrix and Fractures	Classic fractured reservoir double porosity

FUNCTION  $Ei(-u)$  AND  $\exp(-u)$ : APPROXIMATIONS

table 7.2

VARIABLES				FUNCTIONS		
$\omega$	$\lambda t_D$	$\lambda$	$t_D$	$Ei[-\lambda t_D/\omega(1-\omega)]$	$Ei(-\lambda t_D/1-\omega)$	$\exp[-\lambda t_D/\omega(1-\omega)]$
$\omega = 0$	0 - 0.05	$0 - 0.05/t_D$	$0 - 0.05/\lambda$	$Ei(-\infty) \approx 0$	$\ln 1.78 \lambda t_D$	$1/\infty \approx 0$
	0.05 - 10	$0.05/t_D - 10/t_D$	$0.05/\lambda - 10/\lambda$	$Ei(-\infty) \approx 0$	$Ei(-\lambda t_D)$	$1/\infty \approx 0$
	$10 - \infty$	$10/t_D \rightarrow \infty$	$10/\lambda \rightarrow \infty$	$Ei(-\infty) \approx 0$	$Ei(-\infty) \approx 0$	$1/\infty \approx 0$
$\omega = 1$	-	-	-	$Ei(-\infty) \approx 0$	$Ei(-\infty) \approx 0$	$1/\infty \approx 0$
$0 < \omega < 1^*$	$< 0.05$	$\ll 0.01$	small	$\ln 1.78 \times \frac{\lambda t_D}{\omega(1-\omega)}$	$\ln 1.78 \frac{\lambda t_D}{1-\omega}$	$e^{-\lambda t_D/\omega(1-\omega)}$
$0 < \omega < 1$	-	0	-	$\infty$	$\infty$	1
$0 < \omega < 1$	large		small	$Ei[-\lambda t_D/\omega(1-\omega)]$	$Ei[-\lambda t_D/(1-\omega)]$	$\exp[-\lambda t_D/\omega(1-\omega)]$
$0 < \omega < 1$	large	$0 < \lambda < 1$	large	$\rightarrow 0$	$\rightarrow 0$	$\rightarrow 0$

\* The logarithmic expression of  $Ei$  functions requires that  $\lambda t_D/\omega(1-\omega) < 0.05$  and  $\lambda t_D/(1-\omega) < 0.05$

Since the  $E_i$  functions may be approximated by the expressions:

$$Ei(-z) \approx \ln z + .576 \approx \ln 1.78 z \dots \text{if } 0 < z < 0.050$$

$$Ei(-z) \approx Ei(-z) \dots \text{if } 0.05 < z < 10$$

$$Ei(-z) \approx 0 \dots \text{if } 10 < z < \infty$$

simplified equations as presented in table 7.3 are obtained as a function of  $\lambda$ ,  $\omega$  and  $t_D$ .

a. Stages of pressure drawdown

Following the dimensionless time variation, three stages are observed:

- Early stage; for a given  $\lambda$ ,  $\omega$ ,  $\theta$  and very small times, the first right hand term of equation 7.77 will be negligible compared with the second and third terms, and as shown in table 7.3 the dimensionless pressure drop will result as,

$$\Delta P_D = \Delta P_{w, D} = \frac{1}{2} \ln \frac{1}{\omega} \quad (7.78)$$

or in dimensional units as,

## DRAWDOWN PRESSURE EVALUATION

TABLE 7.3

t <sub>D</sub> limits			Function Ei, values			Pressure drop ΔP <sub>D</sub>	Equation Number
Ei(- $\frac{1}{4t_D}$ )	Ei(- $\frac{\lambda}{\omega(1-\omega)}t_D$ )	Ei(- $\frac{\lambda}{1-\omega}t_D$ )	Ei(- $\frac{1}{4t_D}$ )	Ei(- $\frac{\lambda}{\omega(1-\omega)}t_D$ )	Ei(- $\frac{\lambda}{1-\omega}t_D$ )		
0 < t <sub>D</sub> < ∞	0 < t <sub>D</sub> < ∞	0 < t <sub>D</sub> < ∞	unchanged	unchanged	unchanged		
0 < t <sub>D</sub> < 0.05	0 < t <sub>D</sub> < 0.025 $\frac{1-\omega}{\lambda}\omega$	0 < t <sub>D</sub> < 0.025 $\frac{1-\omega}{\lambda}$	≈ 0	$\ln 1.78 \frac{\lambda t_D}{\omega(1-\omega)}$	$\ln 1.78 \frac{\lambda t_D}{1-\omega}$	$\Delta P_D = \frac{1}{2} \left[ -Ei(-\frac{1}{4t_D}) + Ei(-\frac{\lambda}{\omega(1-\omega)}t_D) - Ei(-\frac{\lambda}{1-\omega}t_D) \right]$	7.77
0.05 < t <sub>D</sub> < 10	..	..	-Ei(- $\frac{1}{4t_D}$ )	..	..	$\Delta P_D = \frac{1}{2} \ln \frac{1}{\omega}$	7.78
..	0.025 $\frac{1-\omega}{\lambda}\omega < t_D < 5 \frac{1-\omega}{\lambda}\omega$	..	..	Ei(- $\frac{\lambda}{\omega(1-\omega)}t_D$ )	$\ln 1.78 \frac{\lambda t_D}{1-\omega}$	$\Delta P_D = \frac{1}{2} \left[ -Ei(-\frac{1}{4t_D}) + \ln \frac{1}{\omega} \right]$	7.79
10 < t <sub>D</sub> < ∞	..	..	ln 2.246 t <sub>D</sub>	..	..	$\Delta P_D = \frac{1}{2} \left[ -Ei(-\frac{1}{4t_D}) + Ei(-\frac{\lambda}{\omega(1-\omega)}t_D) - \ln 1.78 \frac{\lambda t_D}{1-\omega} \right]$	7.80
..	..	0.025 $\frac{1-\omega}{\lambda} < t_D < 5 \frac{1-\omega}{\lambda}$	ln 2.246 t <sub>D</sub>	..	Ei(- $\frac{\lambda}{4-\omega}t_D$ )	$\Delta P_D = \frac{1}{2} \left[ \ln 1.26 \frac{1-\omega}{\lambda} + Ei(-\frac{\lambda t_D}{4-\omega}) - Ei(-\frac{\lambda t_D}{1-\omega}) \right]$	7.81
..	5 $\frac{1-\omega}{\lambda}\omega < t_D < \infty$	..	..	..	≈ 0	$\Delta P_D = \frac{1}{2} \left[ \ln 2.246 t_D - Ei(-\frac{\lambda t_D}{1-\omega}) \right]$	7.82
..	..	5 $\frac{1-\omega}{\lambda} < t_D < \infty$	..	..	≈ 0	$\Delta P_D = \frac{1}{2} \ln 2.246 t_D = \frac{1}{2} (\ln t_D + 0.80907)$	7.83

## IMPORTANT CASES

0.05 < t <sub>D</sub> < 10	5 $\frac{1-\omega}{\lambda}\omega < t_D < \infty$	0 < t <sub>D</sub> < 0.025 $\frac{1-\omega}{\lambda}$	Ei(- $\frac{1}{4t_D}$ )	≈ 0	$\ln 1.78 \frac{\lambda t_D}{1-\omega}$	$\Delta P_D = \frac{1}{2} \left[ -Ei(-\frac{1}{4t_D}) - \ln 1.78 \frac{\lambda t_D}{1-\omega} \right]$	7.85
10 < t <sub>D</sub> < ∞	..	..	ln 2.246 t <sub>D</sub>	≈ 0	..	$\Delta P_D = \frac{1}{2} \ln 1.26 \frac{1-\omega}{\lambda}$	7.86
..	0 < t <sub>D</sub> < 0.025 $\frac{1-\omega}{\lambda}\omega$	0 < t <sub>D</sub> < 0.025 $\frac{1-\omega}{\lambda}$	..	$\ln 1.78 \frac{\lambda t_D}{\omega(1-\omega)}$	$\ln 1.78 \frac{\lambda t_D}{\omega(1-\omega)}$	$\Delta P_D = \frac{1}{2} \left[ \ln 2.246 t_D + \ln \frac{1}{\omega} \right]$	7.87

$$\Delta P_w = m' \log 1/\omega \quad (7.78')$$

from which

$$\omega = e^{-2,3} \Delta P_w / m' \quad (7.78'')$$

This last equation shows a direct relationship between the relative storage capacity  $\omega$ , pressure drop  $\Delta P_w$ , and slope  $m'$  of the straight line.

- *Intermediate stage*; this stage corresponds to the transition period between the initial time  $t_{it}$  when flow is no longer governed by equation 7.78 and the final time  $t_{ft}$  when flow is governed by equation 7.84. Various simplified equations based on the magnitude of the dimensionless parameters  $t_D$ ,  $\lambda$ ,  $\omega$  are shown in table 7.3 (equations 7.80 to 7.83, and also 7.85 and 7.86, see figure 7.10).

As observed, if certain relationships among  $\lambda$ ,  $\omega$  and  $t_D$  are fulfilled, the pressure might remain constant with time during the transient period as shown in equation 7.86:

$$\Delta P_D = \frac{1}{2} \ln 1.26 \frac{1 - \omega}{\lambda} \quad (7.86)$$

which, combined with equation 7.78'', might solve the problem of a simultaneous evaluation of both parameters  $\lambda$  and  $\omega$ .

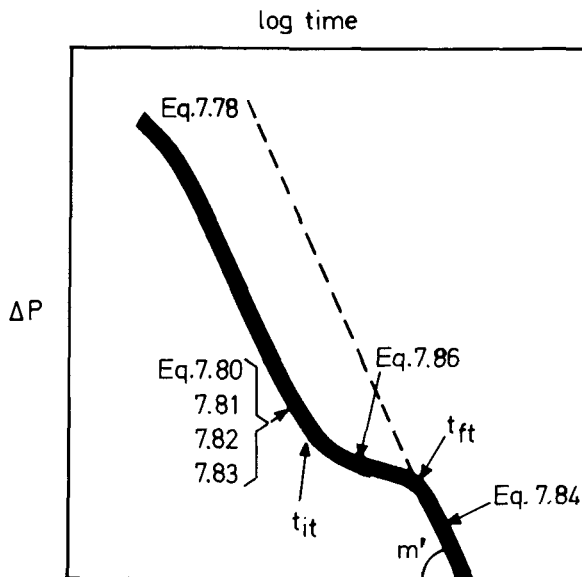
- *Final stage*; the pressure drop at a later stage (expressed by large time  $t_D$ ) is expressed by an equation similar to that used in a conventional reservoir, since both second and third terms of the right hand part of equation 7.77 become negligibly smaller compared with the first term (figure 7.8). This situation is reached when the dimensionless time fulfills the conditions:

$$t_D > 10; t_D > 5 \frac{1 - \omega}{\lambda}; t_D > 5 \frac{1 - \omega}{\lambda}$$

and when the pressure drop will result

$$\Delta P_D = \frac{1}{2} \ln 2.246 t_D = \frac{1}{2} \ln t_D + .80907 \quad (7.84, \text{table 7.3})$$

or in dimensional terms as:



7.10 – Drawdown pressure curve in Warren-Root model for case  $R = \infty$ .

$$P_f = P_i - m' \log 2.246 t_D = P_i - m' \log 2.246 \theta t$$

where  $m' = 1.15$  m (see equation 7.73)

Equation 7.84 expresses a semi steady-state flowing condition and describes the flow in fractures as already discussed in chapter 6.

#### b. Discussion of results

The *early* and *intermediate* stages will only take place if  $\lambda$  and  $\omega$  are very small, which means that important contrasts between the physical properties of the matrix and fractures exists in the fractured reservoir. In fact, if  $\lambda$  and  $\omega$  are high the arguments of the second and third right hand terms of equation 7.77 are large even for small  $t_D$  values, and both second and third Ei functions become negligible compared with the first right hand Ei function. If this is the case, the fractured reservoir in an early transient stage approaches the behaviour of a non-porous fractured reservoir where the pressure drop is expressed by equation 7.84 (see figure 7.4a for  $\omega = 0.1$  and figure 7.3a for  $\lambda < 5 \times 10^{-3}$ ).

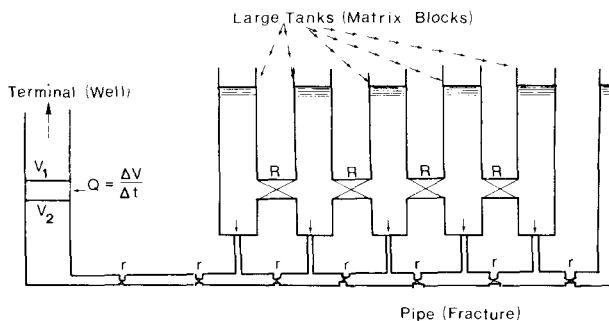
Inversely, if  $\lambda$  and  $\omega$  are small, both the early and intermediate stages will influence the flowing behaviour over long periods of time until the asymptote (equation 7.84) is reached (figure 7.4.a and 7.5). During this time simplified forms of equation 7.77 may result, as shown in table 7.3 from equation 7.78 to equation 7.87. A variety of these equations are controlled by the relationship between  $\lambda$ ,  $\omega$  and  $t_D$ .

The behaviour of the pressure drawdown as shown in figure 7.8 is physically explained in the following way:

- In the *intermediate stage*, after a period of production, the pressure drop developed in a fracture network stimulates the expansion of matrix fluid, and thus the fluid which leaves the matrix is feeding the fractured network. The encroachment of matrix fluid in fractured reduces the pressure drop in

the fractures network similarly to an injection of fluid; only later towards the end of this phase, will the matrix start to adjust its feeding towards the well rate level, *approaching a quasi-steady-state* flowing condition.

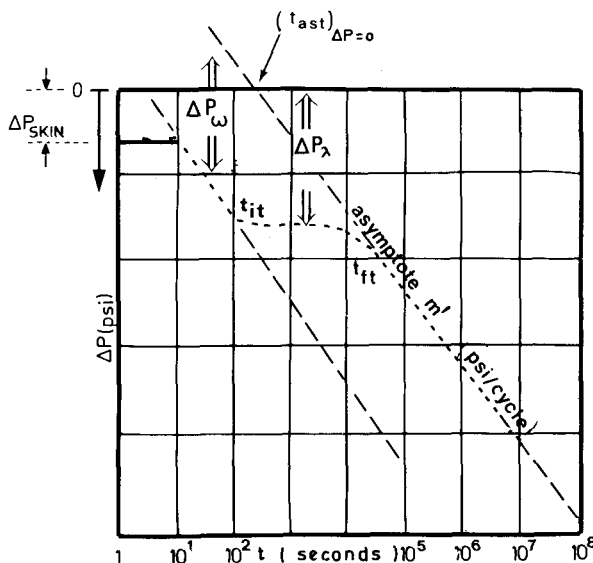
- In the *final stage* the flowing process is *quasi-steady-state*, since the fluid produced by the well is equal to the fluid supplied by the matrix to the fractured network. The relationship  $Q$  vs  $\Delta P$  under steady-state conditions of flow represents *exclusively* the flow through the fractured network as described in chapter 6. By analogy it might be considered that the flow is similar to a series of very *large tanks* (matrix blocks) which supply a *pipeline* (fractured network) in order to assure a certain rate at the *terminal* (well) as illustrated schematically in figure 7.11. The resistance  $R$  between tanks and pipeline is equivalent to flowing conditions between matrix and fractured network.



7.11 – Analogy between tanks containing liquid and fractured reservoir behaviour. R-resistance.

#### 7.2.3.2. Evaluation of a fractured reservoir through transient pressure drawdown

From pressure data recorded in time it is possible to obtain a diagram as shown in the curve in figure 7.12, where pressure is in ordinate and time is in log scale.



7.12 – Fractured reservoir drawdown pressure curve in Warren-Root model for case  $R = \infty$  and  $\Delta P$  necessary for evaluation of basic parameters.

a. Evaluation of permeability  $K_2 = K_f$

From the drawdown plot  $p$  vs.  $\log t$  (figure 7.12) the slope of the straight line ( $m'$ ) is obtained as pressure difference/time cycle on log time scale.

$$m' = \Delta P / \text{cycle}_{10}$$

If  $m'$  is introduced into equation 7.73 it may be written that,

$$k_2 = k_f = 1.15 \frac{q \mu_o B_o}{2\pi h} \times \frac{1}{m'} \quad (7.88)$$

b. Evaluation of the dimensionless time factor  $\theta$  (1/sec)

From equation 7.84, which expresses the dimensionless pressure vs. dimensionless time, in quasi-steady-state conditions (asymptote)

$$P_D = \frac{1}{2} \ln 2,246 t_D = 1.15 \log 2,246 t_D$$

which dimensionally gives:

$$\Delta P = P_i - P_{wf} = m' \log 2,246 t_D = m' \log 2,246 \theta t$$

The parameter  $\theta$  may be obtained as

$$\theta = \frac{.445}{[t_{sat}]_{\Delta P=0}} \quad (7.89)$$

where  $t_{sat}$  at  $\Delta P = 0$  is obtained by the extrapolation of the asymptote (equation 7.84) at  $\Delta P = 0$  (figure 7.12). In the case of a very large contrast between matrix and fractured network the transient time until the asymptote is reached may be so long (compared with recorded time) that the asymptote is not reached, and thus parameter  $\theta$  can not be estimated.

c. Evaluation of the relative storage capacity factor  $\omega$

The relative storage capacity factor  $\omega$  based on equation 7.78 is expressed as:

$$\omega = \exp(-2.3 \Delta P_w / m') \quad (7.78'')$$

where  $\Delta P_w$  is directly obtained from the diagram  $P$  vs.  $\log t$  as shown in figure 7.12.

d. Evaluation of single storage capacities  $\Phi_1 C_1$  and  $\Phi_2 C_2$

Based on equations 7.76 the summation of single storage capacities may be expressed as follows:

$$\Phi_1 C_1 + \Phi_2 C_2 = \frac{K_2}{\mu r_w^2} \times \frac{1}{\theta}$$

and the same summation based on eq. 7.74 will be

$$\Phi_1 C_1 + \Phi_2 C_2 = \frac{\omega}{\Phi_2 C_2}$$

From the combination of these two equations it results that

$$\Phi_2 C_2 = \frac{\omega}{\theta} \frac{K_2}{\mu r_w^2} \quad (7.90)$$

and

$$\Phi_1 C_1 = \frac{\omega}{\Phi_2 C_2} - \Phi_2 C_2 \quad (7.90')$$

#### e. Evaluation of porosities

From single storage capacities obtained through equation 7.90, and if  $C_1$  and  $C_2$  are known, the equation is written as:

$$C_1 = C_o + \frac{S_{wi} C_w + C_{po}}{1 - S_{wi}} \quad (7.91)$$

$$C_2 \cong C_o$$

the result is (see chapter 4):

$$\Phi_m = \frac{\Phi_1}{1 - \Phi_2} \frac{1}{S_{om}} \quad (7.92)$$

#### f. Evaluation of interporosity flowing capacity factor $\lambda$

If the Warren and Root model satisfactorily describes the flowing pressure behaviour, it is necessary for parameter  $\lambda$  to be related to the transient time period between  $t_{it}$  and  $t_{ft}$ , as shown in figure 7.9. The most direct way to evaluate it is given by

the intercept of the tangent to the difference curve in equation 7.31 through the inflection point at  $t_D = 1$ , which is reduced as follows:

$$\Delta P_D \Big|_{t_D=1} = [-\lambda - \ln \lambda/(1-\omega)]/2 \quad (7.31)$$

This equation is similar to equations 7.83 and 7.85 of table 7.3 for  $t_D = 1$ :

$$\Delta P_D \Big|_{t_D=1} = -\frac{1}{2} \ln 1.78 \frac{\lambda}{1-\omega} = \frac{1}{2} \ln \frac{.56(1-\omega)}{\lambda} = 1.15 \times \log \frac{.56(1-\omega)}{\lambda} \quad (7.93)$$

or dimensionally considering the pressure drop in transient conditions at  $t_D = 1$  to be:

$$\Delta P_\lambda = m' \log \frac{0.56(1-\omega)}{\lambda} \quad (7.94)$$

Parameter  $\lambda$  will result thus, in the following expression

$$\lambda = .56(1-\omega) e^{-2.3 \Delta P_\lambda / m'} \quad (7.95)$$

#### g. Evaluation of contact surface parameter $\alpha$

From equation 7.75 parameter  $\alpha$  is given as a function of  $\lambda$ ,

$$\alpha = \lambda \frac{K_2}{K_1} \frac{1}{r_w^2} \quad (7.96)$$

where  $K_2$  and  $\alpha$  may be obtained from the  $P$  vs.  $\log t$  data, while  $K_1$  is generally known from laboratory measurements on matrix samples.

#### h. Evaluation of block characteristic length a

As already discussed (equation 7.34), if a block model of uniformly spaced fractures is used, the following equation will result:

$$L^2 = \frac{n(n+2)}{\alpha} = r_w^2 \frac{K_1}{K_2} \frac{4n(n+2)}{\lambda} \quad (7.97)$$

The relationship of equivalent length  $L$  vs.  $\alpha$  is associated to the number of flowing directions as shown below.

Flowing direction n	$4n(n+2)/\alpha = L^2$	$L^2 = f(\lambda)$
3	$60/\alpha$	$60 r_w^2 \frac{K_1}{K_2} \frac{1}{\lambda}$
2	$32/\alpha$	$32 r_w^2 \frac{K_1}{K_2} \frac{1}{\lambda}$
1	$12/\alpha$	$12 r_w^2 \frac{K_1}{K_2} \frac{1}{\lambda}$

(7.98)

The relationship between average length a in parallelipiped versus orthogonal length characteristics is given by equations 6.48 in chapter 6, and set of equations 7.35. (7.99)

In order to evaluate fracture porosity ( $\Phi_f$ ) and fracture width (b), the models illustrated in chapter 6, table 6.1 may be used. It is necessary to follow the procedure described in section 6.2.1.

### 1. The relationship between $t_{tf}$ and block geometry

When considering the final time of the transition period  $t_{tf}$  equivalent to the time when flow starts to behave as a quasi-steady-state flow, ( $t_{tf} = t_{ss}$ ), a relationship between time, matrix piezconductivity and matrix equivalent length may be written as follows:

$$L \equiv \sqrt{\frac{K_1}{\Phi_1 C_1 \mu}} t \quad (7.100)$$

If transformed into dimensionless time through equation 7.76, the following results:

$$t_{D,ss} = \frac{1}{2} \frac{\Phi_1 C_1}{\Phi_2 C_2 + \Phi_1 C_1} L^2 \frac{K_2}{K_1 r_w^2} \quad (7.101)$$

or based on equation 7.17

$$t_{D,ss} = \frac{1}{2} (1 - \omega) L^2 \frac{K_2}{K_1 r_w^2}$$

If equation 7.101 is combined with equation 7.97 the result is:

$$t_{D,ss} = \frac{1}{2} \frac{1-\omega}{\lambda} \times 4n(n+2) \quad (7.102)$$

or, if

$$\epsilon = \frac{1}{2} 4n(n+2)$$

where,

$$t_{D,ss} = \epsilon \cdot \frac{1-\omega}{\lambda}$$

if  $L/a = 1$  varies from 6 to 16 and 30 according to 1, 2 or 3 flowing directions.

If a cube, as shown in model 6 of table 6.1, has three flowing directions,  $n = 3$  and thus  $4n(n+2) = 60$ . In continuation  $\epsilon = 30$  and

$$t_{D,ss} = 30 \frac{1-\omega}{\lambda}$$

#### *Calculation Example No. 1*

In a naturally fractured reservoir a well is producing at a constant rate. The drawdown pressure is recorded, and the basic data are as follows:

$$q = 3200 \text{ STB/D} \quad \mu_o = 4,6 \text{ C.P}$$

$$h = 240 \text{ m} \quad C_1 = C_{oe} = 13.5 \times 10^{-6} (\text{psi}^{-1})$$

$$r_w = 7.4 \text{ cm} \quad C_2 = C_o = 7.2 \times 10^{-6} (\text{psi}^{-1})$$

$$K_1 = 0.1 \text{ mD (from cores)} \quad B_o = 1,23$$

$$S_{wi} = 0.3 \text{ (from logs)} \quad L_{fD} = 2/\text{m}$$

The variation of pressure drop  $\Delta P$  vs.  $\log t$  as shown in figure 7.13 indicates two parallel straight line segments connected by a transition pressure variation. Since the pressure drop behaviour indicates a behaviour similar to the Warren and Root model, evaluation of the fractured reservoir characteristics by means of the Warren and Root procedure is needed.

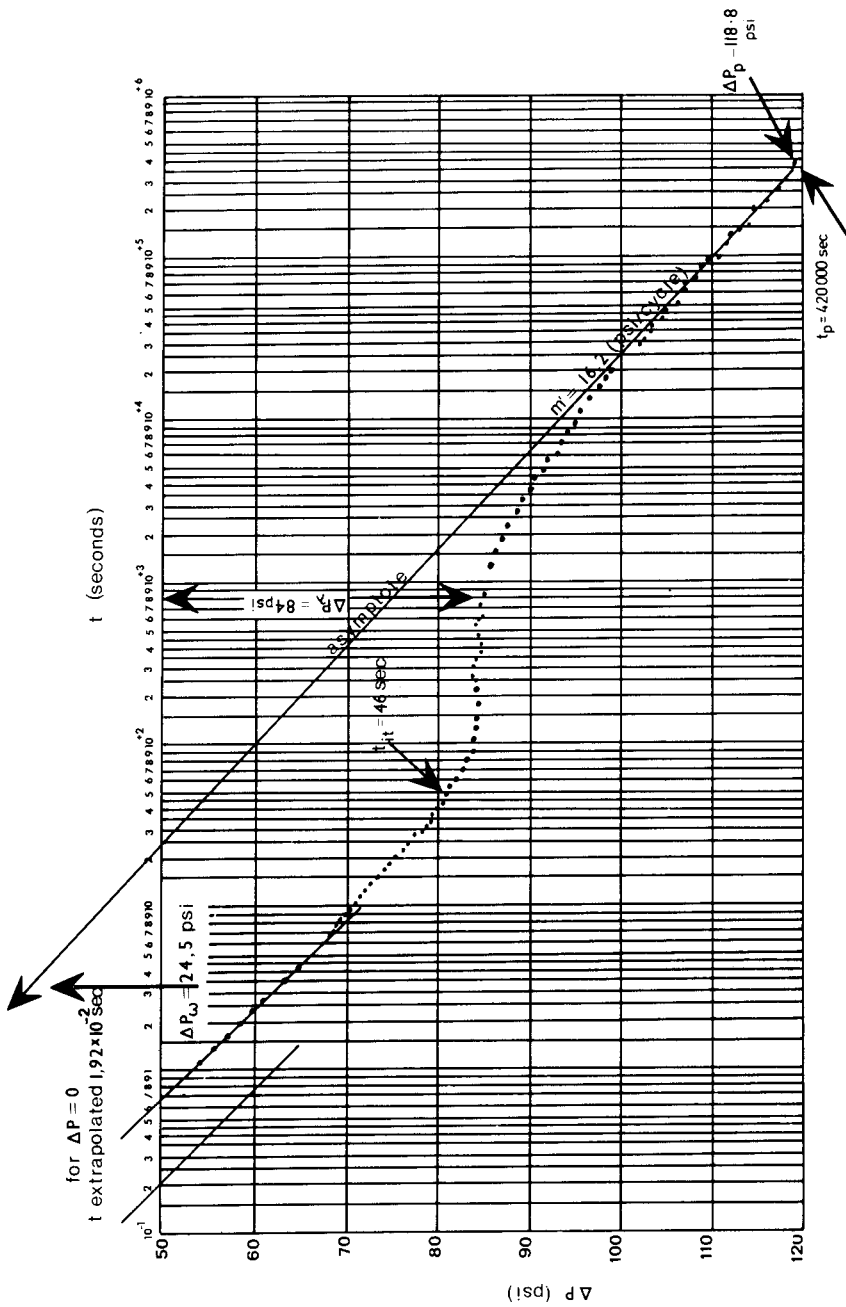
Solution

1. Slope  $m'$  of the straight line log time is:

$$\therefore m' = 16.2 \text{ psi/cycle} = 1.102 \text{ atm/cycle}$$

2. Permeability  $K_2$  is obtained from equation 7.88:

$$K_2 = 1.15 \frac{q \mu_o B_o}{2\pi h} \times \frac{1}{m'} = 1.15 \frac{5890 \times 4,6 \times 1.23}{6.28 \times 24000 \times 1.102} = 0.23 (\text{D})$$



7.13 – Example of pressure drawdown case. Warren-Root model,  $R = \infty$ .

3. Parameter  $\theta$  is obtained from equation 7.89 by extrapolating the asymptote at  $\Delta P = 0$ . The time corresponds to:

$$[t_{ast}]_{\Delta P=0} = 0.0192 \text{ seconds}$$

The result is:

$$\theta = \frac{0.445}{0.0192} = 23 \text{ (1/sec)}$$

4. Parameter  $\omega$  is obtained from equation 7.78':

$$\omega = e^{-2.3\Delta P_w/m'}$$

$$\omega = e^{-2.3 \times 24.5/16.2} = 0.031$$

5. Porosity evaluation from equation 7.90':

$$\Phi_2 C_2 = \frac{\omega}{\theta} \cdot \frac{K_2}{\mu r_w^2} = \frac{3.1 \times 10^{-2}}{23} \cdot \frac{0.23}{4.6 \times 55} = 1.22 \times 10^{-6} \left( \frac{1}{\text{at}} \right) = 8.4 \times 10^{-8} \left( \frac{1}{\text{psi}} \right)$$

$$\Phi_1 C_1 = \Phi_2 C_2 \frac{1 - \omega}{\omega} = 8.4 \times 10^{-8} \times \frac{1 - 0.031}{0.031} = 2.63 \times 10^{-6} \left( \frac{1}{\text{psi}} \right)$$

$$\Phi_2 = \frac{\Phi_2 C_2}{C_2} = \frac{8.4 \times 10^{-8}}{7.2 \times 10^{-6}} = .0117$$

$$\Phi_1 = \frac{\Phi_1 C_1}{C_1} = \frac{2.63 \times 10^{-6}}{13.5 \times 10^{-6}} \cong .20$$

$$\Phi_f \cong \Phi_2 = 0.0117$$

$$\Phi_m = \frac{\Phi_1}{1 - \Phi_2} \frac{1}{S_{om}} = \frac{0.2}{1 - 0.0117} \times \frac{1}{0.7} = 0.252$$

6. Parameter  $\lambda$  is obtained from equation 7.95 as a function of  $\Delta P = 84$  psi (as observed in figure 7.13 by extrapolating the inflection tangent at  $t_D = 1$  or  $t = 23$  sec):

$$\lambda = 0.56 (1 - 0.031) e^{-2.3 \times \Delta P_w/m'}$$

$$\lambda = 0.56 \times 0.97 e^{-2.3 \times 84/16.2} = 3.6 \times 10^{-6}$$

7. Parameter  $\alpha$  will result from equation 7.96 as follows:

$$\alpha = \lambda \frac{K_2}{K_1} \times \frac{1}{r_w^2} = 3.6 \times 10^{-6} \times -\frac{0.23}{10^{-4}} \times \frac{1}{55} = 1.5 \left( \frac{1}{m^2} \right)$$

8. The equivalent length of blocks for the case of flow in 3, 2 and 1 directions is given by:

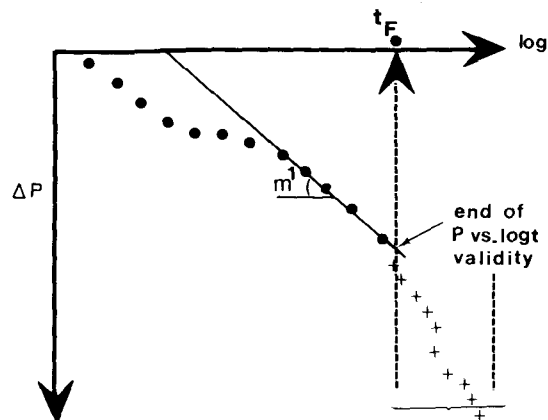
$$L = \sqrt{60/\alpha} \quad \text{if the flow takes place in 3 directions } L = 6.3 \text{ m}$$

$$L = \sqrt{32/\alpha} \quad \text{if the flow takes place in 2 directions } L = 4.6 \text{ m}$$

$$L = \sqrt{12/\alpha} \quad \text{if the flow takes place in 1 direction } L = 2.8 \text{ m}$$

#### 7.2.4. Pressure drawdown behaviour in the case $R = R_o$

Based on recorded pressure drop data the results may be represented in a diagram  $\Delta P$  vs. log time as is illustrated in figure 7.14. The results will be similar to those in the case  $R = \infty$ , up until a time  $t_F$  when linear relationship  $\Delta P$  vs.  $\log t$  loses its validity.



7.14 – Fractured reservoir pressure drawdown behaviour, case  $R = \text{finite}$ .

Based on the same procedure as  $R = \infty$ , it is possible to evaluate:

- $\theta$  from equation 7.89
- $a'$  from  $\theta r_w^2$ , equation 7.76

and then,

$$R_o = \sqrt{4 \times a' \times t_F}$$

Since the finite character of the reservoir is established when pressure changes its decline at  $t = t_F$  (figure 7.14), a new diagram has to be drawn based on equation 7.70, which may be rewritten as follows:

$$\Delta P = P_i - P_w = \frac{1.74 \times m'}{R_o^2} [t_D + F_{tD}] - R_D \quad (7.103)$$

where,

$$F_{tD} = \frac{(1-\omega)^2}{\lambda} \left[ 1 - \exp \left( -\frac{\lambda t_D}{\omega(1-\omega)} \right) \right] \quad (7.103')$$

$$R_D = .87 m' (\ln R_o - .75) \quad (7.103'')$$

The variation of  $\Delta P$  vs. time  $t$  will be drawn as in figure 7.15 and will depend on  $F_{tD}$  as shown in table 7.4.

Table 7.4

$t_D$	Stage	$\frac{\lambda}{\omega(1-\omega)} t_D$	$\exp \left[ -\frac{\lambda t_D}{\omega(1-\omega)} \right]$	$F_{tD}$	$\Delta P$ vs. $t_D$	SLOPE	zone Fig. 7.15
very small	very early	0-0.05	1	0	linear	$m' \frac{1.74}{R_o^2}$	1
small	early	0.05	1	0	linear	»	1
average	average	0.05 ~ 3	$1 \sim 0$	$0 \sim \frac{(1-\omega)^2}{\lambda}$	curve	-	2
very large	late	> 3	0	$(1-\omega)^2/\lambda$	linear	$m' \frac{1.74}{R_o^2}$	3

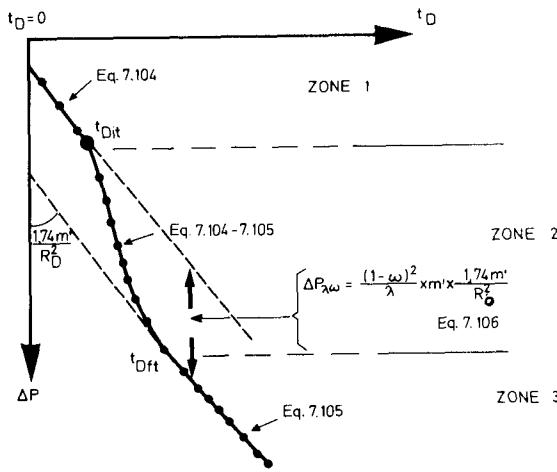
The pressure behaviour will indicate (figure 7.15) the presence of the following zones:

- zone 1 ( $t_D$  small) governed by the equation:

$$\Delta P = \frac{1.74 m'}{R_o^2} t_D + R_D \quad (7.104)$$

- Zone 3 ( $t_D$  large) governed by the equation:

$$\Delta P = \frac{1.74 m'}{R_o^2} \left[ t_D + \frac{(1-\omega)}{\lambda} \right] + R_D \quad (7.105)$$



7.15 – Fractured reservoir pressure drawdown, case  $R = \text{finite}$ . Evaluation of basic data.

- Zone 2 is the transition zone between  $t_{Dit}$  and  $t_{Dft}$  corresponding to an interval of pressure drop which is written as:

$$\Delta P_{\lambda,\omega} = [\text{Eq } 7.105] - [\text{Eq } 7.104] = \frac{(1 - \omega)^2}{\lambda} \frac{1.74}{R_o^2} \times m' \quad (7.106)$$

#### Other evaluation

- The value of  $R_D$  may also be obtained on the intercept of ordinate of equation 7.103 at  $t_D = 0$ .
- The slope of straight line variation  $\Delta P$  vs.  $t_D$  will give the slope  $1.74 m'/R_o^2$  where  $R_o$  is known, and therefore  $m'$ , from which further  $K_2$  could also be determined.
- The value  $\omega$  can be obtained from figure 7.14 as in equation 7.78" in the case of  $R = \infty$ , as a function of  $\Delta P_w$  and  $m'$ .
- The value  $\lambda$  will result from figure 7.15 (where  $\Delta P_{\lambda,\omega}$  is evaluated), since in the relationship expressed by equation 7.106,

$$\lambda = \frac{(1 - \omega)^2}{\Delta P_{\lambda,\omega}} \cdot \frac{1.74 m'}{R_o^2}$$

$\lambda$  is the only unknown parameter.

### 7.2.5. Pressure build-up behaviour in the case $R = \infty$

#### 7.2.5.1. Basic equations

When after a period of production a well is shut-in, the superposition of effects developed during production time and after production was stopped will influence the pressure build-up behaviour (see equation 7.32).

By using equation 7.77 and considering the time  $\Delta t_D$  after shut-in, the result will be:

$$\begin{aligned} \Delta P = m' \times .435 & \left\{ -Ei\left(-\frac{1}{4(t_p + \Delta t_D)}\right) + Ei\left[-\frac{\lambda}{\omega(1-\omega)}(t_p + \Delta t_D)\right] \right. \\ & - Ei\left[-\frac{\lambda}{1-\omega}(t_p + \Delta t_D)\right] + Ei\left(-\frac{1}{4\Delta t_D}\right) - Ei\left(-\frac{\lambda}{\omega(1-\omega)}\Delta t_D\right) \\ & \left. + Ei\left(-\frac{\lambda}{1-\omega}\Delta t_D\right) \right\} \end{aligned} \quad (7.107)$$

Equation 7.107 is presented in various simplified forms in table 7.5 where the variation of the Ei function argument is essential.

The fact that shut-in generally takes place after the pressure drawdown has already reached the quasi-steady-state conditions, means that:

$$Ei\left(-\frac{\lambda}{\omega(1-\omega)}(t_p + \Delta t_D)\right) \cong 0$$

$$Ei\left(-\frac{\lambda}{1-\omega}(t_p + \Delta t_D)\right) \cong 0$$

On the other hand (due to relatively high values of  $\theta$ ), even for small values of time  $t$ , it is expected to give:

$$Ei\left(-\frac{1}{4(t_p + \Delta t_D)}\right) < 0.025$$

$$Ei\left(-\frac{1}{4\Delta t_D}\right) < 0.025$$

and therefore,

$$\text{Ei}\left(\frac{1}{4(t_p + \Delta t_D)}\right) + \text{Ei}\left(-\frac{1}{4\Delta t_D}\right) = \ln \frac{t_p + \Delta t_D}{\Delta t_D}$$

Thus, a first approximation of equation 7.107 is as follows:

$$\Delta P = m' \times .435 \left[ \ln \frac{t_p + \Delta t_D}{\Delta t_D} - \text{Ei}\left(-\frac{\lambda}{\omega(1-\omega)} \Delta t_D\right) + \text{Ei}\left(-\frac{\lambda}{1-\omega} \Delta t_D\right) \right] \quad (7.108)$$

### Discussion

#### •• Expression $\Delta P$ and well pressure $P_w$

From the superposition of effects the following will result:

$$\Delta P = P_s - P_{wf} + P_{wf} - P_w = P_s - P_w$$

therefore, evaluation of pressure in the well during the build-up will give:

$$P_w = P_s - \Delta P$$

and thus based on equation 7.108 the well pressure will be described by

$$P_w \cong P_s + m' \left[ \log \frac{\Delta t_D}{t_p + \Delta t_D} + .435 \text{Ei}\left(-\frac{\lambda}{\omega(1-\omega)} \Delta t_D\right) - .435 \text{Ei}\left(-\frac{\lambda}{1-\omega} \Delta t_D\right) \right] \quad (7.109)$$

The equations shown in table 7.5 indicate the simplified pressure drop expression of equation 7.108 at various values of time  $\Delta t$  after shut-in.

As observed, between the initial stage (equation 7.110) and the final stage (equation 7.114), the difference in pressure between the two parallel straight lines is given by:

$$\Delta P_w = \frac{1}{2} m \times \ln 1/\omega$$

Equations 7.111, 7.112 and 7.113 describe the conditions of flow between initial double porosity behaviour (equation 7.110) and final quasi-stabilized conditions expressed by equation 7.114.

#### 7.2.5.2. Evaluation of fractured reservoirs through transient pressure build-up (figure 7.16)

- In order to evaluate the parameter  $\omega$ , the procedure remains the same as in the drawdown case:

PRESSURE  $\Delta P$  AFTER WELL SHUT-IN

TABLE 7.5

$\omega$	$\lambda$	$\frac{\lambda \Delta t_D}{\omega(1-\omega)}$	$\frac{\lambda \Delta t_D}{1-\omega}$	PRESSURE DROP $\Delta P_{2D}$ EQUATION	EQUATION NUMBER
0-1	0-1	0 → 0.025	0 → 0.025	$\Delta P_2 = \frac{1}{2} \left[ \ln \frac{t_p + \Delta t_D}{\Delta t_D} + \ln \omega \right] = - \frac{1}{2} \left[ \ln \frac{\Delta t_D}{t_p + \Delta t_D} + \ln \frac{1}{\omega} \right]$	7.110
"	"	0.025-5	"	$\Delta P_2 = \frac{1}{2} \left[ \ln \frac{t_p + \Delta t_D}{\Delta t_D} - Ei \left( - \frac{\lambda \Delta t_D}{\omega(1-\omega)} \right) + \ln \lambda \frac{1.78 \Delta t}{1-\omega} \right]$	7.111
"	"	5 - ∞	"	$\Delta P_2 = \frac{1}{2} \left[ \ln \frac{t_p + \Delta t_D}{\Delta t_D} + \ln \frac{1.78 \lambda \Delta t_D}{1-\omega} \right] = \frac{1}{2} \left[ \ln \frac{1.78 (t_p + \Delta t_D) \lambda}{1-\omega} \right]$	7.112
"	"	0.025-5	0.025-5	$\Delta P_2 = \frac{1}{2} \left[ \ln \frac{t_p + \Delta t_D}{\Delta t_D} - Ei \left( - \frac{\lambda \Delta t_D}{(1-\omega)} \right) + Ei \left( - \frac{\lambda}{1-\omega} \Delta t_D \right) \right]$	7.113
"	"	5 - ∞	5 - ∞	$\Delta P_2 = \frac{1}{2} \ln \frac{t_p + \Delta t_D}{\Delta t_D}$	7.114

$$\omega = e^{-2.3\Delta P_w/m'}$$

- Based on slope  $m'$  it is easy to estimate the fracture network permeability:

$$K_2 = 1.15 \frac{q \mu B_o}{2\pi h} \times \frac{1}{m'}$$

- The value  $\theta$  results from the time at the end of the production period:

$$\Delta P_p = m' \log 2.246 \theta t_p \quad (7.115')$$

$$\theta = \frac{1}{2.246 t_p} 10^{\Delta P_p/m'}$$

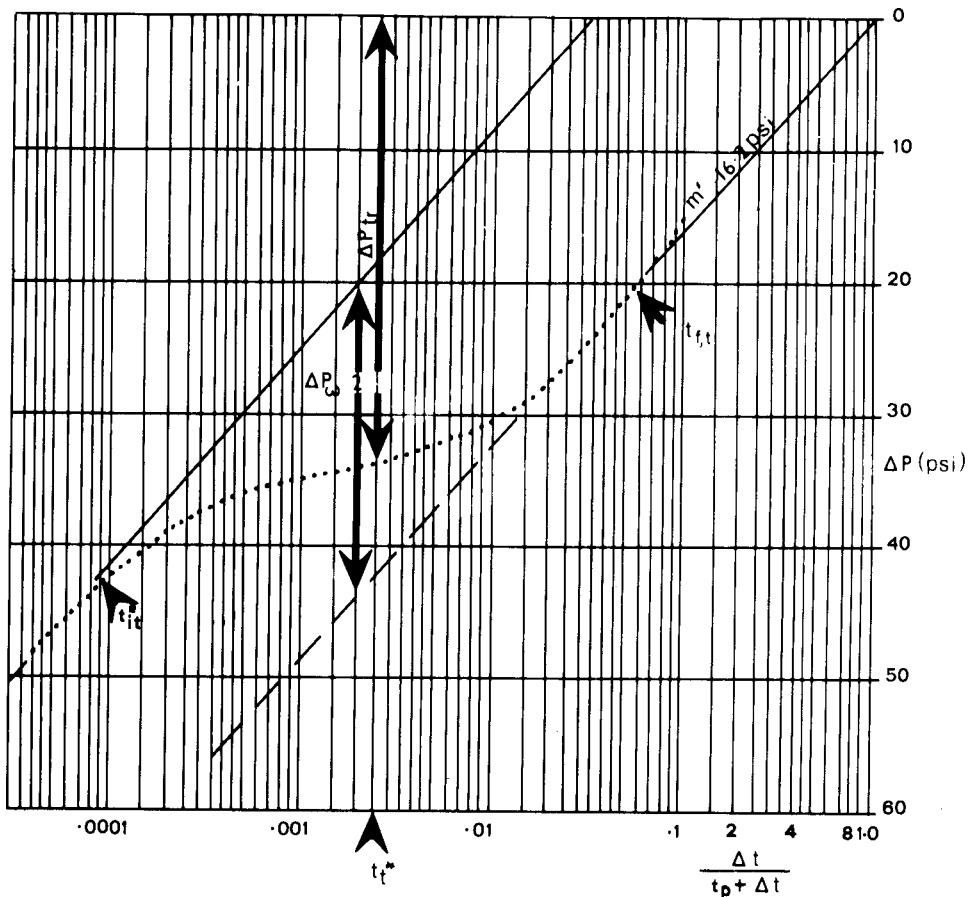


Fig. 7.16

7.16 – Pressure build-up in a fractured reservoir, case R = finite in conventional diagram  $\Delta P$  vs.  $\log \frac{\Delta t}{t_p + \Delta t}$ .

The value  $\Delta P_p$  is obtained through equation 7.115 where  $\theta$  is obtained from the drawdown curve.

- Evaluation of porosities as in the drawdown case is as follows:

$$\Phi_2 C_2 = \frac{\omega}{\theta} \frac{K_2}{\mu r_w^2}$$

$$\Phi_1 C_1 = \frac{1}{\omega} \Phi_2 C_2 (1 - \omega)$$

$$\Phi_1 = \frac{C_1 \Phi_1}{C_1} ; \quad \Phi_2 = \frac{C_2 \Phi_2}{C_2}$$

$$\Phi_f = \Phi_2$$

$$\Phi_m = \frac{\Phi_1}{1 - \Phi_2} \frac{1}{(1 - S_{wc})_m}$$

- The value  $\lambda$  can be obtained from equation 7.112 as a function of  $\Delta P_{tr}$  during the transition period measured at the inflection point (see figure 7.16):

$$\frac{\Delta P_{tr}}{m'} = \log \theta(t_p + \Delta t) + \log \frac{1.78 \lambda}{1 - \omega} = \log \frac{\theta(t_p + \Delta t) 1.78 \lambda}{1 - \omega}$$

from which  $\lambda$  directly results:

$$\lambda = \frac{1 - \omega}{1.78 \theta(t_p + \Delta t)} \times 10^{\Delta P_{tr}/m'} \quad (7.116)$$

- The contact surface parameter  $\alpha$ , similarly to the drawdown case, is:

$$\alpha = \frac{K_2}{K_1} \cdot \frac{\lambda}{r_w^2} \quad (7.117)$$

#### Calculation Example No. 2

If, after producing the same well as in example 1, the shut-in takes place at  $t_p = 450\,000$  sec, the pressure data recorded  $\Delta P$  vs.  $\log \Delta t/(t_p + \Delta t)$  will be drawn as in figure 7.14.

From the results of the build-up the following parameters were obtained:

$$\sim m' = 16,2 \text{ psi/cycle}$$

$$\sim K_2 = 1.15 \frac{q \mu B_o}{2\pi h} \cdot \frac{1}{m'} = 1.15 \frac{5890 \times 4.6 \times 1.23}{6.28 \times 24000 \times 1.102} = 0.23 \text{ D}$$

$$\sim \theta = \frac{1}{2.246 t_p} 10^{\Delta P_r / m'} = \frac{1}{2.246 \times 450000} 10^{119.4i / 16.2} \approx 23 \text{ 1/sec}$$

$$\sim \omega = e^{-2.3 \Delta P_w / m'} = e^{-2.3 \times 24.5 / 16.2} = 3.1 \times 10^{-2}$$

$$\sim \Phi_2 C_2 = \frac{\omega}{\theta} \times \frac{K_2}{\mu r_w^2} = \frac{3.1 \times 10^{-2}}{23} \frac{0.23}{4.6 \times 55} = 1.24 \times 10^{-6} \text{ 1/at}$$

$$= 8.43 \times 10^{-8} \text{ 1/psi}$$

$$\sim \Phi_1 C_1 = \frac{\Phi_2 C_2 (1 - \omega)}{\omega} = 8.43 \times 10^{-8} \times \frac{1 - 0.03i}{0.03i} = 2.63 \times 10^{-6} \text{ 1/psi}$$

$$\sim \Phi_2 = \frac{\Phi_2 C_2}{C_2} = \frac{8.43 \times 10^{-8}}{7.2 \times 10^{-6}} = 0.017$$

$$\sim \Phi_1 = \frac{\Phi_1 C_1}{C_1} = \frac{2.63 \times 10^{-6}}{13.5 \times 10^{-6}} = 0.2$$

From which the respective porosities are:

$$\sim \Phi_f = \Phi_2 \cong 0.017$$

$$\sim \Phi_m = \frac{\Phi_1}{1 - \Phi_2} \cdot \frac{1}{S_{om}} = \frac{0.2}{1 - 0.017} \times \frac{1}{0.7} \cong 0.29$$

and parameter  $\lambda$  (from equation 7.116) is:

$$\lambda = \frac{1 - \omega}{1.78 \times \theta \times (t_p + \Delta t)} \times 10^{\Delta P_w / m'} = \frac{0.97}{1.78 \times 23 (450000 + 1350)} 10^{32/16.2}$$

$$\lambda = 4.95 \times 10^6$$

### 7.2.6. Pressure build-up behaviour in the case $R = R_o$

In a finite reservoir the pressure build-up is expressed through equation 7.72 where, due to superposition of effects, the terms  $R_D$  of equation 103 will disappear.

The equation which governs pressure build-up is written as follows:

$$\Delta P = \frac{1.74 \text{ m}'}{R_o^2} [t_{DP} + F'_{tD}] \quad (7.118)$$

where,

$$F'_{tD} = \frac{(1-\omega)^2}{\lambda} \exp \left( -\frac{\lambda}{\omega(1-\omega)} \Delta t_D \right) \quad (7.119)$$

Table 7.6

Stage	$\frac{\lambda}{\omega(1-\omega)} \Delta t_D$	$\exp \left( -\frac{\lambda}{\omega(1-\omega)} \Delta t_D \right)$	$F(t_D)$	$\Delta P$	Equation no.
early	0–0.05	$\approx 1$	$\frac{(1-\omega)^2}{\lambda}$	$\Delta P = \frac{1.74 \text{ m}'}{R_o^2} \frac{(1-\omega)^2}{\lambda} t_{DP}$	(7.120)
intermediate	0.05 ~ 30	$1 \rightarrow 0$	equation 7.119	$\Delta P = \frac{1.74 \text{ m}'}{R_o^2} (t_{DP} + F'_{tD})$	(7.118)
late	$30 \sim \infty$	$\approx 0$	0	$\Delta P = \frac{1.74 \text{ m}'}{R_o^2} t_{DP}$	(7.121)

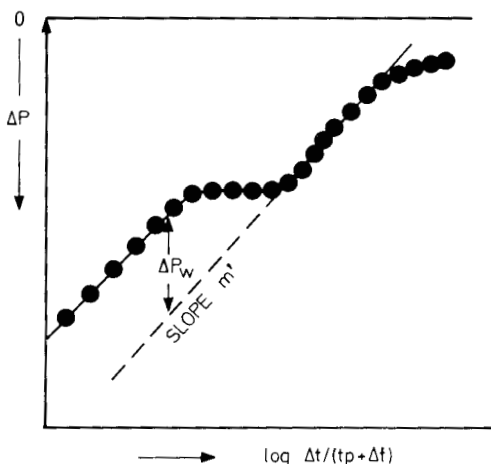
Applying the same criteria as in table 7.4 the results obtained are those shown in table 7.6. As observed, the initial and later stages are represented by constant pressure drop (equations 7.120 and 7.121), while on the contrary in an intermediate stage, equation 7.118, the pressure depends on time.

$$\Delta P = \frac{1.74 \text{ m}'}{R_o^2} t_{DP} + \frac{1.74 \text{ m}'}{R_o^2} \frac{(1-\omega)^2}{\lambda} \frac{1}{e^{-[\lambda/\omega(1-\omega)]\Delta t_D}}$$

If equation 7.118 is rearranged, neglecting the first right hand term, and expressed in log it results,

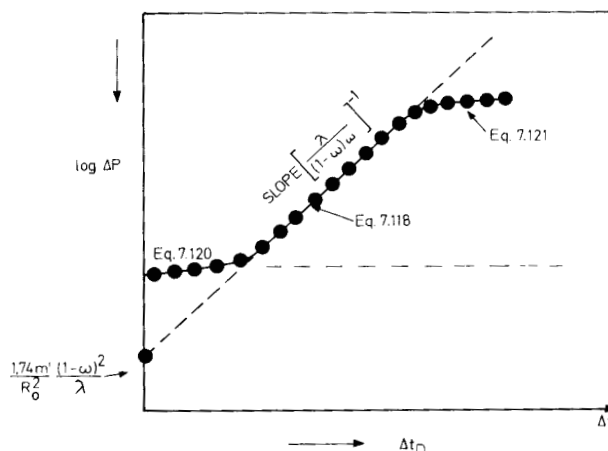
$$\log \Delta P \cong \log \frac{1.74 \text{ m}'}{R_o^2} \frac{(1-\omega)^2}{\lambda} - .435 \frac{\lambda}{(1-\omega)\omega} \Delta t_D \quad (7.122)$$

In practice, if the relationship  $\Delta P$  vs.  $\log \Delta t/(t_D + \Delta t)$  is used, the results give a diagram similar to that of case  $R = \infty$  up until the boundary  $R_o$  is reached, when the pressure deviates from the asymptote (figure 7.17).



7.17 - Fractured reservoir pressure build-up, case R = finite in diagram  $\Delta P$  vs.  $\log t$ .

It is necessary in this case to re-examine the data on another diagram  $\log \Delta P$  vs.  $t_D$  as in figure 7.18, where the three zones are governed by equations 7.120, 7.118 and 7.121, respectively.



7.18 - Fractured reservoir pressure build-up, case R = finite in diagram  $\log \Delta P$  vs.  $\Delta t_D$ .

#### Calculation Procedure

Based on the diagram in figure 7.17 the following may be evaluated:

- $m'$  from the slope of the parallel straight line
- $\omega$  from the pressure difference between parallel straight lines by reading  $\Delta P_w$
- $\theta$  from equation 7.115'

From figure 7.18 the following is obtained:

$$\frac{1.74 m'}{R_o^2} t_{DP} \rightarrow \text{which may give the value } R_o$$

$$\left[ \frac{0.435 \lambda}{(1-\omega) \omega} \right]^{-1} \text{ sec/cycle psi} \quad \left\{ \begin{array}{l} \text{the slope of the straight line of equation 7.118 from} \\ \text{which the only unknown parameter is } \lambda. \end{array} \right.$$

### 7.2.7. Evaluation of $\lambda$ and $\omega$ through dimensionless diagrams

An approach for  $\lambda$  evaluation was proposed by Uldrich<sup>9</sup> in association with a number of dimensionless curves based on transient variations of pressure drawdown and build-up. According to analytical developments of pressure behaviour in the transient zone, the main objective was to relate the inflection point pressure  $P_{wf}^*$  or  $P_{ws}^*$  (flowing wf, and shut-in ws) and their projections on the two parallel straight lines of the Warren and Root curve.

The inflection point pressure (during flowing pressure drop), when projected (figure 7.19a) on the straight line starting at  $P_i$  is denominated *early* ( $P_{wf}^*$ ), and when projected on the parallel straight line it is denominated *late* ( $(P_{wf}^*)_{late}$ ). A similar procedure will be used for the build-up pressure curve (figure 7.19 b).

#### 7.2.7.1. Drawdown pressure

- If the pressure was not recorded over a sufficient period of time, in order to reach the asymptote it is possible to use the parameter:

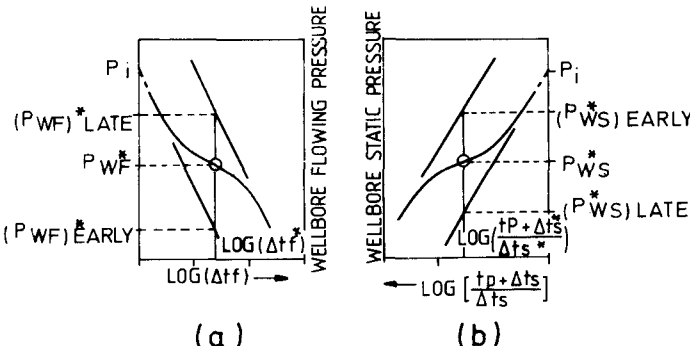
$$F_{DD} = \frac{(P_{wf}^*)_{late} - (P_{wf}^*)_{early}}{m'} \quad (7.123)$$

and then use this parameter in the diagram in figure 7.20 and thus obtain the value  $\omega$ .

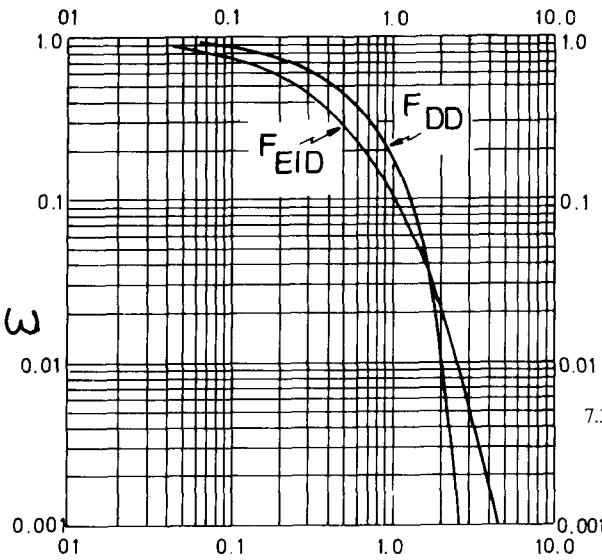
- If the initial transient period is confused by *afterflow effects* the  $(P_{wf}^*)_{late}$ , value may be used as follows:

$$F_{EID} = \frac{(P_{wf}^*)_{late} - P_{wf}^*}{m'} \quad (7.124)$$

and then evaluate through the diagram in figure 7.20 the same value  $\omega$ .



7.19 – Pressure drawdown (a) and build-up (b) associated with inflection pressure and its projections.  
(Uldrich<sup>9</sup>, Courtesy AIME).



7.20 – The relationship  $\omega$  – vs.  $F_{DD}$  and  $F_{EID}$   
(Uldrich<sup>9</sup>, Courtesy AIME).

It should be noted that:

$$\ln \omega = F_{DD} - F_{EID}$$

#### 7.2.7.2. Build-up pressure

Through examination of build-up pressure various options become possible.

##### a. Evaluation of $\lambda$

If the build-up is recorded until the asymptote is reached the parameter  $\omega$  is known, and the value  $\Delta t_s^*/(tp + \Delta t_s^*)$  may be calculated. Through the diagram in figure 7.21 the parameter  $F_B$  is obtained and is considered to be a function of  $\omega$ . The value  $F_B$  is associated with  $\lambda$  through:

$$F_B = \lambda \Delta t_D^* \quad (7.125)$$

and  $\lambda$  then yields:

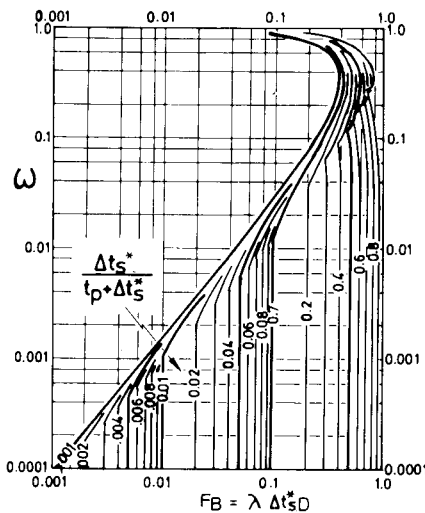
$$\lambda = F_B / \theta \times \Delta t_s^* \quad (7.126)$$

##### b. Evaluation of $\omega$

A similar procedure may be followed if the later part of build-up is not available. The diagram to be used is given in figure 7.22, where the parameter  $\omega$  is obtained from  $(F_{BU})_{early}$  and time expressed by  $t_s/(tp + \Delta t_s^*)$ .

The  $(F_{BU})_{early}$  value is obtained from:

$$(F_{BU})_{early} = \frac{(P_{ws}^*)_{early} - P_{ws}^*}{m} \quad (7.127)$$

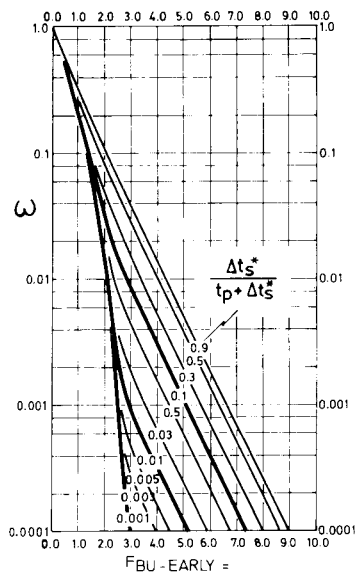


7.22 – The relationship  $\omega$  vs.  $(F_{BU})_{early}$  for various  $\Delta t^*/(t_p + \Delta t_s^*)$ . (Uldrich<sup>9</sup>, Courtesy AIME).

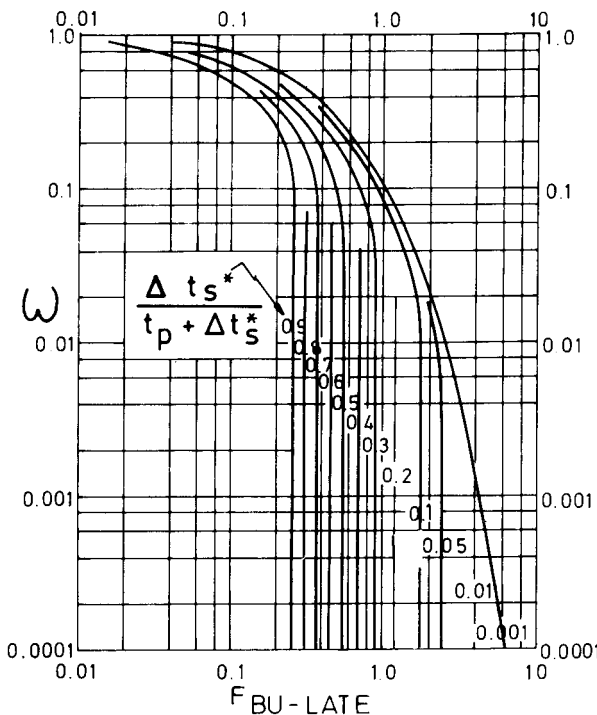
If the *early* part of transient pressure build-up is not clear the *later* part may be used through figure 7.23, where  $\omega$  is obtained as a function of:

$$(F_{BU})_{late} = \frac{P_{ws}^* - (P_{ws}^*)_{late}}{m} \quad (7.128)$$

and of time  $\Delta t_s^*/(t_p + \Delta t_s^*)$ .



7.21 – The relationship  $\omega$  – vs.  $F_B$  for various  $\Delta t^*/(t_p + \Delta t_s^*)$ . (Uldrich<sup>9</sup>, Courtesy AIME).



7.23 - The relationship  $\omega$  vs.  $F_{BU-LATE}$  for various  $\Delta t_s^*/(t_p + \Delta t_s^*)$ .  
(Uldrich<sup>9</sup>, Courtesy AIME).

#### Calculation Example No. 3

- Referring to calculation example no. 2 and its pressure drawdown curve (figure 7.13) it is observed that the inflection pressure point  $\Delta P_f = 84$  psi. If projected on the first straight line, it will give a value of  $(P_{wf}^*)_{early} = 117$  psi.

From equation 7.123 the following is calculated:

$$F_{DD} = \frac{\Delta P}{m'} = \frac{84 - 117}{16,2} = 2,04$$

which gives (see diagram in figure 7.20):

$$\omega \approx 0.03$$

- When referring to calculation example no. 2 (figure 7.16) and based on dimensionless time, where  $2,99 \times 10^{-3}$  is estimated in correspondence to inflection pressure point

$$\frac{\Delta t_s^*}{t_p + \Delta t_s^*} = \frac{1350}{450\,000 + 1350} = 2,99 \times 10^{-3}$$

is easy to evaluate  $\Delta t_s^* = 1350$  sec

Based on,

$$\omega = 0.03$$

from figure 7.22 a value  $(F_{BU})_{early} \approx 0,16$  results. In continuation, applying equation 7.126 where  $\theta = 23$  and  $\Delta t_s^* = 1350$  sec, it results that

$$\lambda = \frac{0.16}{23 \times 1350} = 5,15 \times 10^{-6}$$

Both values of  $\lambda$  and  $\omega$  are similar to those obtained by direct evaluation in calculation example no. 2.

### 7.3. DISCUSSION OF POLLARD METHOD

Pollard's method based on the relationship between logarithm of pressure vs. time requires first a procedure for elaboration of basic reservoir data.

#### 7.3.1. Data processing

- a. The pressure difference is calculated with reference to static pressure, thus, for recorded  $P_{wf}$  the total pressure difference is given by:

$$\Delta P_t = P_s - P_{wf} \quad (7.130)$$

- b. In a diagram,  $\log \Delta P_T$  vs.  $\Delta t$ , a straight line of slope  $m_1$  is obtained as in figure 7.24. If the straight line is extrapolated at  $\Delta t = 0$ , the value obtained is  $C_p$  and the pressure is expressed by equation 7.65 which describes the pressure increment vs. time in the matrix as follows:

$$\Delta P_m = C_p e^{-m_1 \Delta t} \quad (7.66)$$

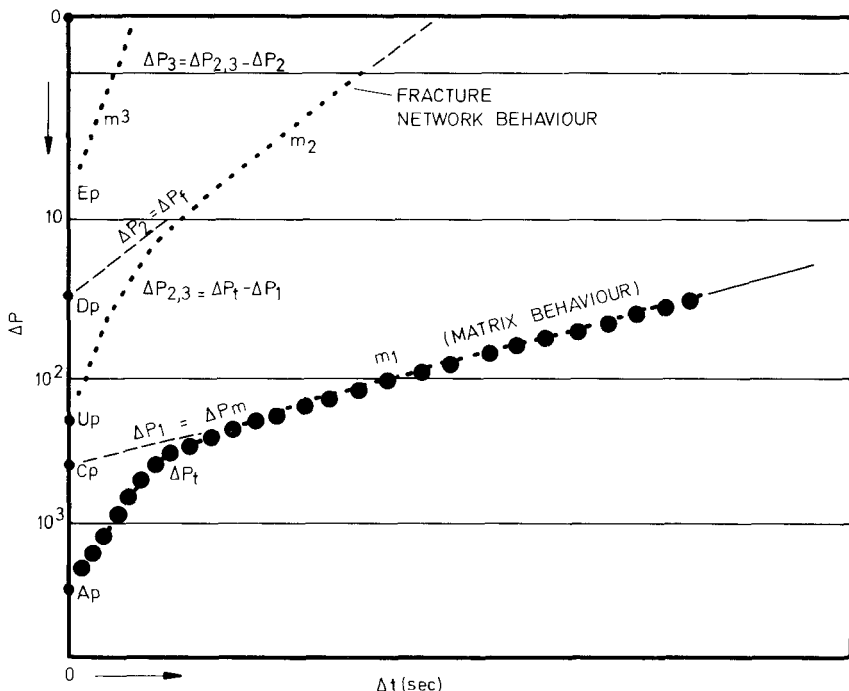
which describes the pressure build-up law in the matrix.

- c. The difference in pressure  $\Delta P_t - \Delta P_1$  represents the total pressure build-up of the fractured network as:

$$\Delta P_{2,3} = \Delta P_t - \Delta P_1 \quad (7.131)$$

- d. Representing the expression,  $\log \Delta P_{f,t}$  vs.  $\Delta t$ , a straight line portion of slope  $m_2$  is obtained as shown in figure 7.24. This straight-line extrapolated at  $\Delta t = 0$  gives a value  $D_p$ , and thus, the pressure build-up in fractures throughout the reservoir may be expressed by:

$$\Delta P_f = \Delta P_{2,3} - \Delta P_2 = D_p e^{-m_2 \Delta t} \quad (7.67)$$



7.24 – Results of Pollard model based on  $\log \Delta P$  vs.  $t$  data.

e. Since as observed in Fig. 7.24 the value,

$$U_p = A_p - C_p$$

in the case of  $U_p > D_p$  the following is obtained:

$$E_p = U_p - D_p$$

which represents the pressure drop in the fractured network around the wellbore.

### 7.3.2. Basic parameters

#### 7.3.2.1. Matrix pores

Based on the classic relationship between volume, compressibility and pressure drop, the following equation can be written:

$$\Delta V_m = V_m C_m \Delta P$$

or expressed as rate:

$$QB_o = \frac{dV_m}{dt} = V_m C_m \frac{dp}{dt}$$

Keeping in mind equation 7.66, the matrix volume obtained is as follows:

$$V_m = \frac{QB_o m_1}{C_m C_p} \quad (7.132)$$

### 7.3.2.2. Fracture pores

Following the same approach:

$$QB_o = V_f C_f \frac{dp}{dt}$$

and through 7.67:

$$V_f = \frac{QB_o}{C_f} \cdot \frac{m_2}{D_p + C_p} \quad (7.133)$$

It is necessary for  $C_p$  to be added to  $D_p$  since the fracture pressure build-up takes place in the presence of both pressure differences ( $C_p$  and  $D_p$ ).

### 7.3.2.3. Porosities $\Phi_m$ and $\Phi_f$

In a simplified way:

$$\Phi_m = \frac{V_m}{V_m + V_f} \quad (7.134)$$

$$\Phi_f = \frac{V_f}{V_m + V_f} \quad (7.134)$$

### 7.3.3. Additional parameters obtained by analogy

Other parameters which can be obtained by *analogy with a conventional porous medium*, with results which are *only orientative*, are as follows:

- a. Productivity index (when referring to fracture network):

$$PI = \frac{QB_o}{\Delta P} = \frac{QB_o}{D_p} \quad (7.135)$$

b. Fracture permeability:

$$K_f \approx PI \frac{\mu_o B_o}{h} \quad (7.136)$$

c. Intrinsic permeability:

$$K_{ff} = K_f / \Phi_f \quad (7.137)$$

d. Skin effect:

$$SE = \frac{U_p - D_p}{A_p} \quad (7.138)$$

e. Completion factor:

$$CF = \frac{C_p + D_p}{A_p} \quad (7.139)$$

This analogy is of limited validity and any evaluation of parameters through these equations has to be considered more as of qualitative and not quantitative interest.

#### *Calculation Example No. 4 (Pollard)*

A well drilled in a fractured reservoir was produced for a time  $t_o \cong 45,000$  sec with a stabilized rate  $q = 3,350$  STB/day/psi. Initial static reservoir pressure was  $P_s = 149.39$  kg/cm<sup>2</sup> = 2190 psi. The pressure recorded at the instant of well shut-in was  $P_w = 2120$  psi. The following parameters are known in addition:

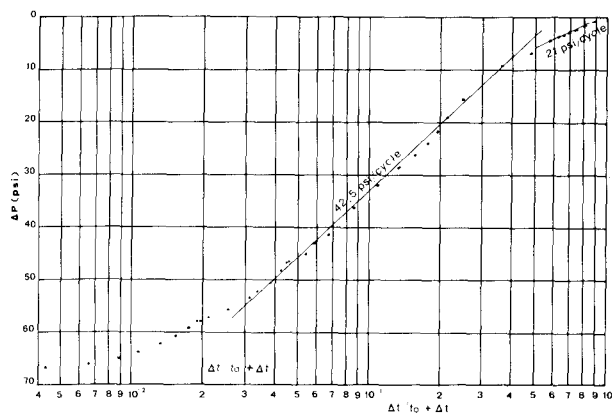
Total pay	$h = 260$ m	Oil viscosity	$\mu_o = 1.2$ cP
Porosity (from logs)	$\Phi = 26\%$	Compressibility	$C_f = 8.2 \times 10^{-6}$ 1/psi
Saturation in water	$Sw_i = .028$	,,	$C_m = 3.8 \times 10^{-6}$ 1/psi
Oil volume factor	$Bo = 1.085$	Well radius	$r_w = 10$ cm

The recorded pressure and time data are listed in columns 1 and 2 of table 7.7, and the conventional dimensionless time ratio  $\Delta t/(t_o + \Delta t)$  is listed in column 3.

Solution

To check if the Warren and Root model corresponds to the reservoir behaviour a conventional representation,  $P_w$  vs.  $\log \Delta t/t_o + \Delta t$ , may be used.

The pressure drop  $\Delta P = P_s - P_w$  in column 4 is plotted against  $\Delta t/(t_o + \Delta t)$  in column 3 (figure 7.25). The result obtained does not resemble the Warren-Root model since both the double parallel straight lines and pressure transient are absent. Apparently the transition zone is around  $t = 1,300$  sec, but the first parallel in the time interval  $1.5 \times 10^{-2} < \Delta t/(t_o + \Delta t) < 2.1 \times 10^{-2}$ , remains uncertain because it may be dissimulated by the afterflow effect. Two different slopes are evidenced later in time when the initial slope is reduced from 42.5 psi/cycle to 21 psi/cycle.



7.25 – Conventional representation  $\Delta P$  vs.  $\log \Delta t / (t_g + \Delta t)$ .

Since the conditions of the Warren and Root model do not seem to be fulfilled, an evaluation of the reservoir characteristics through the Pollard model may be attempted.

In the diagram in figure 7.26 the following representations are illustrated and the results obtained are as follows:

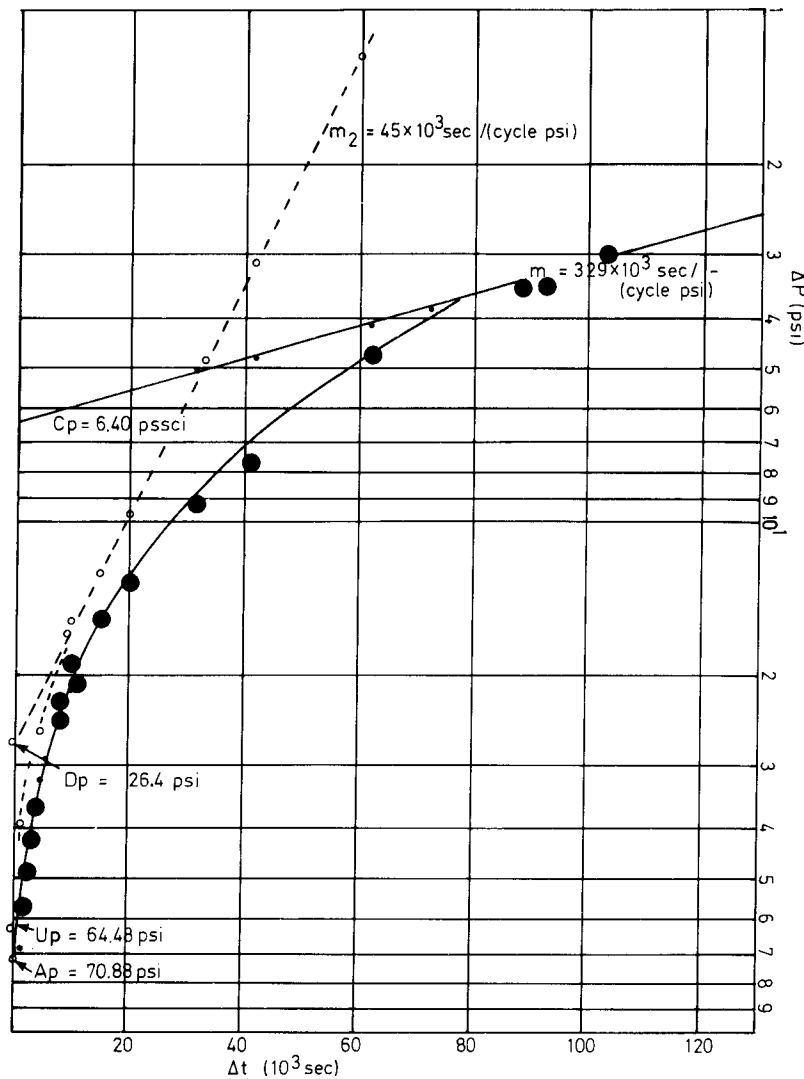
- A first representation is obtained as  $\log \Delta P_T$  (column 4) vs. time  $\Delta t$  (column 1). The straight line portion indicates the following slope,

$$m_1 = 329,000 \text{ sec/cycle (psi)}$$

This slope indicates the time necessary for a cycle of pressure build-up. At  $\Delta t = 0$  the extrapolation indicates,

$$C_p = 6.40 \text{ psi}$$

All values extrapolated indicate the pressure drop in the matrix,  $\Delta P_m = \Delta P_1$ , as shown in column 5.



7.26 –  $\log \Delta P$  vs.  $t$  diagram.

- A second representation is given by the pressure drop in the fractured network, calculated in column 6 of Table 7.7 as follows:

$$\Delta P_{f,T} = \Delta P_{2,3} = \Delta P_T - \Delta P_m$$

as a function of time  $\Delta t$ . The straight line portion (figure 7.26) indicates the following fracture slope:

$$m_2 = 45,000 \text{ sec/cycle (psi)}$$

Since at  $\Delta t = 0$  the total pressure drop in the fractured network is given by:

$$U_p = A_p - C_p = 70.88 - 6.4 = 64.48 \text{ psi}$$

then the total pressure drop in the fractures around the wellbore is expressed by:

$$S_p = U_p - D_p = 64.4 - 26.4 = 40 \text{ psi}$$

Table 7.7

At sec	P <sub>w</sub> (psi)	$\frac{\Delta t}{t_0 + \Delta t}$	$\Delta P_1 =$ $P_s - P_w$	$\Delta P_m = \Delta P_{f1}$	$\Delta P_{f1} =$ $\Delta P_1 - \Delta P_m$
		(3)	(4)	(5)	(6)
1	(2)				
0	2120.00	0	70.88	6.40	64.48
100	2120.98	$2.22 \times 10^{-3}$	69.90	"	63.50
200	2122.68	4.44 "	68.30	"	61.90
300	2123.68	6.62 "	67.30	"	60.90
400	2125.38	8.81 "	65.60	"	59.20
500	2126.88	$1.098 \times 10^{-2}$	64.10	"	57.7
600	2128.78	1.315 "	62.20	"	55.8
700	2130.10	1.531 "	60.80	"	54.4
800	2131.28	1.746 "	59.60	"	53.2
900	2132.78	1.960 "	58.10	"	51.7
1000	2133.28	2.173 "	57.60	"	51.2
1200	2135.18	2.590 "	55.70	6.35	49.3
1400	2137.08	3.017 "	53.80	"	47.4
1600	2138.88	3.433 "	52.00	"	45.6
1800	2140.58	3.846 "	50.30	"	43.92
2000	2142.08	4.255 "	48.80	"	42.46
2200	2143.78	4.661 "	47.10	"	40.75
2500	2145.98	5.52 "	44.90	6.30	38.50
2700	2147.70	5.96 "	43.10	"	36.70
3000	2145.30	6.62 "	41.50	6.25	35.25
4000	2154.60	8.81 "	36.20	"	29.95
5000	2158.70	$1.09 \times 10^{-1}$	32.18	6.20	25.98
6000	2161.70	1.315 "	29.15	6.15	23.00
7000	2164.50	1.530 "	26.30	6.10	20.20
8000	2166.40	1.74 "	24.40	6.05	18.35
9000	2168.30	1.96 "	22.50	6.00	16.50
10000-0	2169.30	2.17 "	19.00	5.95	15.55
15000-0	2172.60	2.50 "	15.50	5.70	12.58
20000-0	2175.40	3.07 "	13.00	5.50	9.98
32000-0	2181.40	3.67 "	9.0	5.01	4.97
42000	2182.90	4.82 "	7.83	4.70	3.13
62000	2186.20	5.79 "	4.68	4.18	0.50
72000	2187.00	6.15 "	3.88	3.88	-
92000	2187.50	6.71 "	3.38	3.38	-
102000	2187.70	6.93 "	3.18	3.18	-

### Interpretation of data (Pollard model)

- Matrix volume obtained from equation 7.132:

$$V_m = \frac{B_o m_1}{C_p \times C_m^*} = \frac{3100 \text{ (STBD)}}{\frac{1}{6.28} \times 1.085 \times \frac{329 \times 10^3}{86400}} = 8.38 \times 10^7 \text{ m}^3$$

- Fracture volume obtained from equation 7.133:

$$V_f = \frac{B_o m_2}{(C_p + D_p)} \frac{1}{C_f} = \frac{3100 \times \frac{1}{6.28} \times 1.085 \times \frac{45000}{86400}}{(26.4 + 6.4) \times 8.2 \times 10^{-6}} = 1.370 \times 10^6 \text{ m}^3$$

- Total volumes:

$$V_m + V_f = 8.38 \times 10^7 + 1.370 \times 10^6 = 85.17 \times 10^7 \text{ m}^3$$

- The porosities obtained are:

$$\Phi_m = \frac{83.8 \times 10^7}{85.17 \times 10^7} \times .26 = 25.58$$

and,

$$\Phi_f = \frac{1.37 \times 10^6}{85.17 \times 10^7} \times .26 = .42\%$$

### Additional parameters (orientative results)

- Productivity index based on equation 7.135:

$$PI = \frac{q}{D_p} = \frac{3350}{26.4} = 127 \text{ STBD/psi}$$

- Fracture permeability based on equation 7.136:

$$K_f \approx PI \frac{\mu_o B_o}{h} = 127 \frac{14.7}{6.28 \times 0.0864} \frac{1.2 \times 1.085}{26000} = 172 \text{ mD}$$

- Intrinsic permeability based on equation 7.137:

$$K_{ff} = K_f/\Phi_f = 0.172/0.0042 = 37.6 \text{ D}$$

- Skin effect based on equation 7.138:

$$SE = \frac{U_p - D_p}{A_p} = \frac{64.48 - 26.4}{70.88} = .537$$

- Completion factor:

$$CF = \frac{C_p + D_p}{A_p} = \frac{6.4 + 26.4}{70.88} = .463$$

NOTE: Regardless of the fact that two different basic concepts are given in the Pollard and Warren and Root models, it is still of interest to observe that the variation  $\log \Delta P$  vs.  $\Delta t$  governs both build-up curves in the case of a finite reservoir. In both cases a straight line portion is obtained (figure 7.18 and 7.24.) However, the significance of the slope is completely different since the Warren and Root model is associated to storage capacity and matrix-fracture interflow, while the Pollard model is only associated to the storage capacity.

The additional parameters as discussed in section 7.3.3 have only a *qualitative* value and therefore the use of these results has to be limited.

## LIST OF SYMBOLS

### LATIN LETTERS

$B_o$	- oil volume factor
$C$	- compressibility
$C_p \}$	- extrapolated pressure (Pollard model)
$D_p \}$	- pressure, $P_c$
$E_p$	- pay
$h$	- permeability
$K$	- matrix block height
$L$	- slope of $P$ vs. $\log t$
$m, m'$	- number of directions of flow
$n$	- pressure
$P$	- productivity index
$Q$	- rate

R, r	- radius
S	- fracture-matrix contact surface
t	- time
v	- velocity
uu	- velocity

### Greek letters:

$\beta$	- turbulence factor
$\Phi$	- porosity
$\Delta$	- difference
$\lambda$	- interflow porosity
$\mu$	- viscosity
$\omega$	- relative storage capacity
$\theta$	- time parameter

### SUBSCRIPTS:

1	- primary (porosity)
2	- secondary
D	- dimensionless
SS	- steady-state
f	- fracture
m	- matrix
min	- minimum
P	- Production
t	- time
tr	- transient
w	- well
$\lambda$	- referring to $\lambda$ parameter
$\omega$	- referring to $\omega$ parameter

## REFERENCES

1. Warren, J.E. and Root, P.J., 1963. The behaviour of naturally fractured reservoirs. *Soc. Petrol. Eng. J.*, p 245–255.
2. Odeh, A.S., 1965. Unsteady-state behaviour of naturally fractured reservoirs. *Soc. Petrol. Eng. J.*, p 60–66.
3. Pollard, P., 1959. Evaluation of acid treatments from pressure build-up analysis. *Trans. AIME*. Vol 216, p 38–43.
4. Kazemi, H., Seth, M.S. and Thomas, G.W., 1969. The interpretation of interference tests in naturally fractured reservoirs with uniform fracture distribution. *SPEJ*, December, p 463–472.
5. DeSwaan, A.O., 1976. Analytic solutions for determining naturally fractured reservoir properties by well testing. *SPEJ*, June, p 117–122.
6. Najurieta, H.L., 1975. A theory for the pressure transient analysis in naturally fractured reservoirs. *SPEJ*, October, New Orleans.
7. Barenblatt, G.I., Zheltov, Y.P. and Kochina, I.N., 1960. Basic concepts in the theory of seepage of homogeneous liquids in fissured rocks. *PMM*, Vol 24, No. 5, p 852–864.
8. Pirson, R.S., 1961. An extension of the Pollard analysis method of well pressure build-up and drawdown tests. Presented at the 36th Annual Fall Meeting of Society of Petroleum Engineers, Dallas, Texas.
9. Uldrich, D.O. and Ershaghi, J., 1979. A method for estimating the interporosity flow parameter in naturally fractured reservoirs. *SPEJ*, October.

This Page Intentionally Left Blank

# CHAPTER 8

## SPECIAL PROBLEMS OF FLOW TOWARD A WELL

### 8.1. INTRODUCTION

The flow through a fracture network or the flow through a double-porosity (fracture-matrix) reservoir toward a well may be considered as the basis of dynamic problems in a fractured reservoir. However, other problems such as well interference, evaluation and role of anisotropy and use of type-curve procedures have to be taken into account.

In this chapter a detailed examination of theoretical aspects of these problems, together with the limits of the validity of equations has been combined with various applications.

The interference in a fractured reservoir opens interesting possibilities for the understanding of a fractured reservoir, but the results are interpretable only when the contrast between the properties of fractures and matrix is very big. If these contrasts are limited, the well interference behaviour describes only the characteristics of the fractured network. It is also of particular interest to understand reservoir anisotropy, especially in designing the location of production and injection wells. The anisotropy evaluation is described under conditions of both steady-state and transient flow. Nevertheless, the processing of such information remains a complex problem.

### 8.2. WELL INTERFERENCE

#### 8.2.1. Interference effects under pressure drawdown conditions.

##### 8.2.1.1. Basic theory

The interference process may be described by the same generalized dimensionless equations obtained in section 7.2.2, where pressure drop results from the following two equations,

$$\frac{1}{r} \frac{\partial}{\partial r_D} \left( r_D \frac{\partial P_2}{\partial r_D} \right) - \omega \frac{\partial P_2}{\partial t_2} - (1 - \omega) \frac{\partial P_{1D}}{\partial t_D} = 0 \quad (8.1)$$

$$(1 - \omega) \frac{\partial P_{1D}}{\partial t_D} - \lambda (P_{2D} - P_{1D}) = 0$$

If the above equations are combined with the boundary conditons,

$$\left. \begin{array}{l} t_D = 0 \rightarrow P_{1D} = P_{2D} = 0 \\ r_D = 1 \rightarrow \frac{\partial P_2}{\partial r_D} = 1; t_D > 0 \\ r_D = \infty \rightarrow P_{1D} = P_{2D}; t_D > 0 \end{array} \right\} \quad (8.2)$$

the pressure drop in fractures (index 2) may be expressed as

$$P_{2D}(r_D, t_D) = \frac{1}{2} \left[ -Ei(-r_D^2 / 4t_D) + \right. \\ \left. + Ei[-\lambda t_D / \omega(1 - \omega)] - Ei[-\lambda t_D / (1 - \omega)] \right] \quad (8.3)$$

for a radius  $r_D$  and a time  $t_D$ , where

$$\left. \begin{array}{l} r_D = r/r_w \\ t_D = a't/r_w^2 \\ a' = K/(\Phi_1 C_1 + \Phi_2 C_2) \mu = K/\overline{\Phi C} \mu \end{array} \right\} \quad (8.4)$$

*Observation.* Due to continuous increase of time  $t$ , the function  $Ei(-r_D^2 / 4t_D)$  may be reduced to the logarithmic expression  $\ln 2.246 t_D/r_D^2$ , and thus equation 8.3 becomes;

$$P_{2D}(r_D, t_D) = \frac{1}{2} \left[ \ln t_D/r_D^2 + Ei[-\lambda t_D / \omega(1 - \omega)] - \right. \\ \left. - Ei\left(-\frac{\lambda t_D}{1 - \omega}\right) \right] \quad (8.5)$$

a. Validity of equations 8.3 and 8.5.

The equations 8.3 and 8.5 have been discussed by Kazemi et al<sup>1</sup> under the assumption that the flow may be examined in two-dimensional flowing conditions, where gravity effects are negligible as well as the vertical pressure gradients. The validity of equations is related to time  $t_D$  and the distance between production and observation well  $r_D$ .

The conditions of validity are similar to those discussed in Chap. 7, but modified in relation to radius  $r_D = r/r_w^2$  so that

$$t_{D,\minim} = 100 r_D^2.$$

or from equation 8.4, the minimum dimensional time is

$$t_{\minim} = 100 r^2/a' \quad (8.6)$$

Beside these validity limitations, which are very restrictive, two other conditions may yield a larger applicability of equations 8.3 and 8.5.

$$\left. \begin{array}{l} t_{D,\minim} = 100 \omega \text{ if } \lambda = 1 \\ t_{\minim} = 100 r_w^2 \omega/a' \end{array} \right\} \quad (8.7)$$

and

$$\left. \begin{array}{l} t_{D,\minim} = 100 - 1/\lambda \text{ for } \omega \ll 1 \\ t_{\minim} = r_w^2 (100 - 1/\lambda)/a' \end{array} \right\} \quad (8.8)$$

b. Discussion of equation 8.3 and 8.5 in relation with parameters of magnitude.

- The equation 8.3 may be substituted by equation 8.5 when the expression

$$r_D^2/4 t_D < 0.25 \quad \text{or} \quad 0.25 r^2/a't < 0.25$$

which corresponds to a minimum time

$$t_{\min} \cong r^2/a' \quad (8.9)$$

Assuming an average value  $a' \cong 10^4 \text{ cm}^2/\text{sec}$  for a radius  $r = 100 \text{ m}$  equivalent for  $r_D \cong 1000$ , a short minimum time  $t_{\minim} = 10000 \text{ sec}$  will result, while for a well located at  $r = 1000 \text{ m}$  the time  $t_{\minim} = 10^6 \text{ sec} \cong 10 \text{ days}$  will be long.

- The time necessary for the pressure wave to reach the observation well, has to be associated to piezo-conductivity and distance from the production well.

If the approximative equation is used

$$r_o \cong \sqrt{2.246 a't} = \sqrt{2.246 kt/\Phi C \mu} \quad (8.10)$$

where

$$\overline{\Phi C} = \Phi_1 C_1 + \Phi_2 C_2 \quad (8.11)$$

a time will result

$$t = .445 \frac{\overline{\Phi C} \mu r_o^2}{K}$$

Assuming the average values  $\overline{\Phi C} = 10^{-5}$  (1/at),  $K/\mu = 1$  and  $r_o = 100$  m and 1000 m, results will be, respectively

$$t(\text{sec}) = 445 \rightarrow \text{for } r_o = 100 \text{ m}$$

$$t(\text{sec}) = 44500 \rightarrow \text{for } r_o = 1000 \text{ m}$$

- The double-porosity pressure behaviour is time dependent. This observation results from equations 8.3 and 8.5, where the second and third right-hand terms tend towards zero when time becomes large. When both terms  $Ei[-\lambda t_D/(1-\omega)\omega]$  and  $Ei[-\lambda t_D/(1-\omega)]$  vanish in equations 8.3 and 8.5, both equations are reduced to the single-porosity pressure behaviour case.

$$P_2(r_D, t_D) = \frac{1}{2} - Ei\left[(-r_D^2/4t_D)\right] \quad (8.12)$$

or

$$P_2(r_D, t_D) = \frac{1}{2} \ln t_D/r_D^2 \quad (8.13)$$

This linear semilog relationship of equation 8.13 represents the asymptote in case of relationship  $P_D$  vs.  $\log t_D$ .

Assuming as an example that  $\lambda \cong 10^{-6}$  and  $\omega \cong 10^{-3}$ , for  $r_w = 100$  m and  $a' = 10^5$  ( $\text{cm}^2/\text{sec}$ ) the following time valid for the two Ei functions will result:

$$\text{Ei} \left[ -\frac{\lambda t_D}{\omega(1-\omega)} \right] = \text{Ei} \left[ -\frac{\lambda}{\omega(1-\omega)} \frac{a'}{r_w^2} t \right] =$$

if

$$\text{Ei} \left[ -\frac{10^{-6}}{10^{-3}} \frac{10^5}{100} t \text{ (sec)} \right] \cong 5$$

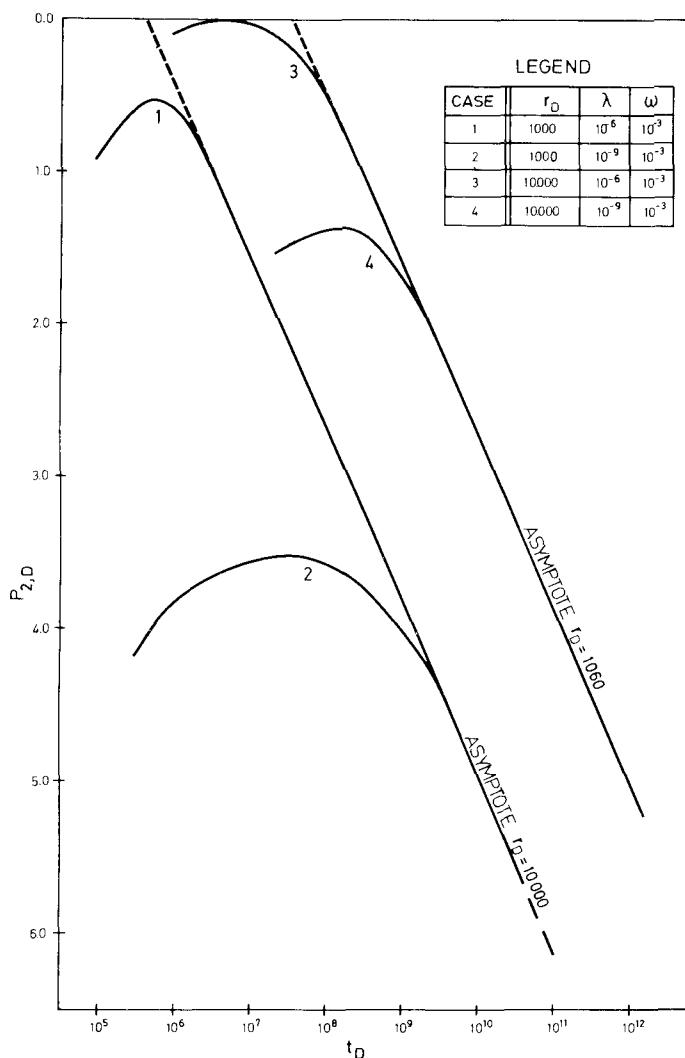
which corresponds to approximately  $t \cong 5$  seconds, when this term becomes negligible. The other term

$$\text{Ei} \left( -\frac{\lambda}{1-\omega} t_D \right) \cong 0 \quad \text{if} \quad \frac{\lambda t_D}{1-\omega} \cong \lambda \frac{a'}{r_w^2} t = 10^{-6} \frac{10^5}{10^2} t \text{ (sec)} = 5$$

which corresponds to  $t = 5000$  sec. when this term becomes zero.

Observation: The interference test can give an indication of double-porosity reservoir characteristics only if all terms of equation 8.5 are still valid during recordings at the observation well. From the above example, equation 8.5 is reduced to equation 8.12 after 5,000 seconds.

- As a consequence of simple observations, the following can be stated:
- Double-porosity behaviour can be interpreted through recordings from observation wells only if  $a'$  and  $\lambda$  are small. Such a condition corresponds to a moderate fracture permeability associated with a large contrast between matrix and fracture permeability.
  - If  $a' = 10^4$  the validity time of the above Ei functions is reduced to 50 seconds and 50,000 seconds, respectively.
  - If  $\lambda > 10^{-6}$  and  $K_f \cong 1$  D there are many chances that pressure drawdown in the observation well behaves similarly to that of a single porosity medium, and
  - If  $\lambda < 10^{-6}$  and  $K_f \cong 0.1$  D the presence of double porosity may be noticed from the pressure behaviour recorded in the observation well.



8.1 – Variation  $P_{2D}$  vs.  $t_D$  in an observation well

An evaluation of the role of parameter  $\lambda$  was done for a constant value  $\omega = 10^{-3}$  and two values of  $r_D$  (1000 and 10000), and the results obtained by using the equation 8.3 are shown in figure 8.1. Since the asymptote represents the *single porosity* pressure-time relationship, all deviations from the straight-line are the effect of double porosity. From the figure 8.1 it results that:

- ~ The values  $\lambda = 10^{-6}$  (cases 1 and 3) are a lower limit of  $\lambda$  values for evaluation of double porosity data. In fact small modifications from single porosity are noticed.

- ~ On the contrary,  $\lambda = 10^{-9}$  corresponding to a very high contrasting matrix-fractures relationship indicates substantial changes in  $P_2D$  during the first period of pressure drop recordings in the observation well.
- ~ The double-porosity is more evident if the distance from the production to the observation well is smaller ( $r_D = 1000$  case 2 compared with  $r_D = 10000$ , case 4).

c. Dimensional expression of pressure draw-down.

Based on equations 8.3, 8.4 and 8.5 the pressure drop may be written as

$$\Delta P_f = m' \left[ -Ei \left( -0.25 \frac{r_o^2}{a't} \right) + Ei \left[ -\frac{\lambda}{\omega(1-\omega)} \frac{a'}{r_w^2} \times t \right] - Ei \left( -\frac{\lambda}{1-\omega} \frac{a'}{r_w^2} \times t \right) \right] \quad (8.14)$$

or

$$\Delta P_f = m' \left[ \log(2,246 a't/r^2) + Ei \left[ -\frac{\lambda}{\omega(1-\omega)} \frac{a'}{r_w^2} \times t \right] - Ei \left( -\frac{\lambda}{1-\omega} \frac{a'}{r_w^2} \times t \right) \right] \quad (8.15)$$

where

$$m' = 1.15 \frac{q_o \mu_o B_o}{2 \pi h} \times \frac{1}{K_f} \quad (8.16)$$

The validity of the above equations was expressed in the previous relationships 8.6, 8.7 and 8.8.

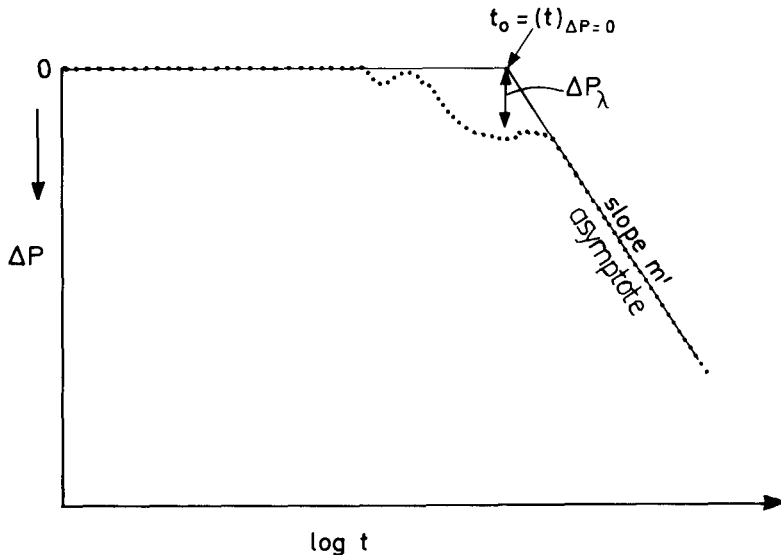
#### 8.2.1.2. Calculation procedure

##### a. Use of basic equations

Based on the recorded pressure  $p$  vs. log time in the observation well, the data obtained may be used as in diagram figure 8.2. When the relationship  $p$  vs.  $\log t$  expresses a straight-line, its slope  $m'$  will indicate the pressure drop per time cycle as in conventional reservoir analysis.

- Evaluation of fracture permeability. Based on slope  $m'$ , the fracture permeability is obtained from the equation:

$$K(D) = 1.15 \times \frac{q (\text{cm}^3/\text{sec}) \times \mu_0 (\text{cP}) \times B_0}{2\pi \times h (\text{cm}) \times m' (\text{at/cycle})} \quad (8.17)$$



### 8.2 – Variation $\Delta P_f$ vs $\log t$ in an observation well

- Evaluation of piezo-conductivity  $a'$ . From the extrapolation of the asymptote at  $\Delta P_f = 0$  it will result that  $\log 2,246 a't/r^2 = 0$  which corresponds to  $2,246 a't/r^2 = 1$ . By reading the time as shown in Figure B.2 it results that

$$a' = \left[ 0.445 r^2/t \right]_{\Delta P_f=0} = 0.445 r^2/t_o \quad (8.18)$$

- Evaluation of composite storage capacity  $\overline{\Phi C}$ . Based on equation 8.4 and using  $a'$  which was previously determined, it results that

$$\overline{\Phi C} = K/\mu a' \quad (8.19)$$

- Evaluation of fracture porosity  $\Phi_2 = \Phi_f$ . From the definition of storage capacity equation 8.4, it is obtained directly

$$\Phi_2 = (\overline{\Phi C} - \Phi_1 C_1) / C_2 \quad (8.20)$$

- Evaluation of relative storage capacity,  $\omega$  is based on the definition given in chapter 7, so that

$$\omega = \Phi_2 C_2 / (\Phi_1 C_1 + \Phi_2 C_2) \quad (8.21)$$

- Evaluation of interporosity flowing capacity  $\lambda$ . In relation with the previous discussion concerning the validity of equation 8.5, the expression of pressure drop may be reduced for small  $\lambda$  value to

$$\Delta P_{2,D} = \frac{1}{2} \left[ \ln t_D/r_D^2 - Ei\left(-\frac{\lambda t_D}{1-\omega}\right) \right] \quad (8.22)$$

from which, by analogy with equation 7.31,

$$\Delta_{2,D} = \frac{1}{2} \left[ -Ei\left(-\frac{\lambda t_D}{1-\omega}\right) \right]$$

The expression  $\Delta_{D,2}$  may be written in dimensional terms as,

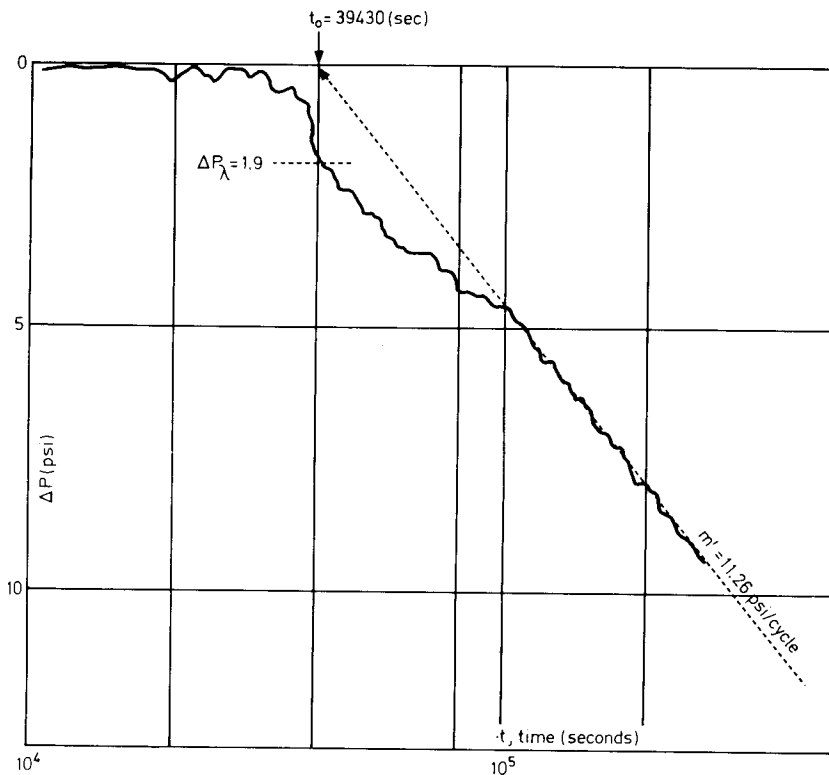
$$\Delta P_\lambda/m = - Ei\left[-\lambda t_D/(1-\omega)\right] \quad (8.22)$$

where  $\Delta P_\lambda$  is measured as in diagram figure 8.2, and  $m = m'/2.3$

### b. Calculation example

Between two wells (production and observation) separated by a distance  $D = 350$  m, an interference test has been carried out. The production well having a rate of 11 000 STB/D, the pressure in the observation well was recorded vs. time and drawn in figure 8.3.

Other basic data are :  $\mu_o = 1.2$  c.P.,  $B_o = 1.27$  ;  $h = 109$ ,  $\Phi_1 = 0.15$  (from cores and logs) ;  $C_1 = 2.6 \times 10^{-4}$  (1/at)  $C_2 = 1.3 \times 10^{-4}$  (1/at) ;  $r_w = 10$  cm.



8.3 – Variation pressure drop vs. time in observation well from recorded data

### SOLUTION

- From semilog diagram  $\Delta P - \log t$  (figure 8.3) the slope is  
 $m' = 11.26 \text{ psi/cycle} = 0.8 \text{ at/cycle}$
- The fracture permeability from equation 8.17 is directly evaluated

$$K_f (\text{mD}) = 1.15 \cdot \frac{20270 \times 1.2 \times 1.27}{6.28 \times 10900} \cdot \frac{1}{0.8} = 0.65 \text{ D}$$

- The complex piezo-conductivity factor results from equation 8.18,  
 $a' = 0.445 r^2 / t_0 = 0.445 \times (3.5 \times 10^4)^2 / 39430 \text{ (sec.)} = 13825 \text{ cm}^2 / \text{sec.}$

- The extrapolated asymptote at  $\Delta P = 0$  indicates a time  $t_0 = 39430$  sec.
- The value  $\Phi C$  from equation 8.19 is

$$\overline{\Phi C} = K/\mu a' = 0.65/1.2 \times 12825 = 3.918 \times 10^{-5} \text{ (1/at)}$$

- The fracture porosity from equation 8.20 will give

$$\Phi_f \cong \Phi_2 = (\overline{\Phi C} - \Phi_1 C_1)/C_2 = (3.918 \times 10^{-5} - .15 \times 2.6 \times 10^{-4})/1.3 \times 10^{-4}$$

$$\Phi_f = 0.00138$$

- Dimensionless storage capacity  $\omega$  from equation 8.27 will give

$$\omega = \Phi_2 C_2 / \Phi C = 0.06138 \times 1.3 \times 10^{-4} / 3.918 \times 10^{-5} = 0.00457$$

- Evaluation of  $\lambda$ . From pressure behaviour curve shown in figure 8.3 the pressure drop at  $t = t_0$  is  $\Delta P = \Delta P_\lambda = 0.168$  psi.

From equation 8.22 it thus obtained that

$$\Delta P_\lambda \cong m \times Ei \left[ -\frac{\lambda}{(1-\omega)} \cdot \frac{a}{r_w^2} \cdot t \right]$$

$$1.9 = (11.26/2.3) \times Ei \left[ -\lambda \frac{13825}{0.995 \times 100} 39430 \right]$$

$$0.719 = \lambda \times 5.47 \times 10^6 ; \lambda \cong 1.312 \times 10^{-7}$$

### 8.2.1.3. Source solution procedure.

By using the pressure distribution differential equation with a source term which represents the fluid flow from the matrix to the fractures when the pressure changes,

$$\Delta^2 (\Delta P_f) = \frac{1}{a_f} \frac{\partial P_f}{\partial t} - \frac{\mu}{K_f} Q = 0 \quad (8.23)$$

Najurieta<sup>3</sup> proposed the use of an approximate solution for initial and boundary conditions expressed by linear source solution

$$\Delta P_f = - \frac{qB_o}{4\pi NT_f} Ei \left( -\frac{r^2}{4a_{co} t} \right) \quad (8.24)$$

where the composed diffusivity

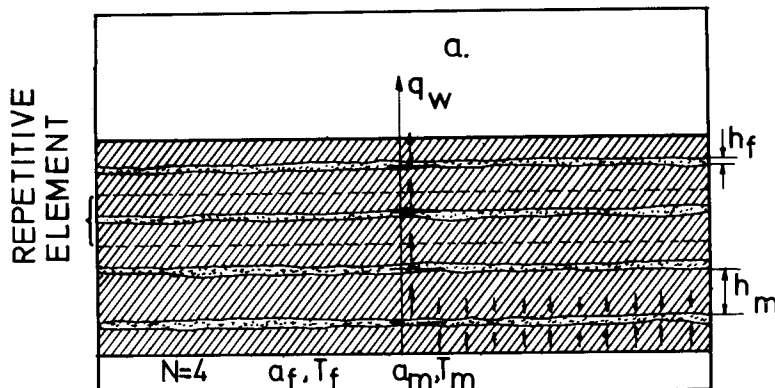
$$a_{co} = \frac{Kh/\mu}{(\Phi ch)_f + (\Phi ch)_m \Psi} = \frac{Kh/\mu}{(\Phi C)_{co}} = \frac{T}{(\Phi C)_{co}} \quad (8.25)$$

where for the two models 1 and 2 as shown in figure 8.4, it will result, respectively, that

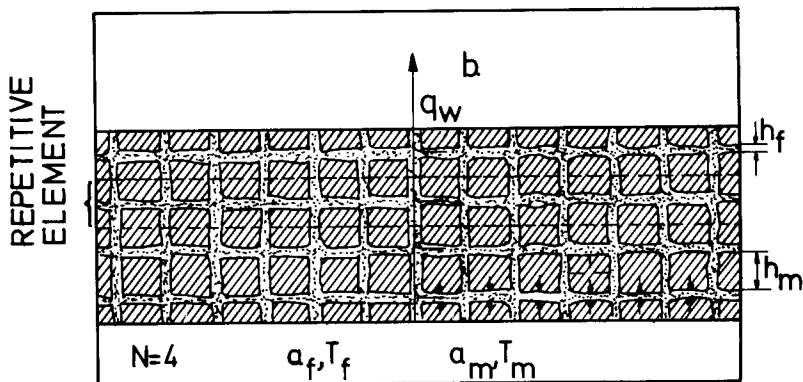
$$\sim \text{model 1} \rightarrow \Psi = \sqrt{t/T} \tanh \sqrt{\delta/t} \quad (8.26)$$

$$\sim \text{model 2} \rightarrow \Psi = \sqrt{t/T} \coth \sqrt{\delta/t} - t/\delta \quad (8.27)$$

### MODEL 1



### MODEL 2



8.4 – Idealized reservoir: model 1 - stratified matrix; model 2 - blocks matrix. (Najurieta<sup>3</sup>, Courtesy AIME)

The parameter  $\delta$  is related to the time response of the matrix during the period when a fluid exchange between matrix and fractures takes place,

$$\delta = h_m^2 / 4 a_m \quad (8.28)$$

During an interference test, by applying equation 8.24, the following may be observed:

- for short times a deviation from single porosity behaviour results as the effect of such fracture-matrix contrast characteristics as  $(\Phi_{ch})_f / (\Phi_{ch})_m$ .
- for longer times, in accordance with the geometry of the model type, the result is

$$\text{for model 1 (layers)} \rightarrow a_{co,1} = T / [(\Phi_{ch})_f + (\Phi_{ch})_m] \quad (8.29)$$

$$\text{for model 2 (cubes)} \rightarrow a_{co,2} = 3T / [3(\Phi_{ch})_f + (\Phi_{ch})_m] \quad (8.30)$$

### 8.2.2. Interference effects under pressure build-up conditions.

The build-up condition develops as a consequence of a change of rate  $q_1$  to a new rate  $q_2$ . This rate could be lower,  $q_2 < q_1$  or even  $q_2 = 0$ . In the case of  $q_2 = 0$ , due to superposition of effects, the dimensionless pressure drop is expressed by

$$P_{2D} = \frac{1}{2} \left[ -Ei \left[ -r^2/4(t_{oD} + \Delta t_D) \right] + Ei \left( -r_D^2/4\Delta t_D \right) - Ei \left[ -\lambda \Delta t_D / \omega (1 - \omega) \right] + Ei \left[ -\lambda \Delta t_D / (1 - \omega) \right] \right] \quad (8.31)$$

which dimensionally will give

$$\Delta P_f = m \left[ - \left( Ei \left( -0.25 \frac{r_o^2}{a'} \cdot \frac{1}{t_o + \Delta t} \right) + Ei \left( -0.25 \frac{r_o^2}{a'} \cdot \frac{1}{\Delta t} \right) \right) \right. \quad (8.32)$$

$$\left. - Ei \left[ - \frac{\lambda}{\omega(1-\omega)} \cdot \frac{a'}{r_w^2} \cdot \Delta t \right] + Ei \left( - \frac{\lambda}{1-\omega} \cdot \frac{a'}{r_w^2} \cdot \Delta t \right) \right]$$

If the first and second right-hand terms of equation 8.31 and 8.32 with long time values,  $\Delta t$ , are substituted by a logarithmic expression, it will result that

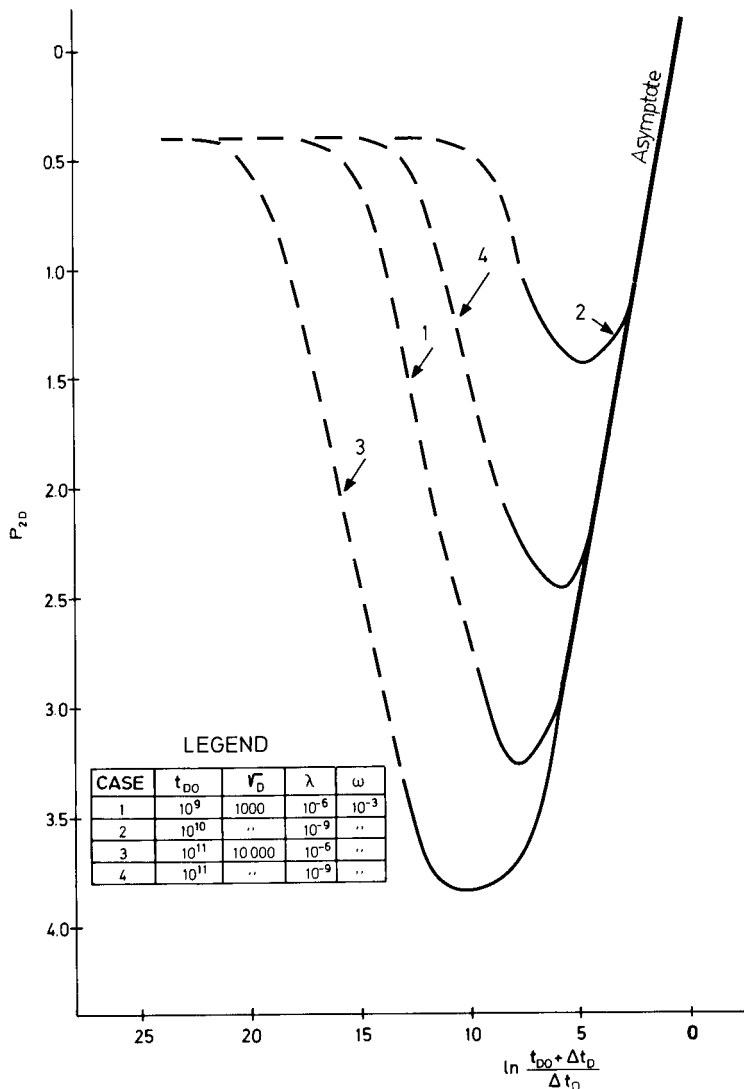
$$\begin{aligned}\Delta P_f = m & \left[ \ln \frac{t_o + \Delta t}{\Delta t} - Ei \left[ -\frac{\lambda}{\omega(1-\omega)} \Delta t_D \right] + \right. \\ & \left. + Ei \left( -\frac{\lambda}{1-\omega} \Delta t_D \right) \right] \quad (8.33)\end{aligned}$$

The validity of equations 8.31 and 8.33 is associated with the magnitude of  $\Delta t_D$ , which may be simplified for small values  $\omega$  and  $\lambda$ , as

$$\begin{aligned}\Delta t_D > 100 \omega & \quad \text{for } \lambda \ll 1 \\ \Delta t_D > 100 - \frac{1}{\lambda} & \quad \text{for } \omega \ll 1\end{aligned}$$

The advantages of build-up recorded in the observation well are the following :

- A reconfirmation of the slope  $m'$  and consequently a better evaluation of the value  $K_h$ , from the asymptote (figure 8.5).
- In the case  $\lambda \ll 10^{-6}$ , which corresponds to either a very significant fracture-matrix contrast in permeability or to very large block dimensions, the last term of the right-hand side of equation 8.32 will modify the linear build-up relationship  $\Delta P_f$  vs.  $\log(t_o + \Delta t) / \Delta t$ . The interpretation of this “anomaly” may help in the basic evaluation parameter or in verifying the basic parameters evaluated from pressure drawdown data.
- For a better understanding of the role of  $\lambda$  and  $r_D$  magnitude, four cases have been studied, where dimensionless pressure build-up has been examined through the equation 8.31. For the same radius, the asymptote is reached earlier for smaller  $\lambda$  ( $\lambda = 10^{-6}$ , cases 1,3) and later for larger  $\lambda$  ( $\lambda = 10^{-9}$ , cases 2,4). It may be stated in general terms that the shut-in-effect on the build-up behaviour of the observation well is delayed if the contrast fracture-matrix is great ( $\lambda = 10^{-9}$ ). This is the consequence of a longer transient time required by matrix-fracture fluid exchange when matrix permeability is substantially lower than fracture network permeability ( $K_f \ll K_m$ ).



8.5 – Dimensionless pressure build-up  $P_{2D}$  versus dimensionless time for various  $\lambda$ ,  $\omega$  and  $r_D$  values.

- The pressure build-up could further be expressed in dimensional values of pressure and time by introducing equations 8.4 for  $t_D$  and  $a'$ , and equation 8.16 for the relationship  $\Delta P_{2D} = \Delta P_f/m$ , as shown in equation 8.33.
- The calculation procedure is similar to that used for the drawdown case, to which a similar approach to those discussed in chapter 7 for production wells may be extended.

### 8.3. EVALUATION OF ANISOTROPY IN A FRACTURED RESERVOIR

#### 8.3.1. Theoretical review.

- Based on discussion developed in Chap. 6, section 6.1, for the vectorial definition of velocity and permeability, the expression of permeability tensor as in 6.16 may be recalled.

$$\bar{\bar{K}}_f = \begin{vmatrix} K_{11} & K_{12} & K_{13} \\ K_{21} & K_{22} & K_{23} \\ K_{31} & K_{32} & K_{33} \end{vmatrix} \quad (8.34)$$

From all concepts developed in formulation of equations from 6.15 to 6.21, the fracture permeability tensor (equation 6.21) is expressed by

$$K_f = \frac{1}{24} \sum_{i=1}^n b_i^3 A_{fD,i} \bar{\bar{I}} \quad (8.35)$$

Which could be further reduced in the case of 3 mutually perpendicular fracture systems to the tensor

$$K_f = \frac{1}{6} b^3 A_{fD,i} \bar{\bar{I}} \quad (8.36)$$

In the case of a single fracture system the tensor is reduced to

$$\bar{\bar{K}}_f = \frac{b^3 A_{fD,i}}{12} \begin{vmatrix} 1 & 0 & 0 \\ 0 & 1 & 0 \\ 0 & 0 & 0 \end{vmatrix} \quad (8.37)$$

and in the case of two orthogonal fracture systems to:

$$\bar{\bar{K}}_f = \frac{b^3 A_{fD,i}}{12} \begin{vmatrix} 1 & 0 & 0 \\ 0 & 1 & 0 \\ 0 & 0 & 2 \end{vmatrix} \quad (8.38)$$

If the tensor  $\bar{\bar{K}}_f$  is associated to the flow in an anisotropic fracture network where flow is governed by Darcy's law

$$\vec{v} = - \frac{\bar{\bar{K}}_f}{\mu} \cdot \overline{\nabla P} \quad (8.39)$$

the components of velocity will be

$$\vartheta_1 = \frac{K_1^o}{\mu} \frac{\partial P}{\partial x_1} ; \quad \vartheta_2 = - \frac{K_2^o}{\mu} \frac{\partial P}{\partial x_2} ; \quad \vartheta_3 = \frac{K_3^o}{\mu} \frac{\partial P}{\partial x_3} \quad (8.40)$$

If further the equations 8.40 are combined with the continuity equation, under steady-state conditions the equation of flow will be

$$K_1^o \frac{\partial^2 P}{\partial x_1^2} + K_2^o \frac{\partial^2 P}{\partial x_2^2} + K_3^o \frac{\partial^2 P}{\partial x_3^2} = 0 \quad (8.41)$$

This equation (8.41) may be transformed into an equivalent flow in an isotropic porous medium by using a relationship of equivalence between geometrical terms and directional permeability. A simplified formulation of such an equivalence is,

$$x'_i / x_i = C \sqrt{K_i^o} \quad (8.42)$$

The equivalence for a 3-component relationship is

$$K = \sqrt[3]{K_1^o K_2^o K_3^o} \quad (8.43)$$

and respectively

$$\left. \begin{aligned} x'_1 &= (K_2^o K_3^o / K_1^{o^2})^{1/6} \cdot x_1 ; \quad x'_2 = (K_1^o K_3^o / K_2^{o^2})^{1/6} \cdot x_2 \\ x'_3 &= (K_1^o K_2^o / K_3^{o^2})^{1/6} \cdot x_3 \end{aligned} \right\} \quad (8.44)$$

while for 2 components

$$K' = \sqrt{K_1^o K_2^o} \quad (8.45)$$

$$x'_1 = (K_2^o / K_1^o)^{1/4} \cdot x_1 ; \quad x'_2 = (K_1^o / K_2^o)^{1/4} \cdot x_2 ; \quad C = (K_1^o K_2^o)^{1/4} \cdot x_3 \quad (8.46)$$

### 8.3.2 Anisotropy and flow toward a well

#### 8.3.2.1. Anisotropy vs. steady-state flow toward a well

##### a. Pressure distribution

In a first simplified approach, an orthogonal system of coordinates  $x, y, z$  may be considered where  $x$  and  $y$  axes correspond to major and minor axes of the permeability ellipse, and the third axis  $OZ$  coincides with the well.

The steady-state equation of flow is then

$$K_x \frac{\partial^2 P}{\partial x^2} + K_y \frac{\partial^2 P}{\partial y^2} = 0 \quad (8.47)$$

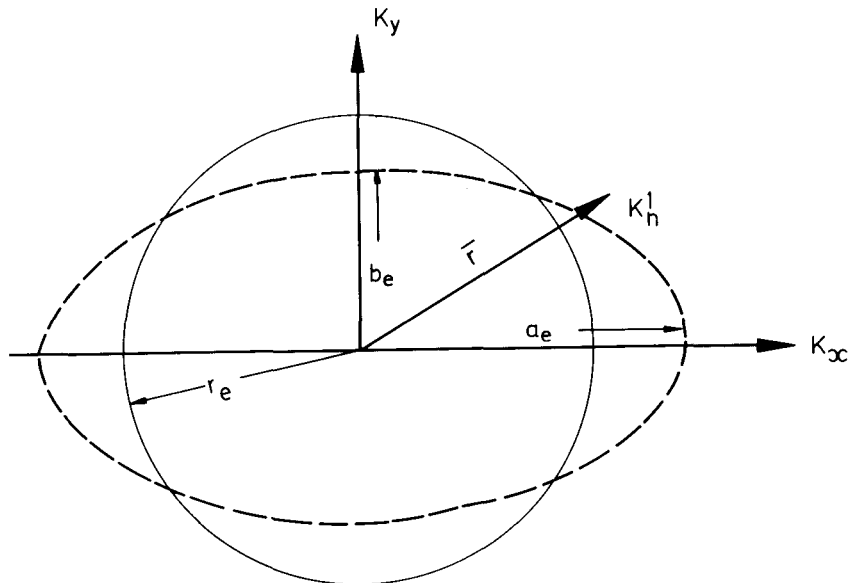
A similar procedure may be used for a stabilized radial plane flow, where the equivalent parameters  $x'_1$  and  $x'_2$  will be associated to an equivalence constant C (depending, for instance, on boundary conditions)

$$P(x', y') = \frac{Q\mu B}{2\pi\sqrt{K_x K_y} h} \ln r' + C \quad (8.48)$$

In cylindrical coordinates (figure 8.6), the pressure distribution may be written as

$$P(\bar{r}) = \frac{Q\mu B}{2\pi\sqrt{K_x K_y} h} \ln \frac{r}{\sqrt{K_n}} + C' \quad (8.49)$$

where  $\bar{r}$  is the radius vector and  $K_n$  the permeability along the same flow direction. For a constant pressure an ellipse will result from equation 8.49 in which the axis ratio is proportional to the ratio  $K_x/K_y$ . This ellipse represents the isobar line similar to that of the external or internal boundary (figure 8.6).



8.6 – Anisotropic and equivalent isotropic boundaries in case of a flow toward a well.

#### b. Equivalent external radial boundary ( $r'_e$ )

The anisotropic reservoir boundary represented by an ellipse of axis  $a_e$ ,  $b_e$ , may be related to an isotropic radial boundary  $r_e$  by the relation

$$r_e = (a_e + b_e)/2 \quad (8.50)$$

where physically the axis ratio is proportional to the permeability ratio

$$a_e/b_e = \sqrt{K_x/K_y} \quad (8.51)$$

It will result that the two axes of the elliptical boundary are

$$a_e = 2r_e \sqrt{K_x} / (\sqrt{K_x} + \sqrt{K_y}) ; b_e = 2r_e \sqrt{K_y} / (\sqrt{K_x} + \sqrt{K_y}) \quad (8.52)$$

From the definition of equivalent length (equation 8.42)

$$a'_e/r'_e = C/\sqrt{K_x} \quad \text{and} \quad b'_e/r_e = C/\sqrt{K_y} \quad (8.53)$$

the equivalent radial supply boundary may be obtained, as a function of anisotropy data,

$$r'_e = \frac{a'_e + b'_e}{2} = \frac{4r_e C}{2} \frac{1}{\sqrt{K_x} + \sqrt{K_y}} = \frac{2r_e C}{\sqrt{K_x} + \sqrt{K_y}} \quad (8.54)$$

#### c. Equivalent radial internal boundary ( $r'_w$ )

Based on the same definition of equivalent length expressed by equation 8.42.

$$a'_w/r = C/\sqrt{K_x} ; b'_w/r_w = C/\sqrt{K_y} \quad (8.55)$$

and further with reference to wellbore data,

$$r'_w = (a'_w + b'_w)/2 = r_w C (\sqrt{K_x} + \sqrt{K_y})/2\sqrt{K_x K_y} \quad (8.56)$$

By analogy, for any radius  $r$  in the flow domain, the equivalent radius will be

$$r' = r C (\sqrt{K_x} + \sqrt{K_y})/2\sqrt{K_x K_y} \quad (8.56')$$

#### d. Equivalent radial flow rate

The well rate for an equivalent radial boundary will result as through equations (8.53) and (8.55)

$$Q = \frac{2\pi\sqrt{K_x K_y} h (P_e - P_w)}{\mu B \ln r'_e/r'_w} = \frac{2\pi\sqrt{K_x K_y} h (P_e - P_w)}{\mu B \ln \frac{r_e}{r_w} 4 \frac{\sqrt{K_x K_y}}{(1 + \sqrt{K_x/K_y})^2}} \quad (8.57)$$

or

$$Q = \frac{2\pi \bar{K} h (P_e - P_w)}{\mu B \ln \frac{r_e}{r_w} \Psi} \quad (8.58)$$

where

$$\Psi = 4\sqrt{K_x/K_y} / (1 + \sqrt{K_x/K_y})^2 ; \bar{K} = \sqrt{K_x K_y} \quad (8.59)$$

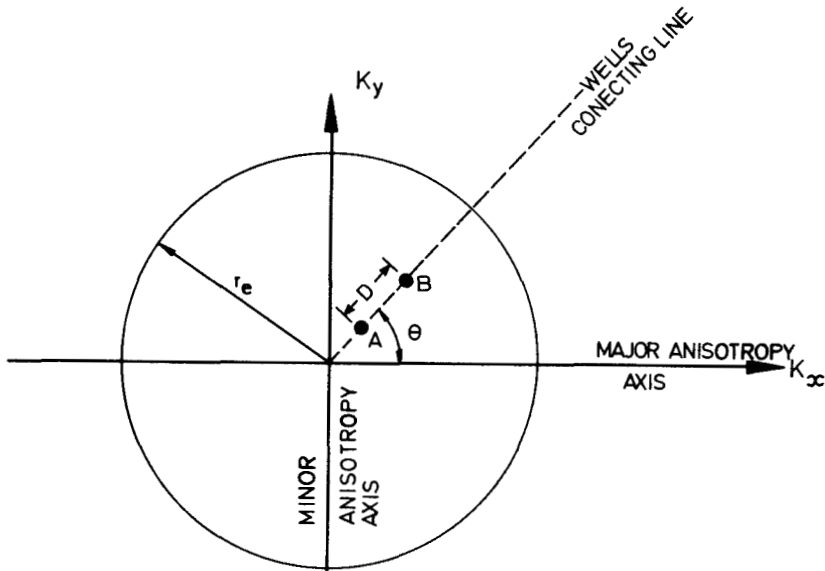
### 8.3.2.2. Anisotropy and steady-state interference

#### a. Case of two production wells.

In the case of two wells A and B producing from the same reservoir and located at a distance D, the classic rate equation expressing the interference effect is

$$Q = \frac{2\pi \sqrt{K_x K_y} h (P_e - P_w)}{\mu B \ln r_e'^2 / 2D' r_w'} \quad (8.60)$$

where  $r_e'$ ,  $r_w'$  and  $D'$  are the equivalent length in a homogeneous reservoir which are substituting for the real anisotropic reservoir (figure 8.7)



8.7 – Two wells producing in an anisotropic reservoir

Since the parameter  $D'$  is written

$$D' = \frac{D}{\sqrt{K_n'}} = D \sqrt{1 - \frac{K_1 - K_2}{K_1} \cos^2 \Theta} \frac{1}{\sqrt{K_2}} \quad (8.61)$$

the single well rate will result from the combination of equation 8.61 with equations 8.60, 8.54 and 8.55,

$$Q = \frac{2\pi \sqrt{K_x K_y} h (P_e - P_w)}{\mu_o B_o \ln \frac{r_e}{r_w} \xi} \quad (8.62)$$

where

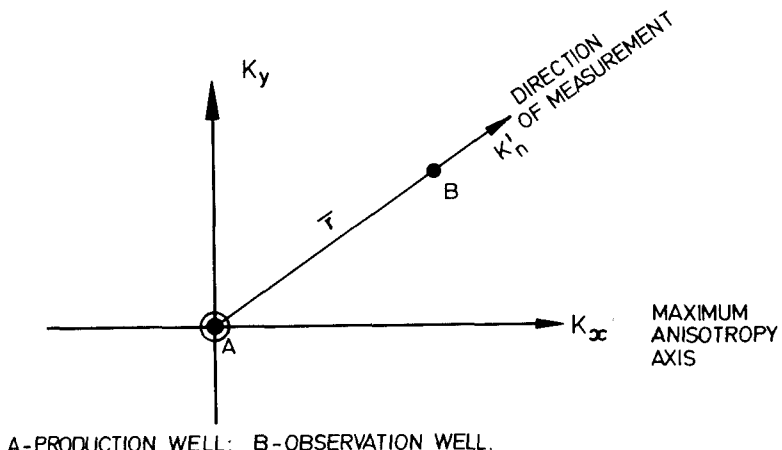
$$\bar{K} = \sqrt{K_1 K_2} \quad (8.63)$$

and

$$\xi = 4 \frac{r_e}{D} \cdot \frac{\sqrt{K_y} / (\sqrt{K_x} + \sqrt{K_y})^2}{[1 - (K_x - K_y) \cos^2 \Theta / K_x]^{1/2} (\sqrt{K_x} + \sqrt{K_y}) / \sqrt{K_x}} \quad (8.64)$$

### b. Case of production and observation well.

If a well A is produced with a rate Q (Fig. 8.8) and an observation well B is located at a distance  $\bar{r}$ , under steady-state flow conditions, the pressure  $p$  ( $r$ ) will be expressed by equation 8.49 with reference to well radius ( $r = r_w$ ) and well pressure ( $p = p_w$ )



A - PRODUCTION WELL; B - OBSERVATION WELL.

8.8 - Producing well A and observation well B in an anisotropic reservoir.

For a radius  $r$ , similarly as in equation 8.56,

$$r' = Cr(\sqrt{K_x} + \sqrt{K_y})/2\sqrt{K_x} K_y \quad (8.65)$$

the pressure vs. radius  $r$  is given by

$$p(\bar{r}) = P_w + \frac{Q\mu B}{2\pi\sqrt{K_x} K_y h} \ln \frac{2\sqrt{K_x} K_y}{r_w (\sqrt{K_x} + \sqrt{K_y})} \frac{r}{\sqrt{K'_n}} \quad (8.66)$$

or

$$2r\sqrt{K_x} K_y / \sqrt{K'_n} r_w (\sqrt{K_x} + \sqrt{K_y}) = e^{2\pi h (P - P_w) / Q\mu \sqrt{K_x/K_y}} \quad (8.67)$$

Substituting the steady-state rate  $Q$  from equation 8.58 under the assumption that  $\Psi = 1$  and combining with equation 8.67, it is obtained along the direction of measurement that

$$\frac{F}{K'_n} \cong (r_w/r) e^{2(P - P_w) \ln r_e/r_w / (P_e - P_w)} = (r_e/r)^2 e^{(P - P_w)/(P_e - P_w)} \quad (8.68)$$

where

$$F = \left[ \frac{2\sqrt{K_x} K_y}{\sqrt{K_x} + \sqrt{K_y}} \right]^2 = \frac{4 K_x K_y}{(\sqrt{K_x} + \sqrt{K_y})^2} = \frac{4 K_x}{(\sqrt{K_x/K_y} + 1)^2} \quad (8.69)$$

In continuation, the angle  $\Theta$  between the major anisotropy axis and the direction of measurement will result from

$$\cos^2 \Theta / K_x + \sin^2 \Theta / K_y = F / K_n \quad (8.70)$$

It becomes evident that if  $F/K'_n$  and  $\Theta$  are known, the orientation of  $K_x$  and  $K_y$  becomes possible.

### 8.3.3 Anisotropy evaluation

#### 8.3.3.1. Major and minor axes of fracture permeability and their orientation

As observed from the basic equation examined above, the production-observation wells' geometry, production rate and pressure data are essential for the determination of anisotropy characteristics :  $K_x$ ,  $K_y$ ,  $\Theta$  and  $K'_n$ . However in the absence of a certain simplified geometry of production-observation wells, the problem is complicated by a larger number of parameters than the number of equations. An explanation is given in Table 8.1.

Table 8.1

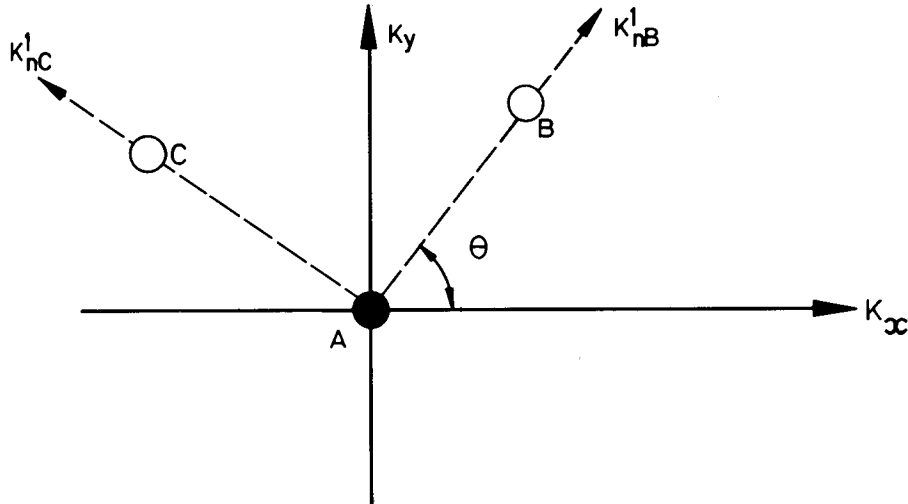
Case	Well	Figure	Equation	Unknown Parameters
1	PRODUCTION, A	8.6	8.58	$K_x, K_y$
2	PRODUCTION, A	8.6	8.58	$K_x, K_y$
	PRODUCTION, A+B	8.7	8.62	
3	PRODUCTION, A	8.6	8.58	$K_x, K_y$ $\Theta, K_n$
	PROD+INTERF A+B	8.8	8.62	
			8.68	

a. Simplified cases

In order to overcome these difficulties in solving the anisotropy problems, a simplified geometry applied to the location of production-observation wells may be very helpful. A number of simple cases are given as examples.

Case 1 : Two mutually orthogonal measurement directions. As observed in figure 8.9, the three wells A, B, C, where A is a production well and B and C are observation wells, form two mutually orthogonal directions similar to the two axes  $K_x$  and  $K_y$ .

The directional permeabilities  $K'_{nB}$  and  $K'_{nC}$  will allow us to write



8.9 – Mutually orthogonal arrangement of wells A,B,C (production well A, observation wells B,C).

$$K'_{n,B}/K'_{n,C} = K_x/K_y \quad (8.71)$$

and in continuation

$$K_x/K_y = K'_{n,B}/K'_{n,C} = r_{AB}^2/r_{AC}^2 = e^{(P_e - P_w)/(P_e - P_w)} / e^{(P_B - P_w)/(P_e - P_w)} \quad (8.72)$$

The ratio  $K_x/K_y$  is determined from equation 8.72 as result of well location data ( $r_{AB}$ ,  $r_{AC}$ ) and dynamic pressure  $P_e$  and  $P_B$  measured in the observation wells. The pressures  $P_w$  and  $P_e$  are respectively the flow pressure in well A and the reservoir static pressure at its external boundary.

The evaluation of other parameters is the following:

- ~  $K_x/K_y$ , if introduced in equation 8.59, gives the parameter  $\Psi$ .
- ~ By introducing  $\Psi$  in equation 8.58 the permeability  $\bar{K} = \sqrt{K_x K_y}$  is obtained
- ~ The single values  $K_x$  and  $K_y$  are obtained from values  $\Psi$  and  $K$ .
- ~ The expression  $F/K_{nB}$  is evaluated from equation 8.68 and in continuation angle  $\alpha$  from equation 8.70

Case 2 : Three wells located along a straightline. Considering the wells located on the same line as wells A, B, C in figure 8.10, the following procedure may be used:

Simultaneous production of wells A, B, C with the same flow pressure in all wells will develop an interference effect between wells A and C and between wells B and C. From equation 8.62 it is possible to write,

$$\frac{1}{Q_A} - \frac{1}{Q_B} = \frac{\mu_0 B_o}{2\pi \bar{K} h (P_e - P_w)} \left( \ln \frac{r_e}{r_w} \xi_{AC} - \ln \frac{r_e}{r_w} \xi_{BC} \right) \quad (8.73)$$

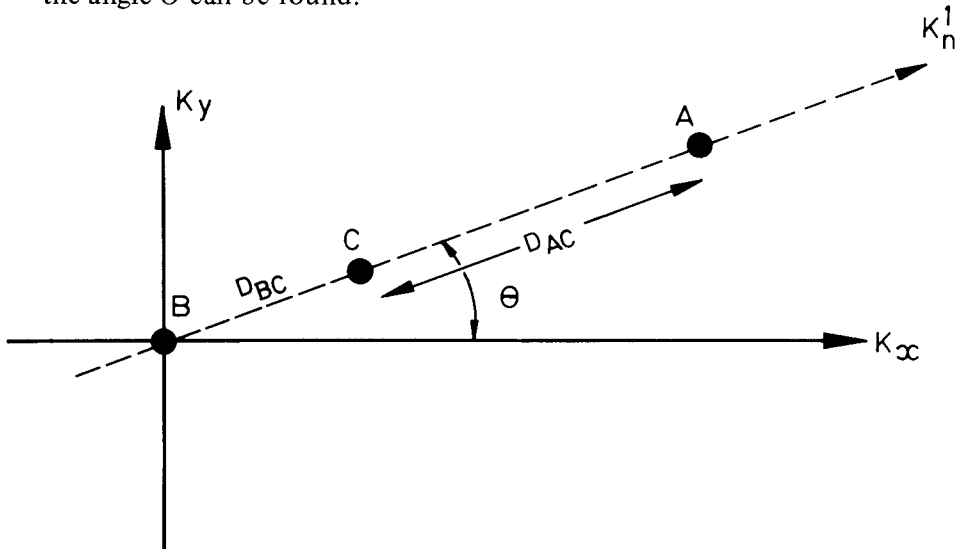
or

$$\frac{Q_B - Q_A}{Q_A \cdot Q_B} = \frac{\mu_0 B_o}{2\pi \bar{K} h (P_e - P_w)} \ln D_{BC}/D_{AC} \quad (8.74)$$

and finally

$$\bar{K} = \sqrt{K_x K_y} = \frac{\mu_0 B_o Q_A Q_B}{2\pi h (Q_A - Q_B) (P_e - P_w)} \ln \frac{D_{BC}}{D_{AC}} \quad (8.75)$$

- ~ If a single well, for example the well C, is produced, the expressions  $\Psi$  and then  $K_x/K_y$  may be directly obtainable from equations 8.58 and 8.59.
- ~ Finally  $K_x$  and  $K_y$  are evaluated, from  $K_x/K_y$  and  $K_x \cdot K_y$ .
- ~ If the single well, for example well C, is producing and A is an observation well, the expression  $F/K_n^1$  results through equation 8.58.
- ~ Knowing the values  $K_x$  and  $K_y$  together with  $f/K_n^1$ , from equation 8.70 the angle  $\Theta$  can be found.



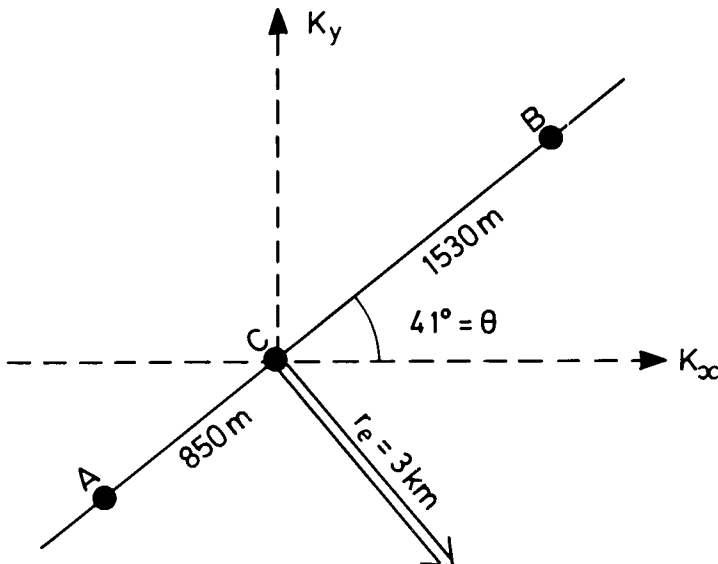
8.10 – Three wells (ABC) located on a common straight-line

#### b. Calculation example

A series of tests have been performed on three wells located along a straightline as shown in Figure 8.11. Is is required to evaluate the reservoir anisotropy.

The basic data to use in the further calculation are:  $H = 150$  m;  $\mu_o = 1.16$  cP;  $B_o = 1.38$ ;  $P_e = 169$  at (with reference to the well C) and the respective boundaries are :  $r_e \approx 3$  Km and  $r_w \approx 10$  cm.

Phase 1 . From simultaneous production of wells A, B, C, with the same flowing pressure at all wells ( $P_w = 166.5$  at), the rates obtained were :  
well A = 5185 STB/D,  
well B = 4610 STB/D



8.11 – Three wells A, B, C aligned on a straight-line.

By using the equation 8.75 it results that:

$$\bar{K} = K_x K_y = \frac{1.16 \times 1.38 \times 8500 \times 9555}{6.28 \times 15000 \times (9555 - 8500) 2.5} \times \ln \frac{1530}{850} = .305$$

Phase 2 : Producing well C and keeping A and B as observation wells, a rate of 3435 STB/D was obtained for a flow pressure  $P_w = 165,45$  at. From equation 8.58

$$\ln \frac{r_e}{r_w} \Psi = \frac{2\pi \bar{K} h \Delta P}{Q \mu_o B_o} = \frac{6.28 \times 0.305 \times 15000 \times 3.55}{6330 \times 1.16 \times 1.38} = 10.06$$

or

$$\Psi = \frac{r_w}{r_e} e^{10.01} ; \quad \Psi = \frac{0.10}{3000} e^{10.01} = 0.779$$

and further from equation 8.59

$$\sqrt{K_x / K_y} = \sqrt{7.72} = 2.77$$

From  $\sqrt{K_x K_y} = 0.305$  and  $\sqrt{K_x / K_y} = 2.77$  it results that

$$K_x = 850 \text{ mD} \text{ and } K_y = 110 \text{ mD.}$$

Phase 3 : If during production of well C the pressure recorded in well B indicated a pressure  $P_w = 166.29$ , it becomes possible to use equation 8.68

$$F/K_n^* = (r_e/r)^2 e^{(P - P_w)/(P_e - P_w)} = (3000/1530)^2 e^{0.847/3.55} = 4.88$$

and further from equation 8.70

$$\cos^2 \Theta / 0.58 + \sin^2 \Theta / 0.11 = 4.88$$

a value results of  $\Theta \approx 41^\circ$  (see figure 8.1).

### 8.3.3.2. Porosity evaluation in the case of an anisotropic fractured reservoir

In a formation which is not isotropic and has  $n$  arbitrarily oriented fracture systems, the permeability and porosity have to take into consideration the orientation of each fracture system. The main components of an ellipsoid will be thus expressed by

$$K_x = K_{fx} = \frac{1}{12} \sum_{i=1}^n b_i^3 \times A_{fD,i} \times \sin^2 \Theta_{x,i}$$

$$K_y = K_{fy} = \frac{1}{12} \sum_{i=1}^n b_i^3 \times A_{fD,i} \times \sin^2 \Theta_{y,i}$$
(8.76)

while porosity is

$$\Phi_f = \sum_{i=1}^n b_i A_{fD,i}$$
(8.77)

In using these equations, the lack of detailed knowledge of fracture distribution makes impossible the evaluation of  $\Phi_f$  as a function of anisotropy expressed by parameters  $K_x$  and  $K_y$ . The only solution is to associate a simplified geometry of fracture network to well testing data.

#### a. Relationship $\Phi_f$ vs. productivity index in an anisotropic reservoir.

In a first approach a simplified case may be assumed where the reservoir is formed by matrix blocks separated by  $n$  vertical fractures of equal width  $b$ .

The anisotropy may be written from equation 8.76 as

$$K_x + K_y = \frac{1}{12} b^3 A_{fD}$$
(8.76')

and similarly

$$\Phi_f = b A_{fD} \quad (8.77')$$

Introducing  $b$  from 8.76' in 8.77' it will result gives

$$\Phi_f = \left[ 12 (K_x + K_y) A_{fD}^2 \right]^{1/3} = \left[ 12 \sqrt{K_x K_y} \left( \sqrt{\frac{K_y}{K_x}} + \sqrt{\frac{K_x}{K_y}} \right) A_{fD}^2 \right]^{1/3} \quad (8.78)$$

since from the equation 8.58 it is possible to approximate that

$$\sqrt{K_x \cdot K_y} \cong \frac{Q_o \mu_o B_o \ln r_e/r_w}{2\pi h \Delta P} = PI \frac{\mu_o B_o \ln r_e/r_w}{2\pi h} \quad (8.79)$$

the porosity as a function of productivity index is

$$\Phi_f = \left[ PI \frac{6 A_{fD}^2 \mu_o B_o \ln r_e/r_w}{\pi h} \left( \sqrt{\frac{K_x}{K_y}} + \sqrt{\frac{K_y}{K_x}} \right) \right]^{1/3} \quad (8.80)$$

b. Various cases.

b.1. *Two mutually orthogonal vertical fracture systems.*

- If  $b_x = b_y$ , but  $A_{fD,x} \neq A_{fD,y}$ , the fracture density is written as,

$$A_{fD} = A_{fD,x} \neq A_{fD,y}$$

and from equation 8.76

$$\sqrt{K_x \times K_y} = \frac{b^3}{12} \sqrt{A_{fD,x} \times A_{fD,y}} = \frac{\Phi_f^3}{12 A_{fD}^3} \sqrt{A_{fD,x} \times A_{fD,y}} \quad (8.81)$$

which yields the fracture porosity

$$\Phi_f = A_{fD} \left( \frac{12 \sqrt{K_x K_y}}{A \sqrt{A_{fD,x} \times A_{fD,y}}} \right)^{1/3} = A_{fD} \left( PI \frac{6 \mu_o B_o \ln r_e/r_w}{\pi h \sqrt{A_{fD,x} \times A_{fD,y}}} \right)^{1/3} \quad (8.82)$$

- If  $b_x = b_y$  and  $A_{fD,x} = A_{fD,y} = A_{fD}$  the fracture porosity from the transformation of equation 8.83 is

$$\Phi_f = 2 \left( \text{PI} \frac{6 \mu_o B_o \ln r_e/r_w}{\pi h} \cdot A_{fD}^2 \right)^{1/3} \quad (8.83)$$

### b.2. Three mutually orthogonal fracture systems.

if  $b_x = b_y = b_z$  but  $A_{fD,x} \neq A_{fD,y} \neq A_{fD,z}$

$$\Phi_f = A_{fD} \left[ \text{PI} \frac{6 \mu_o B_o \ln r_e/r_w}{\pi h \sqrt{(A_{fDx} + A_{fDy})(A_{fDy} + A_{fDz})}} \right]^{1/3} \quad (8.84)$$

In case of a *random* fracturing, or only one horizontal fracture system,  $A_{fD} = (\pi/2) L_{fD}$  (8.85)

and thus

$$\Phi_f = \sqrt[3]{\text{PI} \frac{3\mu_o B_o \ln r_e/r_w}{h} L_{fD}^2} \quad (8.86)$$

#### 8.3.3.3. Fracture permeability and orientation from unsteady-state flow.

The use of transient pressure in case of an anisotropic permeability may be developed with sufficient accuracy, following in general line the method indicated by Elkins<sup>4</sup>, and applied in Spraberry field development.

The procedure indicated hereunder for two wells may be further extended to a large number of observation-production wells located on the same structure

##### a. Calculation procedure

Considering the production well A and the observation well B (figure 8.12), an arbitrary cartesian axis system with a fixed center O is chosen, and the following procedure is used :

~ From the production well A a slope  $m'$  is obtained from the pressure vs. log time relationship from which the permeability results as

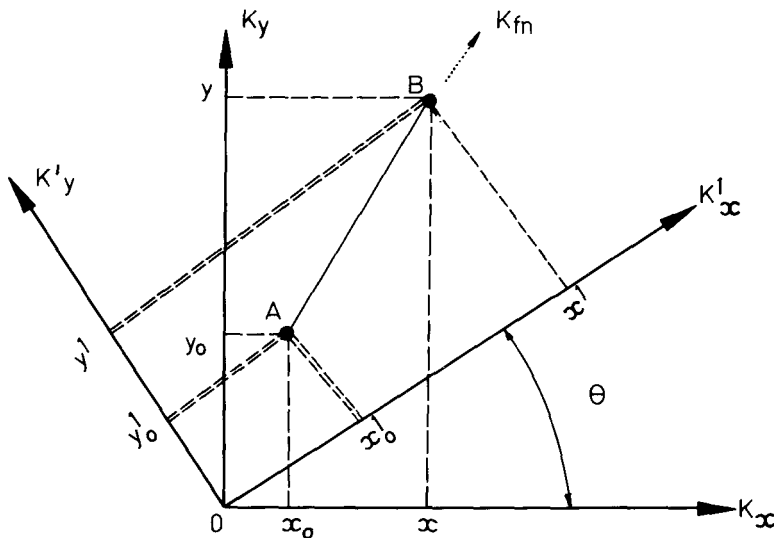
$$\bar{K} = 1.15 \frac{q \mu B}{2\pi h} \frac{1}{m'} \quad (8.87)$$

~ The piezo-conductivity can be calculated as

$$a' = \frac{\bar{K}}{(\Phi_1 C_1 + \Phi_2 C_2) \mu} \cong \frac{\bar{K}}{\Phi C \mu} \cong \frac{\bar{K}}{\Phi_1 C_1 \mu} \quad (8.88)$$

where  $\Phi$  is approximated to matrix porosity  $\Phi_1$ .

~ The values  $x - x_o$  and  $y - y_o$  are evaluated for various angles  $\Theta$ , as shown in figure 8.12.



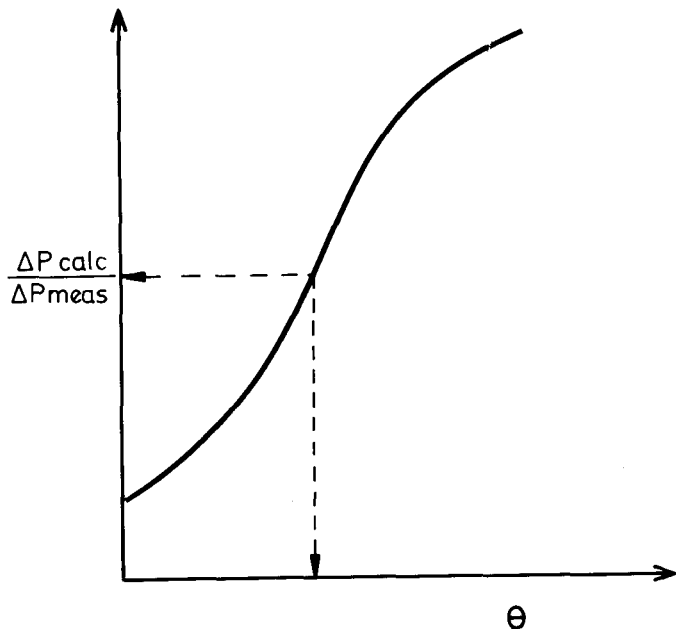
8.12 – Evaluation of angle  $\Theta$  from measured and calculated pressure drop.

~ For each angle  $\Theta$  the calculated pressure drop is given by

$$\Delta P = -m'/2.3 Ei \left[ -D \frac{(x - x_o) + (y - y_o)}{4 a'} \frac{1}{t_m} \right] \quad (8.89)$$

where  $t_m$  is the value of recorded time, when the *pressure drop in observation well  $\Delta P_m$  was measured*.

- ~ The value  $\Delta P_{\text{calc}}$  is the calculated pressure drop from equation 8.89.
- ~ The ratio  $\Delta P_{\text{calc}}/\Delta P_m$  will indicate the most probable  $\Theta$  value when  $\Delta P_{\text{cal}}/\Delta P_m \cong 1$ , as in figure 8.13
- ~ Distance  $D$  remains unchanged, but its projections are modified with the variation of angle  $\Theta$



8.13 – Variation  $\Delta P_{\text{calc}}/\Delta P_{\text{meas}}$  versus  $\Theta$

- ~ Knowing the direction of major permeability axis  $K_n$ , it is possible to try to evaluate the  $K_x$  and  $K_y$  values by considering that for the resulting  $\Theta$  value,

$$\frac{K_y}{K_x} = \frac{y - y_o}{x - x_o} \quad (8.90)$$

If combined with

$$K_x K_y = \bar{K}^2 \quad (8.91)$$

where  $\bar{K}$  is obtained from eq. 8.87, both values  $K_x$  and  $K_y$  may be evaluated.

#### b. Discussion about equation 8.89.

Basically the pressure drop in an observation well in case of an anisotropic fractured reservoir may be expressed<sup>4</sup> by the following equation

$$\Delta P = -\frac{1}{2} \frac{q \mu B}{2\pi \sqrt{K_x K_y h}} Ei \left[ -\frac{(x - x_o)^2 / K_x + (y - y_o)^2 / K_y}{4/\Phi C \mu} \cdot \frac{1}{t} \right] \quad (8.93)$$

where if  $x - x_o$  and  $y - y_o$  are the projected values of straight-line D on the orthogonal axis system  $K_x$  and  $K_y$ .

$$K_x = \bar{K} [D/(x - x_o)] \text{ and } K_y = \bar{K} [D/(y - y_o)] \quad (8.94)$$

The combination of equations 8.93 and 8.94 reduces the pressure drop in the observation well to the simplified equation 8.89.

### c) Calculation example

Two wells A (production) and B (observation) are examined during the transient period of well A production (Figure 8.14).

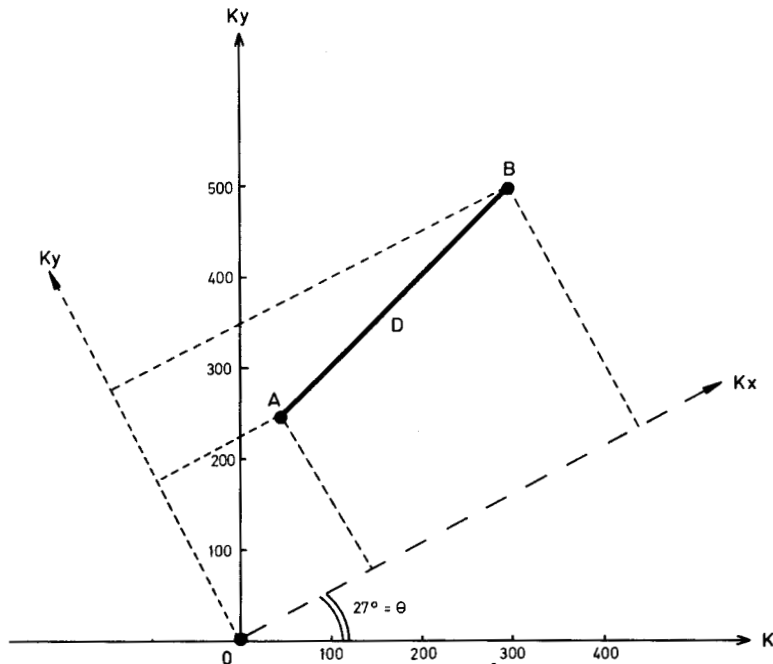
It is required to find the anisotropy of the reservoir based on pressure vs. time recording data in both wells A and B.

The following data are known :

$$q = 8420 \text{ STB/D} ; h = 50 \text{ m} ; \mu_o = 1.4 \text{ cP} ; B_o = 1.26 ;$$

$$\Phi_{\text{matrix}} \cong 14.8 \% ; C_1 \cong 12 \times 10^{-6} \text{ l/psi} ; D = 350 \text{ m.}$$

In the observation well at time  $t_m$  a pressure drop  $\Delta P_{\text{measured}}$  was recorded ( $t_m = 200.000 \text{ sec.} ; \Delta P_{\text{measured}} = 1.345 \text{ at}$ ).



8.14 – Production well A and observation well B associated with anisotropy axis  $K_x$  and  $K_y$ .

## SOLUTION

- Preparation of basic equation 8.89

~ From production well A, a linear variation  $\Delta P_f$  vs.  $\log t$  results from which slope  $m'$  gives the permeability  $\bar{K}$  through equation 8.87

$$m' = 2.18 \text{ at/cycle and further}$$

$$\bar{K} = \frac{1.15 q \mu_o B_o}{2\pi h x m'} = \frac{1.15 \times 15520 \times 1.4 \times 1.26}{6.28 \times 5000 \times 2.18} = 0.459 \text{ D}$$

~ The value  $a'$  which expresses the piezo-conductivity is obtained through equation 8.88,

$$a = \bar{K}/\Phi C \mu = .459/0.148 (12 \times 10^{-6} \times 14.7) \times 1.4 = 12500 \text{ (cm}^2/\text{sec)}$$

~ The value

$$m = \frac{1}{2} \cdot 3 = 2.18/2.3 = 0.949 \text{ at/cycle}$$

~ For  $D = 350 \text{ m}$  and  $t_o = 200 \text{ 000 seconds}$  it results that

$$\begin{aligned} \Delta P_{\text{calc}} &= -m \text{ Ei} \left[ -D \frac{(x - x_o) + (y - y_o)}{4a t_o} \right] = \\ &= 0.949 \times \text{Ei} \left[ -\frac{35000 (x - x_o) + (y - y_o)}{4 \times 12500 \times 2 \times 10^5} \right] \end{aligned}$$

or

$$\Delta P_{\text{calc}} = -0.949 \text{ Ei} \left[ -3.5 \times 10^{-6} [(x - x_o) + (y - y_o)] \right]$$

- Evaluation of  $(x - x_o)$  and  $(y - y_o)$  vs.  $\Theta$ .

By rotating the orthogonal axis with angle  $\Theta$  the values  $(x - x_o)$  and  $(y - y_o)$  are the projection of line D on the  $K_x$  and  $K_y$  axes.

If angle  $\Theta = 10^\circ$ , it results that  $x - x_o = 28671 \text{ cm}$  and  $y - y_o = 20075 \text{ cm}$ .

- Evaluation of  $\Delta P_{\text{calc}}$ .

Introducing for  $\Theta = 10^\circ$  the values  $x - x_o$  and  $y - y_o$ , it results that

$$\Delta P_{\text{calc}} = 0.949 \text{ Ei} (-0.1706) = 1.2717 \text{ at}$$

and further

$$\frac{\Delta P_{\text{calc}}}{\Delta P_{\text{measured}}} = \frac{1.2717}{1.345} = 0.945$$

- Angle  $\Theta$  evaluation

Repeating the above calculation of  $\Theta$  between  $0^\circ$  and  $45^\circ$ , the results are given in diagram figure 8.15, from which it results that  $\Theta = 27^\circ$  for a ratio  $\Delta P_{\text{calc}}/\Delta P_{\text{measured}} \approx 1$

- Evaluation of  $K_x$  and  $K_y$ .

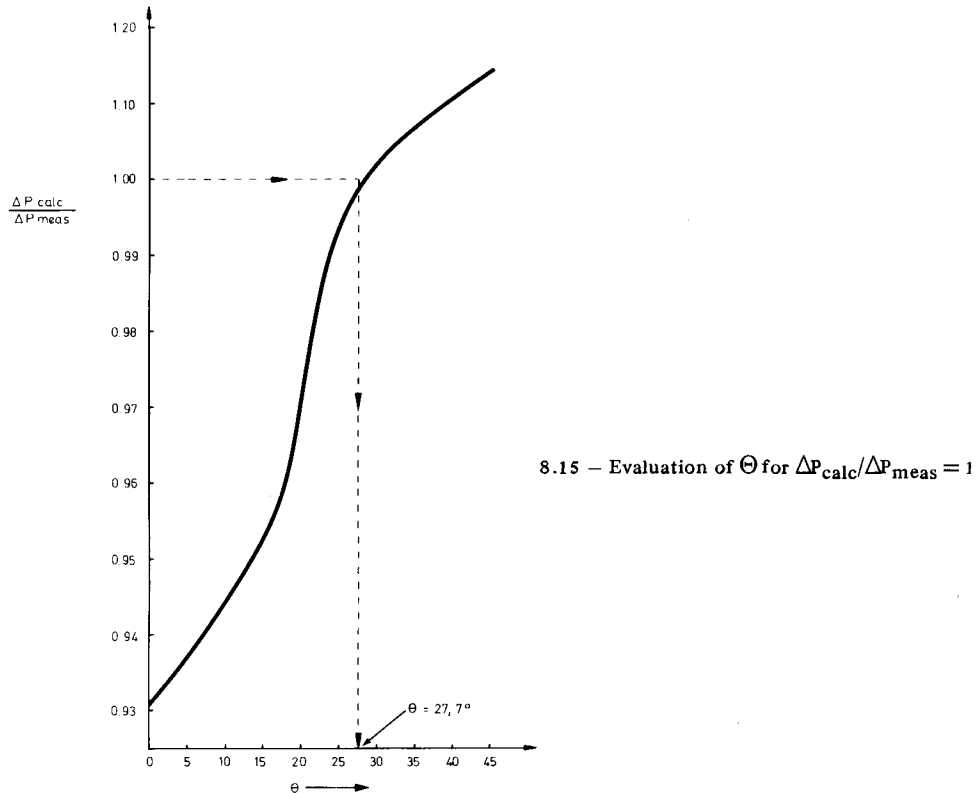
Based on equations 8.90 and 8.91 for  $\Theta = 27^\circ$  the ratio

$$K_x/K_y = (x - x_o) / (y - y_o) = 33250/10806 = 3.07$$

and on permeability  $K$  expressed by

$$\bar{K} = \sqrt{K_x K_y} = 0.459$$

then  $K_x = 0.801$  D and  $K_y = 0.261$  D.



## 8.4. USE OF TYPE-CURVES FOR ANALYSIS OF FLOW TOWARD A WELL

The type-curves have been extensively developed for fractured wells in conventional reservoirs; these are not the same as the type-curve for a natural fractured reservoir when a well is producing under transient conditions. The use of a fractured-well type-curve for a natural fractured reservoir well will have only a limited qualitative value and will not indicate any particular characteristic of the fractured reservoir. Recently, two papers<sup>5,6</sup> have developed specific fractured reservoir type-curves; one for the case of a well producing under a constant rate<sup>5</sup> and another for a well producing under constant pressure drop<sup>6</sup> at the wellbore. In these papers the theoretical development is based on the rigorous approach of Barenblatt and Warren-Root theory.

### 8.4.1. Type-curve of a producing well under constant rate conditions (Bourdet-Gringarten<sup>5</sup>)

The type-curve substitutes for the pressure vs log time analysis with log pressure - log time relationship. Without developing the basic concepts in detail, the procedure recommends the plotting of recorded data in a diagram  $\log \Delta P$  vs log time. The data are later matched with the diagram figure 8.16 where the ratio dimensionless pressure versus dimensionless time-storage is drawn.

From matching the measured data with the dimensionless value, a procedure of evaluation of fractured reservoir parameters becomes possible,  
~ flowing capacity  $K_f h$  from

$$K_f h \text{ (mD x feet)} = 141.2 q B \mu (P_D / \Delta P)_M \quad (8.95)$$

where M indicates matching point data ; q,rate ; B, volume factor ;  $\mu$  – viscosity (cp).

~ well storage capacity C is given by

$$C = \frac{Kh}{3389 \mu} \left[ \frac{\Delta t}{t_D / C_D} \right]_M \quad (8.96)$$

where C (bbl/psi); Kh (md x feet),  $\mu$  – viscosity (cp).

~ total storage capacity  $(C_D)_{f+m}$  is expressed by

$$(C_D)_{f+m} = \frac{0.8396 C}{(\Phi V C_t)_{f+m} \times h r_w^2} \quad (8.97)$$

where  $(\Phi V C_t)_f + m$  is the storage capacity of the entire system ;  $h$  is the pay ;  $r_w$  - well radius.

~ Skin effect is expressed by

$$S = 0.5 \ln \frac{(C_D e^{2S})_{f+m}}{(C_D)_{f+m}} \quad (8.98)$$

where  $C_D e^{2S}$  results from the type-curve

~ The relative storage capacity  $\omega$  and interporosity parameter are finally obtained as

$$\omega \cong \frac{(C_D e^{2S})_{f+m}}{(C_D e^{2S})_f} \quad (8.99)$$

and

$$\lambda = (\lambda e^{-2S}) e^{-2S} \quad (8.100)$$

where  $\lambda e^{-2S}$  represents the curve with which the reservoir behaviour matches the best.

Example.

The pressure vs. time recorded in a production well of a fractured reservoir is expressed in double-log diagram (figure 8.16) as  $\Delta P$  (psi) vs time  $t$  (hours). The other basic data are :  $q = 3600 \text{ STB/D}$ ,  $\mu_o = 116 \text{ cP}$ ,  $B_o = 1.21$ ,  $h = 736 \text{ feet}$  ;  $(\Phi V C_t)_{f+m} = 2.1 \times 10^{-6} \text{ (1/psi)}$  ;  $r_w = 7.5 \text{ cm}$ .

Matching procedure.

Fixing the pressure drawdown on  $\lambda e^{-2S} = 10^{-6}$  curve, and  $C_D e^{2S} \cong 10^3$ , the matching point M will indicate (figure 8.16) the following:

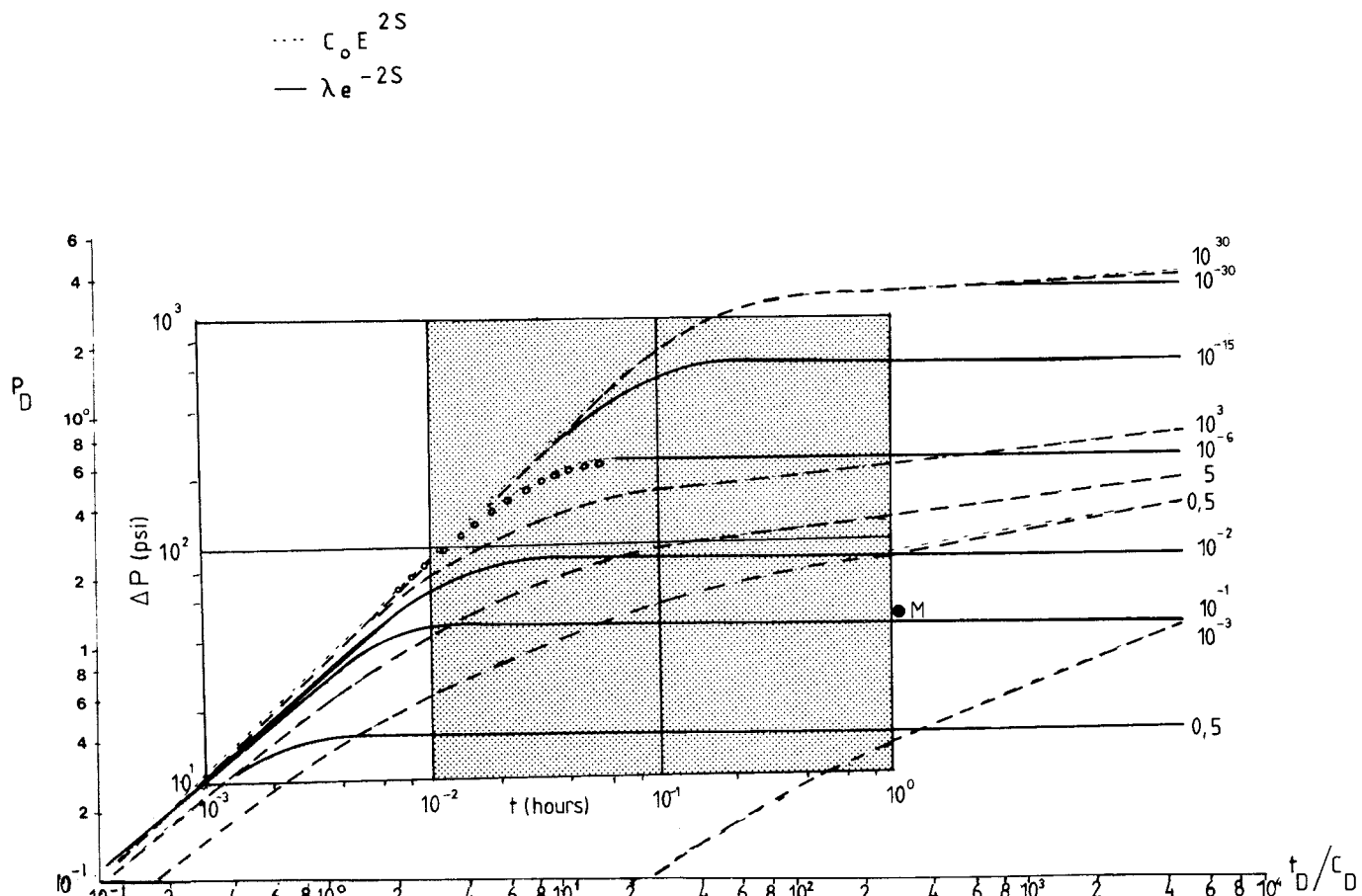
$$P_D = 1.42 \quad \text{and} \quad \Delta P = 50 \text{ psi}$$

$$t_D / C_D = 337 \quad \text{and} \quad \Delta t = 1 \text{ hour}$$

Calculation of basic data:

~ from equation 8.95

$$K_f h = 141.2 \times 3600 \times 1.16 \times 1.21 \times \frac{1.42}{50} = 20262 \text{ (mD x feet)}$$



8.16 – Type curve and well pressure drawdown data (Bourdet<sup>5</sup> Courtesy AIME)

~ from equation 8.96

$$C = \frac{20262}{3389 \times 1.16} \left( \frac{1}{337} \right) = 1.52 \times 10^{-2} \text{ (bbl/psi)}$$

~ from equation 8.97

$$(C_D)_f + m = \frac{0.8936 \times 1.52 \times 10^{-2}}{2.1 \times 10^{-6} \times 736 \times (0.243)^2} = 152$$

~ from equation 8.98

$$S = 0.5 \ln \frac{10^3}{100} = 1.15$$

~ through equation (8.100) the  $\lambda$  value is verified

$$\lambda = 10^{-6} e^{2.3} \cong 10^{-5}$$

#### 8.4.2. Type-curve of a producing well under constant pressure drop conditions (Da Prat<sup>6</sup>)

In this case the rate decline vs. time is examined for the simplified Warren-Root model. The method indicates that for relatively large reservoirs after an initial rate decline a constant rate follows for a long period of time.

The data obtained from matching are the following :

$$K_f = \frac{\mu_o B_o}{h \Delta P} \times \left( \frac{q}{q_D} \right)_M \quad (8.101)$$

and

$$\overline{\Phi C} = \left[ (\Phi V C)_m + (\Phi V C)_f \right] = \frac{K_f}{\mu r_w^2} \left( \frac{t}{t_D} \right)_M \quad (8.102)$$

### Calculation example

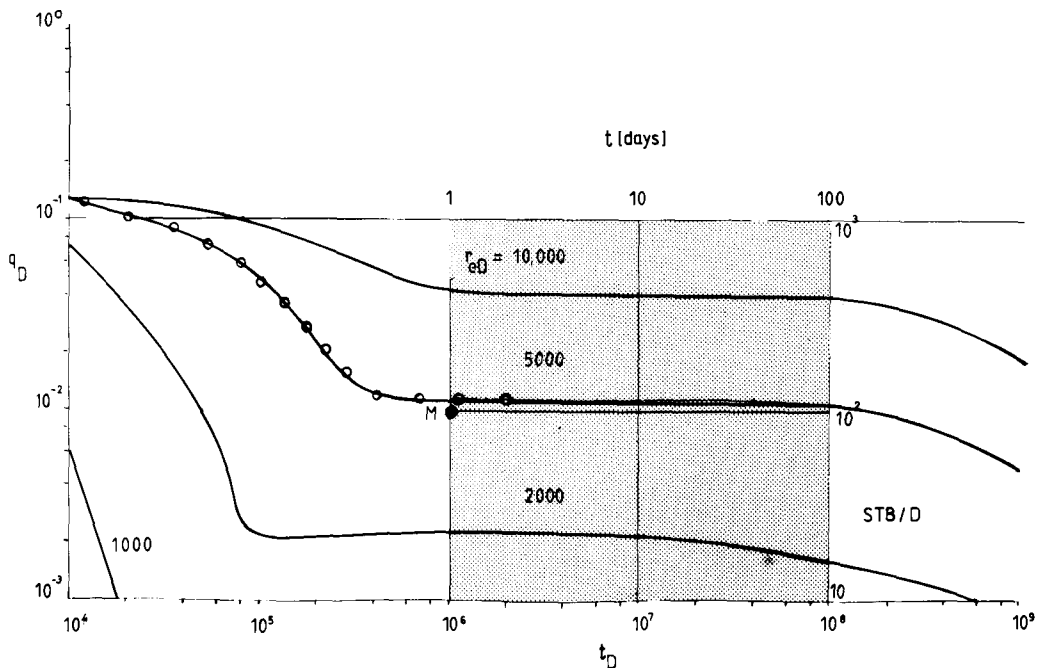
Based on production data and using a diagram such as figure 8.17 where  $\omega = 10^{-3}$  and  $\lambda = 10^{-9}$ , the matching point indicates

$$q = 10^2 \text{ STB/D} - \text{for } q_D = 10^{-2}$$

$$t = 1 \text{ Day} - \text{for } t_D = 10^6$$

It results thus from equation 8.101 that

$$k_f = \frac{1.2 \times 1.26}{6.28 \times 12000 \times 16} \times \frac{10^2 / .0864 \times 6.28}{10^{-2}} = 0.023 \text{ D}$$



8.17 – Type curve and well data, for case of  $\Delta P = \text{constant}$ . Case  $w = 10^{-3}$  and  $\lambda = 10^{-9}$  (De Prat<sup>6</sup>, Courtesy AIME)

and from equation 8.102

$$\overline{\Phi C} = \frac{0.023 \times 86400}{1.2 \times 100 \times 10^6} = 1.66 \times 10^{-5} \text{ (1/at)} = 1.12 \times 10^{-6} \text{ (1/psi)}$$

from where

$$\overline{\Phi} \cong 1.12 \times 10^{-6} / 9 \times 10^{-6} = 12.4 \%$$

The basic data used in calculation were :  $\mu_0 = 1.2 \text{ cP.}$  ;  $B_0 = 1.26$  ;  $h = 120 \text{ m}$ ;  
 $\Delta P = 16 \text{ at}$  ;  $r_w = 10 \text{ cm}$  ;  $C \cong 9 \times 10^{-6} \text{ (1/psi)}$ .

## SYMBOLS

### Latin letters

$a'$	— piezo - conductivity
$A_f$	— areal fracture density
$B$	— volume factor
$C$	— constant
$D$	— distance between two wells
$F$	— function of permeability ratio in an anisotropic reservoir
$h$	— pay
$K$	— permeability
$\bar{K}$	— anisotropic permeability
$m$	— slope
$P$	— pressure
$Q, q$	— rate
$r$	— radius
$S$	— skin
$t$	— time
$v$	— velocity
$V$	— volume

### Greek letters

$\Phi$	— porosity
$\lambda$	— interporosity flow
$\mu$	— viscosity
$\Theta$	— angle
$\omega$	— relative storage capacity

## Subscripts

c	- calc.
D	- dimensionless
e	- equivalent
f	- fracture
m	- matrix
meas	- measured
o	- oil
w	- well
X	- major anisotropy axis
y	- minor anisotropy axis
1	- matrix
2	- fracture

## REFERENCES

1. Kazemi, H., Seth, M.S., and Thomas, G.W. (1969) The Interpretation of Interference Tests in Naturally Fractured Reservoirs with Uniform Fracture Distribution, Soc. Pet. Eng. J. (Dec).
2. Warren, J.E. and Root, P.J. : (1963) The Behaviour of Naturally Fractured Reservoirs. Soc. Pet. Eng. J. (sept) 245 - 255.
3. Najureta, H.L. (1979) Interference and pulse testing in uniformly fractured reservoir. Paper presented at Las Vegas, Nevada, 54th Anual Fall muting. SPE 8283.
4. Elkins, L.F. and Skov, A.M., (1960). Determination of fracture orientation from pressure interference.
5. Bourdet, D. Gringarten, A.C. (1980) Determination of fissure volume and block size in fractured reservoir by type-curve analysis. Paper present at Fall meeting in Dallas, Texas.
6. Da Prat, G., Cinco-Ley, H., Ramey, H.J. 1981, Decline curve analysis using type curves for two-porosity System. SPEJ, june, 354 - 362.

This Page Intentionally Left Blank

## **THIRD PART**

This Page Intentionally Left Blank

# Reservoir Dynamics

The dynamic problems of naturally fractured reservoirs are much more complex than those of conventional reservoirs as result of their specific pore structure. The fracture network pores delimitate matrix blocks which, although they are not directly intercommunicating, form the *reservoir body*. This discontinuity from block to block and this «*totum*» of reservoir body is apparently a *contradiction*. In order to overcome these difficulties, the problems of reservoir dynamics have to be treated at two levels: single block and entire reservoir body. The displacement of oil from the single blocks has to be integrated in a *generalized material balance* referred to fractures-matrix exchange of fluid, where fluid feeding the fracture has to be equal to fluid produced from fractures (under steady-state conditions). In chap. 9 single block problems are examined in association with the relationship recovery vs. time of a single block producing under drainage and imbibition displacement. Particular attention is given to the role played by capillary forces and gravity forces in the displacement process in relation to block size and shape, as well as in relation to physical properties of fluids and rock. The results obtained have been expressed dimensionless, in order to *scale* the laboratory results to field applications.

In chapter 10, the material balance is discussed in relation to the production mechanism as a direct result of fluid saturation in matrix blocks and surrounding fractures where various zones have been defined according to fluid distribution in the fracture network. In chapter 11, various numerical models are reviewed which simulate the flow process in a single block and in an entire reservoir for one, two or three phases. In chapter 12, after some data concerning certain well-known reservoirs, a number of simplified calculation examples are given. The applications are to single blocks, rate of flow to wells and finally to reservoir material balance.

This Page Intentionally Left Blank

# CHAPTER 9

## FLUID DISPLACEMENT PROCESS IN A SINGLE MATRIX BLOCK

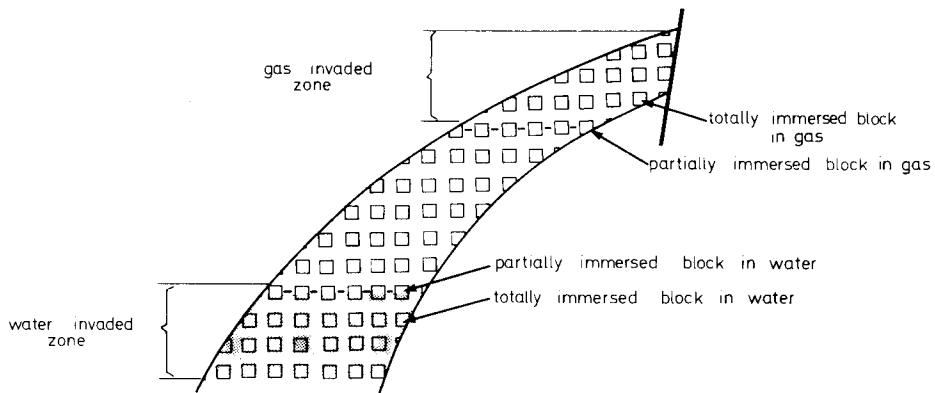
### *9.1. INTRODUCTION*

A single block, as defined in Chapter 2, is a volumetric matrix unit completely surrounded by a network of fractures without any communication with other blocks. The assumption that communication with other blocks does not take place is hydrodynamically acceptable if the contact surface among various blocks is small (punctual contact). Consequently, the continuity of flow from one matrix block to another virtually does not exist, thus the problem of fluid displacement only affects the interaction between fluids which saturate the matrix and fluids which saturate the surrounding network of fractures. The change in saturation as a result of the displacement process may take place under imbibition or drainage conditions, where capillary pressure and gravity forces could work for or against the displacement.

In this chapter, matrix fluid displacement has been approached through use of simplified dynamic models, where more attention has been given to the forces involved in the process and less attention to the shape of the displacement front. After a physical description of the imbibition and drainage processes, a critical evaluation of various authors' concepts and experiments has been carried out. The main objective of such an evaluation was to examine the relationship of recovery versus time and to scale the laboratory results for prediction of reservoir behaviour.

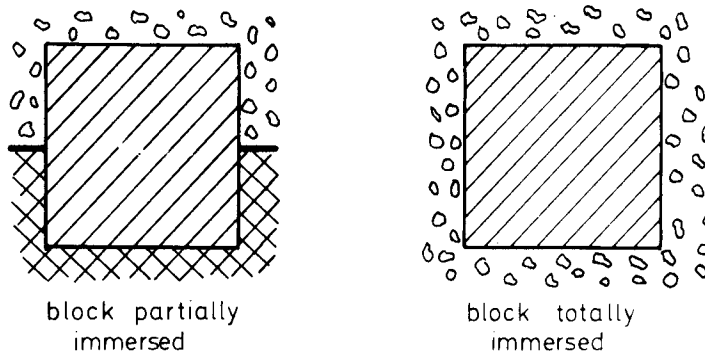
### *9.2. SIMPLIFIED DYNAMIC APPROACH TO MATRIX FLUID DISPLACEMENT*

The displacement process in a fractured reservoir occurs when the matrix block saturated with oil is partially or entirely surrounded by another fluid, gas and/or water. As schematically shown in figure 9.1, a reservoir built by uniform geometrical blocks may be invaded by the expanded gas cap in the upper part of the reservoir, and by the expanded aquifer in the lower part of the reservoir. Thus, the oil saturated matrix blocks will be in contact with a different fluid in the invaded zones and a displacement process will take place. A different type of displacement will govern the oil recovery in the gas invaded zone (drainage displacement) in the case of a

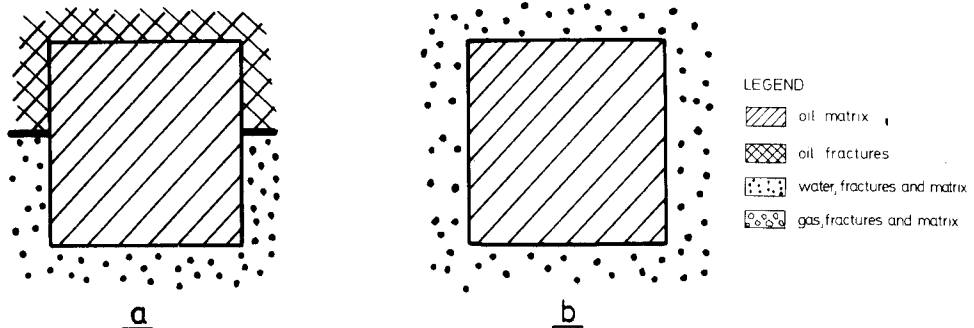


9.1 – Fractured reservoir invaded by water and gas-cap.

block partially immersed in gas (figure 9.2a) or a block totally immersed in gas (figure 9.2b). The displacement process will be different in the water invaded zone (imbibition displacement), in both cases of a partial immersion (figure 9.3a) and/or a total immersion (figure 9.3b).



9.2 – Block invaded by gas from gas-cap (a) partially invaded (b) totally invaded.



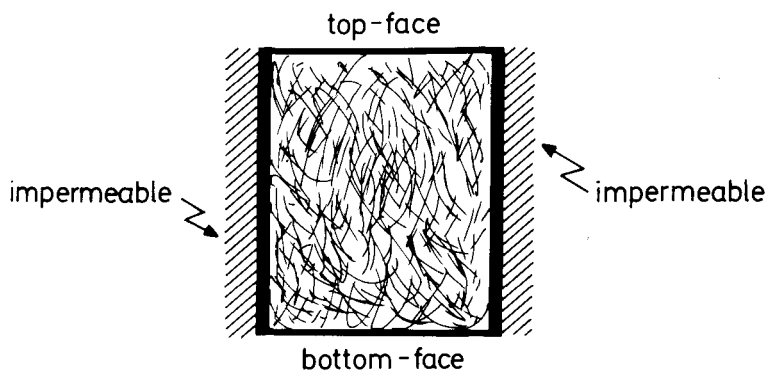
9.3 – Block immersed in water (a) partially immersed (b) totally immersed.

### 9.2.1. Basic model

A detailed examination of the displacement mechanism must be related to the specific conditions of the fluid saturation in the fractures and matrix, especially to those associated with the wettability conditions and the saturation history. Therefore, the equations governing the displacement of oil by water or of oil by gas from a block of a fractured reservoir would have to be those of simultaneous flow, where the relative permeabilities and capillary pressure are functions of saturation. A solution to these equations can be obtained only by a numerical method. In order to investigate the influence of some of the parameters involved in the process, a simplified displacement model having a sharp interface between the two fluids may be used. The analytical solutions of such a model will constitute part of the theoretical support of further discussions.

The basic assumptions of the models are as follows:

- a. The flow is considered uni-dimensional.
- b. The capillary pressure at the interface is assumed constant.
- c. The irreducible wetting liquid saturation and residual non-wetting liquid saturation are assumed constant and, therefore the relative permeabilities are constant. This assumption has been used by Muskat<sup>1</sup> to explain the influence of the mobility ratio in a horizontal displacement in a reservoir with constant pressure at the boundaries.
- d. The procedure developed is slightly different from Birks approach<sup>2</sup> used to explain the displacement of fluid from a fractured reservoir block.
- e. The uni-dimensional displacement from the matrix block is understood as lower and upper sides open to flow while the lateral faces are impermeable (figure 9.4).
- f. In the surrounding fractures the pressure distribution is approximated by a hydrostatic relationship and therefore the potential  $\Phi = p + \rho g z$  is considered constant.
- g. Darcy's fluxes of the wetting (w) and the non-wetting (nw) fluids in the block are:



9.4 – Matrix block with lateral impermeable faces.

$$u_w = - \frac{k k_{rw}}{\mu_w} \frac{\partial \Phi_w}{\partial z} \quad (9.1)$$

$$u_{nw} = - \frac{k k_{rnw}}{\mu_{nw}} \frac{\partial \Phi_{nw}}{\partial z}$$

h. The fluids are considered as imcompressible and thus, the equations of conservation of mass in each phase are:

$$\partial u_{nw}/\partial z = 0 , \quad \partial u_w/\partial z = 0 \quad (9.2)$$

from which it follows that, at a considered time, in each phase the flux is constant. In addition, across the boundary the flux of the two phases is constant and, therefore, in view of the two equations presented in equation 9.2 the flux should be considered constant over the whole flow domain, i.e.  $u_w = u_{nw} = u$ . With constant fluxes the two equations presented in equation 9.1 can be easily integrated.

### 9.2.2. Displacement of oil by water

Water entering the lower side of the block displaces oil which is produced at the upper side in an oil or water environment. Water is considered a wetting phase and oil a non-wetting phase. The two cases to be examined will be related to the model, presence or absence of water in the fracture delimiting the upper face of the block. Usually when both faces are water saturated through respective fractures, this is referred to as block *totally surrounded by water or* block totally immersed in water.

#### 9.2.2.1. Oil saturated block totally immersed in water

In the case of an oil saturated block totally immersed in water (figure 9.5) the boundary conditions are as follows:

$$\begin{aligned} Z = 0 ; \Phi_w &= \Phi_{w_1} \\ Z = H^- ; \Phi_o &= \Phi_{o_2} \end{aligned} \quad (9.3)$$

where  $H^-$  denotes the length of the block in the medium of the block ( $H^+$  is block length expressed outside of the block field), and numbers 1 and 2 denote the entrance and exit faces. Integration of equation 9.1 under boundary conditions with equation 9.3 gives:

$$\begin{aligned}\Phi_{w_1} - \Phi_{wZ} &= u \frac{\mu_w}{k_w} Z \\ \Phi_{oZ} - \Phi_{o_2} &= u \frac{\mu_o}{k_o} (H - Z)\end{aligned}\quad (9.4)$$

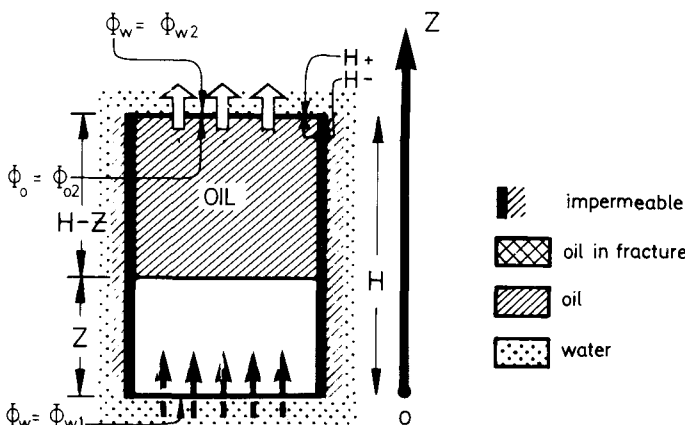
where  $Z$  is the height of the water front in the block above the bottom (figure 9.5).

The addition of equations 9.4 and substitution of  $\Phi_Z = p + \rho g Z$  for the water and oil phases gives:

$$\Phi_{w_1} - \Phi_{o_2} + P_c - gZ\Delta\varrho = u \left[ \frac{\mu_w}{k_w} Z + \frac{\mu_o}{k_o} (H - Z) \right] \quad (9.5)$$

where,

$$\Delta\varrho = \varrho_w - \varrho_o$$



9.5 – Advancement of displacement front in the case of a block totally immersed in water.

The potential  $\Phi_{o2}$  at  $H^-$ , in the block, is related to the potential  $\Phi_{w2}$  of water at the exit from the block ( $H^+$ ) by:

$$\Phi_{o2} = \Phi_{w2} + P'_c - gH\Delta\varrho \quad (9.6)$$

where  $P'_c$  is the capillary pressure at the producing face.

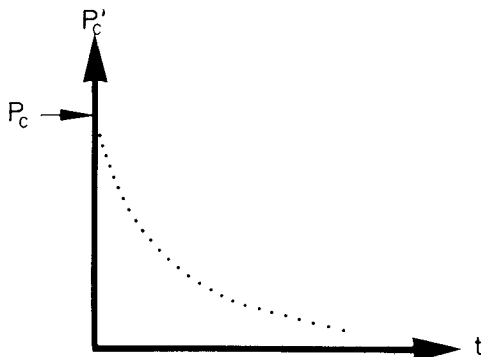
In a water environment at hydrostatic equilibrium  $\Phi_{w2} = \Phi_{w1}$  and substitution of equation 9.6 in 9.5 yields:

$$u = \frac{P_c - P'_c + g(H - Z)\Delta\varrho}{\frac{\mu_w}{k k_{rw}} Z + \frac{\mu_o}{k k_{ro}} (H - Z)} \quad (9.7)$$

In the imbibition experiment with the sample totally immersed in water it was observed that the oil was produced as bubbles at the upper face. This production mechanism is the result of a continuous increase in time of the dimensions of the bubbles, and thus at a given stage the buoyancy exceeds the capillary forces and the bubbles leave the matrix. In fact, the capillary pressure  $P'_c$  is variable in time starting with a maximum  $P_c = P'_c$ , and thereafter capillary pressure in the block decreases very quickly with an increase in bubble dimension. Production of oil as bubbles at the exit face is an intermittent process. In a cycle of production of one bubble, the time during which  $P'_c$  has values close to  $P_c$  is relatively short (figure 9.6), thus  $P_c$  very quickly becomes negligible (equation 9.7) in comparison with  $P_c$ , and the following is obtained:

$$u = \frac{P_c + g(H-Z)\Delta\varrho}{\frac{\mu_w}{k k_{rw}} Z + \frac{\mu_o}{k k_{ro}} (H-Z)} = \frac{P_c + g(H-Z)\Delta\varrho}{\frac{\mu_w}{k k_{rw}} [MH + (1-M)Z]} \quad (9.8)$$

where  $M = (\mu_o/k_o)/(\mu_w/k_w)$  is the mobility ratio of constant value in the present case.



9.6 – Variation of bubble capillary pressure  $p'_c$  vs. time.

#### a. Discussion of equation 9.8

Equation 9.8 is a function of the difference in magnitude between capillary and gravitational pressure, magnitude of mobility M and of front height Z, and each of these components must be examined.

##### a.1 Relationship between gravitational and capillary pressure

Between the two forces expressed as capillary pressure and gravitational pressure,

$$P_c + G = P_c + (H-Z)g\Delta\varrho = h_c\Delta\varrho + (H-Z)\Delta\varrho$$

one of them may be predominant by comparison with the other and thus displacement is governed only by one of them.

Gravitational pressure governs displacement when,

$$G = (H-Z)g\Delta\varrho \gg P_c = h_c g\Delta\varrho$$

which becomes possible if:

- blocks are very high, therefore  $(H-Z) \gg h_c$  which implies also that  $Z$  is small (at the initial phase of displacement).
- wettability is small, therefore  $P_c$  is small. In this case equation 9.8 may be rewritten as,

$$u = \frac{g(H-Z)\Delta\varrho}{\frac{\mu_w}{k \times k_{rw}} [MH + (1-M)Z]} \quad (9.9)$$

Capillary pressure governs the displacement when,

$$P_c = h_c \times g \times \Delta\varrho \gg (H-Z)g\Delta\varrho$$

Which becomes possible if:

- blocks are very small  $H \ll h_c$
- displacement front has already advanced so much that  $Z \approx H$  and  $h_c > 0$ . In this case equation 9.8 may be rewritten as,

$$u = \frac{P_c}{\frac{\mu_w}{k \times k_{rw}} [MH + (1-M)Z]} \quad (9.10)$$

### a.2 Initial rate

The initial rate corresponds to  $Z = 0$ , thus equations 9.9 and 9.10 are reduced to the following expressions:

- for gravitational pressure,

$$U = U_{GI} = \frac{K_o}{\mu_o} g \Delta\varrho = \frac{K_o}{\mu_o} \Delta\gamma \quad (9.11)$$

- for capillary imbibition pressure

$$U = U_{CI} = \frac{K_o}{\mu_o} - \frac{h_c}{H} g \Delta\varrho = \frac{K_o}{\mu_o} - \frac{h_c}{H} \Delta\gamma \quad (9.12)$$

It is observed that:

- the initial gravity rate  $U_{GI}$  is independent of block magnitude, depending only on physical properties of rock and fluid. This equation was expressed by Muskat<sup>1</sup> for gravitational displacement in a conventional reservoir, and was called *gravity rate*.
- The initial rate under capillary conditions  $U_{CI}$  depends on the magnitude of the block height becoming negligible in the case of large  $H$  and very significant in the case of small  $H$ . This reconfirms the important role of capillary forces in the case of small matrix blocks (small  $H$ ).

### a.3 Mobility vs. rate

In order to examine the role of  $M$  it is necessary to rewrite equation 9.8 as follows:

$$U = \frac{K_o}{\mu_o} \frac{h_c \Delta\gamma + (H-Z) \Delta\gamma}{H-Z + Z/M} \quad (9.13)$$

As observed, equations 9.11 and 9.12 are obtained when the term  $Z/M$  is negligible. This corresponds to the situation of large mobility  $M$  equivalent to highly viscous (heavy) oil. It is interesting to observe that in the case of heavy oil reservoirs with tall blocks, the gravitational velocity remains constant (equation 9.11) and independent of the relative position of the displacement front, expressed by  $H-Z$ . This observation was verified in various heavy oil fractured reservoirs.

### b. Water front advancement vs. time

The advancement of the water front in time  $dZ/dt$  expresses the real front velocity (which is related to the filtration velocity by effective porosity  $\Phi$ ) through the classic relationship,

$$U = \Phi \times dZ/dt \quad (9.14)$$

#### b.1 Case of predominant capillary pressure

Substitution of equation 9.10 in 9.14 and integration with the initial condition  $t=0$ ,  $Z=0$  yields:

$$t = \frac{\Phi \mu_w}{P_c k k_{rw}} [MHZ + (1-M) Z^2/2] \quad (9.15)$$

In general the capillary pressure  $P_c$  is a function of saturation which can be expressed through the Leverett<sup>3</sup> function  $J(S_w)$  as:

$$P_c = (\sigma f(\theta) / \sqrt{k/\Phi}) J(S_w) \quad (9.16)$$

where  $\sigma$  is the interfacial tension. For a constant value of capillary pressure  $J(S_w) = 1$  and substitution of equation 9.16 in 9.15 the result is:

$$t = \frac{\mu_w H^2 \sqrt{\Phi}}{\sigma f(\theta) \sqrt{k} k_{rwmax}} [MZ_D + (1-M)Z_D^2/2] \quad (9.17)$$

where  $Z_D = Z/H$ , represents the equivalent to recovery factor.

Equation 9.17 shows that the time required to produce a given fraction of oil ( $Z_D$ ) by imbibition is directly proportional to the square of the block height ( $H$ ), and inversely proportional to interfacial tension ( $\sigma$ ), relative permeability for water ( $K_w$ ) and the square root of permeability ( $K$ ).

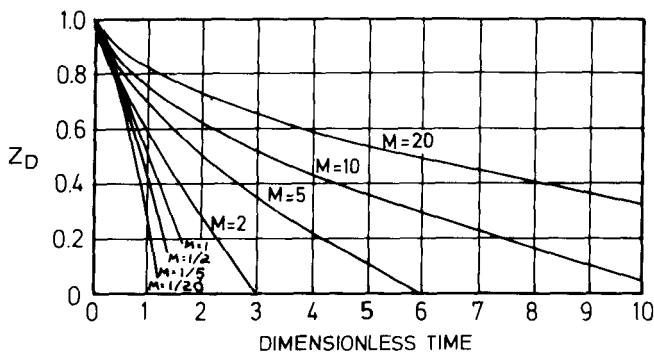
By defining the dimensionless time for displacement by capillary imbibition,

$$t_{D,P_c} = \frac{\sigma f(\theta) \sqrt{K/\Phi} k_{rwmax}}{\mu_w H^2} t \quad (9.18)$$

equation 9.18 may be written in a dimensionless form as,

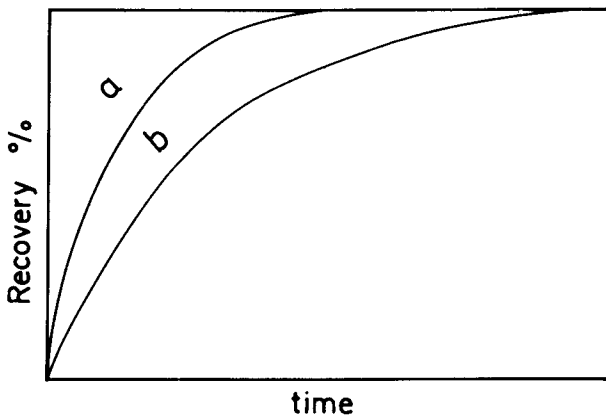
$$t_{D,P_c} = M Z_D + (1-M)Z_D^2/2 \quad (9.19)$$

The fraction of oil recovery versus dimensionless time for different mobility ratios was elaborated by Muskat<sup>1</sup> as shown in figure 9.7.



9.7 – Variation of recovery vs. time for various mobility ratios (Muskat<sup>1</sup>).

Because of the assumption that relative permeabilities and capillary functions are expressed by constant values and not by functions of saturation, as in a real matrix, the time of recovery will be underestimated. Compared with experimental results<sup>4</sup> this may give the impression of higher porosity than the measured porosity (figure 9.8).



9.8 – Variation of recovery vs. time (a) based on equation 9.8 (b) based on experiments.

### b.2 Case of gravity and capillary imbibition

If both capillary pressure and gravitational pressure are considered, the integration of equations 9.8 and 9.14 will give the following:

$$t = \frac{\mu_w \Phi H}{k k_{rw} g \Delta \varrho} \left[ (M-1) Z_D - \left[ M + (1-M) \left( 1 + \frac{P_c}{Hg\Delta\varrho} \right) \right] \ln \left( 1 + \frac{P_c}{Hg\Delta\varrho} - Z_D \right) \right] \quad (9.20)$$

In such a case another dimensionless time is defined as,

$$t_{D,G,P_c} = \frac{k k_{rw} \max g \Delta \varrho}{\mu_w \Phi H} t \quad (9.21)$$

and with this dimensionless time equation 9.20 becomes:

$$t_{D,G,P_c} = (M-1) Z_D - \left[ M + (1-M) \left( 1 + \frac{P_c}{Hg\Delta\varrho} \right) \right] \ln \left( 1 + \frac{P_c}{Hg\Delta\varrho} - Z_D \right) \quad (9.22)$$

As may be observed, there is a substantial difference between equation 9.19 (resulting from only capillary pressure displacement drive) and equation 9.22 (resulting from the combined displacement forces, capillary and gravitational).

### b.3 Case of predominant gravity (imbibition) pressure

If displacement is only governed by gravitational forces, the time results either from the combination of equations 9.14 and 9.9, or by neglecting capillary pressure ( $P_c/H_g \Delta Q$ ) in equation 9.22. The result is,

$$t_{DG} = (M - 1)Z_D - \ln(1 - Z_D) \quad (9.23)$$

#### *Observations*

From the theoretical results obtained above the following is retained:

c.1 Relationship  $t$  vs.  $H$ . This relationship shows the influence of block height  $H$  on time in both cases examined

- if capillary forces are predominant  $\rightarrow t \equiv H^2$  (equation 9.18).
- if gravitational forces are predominant  $\rightarrow t \equiv H$  (equation 9.21)

This result shows that in case of capillary predominant displacement which corresponds to small blocks (small  $H$ ) the time depends parabolically of block height.

c.2 Relationship  $t$  vs.  $Z_D$ . This relationship is in fact showing the recovery vs. time behaviour.

- ~ If capillary forces are predominant (equation 9.19),  $M$  plays an important role.

$$t_{D,P_c} \cong Z_D^2/2 \quad \text{if } M \ll 1$$

$$t_{D,P_c} \cong MZ_D \quad \text{if } M \cong 1$$

- ~ If gravity forces are predominant (equation 9.23)

$$\begin{aligned} t_{D,G} &\cong \ln(1 - Z_D) - Z_D \quad \text{if } M \ll 1 \\ t_{D,G} &\cong \ln(1 - Z_D) \quad \text{if } M \cong 1 \end{aligned} \quad (9.24)$$

Equation 9.24 is similar to results observed in experimental work, and in various theoretical<sup>5</sup> approaches when recovery vs. time is written as

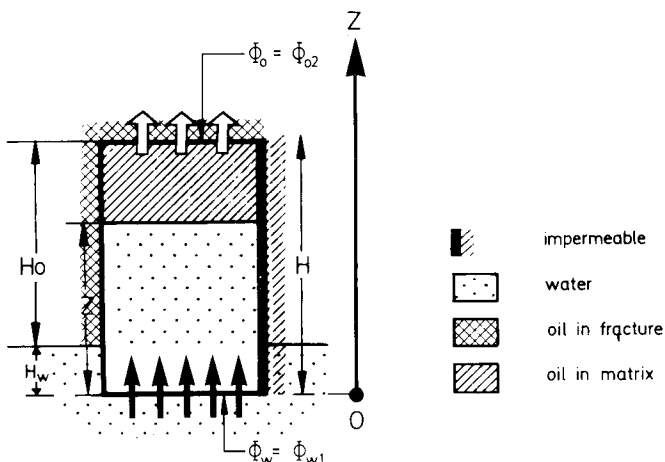
$$Z_D = 1 - e^{t_{DG}} \quad (9.24')$$

### 9.2.2.2. Oil saturated block partially immersed in water

An oil saturated block partially immersed in water corresponds to a slow advance of water in the fracture so that the water-oil front in the block is higher than the water-oil front in the fracture. A simplified assumption is that the advance of the front in the fracture is negligible in comparison with the advance of the front in the block, i.e.  $H_w = \text{const.}$  (figure 9.9).

In such a case the upper face of the block is producing in an oil environment and the potentials  $\Phi_{w1}$  and  $\Phi_{o2}$  (figure 9.9) are related through the capillary pressure in the fracture as follows:

$$\Phi_{w1} - \Phi_{o2} = - P_{cf} + gH_w\Delta\rho \quad (9.25)$$



9.9 – Advancement of displacement front in the case of a block partially immersed in water.

Substituting equation 9.25 in 9.8 gives,

$$U = \frac{P_c - P_{cf} - g(Z - H_w)\Delta\rho}{\frac{\mu_w}{KK_{rw}} [MH + (1 - M)Z]} \quad (9.26)$$

The capillary pressure in fracture  $P_{cf}$  may be ignored being of constant value and much smaller than the capillary pressure  $P_c$  in the block. Equation 9.27 is thus obtained,

$$U = \frac{P_c + g(H_w - Z)\Delta\rho}{\mu_w / KK_{rw} [MH + (1 - M)Z]} \quad (9.27)$$

The uni-dimensional displacement of oil, by *imbibition only*, from a block with impervious lateral sides is not affected by the position of the water front in the adjacent vertical fractures as much as  $h_c > H_w - Z$ .

As long as  $Z < H_w$  gravity will contribute to oil displacement, but in the case that  $Z > H_w$ , gravity will have a retardation effect on the displacement process. Therefore, oil displacement from a block completely surrounded by water will occur at a faster rate than oil displacement from a block partially immersed in water, even if the lateral sides of the block are inactive.

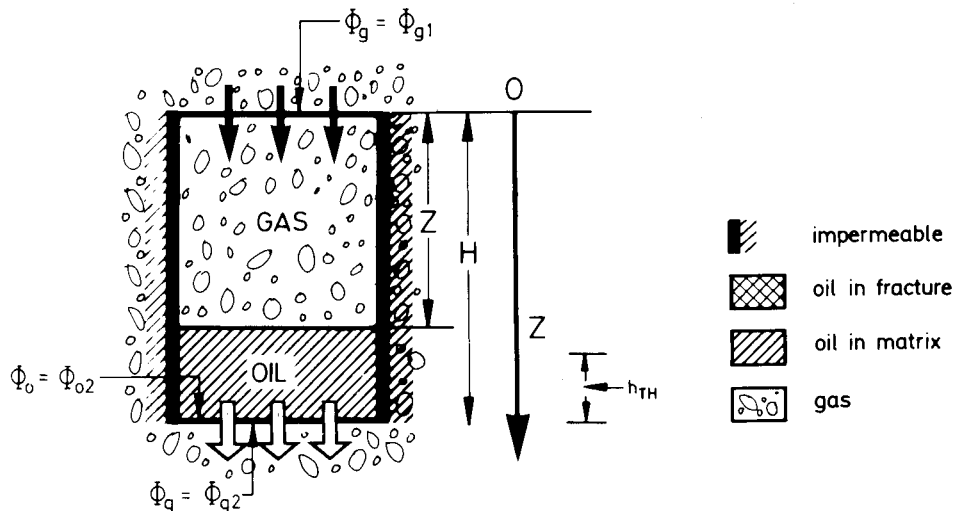
This observation is in accordance with Mattax's<sup>4</sup> experiments which define, under similar conditions, a critical rate *above* which the recovery is rate-dependent and *below which* the recovery remains constant (the rate is understood as advancement of the water-oil contact in fractures).

### 9.2.3. Displacement of oil by gas

Gas entering the upper side of the block will displace oil which is produced at the bottom of the block in a gas or oil environment. The gas is considered to be the non-wetting phase and gas compressibility is ignored.

#### 9.2.3.1. Case of an oil saturated block totally surrounded by gas

A block initially saturated with oil and totally surrounded by gas is shown in figure 9.10. The initial pressure of the gas column is considered to be above the threshold pressure, therefore, gas can enter the block.



9.10 – Advancement of displacement front in the case of a block totally immersed in gas.

The boundary conditions corresponding to this case are:

$$\begin{aligned} Z = H & \quad \Phi_g = \Phi_{g1} \\ Z = O^+ & \quad \Phi_o = \Phi_{o2} \end{aligned} \quad (9.28)$$

where  $Z = 0^+$  is a point at the boundary within the block.

Integration of equation 9.1 with equation 9.28 gives:

$$\begin{aligned} \Phi_{g1} - \Phi_{gz} &= \frac{\mu_g U}{K K_{rg}} Z \\ \Phi_{oz} - \Phi_{o2} &= \frac{\mu_o U}{K K_{ro}} (H - Z) \end{aligned} \quad (9.29)$$

By adding these equations and substituting  $\Phi_{gz} - \Phi_{oz} = P_c - g(H - Z)\Delta\rho$  the following is obtained:

$$\Phi_{g1} - \Phi_{o2} - P_c + g(H - Z)\Delta\rho = \frac{U}{K} \left[ \frac{\mu_g}{K_{rg}} Z + \frac{\mu_o}{K_{ro}} (H - Z) \right] \quad (9.30)$$

where,

$$\Delta\rho = \rho_o - \rho_g$$

By substituting, in equation 9.30, the relationship between the potential of oil in the block and that of the gas in the fracture at the exit face  $\Phi_{o2} = \Phi_{g2} - P'_c$  (where  $P'_c$  is the capillary pressure at the exit face), and with  $\Phi_{g1} = \Phi_{g2}$  the result is,

$$P'_c - P_c + g(H - Z)\Delta\rho = \frac{U}{K} \left[ \frac{\mu_g}{K_{rg}} Z + \frac{\mu_o}{K_{ro}} (H - Z) \right] \quad (9.31)$$

or by ignoring the capillary pressure at the exit face,

$$U = \frac{g(H - Z)\Delta\rho - P_c}{\frac{\mu_g}{K K_{rg}} [M H + (1 - M) Z]} \quad (9.32)$$

where  $M = (\mu_o / K_o) / (\mu_g / K_g)$  is the mobility ratio.

In such a displacement the capillary pressure has a negative effect on production. Oil can be produced to the extent that gravitational forces exceed capillary forces

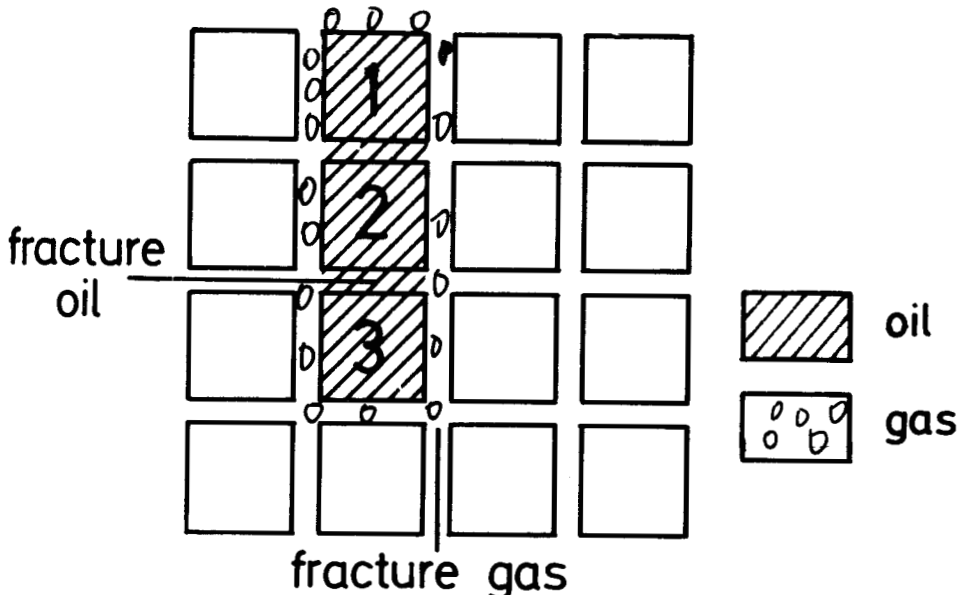
$H_g >> h_{TH}$ . Depending on the value of the capillary pressure and the length of the block, if  $H_g > Z_{cr}$  an equilibrium is reached when

$$H - Z = Z_{cr} = H - h_{TH} \quad (9.33)$$

and oil will no longer be displaced.

The conclusion reached is as follows: In a displacement by a sharp interface, under certain conditions (depending on the value of the gas-oil capillary pressure, and the blocklength) the block saturated with oil can be totally entrapped by gas circumventing the block if  $h_{TH} > H$ . This could never be possible in a displacement of oil by water.

On the other hand, to penetrate and move into the block, the gas must reach the *entry value* or the threshold pressure  $P_{cTH}$ , i.e.  $gH \Delta \rho > P_{cTH} = h_{TH} \times \Delta \gamma$  (equation 9.32). In the case of small blocks totally surrounded by gas, it is very unlikely that such a value of  $gH \Delta \rho$  may be achieved and the oil displaced. However, it could be that considering the length of the individual block to satisfy  $gH \Delta \rho > P_{cTH}$  too restrictive, since the gas reaching the bottom of individual block does not displace the oil from horizontal adjacent fractures. Thus, there is a possibility that oil will remain as a continuous phase between several blocks (figure 9.11). Gas will thus completely circumvent blocks 1, 2 and 3 (similar to a block height  $H = H_1 + H_2 + H_3$ ) and displacement will cease only after displacement gas-oil front reaches the level  $Z_{cr} = H_1 + H_2 + H_3 - h_{TH}$ .



9.11 – Example of blocks where oil was not displaced in horizontal fractures between blocks forming a continuum of oil phase.

In such a case the pressure acting on the first block (block 1, figure 9.11) is the pressure corresponding to the total length ( $H$ ) of the circumvented blocks (1, 2 and 3), which increases the chances of overcoming the threshold pressure  $P_{TH}$ , and thus displacing the oil from block 1.

To obtain the relationship between the fraction of the recovered oil and time,  $U = \Phi dz/dt$  is substituted in equation 9.32, and when integrated with initial condition  $t = 0, Z = 0$ , the result obtained is:

$$t_{D,G,P_c} = Z_D(M-1) - \left[ M + (1-M) \left( 1 - \frac{P_c}{gH\Delta\varrho} \right) \right] \ln \left( 1 - \frac{P_c}{gH\Delta\varrho} - Z_D \right) \quad (9.34)$$

where  $Z_D = Z/H \sim$  is the fraction of oil produced, and  $t_{D,G} = K K_{rg} \max g \Delta\varrho / \Phi \mu_g H \sim$  dimensionless time (equation 9.21). The dimensionless displacing time in case  $P_c \ll H_g \Delta\gamma$  will be reduced to a displacement by gravitational forces only and equation 9.34 will become

$$t_{DG} = (M-1)Z_D - \ln(1-Z_D) \quad (9.35)$$

which is similar to the gravitational dimensionless time obtained for the displacement of oil by water (equation 9.23).

#### 9.2.3.2. Case of an oil saturated block, partially surrounded by gas.

An oil saturated block partially surrounded by gas corresponds to the gas front which did not reach the lower face of the block (figure 9.12), and thus the problem will be the same as in the case of a totally immersed block.

- Displacement will start only if the column of gas in fractures ( $H_g$ ) is higher than the threshold height, as follows:

$$H_g > P_{TH} / \Delta\varrho \times g = h_{TH} \quad (9.36)$$

- Displacement will cease when the gas-oil contact in the matrix reaches the limit height of  $H - h_{TH}$  equivalent to the following height:

$$H - h_{TH} = Z_{cr} = P_{TH}/\Delta\varrho \times g = h_{TH} \quad (9.37)$$

- By analogy with equation 9.32 the rate of advancement of the gas-oil contact in the matrix will be:

$$U = \frac{\frac{g}{KK_{rg}} [H_g - (H - Z)] \Delta\rho - P_c}{\frac{\mu_g}{KK_{rg}} [MH + (1 - M)Z]} \quad (9.38)$$

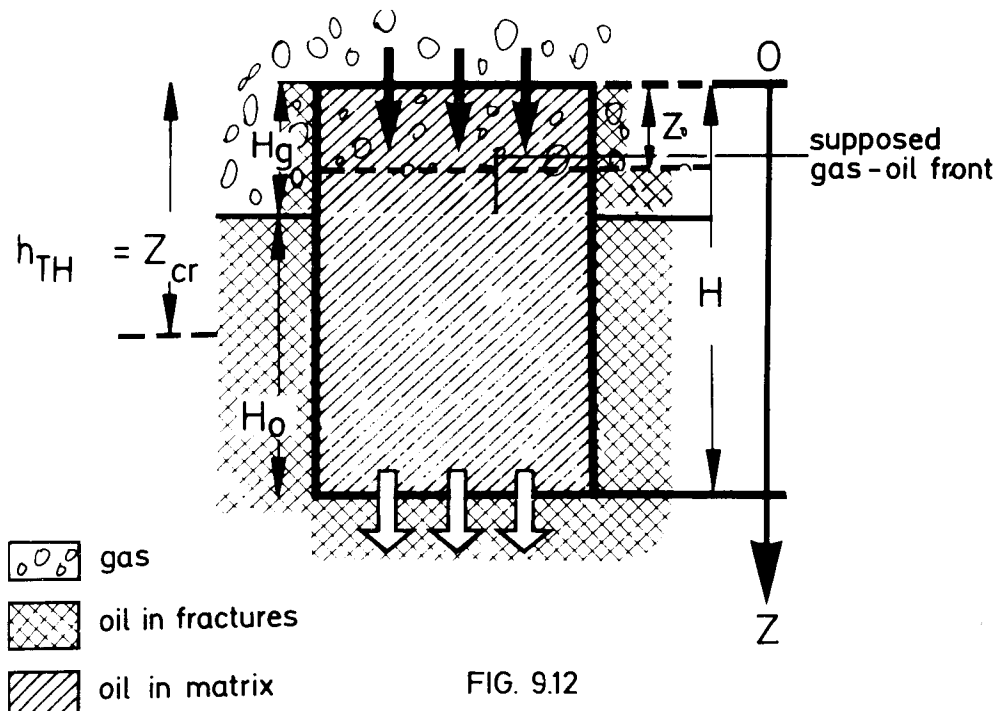


FIG. 9.12

9.12 – Displacement front in the case of a block partially invaded by gas.

#### 9.2.4. Conclusions

From the results obtained through this simplified dynamic approach the following conclusions are reached:

- In an imbibition displacement the *time of recovery* is proportional to the *square of the block height*, while in a displacement by gravitational forces the time of recovery is *proportional to the block height*.
- Gravitational forces in an imbibition process may play an important role in the displacement if either the blocks are large in size, or if the capillary pressure is negligible.
- In a drainage displacement of oil by gas the capillary forces will act against the displacement, and therefore the displacement will result only through gravitational forces, which must exceed the capillary pressure.
- To displace oil (as wetting phase), the gas pressure must reach the *entry pressure* or the threshold pressure. In a reservoir of small size blocks, there is a possibility that gas will circumvent the blocks without reaching the threshold pressure, and in such a case the oil will not remain entrapped in the blocks.

## **9.3. SIMPLIFIED PHYSICAL APPROACH TO FLUID DISPLACEMENT IN MATRIX BLOCK**

### ***9.3.1. Basic discussion of displacement process***

The heterogeneous flow in the matrix depends on the nature of fluids saturating the matrix and surrounding fractured network, as well as on the relationship between rock and fluids at various stages of the saturation history during the displacement process. For this reason the wettability, average pore size and pore size distribution play an essential role in the biphasic flowing conditions in the matrix-fracture network.

#### **9.3.1.1. Wettability role**

The importance of wettability in the displacement process has already been discussed in chapter 4, but its role in the matrix-fracture relationship must be reviewed in order to correlate it with the dynamic process.

If the relationship of the capillary pressure versus contact angle results in the comparison of the preferential wettability of one fluid with another, then displacement will essentially depend on the saturation history. In other words, the displacement will depend on the matrix desaturation process of a wetting or a non-wetting phase.

Experience has shown, in regard to the drainage case, that if the contact angle is below  $49^\circ$ , capillary pressure will remain unchanged. Consequently, the oil-gas capillary pressure will remain unchanged for a given rock, and the threshold pressure or the critical block height will therefore remain a constant value.

Contrary to this, imbibition shows a large sensitivity to the contact angle. A spontaneous imbibition is observed if the contact angle is below  $49^\circ$ , a limited imbibition will result in angles between  $49^\circ$  and  $73^\circ$ , but imbibition will not take place when the angle is over  $73^\circ$ . Since the oil-water contact angle is, in general, below  $49^\circ$ , the capillary imbibition curve will mainly be a function of pore size and pore size distribution.

A major problem, especially in limestone reservoirs, will remain in the case of a water-oil displacement process, the preferential wettability of the water phase or the oil phase. In the case of a water-wetting rock, all advantages of capillary and gravity imbibition assist oil recovery; while for an oil-wetting reservoir, the recovery will be controlled by a drainage process. This may be extremely disadvantageous especially for small matrix blocks (see section 9.2).

It would probably be more advantageous in the case of an oil-wetting reservoir

(where both gas and water are non-wetting phases) to develop the gas cap expansion instead of the aquifer expansion, since the gravity difference,

$$G_{og} = \gamma_o - \gamma_g > G_{wo} = \gamma_w - \gamma_o \quad (9.39)$$

may better overcome the opposing capillary forces (for the same block height).

### 9.3.1.2. Type of displacement

In order to evaluate a displacement process it is necessary to know the relationship of capillary pressure and relative permeability versus saturation. This relationship behaves as a function of saturation history, which is basically indicated by two types of behaviour – drainage and imbibition.

Drainage applies to the displacement processes in which the wetting phase saturation in the matrix block decreases. Imbibition applies to all those processes where wetting phase saturation inside the matrix increases.

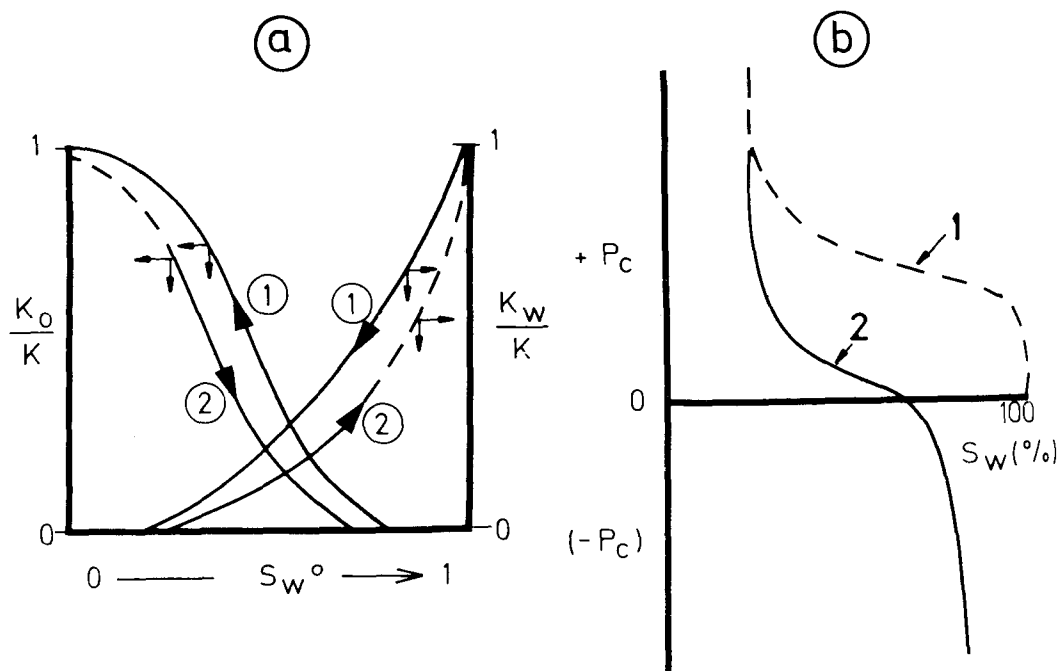
In a unitarian block the matrix displacement process is related to fluid saturation in matrix and in fractures, and also to preferential wettability. The type of displacement – drainage or imbibition – and displacement history is examined in the six cases outlined in table 9.1.

Table 9.1

Case	Fluid saturation		Wetting phase in matrix	Oil Displacement Process	Displacement History
	Matrix Block	Fracture network			
1	oil	water	water	imbibition	Reservoir production
2	oil	water	oil	drainage	Reservoir production
3	oil	gas	oil	drainage	Reservoir production
4	gas	water	water	imbibition	Reservoir production
5	water	oil	water	drainage	Reservoir migration
6	water	gas	water	drainage	Reservoir migration

The process is controlled by the relative permeability curves and capillary pressure curves in both cases, drainage and imbibition.

The relative permeability curve has a similar trend in both drainage and imbibition (figure 9.13a), while the capillary pressure curves have a substantially different trend in both cases (figure 9.13b). Consequently, the combined effect of gravity-capillary forces under imbibition displacement will behave differently from the displacement under drainage conditions.

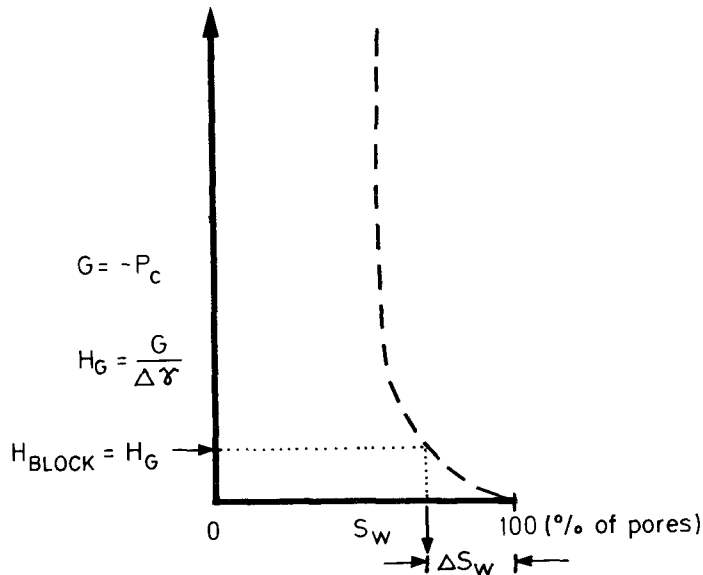


9.13 – Relative permeability curve (a) and capillary pressure curve (b) for (1) drainage and (2) imbibition displacement.

- ~ The lower branch of figure 9.13b indicates the oil produced through gravitational pressure  $G$ , as a result of the equivalence between  $\Delta S_o$  and  $\Delta S_w$ .
- ~ If the block is totally immersed in water, gravitational pressure is associated to the block height:

$$G = H_B \times \Delta\gamma$$

Thus, it is evident that for a given  $\Delta\gamma$  the block height  $H_B$  will indicate the equivalent gravitational recovery read as the value  $\Delta S_w = \Delta S_o$  shown on the curve  $H_G$  vs. saturation in figure 9.14.



9.14 | – Gravity variation ( $G$ ) vs. saturation ( $s_w$ ).

### 9.3.2. Analysis of the displacement process

It is necessary to discuss displacement (in the case of imbibition or drainage) in its most specific physical aspects. The behaviour of the forces which takes place and the implications concerning oil recovery are the basis of this discussion.

#### 9.3.2.1. Analysis of drainage displacement

Drainage displacement takes place when the wetting phase, which saturates the matrix, is displaced by a non-wetting phase, which saturates the fractured network. A common case will be represented by the expansion of the gas-cap. Gas (non-wetting phase) invades the fractures while the matrix blocks are saturated by oil. Similar behaviour patterns occur throughout the oil migration history when, initially, the fractures are invaded by oil (as a non-wetting phase) which displaces the water (wetting phase) from the matrix blocks. A less common case may be that of an oil-wetting rock corresponding to a matrix block saturated with oil (wetting phase), which must be displaced by the water saturating the fractures as a non-wetting phase.

##### a. Critical height of matrix block

In the so-called gas-invaded zone, the blocks saturated with oil are surrounded by gas as a result of the gas-cap expansion. The position of the gas-oil contact in the fractures, with reference to the block's lateral face, is essential in the calculation of oil displacement.

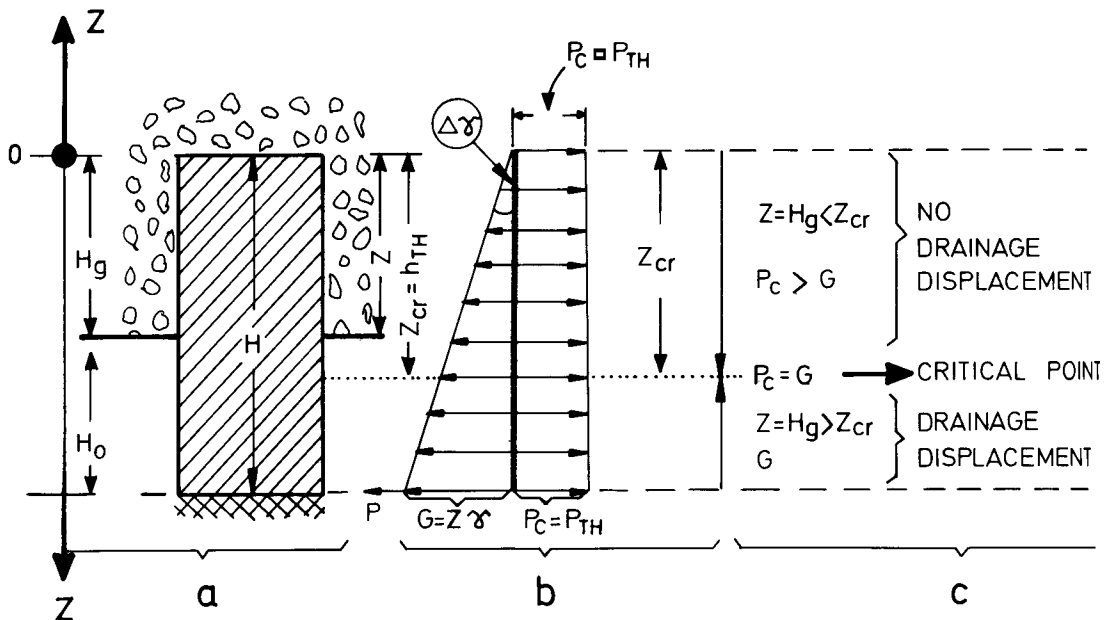
Gas pressure, oil pressure and capillary pressure respectively will act on the lateral face of the block (figure 9.15a) as expressed by the equilibrium relationship at a

given depth  $Z$

$$P_c + P_o = P_g$$

or

$$P_c = P_g - P_o = Z\gamma_g - Z\gamma_o = -Z(\gamma_o - \gamma_g) = -Z\Delta\gamma = -G \quad (9.40)$$



9.15 – Gas invading an oil saturated block (a) zone of gas and oil around the block (b) pressure distribution versus depth (c) zone distributions.

The oil displacement in the matrix is then conditioned by a pressure difference  $P_g - P_o$  higher than the capillary pressure which, in this case, corresponds to the threshold pressure  $P_{TH} = P_c$ . It is therefore necessary that,

$$P_g - P_o > P_c = P_{TH} \quad (9.41)$$

or

$$Z(\gamma_g - \gamma_o) > h_c(\gamma_g - \gamma_o) = h_{TH}(\gamma_g - \gamma_o) \quad (9.42)$$

or

$$Z > h_{TH} \quad (9.43')$$

In other words, in order to assure displacement of matrix oil by the gas in fractures, block height must be higher than threshold capillary height. For a better understanding, figure 9.15b illustrates the capillary pressure which opposes the entrance of gas and remains constant over the total block height. Meanwhile, the gravity force represented by  $Z \times \Delta\gamma$  (which aids displacement) increases with the depth  $Z$ . Above the depth  $Z_{cr}$  (where  $Z < Z_{cr}$ ) the  $P_c > G$  and it is not possible to develop a displacement process; while below  $Z_{cr}$  (where  $Z > Z_{cr}$ ) the gravity forces are higher than the capillary forces  $P_c < G$ , and the drainage displacement takes place.

If gas invades the entire block the displacement *will not begin*, if the gas-oil contact in fractures is  $0 < Z < Z_{cr}$ . Displacement *will only begin when*  $Z > Z_{cr}$  (figure 9.15c). The conclusion is that oil recovery by gas displacement is possible only if the block height  $H > h_{TH}$ .

#### b. Equilibrium of gas-oil contact

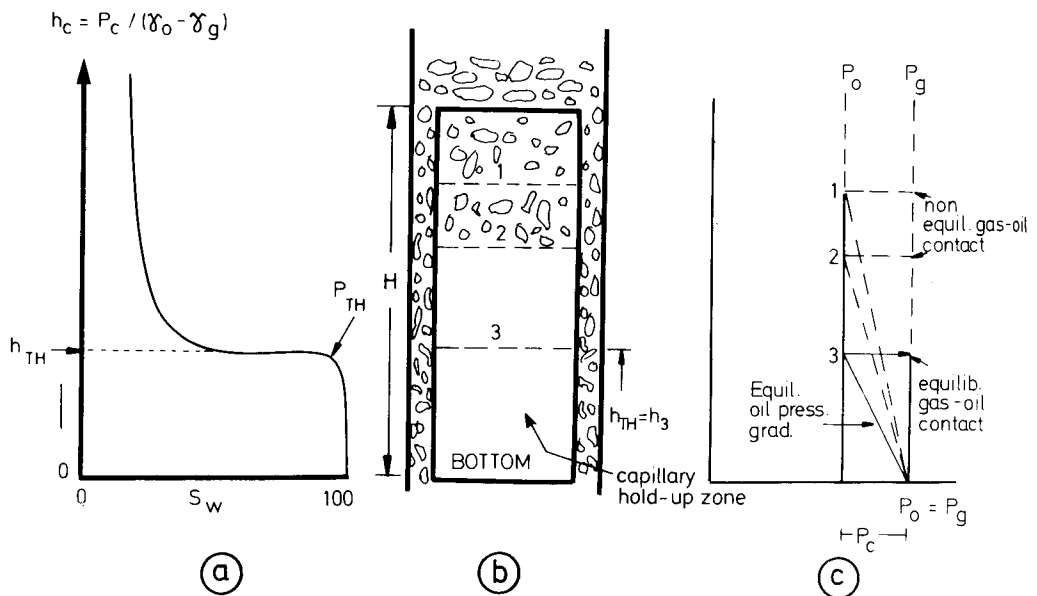
By using the representation indicated in figure 9.16, the level  $h_c = 0$  of the capillary pressure curve (figure 9.16a) is related to the bottom of the matrix block. The advancement in the matrix of the gas front is possible since the matrix block height  $H > h_{TH}$  and the advancement of the gas-oil displacement front will reach positions 1 and 2, respectively (figure 9.16b). Both positions indicate gravitational gradients (as result of front positions 1 and 2) substantially higher than the capillary pressure gradient (figure 9.16c). The static equilibrium will be reached when the displacement front arrives in position 3, and gravitational and capillary forces become equal.

The block will retain a column of unrecoverable oil due to capillary forces named *capillary hold-up zone*, of height  $h_3 = h_{TH}$ .

As observed in figure 9.16c the equilibrium between the oil pressure gradient and capillary pressure gradient controls the fracture-matrix exchange of fluid. On this basis it may further be concluded that if block height  $h_B < h_{TH}$  recovery cannot take place at all since the block height is smaller than the capillary hold-up zone.

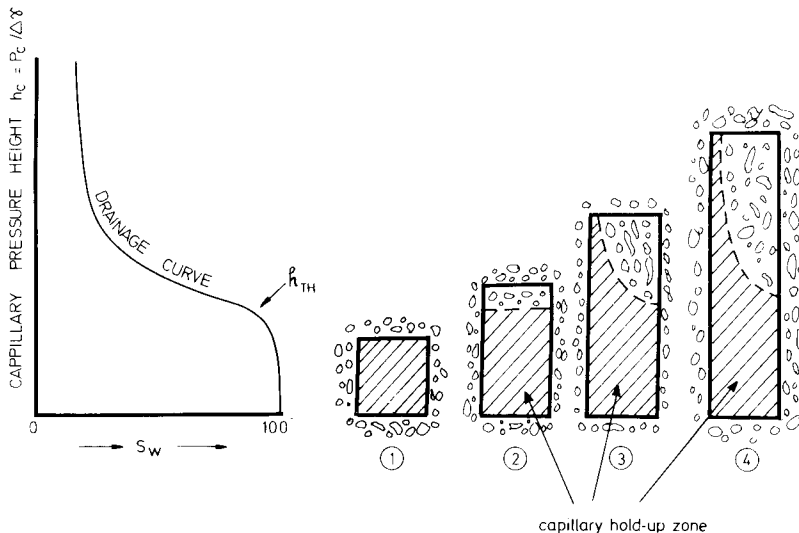
#### c. Role of block height vs. recovery

For a given capillary pressure curve (figure 9.17), four single matrix blocks of different heights will behave differently. Block 1 (small) will contain unrecoverable oil, block 2 (higher) will be recovered slightly, and more and more oil will be



9.16 – Relationship between gravity and capillary forces in drainage displacement (a) capillary curve (b) drainage displacement in the block (c) equilibrium of gas-oil contact at matrix-fracture interface. Zone  $h$ , equal to capillary hold-up zone.

recovered in blocks 3 and 4. This means that in taller blocks the gravity forces could overcome, at least for a part of the block height, the capillary resistance to the entrance of the displacing fluid.



9.17 – Capillary hold-up zone of various block heights.

#### d. Role of rock characteristics, recovery

If the reservoir is not formed by matrix blocks of similar petrophysical characteristics, recovery will vary for different capillary pressure curves. Assuming blocks A, B and C (fig. 9.18) to have the same block height with the following characteristics,

$$K_A > K_B > K_C$$

$$\Phi_A > \Phi_B > \Phi_C$$

the result will be that block C height is below the capillary hold-up height (figure 9.19), while block A is recovered with a very limited hold-up height.

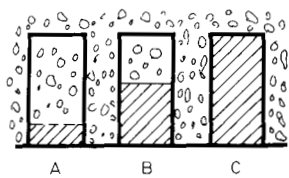
$$K_A > K_B > K_C$$

$$\Phi_A > \Phi_B > \Phi_C$$

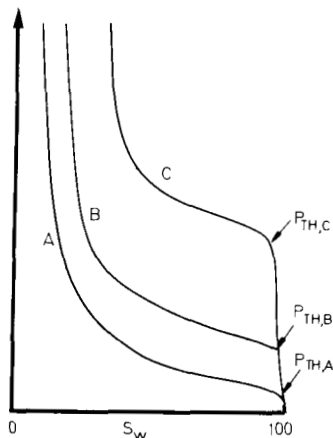
$$h_{BLOCK} > h_{TH,A}$$

$$h_{BLOCK} > h_{TH,B}$$

$$h_{BLOCK} < h_{TH,C}$$



9.18 – Blocks A, B, C of equal size but of different properties, displaced oil and oil hold-up zones function of capillary pressure.

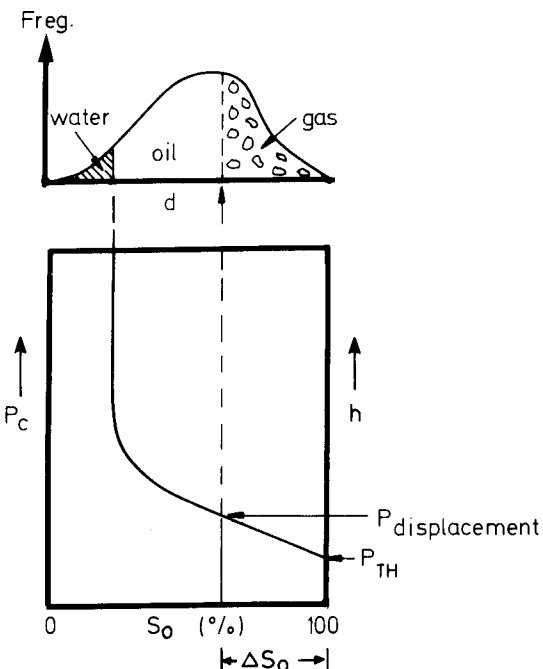


9.19 – Drainage capillary curves of blocks A, B, C.

e. Role of displacement forces vs. recovery

The recovery will depend on gravity (as result of block height) and on injection pressure of the gas. These two parameters together with capillary pressure-saturation distribution (figure 9.29) may indicate the recovery vs. height. For various types of drainage capillary pressure curve, the displacement pressure may be expressed in a general form by

$$P_{\text{displ}} = P_{\text{gravit}} + P_{\text{ing}} - P_c \quad (9.44)$$



9.20 – Role of displacement pressure ( $P$ ) and oil desaturation  $\Delta S_0$ .

### 9.3.2.2. Analysis of imbibition mechanism

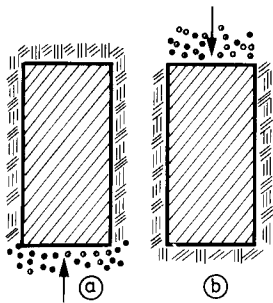
When the matrix is saturated by a non-wetting phase (oil, gas) and the fracture network is saturated by a wetting phase (water), an imbibition process will take place if capillary, gravitational and, eventually, injection pressure contribute to the displacement of the wetting phase in the matrix block, thus reducing the saturation of the non-wetting phase. Imbibition is normally examined under the effect of capillary and gravitational forces (which could include injection pressure if the water is injected in the reservoir). Imbibition may take place in the water-invaded zone

(figure 9.1) if the matrix block is totally immersed (figure 9.3a) or partially immersed in water (figure 9.3b).

#### a. Counterflow and direct flow

Counterflow and direct flow express the flowing direction's relationship between the displaced fluid and the displacing fluid.

Counterflow takes place when, on the same face of the matrix block, the production of a non-wetting phase has a flowing direction opposite to that of the imbibing wetting phase. On the contrary, when the displacing fluid (wetting phase) and displaced fluid (non-wetting phase) have the same direction, the production phase indicates a direct flow.



9.21 – Example of counterflow (a) through bottom face (b) through top face.

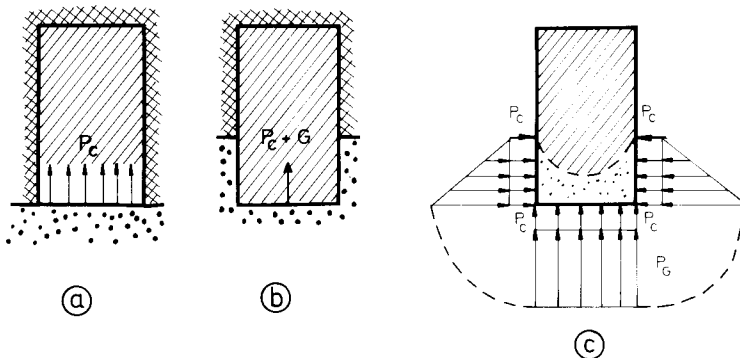
In order to acquire a better understanding of the problem, refer to the two blocks shown in figure 9.21 where all faces are made impermeable except one. If the blocks are saturated with oil and the permeable face is in contact with water (wetting phase), the inflow of the imbibed water and the outflow of the produced oil must take place on the same permeable face. In both cases (a and b) the outflowing oil direction is opposite to the inflow direction of the imbibing water — a classic case of *counterflow*.

It is also interesting to observe that imbibition in case a (bottom face permeable) is only supported by capillary forces, while in case b displacement is sustained by both forces — capillary and gravity. In fact, gravity will aid the water in advancing downwards into the matrix block (case b), and oil buoyancy will aid the oil to flow towards the upper face in a typical counterflow production, resulting from both capillary and gravity forces.

#### b. Influence of impermeable faces

If all faces are impermeable and only the lower face of the matrix block is kept in contact with water (figure 9.22a), the only displacing forces will be the capillary forces. If the water level increases (figure 9.22b) but lateral faces are impermeable, capillary and gravity forces will assist displacement at the bottom face.

The capillary forces on the *lateral permeable faces* remain constant while gravity increases proportionally with the depth below the oil-water contact in the fracture (figure 9.22c). Since capillary pressure  $P_c$  remains uniformly distributed in all zones of water-oil contact, and gravitational pressure varies with depth, it is easy to understand that the maximum gravity force will act on the bottom face of the block. On the other hand, gravity force will decrease upwards until it reaches zero at the water-oil contact in the fractures. This will influence the shape of water-oil displacement contact which follows the pressure distribution (figure 9.22c).



9.22 – Role of forces in the case of impermeable lateral faces (cases a and b) and permeable lateral faces, (case c). (a) capillary forces; (b) capillary and gravity forces on bottom face; (c) gravity and capillary forces on lateral faces and on bottom.

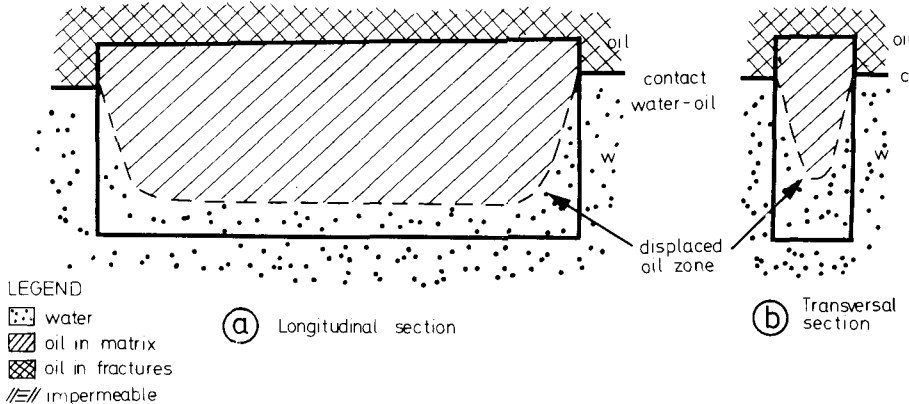
#### c. Influence of block size

If the *blocks are large*, displacement in the vicinity of the lateral face is reduced to a local effect compared with displacement through the bottom face (figure 9.23a). On the other hand, if the blocks are vertically elongated (as described in Chapter 2), capillary effect on the lateral faces will play a very important role. Figure 9.23b illustrates that recovery could be accelerated in thin blocks if capillary pressure is high. However, a delay in time may occur in high, thin blocks if the lateral capillary displacement reduces the upward vertical displacement efficiency which starts at the bottom face. In practice, if the blocks are very large, simulated displacement tests may be performed on the small, thin cores after the lateral faces have been impermeabilized.

#### d. Influence of water table vs. block faces

Displacement behaviour in large blocks can be examined in the laboratory on samples as shown in figure 9.24a, where lateral faces are made impermeable, and therefore the displacing forces only work on the upper and lower faces.

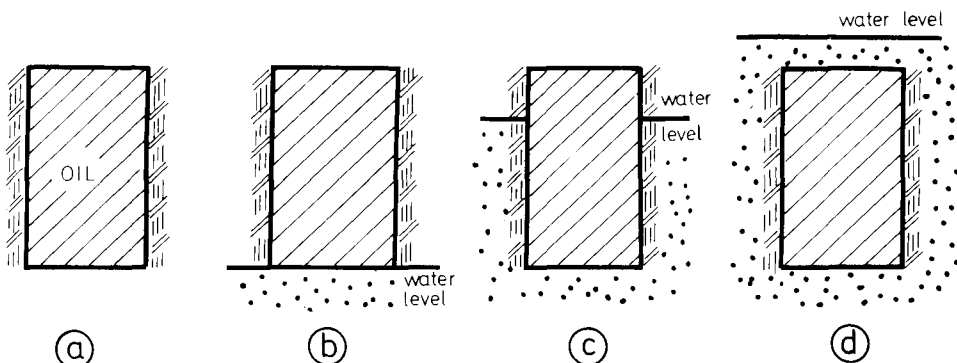
If water is in contact with the oil in the lower face and oil is produced through the upper face, a direct flow displacement takes place under the effect of the capillary forces acting on the lower face (figure 9.24b). If the water level reaches the top of the block, both the gravity and capillary effects will be measured through the oil recovered at the upper face (figure 9.24c). If the block is completely immersed (figure 9.24d), gravity is proportional to the block height and  $\Delta\gamma$ , while capillary



9.23 – Role of vertical face displacement vs. block dimension (a) large blocks (b) thin blocks.

forces will aid imbibition through both lower and upper permeable faces. Production in this case will be through the top face in *direct flow* with reference to the bottom face water imbibition, and in *countercurrent* with reference to the upper face water imbibition.

It is important to remember that for time-recovery relationships, block height is an essential parameter, and therefore the results obtained on a small sample in the laboratory will have to be scaled to real block dimensions in reservoir conditions.



9.24 – Direct flow displacement (impermeable lateral faces): (a) sample; (b) water in fractures in contact with sample bottom face; (c) water in fractures at higher level than bottom level (d) block totally immersed in water.

### e. Role of composite capillary curve

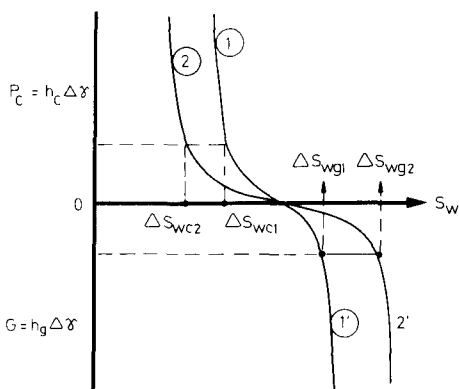
The composite imbibition curve or composite capillary curve (as referred to in Chapter 4) is illustrated in figure 9.25. As already established, for a uniform regular pore distribution the average pore size will influence the *composite curve*.

For the small pore size  $d_1$  (fig. 9.26) and larger pore size  $d_2$ , two different capillary curves can be expected as shown in figure 9.25. Curve 2 indicates a lower capillary and gravity pressure for the same saturation compared with curve 1. Therefore, for a smaller average pore size ( $d_1$ ) at the same pressure and gravity forces ( $P_c = G$ ) a smaller desaturation in water than that obtained for large pore size ( $d_2$ ) will result during the displacement process.

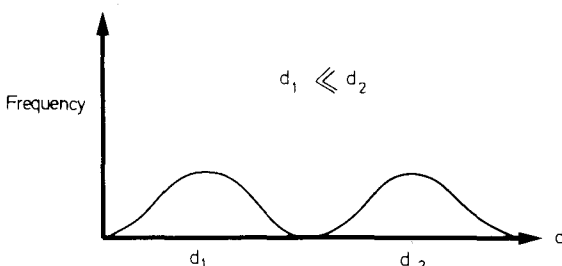
In other words, for the same block height, a higher recovery in oil will occur in curve 2 than in curve 1, since

$$\Delta S_{wc2} > \Delta S_{wc1} \quad (9.45)$$

$$\Delta S_{wg2} > \Delta S_{wg1}$$

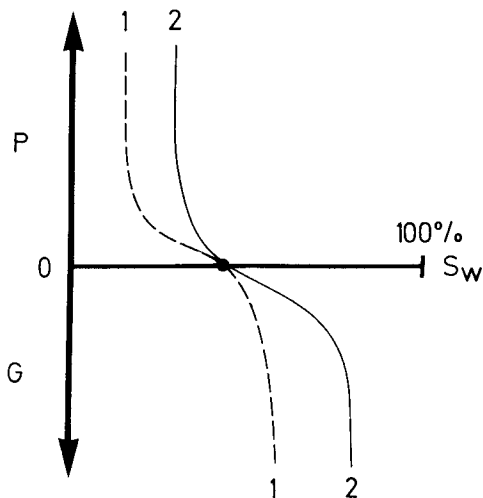


9.25 – Two capillary curves (1) and (2) corresponding to two types of rocks, of different average pore size.



9.26 – Frequency curve for small (1) and large (2) pore sizes.

Based on various composite curves it is possible to estimate the final imbibition recovery as a result of one or another preferential displacement mechanism during field production. For example, in figure 9.27, curve 1, the total gravitational recovery is negligible while capillary recovery is very large. Contrary to this, gravitational recovery in curve 2 is very large, which means that recovery in this case is directly dependent on block height. If the block is small, recovery will be limited, and if it is large, recovery will increase substantially for curve 2 rock type.



9.27 – Capillary-gravity recovery curves, with different behaviour.

#### 9.4. CONCEPTS AND EXPERIMENTS: SINGLE BLOCK IMBIBITION DISPLACEMENT

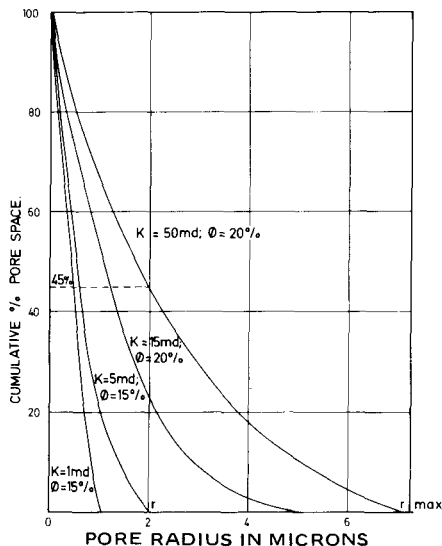
Imbibition is a primary mechanism of oil production in a fractured reservoir as a result of the drastic variations in permeability between fractures and matrix helping the fractures water to imbibe the matrix. Based on a simplified model, it is possible to develop a thorough understanding of the quantitative relationships of the basic parameters which describe and control the imbibition process. An attempt will be made to evaluate the dependence of the imbibition rate on the physical parameters of rocks and fluids, and finally to correctly scale the relationship between the laboratory model and field conditions in order to reach an accurate prediction of recovery versus time.

##### 9.4.1. Concepts of a simplified model

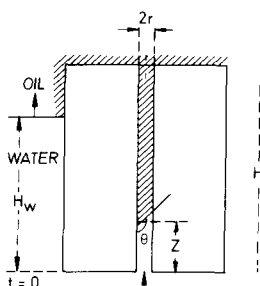
#### 9.4.1.1. Capillary tube model

The model developed by Birks<sup>2</sup> assumes that the matrix block is equivalent to a group of capillary tubes. The number and radius of the tubes are defined through the pore size distribution curve in figure 9.37. In a single capillary tube of height H (figure 9.38) the water-oil contact advancement Z in the capillary is related to the advancement of water-oil contact  $H_w$ , through the equilibrium between capillary, gravity and friction forces. Thus, the basic equation is written as follows:

$$H_w g \rho_w \pi r^2 + 2\pi r \cos\theta = 8\pi\mu_w Z \frac{dz}{dt} + \\ + 8\pi\mu_o (H - Z) \frac{dZ}{dt} + \pi r^2 g [\rho_w Z + \rho_o (H_w - Z)] \quad (9.46)$$



9.28 – Pore size distribution curve of matrix limestone (Birks<sup>2</sup>, courtesy of Elsevier).



9.29 – Water advancement in fracture (Birks<sup>2</sup>, courtesy of Elsevier).

If water-oil advancement in fractures is constant ( $H_w = at$ ) the equation is,

$$8[(\mu_w - \mu_o)Z + \mu_o H] dz/dt + r^2 g (\rho_w - \rho_o) Z = ar^2 g (\rho_w - \rho_o)t + 2r\sigma \cos\theta \quad (9.47)$$

If viscosities of water and oil are equal ( $\mu_o = \mu_w$ ) the equation is written as,

$$\frac{dz}{dt} + AZ = Bt + C \quad (9.48)$$

where A, B and C are constant terms resulting from equation 9.52, respectively  $A = r^2 \Delta \gamma / 8\mu H$ ;  $B = aA$ ;  $C = 2r\sigma \cos\theta / 8\mu_o H$ .

The solution of equation 9.52 is,

$$Z = \frac{B(At - 1)}{A^2} + \frac{C}{A} + De^{-At} \quad (9.49)$$

Recovery of each group of capillary tubes is given by,

$$R = \frac{Z}{H} \approx f(e^{-At}) \quad (9.50)$$

which indicates that the basic relationship of recovery versus time is given by an exponential expression.

If a scaling parameter for tortuosity is introduced for each cylindrical capillary tube, equation 9.48 will be rewritten as,

$$\frac{dx}{dt} + A'x = B't + C' \quad (9.51)$$

$$A' = A \left( \frac{L}{L_e} \right)^2; \quad B' = B \left( \frac{L}{L_e} \right)^2; \quad C' = C \left( \frac{L}{L_e} \right)^2 \quad (9.52)$$

#### CALCULATION EXAMPLE:

The average radii of capillaries and their percentages (table 9.2) are given in Birks' calculation example, from a curve similar to that shown in figure 9.28. The physical

parameters are:  $\mu_w = \mu_o = 1 \text{ cP}$   $q_w - q_o = 0.4 \text{ gr/cm}^3$   $\sigma \cos \theta = 10 \text{ dyne/cm}$

$H = 100 \text{ feet}$   $a = 24 \text{ feet/year}$

The recovery at the time of total immersion when  $Z=L$  will correspond to a time  $t = 100(\text{feet})/24(\text{feet/year}) = 4.15 \text{ years}$ , is given for each group of capillary tubes in columns 3 and 4 of table 9.2 below.

Table 9.2

Radius r (microns)	Pores % of total	Recov. R at Z=L	Recovery (% pore)
0.00–0.25	0.25	3,1%	0,8 %
0.25–0.50	0.25	11.2	9.8
0.50–1.00	0.30	29.3	8.79
1.00–1.50	0.125	53.8	5.72
1.50–2.00	0.075	72.6	5.45

#### 9.4.1.2. Piston-like displacement model

##### a. Dipping reservoir block

The model shown in figure 9.30 illustrates a displacement front advancing in the matrix as a piston, leaving a constant saturation in water and residual oil behind the front. Oil displaced from the matrix is expressed by,

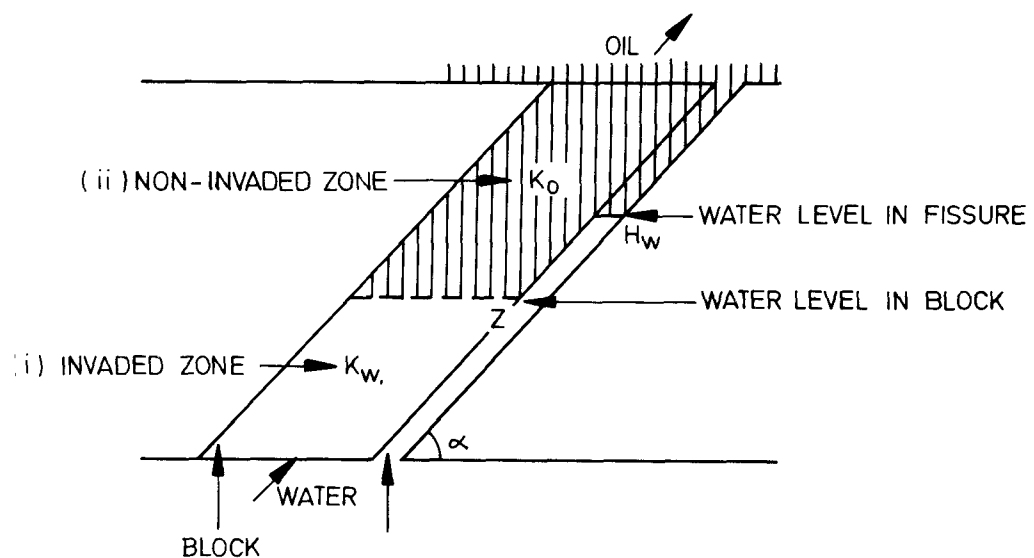
$$\Phi (S_w - S_{wi})$$

and the rate of water advancement in matrix similar to equation 9.7 is expressed as follows,

$$U = \frac{dZ}{dt} = \frac{1}{\Delta S_w \Phi} \cdot \frac{P_c + \Delta \rho (H - Zg \sin \alpha) \sin \alpha}{\frac{\mu_w}{K_w} Z + \frac{\mu_o}{K_o} (H - Z)} \quad (9.53)$$

where  $\Delta S_w = S_w - S_{wi}$ ;  $\Delta \rho = q_w - q_o$

As observed, this result is similar to that obtained in equation 9.7 where  $\alpha = 90^\circ$ .



9.30 – Water advancement in matrix block and fractures (Birks<sup>2</sup>, courtesy of Elsevier).

The recovery will be expressed by,

$$R = \frac{Z \times \Phi \times \Delta S_w}{H \Phi} = \Delta S_w \times \frac{Z}{H} = \Delta S_w Z_D \quad (9.54)$$

b. Vertical reservoir block (developed in section 9.2.2.)

The dimensionless equations obtained in section 9.2.2 which give the relationship time recovery are,

Equations 9.19, 9.22 and 9.23

If gravitational pressure is predominant in the imbibition process, then,

$t_{DG}$  is expressed by Eq. 9.23, and 9.21.

If capillary pressure is predominant in the imbibition process, then,

$t_{D,pc}$  is expressed by Equation 9.19 and 9.18.

#### *9.4.2. Recovery versus time: basic theory and basis of experiments*

A number of theoretical and experimental studies<sup>4 5 6</sup> have been dedicated to the relationship between time and rate of exchange of oil and water in a single matrix block. The displacement front will be influenced by matrix and fracture parameters as well as by physical properties of fluids. In the case of highly permeable vertical fractures the displacement front in a simplified approach is considered to be a horizontal plane.

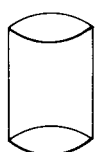
Various authors are using in their experiments a number of models of different block geometry, shape of producing-imbibing surfaces, and rate of water table advancement in fractures (equivalent to rate of immersion) and forces involved in displacement, etc.

##### **9.4.2.1. Types of experiments**

The experiments developed by various authors consider various geometrical and physical elements according to the objective of their study. Table 9.3 describes the basic elements of each research:

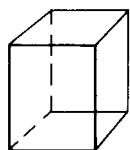
- a. Type of model; refers to experimental or theoretical models. This second category can refer to a theoretical approach<sup>5 6</sup> or a mathematical model<sup>14 15 16</sup>. Often mathematical models are associated with experimental data in order to test the validity of the model<sup>14 15</sup>.
- b. Forces; refers to those forces entering in the displacement of oil by water and corresponding to natural pressure gradients (capillary and gravity) or artificially imposed pressure gradients (due to external injection pressure).
- c. Block shape; generally of regular geometry – cylindrical, parallelepiped, cube (figure 9.31), and partially sealed in order to examine the effects of flow in each direction.

#### **GEOMETRY**



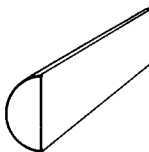
(CYL)

CYLINDRICAL



( PAR )

PARALLELIPIPED



( SCYL )

SEMICYLINDRICAL



( CUBE )

CUBE

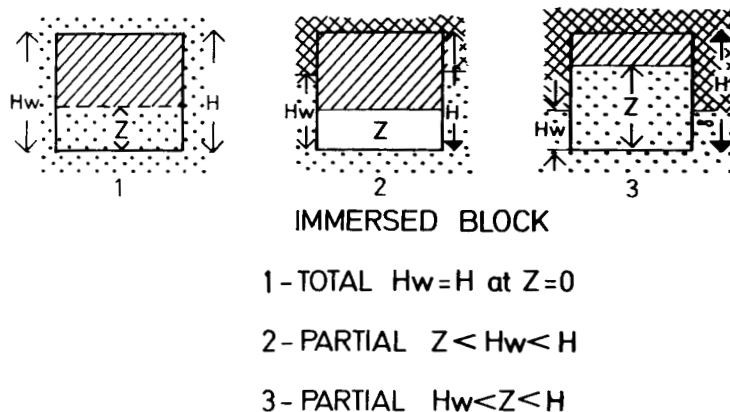
9.31 – Various block shapes

Table 9.3 Basic Characteristics of Experimental and Theoretical Models

No.	Author	Type of Model	Forces $P_c, G, P_{inj}$	Block Shape (Fig. 9.40)	Sealed (Fig. 9.32)	Water-table rate (Fig. 9.41)	Type of flow (Fig. 9.33)	Type of experiment
1	Aronofsky <sup>5</sup>	theoretical	$P_c$	CYL		1	3	conventional
2	Boxerman <sup>6</sup>	theoretical	$P_c$	CYL		2	3	
3	Mattax <sup>4</sup>	theoretical & experimental	$P_c + G$	SCYL	lateral	1	1	displacement
	Iffly <sup>11</sup>	experimental	$P_c + G$	CUBE	no	1, 2, 3	3	
	Kyte <sup>7</sup>	experimental	$P_c + G + P_{inj}$	CYL	no	1, 2	counter + direct	centrifuge
	Du Pray <sup>9</sup>	experimental		PAR	3 lateral faces	1	direct	
				CYL	lateral		dir. + counterflow	centrifuge
	Blair <sup>12</sup>	mathematical	$P_c, P_G$	CYL	top + bottom		direct	
	Parsons <sup>10</sup>	theor. + exper.	$P_c, P_G$	PAR+CUBE	—	1	direct	
	Kleppe <sup>14</sup>	theor. + exper.	$P_c, P_G, P_{inj}$	CUBE	—	1, 2, 3	direct	
	Graham <sup>13</sup>	experiment	$P_c, P_{inj}$	PAR	lateral	—	—	conventional

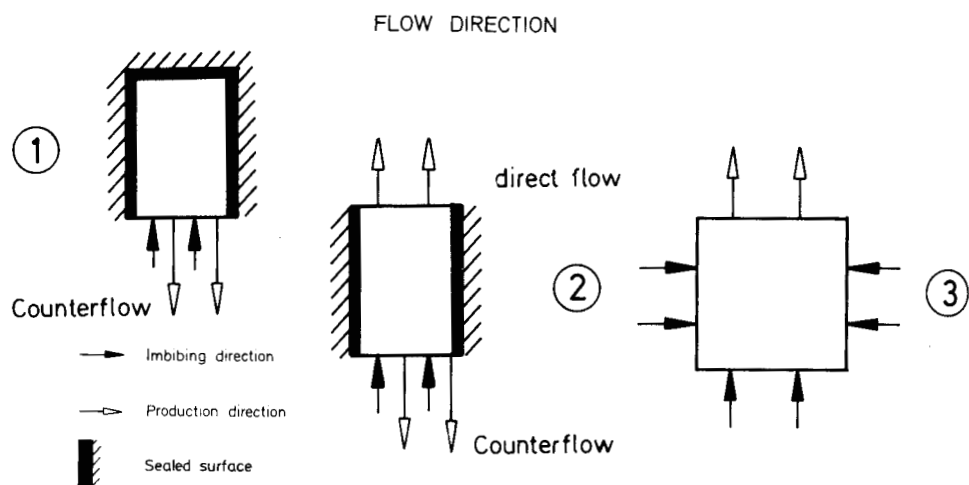
- d. Water table rate; rate of advancement of water-oil contact in fractures equivalent to block immersion in water may schematically present one of the three situations indicated in figure 9.32.
- e. Type of flow; direct or counterflow is indicated in figure 9.42, while type of experiment – conventional imbibition or centrifugal analogical procedure – is indicated in the last column of table 9.3.

### WATER TABLE = BLOCK IMMERSION RATE



$H_w$  - water table height (in fractures);  $Z$  - water-oil height (in matrix)

9.32 – Relative water-oil contact advancement in fractures and matrix.



9.33,- Flowing directions during imbibition.

#### 9.4.2.2. Basic theories

##### a. Aronofsky's model<sup>5</sup>

In a matrix block of low height, saturated with oil and totally immersed in water at time  $t=0$  (see table 9.3), an imbibition displacement controlled by capillary pressure will take place.

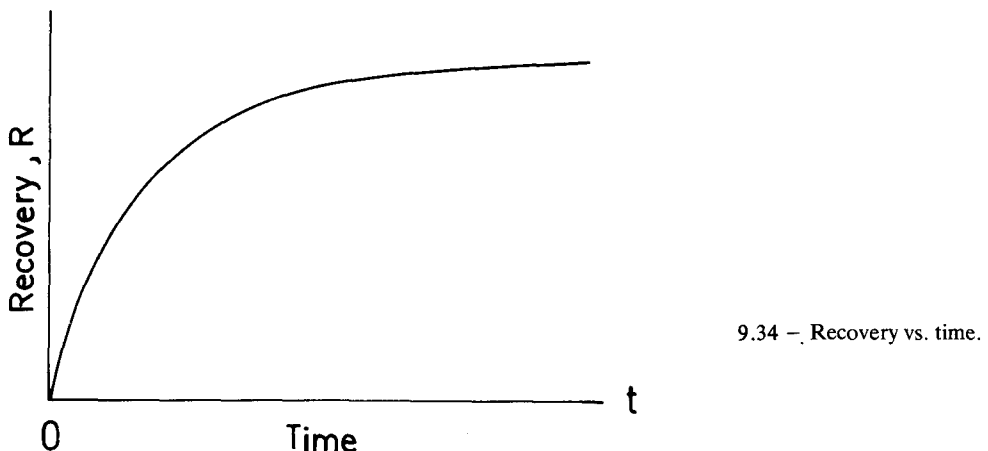
Aronofsky assumes that the function of time relative to production from the matrix is expressed by

$$R = R_{\infty} (1 - e^{-\lambda t}) \quad (9.55)$$

where  $\lambda$  is a constant giving the rate of convergence, and  $R_{\infty}$  is the limit towards which  $R$  converges at time  $t=\infty$ .

#### DISCUSSION

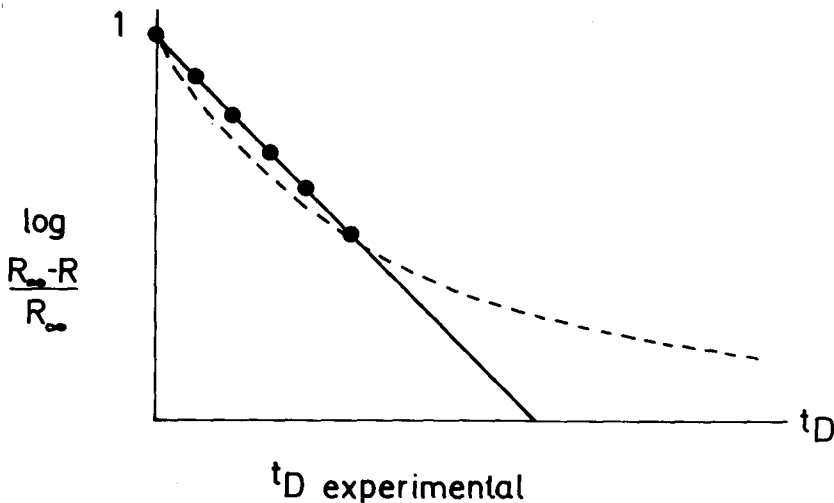
Equation 9.59 represented in figure 9.34 illustrates the important increments of recovery at the initial stage and the tendency to become constant with longer time.



If it is acknowledged that total time is the time necessary to approach the total recovery  $R_{\infty}$ , equation 9.59 can then be rewritten as,

$$\ln \left( \frac{R_{\infty} - R}{R_{\infty}} \right) = -\lambda t = -\left( \frac{t}{t_T} \right) = t_D \quad 9.56$$

and thus represented as in figure 9.44 for various experimental points of time  $\underline{t}$  and recovery  $\underline{R}$ .



9.35 – Relative recovery vs. dimensionless time,

If  $t \rightarrow t_T$ , recovery  $R$  will tend to equal  $R_T$  expressed by the relationship

$$R_T = R_\infty (1 - e^{-t/t_t}) = R_\infty (1 - 1/e) = R_\infty \times 0.63$$

which corresponds to 63% of total recoverable oil.

The rate of imbibition based on Aronofsky's model can be written in the following way,

$$q = \frac{R_\infty}{t_t} e^{t/t_t} \quad (9.57)$$

as proposed by DeSwaan<sup>16</sup>. This further allows the rate of water imbibition per unit of fracture to be written as,

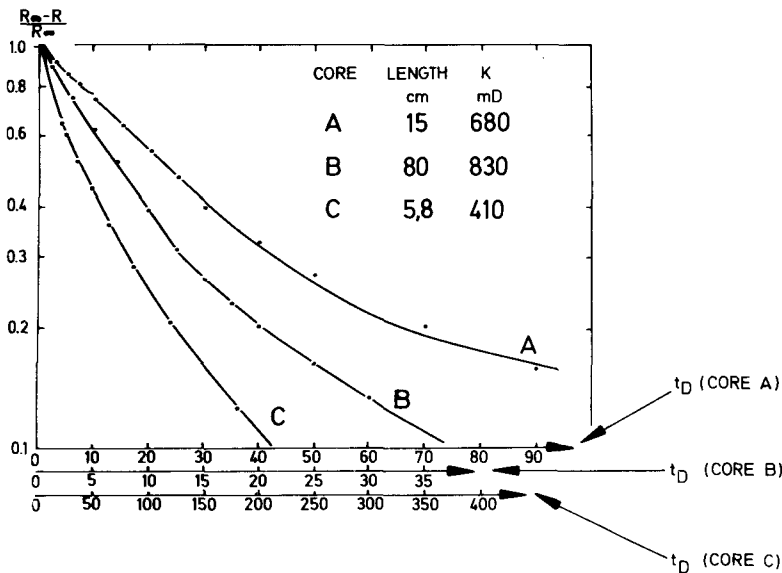
$$q = \frac{R_\infty}{t_t} \int_0^t e^{-(t-\Theta)t_t} \frac{\partial S_w}{\partial \Theta} d\Theta \quad (9.58)$$

### OBSERVATIONS

The relationship  $\ln R$  versus time  $t$  expressed by equation 9.55 was not verified in Iffly's experiments (figure 9.36). However, the deviations from a straight line in a semilog diagram are less important in the case of low height and low permeability (the comparison of core C with core B, figure 9.36).

The total recovery (63%) was indicated in Mattax's experiments on alundum cores, where saturation in water was  $S_{wi} = 0$  (similar to equation 9.60 when  $t \rightarrow t_T$ ).

A similar approach to that obtained in theoretical development of equation (9.56) may be used if mobility  $M=1$  in equation 9.23 since  $Z_D = Z$  is equivalent to recovery. Physically the time  $t_{D,G}$  has the following meaning (DuPrey<sup>9</sup>): time will correspond



9.36 – Relative recovery vs. dimensionless time (Iffly<sup>11</sup>, courtesy of French Institute of Petroleum).

to the rise of the saturation front to the height of,

$$(1 - \frac{1}{e})H = 0.63H \quad (9.59)$$

when the gravitational forces for a total immersion govern the flow and mobility  $M \approx 1$ .

#### b. Bokserman's equation<sup>6</sup>

The relationship developed by Bokserman may be seen as an analytical approach as well as a simplification of equation 9.19 of the basic model discussed in section 9.2. The solution of this equation shows that for very small M values,

$$Z_D^2 \cong \text{const } t_{D,PC} \quad (9.60)$$

which is equivalent to,

$$R \cong C \sqrt{t_D} \quad (9.60')$$

From Iffly's<sup>11</sup> experiments, this equation shows an inferior correlation to that of Aronofsky, but seems to match better to Mattax's experimental results.

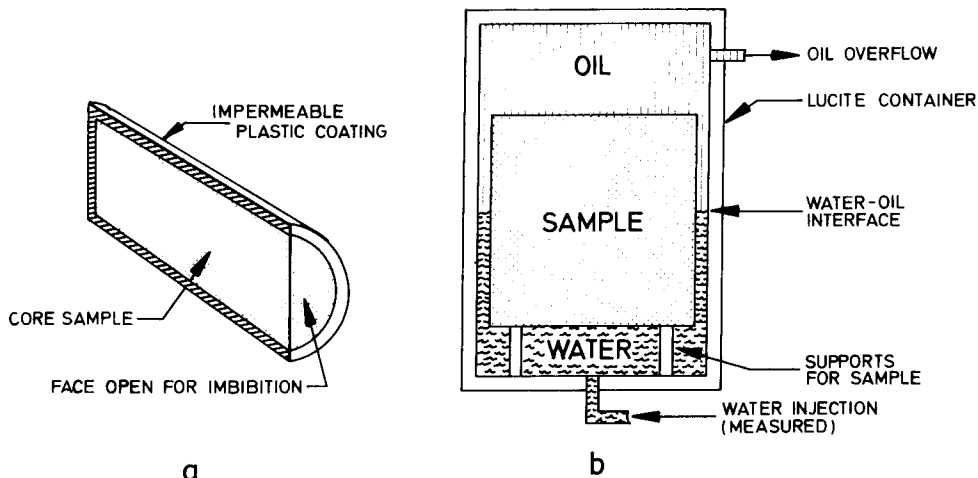
c. Mattax and Kyte models<sup>7</sup>

Their experiments have been carried out on two categories of cores:

	<u>alundum cores</u>	<u>sandstone cores</u>
shape →	semi-cylindrical	cubes
sealing →	sealed laterally	no sealing
water saturation →	$S_{wi} = 0$	$S_{wi} = 0$
experimental scheme →	Figure 9.37a	Figure 9.37b

The results obtained from counterflow on alundum cores are shown in figure 9.38. During the same imbibition time, recovery is higher for a lower water viscosity, for a greater core length, and for cores having a higher permeability.

The three-dimensional imbibition test has been examined for a different uniform rate of advancement of water-oil contact in fractures (similar to cases 2 and 3, figure 9.32). In order to interpret the results, the concept of critical rate was elaborated. This concept corresponds to equal advancement of water-oil contact in fractures

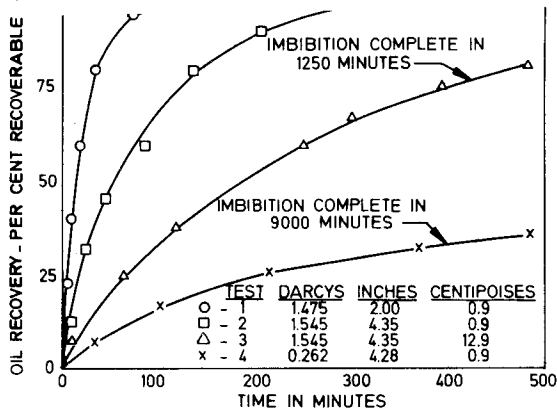


9.37 – Mattax's<sup>4</sup> imbibition procedure (a) counterflow (b) tridimensional flow (courtesy AIME).

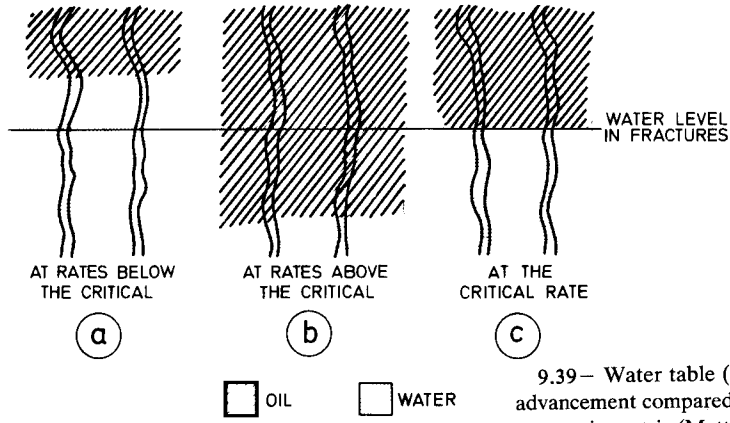
(water table) and in matrix (displacement front) where a *higher than critical rate* corresponds to a more rapid advancement of contact in fractures than in matrix (figure 9.39b), and vice-versa for a *lower than critical rate* (figure 9.39a). Advancement *at the critical rate* corresponds to a similar rate in matrix and fractures (figure 9.39c).

Based on this concept it was considered that *total recovery of the matrix* at water table rates below the critical rate (case a, figure 9.39) corresponds to the period when the water-oil front of displacement in the matrix reaches the top of the matrix block. It was observed that the *recovery is rate-sensitive* any time the rate is *below* the critical rate. Consequently, in order to evaluate the

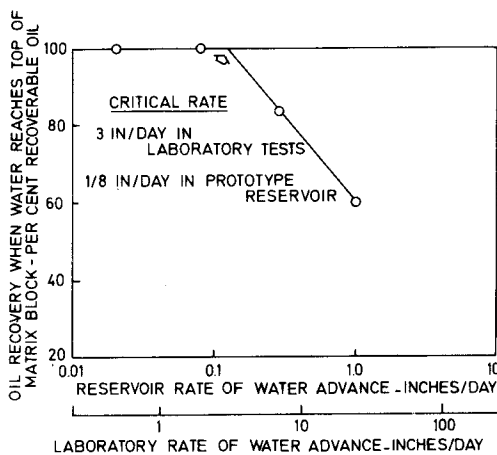
critical rate, a number of tests performed with water table rate below critical rate will give, by extrapolation as shown in figure 9.40, the magnitude of the critical rate.



9.38 – Counterflow imbibition test results (Mattax<sup>4</sup>, courtesy AIME).



9.39 – Water table (oil-water contact in fracture) advancement compared with displacement oil-water contact in matrix (Mattax<sup>4</sup>, courtesy AIME).



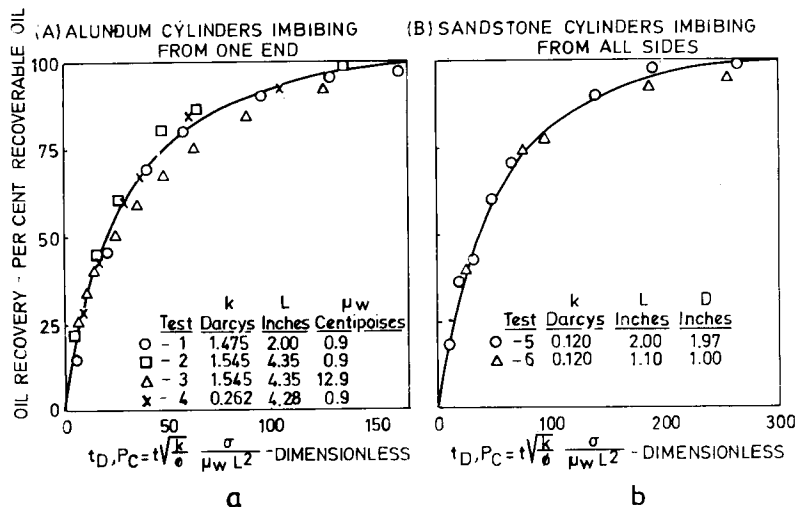
9.40 – Recovery vs. time correlation for evaluation of critical rate (Mattax<sup>4</sup>, courtesy AIME).

## DISCUSSION

- The results obtained from both experimental categories (uni-dimensional and three-dimensional flow) show that recovery versus time depends on sample geometry and physical properties of cores and fluids. But if time is expressed as a dimensionless parameter  $t_{D,P_c}$  similar to that in equation 9.18 (resulting from a theoretical approach),

$$t_{D,P_c} = \frac{\sigma f(\Theta) \sqrt{K/\Phi}, K_{rw,max}}{\mu_w H^2} t \quad (9.18)$$

then all experimental curves will be reduced to a unique curve as shown in figure 9.41a and b. In other words, for a given rock type ( $K, \Phi$ ), given fluids ( $\mu_w, \mu_o, \sigma, \theta$ ) and a given sample geometry, it is possible to generalize the results through a dimensionless relationship – recovery versus time.



9.41 – Recovery vs. time correlation for evaluation of critical rate (Mattax, courtesy AIME).

## OBSERVATIONS

- The basic assumptions of the results obtained are as follows:
  - The oil contained in fractures is negligible if compared with the oil contained in the matrix.
  - The fractures are large enough that resistance to flow is negligible.
  - The flow is governed by capillary forces since gravity forces are negligible.
  - The water-oil contact is uniform in all fractures as result of their intercommunication.
- The relationship obtained for recovery versus dimensionless time suggests that in

the case of capillary imbibition equation 9.18 can be used as a basic scaling correlation between the laboratory sample and reservoir matrix block.

#### d. Kyte's centrifuge method

The relationship between experimental recovery and time, which was developed through use of the centrifuge, has already been discussed in chapter 4. The basic law of displacement of a sample in a centrifuge is expressed by gravity-capillary forces and their relationship with the centrifuge speed, as follows:

$$\frac{G}{P_c} \sim \frac{\omega^2 \Delta\rho (3RH + H^2) / 6}{\sigma f(\Theta) / \sqrt{k/\Phi} J(S_w)} \quad (9.61)$$

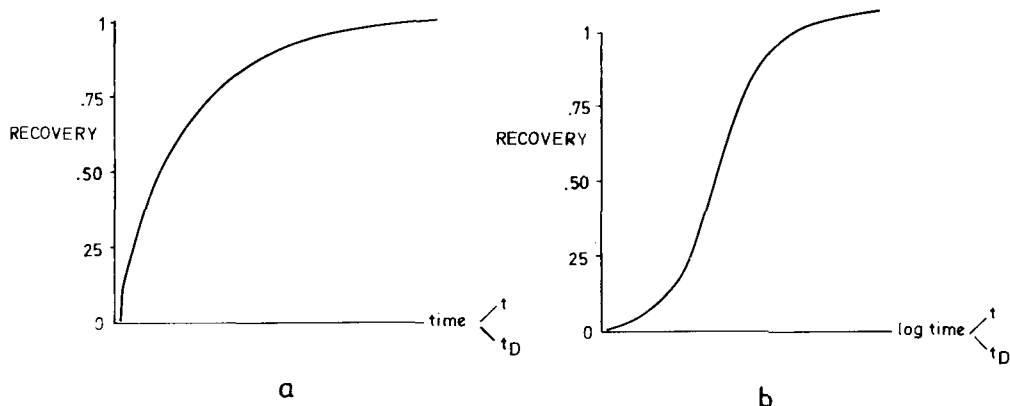
where R is the length of the centrifuge arm and H is the core height (figure 4.72, Chap. 4).

The combined influence of capillary imbibition and gravity on the displacement of oil by water is associated to block dimension (H) and capillary pressure  $P_c$ , when compared with rotation rate  $\omega$ .

The centrifuge results will give a similar recovery versus time curve as that obtained by conventional imbibition experiments (figures 9.38 and 9.41).

#### 9.4.2.3. Final conclusions

In all imbibition experiments where either gravity or capillary pressure is the predominant driving force, or both forces together contribute to imbibition displacement, the predicted recovery versus time curve is similar to that illustrated in figure 9.42a. If represented as recovery versus log time, the curve is similar to that shown in figure 9.42 b.



9.42 – Type of recovery vs. time diagram (a) R vs. t (b) R vs. log t.

The curve in figure 9.42b assumes a certain linear variation in semilog scale for intermediate time values.

Based on theoretical development (section 9.2.2) and on the results obtained by Mattax through dimensionless curves (figure 9.41) the following can be assumed:

- In small height blocks where capillary imbibition controls displacement, the recovery time is proportional to the square of the block height ( $H^2$ ).
- In tall blocks where gravity pressure controls displacement, the recovery time is proportional to the block height ( $H$ ).
- In case a, recovery may be represented as a function of  $t_{D,Pc}$  (equation 9.18) and in case b as a function of  $t_{D,G}$  (equation 9.22).

In the curve recovery versus log time an interesting yardstick<sup>9</sup> can be obtained from the necessary time to obtain 50% recovery  $t_{0.5R}$ . A comparison of  $t_{0.5R}$  from experiments obtained under various displacement conditions may be useful in reservoir evaluation.

#### 9.4.3. Recovery versus time: Scaling laws

The scaling of the immiscible displacement process in a porous medium was examined in detail by Rapoport<sup>8</sup>, and the basic premises for the relationship between laboratory model and reservoir block may help in predicting fractured reservoir behaviour. Since the flowing pressure gradient in fractures is negligible if compared with gravity and capillary forces, it is necessary that scaling should take into consideration these last two forces only. If a correct scaling procedure is established, the reservoir rock samples can be used to duplicate the reservoir matrix block behaviour.

##### 9.4.3.1. Scaling requirements

If, through model (m), one wishes to predict the behaviour of reservoir (R) formed by matrix blocks of given characteristics, it is necessary to fulfill a number of basic requirements. These requirements are based on classic Rapoport<sup>8</sup> principles developed for immiscible displacement processes, and are as follows:

$$\left[ \frac{H}{L} (K_x / K_z)^{1/2} \right]_m = \left[ \frac{H}{L} (K_x / K_z)^{1/2} \right]_R \quad (9.62)$$

$$\left[ (K_w \max / \mu_w) / K_o \max / \mu_o \right]_m = \left[ (K_w \max / \mu_w) / (K_o \max / \mu_o) \right]_R \quad (9.63)$$

$$\left[ \frac{P_c}{Ha \Delta \rho} \right]_m = \left[ \frac{P_c}{Hg \Delta \rho} \right]_R \quad (9.64)$$

- equality of initial water saturation.
- same shape as the relative permeability curves and,
- the capillary pressure curves.

In equations 9.66, 9.67 and 9.68 the three dimensionless groups represent the *shape factor* (SF), the *mobility factor* (M) and the *capillary-gravity ratio* (CGR), listed below:

$$\left. \begin{aligned} SF &= \frac{H}{L} \sqrt{K_x/K_z} \\ M &= \frac{K_{w,\max} / \mu_w}{K_{o,\max} / \mu_o} \\ CGR &= P_{c,t} / \Delta \rho g H \end{aligned} \right\} \quad (9.65)$$

In the literature the three factors are often written as  $\pi$  coefficients:  $\pi_1 = SF$ ;  $\pi_2 = M$  and  $\pi_3 = CGR$ .

In equation 9.65 H and L represent the block height and extension respectively,  $P_{c,t}$  is the threshold pressure and parameters a and g represent respectively the accelerations in simulated model and reservoir.

If a representative core of reservoir rock is used for simulation, then scaling is reduced to,

$$\pi_1 = SF = H/L \quad \text{or} \quad (H/L)_m = (H/L)_R \quad (9.66)$$

$$\pi_2 = \mu_o / \mu_w \quad \text{or} \quad (\mu_o / \mu_w)_m = (\mu_o / \mu_w)_R \quad (9.67)$$

$$\pi_3 = CGR = \frac{P_{c,t}}{\Delta \rho g H} \quad \text{or} \quad (P_{c,t} / \Delta \rho g H)_m = (P_{c,t} / \Delta \rho g H)_R \quad (9.68)$$

since the conditions d, e and f are fulfilled implicitly

#### 9.4.3.2. Principles of experimental scaling

##### a. Model shape

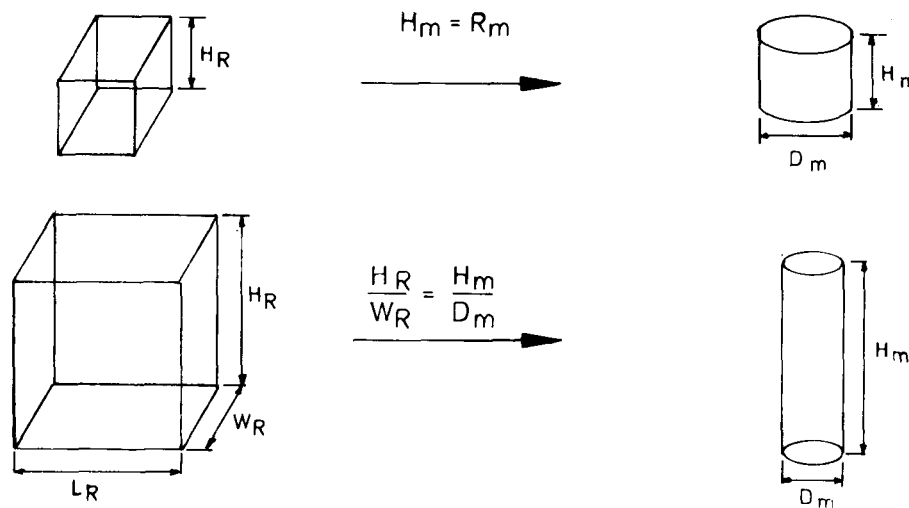
The shape of the model should be identical to that of the reservoir matrix block; but if the plugs already have a given shape, it is necessary to adapt to experimental conditions. A cylindrical model may be adapted as shown in figure 9.43 where the

requirements are as follows:

<i>Reservoir</i> cube ; $ H _R$	<i>Model requirements</i> $\rightarrow$ cylinder; $ H _m =  D _m$	}
	parallelepiped; $ H, L, W _R \rightarrow$ cylinder ; $\left  \frac{H}{D} \right _m = \left  \frac{H}{W} \right _R$	

(where  $W \ll L$ ) (9.69)

In certain cases the amount of error may reach 20% – 30%. When the amount of error is too high, it is necessary to simulate the imbibition with plugs having an identical shape as the idealized matrix block.



9.43 – Equivalence of a cylindrical core to a non-cylindrical core.

### b. Time scaling

It is necessary for time scaling to be associated to the forces which contribute to the driving of oil. If the displacement process is controlled by capillary forces (equation 9.18) as discussed by Mattax<sup>4</sup>, then,

$$(t_{D, P_c})_m = (t_{D, P_c})_R$$

$$\left[ \frac{\sigma_f(\Theta) \sqrt{K/\Phi} K_{rw,max}}{\mu_w H^2} t \right]_m = \left[ \frac{\sigma_f(\Theta) \sqrt{K/\Phi} K_{rw,max}}{\mu_w H^2} t \right]_R \quad (9.70)$$

or if  $f(\theta)$  and  $K_{rw,max}$  are the same then,

$$\left[ \frac{\sigma \sqrt{K/\Phi}}{\mu_w H^2} t \right]_m = \left[ \frac{\sigma \sqrt{K/\Phi}}{\mu_w H^2} t \right]_R \quad (9.71)$$

If displacement is controlled by gravity forces (predominant forces), it is possible to write the scaling law as,

$$(t_{D,G})_m = (t_{D,G})_R$$

$$\left( \frac{K}{\Phi} \frac{\Delta \gamma}{\mu_w H} t \right)_m = \left( \frac{K}{\Phi} \frac{\Delta \gamma}{\mu_w H} t \right)_R \quad (9.72)$$

NOTE: If the rock used in the experimental model is fully representative for reservoir rock and fluid characteristics are the same in the model as in the reservoir, the equations 9.71 and 9.72 are reduced to the following:

~ for predominant capillary pressure:

$$\left( \frac{t}{H^2} \right)_m = \left( \frac{t}{H^2} \right)_R \quad (9.73)$$

~ for predominant gravity force:

$$\left( \frac{t}{H} \right)_m = \left( \frac{t}{H} \right)_R \quad (9.74)$$

c. Physical scaling in the presence of  $P_c$  and  $G^{10}$ .

When gravity forces are working together with capillary forces it is necessary, in addition to time scaling, to assure a physical scaling which will result from the two dimensionless times (equations 9.18 and 9.22),

$$\frac{t_{D,P_c}}{t_{D,G}} = \frac{\sigma f(\Theta) K_{rw,max} \sqrt{K/\Phi} / \mu_w H^2}{K \times g \Delta \rho \times K_{rw,max} / \Phi \mu_w H} \approx \frac{\sigma \sqrt{\Phi/K}}{\Delta \rho H} \quad (9.75)$$

and consequently, the scaling relationship may be expressed as,

$$\left( \frac{L\Delta\rho}{\sigma} \sqrt{\frac{K}{\Phi}} \right)_m = \left( \frac{L\Delta\rho}{\sigma} \sqrt{\frac{K}{\Phi}} \right)_R \quad (9.76)$$

d. Scaling of displacement front advancement<sup>10</sup>

When considering a piston-like displacement (figure 9.9), the water-oil displacement front is expressed by the scaling of parameter  $Z_D$  as follows,

$$\left. \begin{array}{l} (Z_D)_m = (Z_D)_R \\ (Z/H)_m = (Z/H)_R \end{array} \right\} \quad (9.77')$$

which if associated to velocities  $V_m$  and  $V_R$  will give

$$\frac{V_m}{V_R} = \frac{\left( \sigma \sqrt{K/\Phi} / \mu_w H \right)_m}{\left( \sigma \sqrt{K/\Phi} / \mu_w H \right)_R} \quad (9.78)$$

e. Scaling gravity force through acceleration (centrifuge).

If the gravity force in the reservoir  $(H_g \Delta Q)_R$  is simulated through a model of the same  $\Delta Q_m$  but of smaller  $H_m$ , it is necessary for the simulation to increase the acceleration until equation 9.64 is satisfied.

When considering the gravity force in the reservoir,

$$(G)_R = \left[ \frac{1}{2} \Delta \rho g H \right]_R \quad (9.79)$$

and the capillary force,

$$(P_c)_R = \left[ \sigma f(\Phi) \sqrt{K/\Phi} J(S_w) \right]_R \quad (9.80)$$

the following ratio will result,

$$\left[ \frac{G}{P_c} \right]_R = \frac{\left[ \frac{1}{2} \Delta \rho g H \right]_R}{\left[ \sigma f(\Theta) \sqrt{K/\Phi} J(S_w) \right]_R} \quad (9.81)$$

By using the scaling law,

$$(G/P_c)_m = (G/P_c)_R \quad (9.81')$$

and combining it with the Kyte equation (9.61) expressing  $(G/P_c)_m$ , the result is

$$\omega = \left\{ \left( \frac{3gH\Delta\rho}{\sigma} \right)_R \left[ \frac{\sigma}{(3RH + H^2)\Delta\rho} \right]_m \right\}^{1/2} \quad (9.82)$$

or as a number of rotations per minute,

$$N = \frac{60}{2\pi} \omega \quad (9.83)$$

As previously discussed, the relative importance of the capillary and gravity forces in the process of displacement is closely related to block dimension, and gravity may play a relevant role in reservoirs formed by tall blocks or having large pores equivalent to small values of capillary pressure. Kyte's centrifuge circumvented the difficulty of testing large size blocks by scaling the acceleration and performing the experiments in small cores. Simulation may be developed through conventional imbibition displacement or centrifuge experiments. In both cases the scaling laws must be rigorously maintained.

#### 9.4.3.3. Examples of scaled experiments in the literature

##### a. Mattax's<sup>4</sup> scaling example: conventional imbibition displacement.

In the imbibition displacement carried out in the laboratory by Mattax, the reservoir matrix block was represented by a sample model. The basic data ( $K, \Phi, S_{wi}, \sigma$ ) for sample model and reservoir were the same, but block geometry and fluid were different (table 9.4). The time ratio was based on equation 9.71',

$$t_R = t_m \left( \frac{\sigma\sqrt{K/\Phi}}{\mu_w H^2} \right)_m \left( \frac{\mu_w H^2}{\sigma\sqrt{K/\Phi}} \right)_R$$

or,

$$t_R = t_m \frac{H_R^2}{H_m} \cdot \frac{\mu_w, R}{\mu_w, m} = t_m \left( \frac{9'}{3''} \right) \frac{0.6}{0.9}$$

$$t_R = 864 t_m$$

Table 9.4. Model and Prototype Data (Mattax<sup>4</sup>)

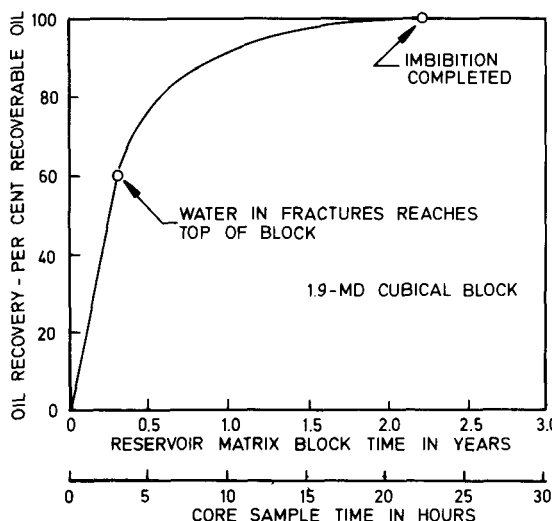
DATA	Symbol	Model (m)	Reservoir (R)
Permeability	K		1.9 mD
Porosity			9.1%
Saturation	$S_{wi}$		24.3%
Tension			35 dgne/cm
Block shape	H	Cube	Cube
Block height	H	3"	9'
Water viscosity	w	0.9 cP	0.6 cP
Oil viscosity	o	2.7 cP	1.8 cP

The rate of advancement, based on equation 9.78 will be reduced to,

$$V_R = V_m \frac{H_m}{H_R} \frac{\mu_{w,m}}{\mu_{w,R}} = V_m \frac{3''}{9'} \cdot \frac{0.9}{0.6} \quad (9.78)$$

$$V_R = V_m / 24 \text{ (inches/day)}$$

The results obtained for a constant water table rate, higher than the critical rate (figure 9.39b), are presented in figure 9.44 for both times –  $t_m$  and  $t_R$ . The laboratory results obtained in hours correspond to years in the reservoir matrix block. The top of the block is reached after a certain period of time due to a constant rate of advancement of the water table, after which recovery continues. When the water table reaches the top of the block, 60% of recoverable oil is produced, while the final oil recovered represents 48.8% PV.



9.44 Conventional imbibition recovery vs. time, model and reservoir (Mattax<sup>4</sup>, courtesy AIME).

b. Kyte's<sup>7</sup> scaling example: centrifuge displacement.

In the example examined by Kyte, some of the physical properties of rock and fluid in the model (core sample) and reservoir (matrix block) are identical, such as the following basic data:

$$K_m = K_R = 350 \text{ mD} \quad \Phi_m = \Phi_R = 20.3\% \quad \mu_o/\mu_w = 6.5 \quad \sigma_m = \sigma_R = 21 \text{ dyne/cm}$$

The different properties of the model and reservoir are as follows:

$$\mu_{o,m} = 5.85 \text{ cP} \quad \mu_{o,R} = 1.95 \text{ cP}$$

$$\mu_{w,m} = 0.90 \text{ cP} \quad \mu_{w,R} = 0.3$$

$$\Delta \rho_m = 0.180 \text{ g/cc} \quad \Delta \rho_R = 0.166 \text{ g/cc}$$

The dimensions of the matrix block are  $H_R = 182 \text{ cm}$  and  $D = 69.8 \text{ cm}$ .

The data are as follows: core (1)– $H_{m1} = 4.90 \text{ cm}$  and  $D_{m1} = 1.88 \text{ cm}$ ; core (2)– $H_{m2} = 9.80 \text{ cm}$  and  $D_{m2} = 3.76 \text{ cm}$ . The centrifuge radii of the two cores are  $R_1 = 14.5 \text{ cm}$  and  $R_2 = 11.70 \text{ cm}$ .

From equation 9.83, the numbers of rpm (rotations per minute) for simulation of displacement through cores (1) and (2) were obtained based on the above data.

It resulted that  $N_1$  and  $N_2$  are:

$$N_1 = \frac{60}{2\pi} \left[ \frac{3 \times 981 \times 182 \times 0.66}{21/981} \times \frac{21/981}{(3 \times 14.15 \times 4.90 + 4.9^2) \times 0.180} \right]^{1/2}$$

$$N_1 = 441 \text{ rpm}$$

and similarly,

$$N_2 = 320 \text{ rpm}$$

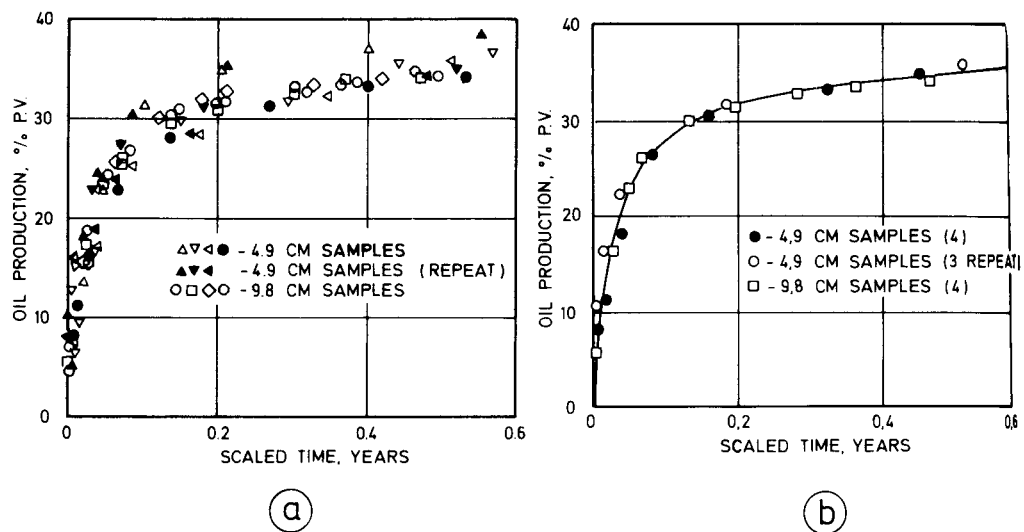
Using equation 9.71 and simplifying it, the only parameters to be scaled are  $t$ ,  $\mu_w$  and  $H$ . The results are as follows,

$$\left[ \frac{t}{\mu_w H^2} \right]_m = \left[ \frac{t}{\mu_w H^2} \right]_R$$

$$\frac{t_m}{t_R} = \frac{\mu_{w,m}}{\mu_{w,R}} \left[ \frac{H_m}{H_R} \right]^2$$

which, for core 1, will further correspond to,

$$\left[ \frac{t_m}{t_R} \right]_1 = \frac{0.9}{0.3} \left[ \frac{4.9}{182} \right]^2 = \frac{1}{460} = 0.00217$$



9.45 – Experimental results of recovery vs. time by use of the centrifuge (a) experimental data; (b) averaged experimental data (Kyte<sup>7</sup>, Courtesy AIME).

$$t_R \cong 115 t_{m,1}$$

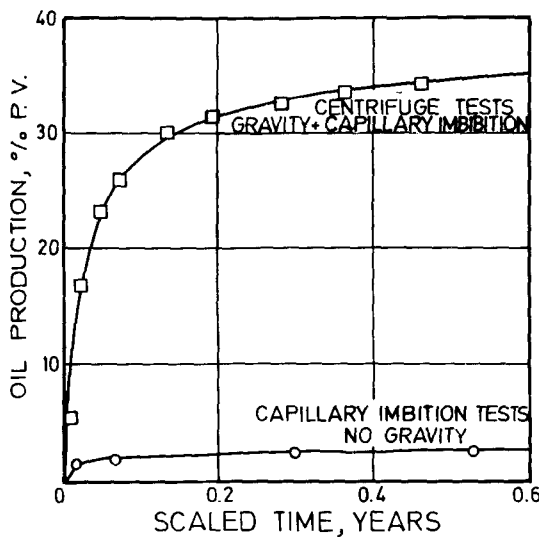
and for core 2,

$$\left(\frac{t_m}{t_R}\right)^2 = \frac{0.9}{0.3} \left(\frac{9.80}{182}\right)^2 = \frac{1}{116} = 0.0087$$

$$t_R \cong 460 t_{m,2}$$

The experimental results are shown in figure 9.45a where the recoveries versus time are presented for four cores measuring 4.9 cm, tested once and repeated on only three of the cores. In addition, four cores measuring 9.8 cm were tested under similar conditions. The resulting data indicate maximum differences in the range of 5%, showing greater recoveries for smaller cores. By averaging the results of cores of different lengths, the scaled results are obtained and shown in figure 9.45b.

If the combined effects of gravity-imbibition are compared with the effects of only capillary imbibition on the reservoir block of only  $H = 1.82$  m, then there will be one curve for recovery versus time for gravity and capillary imbibition and another for imbibition (fig. 9.46). The laboratory results scaled for the reservoir block indicate the predominance of gravity forces as a result of a significant block height (figure 9.46).



9.46 – Comparison of gravity and capillary imbibition and capillary imbibition at reservoir block scale (KYTE<sup>7</sup>, courtesy AIME)

#### 9.4.4. Recovery versus time: critical discussion

The basic laws of scaling are valid if properly applied and if all basic assumptions concerning the homogeneity of the matrix-fracture system are observed. However in experimental work, as well as in any further extrapolation of the results, a series of precautions must be taken.

##### 9.4.4.1. Discussion of conventional imbibition displacement

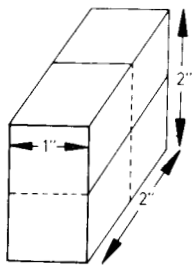
The basic factors which influence experimental results and their use are related to rock homogeneity, types of rock and fluid characteristics as well as experimental conditions.

###### a. Rock heterogeneity

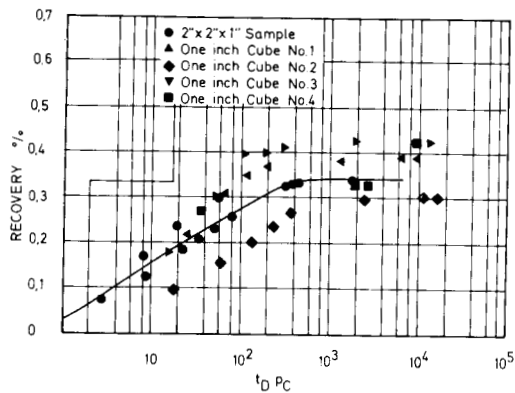
Inside a reservoir, heterogeneity limits the validity of the relationship between recovery and time obtained through Mattax's<sup>4</sup> experiments (shown in figure 9.47). Parsons<sup>10</sup> examined this role of heterogeneity by using a core measuring 2" × 2" × 1" (figure 9.47a) on which imbibition was carried out and a recovery-time relationship was obtained. The core was divided into four cubes and an imbibition performed on each of them. The results obtained from core 1 indicate a large spread of recovery, while the results from core 2 indicate a significant homogeneity (figure 9.47b and c).

###### b. Reservoir lithology

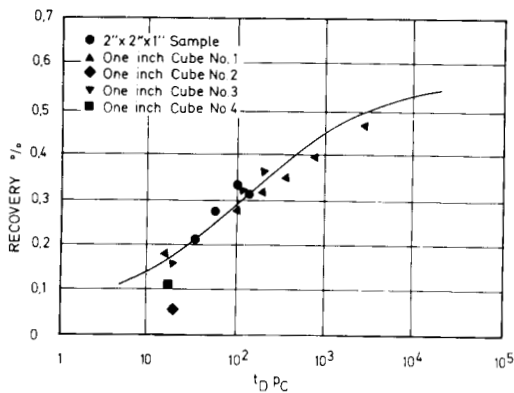
The experiments carried out in similar conditions may show different results because of mineralogical characteristics (Iffly<sup>11</sup>). The experiments performed (schematically shown in figure 9.47 a) are referred to as Type A1 and Type A2. For various values of CGR the results will be quite different as a direct effect of lithological variations (figure 9.47b).



(a)



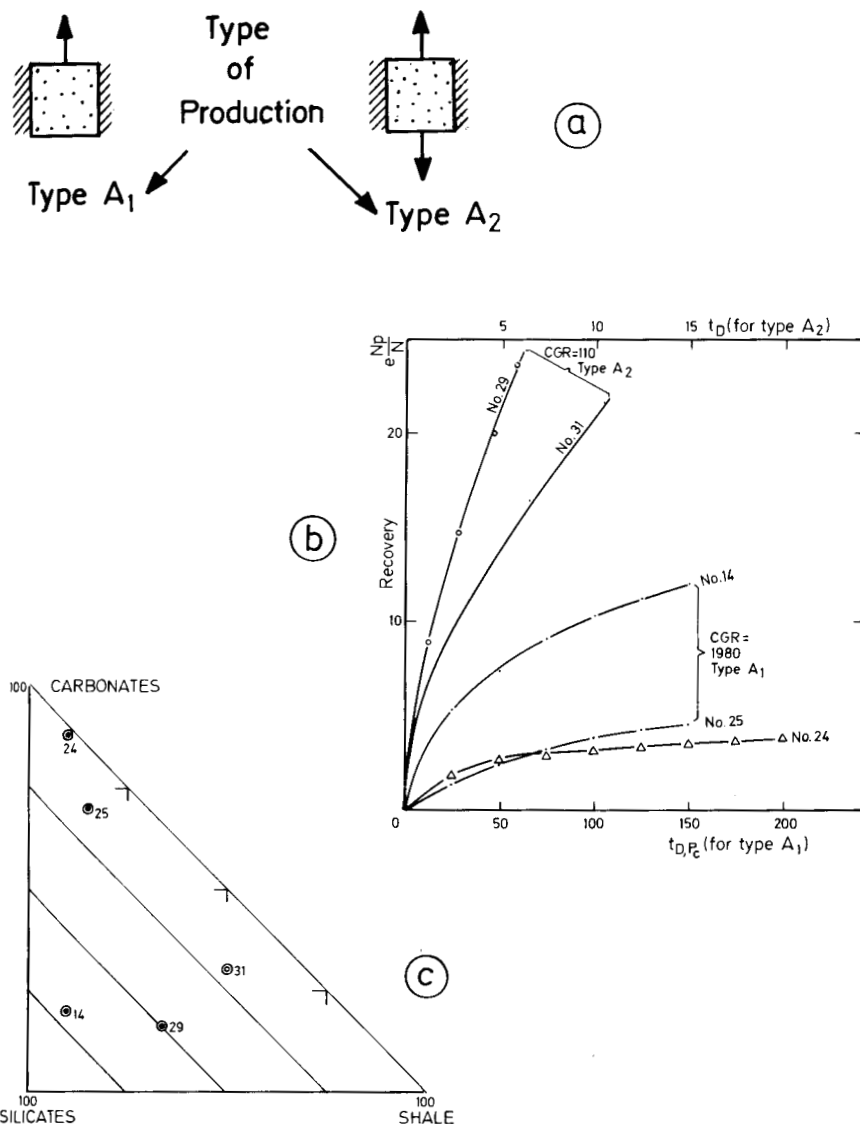
(b)



(c)

9.47 – Influence of rock heterogeneity on recovery vs. time  $t_D \cdot P_C$  (a) shape of core used (b) scattered points of heterogeneous rock (c) similar result in a homogeneous rock (Parsons<sup>10</sup>, courtesy AIME).

Recovery versus time shows a very large divergence (figure 9.48b) resulting from the relationship between lithology and spontaneous oil displacement (figure 9.48d). The observed trend is appropriate as consequence of the fact that a higher content in carbonates causes a higher oil wettability in the rock and a reduction in recovery (cores 24 and 25).

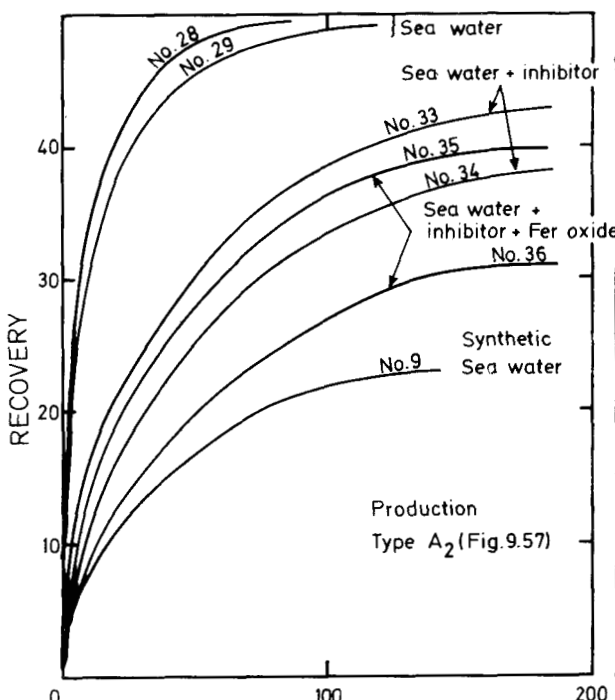


9.48 – Influence of lithology on recovery vs. time  $t_{D,P_c}$  (a) type of displacement (b) recovery vs. time for various rocks (c) rock mineralogical composition (Iffly<sup>11</sup>, courtesy of French Institute of Petroleum).

### c. Nature of fluid

Experiments performed under similar conditions on similar cores but with a different injected fluid, have shown substantial variations in recovery behaviour versus time (Iffly<sup>11</sup>). The results given in figure 9.49 demonstrate the important difference between conventional sea water and sea water with inhibitors. When synthetic sea water was used, unpredictable results were obtained. This strong reduction in recovery is due to a more rapid decreasing of interfacial tension of synthetic sea water. This means that the interfacial tension, if modified in time, may change the entire simulation between laboratory results and field predictions. It is therefore absolutely essential to add to the simulation conditions the ratio,

$\frac{(\sigma \cos \theta)_{t_D}}{(\sigma \cos \theta)_{t_D=0}}$  which expresses the variation in time of the  $\sigma \cos \theta$  factor.



9.49 – Recovery vs.  $t_D$  for various types of fluids and cores characteristics (Iffly<sup>11</sup>, courtesy of French Institute of Petroleum).

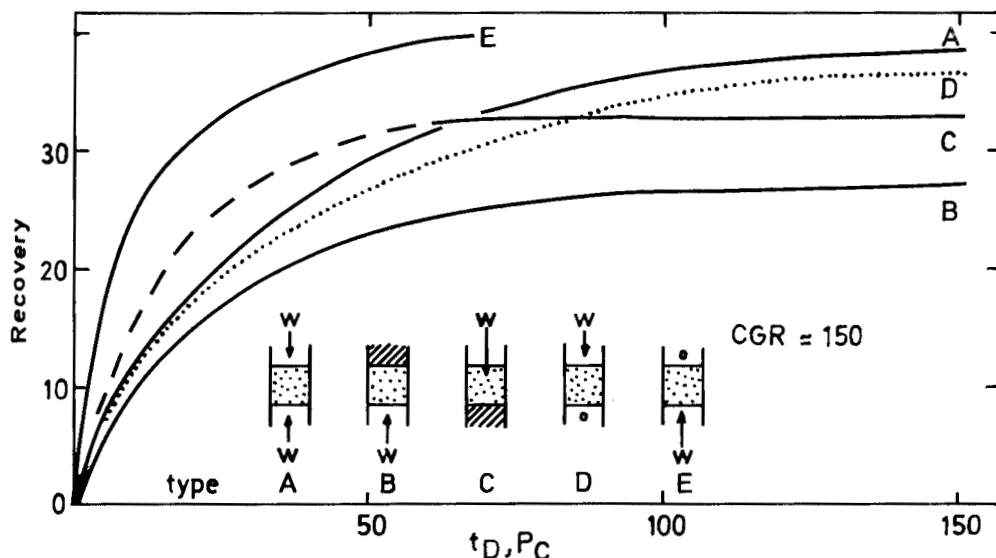
No	h (cm)	$\phi$ %	$S_{wi}$ %	k mD	CGS
9 -	25	42	40	160	180
28 -	20	42	20	130	103
29 -	20	41	39	434	132
33 -	20	40	28	442	140
34 -	20	45	29	418	135
35 -	20	44	30	600	117
36 -	20	42	42	224	187

### d. Role of fluid entering-exit surface

It is essential to associate the displacement process results to the fluid entering-exit surfaces which influence the type of flow and the direction of flow during displacement. A number of representative cases were examined by Iffly (figure 9.43). The cores were all sealed laterally but in cases A, D and E the top and bottom surfaces were left open, and in cases B and C only one surface was left open. The CGR was constantly maintained around CGR=150, but in all five cases examined the recovery behaviour indicated substantial differences due to the flowing surfaces.

From the results presented in figure 9.50 the following was determined:

- Experiment B was the most unfavourable since oil production was working in counterflow and also against gravity.
- The inverse situation of case C indicates the favourable role of gravity under similar counterflow conditions.
- The most favourable conditions were observed in case E, where all forces (gravity and capillary) favour the displacement.
- Better results were obtained in case A than in case D due to the fact that production through the bottom face was performed against gravity forces (case D), while in case A the counterflow on both faces seems more efficient.



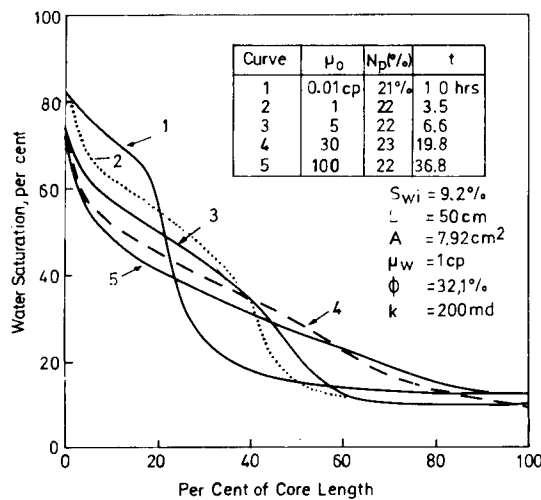
9.50 – Recovery vs.  $t_D, P_C$  examined on five models of rock/fluid surface contacts for the same CGR = 150 (Iffly<sup>11</sup>, courtesy of French Institute of Petroleum).

#### e. Role of oil viscosity

The function of oil viscosity on the imbibition process was examined through numerical models (Blair<sup>12</sup>) in five cases of viscosity ( $\mu_o = 0.01; 1; 5; 30; 100 \text{ CP}$ ) and in the case of a constant water viscosity  $\mu_w = 1 \text{ CP}$ .

Counterflow imbibition developed a saturation distribution at various times during the displacement process, from which it was discovered that only in low viscosities did a displacement front effectively develop. On the contrary, with high viscosities of oil no apparent front was observed and a continuous increase of water saturation versus core length was noticed (figure 9.51).

The influence of oil viscosity on rate of imbibition is presented in figure 9.52 where, for a recovery higher than 6%, the recovery versus time plot illustrates an approximately linear relationship in a log-log diagram. At a lower oil viscosity, a higher recovery was obtained for the same time of displacement.

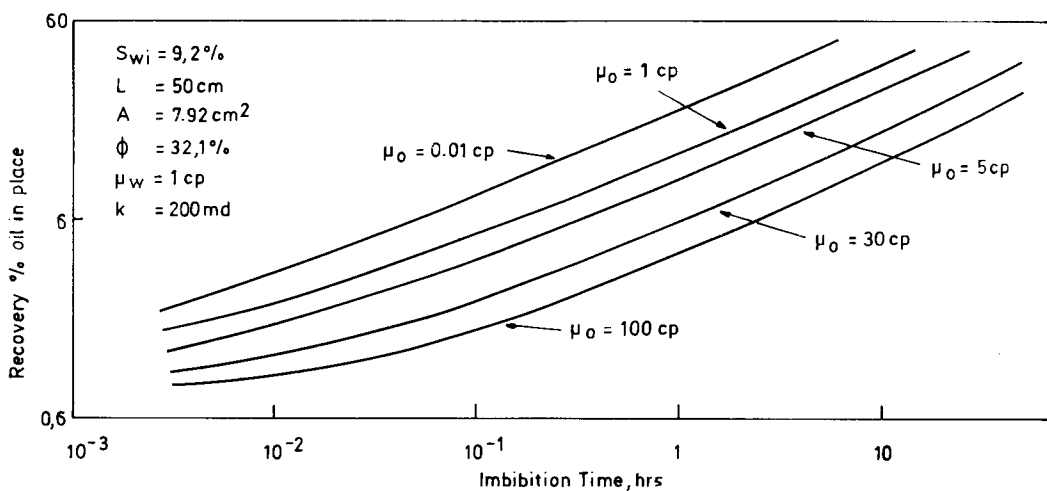


9.51 – Saturation distribution at various times of displacement for various oil viscosities (Blair<sup>12</sup>, courtesy AIME).

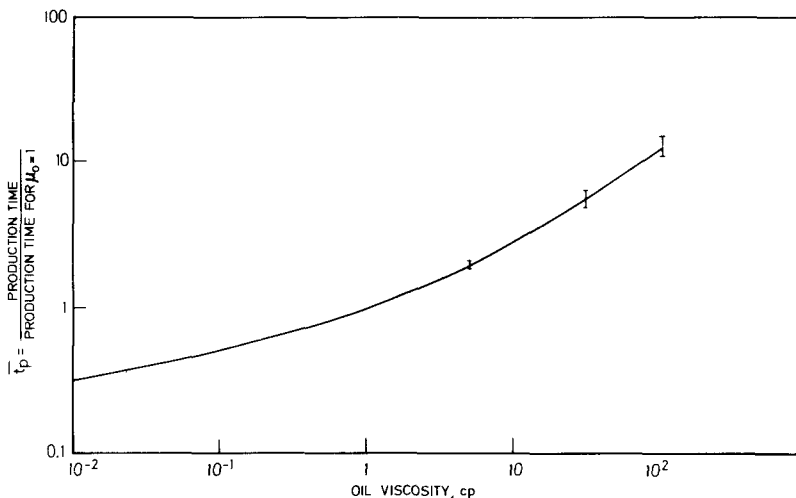
Another relationship is shown in figure 9.53 where the relative production time  $t_p$  is expressed as a function of viscosity. The time ratio  $t_p$  is,

$$t_p = \frac{\text{Production time}}{\text{Production time for } \mu_o=1}$$

which indicates the additional time necessary for the displacement process in case viscosity  $\mu_o$  increases. The evaluation has been performed on a core of section  $A = 7.92 \text{ cm}^2$  and length  $L = 50 \text{ cm}$ , having a porosity  $\Phi = 32\%$ , water saturation  $S_{wi} = 9.2\%$ , and a water viscosity  $\mu_w = 1 \text{ CP}$ .



9.52 – Recovery vs. imbibition for various oil viscosities.



9.53 – Variation of  $t_p$  vs. viscosity ( $t_p \sim$  production time referred to production time for  $\mu_0 = 1$  cp). (Blair<sup>12</sup>, courtesy AIME).

#### f. Special rock characteristics

The capillary pressure is influenced by any change in porosity, permeability, pore size distribution, etc. as results from equation 9.16. It was observed that relative permeability and interstitial water saturation plays a minor role, so that imbibition by capillary forces will mainly be a function of  $\sqrt{K/\Phi}$ .

#### g. Mobility $M = \pi_2$

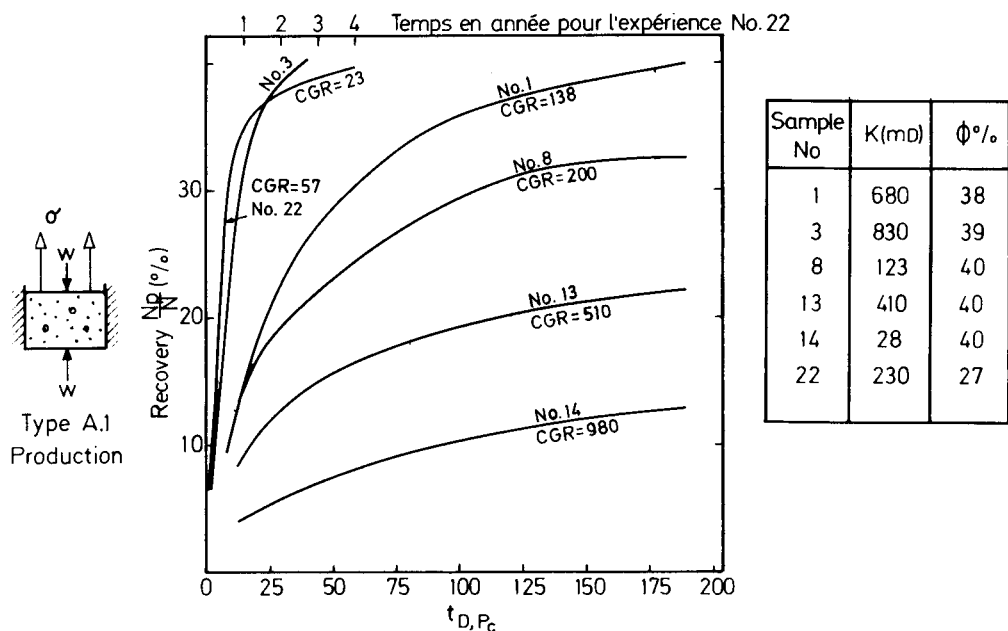
From DuPrey's<sup>3</sup> experiments it was found out that if  $M = \pi_2$  varied between 0.25 and 0.9, relatively few changes were observed in the relationship between recovery and dimensionless time.

#### h. Role of capillary-gravity ratio, CGR = $\pi_3$

The capillary-gravity ratio indicates the contribution of each of the two forces to the imbibition displacement, resulting in the recovery-time relationship.

Experiments were carried out by Iffly<sup>11</sup> on cores varying in height between 5 cm and 200 cm, and permeability varying between 10mD and 1000mD. Displacement was performed with real fluid; no additives on rocks of the same composition (silica  $\approx 60\%$ , shale  $\approx 15\%$ , carbonate  $\approx 25\%$ ). The type of experiment (denoted A.1), corresponds to production on the top contact surface. The variations of CGR, expressed as,

$$\pi_3 = \text{CGR} = \frac{\sigma f(\Theta) \sqrt{K/\Phi}}{\Delta \rho \times g \times h} \quad (9.84)$$



9.54 — Recovery vs.  $t_D, P_c$  for various CGR values (Iffly<sup>11</sup>, courtesy of French Institute of Petroleum).

were between 20 and 1000. The results are shown in figure 9.54, from which it is evident that CGR directly influences recovery, independent of the other experimental conditions. The basic conclusion is that recovery is more rapid and more significant if CGR is smaller, which shows the role of increased gravitational forces in reducing the time of recovery.

Similar experiments have been carried out on parallelepipeds with only one lateral face open for imbibition (DuPrey<sup>9</sup>). Presented as recovery versus  $t_{d,C}$  and  $t_{D,G}$  the trend is similar to that shown in figure 9.54. Thus, smaller CGR or increased gravitational forces are associated with a faster recovery.

#### 9.4.4.2. Discussion of imbibition displacement by use of a centrifuge

The scaling procedure used in Kyte's<sup>7</sup> experiments for the evaluation of recovery under gravitational conditions is a fast and relatively accurate method, and therefore, it continues to be a useful and significant aid in basic data preparation.

As mentioned earlier, if the imbibition process is to include gravitational effects by use of the numerical method (Blair<sup>12</sup>), an accurate capillary pressure curve and relative permeability data are necessary. The centrifuge test does not require this data as long as the sample is fairly representative of the matrix block.

Kyte noticed that the relative permeability curve is often obtained at high flow rate tests, where capillary and gravity pressures are negligible compared with the flowing gradients. If these laboratory results are used further in numerical models, it is quite obvious that the field results will differ from the laboratory results.

There is also the additional advantage that boundary effects could be better simulated in centrifuge tests than through numerical models, where arbitrary saturation would have to be used at matrix block boundaries.

#### a. Role of capillary-gravity ratio ( $CGR = \pi_3$ )

The function of gravity was evidenced in Mattax's<sup>4</sup> experiment (figure 9.46), where for given conditions of a matrix block with a height of  $H_R = 1.82\text{m}$ , gravitational forces were twelve times more effective in the displacement process than capillary forces were.

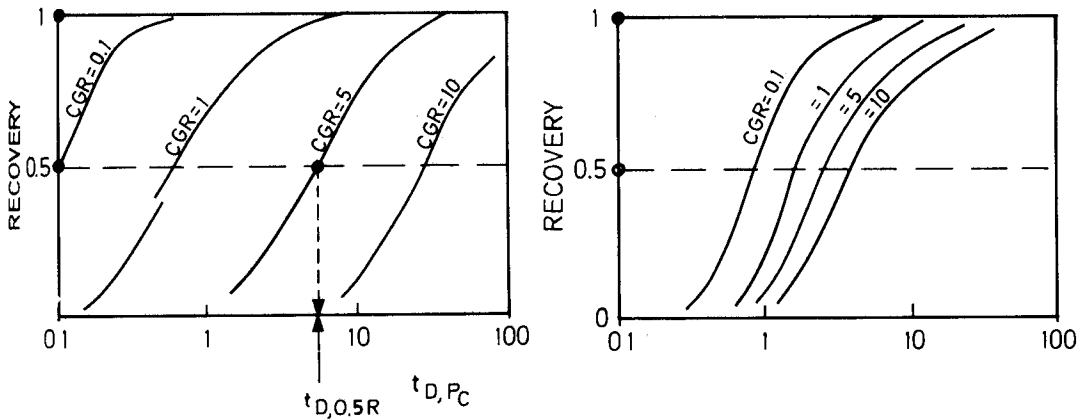
Other experiments performed by DuPrey<sup>9</sup> compared the centrifugal and conventional imbibition results for various CGR values.

The relationship between recovery and time is directly influenced by CGR, and an examination of the results may be carried out by referring to either capillary dimensionless time ( $t_{D,P_c}$ ) or gravity dimensionless time ( $t_{D,G}$ ).

With reference to the  $t_{D,P_c}$  scale, recovery is faster when CGR decreases and gravity assumes a greater role (figure 9.55a), but the resulting curves are relatively dispersed.

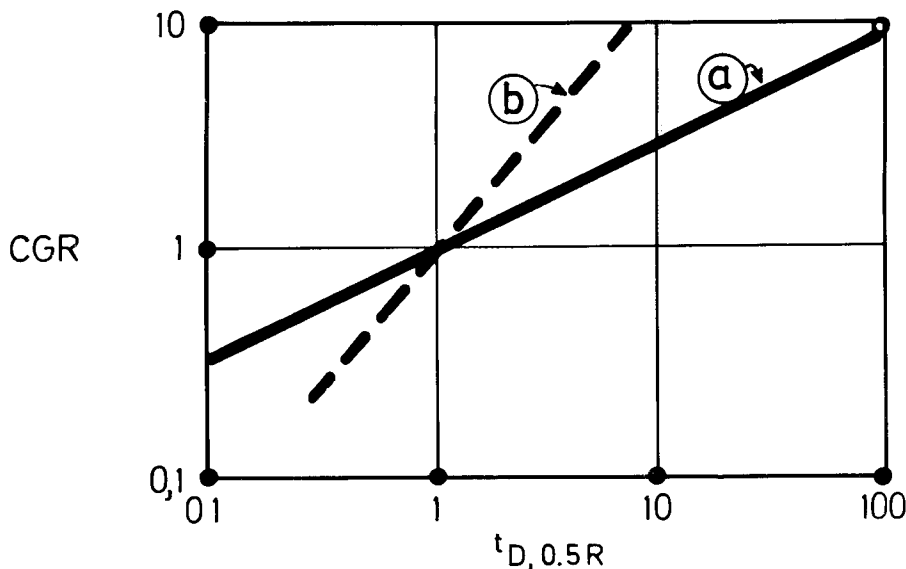
Recovery with reference to the  $t_{D,G}$  is similarly influenced by CGR values — recovery is faster when gravity increases, but the curves are closer to one another without superimposing as would be expected (figure 9.55b).

Due to the dispersion of the relationship between recovery and time in the log-log scale, the examination of the results as a function of *half-recovery time* was suggested by DuPrey<sup>9</sup>. Half-recovery time corresponds to the dimensionless time  $t_D$  for a recovery of 50%, shown in the diagram in figure 9.55. This time is denominated as  $t_{D,0.5R}$ .



9.55 — Recovery vs. dimensionless time<sup>9</sup>; (a) in terms of capillary dimensionless time and (b) gravitational dimensionless time.

In examining the CGR values between 1 and 10 versus  $t_{D,0.5R}$ , it is found that a linear relationship between these two parameters exists in a log-log scale. A difference in slope was noticed between CGR versus time in terms of capillarity ( $t_{D,Pc}$ ) and gravity ( $t_{D,G}$ ). It was observed (figure 9.56) that CGR versus  $t_{D,0.5R}$  gave a higher slope in terms of gravity than in terms of capillarity.



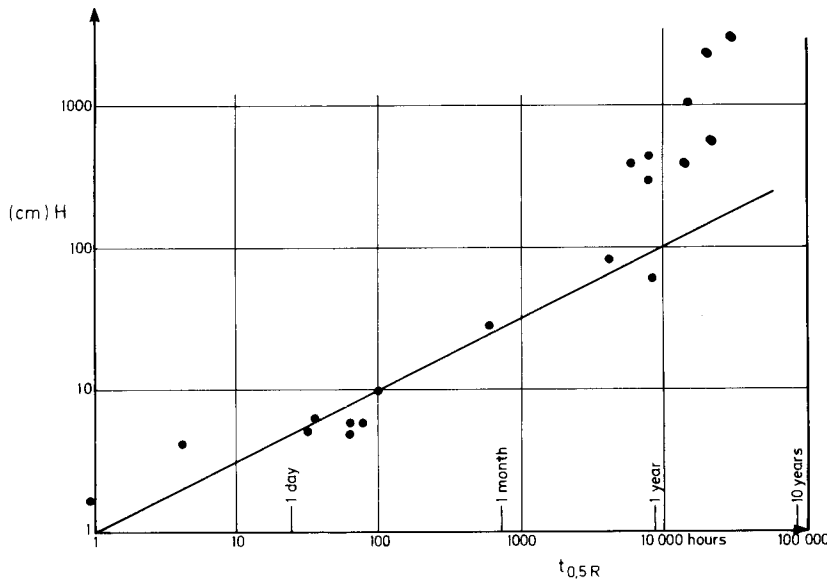
9.56 – Variation of CGR vs. half recovery dimensionless time  $t_{D,0.5R}$  (a) in terms of capillarity<sup>9</sup> (b) in terms of gravity<sup>9</sup>.

#### b. Role of block height and diameter.

Block height was examined in relation to half-recovery time after the experimental laboratory results were scaled to field conditions. Based on recovery versus dimensional time, the values of dimensional half-recovery time ( $t_{0.5R}$ ) were examined as a function of block height (fig. 9.57), which, through DuPrey's experiments reveals a linear relationship in the log-log scale. This results of limited linearity up to the heights of 1m, indicates that in this interval  $t_{0.5R} \propto H^2$ . The lack of continuity in this relationship in the case of  $H > 1m$  may be the result of difficulties in using a centrifuge type of experiment at very high acceleration  $a > 10g$ . In DuPrey's experiments, in conditions of a constant CGR, a faster recovery resulted for larger block diameters, but the experiments cannot be considered conclusive and further studies are necessary.

#### 9.4.5. Observations and conclusions on single block imbibition process

- a. Through use of theoretical analysis of the imbibition process and the experimental results, some satisfactory correlations were obtained.



9.57 — Variation of scaled reservoir block height  $H$  vs. dimensional time  $t$  (hours) of experiments carried out by du Prey<sup>9</sup> (courtesy AIME).

- b. Displacement is governed mainly by capillary forces in small blocks and by gravitational forces in large blocks.
- c. If capillary pressure is predominant, recovery time is proportional to the square root of the block height, while if gravity forces are predominant, recovery time is proportional to block height.
- d. Recovery versus dimensionless time  $t_{D,P_c}$  and  $t_{D,G}$  have shown an interesting similarity between theoretical analysis and experimental results. Evidently these results are less valid if the rock is very heterogeneous or if lithology and fluid characteristics interfere with the experiments on models.
- e. Simulation of behaviour of the large matrix blocks using a centrifuge proved to be a rapid and useful method; nevertheless, at very high speeds the centrifuge results lose their validity for simulation.
- f. Based on the results obtained through conventional and centrifuge imbibition tests, a significant step is developed for approaching a valid prediction of recovery in time for a single matrix block.
- g. The criticism of physical simulation and substitution by numerical methods appears logical at first sight. However, the fact is neglected that by using numerical methods the relative permeability curves are seldom sufficiently representative for a capillary-gravity governed flowing process.
- h. The complexity of processes which take place in the imbibition phenomenon suggests that both procedures, experimental (with scaling) and numerical techniques, must be further developed through additional comprehensive studies.

## 9.5. OTHER ASPECTS OF SINGLE BLOCK FLUID DISPLACEMENT

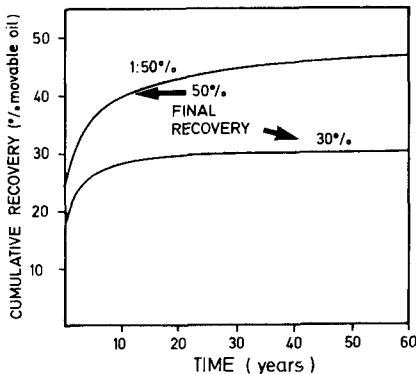
### 9.5.1. Drainage displacement

Oil drainage from the matrix by gravity, which occurs when the gas-cap advances, was discussed in sections 9.2.3. and 9.3.3. The displacement behaviour of a single block in drainage conditions can be calculated if block dimensions as well as rock and fluid characteristics are known.

It is of particular importance, to compare the block height ( $H_B$ ) with hold-up height ( $H_C$ ) and threshold ( $H_{TH}$ ) resulting from the capillary pressure curve.

If the rock is very poor and block heights small, the capillary height will be bigger than block height and so all the oil will be left in the matrix block (figure 9.18, 919, case of block C). If the block height is higher than capillary height, a recovery will be obtained until an equilibrium is reached between gravity and capillary forces. The oil left at the bottom of a block of height equal to capillary height represents the hold-up zone (figures 9.16 and 9.17), thus, only in highly permeable rocks having a low capillary pressure or in very tall blocks will a greater oil recovery be expected. Therefore, block height and capillary pressure are crucial parameters for designing the field performance.

A simulation was carried out by Saidi<sup>16</sup> for block height of  $H_B = 3\text{m}$ ,  $\Delta\sigma = 0.6\text{g/cm}^3$ ,  $\mu_o = 1\text{C.P.}$ ,  $(K_o)_{swi} = 1.26\text{mD}$ ,  $\Phi(1-S_{wi}) = 0.083$  and  $K_{or} = [S_o]^7$ . Recovery increases very rapidly to  $R_\infty$ , especially for lower final recovery values ( $R_\infty = 30\%$  compared with  $R_\infty = 50\%$  of movable oil). The results of the numerical models are shown in figure 9.58.



9.58— Recovery vs. time under gas-cap drainage displacement (Saidi<sup>16</sup>).

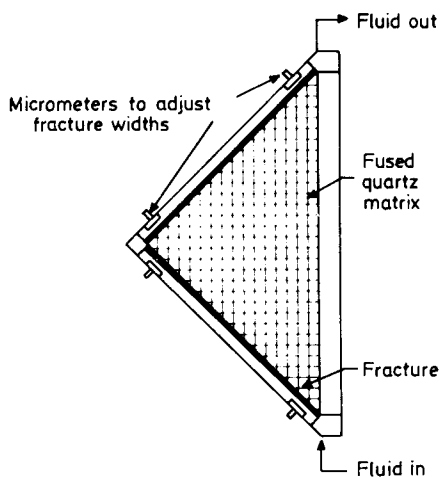
Gravitational drainage displacement can be simulated through use of the centrifuge, but a number of precautions must be taken into consideration. Since the maximum gravity potential will be at the top and not at the bottom of the matrix block, it is necessary to modify the core holder and to immerse the sample in an inert gas.

### 9.5.2. Production by water injection

The problem of water injection has been examined by various authors<sup>9 13 14 15</sup>, and in all the theoretical and experimental work the object was to evaluate the relationship between recovery and time, and water-cut versus cumulative injection. Various parameters have been considered to be the function of permeability – fracture-matrix ratio, pressure gradients, etc.

#### 9.5.2.1. Graham's model<sup>13</sup>

A laboratory investigation was performed on a sandstone block (figure 9.68) shaped as a right isosceles triangle 1 foot long and 1.5 inches thick. As a result of its symmetry, this triangle represents a half-square shape since the entrance and exit of fluids are at opposite corners.

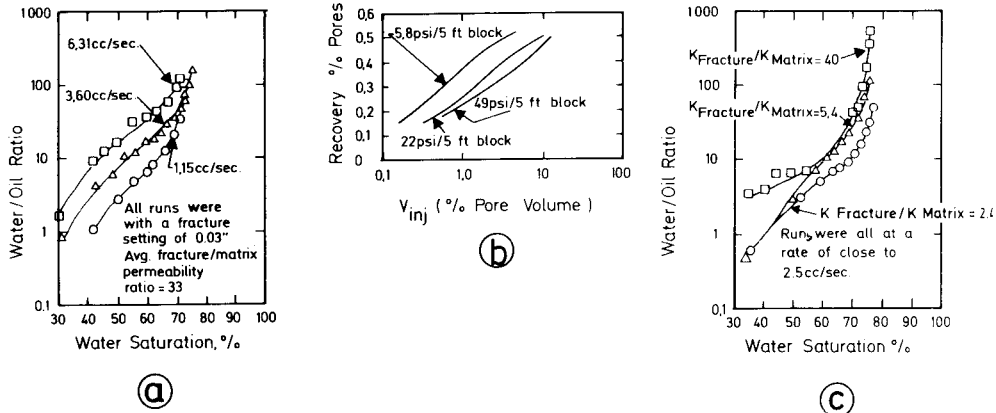


9.5x – Graham's<sup>18</sup> experimental model (courtesy AIME).

Experiments have demonstrated the following:

- a. The injected water-oil ratio versus water saturation (equivalent to desaturation in oil) was measured for the following three rates: 1.15cc/sec; 3.60cc/sec; 6.31cc/sec, and as observed, if the injection rate is high, it is necessary to inject more water in order to produce the same amount of oil (figure 9.60a).
- b. Similar results were obtained for pressure gradients.
- c. On the other hand, if recovery is expressed as percentage of pores versus water injection (% of pores), the result is that recovery is higher for low pressure gradients for the same amount of water injected. In a semi-log scale, recovery versus  $\log V_{inj}$ , the relationship is indicated by a straight line (figure 9.60b).

- d. The influence of matrix-fracture conductivity expressed by the permeability ratio  $K_f/K_m$  is observed in the early stages. After a certain amount of production (increased water saturation) the difference in recovery is not of much importance (figure 9.60). The water-oil ratio initially increases 3-fold in order to produce the same amount of oil, whereas the fracture-matrix permeability ratio increases 17-fold.



9.60 – Results of Graham's<sup>13</sup> experiments (a)  $Q_{inj}$  vs. WOR for constant fracture width (b) recovery vs.  $V_{inj}$  for various  $Q_{inj}$  ( $K = 0.2\text{mD}$ ;  $\Phi = 12\%$ ;  $K_f/K_m = 33$ ) (c) WOR vs.  $S_w$  for  $Q_{inj} = 2.5\text{cc/sec}$  and variable  $K_f/K_m$  ratios.

#### 9.5.2.2. Kleppe's model<sup>14</sup>

The results of Kleppe's experimental model were compared with the numerical model results. The block was formed by a Berea cylindrical sandstone having a diameter and height of 4 inches. During the imbibition displacement of oil, brine was injected at a constant rate into the lower part of the core.

The injection rates have been expressed dimensionless as a multiple of the gravitational rate (equation 9.12). This ratio may be written as follows:

$$Q_{ID} = \frac{Q_{inj}}{Q_{gravit}} = \frac{Q_{inj}}{\Delta \frac{K_o}{\mu_o B_o} \Delta \gamma} \quad (9.85)$$

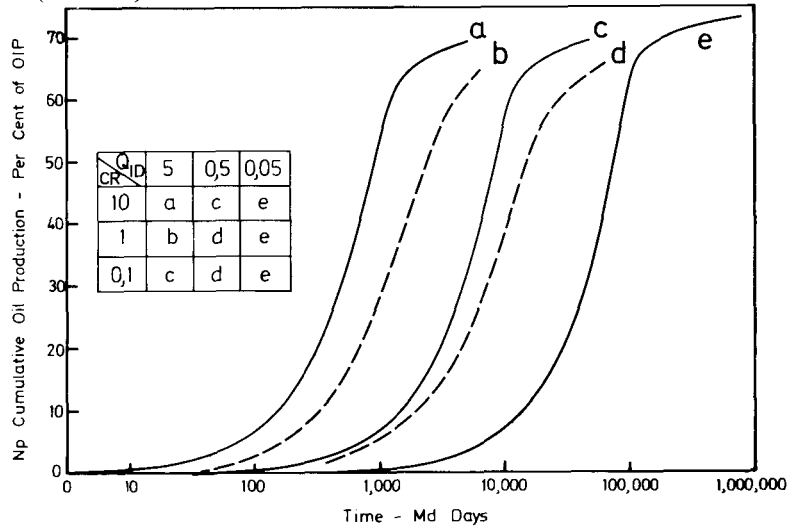
Three rates have been used:  $Q_{ID} = 0.05, 0.5$  and  $5$ . It was determined that when  $Q_{ID}$  was very small, the behaviour was similar to that of gravitational and capillary forces, but when  $Q_{ID}$  was large the displacement was controlled by injection pressure gradients.

Particular attention has been given to the conductivity ratio which expresses the fracture-matrix vertical permeability ratio,

$$CR = (K_f/K_m)_{\text{vertical}} \quad (9.86)$$

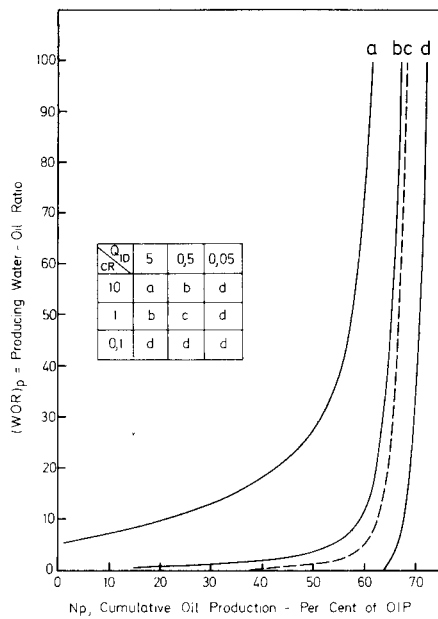
The ratios chosen were 10, 1 and 0.1 for wider to narrower fractures in the case of a constant matrix permeability. The results obtained are expressed in the figures mentioned below with the following information:

- a. Cumulative oil production versus time shown in figure 9.61 illustrates the classic «S» curve, where at any given time higher production is obtained for higher injection rates (comparison of curves a, c and e in case of constant CR = 10 and  $Q_{ID} = 5; 0.5$  and  $0.05$ ). Time is longer if the conductivity ratio diminishes for the same constant rate (for  $Q_{ID} = 5$  the variation effect of CR from 10 to 1 and 0.1 is shown in curves a, b, c). When using low rates and a low CR, imbibition will reduce to a classic porous medium under capillary-gravity imbibition (curve e).



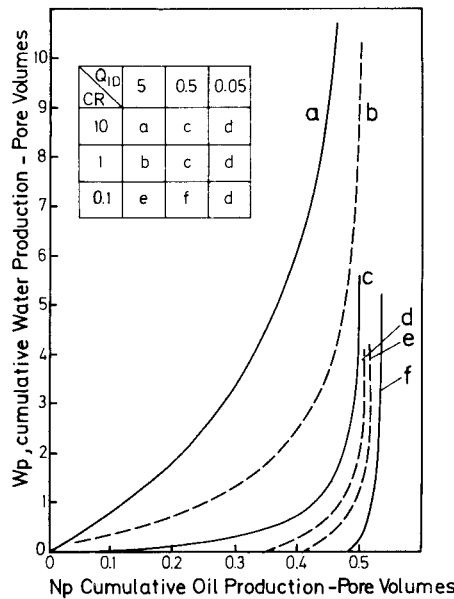
9.61] – NP vs. time for various  $Q_{ID}$  and CR (Kleppe<sup>14</sup>, courtesy AIME).

- b. The water-oil production ratio versus cumulative water production illustrates the risk of water breakthrough at an early stage if both  $Q_{ID}$  and CR are high. On the other hand, with a low CR and  $Q_{ID}$  it is possible to produce free-water oil recovery up to 60% (figure 9.62). In addition, for small  $Q_{ID}$  ( $Q_{ID} = 0.05$ ) independent of the magnitude of CR, or for a low CR ( $CR = 0.1$ ) independent of the magnitude of  $Q_{ID}$ , the result is the same (curve d).



9.62 – WOR vs. Np for various  $Q_{ID}$  and CR (Kleppe<sup>14</sup>, courtesy AIME).

- c. Cumulative water production versus cumulative oil production reinforces the statement that a moderate  $Q_{ID}$  and CR assumes a high recovery through free-water oil production (figure 9.63).

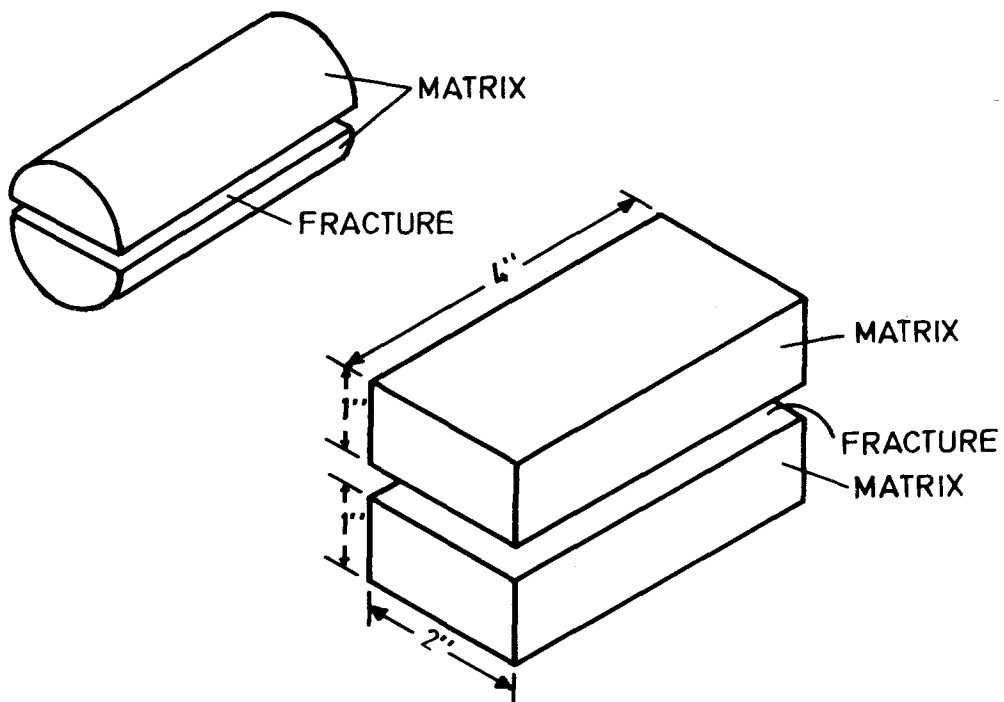


9.63 –  $W_p$  vs.  $N_p$  for various  $Q_{ID}$  and CR (Kleppe<sup>14</sup>, courtesy AIME).

### 9.5.2.3. Kazemi's model<sup>15</sup>

The experimental work carried out by Kazemi on artificially fractured cores was performed by cutting cylindrical cores or rectangular blocks along the fracturing plane (figure 9.64). The cylindrical cores measured 3 inches in length and 1 inch in diameter, while the rectangular blocks were 4 inches in length and 2"×2" square or 2"×1" rectangular. The cores were completely saturated with either oil or brine and water. The experiments have been conducted at low and high rates of water advancement in fractures and observations were as follows:

- a. at low rates of water advance in fractures (1 foot/day) imbibition prevailed and advancement in the matrix was faster than in fractures,
- b. at high rates of water advance in fractures (5 feet/day) and low capillary pressures, a breakthrough occurred much sooner in fractured rock than in non-fractured rock,
- c. oil recovery by imbibition is closely related to recovery by water flooding, and
- d. when water advanced in fractures, only in the case of 100% oil-saturated matrix was a lag time observed before the imbibition became fully effective. No similar observations were made in the case of water saturation present in the core.



9.64 – Kazemi's<sup>15</sup> experimental cores (a) cylindrical (b) rectangular.

## 9.6. OIL PRODUCED FROM A SINGLE BLOCK: THEORETICAL APPROACH

The previous sections have been devoted to oil production from a single block and the discussion was focused on the physical aspects of displacement of oil either by imbibition, e.g. water-oil displacement, or by drainage, e.g. gas-oil displacement.

The single block was considered to be homogeneous, and thus displacement was described accordingly by the equations of flow through homogeneous rocks.

In reality the problem is much more complex, since in a fractured reservoir the matrix block can exchange fluids only through the adjacent fractures. Therefore, along the direction of displacement the displacing fluid has the tendency to advance faster through the fractures than through the blocks due to a large inhomogeneity introduced by the fracture network. On the other hand, *the continuous penetration of the displacing fluid from the fracture into the blocks* has the tendency to reduce the difference in advancement velocity of the fluid in the two media: fractures and blocks.

The mutual dependence of the conditions governing the displacement in fractures and blocks requires a new approach to treatment of the problem of oil produced from the matrix blocks in a fractured reservoir. This approach is based on treatment of the fractured reservoir as a whole. Thus, the analytical treatment of a fractured reservoir is based on the *continuum* approach as formulated by Barenblatt<sup>18</sup>. In numerical simulators a discrete representation of the fractured reservoirs as individual fractures and blocks is also possible.

In the present section only the *continuum* approach will be presented while numerical simulators will be included in the following chapter.

### 9.6.1. Barenblatt's<sup>18</sup> continuum approach for simultaneous flow of immiscible fluids in fractured reservoirs

The *continuum* approach for one-phase flow through fractured reservoirs (chapter 7) was generalized to two-phase flow of immiscible fluids. The equations of flow are written for flow of each fluid through the constituent media of the fractured reservoirs – fractures and blocks; the transfer of the displacing fluid from the *fractures to blocks* and production of the displaced fluid from *blocks into the fractures* is represented by a source/sink term in the equations of conservation of mass, according to the law governing the displacement of fluid from the block, e.g. an imbibition function in water-oil displacement.

#### 9.6.1.1. Gas-oil displacement

The equations of flow for a gas-oil displacement from a fractured reservoir were formulated by Barenblatt<sup>18</sup> as follows:

The conservation of oil (subscript 0) in blocks (subscript 1) and fractures (subscript 2), is expressed as,

$$\frac{\partial}{\partial t} \left[ \Phi_1 \rho_o (P_1) S_{o1} \right] + \operatorname{div} \left[ \rho_o (P_1) \vec{U}_{o1} \right] + U_o^* = 0 \quad (9.87)$$

and

$$\frac{\partial}{\partial t} \left[ \Phi_1 \rho_o (P_2) S_{o2} \right] + \operatorname{div} \left[ \rho_o (P_2) \vec{U}_{o2} \right] - U_o^* = 0 \quad (9.88)$$

The conservation of gas (subscript g) in blocks and fractures, is expressed as,

$$\begin{aligned} \frac{\partial}{\partial t} & \left[ \Phi_1 \rho_g (P_1) S_{g1} + \Phi_1 \rho_o (P_1) R (P_1) S_{o1} \right] + \\ & + \operatorname{div} \left[ \rho_g (P_1) \vec{U}_{g1} \right] + U_g^* = 0 \end{aligned} \quad (9.89)$$

and

$$\begin{aligned} \frac{\partial}{\partial t} & \left[ \Phi_2 \rho_g (P_2) S_{g2} + \Phi_2 \rho_o (P_2) S_{o2} \right] + \\ & + \operatorname{div} \left[ \rho_g (P_2) \vec{U}_{g2} \right] - U_g^* = 0 \end{aligned} \quad (9.90)$$

where  $R$  is gas solubility and  $U^*$  are functions representing the transfer of fluid between the two media suggested by Barenblatt as,

$$U_o^* = \frac{sK_1 K_{r1} (S_o)}{\mu_o} \left[ \int_o^{P_1} \rho_o (P_1) dp_1 - \int_o^{P_1} \rho_o (P_2) dp_2 \right] \quad (9.91)$$

and

$$\begin{aligned} U_g^* = & \frac{SK_1 K_{r1} (S_o)}{\mu_o} \left[ \int_o^{P_1} \rho_o (P_1) dp_1 - \int_o^{P_2} \rho_o (P_2) dp_2 \right] - \\ & - \frac{SKK_{r1} (S_g)}{\mu_g} \left[ \int_o^{P_1} \rho_g (P_1) dp_1 - \int_o^{P_2} \rho_g (P_2) dp_2 \right] \end{aligned} \quad (9.92)$$

where  $s$  is a similar coefficient as in equation 9.90. No solution of these equations is known.

#### 9.6.1.2. Water-oil displacement

Bokserman, Zheltov and Kocheshkov<sup>6</sup> considered the equations of conservation of mass of oil and water in fractures to be,

$$\Phi_1 \frac{\partial S_{w2}}{\partial t} + \operatorname{div} \vec{U}_{w2} + U_w^* = 0 \quad (9.93)$$

and

$$-\Phi_1 \frac{\partial S_{o2}}{\partial t} + \operatorname{div} \vec{U}_{o2} + U_o^* = 0 \quad (9.94)$$

where  $U_w$  and  $U_o$  are Darcy's fluxes of water and oil, presented as follows, respectively,

$$\vec{U}_{w2} = - \frac{K_2 K_{rw2} (S_{w2})}{\mu_w} \operatorname{grad} \Psi \quad (9.95)$$

and

$$\vec{U}_{o2} = \frac{K_2 K_{ro2} (S_{o2})}{\mu_o} \operatorname{grad} \psi \quad (9.96)$$

Since the volume of the fracture system is very small *it is assumed that the total amount of water entering the fractures is consumed in the imbibition of the blocks.* In incompressible flow the volume of water entering the block equals the volume of oil produced in the fractures, and therefore  $u_w^* = -u_o^* = |u^*|$ . This source function is assumed as a known function of time resulting from experimental investigations.

Denoting the surface delimiting the volume  $V(t^*)$  imbibed by water by  $S(x_1, x_2, x_3, t^*)$ , one may obtain the unknown function  $t^*(x_1, x_2, x_3)$  from the following integral equation, expressing the balance of water imbibing the blocks of a fractured reservoir:

$$\int u_w^* [t - t^*(x_1, x_2, x_3)] dv = q(t) \quad (9.97)$$

The transfer function considered by Bokserman et al<sup>6</sup> is as follows:

$$U''(t) = \frac{A}{2} \Phi_1 S_1 \frac{s \sigma \cos \Theta \sqrt{K_1/\Phi_1}}{\mu_o} \left( t \frac{s^2 \cos \Theta \sqrt{K/\Phi_1}}{\mu_o} \right)^{-\frac{1}{2}} \quad (9.98)$$

where A is a constant coefficient.

Bokserman et al<sup>6</sup> present a solution for uni-dimensional water-oil displacement. In such a case the problem is reduced to the solution of the following integral and differential equations:

$$x_D(t^* = t_D) \\ \int_0^{x_D} U^* \left[ t_D - t^*(x_D) \right] dx_D = q(t_D) \quad (9.99)$$

and

$$-q(t_D) F'(S_w) \frac{\partial S_w}{\partial x} + \frac{\Phi_1 \sigma \cos \Theta \sqrt{K_1/\Phi_1}}{\mu_o} \frac{\partial S_w}{\partial t_D} + \\ + U^* \left[ t_D - t^*(x_D) \right] = 0 \quad (9.100)$$

where,

$$\left. \begin{aligned} X_D &= X/L \\ t_D &= t \sigma \cos \Theta \sqrt{K_1/\Phi_1} s^2 / \mu_o \\ F(S_w) &= K_{rw}(S_w) / \left[ K_{rw}(S_w) + (\mu_w / \mu_o) K_{ro}(S_w) \right] \\ U^*(t_D) &= (A/2) \Phi_2 S_w \left[ \sigma \cos \Theta s^2 \sqrt{K_2/\Phi_2} s^2 t_D^{\frac{1}{2}} / \mu_o \right] \end{aligned} \right\} \quad (9.101)$$

L is a reference length, e.g. the average size of the block.

The imbibition of a considered volume of block takes place during time  $t_{Di}$ , which provides the condition  $t_D - t^*(x) \leq t_{Di}$ .

The solution of equations 9.99 and 9.100 for a constant rate of flow  $q = \text{const}$  and initial conditions  $x_D = 0$  at  $t_D = 0$  is,

$$t^* = ax_D^2 \quad (9.102)$$

where,

$$a = \left( \frac{\pi A}{4q} \times \frac{s^2 \sigma \cos \Theta \sqrt{K_2/\Phi_2}}{\mu_o} \Phi_2 S_w \right)^2 \quad (9.103)$$

### 9.6.2. Braester theoretical approach

Braester<sup>19</sup> considered the equations of simultaneous flow of water and oil in a fractured reservoir, as a source function representing the displacement of oil from the blocks by imbibition, gravity and pressure gradients in the fractures. In addition, the model enabled flow of fluids through the blocks without displacement, i.e. exchange of the same kind of fluid between fractures and blocks as for one-phase flow (figure 4.51; chap. 4). Such an exchange can take place only in a region of the blocks saturated with the considered fluid. From this point of view, the flow of the same fluid through fractures and blocks in this model, may be regarded as a system of fractures connected in parallel to that region of the blocks saturated with the considered fluid. Increase in saturation of one kind of fluid in the blocks is similar to an increase in the effective permeability of the fracture system, and therefore the effective permeabilities for the fluxes in the fracture system include the average permeability of the fractured reservoir (fracture system and blocks) and a relative permeability, depending on saturation in both fractures and blocks.

For a system of fractures and blocks in parallel the average permeability of the reservoir is  $k = (k_1 B_1 + k_2 B_2)/(B_1 + B_2)$  where  $k$  and  $B$  represent the permeability and the width of the considered medium. Since  $B_2 \ll B_1$ , it results  $k \cong k_1 + k_2 B_2/B_1$ . In some reservoirs with large size blocks the contribution of the blocks ( $k_2 B_2/B_1$ ) to the total permeability may be important. Therefore, such a model may be valuable in cases of reservoirs of non-negligible average block permeabilities.

The equations of flow are as follows:

- Darcy's fluxes of water and oil in the fracture system:

$$\vec{U}_w = \frac{KK_{rw}(S_{w1}, S_{w2})}{\mu_w} (\text{grad } P_w - \rho_w - \rho_w \vec{g}) \quad (9.104)$$

$$\vec{U}_o = \frac{KK_{ro}(S_{w1}, S_{w2})}{\mu_o} (\text{grad } P_o - \rho_o \vec{g}) \quad (9.105)$$

– The equations of conservation of mass of fluids in fractures (subscript 2) and blocks (subscript 1) are:

$$\left. \begin{array}{l} \Phi_2 \frac{\partial S_{w2}}{\partial t} + \operatorname{div} \vec{U}_w - U^* = 0 \\ \Phi_2 \frac{\partial S_{w2}}{\partial t} + \operatorname{div} \vec{U}_o + U^* = 0 \\ S_{w2} + S_{o2} = 1 \end{array} \right| \quad \left. \begin{array}{l} \Phi_1 \frac{\partial S_{w1}}{\partial t} + U^* = 0 \\ \Phi_1 \frac{\partial S_{o1}}{\partial t} - U^* = 0 \\ S_{w1} + S_{o1} = 1 \end{array} \right\} \quad (9.106)$$

The considered source function is:

$$U^* = \frac{K_1 s}{\mu_w} \left[ - \frac{\partial P_w}{\partial s} + \frac{P_c}{L_1} - S_{w1} g \Delta \rho \right] F_1(S_{w1}) \times F_2(S_{w2}) \quad (9.107)$$

where  $L_1$  is the characteristic length of the block and  $F_1(S_{w1}) F_2(S_{w2})$  are functions of saturation in the media of blocks and fractures, respectively.

Substituting the equations 9.104, 9.105 and 9.107 into equation 9.106 gives,

$$\left. \begin{array}{l} \Phi_1 \frac{\partial S_w}{\partial t} + \operatorname{div} \left\{ \left[ \vec{U} - (K K_{ro}/\mu_o) (g \Delta \rho \operatorname{grad} Z + \right. \right. \right. \\ \left. \left. \left. + \operatorname{grad} P_c \right) Z_w \right] - U_w^* = 0 \right\} \\ \Phi_1 \frac{\partial S_w}{\partial t} - U^* = 0 \end{array} \right\} \quad (9.108)$$

where,

$$\left. \begin{array}{l} f_w = 1 / (1 + K_{ro} \mu_w / K_{rw} \mu_o) \\ \vec{U} = \vec{U}_w + \vec{U}_o \\ \Delta \rho = \rho_w - \rho_o \end{array} \right\} \quad (9.109)$$

A solution to equation 9.108 for uni-dimensional water-oil horizontal displacement by neglecting the capillary pressure in the medium of fractures was given.<sup>19</sup> In such a case equation 9.108 can be rewritten as,

$$\left. \begin{array}{l} \Phi_2 \frac{\partial S_{w2}}{\partial t} + U \frac{\partial f_w}{\partial S_{w2}} \frac{\partial S_{w2}}{\partial x} + U \frac{\partial f_w}{\partial S_{w1}} \frac{\partial S_{w1}}{\partial x} + U^* = 0 \\ \Phi_1 \frac{\partial S_{w1}}{\partial t} - U^* = 0 \end{array} \right\} \quad (9.110)$$

and,

$$U = U_w + U_o = K \left( \frac{K_{rw}}{\mu_w} + \frac{K_{ro}}{\mu_o} \right) \frac{\partial P}{\partial x} = - K \frac{K_{rw}}{\mu_w} \frac{1}{f_w} \frac{\partial P}{\partial x}$$

Equation 9.110 represents a quasi-linear hyperbolic system of equations with  $S_{w_1}$  and  $S_{w_2}$  as unknowns. The appropriate method to obtain a solution of these equations is through characteristics.

The slopes of the characteristics of the set of equations in 9.110 are,

$$m_\alpha = (dx/dt)_\alpha = \frac{U_o}{\Phi_2} \frac{\partial f_w}{\partial S_{w_2}} \quad (9.111)$$

$$m_\beta = (dx/dt)_\beta = 0$$

In characteristic coordinates, the equations in 9.110 become,

$$\frac{\partial x}{\partial \alpha} - \frac{U}{\Phi_2} \left( \frac{\partial f_w}{\partial S_{w_2}} \frac{\partial t}{\partial \alpha} \right) = 0 \quad (9.112)$$

$$\frac{\partial f_w}{\partial S_{w_2}} \cdot \frac{\partial S_{w_2}}{\partial \alpha} + \frac{\partial f_w}{\partial S_{w_1}} \cdot \frac{\partial S_{w_1}}{\partial \alpha} + \frac{u^*}{\mu} \left[ \left( 1 - \frac{\Phi_2}{\Phi_1} \frac{\partial f_w}{\partial S_{wi}} \right) \cdot \left/ \frac{\partial f_w}{\partial S_{w_2}} \frac{\partial x}{\partial \alpha} \right. \right] = 0$$

on  $\beta = \text{constant}$

The boundary and initial conditions considered were,

$$\begin{aligned} t &= 0 & S_{w_2} &= S_{wi2} = 0 \\ &\quad 0 \leq x \leq L & S_{w_1} &= S_{wi1} = 0 \\ x &= 0 & U &= U_w = \text{const.}, S_{wz} = 1 \end{aligned} \quad (9.113)$$

where  $S_{wi}$  is the irreducible water saturation.

In impervious blocks the fractured rock is reduced to a conventional homogeneous reservoir. As known, in such a case there is an inflection point in the function  $f_w(S_w)$  for water-oil displacement.

In a fractured reservoir,  $f_w$  is a function of both  $S_{w_1}$  and  $S_{w_2}$  saturations. In the  $f_w(S_w)$  plane for a constant saturation in the blocks the function  $f_w$  preserves its general shape. It must also consider in the present case an inflection point in the  $f_w(S_{w_1}, S_{w_2})$  curves.

With an inflection point in the  $f_w$  curve and initial conditions (equation 9.113), three families of characteristics are obtained which lead to a multiple solution to the saturations.

For a homogeneous reservoir a front (a jump in saturation) is introduced to avoid the multiple solution. The jump conditions determined from the equations of conservation of mass through the front are,

$$V_{fz} = \frac{U}{\Phi_2} = \frac{f_w^+ - f_w^-}{S_{w_2}^+ - S_w^-} \quad (9.114)$$

and

$$V_{f1} = 0 \quad \text{or} \quad S_{wi}^+ = S_{wi}^- \quad (9.115)$$

where  $v_f$  is the velocity of the front and the (+) sign denotes the values of the parameters before the front, and the (-) sign denotes the values behind the front.

For the initial conditions considered (equation 9.113) the jump in saturation  $S_{w2}$  is determined from the equation,

$$\left. \frac{\partial f_w}{\partial S_w} \right|_{S_{w2} = \bar{S}_{w2}} = \frac{f_w(S_{w2}, S_{w1t}) - f_w(S_{w1t}, S_{w12})}{S_{w2} - S_{w12}} \quad (9.116)$$

Since  $(\Phi_2/\Phi_1)(\partial f_w/\partial S_{w1}) / (\partial f_w/\partial S_{w2}) \ll 1$  in the third term of the third group of equations in 9.112, and defining the dimensionless parameters,

$$x_D = x/L; t_D = t(\kappa_1/\Phi_1)^{1/2} \sigma/\mu_w L_1^2; U_D = U/L \Phi_2$$

$$U_D^* = U^*/\Phi_2 \left[ (\kappa_1/\Phi_1)^{1/2} \sigma/\mu_w L_1^2 \right]$$

The group of equations 9.112 may be rewritten as,

$$\begin{aligned} \partial x_D / \partial t_D - U_D \sigma f_w / \sigma S_w &= 0 && \text{(on } \beta = \text{ const)} \\ \partial x_D / \partial t_D &= 0 && \text{(on } \alpha = \text{ const)} \\ \partial f_w / \partial x_D + (\Phi_1/\Phi_2) U_D^* / U_D &= 0 && \text{(on } \beta = \text{ const)} \\ \partial S_{w1} / \partial t_D - U_D^* &= 0 && \text{(on } \alpha = \text{ const)} \end{aligned} \quad (9.117)$$

Fractured reservoir behaviour was investigated by solving equations 9.117 for particular values of the functions involved in the equations.

The considered expressions for the relative permeabilities, capillary pressure, and the source function were,

$$\begin{aligned} K_{ro} &= \left[ \frac{K_2}{K} + (1 - \frac{K_2}{K})(1 - S_{w1}^*) (1 - S_{w1})^2 \right] (1 - S_{w2})^2 (1 - S_{w2}^2) \\ K_{rw} &= \left[ \frac{K_2}{K} + (1 - \frac{K_2}{K}) S_{w1}^4 \right] S_{w2}^4 \\ P_{c1} &= \sigma F(\Theta_c) J(S_{w1}) / (\kappa_1/\Phi_1)^{1/2} \end{aligned} \quad (9.118)$$

$$U^* = sF_2(S_{w2}) \left[ \frac{K_1}{K} \frac{f_w}{K_{1w}} F_1(S_{w1}) U + \frac{(\kappa_1/\Phi_1)^{1/2} \sigma F(\Theta_c)}{\mu_w L_1} J(S_{w1}) F(S_{w1}) \right]$$

If in the group of equations 9.118 a logarithmic relationship  $J(S_{w2})$  is introduced in the last equation, the result will be,

$$\frac{(\kappa_1/\Phi_1)^{1/2} \sigma F(\Theta_c)}{\mu_w L_1} J(S_{w1}) F(S_{w1}) = \frac{(\kappa_1/\Phi_1)^{1/2} \sigma F(\Theta_c)}{\mu_w L_1} C_1 S_{w1}^{-1}$$

which is identical to Bokserman's<sup>6</sup> assumption based on Mattax's<sup>4</sup> and Kyte's<sup>7</sup> experiments.

As for the functions  $F_2(S_{w2})$  representing the influence of the water saturation in the fracture on oil displaced from matrix under imbibition effects, the relationship was assumed linear, expressed as,

$$F_2(S_{w2}) = C_2 S_{w2}$$

$C_1$  and  $C_2$  being constant values. Numerical values of the parameters are given in the following example:

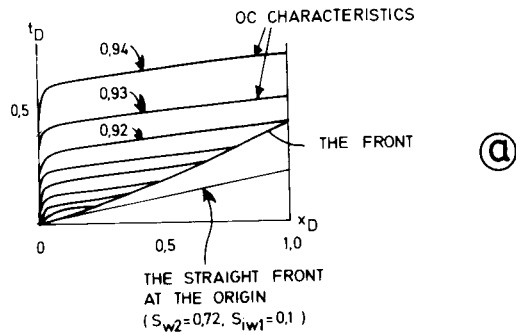
### EXAMPLE

Based on the data<sup>19</sup> presented in the table

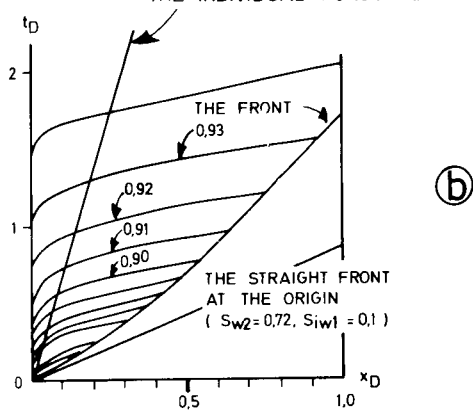
Parameter	Value
Length of the horizontal column ( $L$ )	50 m
Characteristic length of the block ( $L_2$ )	25 cm
Specific surface of the block ( $sA_2$ )	0.04 cm <sup>-1</sup>
Porosity of blocks ( $\Phi_1$ )	0.15
Porosity of fissures ( $\Phi_2$ )	0.02
Permeability of the porous fissured medium ( $k$ )	75 md
Permeability of the fissure system ( $k_2$ )	25 md*
Permeability of the blocks ( $k_1 - k - k_2$ )	50 md
Relative permeabilities ( $k_{ro}, k_{rw}$ )	Eqs. 32
Leverett function $J(S_{w2})$	$J(S_{w1}) - \ln S_{w2}$
Viscosity of water ( $\mu_w$ )	1 cp
Viscosity of oil ( $\mu_o$ )	4 cp
Interfacial tension ( $\sigma$ )	25 dyne/cm
Irreducible saturation of water in fissures ( $S_{wi2}$ )	0
Irreducible saturation of water in the blocks ( $S_{wi1}$ )	0
Constant ( $C$ )	$2 \times 10^{-3}$
Function of contact angle [ $F(\theta_c)$ ]	0.8

\*The permeability of the fissure system is defined in the introduction as an average over the whole system.

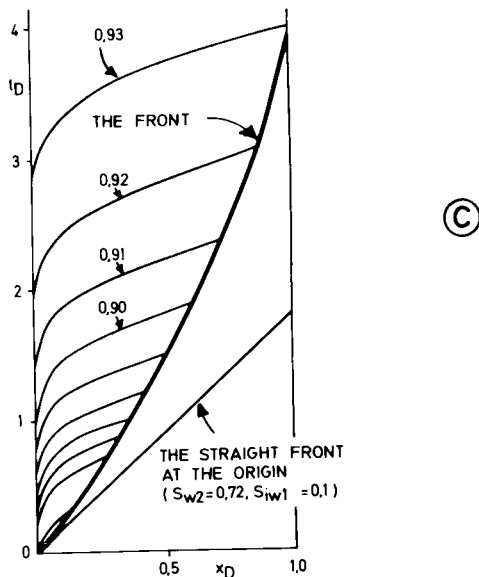
The results of numerical computation are presented in figures 9.65 and 9.66. Figure 9.65 illustrates the advance of the water front in the fracture in the  $(x_D, t_D)$  plane for different rates of injection  $u_D$ . As observed, at the origin the front begins with a slope equal to the slope of the front of a homogeneous medium with equivalent properties to those of the fracture system. Then the front bends and the velocity of the front decreases in time, reflecting the loss of water from fractures into the blocks.



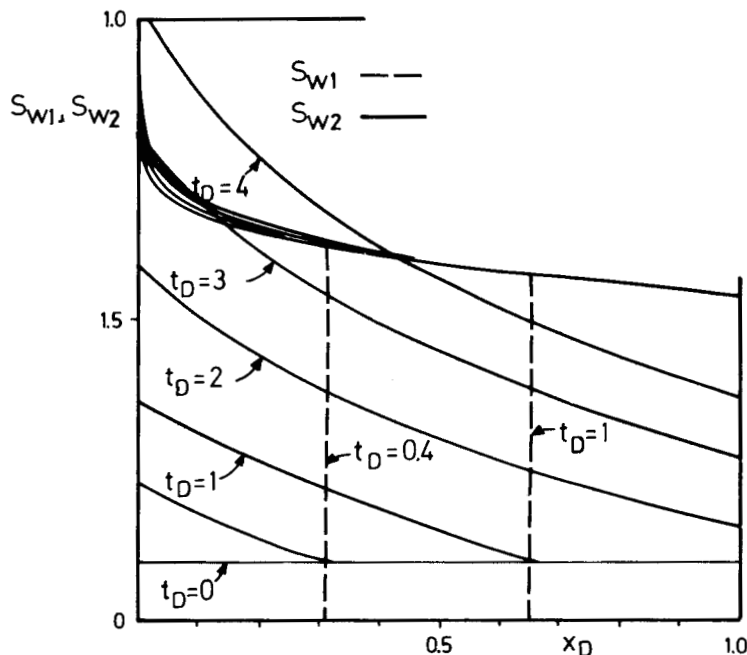
THE STRAIGHT FRONT ( BUCKLEY - LEVERETT )  
FOR A HOMOGENEOUS MEDIUM WITH  
PROPERTIES EQUIVALENT TO THOSE OF  
THE INDIVIDUAL POROUS BLOCKS.



9.65 – Graphical representation of the  $\alpha$  characteristics and the front for (a)  $\mu_D = 2.5$ ; (b)  $\mu_D = 1$  and (c)  $\mu_D = 0.6$  (Braester<sup>12</sup>, courtesy AIME). (Values on the Characteristics indicate the corresponding values of the saturation  $S_{w2}$  at the origin).



This decrease in velocity is a function of the rate of injection  $u_D$ .



9.66 – The saturation distribution in the medium of blocks and fractures for  $\mu_D = 1.25$  (Braester<sup>18</sup>, courtesy AIME).

After a certain time the velocity of the front in the fracture becomes approximately constant, i.e. the transition zone in the fracture system stabilizes.

In the medium of blocks the saturation profile changes gradually. Due to the small porosity of the fracture system the average saturation of the fractured reservoir can be approximated by the saturation of the medium of blocks. Therefore, one may conclude that in contradistinction with a conventional homogeneous reservoir, the transition zone of a fractured formation spreads over a large length of the reservoir (fig. 9.77).

The function used in the numerical computation cannot be determined experimentally. Despite the synthetic data used, the model and solution contribute to a better understanding of the qualitative behaviour of the fractured reservoir.

The Buckley-Leverett<sup>20</sup> solution for water-oil displacement at a constant rate from a homogeneous reservoir is obtained from the above solution by considering the blocks as impervious. In such a case the fracture system plays the role of the interconnected voids, and the blocks act as solid grains.

## SYMBOLS

### Latin letters

A	— constant
a	— velocity
B	— constant
CGR	— capillary/gravity ratio
d	— pore diameter
f	— function
G	— gravity
g	— gravity
H	— height
J	— Leverett function
k	— permeability
l	— length
M	— mobility
N	— number of rotations
P	— pressure
R	— recovery
s	— coefficient
SF	— shape factor
t	— time
U	— velocity, rate
V	— velocity
Z	— distance along axis OZ

### Greek letters

$\alpha$	— reference to equation
$\Delta$	— difference
$\delta$	— difference
$\Phi$	— potential
$\gamma$	— specific weight
$\mu$	— viscosity
$\pi$	— dimensionless parameter
$\beta$	— reference to equation
$\varrho$	— specific mass
$\Sigma$	— summation
$\sigma$	— interfacial tension
$\theta$	— angle

## SUBSCRIPTS

B	- block
c	- capillary
cr	- critical
displ.	- displacement
f	- fracture
g	- gas
gravit	- gravity
i	- index
inj.	- injection
m	- model
nw	- non-wetting
o	- oil
o, max	- oil maximum
og	- oil-gas
or	- oil residual
R	- reservoir
rnw	- relative non-wetting
ro	- relative oil
rw	- relative water
t	-- total
TH	- threshold
k	- water
wi	- water interstitial
wo	- water oil
x	- direction along ox axis
$\infty$	- for very long time
1	- matrix
2	- fractures

## REFERENCES

1. Muskat, M., 1949. Physical principles of oil production. McGraw-Hill Book Co., Inc., New York.
2. Birks, T., 1955. A theoretical investigation into the recovery of oil from fissured limestone formations by water drive and gas-cap drive. Proc., Fourth World Petroleum Congress, Section II/F, Paper 2.
3. Leverett, M.C., 1940. Capillary behaviour in porous solids. Trans. AIME, 152-159.
4. Mattax, C.C. and Kyte, J.R., 1972. Imbibition oil recovery from fractured water drive reservoir. Soc. Pet. Eng. J. (June), 177-184. Trans. AIME, Vol. 225.
5. Aronofsky, J.S., Massee, L. and Natanson, S.G., 1958. A model for the mechanism of oil recovery from the porous matrix due to water invasion in fractured reservoirs. Trans. AIME, Vol. 213, 17.
6. Bokserman, A.A., Zheltov, Y.P. and Kocheshkov, A.A., 1964. Motion of immiscible liquids in a cracked porous medium. Soviet Physics Doklade (Oct). Vol. 9, No. 4, 285.
7. Kyte, J.R., 1970. A centrifuge method to predict matrix block recovery in fractured reservoirs. Soc. Pet. Eng. J. (June), 164-170.

8. Rapoport, L.A., 1955. Scaling laws for use in field and operation of water-oil flow models. Trans. AIME, Vol. 204, 143.
9. Lefebure du Prey, E., 1978. Gravity and capillarity effects on the matrix imbibition in fissured reservoirs. Soc. Pet. Eng. J. (June), 195-205.
10. Parsons, R.W. and Chaney, P.R., 1966. Imbibition model studies on water-wet carbonate rocks. Soc. Pet. Eng. J. (March), 26-34.
11. Ifly, R., Rousselet, D.C. and Vermeulen, J.L., 1972. Fundamental study of imbibition in fissured oil fields. Paper SPE 4102 presented at the SPE-AIME 47th Annual Fall Meeting, San Antonio, Tex., Oct.
12. Blair, P.M., 1960. Calculation of oil displacement by countercurrent water imbibition. Paper 1475-G presented at the Fourth Biennial Secondary Recovery Symposium of SPE in Wichita Falls, Tex., May.
13. Graham, J.W. and Richardson, T.G., 1950. Theory and application of imbibition phenomena in recovery of oil. Trans., AIME, 216, 377-385.
14. Kleppe, J. and Morse, R.A., 1974. Oil production from fractured reservoirs by water displacement. Paper SPE 5034 presented at the SPE-AIME 49th Annual Fall Technical Conference and Exhibition, Houston, Tex., Oct.
15. Kazemi, H., 1979. Numerical simulation of water imbibition in fractured cores. Soc. Pet. Eng. J. (June), 175-276.
16. De Swaan, A., 1978. Theory of waterflooding in fractured reservoirs. Soc. Pet. Eng. J. (April), 117-226.
17. Saidi, A.M. and Tehrani, D.H., 1980. Mathematical simulation of fractured reservoir performance, based on physical Mobil experiments. 10th World Oil Congress, P.D. 10.
18. Barenblatt, G.I., 1964. On the motion of a gas-liquid mixture in a porous fissured medium. Mekhanika I Mashinostroismic Izvestial Akademii Nauk USSR, No. 3, 47-50.
19. Braester, C., 1972. Simultaneous flow of immiscible liquids through porous fissured media. Soc. Pet. Eng. J. (Aug), 297-305.
20. Buckley, S.E. and Leverett, M.C., 1942. Mechanism of fluid displacement in sands. Trans., AIME, 146, 107-116.

This Page Intentionally Left Blank

# CHAPTER 10

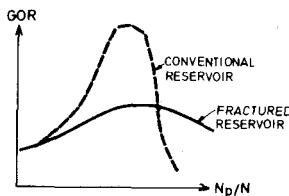
## PRODUCTION MECHANISM OF A FRACTURED RESERVOIR

### 10.1. INTRODUCTION

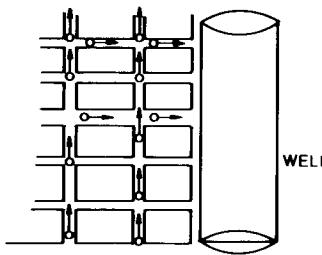
Reservoir engineers often try to predict the future behaviour of a fractured reservoir by examining its past history and estimating its future behaviour through *conventional reservoir approaches* and procedures. But, unfortunately, very seldom will the behaviour resulting through conventional reservoir calculation procedures match with the real past history of a fractured reservoir. A matching may be obtained only modifying the basic data to a completely unrealistic extent. Thus, an example, a matching may be obtained *artificially* by increasing by several times the volumetric oil in place. The impossibility of a *valid matching* when the methods of predicting a conventional reservoir are used for a fractured reservoir is a direct result of *specific production mechanisms* which develop in a fractured reservoir due to fracture-matrix characteristics.

These differences can be understood by comparing the behaviour of a conventional reservoir where fluid and rock characteristics are in the same range of magnitude as a fractured reservoir but where in addition a network of fractures of very different characteristics is extensively developed throughout the reservoir. Some of these results are discussed below.

- *The reservoir gas-oil ratio, GOR vs. recovery*, is substantially lower in a fractured reservoir than in an unfractured reservoir (figure 10.1). This behaviour is due to the liberated gas, which will rapidly segregate towards the top of the reservoir through fractures instead of flowing towards the well (figure 10.2). The segregation of gas during the flow of fluid toward the wellbore is possible since the pressure drop in the fracture network is generally very small. Consequently, pressure gradients supporting the movement of fluid toward the wellbore are below gravity gradient, especially far from the wellbore surroundings.

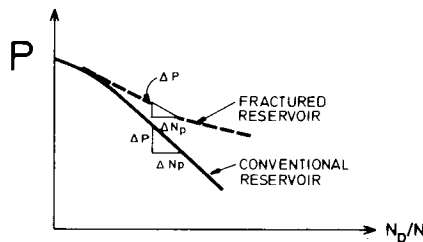


10.1 – Comparison of GOR vs. Recovery in a conventional and a fractured reservoir.



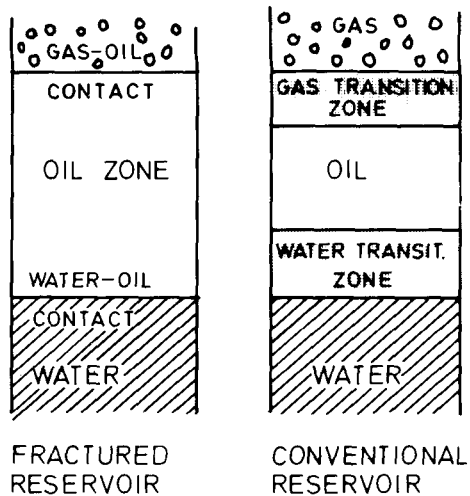
10.2 – Tendency of gas to flow towards top of reservoir through fractures.

- The rate of pressure decline per unit of oil produced ( $\Delta P/\Delta N_p$ ) is normally low in a fractured reservoir (figure 10.3). Such improved behaviour in a conventional reservoir may be obtained only if a large amount of produced gas should be reinjected. Comparing two identical reservoirs of which one is fractured and the other is not, the conventional reservoir may show a similar behaviour to that of a fractured reservoir if up to 80% of produced gas has been reinjected. The explanation of this improved behaviour in a fractured reservoir is the result of new types of production mechanisms which take place in a double porosity system. These mechanisms assure a great supply of fluids from matrix toward fractures as a result of gravity and imbibition combined with fluid expansion, segregation, convection, etc.



10.3 – Reservoir decline ( $\Delta P/\Delta N_p$ ) behaviour in a conventional and a fractured reservoir

- The absence of transition zones in a fractured reservoir represents a specific characteristic of this reservoir. In fact, the two-phase contact of water-oil or gas-oil is represented in a fractured reservoir by distinct separation surfaces and not by large transition zones as in a conventional reservoir (figure 10.4). In a fractured reservoir the two-phase contact is sharp and horizontal in static or dynamic conditions since the transmissivity in a fractured network is high due to large permeability of fractures, and any change in level is rapidly reequilibrated. On the contrary, in a conventional reservoir the transition zone may be large in static conditions and thus will remain so in dynamic conditions too.



10.4 – Schematisation of water-oil and gas-oil contact in a conventional and a fractured reservoir

- Pressure drop around a producing well in a fractured reservoir is very low, since the high permeability of the fractures even for very high well rates does not call for significant pressure drop. The resulting small pressure gradients are sufficient for transportation of oil through fractures, but are too small to control the exchange of fluid between matrix and fractured network. Thus, the production process of the matrix block is controlled by the specific producing mechanisms which are developed as a result of different fluid saturations of fractures and matrix blocks (where capillary and gravity play a substantial role), and not by pressure gradients resulting from producing wells.
- The free-water oil production in a fractured reservoir is essentially a function of production rate, while in a conventional reservoir free water-oil production depends on rock characteristics, PVT characteristic distribution, and also on production rate.
- Constant PVT properties with depth usually occurs in a fractured reservoir if a convection process takes place as a result of thermal expansion and fluid compression conditions inside the reservoir. The constant PVT properties with depth are totally different from the general behaviour of a conventional sandstone reservoir where a variable bubble point always results from PVT analysis of oil samples taken at various depths.

As a result of these specific aspects of a fractured reservoir where the production behaviour is so different from that of a conventional sandstone reservoir, a detailed examination of the production mechanism as presented in the following sections becomes necessary.

## 10.2. RESERVOIR DESCRIPTION DURING DEPLETION

In the absence of a largely distributed fracture-fissure network, low-permeability reservoirs are practically unrecoverable, but the presence of fractures transforms them into excellent reservoirs. The fractures assure the flow of hydrocarbons from the matrix where those hydrocarbons are stored to wells from which they will be later lifted to the surface. In general, the fractured network is divided into a number of zones, each of them practically saturated with only one phase, while inside each zone the matrix block may be saturated with one, two or even three phases. A given reservoir zonation will already exist before reservoir production begins (under static equilibrium) and another zonation will result from reservoir production conditions during field exploitation (dynamic state). The matrix-fracture *interaction* and fluid exchange will depend on the relative position of the single block in the reservoir and the respective water-oil and gas-oil contact.

### 10.2.1. Reservoir zoning

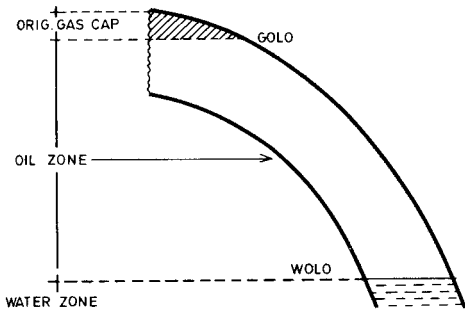
As previously mentioned, the division of a reservoir into zones depends essentially on the fractured network saturation. The magnitude of the three essential zones of water, oil and gas is therefore associated with the water-oil contact and gas-oil contact in the fractured network.

Sub-zones may also develop during the production of the reservoir, as a result of fluid equilibrium inside the matrix block as well as fluid exchange between matrix and fracture.

The extension of zones and subzones is continuously changing during reservoir production due to the exchange of matrix-fracture fluid, fluid segregation in fractures, changes in phases provoked by gas liberation, fluid produced from reservoir, etc.

#### 10.2.1.1. Reservoir zoning under static conditions

A fractured oil reservoir may have an oil, water and gas-cap zone before any production begins (figure 10.5), in agreement with the fracture saturation distribution. The original limits are then represented by GOLO (original gas-oil level) and WOLO (original water-oil level). Both limits provide the static equilibrium of the three phases — water, oil and gas — inside the fractured network and between the fractured network and matrix blocks. The two-phase contacts in the fractured network are always sharp, distinct and horizontal, as schematically shown in figure 10.6a.



10.5 – Vertical cross-section in a fractured reservoir and fluid zonation in static condition

FIG. 10.5

Originally, the pressure distribution is schematised as in figure 10.6b where the bubble point pressure  $B_{pp}$  is constant throughout the reservoir and thus constant with depth. At the level of gas-oil contact (GOLO) the initial static pressure ( $P_{si}$ ) is equal with bubble point pressure ( $B_{pp} = P_{si}$ ). The pressure increases with depth from the gas-oil limit towards the water-oil limit with a gradient equivalent to oil density (figure 10.6b), and thus the pressure difference  $P_{si} - B_{pp}$  is increasing with the depth.

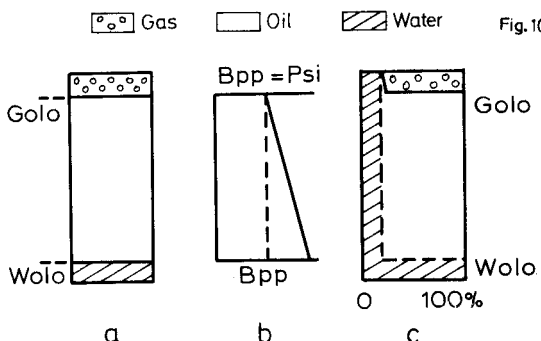


Fig. 10.6

10.6 – Schematisation of zones under static reservoir conditions: a) zone distribution  
b) pressure distribution c) matrix saturation distribution

The fluid saturation distribution in the fracture-matrix system is schematically shown in figure 10.6c. The saturation takes into consideration the overall saturation of the reservoir formed by the matrix-fracture pores. Thus, the interstitial saturation of matrix pores is represented in the oil zone and gas zone.

Initially, the oil zone may then be considered to be between GOLO and WOLO. Below WOLO the matrix pores are saturated with water, while between WOLO and GOLO the matrix blocks are saturated with oil and interstitial water and the fractures with oil only. Above GOLO, gas saturates the fractures, and gas with interstitial water saturates the matrix.

#### 10.2.1.2. Reservoir zones under dynamic conditions

When the reservoir begins to be produced the initial static reservoir pressure  $P_{si} = B_{pp}$  is reduced to a lower static pressure  $P_s < B_{pp}$ . The depletion of the oil zone and the consequent expansion of the gas-cap and aquifer will modify the levels of GOLO and WOLO to new levels of GOL and WOL (figure 10.7a).

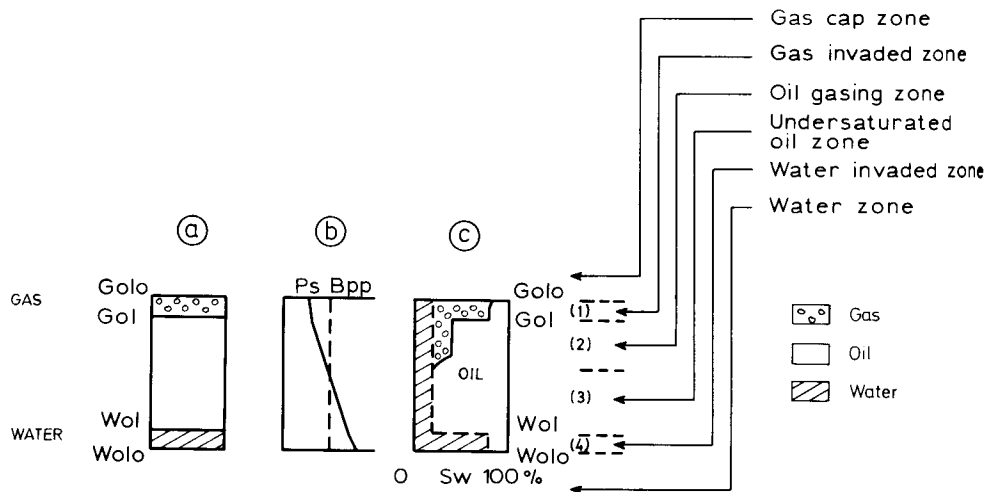
### a. Main zones.

The following main zones will result and are illustrated in figure 10.7a:

- a water-invaded zone between WOLO and WOL
- a gas-invaded zone between GOLO and GOL
- an oil zone between WOL and GOL

In addition it is possible to develop sub-zones inside the oil zones as a result of reservoir pressure decline. As observed in figure 10.7b, the pressure decreasing below original pressure, at the level of gas-oil contact (GOLO) will no longer equal bubble point pressure ( $P_s = B_{pp}$ ) but will decrease below bubble point pressure ( $P_s < B_{pp}$ ).

Pressure will increase with depth in the gas-invaded zone as a function of gas density, while in the oil zone pressure will increase with depth with a gradient related to the oil density. At a given depth below GOL level the  $B_{pp}$  will intersect with reservoir pressure  $P_s$  and there pressure  $P_s = B_{pp}$ . Below this point  $P_s > B_{pp}$  and the pressure increases with depth as a function of oil density until the water-oil limit WOL. Below the WOL level in the water-invaded zone, the pressure varies with depth as a function of water density (figure 10.6b).



10.7 – Schematisation of zones under dynamic reservoir conditions: a) zone distribution through fluid contact in fractures b) pressure vs. depth in reservoir and relationship  $P_s$  vs.  $B_{pp}$  c) saturation distribution in matrix.

### b. Sub-zones

As a result of pressure variation with depth the oil zone may be divided into two additional zones:

- the gassing zone, between GOL and  $P_{ss} = B_{pp}$  (figure 10.7)
- the undersaturated zone, between  $P_s = B_{pp}$  and WOL (figure 10.7).

Upon a more detailed examination of these two zones the following may be stated:

– In the *gassing zone*, because the reservoir pressure is below the bubble point pressure, a volume of gas will be liberated from the oil. The driving mechanism will be influenced in this case by the presence of free gas in matrix blocks and in the oil saturated fractured network. The fluid interchange between matrix and fractures will become a complex process influenced by gravity and capillary pressures and developing phenomena of convection, supersaturation, etc. The phenomena taking place in a fractured reservoir are substantially more complex than the equivalent solution gas drive in a conventional reservoir.

– In the *undersaturated zone*, as a result of reservoir pressure being higher than bubble point pressure ( $P > B_{pp}$ ), the entire fracture-matrix system is saturated with only one movable phase, oil. The matrix-fracture fluid interchange is the unique result of fluid expansion associated to reservoir depletion and compressibility of the fracture-matrix system fluids and rock.

### c. Saturation distribution

The four zones in a fractured reservoir (gas-invaded zone, gasing zone, undersaturated zone and water-invaded zone) show the following saturations (figure 10.7c):

– In the *gas-invaded zone* the gas saturation increases to a value equivalent to  $S_g = 1 - S_{wi} - (Sor)_g$ . The magnitude of residual oil ( $Sor$ )<sub>g</sub> depends on conditions of gas front advancement (figure 10.7c) and on specific characteristics of drainage displacement. The volume of gas in the invaded zone refers to pore volume of the matrix between GOLO and GOL.

– In the *oil gassing zone* the saturation in gas corresponds to the oil recovered from the matrix as a result of reservoir pressure decline below bubble point pressure. The oil remaining in this zone at a given stage of reservoir depletion is expected to be substantially higher than the residual oil in the gas-cap zone.

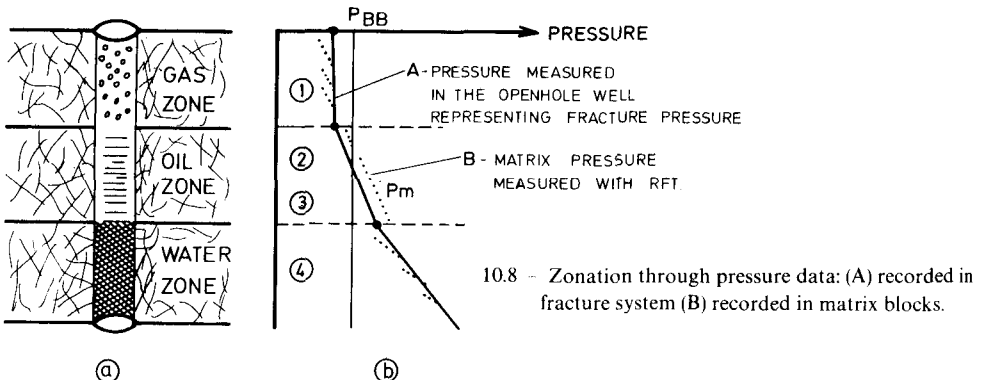
– In the *undersaturated oil zone* only two phases – oil and interstitial water – exist since the gas has not yet been liberated from the oil.

– In the *water-invaded zone* there is a saturation in water (interstitial and invaded) and a saturation in residual oil ( $Sor$ )<sub>w</sub> as a result of imbibition displacement of oil contained in blocks by water saturating the surrounding fractures.

## 10.2.2. Zoning vs. pressure distribution

### 10.2.2.1. The role of fracture pressure vs. depth

Reservoir zoning may be continuously evaluated by pressure recording vs. depth in *an open hole observation well*. The fluid intercommunication between the fractured network and well is equivalent to the intercommunication of a vertical, large fracture represented by the wellbore and the rest of the fractured network (figure 10.8a). The four zones may be delimited if the pressure vs. depth variation (expressed by curve A in figure 10.8b) is associated with the bubble point pressure  $B_{pp}$ .



#### 10.2.2: Zoning vs. pressure distribution

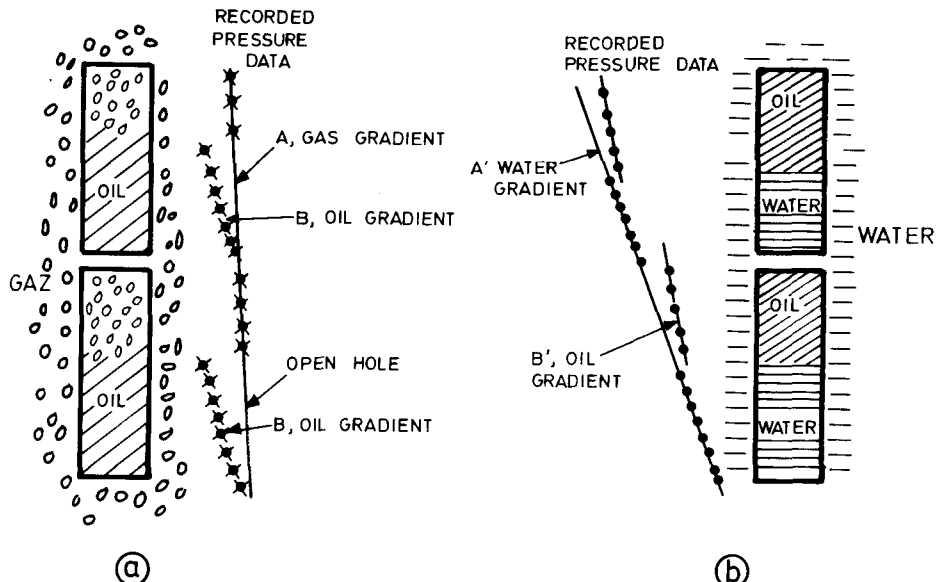
The matrix pore pressure may be actually measured by use of a modern tool such as the repetitor formation tester (RFT). In the open hole of a new well, the pore pressure obtained from the RFT may indicate a different profile from line A in figure 10.8b, obtained as a result of fluid equilibrium in the fractured network.

By examining the invaded zones first, it is possible to obtain pore pressure which deviates from line A as a result of local saturation distributions in each block (dotted lines in figure 10.8b).

If the single blocks are separated in the gas-invaded zone, the matrix pore pressure will not stay on line A (figure 10.9a), and its deviation will correspond to the mobile phase gradient. The upper part of the block saturated with gas as a result of oil displaced in the upper zone of each block, will have the same pressure gradient as the gas saturating the surrounding fractures. The non-displaced oil in the hold-up zone will not modify its equilibrium during the displacement of oil by gas in the upper zone, as shown in figure 10.9a where line B represents the oil gradient. At any depth the difference between the two gradients indicates the limit of drainage displacement in the block.

In a similar way, in figure 10.9b line A' represents the presence of water in fractures measured in the open-hole well, while line B' represents the matrix intergranular pore pressure recorded by RFT. Where water displaced the oil, the pore pressure and fracture have the same water gradient, but the non-displaced zone containing oil will indicate a pore pressure following the oil gradient.

In the oil zone, the pressures of both gassing and undersaturated zones are less depressed than fracture voids. In fact, in the undersaturated zone the difference in pressure  $\Delta P = P_m - P_f$  generates the oil production by a monophase expansion mechanism (Fig. 10.8b, zone 3). The difference in pressure  $\Delta P$ , may be observed «only» in an open hole observation well, drilled when the reservoir is producing and the fractured network is more depressed than the matrix. But the pressure difference will not be observed if matrix blocks are small or the reservoir is not producing during RFT measurement.



10.9 – Matrix and fracture pressure recordings a) Blocks in gas-cap zone b) Blocks in water-invaded zone

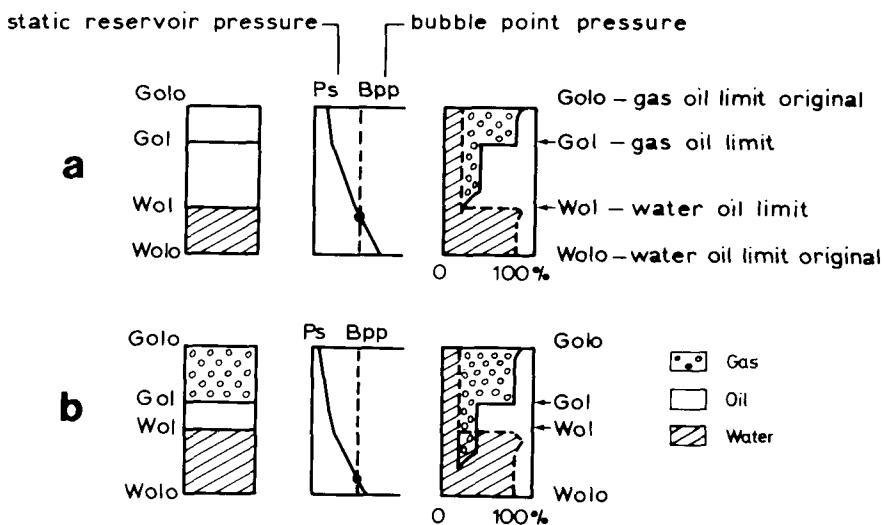
### OBSERVATION

Such pressure measurements as RFT recordings in wells drilled during field life or pressure recordings in open hole observation wells, together with log data may aid in the understanding of the production mechanism of a fractured reservoir. Variations of lengths of lines B and B' (Fig. 10.9) may help to define in-situ the imbibition recovery vs. time relationship, which then may further be extended to the entire reservoir as *reservoir pseudo-function*. In both cases, gas-invaded or water-invaded zones, by means of the pressure gradients B and B', it becomes possible to evaluate the drainage and inhibition performance in situ. A comprehensive analysis of the recorded data vs. time may also help in establishing a valid scaling factor between lab data and effective field behaviour data.

#### 10.2.2.3. Zoning at a late stage of reservoir depletion

In an advanced stage of reservoir production (figure 10.10 a and b) a superposition of zones becomes possible especially if the reservoir height is not very significant. A stage may be reached when reservoir pressure is below  $B_{PP}$  in the water-invaded zone as shown in figure 10.10b.

In the upper part of the water-invaded zone (between WOLO and WOL) there will be a sub-zone where, in the matrix beside the water displacing oil, a saturation in gas will result from gas liberated from solution. The residual oil saturation in this case will have to decrease, due to the more favourable condition of displacing oil by water in the presence of a certain amount of gas, (fig. 10.10b).



10.10 – Zonation at later stage of depletion: a) before and b) after the interference of gas-cap invaded zone with water-invaded zone

### 10.3. RESERVOIR ZONING VS. PRODUCTION MECHANISM

In the four zones which are developed during the depletion of the reservoir (figure 10.7), it is evident that the presence of four different production mechanisms is due mainly to the *difference in fluid saturation* of matrix and fractures (figure 10.11).

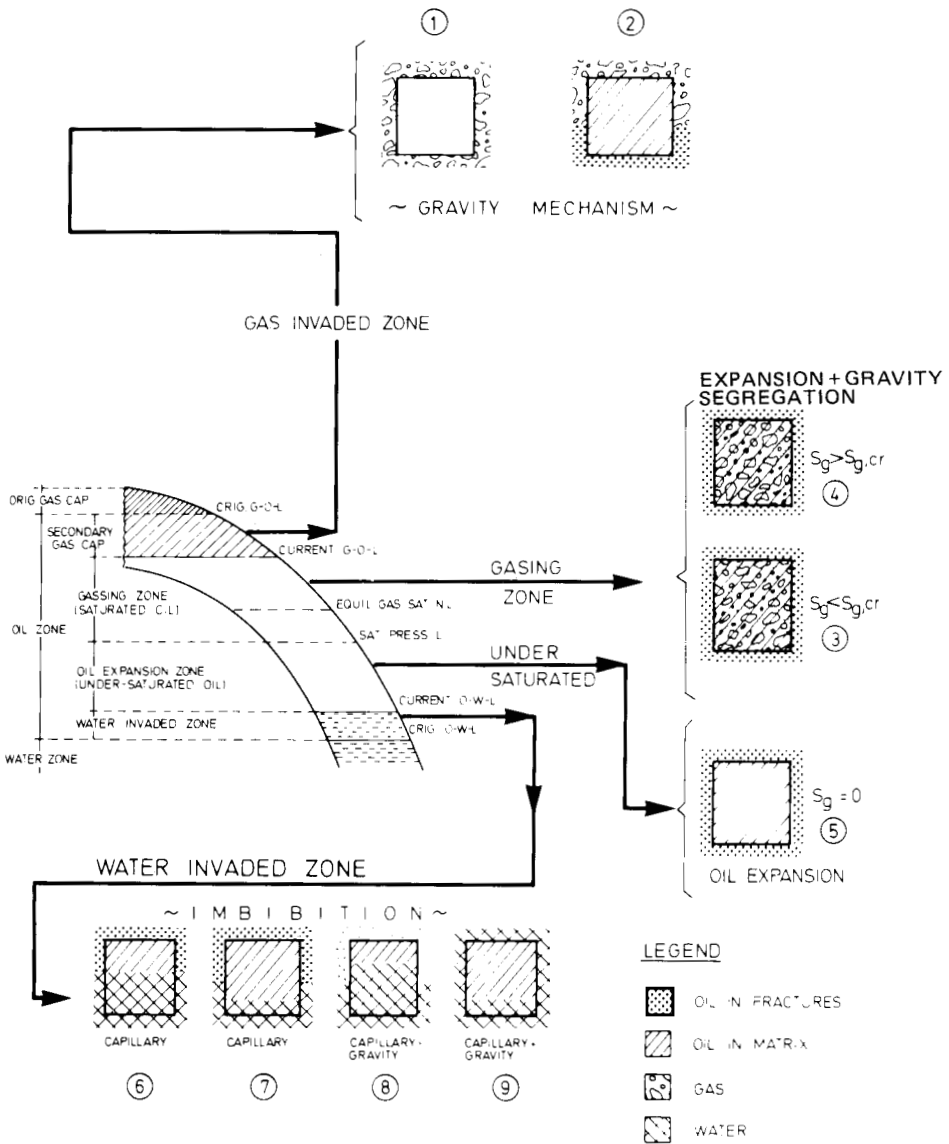
Through pressure gradient interpretation, the zones of different production mechanisms may be established during the reservoir production history from continuous pressure recordings in the observation wells. A simplified model is shown in figure 10.11, where reservoir zones are examined vs. single block behaviour.

The desaturation history of the matrix block will be examined with reference to the modification in saturation and wettability relationship which takes place in the matrix and the environment (fractured network). The production zones and their mechanisms are as follows:

#### a. *Gas-invaded zone*: Gravitational drainage displacement mechanism

In the gas-invaded zone between GOLO and the current GOL (where the secondary gas-cap is developing in the fractured network) the matrix blocks will be partially or completely surrounded by gas (figure 10.11).

Based on the discussions in chapter 9, the matrix will adopt a different behaviour if it is partially or totally surrounded by gas (blocks 2 and 1, figure 10.11), but the capillary pressure and block height will still be the main parameters upon which the block hold-up zone depends.



10.11 – Schematisation of four basic zones and production mechanism in nine blocks taken as examples.

b. *Gassing zone:* Liberated gas expansion + buoyancy + imbibition + convection mechanisms

The gassing zone is limited (in the upper part) by current GOL and  $B_{pp}$ . In addition *two sub-zones may be developed as a result of critical gas saturation* vs. effective gas saturation in the matrix. If reservoir conditions are such that the liberated gas expansion is a predominant driving mechanism, the matrix block inside the upper subzone should develop more gas than those of the lower sub-zone for the same time lag.

Therefore there is a greater chance of having a gas saturation of  $S_g > S_{gc}$  in the upper sub-zone (block 4) than in the lower sub-zone (block 3) where  $S_g < S_{gc}$  (figure 10.11). In addition to the liberated gas mechanism of the internal matrix block, other mechanisms develop, such as segregation of gas inside the matrix block and the interchange of fluids between matrix and fractures. In fact, the circulation of liberated gas in fractures saturated with oil, as well as the contact between the heavier oil of fractures with the lighter oil remaining in the matrix, develops more complex transfer processes. It was also observed that in the case of non-uniform distribution of matrix pores and low decline rate of reservoir pressure, supersaturation pressure phenomena had occurred, so that gas remains dissolved at reservoir pressure below the original bubble point pressure. A detailed discussion of all these mechanism is developed in the next section.

c. *Undersaturated zone*: Simple expansion drive mechanism

This zone is between the level of  $B_{pp}$  and the level of the current WOL, with only oil as a monophase without free-gas. The difference in pressure between higher pressure in the matrix block and lower pressure in fractures produces an expansion of the fluidrock system, which drives the fluid from pores towards the fractured network. The expansion drive mechanism will be bigger if the compressibility and pressure decline rate are higher while production rate increases if block dimensions (block 5, fig. 10.11) are smaller.

d. *Water-invaded zone*: Gravitational + capillary imbibition displacement mechanisms

In the zone between the current WOL and the original WOLO, the matrix blocks surrounded by fractured network saturated with water produce the oil through gravitational and capillary imbibition. Oil recovered from the matrix pores as a result of progressive exposure of the matrix pores to a water environment in the fractures, is rate sensitive to rate of water table advancement.

In the schematisation of blocks 6, 7, 8 and 9 of figure 10. the water-oil contact in fractures (water table) is compared with the matrix front displacement rate. The prevailing of contact advancement in fractures or matrix, influences the predominance of capillary or gravity forces during imbibition displacement.

The *critical rate* of Mattax's<sup>1</sup> simplified model corresponds to an equal advancement of water-oil contact in matrix and fractures (block 6, figure 10.11). The rates are considered to be *above the critical rate* if water-oil contact rate in fractures is higher than water-oil contact rate in matrix (block 7, figure 10.11), or *below the critical rate* if water-oil contact rate in fractures is lower (block 8, figure 10.11).

A unique case is shown in block 9, where the entire block is surrounded by water or *totally immersed* in water.

In all water imbibition cases described above, the production mechanism will be a function of capillary and gravity forces, where often during displacement one or another of these forces may prevail (discussed in chapter 9). Without going into further detail, it is evident that in blocks 6 and 8 the capillary forces prevail, while in block 7 and 9 the capillary forces work jointly with the gravity forces. If the blocks are very tall, as in the case of block 9, gravity will be predominant during the imbibition process.

The simultaneous presence of all these production mechanisms discussed, represents a generalization which is resumed in table 10.1. It is easy to assume that this situation may be simplified in the case that only part of this production is present in the reservoir. For example, in the case of only a water drive mechanism or only a liberated gas expansion combined with the gas-cap production mechanism, the field production forecast becomes substantially simpler.

- The presence of a strong water drive may maintain a reservoir pressure equal to the initial reservoir pressure and, thus, reduce all those mechanisms associated to reservoir pressure depletion. Recovery is then the result of imbibition displacement only, through capillary and gravity forces. This corresponds to the behaviour of the Gela (Italy), Amposta (Spain) and Nido (Philippines) reservoirs.

Table 10.1 *Production mechanism*

Zone (Fig. 10.7)	Saturation				Block no. Observations fig 10.11
	Matrix	Fractures network	Production mechanism		
Gas invaded (1)	oil	gas	Gravity drainage	1	$P < P_{BB}$
»	»	gas + oil	»	2	$P < P_{BB}$
Gasing zone (2)	oil gas	oil	• expansion of liberated gas	3 & 4	»
$Sg < Sga$	oil + gas	oil	• convection	3	• immobile gas
$Sg > Sga$	»	oil		4	• mobile gas
under-saturated oil (3)	oil	oil	monophase expansion	5	$P > P_{BB}$
water invaded (4)	water & oil	water & oil	capillary imbibition	8	Fracture water – oil contact below critical
			gravity & imbibition	6	
				7,9	Fracture water – oil contact above critical

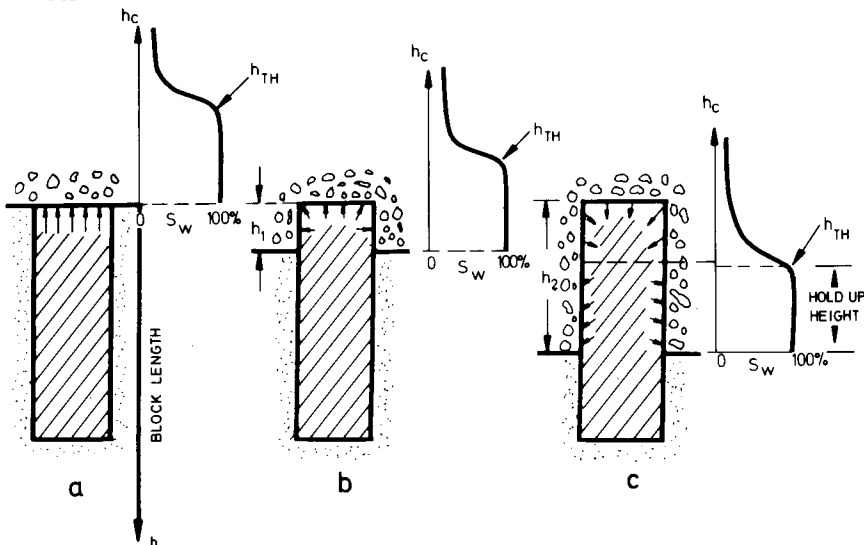
- If the aquifer is limited or non-existent, reservoir pressure depletion will take place and the oil will be produced as a result of the expansion of gas liberated from solution in the oil zone, and of gravity drainage in the gas-invaded zone. If favourable conditions develop in the gas-invaded zone, oil displacement will occur as a result of gravitational drainage displacement. The main problems during the drainage displacement concern the conditions in which gravity forces prevail in comparison with capillary forces, which oppose oil displacement.

- The oil produced from the blocks during drainage displacement, if moving downward in the fracture network, may be re-imbibe the lower located matrix blocks with oil, if these are desaturated in oil, or may move towards the wells if the pressure gradients in the fractured network are big enough to overcome the segregation effects.

### 10.3.1 Production mechanism in the gas-invaded zone

#### 10.3.1.1 Single block behaviour

As discussed above and also examined in detail in chapter 9, the oil producing mechanism in the matrix blocks of the gas-cap is gravity drainage. The production of oil is based on the *single block concept* where for a given block geometry and given fluids and rock properties the recovery vs. time relationship may be calculated as described in chapter 9, section 9.3.2. The forces which resist the displacement of oil by gas are related to pore distribution and the average diameter which influences the capillary height ( $h_c$ ) and threshold height ( $h_{TH}$ ). The example given in figure 10.12 illustrates that in case  $h_{TH} \geq h_c$ , displacement does not take place if the gas is in contact with the upper block surface (figure 10.12a), or even if it reaches a depth of  $h_1 < h_{TH}$ . Only when the block is surrounded at a depth of  $h_2 > h_{TH} \geq h_c$  will recovery take place (figure 10.12c). In addition, in case c (figure 10.12), recovery is limited only to the matrix block height  $h_2 - h_{TH}$  while  $h_{TH}$  will represent the height of the block hold-up zone.



10.12 – Role of gas-oil contact advancement in drainage displacement.

#### Observations

- It is essential to know the relationship of *capillary height vs. block height* in order to calculate block recovery behaviour.

- Since gas-oil interfacial tension increases with reservoir depletion, the hold-up height may increase in the absence of a pressure maintenance by gas injection.
- An oil re-imbibition process may take place when some of the oil produced through gas gravity drainage may re-imbibe into lower blocks which have been partially desaturated. In fact, during the descent of oil drops (displaced by gas) through fractures, the oil may enter into contact with the gassing zone blocks which are partially saturated with gas and oil. The re-imbibition of these blocks with oil is, in effect, a reduction of the overall oil production in the reservoir.

#### 10.3.1.2. The interaction effect of the blocks

This effect was experimentally developed by Saidi<sup>2</sup> and may be called block-block interaction, as a result of oil entering (supplied) into the upper face of a tilted block, or infiltrating from the surrounding fractures after having left an upper located block.

##### a. Description of phenomenon

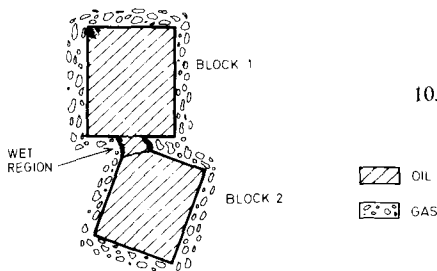
Between the two adjacent blocks 1 and 2 shown in figure 10.13 (both located in the gas-invaded zone), a wet region may create an oil bridge and thus a continuous oil phase among the blocks. This continuous oil phase due to irregularities in fractures is represented by a film of oil remaining between the blocks in the case of narrow fractures. The extension of this wet region is estimated to be of the same order of magnitude as the cross-flow section of the block if the extension of the block is not too big compared with the capillary height.

The oil flow from block 1 to 2, due to capillary continuity, is controlled by capillary pressure gradients and the potential difference of gravity. The rate of effective permeability  $K_o$  depends on matrix saturations  $S_o^*$  and is expressed by,

$$q = - \frac{k_o(S_o^*)}{\mu_o} \left( \Delta \rho g - \frac{dP_c}{dZ} \right) \quad (10.1)$$

where,

$$q = - \frac{k_o(S_o^*)}{\mu_o} \left( \Delta \rho \times g - \frac{dP_c}{dS_o^*} \cdot \frac{dS_o^*}{dZ} \right) \quad (10.2)$$



10.13 – Two blocks and the wet zone of fluid continuity

Since capillary pressure is also a function of saturation  $h_c(S_o^*)$ , the equation may be rewritten as.

$$S_o^* = (S_o - S_{or}) / (1 - S_{cw} - S_{or})$$

The oil produced from the matrix in fractures but re-imbibed in the lower matrix blocks during the descent of oil in the fractured network is disregarded in this rate  $q$ . Such a reimmersion will evidently reduce the efficiency of the gas-invaded zone producing through the drainage displacement mechanism.

#### b. Definition of rates

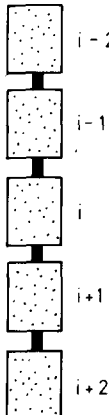
In the case of continuity of flow over several blocks forming a stack of blocks of different dimensions and physical characteristics (figure 10.14), in the block  $i$  the rate may be expressed as follow:

- the *drainage rate* of single block is expressed in chapter 9 figure 9.12 by equation 9.38 as follows,

$$Q_{DR} = A \frac{(Hg - Z) \Delta\gamma - P_c}{\frac{\mu_g}{k k_{rg}} [MH + (1 - M)Z]} \quad (10.4)$$

or by rearranging the terms as,

$$Q_{DR} = A \frac{(Hg - Z) \Delta\gamma - P_c}{\frac{\mu_o}{k k_{ro}} \frac{1}{M} [MH - (1 - M)Z]} = A \frac{k_o}{\mu_o} \left[ \frac{(H - Z) - h_c}{H - \left( \frac{1}{M} - 1 \right)Z} - \Delta\gamma \right] \quad (10.4')$$



10.14 – Stack of interacting blocks

- The *maximum drainage rate*, often referred to as gravitational rate, is expressed by equation 9.38 in chapter 9, when  $P_c = 0$  (equivalent to  $h_c \ll H$ ) and  $Z = 0$  (equivalent to  $z \ll H$ ) as follows,

$$Q_{GR} = Q_{MAX} = A \frac{k_o}{\mu_o} \Delta \gamma \quad (10.5)$$

- the supply rate from block  $i-1$  towards block  $i$  (figure 10.14) along the wet region is expressed by  $Q_{i-1, SUPP, i}$  which may be higher or lower than the drainage maximum rate  $Q_{max, i}$  of block  $i$ .

- \* If  $Q_{i-1, SUPP, i} < Q_{MAX, i}$ , all oil coming from above is sucked into block  $i$ .
- \* If  $Q_{i-1, SUPP, i} > Q_{MAX, i}$ , some of the oil (the excess) passes through the fractured network of block  $i$ .

The supply rate will then be expressed as,

$$Q_{i-1, SUPP, i} = Q_{DR, i-1} + Q_{PASS, i-1}$$

where  $Q_{DR}$  is expressed by equation 10.5 rather than 10.4.

- the *reinfiltration rate* is then equal to the rate of supply under the condition that the supply rate is lower than the maximum drainage rate. This is expressed as,

$$Q_{REINF, i} = Q_{i-1, SUPP} \text{ if } Q_{i-1, SUPP, i} < Q_{MAX, i}$$

- the *passing rate* is the excess of the rate which moves through the fractured network. This rate is given by,

$$Q_{PASS, i} = Q_{i-1, SUPP, i} - Q_{DR, i}$$

and takes place only if,

$$Q_{i-1, SUPP, i} > Q_{MAX, i}$$

### c. Degree of block interaction

If the degree of interaction is expressed by an interaction parameter  $\alpha$ , it may be stated that:

- full interaction corresponds to  $\alpha = 1$
- partial interaction corresponds to  $0 < \alpha < 1$
- non-interaction corresponds to  $\alpha = 0$

Based on the above definitions, the relationships between  $\alpha$  and the rate are as follows,

$$\alpha = 1 - \text{corresponds to } Q_{i-1, SUPP, i} < Q_{MAX, i}$$

$$\alpha < 1 - \text{corresponds to } Q_{i-1, SUPP, i} > Q_{MAX, i}$$

In other words, when  $\alpha = 1$  the total supply rate of block  $i - 1$  is sucked into block  $i$ , while in the case of  $\alpha < 1$ , only some of the supply rate is obliged to pass block  $i$  moving through the fractures which surround it.

In the case of  $\alpha < 1$ , a part of the supply rate which is down-falling may become a *reinfiltrated rate* while the difference among them is just the passing rate. This corresponds to

$$Q_{i-1, \text{SUPP}, i} > Q_{\text{MAX}, i}$$

If  $\alpha = 0$  the problem is reduced to the case of a single block without any interaction with adjacent blocks.

#### d. Observations from experiments

From the experiments performed in the laboratory and with reference to the two blocks shown in figure 10.12, the results were as follows:

- the oil from block 1 moved through block 2 instead of travelling along its surface
- even though the wet region of supply was small, infiltration rates were often high
- reduction of infiltration rates was observed in flat blocks where the wet region was located at one side of the blocks' surface
- the infiltration rate depended on block shape and size, as well as on supply point location, matrix isotropy and presence of impermeable layers.

#### e. Saturation behaviour if supply takes place at top during oil drainage from block

In matrix block  $i$  the entering rate  $Q_{\text{SUPP}}$  and the produced drainage rate (gravitational  $Q_{\text{MAX}}$ ) will generally reach a steady-state internal saturation if both rates remain constant. The ratio of the two rates  $\bar{Q} = Q_{\text{SUPP}}/Q_{\text{MAX}}$  will determine a capillary hold-up height and an oil desaturation distribution through the equation.

$$\frac{d(Z/H_B)}{dS_o^*} = \frac{d}{dS_o^*} \left[ \frac{h_c(S_o^*)}{H_B} \right] \left[ 1 - \bar{Q} \frac{1}{k_{or}(S_o^*)} \right] \quad (10.6)$$

obtained from equation 10.3 where  $dP_c/dS_o^*$  was introduced from the Leverett equation,

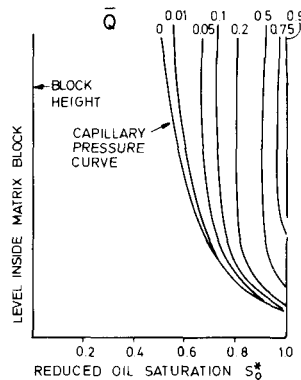
$$P_c = \sigma \sqrt{\Phi/KJ(S_o^*)} \quad (10.7)$$

In a calculation example<sup>2</sup> where relative permeability of oil is expressed by  $K_{or} = (S_o^*)^7$  and final recovery by  $R_f = 31,5\%$ , the desaturation of oil depends on supply-drainage rate ratio  $\bar{Q}$ . The curves in figure 10.15 illustrate the steady-state oil saturation distribution for  $\bar{Q}$  varying between 0 and 1.

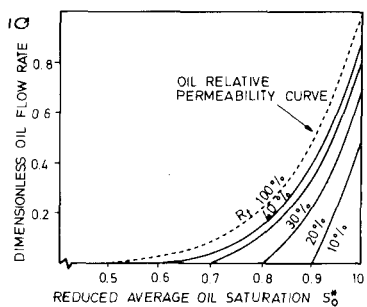
- when  $\bar{Q} = 0$  (which means that  $Q_{\text{SUPP}} = 0$ ) the saturation profile is equal to the capillary pressure curve (figure 10.15)
- if  $0 < \bar{Q} < 1$ , the increasing supply-drainage ratio results in higher oil saturation  $S_o^*$ ,

- which means that the oil supplied will compensate for the oil produced
- if  $Q = 1$ , the saturation in oil in the block is practically unchanged, which corresponds to a lack of oil production; nevertheless a drainage process takes place in each single block.

As observed, the oil hold-up zone is large at the bottom and starts to decrease up to a given height. Therefore, at the top of the block,  $S_o^*$  is large even for reduced wet zones and  $K_o$  is high enough to assure the entrance of oil into the matrix. The average block oil saturation vs. dimensionless rate  $\bar{Q}$  for given final recoveries are shown in figure 10.16. It may be observed that if  $R_f = 100\%$  corresponding to  $P_c = 0$ , the curve is similar to the relative permeability curve of oil in which the variations of  $Q$  behave as a relative permeability curve. For lower final recoveries, the shape of the curves remains the same, which means that the curve  $K_o(S_o^*)$  may be shifted downwards according to the product  $K_{or}(1 - R_f)$ .



10.15 Saturation profile when oil passes through a block from wet zone to block bottom (Saidi<sup>2</sup>)



10.16 – Relative ratio  $\bar{Q}$  vs. block oil average saturation  $S_o^*$  for various recovery values (Saidi<sup>2</sup>)

### 10.2.1.2. Gravity drainage from stacks of equal blocks

In the case of a stack of equal blocks with identical physical properties in communication through supply points of various extensions (figure 10.14), the oil will move through all blocks. The time which results is as follows:

$$t_{\text{drainage stack}} = t_{\text{drainage single block}} \times \text{number of blocks}$$

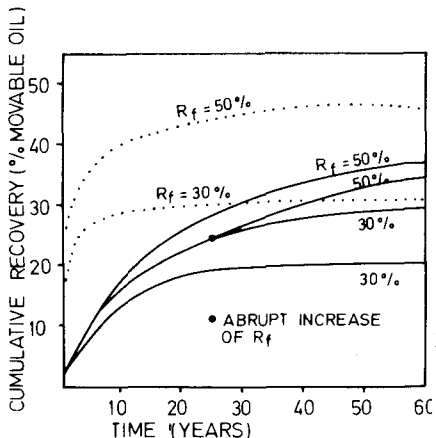
Due to this long period of time, the rate in a stack will evidently be very slow compared with the drainage rate of a single block, and this suggests that the drainage in a stack of equal blocks may be approximated as a semi-steady-state process.

The drainage process described by a single block behaviour may be unrealistic since it is too rapid and too optimistic compared with stacked blocks. A detailed examination of the process is resumed as follows:

- The semi-steady-state stack production rate will be determined by the *pseudo-relative permeability curve* for the oil phase in relation to the recovery  $R_f$  at an average saturation in oil  $S_o^*$ . This saturation corresponds to average saturation in oil remaining in the mobile phase for a given  $R_f$ .

By using the function  $F(S)$ , which is similar to a pseudo-relative permeability curve, and which takes into consideration the capillary hold-up height, the process is similar to a gravity drainage process, but without the capillary effects. In fact, if the recovery approaches the  $R_f$  value, each block will have its proper fluid saturation distribution including the capillary hold-up zone.

In a calculation example<sup>2</sup>, a stack of 50 equal blocks interacting among themselves and having the same properties, illustrates the difference between the single block and the stack of 50 blocks. The characteristics of the single block are: height 3 meters;  $(1 - S_{wi}) = 0.083$ ;  $K_{or} = (S_0^*)^7$ ;  $K_o (S_{wi}) = 1.26 \text{ md}$ ;  $\Delta\rho = 0.6 \text{ gr/cm}^3$  and  $\mu_o = 1 \text{ c.P.}$



10.17 – Drainage performance of a stack of interacting equal blocks. Cumulative recovery (% movable oil) vs. time (years) for various  $R_f$  – case of stack of 50 equal blocks: ... case of single block drainage (Saidi<sup>2</sup>)

It is evident from the results that the single block corresponds to a fast drainage process, especially if passing from a small  $R_f$  to a larger  $R_f$  by reducing the capillary pressure due to reservoir repressuring (figure 10.17). In fact, by repressuring the reservoir, the effects of capillary pressure will be reduced.

### 10.3.1.3. Gravity drainage from stacked heterogeneous blocks

Based on the observation discussed above, the variations in dimensions and physical rock properties influence the supply and drainage rates in a stack of heterogeneous blocks. From one block to another the degree of interaction  $\alpha$  will be different; in addition, for each block in a stack, the relationship between the drainage rate and its average oil saturation will be given by a pseudo-relative permeability  $F$ .

Parameter  $F$  could be approximated as,

$$F = (S_o^*)^N - (1 - R_f)^N \quad (10.8)$$

and therefore, the ratio of the drainage-gravity ratio vs. time may be expressed in each block  $i$  as the rates of equations 10.4 and 10.5 given by,

$$\frac{Q_{DR, i}}{Q_{MAX, i}} = F \left[ \bar{S}_o^*(t), R_f(t) \right] \quad (10.9)$$

Saturation vs. time is given by,

$$\frac{d\bar{S}_o^*}{dt} = \frac{1}{H_{Bi} \Phi_i (1 - S_{cwi})} \left[ Q_{i-1, SUPP, i} - Q_{DR} \right] \quad (10.10)$$

### CALCULATION EXAMPLE

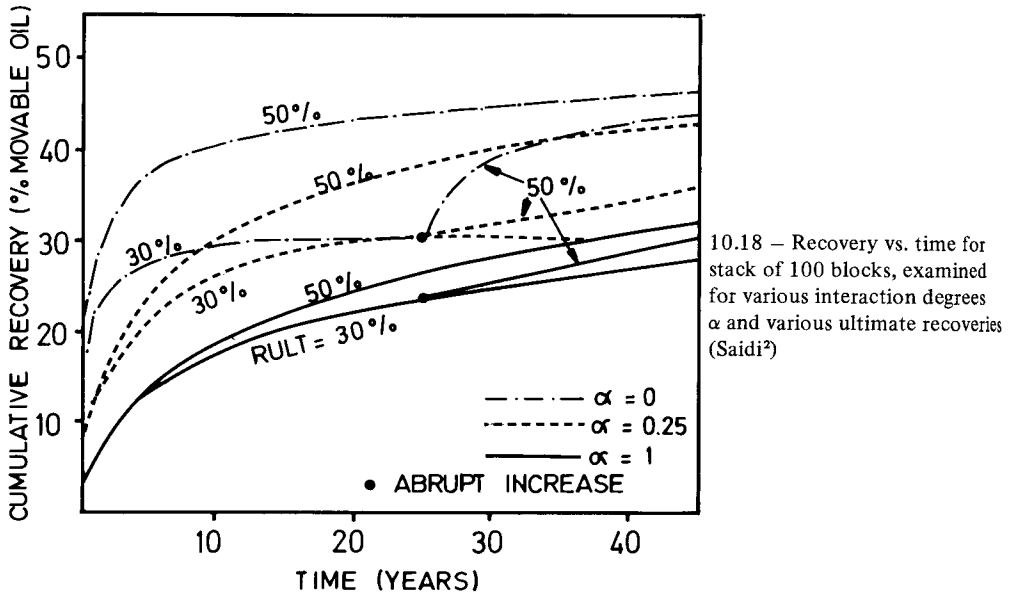
- a. An interesting experiment<sup>2</sup> was performed on a stack of 100 matrix blocks having an average height of 3 meters, but with different physical properties. The data given in Table 10.2 indicate porosity, permeability, initial saturation and oil content.

Table 10.2 Basic data of stacked heterogeneous blocks

Permeability (mD) ( $10^{-15}$ m $^2$ )	Porosity (%)	Initial oil saturation (%)	Oil content (% of OOIP)
0.20	6.3	58.5	5.0
0.30	7.0	63.0	5.9
0.46	7.8	66.0	6.9
0.63	8.5	70.5	8.1
0.87	9.2	73.5	9.1
1.26	10.0	76.0	10.2
1.70	10.7	77.5	11.1
2.29	11.4	79.0	12.1
5.00	13.3	82.0	14.6
9.55	15.1	84.0	17.0
			100.0

The viscosity of oil used was  $\mu_o = 10$  c.P., the difference in specific mass was  $\Delta\rho = 0.6 \text{ g/cm}^3$  and  $K_{or} = (S_o^*)^7$

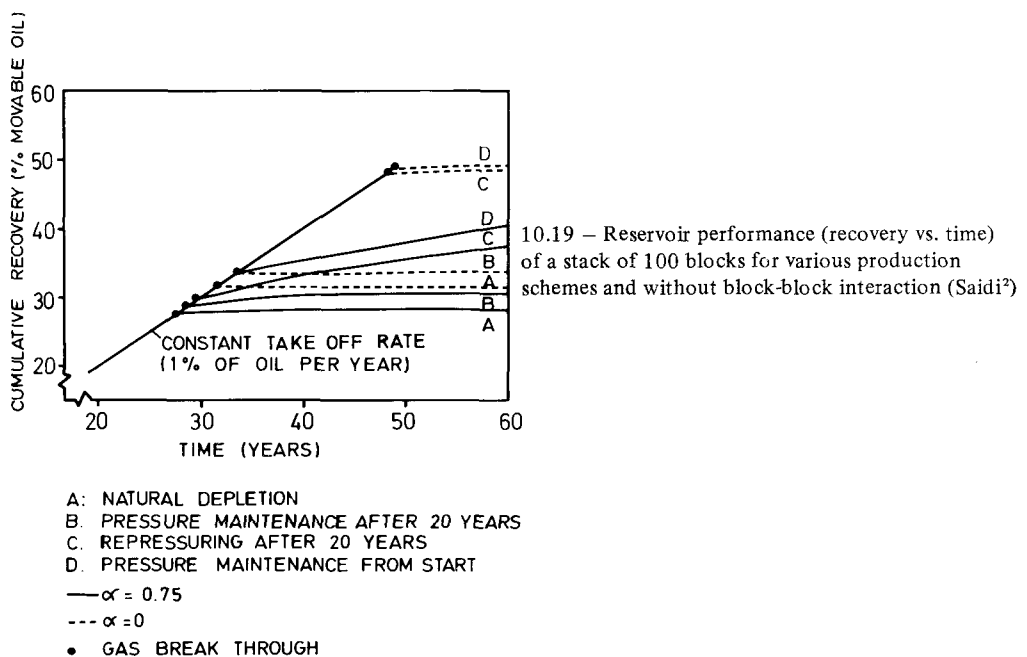
The sensitivity calculation performed for block-block interaction  $\alpha = 0; 0.25; 1$  and final recoveries  $R_f = 30\%; 50\%$  resulted in a variation in recovery vs. time as shown in figure 10.18.



From the calculation performed the following was observed:

- The drainage rate was initially controlled by high permeability blocks and the less permeable blocks were by-passed by the oil.
- When the drainage rate of the stack decreased, the lower permeability blocks are also involved in the drainage process, and at a later stage if rate is very slow all blocks were drained.
- The parameter  $\alpha$  greatly influences the recovery-time relationship, and thus, it may be mentioned that  $R_f$  is proportional to  $\alpha$ .
- In high interaction conditions ( $\alpha = 1$ ) the ultimate recovery did not show any sensitivity, but final recovery seemed to be very sensitive through the relationship recovery vs. time for a moderate interaction ( $\alpha = 0.25$ ) or no interaction at all ( $\alpha = 0$ ).
- A sudden increase in recovery from 30% – 50% after 25 years of production showed that in the case of  $\alpha = 1$  (total interaction), negligible additional oil could be produced; but in the case of  $\alpha = 0$  (no interaction), significant improvements in recovery became possible in the same period of time (Fig. 10.18).

- b. In a comparative calculation for various driving conditions, the same stack has shown the role of block-block interaction. The conditions examined were: A-natural depletion; B-pressure maintenance after 20 years; C-repressuring after 20 years; and D-pressure maintenance from start for  $\alpha = 0.75$  and  $\alpha = 0$  (figure 10.19). The constant yearly rate was 1 % of original oil in place. In the case of natural depletion, recovery was stopped in each block when oil saturation corresponded to the capillary hold-up curve. Consequently, inside the stack the lower blocks surrounded by gas had a lower recovery. As observed in the example studied, the difference in recovery between  $\alpha = 0.75$  and  $\alpha = 0$  is not too sensitive. But repressuring or pressure maintenance at an early stage showed significant increases in recovery, while if repressuring or pressure maintenance began at a later stage of depletion, the improvement in recovery was less significant.



- c. Comments on calculation example: Since any additional recovery obtainable from gas injection seems very favourable, the understanding and evaluation of the block-block interaction process with all implications is very important for the design of reservoir behaviour. The evaluation of interaction through matching the past history of reservoir performance of the reservoir with calculated results is the general procedure. In the case of depletion independent of block-block interaction, matching may be obtained by adjusting block height which influences the recovery  $R_f$  and permeability, and consequently, adjusts the time scale of the gravity drainage process.

### 10.3.2. Production mechanism in the gassing zone

In the gassing zone the oil-saturated blocks are surrounded by fractures saturated with oil (figure 10.11). The matrix pore pressure is lower than the bubble point pressure. During the reservoir depletion, different fluid exchanges between matrix and fractures take place. The liberated gas from matrix blocks percolates upward in fractures while the oil from matrix moving in a downward direction may replace the oil lost previously to the fracture by the lower located matrix blocks by re-imbibition.

In this zone it is considered that the presence of fractures changes the production mechanism *from a conventional solution gas-drive* to a more complex production mechanism and flowing process. Besides the simple expansion of fluids and rock, it is possible to have 1) *oil circulation* due to convection phenomena, 2) *displacement of matrix oil* by fracture oil as a result of differences in densities between the oil in matrix and that in fractures, 3) *gas diffusion* between oil in matrix and fissures, as a result of higher gas concentration in matrix oil, etc.

#### 10.3.2.1. Oil circulation and implications on PVT properties

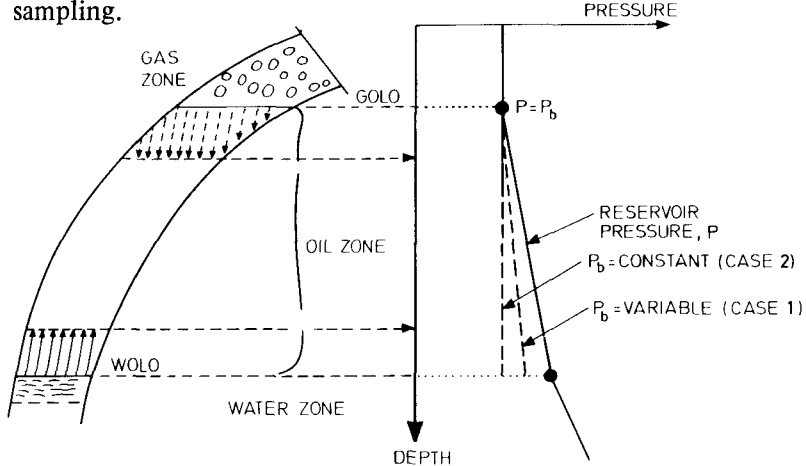
The original pressure distribution in a reservoir is shown in figure 10.20. The variations of reservoir pressure in the gas, oil and water zones are the results of original static equilibrium in the fractured network associated to the fluid distribution in the matrix blocks.

At the original gas-oil contact level (GOLO) the reservoir pressure is equal to the saturation pressure; but below this level the saturation pressure may either in case 1 vary with depth (as in a conventional reservoir), or in case 2 remain constant along the entire oil column (typical for a fractured reservoir having a very good intercommunicating fractured network). The constant value of  $P_b$  with the depth is the result of a convection process inside the reservoir due to the combined effect of pressure and the thermal gradient in a fractured reservoir. Under the influence of increasing pressure, oil contracts, and under the influence of the increasing temperature it expands. Thus, for a given system, a state of disequilibrium may develop if the expansion, resulting from the increase of temperature with depth, is counter-balanced by the contraction, due to the increase of pressure with depth. As a result, a further convection process may develop inside the reservoir, causing the heavier oil from the upper part of the reservoir to move rapidly through the fractures towards the lower part, while the light oil of the lower part of the reservoir moves upwards.

A homogeneity of PVT properties with depth will be the result of this continuous fluid circulation throughout the fracture network. Such PVT behaviour is impossible in a conventional reservoir, but is possible only if an excellent intercommunication between fractures is developed over the entire reservoir.

On the other hand, if the effect of compressibility resulting from the increased pressure vs. depth is not compensated for by a thermal expansion, a static equilibrium

without any convection will govern over the entire reservoir; thus, a segregation process of oil will take place along the reservoir depth, and consequently, a variation of PVT properties with depth. A relationship  $P$  vs. depth followed by the relationship  $P_b$  vs. depth (figure 10.20 case 1) will result from reservoir sampling.



10.20 Variation of pressure and bubble point pressure with depth: case 1,  $P_b$  = variable and case 2  $P_b$  = constant.

#### a. Segregation vs. convection of oil in a fractured reservoir

Segregation means that the heavy and light components in the reservoir are distributed under gravity forces. Such a variation in oil composition will influence the bubble point pressure  $P_b$  as a function of depth.

Analytically the basic relationship which correlates temperature, pressure and volume of the liquid hydrocarbons may be expressed as follows:

- The variation of the volumetric mass (in isothermal conditions) of a compressible liquid under the influence of a pressure variation (as discussed by Saidi and van Golf-Racht<sup>3</sup>) is,

$$\delta_T = \delta_o e^{C\Delta P} \quad (10.11)$$

where  $\delta_T$  is the volumetric mass under constant temperature,  $C$  is the compressibility, and  $\Delta P$  is the pressure difference. The isobaric variation of the volumetric mass of a compressible liquid under a temperature variation is,

$$\delta_p = \delta e^{\lambda \Delta T} \quad (10.12)$$

where  $\delta_p$  is the volumetric mass under constant pressure,  $\lambda$  is the coefficient of thermal expansion, and  $\Delta T$  is the temperature difference.

b. Condition of convection and segregation

For a given oil composition and a given geothermic gradient based on equations 10.11 and 10.12, the results are as follows:

$$\left\{ \begin{array}{l} \delta_p - \delta_T \text{ if positive - convection} \\ \delta_p - \delta_T \text{ if negative - segregation} \end{array} \right\} \quad (10.13)$$

c. Example

Considering the following temperature and pressure data in a reservoir,

$$\lambda = 6.4 \times 10^{-4} \text{ vol/vol/}^{\circ}\text{F}$$

$$C = 1.45 \times 10^{-5} \text{ vol/vol/psi}$$

$$T_G = 0.02^{\circ}\text{F/ft}$$

$$P_G = 0.3 \text{ psi/ft}$$

the result is,

$$6.4 \times 10^{-4} \times 0.02 - 1.45 \times 10^{-5} \times 0.3 = 3.45 \times 10^{-5} > 0$$

Since the result is positive, the PVT properties are uniform and therefore,  $P_b = \text{const}$  with the depth.

### 10.3.2.2. A different concept of solution gas-drive as a result of diffusion (non-dispersion)

Applying the conventional methods for simple expansion and solution gas-drive of a fractured reservoir it was difficult to match the past history without assuming either a high OOIP or an extremely efficient water-drive.

It was, however, observed that the material balance results could be matched with the past history for the most probable OOIP and for a reasonable displacement efficiency only by assuming a very low gas saturation in the gassing zone, which implies a higher gas displacement efficiency in the gas-invaded zone.

Based on the above observation, a theory was developed by Dumoré<sup>4</sup>. The theory, supported by experimental results, indicates that at a *low reservoir pressure decline rate*

$\left( \frac{dp}{dt} \right) < 10^{-6} \frac{\text{at}}{\text{sec}}$ , a supersaturation phenomena would be developed in the pores. In other words, *it would be a pressure (supersaturation pressure) at which gas would remain in a liquid phase below its equilibrium bubble point (obtained from conventional PVT experiments)*. Analysing the phenomena the following may be stated:

- The largest pore having a lower capillary pressure would be the first pore in which a gas bubble would develop.
- Because of supersaturation, a gas concentration gradient exists between the bubble of gas in the large pore and its surrounding. If the reservoir pressure drops at a very low decline rate there will be enough time for the diffusion of gas through liquid in the surrounding area to feed the bubbles of gas. In this manner the bubbles of gas grow larger and larger until the gas bubble channel reaches the upper boundary of a block, where it delivers gas to fractures.
- During such a process, the spherical drainage of a bubble changes into a cylindrical drainage, and at any time a new gas *nucleus* will develop into the largest pore undergoing a similar process, since the pore pressure is below the bubble pressure, but greater than a critical supersaturation pressure.
- A mathematical derivation was developed based on physical characteristics and Fik's law for unsteady and steady-state periods, and preliminary studies indicate that for a pressure decline rate ( $10^{-6}$  atm/sec) and a non-homogeneous reservoir rock, a gas saturation of about 1% would be developed in the gassing zone.
- If diffusion takes place in the undersaturated part of the reservoir, where the bubble point pressure drops considerably below the original value, the free-gas saturation is low when this part of the reservoir becomes a gassing zone. If, on the contrary, the pressure decline rate is high, supersaturation oil capacity is low and if in addition the reservoir rock is homogeneous, a tendency of gas dispersion phenomena occurs and a classic solution gas-drive calculation must be applied even in the fractured reservoir.

All this may very well explain why it is impossible to apply automatically the conventional solution gas-drive performance in the fractured reservoir material balance calculation before examining if conditions of diffusion may occur or not.

#### a. Experiments and interpretation of results

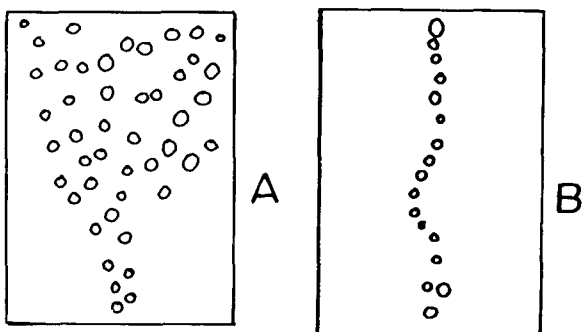
A series of experiments have been carried out by Dumoré<sup>4</sup> on models where visual observations were possible during the flow of liquid and gas in the model as a result of the transparency of the glass pack. The experiments have been performed at low, medium and high pressures on crushed glass pack grains and on Bentheim sandstone blocks.

#### b. Basic experiment

In a transparent model (figure 10.21) containing crushed pyrex glass and saturated with a liquid which assumes transparency, air was injected through a hypodermic needle near the bottom of the pack model. The gas, injected at various rates, was successively examined in coarse-grain and fine-grain packs (figure 10.21), and the results obtained led to the following conclusions:

- In a coarse-grain pack, a conic gas-saturated region develops (figure 10.21 A) when gas moves upwards (gas dispersion), while in a fine-grain pack only one gas channel develops (figure 10.21 B).

- It was observed that the gas phase is not a continuous stream of upward moving gas, but rather an agglomeration of small mutually interconnected gas channels and thus forming a continuous stream.
- In a non-homogeneous grain pack the non-dispersed single channel follows a more tortuous pattern than in a more uniform grain pack.
- The transition of upward gas flowing from dispersion to non-dispersion conditions is restricted to a particular permeability interval or a particular permeability – porosity ratio.
- The upward gas flow at low rates is governed mainly by gravity and capillary forces alone, which helps a non-dispersion state of flow.



10.21 . . . Bubbles of gas liberated. A)  
Dispersion B) Non-dispersion

### b. Qualitative explanation of dispersion and non-dispersion

Gas is assumed to be injected into a porous media (matrix) saturated with liquid. In a single pore (figure 10.22) connected to other pores only by different restrictions – 1 and 2 – of different radii –  $r_1$  and  $r_2$  – gas can leave the pore only if pore pressure  $P$  is higher than the capillary pressure in the two restrictions.

If the two capillary pressures are respectively,

$$P_{c1} \cong \frac{2\sigma}{r_1} \text{ and } P_{c2} \cong \frac{2\sigma}{r_2}$$

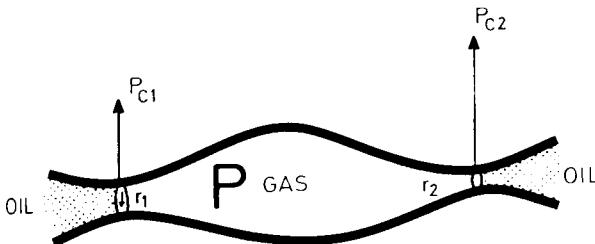
then the following applies:

$$\text{when } r_2 \ll r_1 \rightarrow P_{c2} \gg P_{c1} \rightarrow \text{if } \begin{cases} P > P_{c2} - \text{dispersion state} \\ P_{c2} > P > P_{c1} - \text{non-dispersion state} \end{cases}$$

$$\text{when } r_2 = r_1 \rightarrow P_{c2} = P_{c1} \rightarrow \text{if } \begin{cases} P > P_{c1} - \text{dispersion since,} \\ \quad \quad \quad \text{automatically } P > P_{c2} \end{cases}$$

From this simplified qualitative discussion the following is concluded:

- If pores are *uniform* and of *large radii*, this is equivalent to small capillary forces and a state of *dispersion* will take place.
- If pores are *non-uniform* and of *small radii*, there is a great chance that a *non-dispersion* condition of gas flow will take place.



10.22 Pores having two entrances of different radii.

If the capillary pressure between the two restrictions is expressed as capillary differential pressure,

$$\Delta P_c = \frac{2\sigma}{r_1} \left[ \frac{r_1}{r_2} - 1 \right] \quad (10.17)$$

dispersion will occur for a small  $P_c$ , and non-dispersion will occur when  $P_c$  is high.

Associated with Leverett's expression, the limit of the states of dispersion and non-dispersion could be expressed by a transition capillary magnitude,

$$\sigma \sqrt{\Phi/K} \cong 1.5 \times 10^4 \sim 2 \times 10^4 \text{ dyne/cm}^2$$

### c. Large scale experiments

Laboratory experiments have been carried out on various materials at various reservoir pressures with oil saturated with gas in order to review the behaviour of gas in the case of a gas liberation process.

- The porous medium was either a crushed-glass pack, where transparency helped the qualitative gas behaviour, or sandstone, when the data was examined only quantitatively.
- The fluid-material relationship was examined in association with the critical Leverett parameter,  $\sigma \sqrt{\Phi/K}$  in order to evaluate the transition zone between non-dispersion and dispersion states.
- The pressure used varied from low ( $3.7 \text{ kg/cm}^2$ ) to medium ( $21 \text{ kg/cm}^2$ ) and high ( $250 \text{ kg/cm}^2$ ) pressures.
- Gas liberation was controlled by the pressure decline rate  $dp/dt (\text{kg/cm}^2/\text{sec})$ .

The types of experiments are shown in table 10.3, and a discussion of these results is based on the diagrams shown in figures 10.23 and 10.24, where various correlations between parameters have been represented.

$$\delta_p - \delta_T = \delta_o \left( e^{\lambda T_G Z} - e^{CP_G Z} \right) \text{ or } \delta_p - \delta_T \cong \delta_o (\lambda T_G - CP_G) \quad (10.15)$$

$$\begin{aligned} T_G - CP_G &> 0 & \text{convection} \\ T_G - CP_G &< 0 & \text{segregation} \end{aligned} \quad (10.16)$$

Table 10.3 *Supersaturation experiments: Basic data*

No. of experiment	Type of rock	K Darcy	$\Phi$ fraction)	$P_B$ kg/cm <sup>2</sup>	Temp. F	$R_s/R_{S,O}$	$dp/dt$ (kg/cm <sup>2</sup> . sec)	$\sigma \sqrt{\Phi/K}$ (psi)
1	Glass grains pack	350	.39	3.7	72	1.5	$10^{-5}$	0.15
2	»	»	»	»	»	»	$10^{-6}$	»
3	»	15	»	»	»	»	$10^{-5}$	0.70
4	»	15	»	»	»	»	$10^{-6}$	»
5	Sand-stone	2		21		1.2		
6	»	2		250				
7	»	2		»			$8 \dots 10^{-5}$	

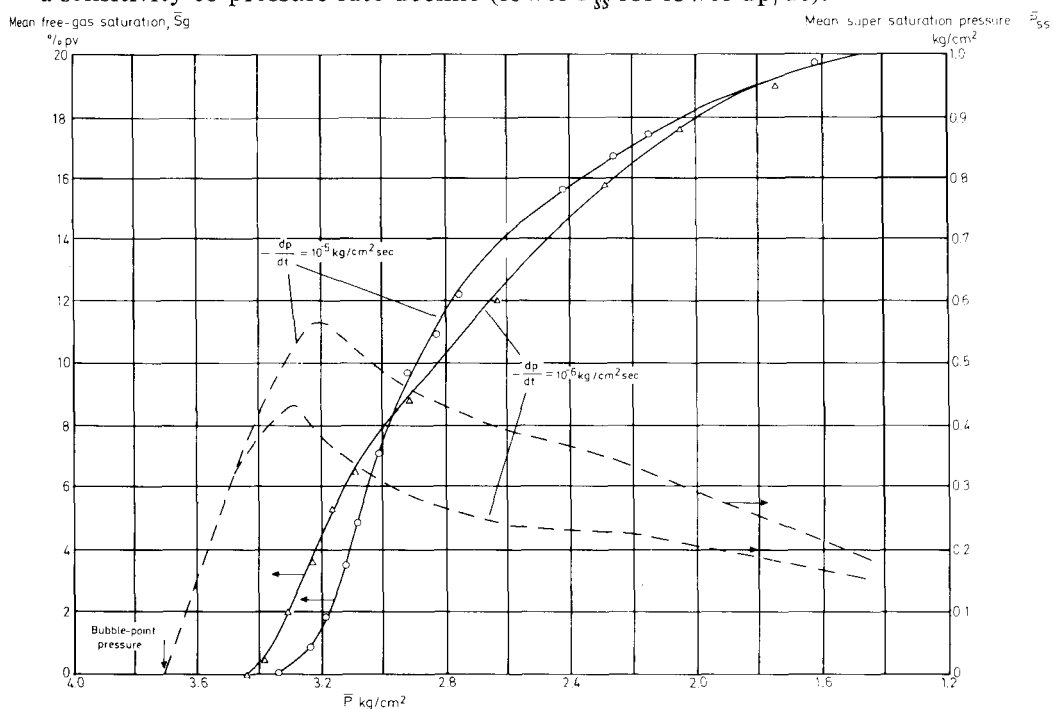
The two essential parameters resulting from supersaturation flowing conditions are the *mean average saturation*  $\bar{S}_g$  (% of pore volume) and the *mean supersaturation pressure*  $\bar{P}_{ss}$ . These two parameters are often expressed in relation to the *mean oil pore pressure*  $\bar{P}$ , which is associated to reservoir depletion.

Physically the pressure  $\bar{P}$  is the same in the totality of the block matrix, but the relationship of pressure vs. gas liberation is different on the surface of oil-gas contact, at the boundary of gas channels and inside the oil in the interchannel pores. The oil at the contact surface of the gas channels will liberate the gas according to the relationship  $R_s$  vs.  $P$  obtained in the laboratory PVT analysis, while outside the channels the oil will not liberate the gas as result of oil supersaturation. During the production phase part of the non-liberated gas, which remained in oil (at lower pressure than indicated by PVT) as a result of supersaturation, will move by diffusion towards the gas channels, and then break away from the oil after the gas-oil contact is reached. The gas so liberated will flow through the channels towards the fractures.

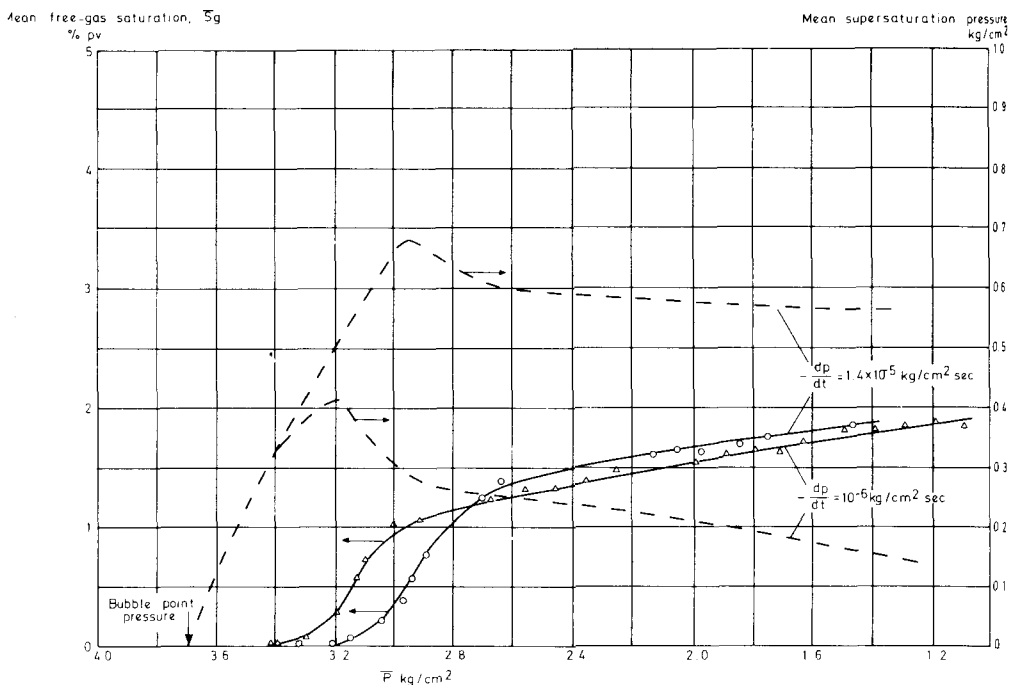
If, during the gas liberation under these specific conditions, the rate of pore pressure decline is high, a non-equilibrium will be created between pore pressure and channel pressure. This overly high supersaturation pressure will reach a new equilibrium only by developing new gas channels. It becomes evident that the number of gas channels, the spacing between channels, and the mean gas saturation are all associated to the rate of pore pressure decline.

*1. Role of permeability K.* In figure 10.23 the results obtained on a 350 Darcy glass pack show the variation of mean-free gas saturation  $\bar{S}_g$  and of mean supersaturation pressure  $\bar{P}_{ss}$  with mean oil pressure  $\bar{p}$ , for various rates of pressure decline, in the case of low pressure experiments at the low value of  $\bar{p}$ . As observed, independent of pressure decline rate ( $dp/dt$ ), the gas saturation in both conditions builds-up to  $\bar{S}_g = 20\%$ . The mean-supersaturation pressure  $\bar{P}_{ss}$  shows a maximum and then a rapid decline (figure 10.23). The  $\bar{P}_{ss}$  behaviour shows a sensitivity to  $dp/dt$  magnitude, and its maximum is increasing for higher rates of pressure-decline.

The same experiment repeated on 15 Darcy glass packs (figure 10.24) shows completely different results. Whenever capillary pressure increases, the saturation  $S_g$  is small (below 2%) and supersaturation  $\bar{P}_{ss}$  again shows a sensitivity to pressure rate decline (lower  $P_{ss}$  for lower  $dp/dt$ ).



10.23 -  $S$  and  $P_{ss}$  vs.  $P$  obtained in a model of 350 Darcy glass packs (Dumoré<sup>4</sup>, courtesy AIME)



10.24.  $S_g$  and  $\bar{P}_{ss}$  vs.  $\bar{P}$  obtained in a model of 15 Darcy glass packs (Dumoré<sup>4</sup>, courtesy AIME)

2. *Role of pressure decline rate  $dp/dt$ .* The rate of pressure decline is an essential parameter in the case of dispersion and non-dispersion behaviour of liberated gas.

At very high pressure decline rates vertical channelling in matrix is not developed at all, while at very low pressure decline rates vertical channels develop at the initial stage. In this last case it was observed that, during reservoir pressure depletion, the gas channels tend to expand out in thickness, and towards the final stage they extend throughout the entire matrix.

#### d. Critical values

From the large number of experiments it may be concluded that dispersion vs. non-dispersion is mainly controlled by the rock characteristics and by the rate of pressure decline.

1. *Leverett parameter.* From the experiments carried out it was found that  $\sigma \sqrt{\Phi/K}$  is a good criterion for both glass pack or sandstone experiments. It may be stated that higher values than the critical parameter will correspond to non-dispersion and lower values than the critical parameter to the dispersion case. This is in line with the idea that high permeability and porosity favour the dispersion. The *critical value for glass pack* is,

$$\text{critical } \sigma \sqrt{\Phi/K} \rightarrow 1.5 \times 10^4 \sim 2 \times 10^4 \text{ dyne/cm}^2$$

which corresponds to .22 – .29 psi, and reaches the range of,

$$\text{critical } \sigma \sqrt{\Phi/K} \rightarrow 20 \sim 30 \times 10^4 \text{ dyne/cm}^2$$

for intergranular consolidated rock.

Since the matrix block of the fractured limestone generally has a permeability of  $K \leq 1 \text{ mD}$  and a porosity  $\Phi$  between 20% and 30%, the result for  $K = 1 \text{ mD}$ ,  $\Phi \approx 20\%$  and  $\sigma (\text{gas-oil}) \approx 5 \text{ dyne/cm}$ , is

$$\text{critical } \sigma \sqrt{\Phi/K} \approx 5 \sqrt{0.2/10^{-11}} = 70 \times 10^4 \text{ dyne/cm}^2 \gg 40 \text{ dyne/cm}^2$$

which shows that non-dispersion conditions are normally obtained in an average fractured limestone reservoir.

2. *Pressure decline rate.* The experiments have shown that a non-dispersion condition is reached at a pressure decline rate in the range of  $10^{-5}$  and  $10^{-6} \text{ kg/cm}^2/\text{sec}$ , but effectively a non-dispersion condition is evident in the case of,

$$\text{critical } dp/dt \leq 10^{-6} \text{ kg/cm}^2/\text{sec} \approx 30 \text{ kg/cm}^2/\text{year}$$

3. *Dynamic criteria.* The gas movement in non-dispersion conditions requires that the flow in matrix is controlled only by gravity and capillary forces, and not by the flow pressure gradient. In order to check this specific situation it is important to remember that in a fractured reservoir, the flow is developed only through fractures in which permeability is high and the pressure drop in the fracture network is small. Assuming that the total pressure drop in the fractured network is around  $2 \text{ kg/cm}^2$  for a relatively high rate in case of a radial-plane pressure distribution, the pressure gradient is expressed by,

$$\frac{dp}{dr} = \frac{\Delta P}{\ln r_e/r_w} \times \frac{1}{r} = \frac{2}{7.6} \times \frac{1}{r \text{ (cm)}}$$

where  $r_e/r_w \approx 2000$ . At radii of 10 cm, 100 cm, 1000 cm and 10 000 cm, gradients of  $dp/dr = 2.63 \times 10^{-2}$ ,  $2.63 \times 10^{-3}$ ,  $2.63 \times 10^{-4}$  and  $2.63 \times 10^{-5} \text{ kg/cm}^2/\text{cm}$  will result. If compared with gravity forces  $\Delta\gamma$  (oil-gas) =  $2 \times 10^{-4} \text{ kg/cm}^2/\text{cm}$  it is understandable that, except for a limited area around the wellbore (approximately 10 m radius), the pressure gradient, resulting from the pressure drop of radial flow towards the well, will not influence the upward movement of gas.

#### e. Diffusion of gas through oil saturated matrix.

In order to verify the diffusion theory in different fractured oil reservoirs, the bubble point pressure was examined on some Iranian reservoirs. The study was made on oil

samples taken from the lower part of the oil zone (no gassing zone called zone 2, but undersaturated zone called zone 3 in figure 10.7). From examination of the sample the bubble point pressure was found to be continuously decreasing from the initial value.

This difference in bubble point pressure could not be attributed to the circulation that has taken place within the fracture system, since the volume of fractures is very small compared to the matrix, and the rate of production is very high. Therefore, the samples of oil taken from this part of the reservoir should represent the composition of oil supplied by matrix to fractures, and thus such a low bubble point of reservoir oil could be attributed only to the mechanism of gas diffusion through the oil phase inside the matrix. In particular it was noticed that a better diffusion in the fractured system is associated to a lower bubble point.

Calculation of an Iranian oil reservoir indicates that for a matrix system where the smallest size block is about 4–5 ft., the bubble point of oil in the matrix has dropped by 500 psi within 10 years of life. If the above mechanism can be determined in a certain reservoir, a new bubble point pressure distribution should be calculated and used in the material balance analysis. Some experiments have shown the validity of this process in different flowing conditions. Some of these results are given below:

- It was observed that better conditions (lower liberated gas saturation) are obtained in a low-permeability matrix (compare figure 10.23 with 10.24).
- Improved diffusion is obtained when the pressure decline rate  $\left(\frac{dp}{dt}\right)$  is lower (see figures 10.23 and 10.24).
- Supersaturation pressure improves (especially in the initial depletion stage), with decreasing pressure decline rate  $\left(\frac{dp}{dt}\right)$ .
- Better diffusion conditions are also obtained when bubble point pressure decreases.

During the diffusion process some of the gas is transported from the matrix through the liquid to fractures, where it is instantaneously liberated toward the gas-cap.

It is obvious that during this process the small amount of gas present in the matrix will increase the flowing efficiency (through improved relative permeability for oil) if compared with a case where no diffusion takes place.

#### g. Conclusions

- \* Due to the special conditions of a fractured reservoir, the conventional gas-drive solution must be modified if certain conditions develop during reservoir depletion.
- \* If the flowing pressure gradients are not large enough to prevail over capillary and gravitational forces, the liberated gas will behave differently from the classic gas-drive solution.
- \* In this case a series of vertical gas channels will develop and the liberated gas will quickly move toward the fractures surrounding the matrix block. This *non-dispersion* behaviour of the liberated gas will keep the rest of the gas in solution, and a supersaturation pressure will take place.

\* The consequences of this *unique behaviour* resulting from diffusion (non-dispersion) are:

1. The free-gas saturation  $S_g$  (% of pore volume) is lower if diffusion takes place, and consequently a better relative permeability for oil will result in the matrix block.
2. The lower pressure decline rate will, in general, be associated with lower free-gas saturation.

#### 10.3.2.3. Classic production mechanism (dispersion of liberated gas)

Inside the matrix block the liberated gas may react as in a classic case of a *solution gas-drive mechanism*. In other words, the liberated gas in the matrix will depend on the relationship between the relative permeability of gas vs. gas saturation.

If  $S_g < S_{g, cr}$  the liberated gas will remain immobile and its expansion will drive the oil out of the matrix block towards the fractures. If  $S_g > S_{g, cr}$  the liberated gas will become a movable phase, and inside a single matrix block the mechanism will be a combination between solution gas-drive and segregation. At this point the mechanism will become more complex since some of the liberated and segregated gas will leave the matrix and drive some of the oil towards the fractures. At the same time, as the desaturation in oil of the matrix blocks increases, the oil from the surrounding fractures may be re-imbibe the matrix and thus the resaturation in oil of the same block will reduce the single block production performance.

#### 10.3.3 Production mechanism in the undersaturated oil zone

The undersaturated zone of the reservoir is usually below the gassing zone ( $P = B_{pp}$ ) and the actual water-oil contact in fractures (WOL) as shown in figure 10.7. Since in this zone the gas is entirely dissolved in the oil which saturates the matrix and fractures, the production mechanism is the result of the single phase expansion of matrix oil under the pressure difference between the matrix and fractured network.

$$\Delta P_{MF} = P_M - P_F \quad (10.18)$$

In this case the effective compressibility is given by the totality of effects resulting from oil, water and rock compressibility,

$$C_{oe} = C_o + C_w \frac{\Phi_m S_{wm}}{\Phi_m (1 - S_{wm}) + \Phi_f} + C_{pw} \frac{\Phi_m}{\Phi_m (1 - S_{wm}) + \Phi_f} + C_{pf} \frac{\Phi_f}{\Phi_m (1 - S_{wm}) + \Phi_f} \quad (10.19)$$

or since  $\Phi_f \ll \Phi_m$  and  $C_{pm} \cong C_{pf}$ ,

$$C_{oe} \cong C_o + C_w \frac{S_{wm}}{1 - S_{wm}} + C_{pm} \frac{1}{1 - S_{wm}} \quad (10.20)$$

As observed, the compressibility of fractures is negligible, therefore the energy developed in the undersaturated zone is mainly due to the expansion energy of matrix oil.

The volume produced by simple expansion is given by,

$$\Delta N_{p, \text{UZ}} = V_{o, \text{UZ}} \times C_{oe} \times \Delta P_{MF} \quad (10.21)$$

where,

$$V_{o, \text{UZ}} = V_{\text{BULK, UZ}} \times \Phi_m \times (1 - S_{wi}) \quad (10.22)$$

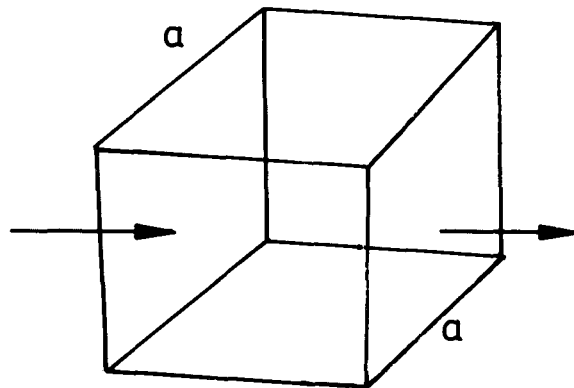
The rates of oil produced from the matrix are a function of geometrical size and dimension of matrix blocks, physical parameters of rock and matrix-fracture pressure drop (see zone 3 of figure 10.8b).

In a simplified case of uniform cubic blocks (figure 10.25) the total rate for n blocks will be given in steady-state conditions of flow by,

$$n_{\text{BLOCKS}} = \frac{V_{\text{BULK, UZ}}}{a^3} \quad (10.23)$$

where,

$$Q_{o, \text{UZ}} = V_{\text{BULK, UZ}} \frac{12 K_m}{a^2} \frac{\Delta P_{MF}}{\mu} \quad (10.24)$$



10.25 : Cubic matrix block saturated and surrounded by oil ( $p < B_{pp}$ )

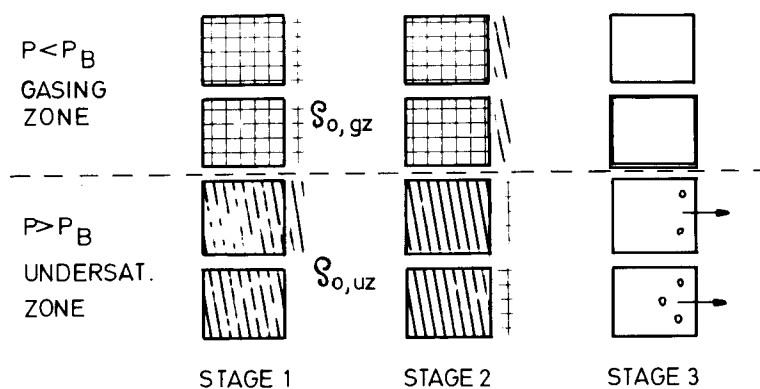
The relationship between  $N_{p,uz} Q_{o,uz}$  and time could be easily evaluated if the transient time is small and a rapid pseudo-steady-state condition is reached inside the matrix block. The time lag to reach a steady-state rate is given by,

$$t_{ss} (\text{sec}) \cong 0,5 \frac{a^2 (\text{cm}^2) \times \varphi_m (\text{fraction}) \times \mu_o (\text{CP}) \times \text{Coe (1/at)}}{K (\text{Darcy})}$$

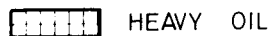
#### 10.3.4. Convection process in gassing and undersaturated zones

The oil contained in the fissures of the gassing zone will continuously reduce its dissolved gas during reservoir depletion. Consequently, during the depletion, the oil of the gassing zone will become heavier than the underlying oil in the fissures of the undersaturated zone (figure 10.10 and 10.26, stage 1).

The heavier oil on top and lighter oil on the bottom will create an *unstability*, and as a result a *convection mixing* takes place in which the heavy oil moves downwards through the fractures where (figure 10.26, stage 2) it enters in contact with the lighter oil (higher content in dissolved gas) in the matrix block. The calculation has shown that the density contrast between the oil in the matrix and fissures (figure 10.26) causes *convective mixing* within the matrix. The *convective mixing* causes more of the dissolved gas to transfer from matrix to fissure than does molecular diffusion (figure 10.26, stage 3).



#### LEGEND:



10.26 – Various stages in a convection process

The problem of convection was examined by Peaceman<sup>5,6</sup>, who suggested the examination of convection in two extreme cases:

1. Convection will not take place in the undersaturated zone, and thus no additional dissolved gas will be produced from this zone. Consequently, the saturation pressure in fissure and matrix remains equal to its original value. The gas produced in the gas-cap will *only* be the result of the gasing zone.
2. A very strong (infinitely rapid) convection takes place in the undersaturated zone. As a result the saturation pressure at each level is equal to the pressure at the current gas-oil level. A *maximum* transfer of gas from matrix to fractures takes place.

These *extreme* cases are *non-existent* and field sampling indicates significant saturation-pressure depression which confirms that convection phenomena take place in undersaturated zones.

Convection in a fissure with transport between matrix and fractures has also been examined by Peaceman<sup>5</sup>, by using a vertical fissure of width  $b$  with a permeability of  $K_f = b^2/12$ .

- Basic equations

A material balance of the dissolved gas in a fissure must take into account diffusion, convection, transport from matrix to fissure and accumulation:

$$D_F \left( \frac{\partial^2 R_{SF}}{\partial x^2} + \frac{\partial^2 R_{SF}}{\partial y^2} \right) - v_x \frac{\partial R_{SF}}{\partial x} - v_y \frac{\partial R_{SF}}{\partial y} + q_{M-F} = \frac{\partial R_{SF}}{\partial t} \quad (10.25)$$

A material balance of dissolved gas in the matrix will give:

$$q_{m-F} = -\frac{V_m}{V_F} \frac{\partial R_{sm}}{\partial t} \quad (10.26)$$

where  $V_M/V_F$  is the hydrocarbon volume of matrix per unit of volume of fissures.

In order to correlate the density and  $R_s$ , a linear relationship is admitted:

$$\rho = a^1 + b^1 R_s$$

and therefore, equations 10.25 and 10.26 become:

$$D_F \left( \frac{\partial^2 \rho_F}{\partial x^2} + \frac{\partial^2 \rho_F}{\partial y^2} \right) - v_x \frac{\partial \rho_F}{\partial x} - v_y \frac{\partial \rho_F}{\partial y} = \frac{\partial \rho_F}{\partial t} + \frac{V_M}{V_F} \frac{\partial \rho_m}{\partial t} \quad (10.27)$$

and,

$$\frac{V_m}{V_F} \frac{\partial \rho_m}{\partial t} = K_m (\rho_F - \rho_M) \quad (10.28)$$

where  $K_M$  is the transfer coefficient.

- Perturbation analysis

If no matrix-fissure transport takes place ( $K_M = 0$ ) in a fissure of width  $b$  and height  $H$  (considered as a convection cell), a perturbation will result due to an inverse density gradient. The finger will grow exponentially by factor  $e^{\omega t}$ , where  $\omega$  expresses the growth factor for perturbation (figure 10.27).

Factor  $\omega$  depends on physical parameters and must be equal in matrix and fractures. The mathematical expression of finger growth is thus,

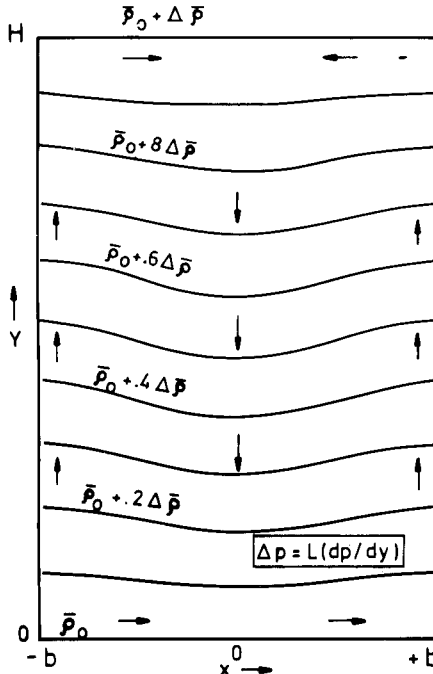
$$\frac{1}{D_F} \left[ \omega + \frac{K_M V_M / V_F}{K_M + V_M / V_F} \right] = -(\varepsilon^2 + v^2) + \frac{\varepsilon^2 v}{\varepsilon^2 + v^2} \quad (10.29)$$

where,

$$\varepsilon^2 = \frac{m\pi}{w} \quad (10.30)$$

$$v = \frac{n\pi}{L} \quad (10.31)$$

$$\chi = \frac{K_F g(d\rho/dy)}{\mu D_F} \quad (10.32)$$



10.27 - Density contours in a sinusoidally perturbed inverse density gradient (Peaceman<sup>5</sup>, Courtesy AIME)

Equation 10.29 indicates the mass transfer through parameters  $K_M$  and  $V_M/V_F$ , and therefore the growth factor perturbation may be redefined, in the absence of matrix-fracture transfer, as follows:

$$\omega_o = \omega + \frac{K_M \omega V_M/V_F}{K_M + (\omega V_M/V_F)} \quad (10.33)$$

The *stability* and *instability* of density inversion could be examined by equation 10.29. Instability is indicated by the positive values of  $\omega$  since any finger will grow exponentially, while a negative  $\omega$  represents a stability and this corresponds to a stable density inversion.

Based on equation 10.24 the stability or instability of the density inversion depends on  $\omega$  values.

$\omega > 0$  indicates instability – the finger perturbation  
grows exponentially

$\omega < 0$  indicates stability – the perturbation will die

$\omega = 0$  indicates a neutral stability

#### c. General observations

The results of various factors examined are as follows:

For  $K_M/\omega_o > 10$   $\omega/\omega_o = 1 - K_M/\omega_o$

For  $K_M/\omega_o < 0.5$   $\omega/\omega_o = 1/(1 + V_M/V_F)$

In normal cases the above parameters are expected to be of the following order of magnitude,

$K_M > 10^{-6} \text{ sec}^{-1}$

$50 < V_M/V_F < 100$

$\omega/\omega_o$  units of percent

The instability of density inversion is independent of the matrix-fissure transfer. For a fissure having a height of 1000 feet, the horizontal spacing of the density finger is expected to be approximately 30 feet.

The inverse density gradient grows with time exponentially  $e^{\omega t}$ .

For large fractures the growth factor  $\omega$  is totally dependent on the magnitude of  $D_f$ .

#### 10.3.5. Production mechanism in the water-invaded zone

The production mechanism of a single matrix block in the water-invaded zone caused by gravity and capillary imbibition was discussed in detail in chapter 9. If a stack of vertical blocks is separated by horizontal fractures, the (oil) displacement process is

associated with the advance of the water-oil contact in fractures and single block production starting time.

The methods and physical considerations are practically limited to the criteria discussed in chapter 9, in which the extension of results for the entire field may be solved by different approaches, experimental, theoretical, numerical simulation, etc.

#### 10.3.5.1. Experimental approach – Mattax method

In chapter 9 the imbibition behaviour of the matrix block was verified by experimental laboratory tests to be controlled by the dimensionless group,

$$\left[ \frac{\sigma}{\mu_w H_B^2} \sqrt{\frac{K}{\Phi}} t \right]_M = \left[ \frac{\sigma}{\mu_w H_B^2} \sqrt{\frac{K}{\Phi}} t \right]_{RB} \quad (10.34)$$

In this way the recovery vs. time behaviour obtained from laboratory tests on cores may be used for a stack of vertical matrix blocks.

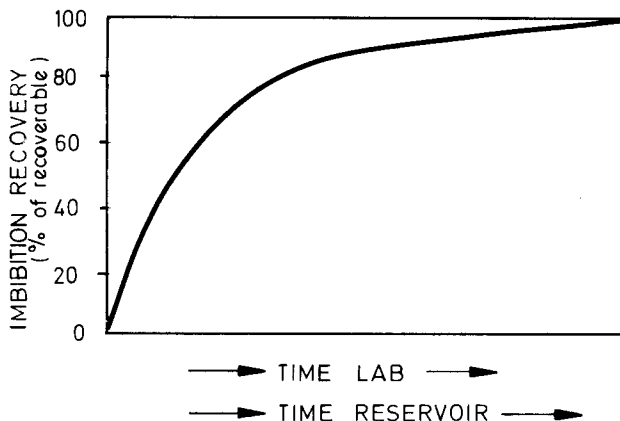
The necessary basic data are as follows:

- fluid data
- block characteristics –  $K$ ,  $\Phi$ ,  $S_{wi}$ ,  $H_B$
- reservoir characteristics – reservoir height  $H_r$  and area  $A$
- rate of water front advancement in fractures,  $V_{wo}$
- recovery vs. time resulting from laboratory tests (figure 10.28).

The calculation procedure is as follows:

- Based on results obtained from laboratory tests on cores, the recovery-time relationship of figure 10.28 is transformed to recovery-time reservoir relationship through equation 10.34 and drawn in figure 10.28 as a new time scale:

$$t_{RB} = \frac{(\sigma/\mu_w H_B^2)_M}{(\sigma/\mu_w H_B^2)_{RB}} \times \frac{\left[ \frac{K}{\Phi} \right]_M^{1/2}}{\left[ \frac{K}{\Phi} \right]_{RB}} \times t_M \quad (10.35)$$



10.28 – Recovery vs. time in a single matrix block

where M represents the model and RB represents the reservoir block.

- Considering that there are n blocks in a stack of vertical blocks (figure 10.29) and that recovery of each block i begins at time  $t_{oi}$  as effect of rate  $V_{wo}$ , the stack recovery vs. time will result from the simulation of recoveries of all blocks between 1 and n.
- The imbibition recovery expressed as a percentage of total oil recovery for each matrix block results from figure 10.28 as a function of time  $t = t_{oi} - t_{o,i-1}$ ,

$$R_i = f(t - t_{o,i-1})$$

where  $t_{o,i-1}$  indicates the time when imbibition begins in block i.

- This time  $t_{o,i-1}$  will result in the case of a constant rate of water-oil advance-

$$t_{o,i-1} = \frac{\sum_{i=1}^i h_B}{v_f} \quad (10.36)$$

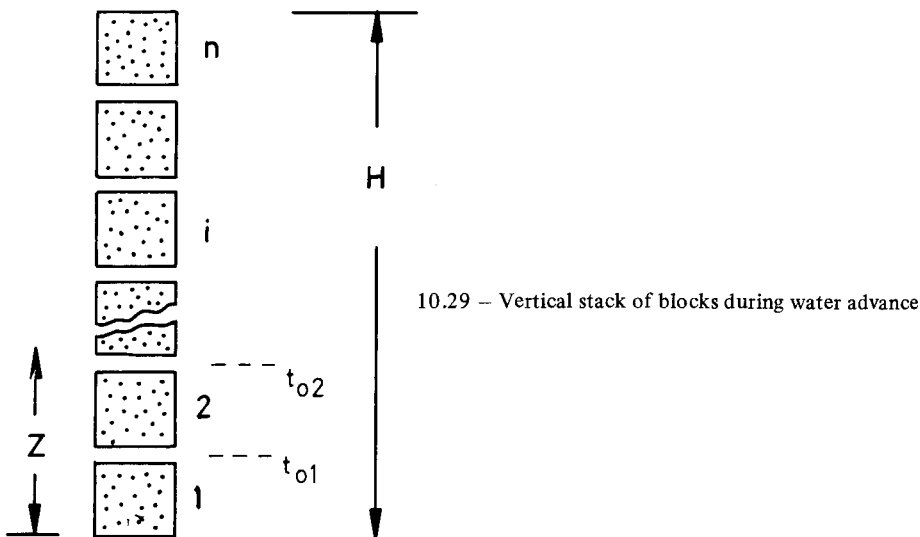
- The total oil recovery for n blocks will be,

$$R_R = \frac{\sum_{i=1}^n R_i \times \left[ V_B \times \Phi \times (1 - S_{wi}) \right]_i}{\sum_{i=1}^n \left[ V_B \Phi (1 - S_{wi}) \right]_i} \quad (10.37)$$

which, in the case of blocks of equal sizes, will give,

$$R_R = \frac{1}{n} \sum_{i=1}^n R_i \quad (10.37)$$

where  $R_i$  is a function of time



### 10.3.5.2. Theoretical approach

#### a. Aronofsky's<sup>8</sup> abstract model

In the case of a series of matrix blocks vertically stacked and separated by fractures, the water rises in the fractures and the oil production of the block begins when water comes in contact with the block. As discussed in chapter 9, the single block recovery may be expressed by,

$$R = R_f (1 - e^{-\lambda t}) \quad (10.38)$$

which is based on a theoretical approach. The value  $\lambda$  may be considered as the basic recoverable rate, while its reciprocal value  $t_f = 1/\lambda$  represents the time necessary to obtain the final recovery  $R_f$ . In fact, at times when  $t = t_f$ , then  $\lambda t_f \cong 1$  and therefore  $(1 - 1/e) \cong 0.63$ .

In the case of vertically stacked blocks of equal dimensions (figure 10.29), the oil in place in each block will be given by,

$$a_e H_B = a \times \Phi (1 - S_{wi}) H_B \quad (10.39)$$

and in  $i$  blocks will be,

$$N_i = a_e Z_i \quad (10.40)$$

where  $a_e$  is the effective flowing cross-section of the block.

Oil recovery will begin at time  $t > t_{o,i}$  when the water comes in contact with block  $i$ , and therefore the oil produced will be given for block  $i$  as,

$$N_{p,i} = N_i \times R_f (1 - e^{-\lambda t_i}) \quad (10.41)$$

or

$$N_{p,i} = \sum_i^i R_f (1 - e^{-\lambda t_i}) a_e z_i \quad (10.42)$$

If the oil produced is expressed as a continuous function of rising water level  $z$ , equation 10.42 becomes,

$$N_{p,i} = a_e R_f \int_0^z \left[ 1 - e^{-\lambda(t-t_i)} \right] dz \quad (10.43)$$

or as a recovery function of time (since  $N_p = aHR$ ),

$$R = \frac{1}{H} R_f \int_0^t (1 - e^{-\lambda t}) dt \quad (10.44)$$

b. De Swaan's approach

The rate of water imbibition per unit of fracture length is based on the unitarian rate of a single block,

$$q = a R_f \lambda e^{-\lambda t} \quad (10.45)$$

which, for the total number of blocks, becomes the integral of variation in time of surrounding water saturation.

$$q_i = a_e R_f \lambda \int_0^t e^{-\lambda(t-t_i)} \times \frac{\partial S_w}{\partial t_i} \times dt_i \quad (10.46)$$

c. Other simplified methods

If the reservoir is preferentially fractured with sub-vertical fractures and the horizontal fractures are not interrupting the flowing continuity process from block to block, the matrix block may be idealized to a matched type model as discussed in chapter 4, Fig. 4.20.

Since in this case the blocks will be vertically elongated, it may be considered that gravity will be the predominant flow mechanism since the blocks are tall, and the reservoir rate is given by the following equation,

$$Q = A \frac{K_o}{\mu_o} \Delta \gamma \quad (10.47)$$

In this case each class of matrix blocks will be classified through its permeability and porosity. It will follow that each class has a certain amount of oil in place which will flow at a certain rate, a function of both class percentual magnitude and respective  $\Phi$ ,  $S_{wi}$ ,  $K$  of the class.

The field rate could be calculated as the total of all single rates of each class.

$$Q = \frac{\Delta \gamma}{\mu_o} \sum_{i=1}^h A_i K_{o,i} \quad (10.48)$$

## 10.4. SPECIFIC ASPECTS OF A FRACTURED RESERVOIR

### 10.4.1. Material balance relationship

A material balance in a fractured reservoir where several production mechanisms coexist, is developed as a result of interaction among single zones and a combination of the simultaneous behaviour of all production mechanisms.

A material balance where the gas-invaded and water-invaded zones show different efficiencies as a result of imbibition and drainage production mechanisms, must be associated with the gassing zone and undersaturated zone production mechanisms, which depend more on reservoir pressure decline and the parameters associated with reservoir pressure.

#### 10.4.1.1. Global material balance

If the reservoir zones are similar to those shown in figure 10.7, the material balance may be written as the relationship between cumulative oil produced  $N_p$  and oil delivered by matrix pore volume of each zone to the fractured network. In reservoir conditions the result is,

$$N_p B_o = V_{GIZ} \times R_G + V_{WIZ} \times R_W + V_{SGZ} \times R_{SGD} + V_{UZ} \times R_{EXP} \quad (10.49)$$

which may be expressed in a differential form for an interval of time  $t$  as,

$$\Delta N_p B_o = \Delta N_{p,GIZ} + \Delta N_{p,WIZ} + \Delta N_{p,SGZ} + \Delta N_{p,UZ} \quad (10.50)$$

Often the material balance may be associated to the changes in fluid saturations inside the reservoir matrix and fractures. For example:

- change in residual oil volume

$$\Delta V_{RO} = \Delta [PV \times S_o/B_o] \quad (10.51)$$

- change in free-gas volume

$$\Delta V_{FG} = \Delta [PV \times S_g/B_g] \quad (10.51')$$

- change in water volume

$$\Delta V_w = \Delta [PV \times S_w/B_w] \quad (10.51'')$$

In this case the changes in oil saturation throughout the reservoir pore volume must be associated with changes in free-gas in the gas-invaded zone and gasing zone, and changes in water in the water-invaded zone.

#### 10.4.1.2. Material balance of single zones

At any stage the single zones are delimited by the gas-oil contact (GOL), water-oil contact (WOL) and pressure distribution vs. bubble point pressure.

In each zone it is necessary to know the respective volumes of pores expressed by  $V_{GIZ}$ ,  $V_{WIZ}$ ,  $V_{SGZ}$  and  $V_{UZ}$ , as well as matrix block characteristics (geometry, height, permeability, porosity, saturation in water, etc.).

In order to satisfy equation 10.50 it is necessary for a given time stage to fix a given pressure decline, and therefore evaluate the oil produced in each single zone as a result of various production mechanisms.

The material balance of fractures for each zone may be written for various phases – oil, gas and water – as follows:

- oil phase (remained oil RO);

$$\sum \text{change ROM} + \sum \text{change ROF} = \sum \text{vol ROT} + \sum \text{vol ROP} \quad (10.52)$$

- gas phase (free-gas FG);

$$\sum \text{change FGM} + \sum \text{change FGF} = \sum \text{vol FGT}$$

$$+ \sum \text{vol FGP} - \sum \text{vol FGI} \quad (10.53)$$

- water phase (W);

$$\sum \text{change WM} + \sum \text{change WF} = \sum \text{vol WT}$$

$$+ \sum \text{vol WP} - \sum \text{vol WE} - \sum \text{vol WI} \quad (10.54)$$

In these equations M and F represent the matrix and fractures while T, P, E and I are transferred, produced, encroached and injected fluid, respectively.

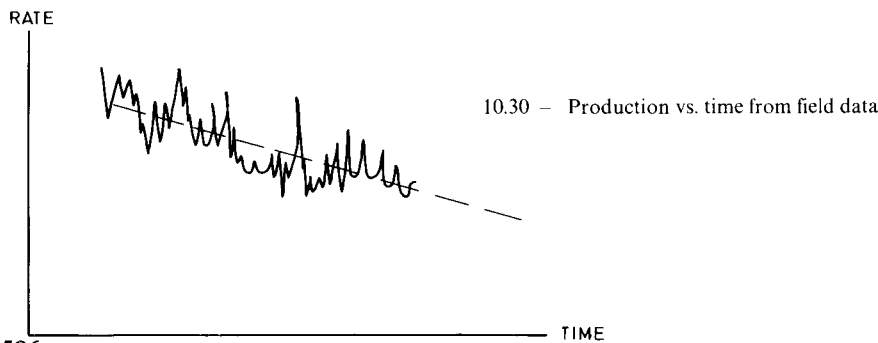
#### 10.4.1.3. Oil recovery forecast of a fractured reservoir

There are several ways to estimate a reserve. They are as follows:

a. Extrapolation method

If in a reservoir, past history data such as pressure, water-oil and gas-oil advancement and cumulative production are known, it is possible to evaluate its future behaviour by conventional extrapolation (Fig. 10.30). This extrapolation may be rate vs. time, rate vs. cumulative oil produced, etc. The validity of this method is limited in cases of substantial modification of rate of production, of high water-cut, and of high GOR as a result of gas coning.

This type of quick procedure has however more validity in reservoirs which are producing oil above bubble point (undersaturated), where water encroachment in fractures offers simultaneously a pressure maintenance and a production of oil through imbibition of matrix.



b. Material balance method

— Matching the past history by varying block size and magnitude of gas diffusion; In this method the magnitude of water influx is estimated by using equation 10.49 after a volume of liberated gas has moved from the oil zone to the gas-cap and gas-invaded zones.

Water and gas efficiency are obtained by dividing the volume of encroached water by the pore volume of the water-invaded zone, and the volume of gas from the invaded zone by the respective pores. In this way the two unknown parameters of oil in place and bubble point depression, and a simultaneous solution of the material balance equations may be obtained by the method of least squares. In order to match the calculated reservoir behaviour with the past history, a variation of block size and magnitude of diffusion can be used.

- Matching the past history for the most probable water and gas displacement efficiency. Since the total contribution of expansion and dissolved gas drive can be calculated for each given reservoir pressure, equation 10.50 becomes,

$$R_G \times V_{GIZ} + R_W \times V_{WIZ} = \text{Production}$$

$$- R_{SGD} \times V_{GZ} - R_{EXP} \times V_{UZ} = P_{NET} \quad (10.55)$$

Dividing equation 10.55 by  $V_{GIZ}$  and then multiplying by  $V_{WIZ}/V_{GIZ}$ , the result is as follows,

$$R_G \frac{V_{WIZ}}{V_{GIZ}} + R_W \left( \frac{V_{WIZ}}{V_{GIZ}} \right)^2 = P_{NET} \times \frac{V_{WIZ}}{(V_{GIZ})^2} \quad (10.56)$$

and if the past history data can be used for X steps, it will result

$$R_G \sum_1^x \frac{V_{WIZ}}{V_{GIZ}} + R_W \sum_1^x \left( \frac{V_{WIZ}}{V_{GIZ}} \right)^2 = \sum_1^x P_{NET} \frac{V_{WIZ}}{(V_{GIZ})^2} \quad (10.57)$$

Similarly, for X steps equation 10.55 will give

$$X R_G + R_W \sum_1^x \frac{V_{WIZ}}{V_{GIZ}} = \sum_1^x \frac{P_{NET}}{V_{GIZ}} \quad (10.58)$$

By solving equations 10.57 and 10.58 the most probable efficiency  $R_G$  and  $R_W$  can be estimated. An application is given in chapter 11.

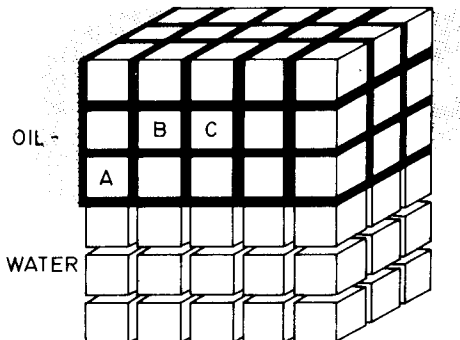
#### 10.4.2. Migration of hydrocarbons in a fractured reservoir

The migration process of oil and/or gas in a fractured reservoir is related to a drainage displacement process of a wetting phase (water) by a non-wetting phase (oil/gas). Consequently, capillary forces, threshold pressure, pore size and distribution will play an essential role in this process. In addition, a different saturation distribution is resulting in a reservoir if the migration of hydrocarbons took place *before* or *after* reservoir fracturing.

#### 10.4.2.1. Fracturing followed by hydrocarbon migration – Case 1

In a fractured reservoir the migration is governed by the flow law of drainage displacement where matrix blocks saturated with the wetting phase (water) are surrounded by migrated oil in fractures, (figure 10.31). Assuming, for simplification purposes, that the reservoir is formed by regular geometrical shaped blocks having either the same dimensions or the same properties, the exchange of fluid between fracture and matrix may be examined in detail.

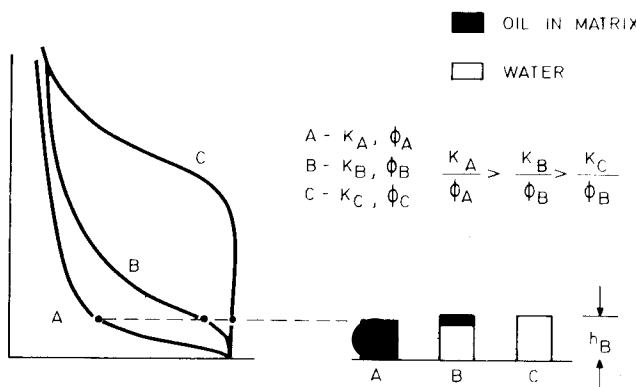
Desaturation in water of these blocks will depend on the physical properties of the rock and especially on the capillary pressure curve.



10.31 – First stage of migration in a fractured reservoir. (Fractures filled by oil).

##### a. Uniform blocks: equal $H_B$ , but different $\Phi$ , $K$

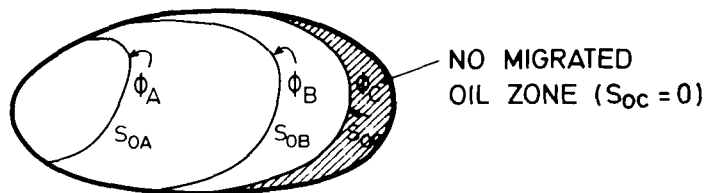
If the reservoir is formed by blocks of uniform heights  $H_B$ , in the blocks of type A, oil saturation will be high; if formed by type B blocks, oil saturation will be low, and if formed by type C, only the fractures in the reservoir will contain oil. The result is obtained in agreement with respective capillary pressure curves A, B and C of figure 10.32.



10.32 – Second stage of migration.

Equal blocks differently saturated with hydrocarbons as a result of  $\Phi$ ,  $K$ , and  $P_c$  magnitudes

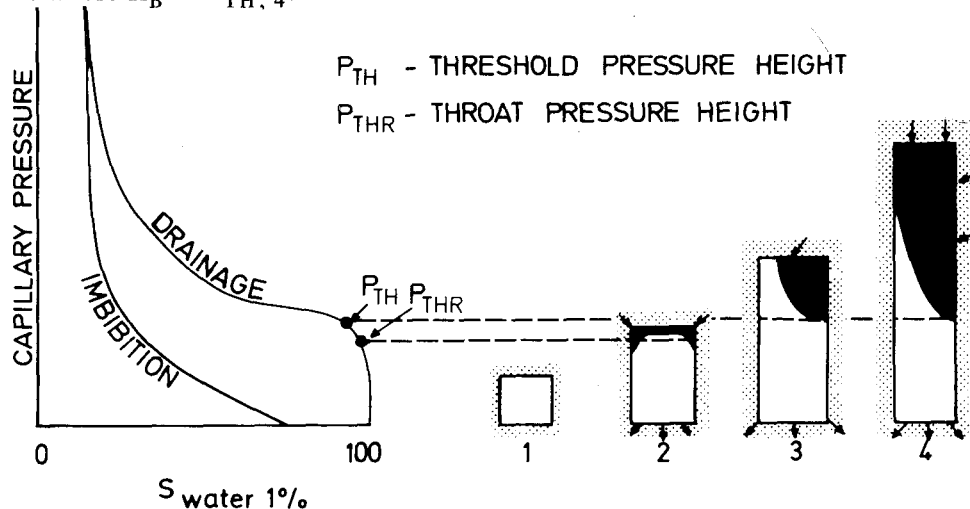
It is evident that the tighter zones will have less oil and more permeable rocks will contain more oil, if block height is uniformly distributed throughout the entire reservoir. The iso-saturation lines are expected to follow the isoporosity lines. In a simplified case based on capillary properties of blocks A, B and C of figure 10.33, the iso-saturation in oil  $S_{o,c} = 0$  will correspond to iso- $\Phi_c$  lines, while iso- $\Phi_B$  will represent lines of higher saturation and iso- $\Phi_A$  will represent lines of highest oil saturation.



10.33 – Iso-saturation lines influenced by rock characteristics in the case of a fractured reservoir formed by blocks of uniform heights but different physical properties.

b. Equal block properties ( $\Phi$ ;  $K$ ) and various block heights ( $H_B$ )

If block properties are identical, the difference in oil saturation will result from the relationship between block height and capillary height vs. saturation (figure 10.34). In block 1 (small block) the saturation in oil is zero, but increases in blocks 2 and 3. The saturation in oil is effectively high in block 4 where  $H_B \gg H_{TH, 4}$ .



10.34 – Water drained by migrated oil as a function of block height and capillary pressure curve, in case of uniform matrix but different block heights.

c. Various block heights ( $H_B$ ) with various physical properties

This represents the most probable case since, in addition to a variation of rock properties, a variation of block height during the fracturing process is expected. If migration took place after rock fracturing, the well logging results may explain the process which took place in the reservoir during migration.

By examining the logs illustrated in figure 10.35 the following comments can be made:

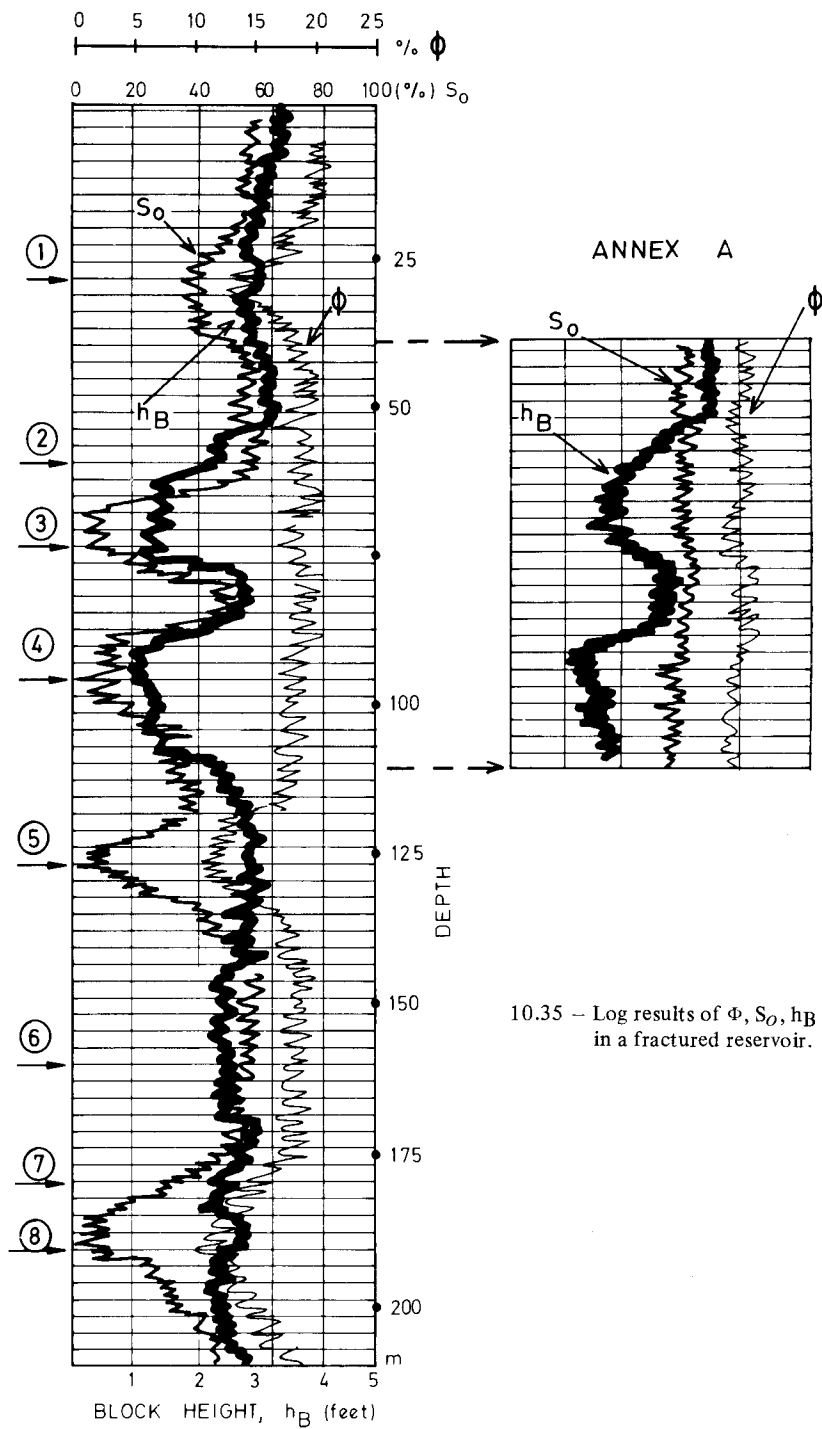
- If block height  $h_B$  remains constant and saturation  $S_o$  is simultaneously reduced with porosity, the explanation is similar to that of blocks A and B of figure 10.32. If the rock becomes tighter, capillary pressure will limit the drainage of water by migrated oil. These examples are shown in zones 1,5 and 8 of figure 10.35. As may be observed in cases 5 and 8 for blocks having a height of  $h_B = 2.5$  feet and  $\Phi = 12\%$ , the saturation in oil is zero, which is similar to C in figure 10.32.
- On the other hand if  $\Phi$  remains constant in the range of  $\Phi = 18\%$  and fracture density increases (which corresponds to  $h_B = 1.2 - 1.5$  feet), this will result in a lack of oil saturation (figure 10.35, zones 3 and 4). The reduction in saturation in zones 3 and 4 corresponds to case 1 and 2 illustrated in figure 10.34. A small block (height) will reduce saturation in oil for the same rock as a result of capillary forces opposing the migrated oil from draining the oil in the pores.

#### 10.4.2.2. Migration followed by reservoir fracturing – Case 2

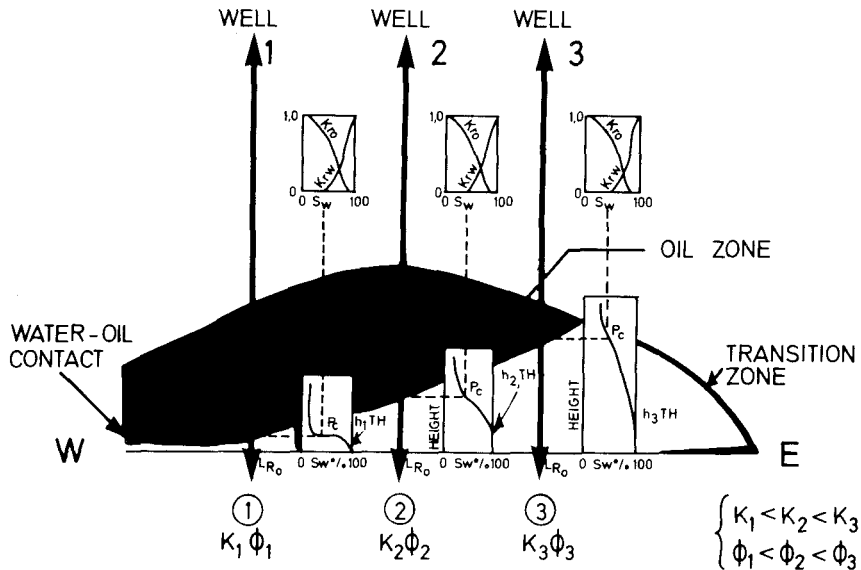
In any reservoir with intergranular porosity, during the migration phase the fluids will be distributed in the reservoir according to rock characteristics. A transition zone will be observed if various facies exist in the reservoir as shown in the west-east cross-section in figure 10.36. On the eastern side of the cross-section (well 3), since the pores are very fine the capillary pressure will be high and the saturation in water will remain elevated. In the western zone, coarse pores will correspond to reduced capillary pressure, and thus to the absence of a transition zone (well 1). The variation of the transition zone through wells 1, 2 and 3 very clearly indicates the west-east direction of the facies variation.

Assuming that at a later geological stage the reservoir was fractured, a redistribution of fluids will take place as a result of a new equilibrium due to fracture intercommunication. Inside the fractured network the water-oil contact will become a horizontal plane and the hydrocarbons will migrate under imbibition and drainage conditions. In a schematic case (discussed above and illustrated in figure 10.37), the hydrocarbons displaced by water imbibition will migrate upwards in the west side (well 1) and downwards in the east side, draining the remaining water in this zone (well 3).

After long periods of geological time an equilibrium will be reached, and thus the zone of oil will be limited by water-oil contact in the fractured network. Saturation of the oil zone depends on the height and characteristics of the blocks.



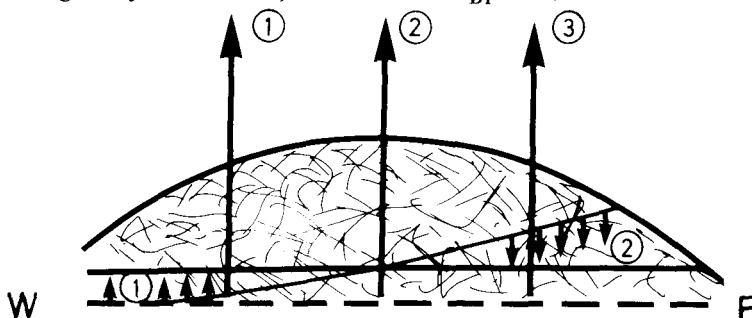
10.35 - Log results of  $\Phi$ ,  $S_o$ ,  $h_B$  of a well drilled in a fractured reservoir.



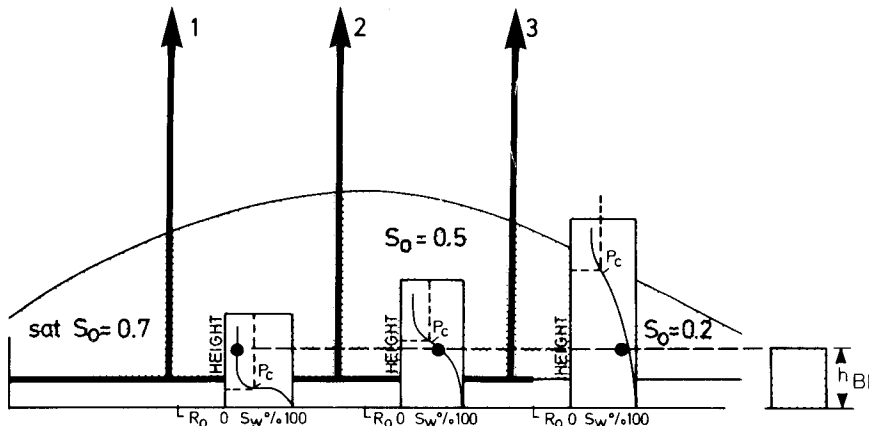
10.36 – Saturation distribution in a non-fractured reservoir as a function of facies variations

– If it is assumed that all blocks have a uniform height ( $h_B > h_{TH3}$ ), saturation will vary according to the capillary pressure curve. If, for example, a reservoir having blocks of uniform height  $h_B$  (right side of figure 10.38) is investigated, the average saturation of each well will result as a function of block height related to capillary curve heights. This second phase of migration will redistribute the saturation in fluid in the east zone of the reservoir cross-section, but throughout the reservoir the increasing trend in saturation results in an east-west direction.

– If blocks were reduced in dimension to  $h_{BL} < h_{3TH}$ , the saturation in oil in the well 3 zone would remain  $S_o = 0$ , since oil would not be capable (after rock fracturation took place) of draining the water of small blocks only by the gravity difference, the result of  $h_{BL} \times \Delta\gamma$ .



10.37 – Water-oil contact in fractures after reservoir fracturing. Zone (1) – water displaces oil by imbibition; zone (2) – oil drains water from matrix



10.38 – Saturation redistribution after reservoir fracturing

– The logs examined in figure 10.35 showing the behaviour of zones 3 and 4, where rock properties are unchanged and the oil saturation is reduced to zero due to small block height, very clearly indicate that oil migration took place *after* reservoir fracturing. Inversely, if in zones 2, 3 and 4 the logs (Annex A, figure 10.35) indicate that  $S_o$  is not a function of  $h_{BL}$ , but a function of  $\Phi$  (regardless of reservoir fracturing characteristics), it may be concluded that oil migration took place *before* reservoir fracturing.

## SYMBOLS

### Latin letters

$a$	– cubic block dimension
$a'$	– constant
$b'$	– constant
$B_{pp}$	– bubble point pressure
$C$	– compressibility
$D_f$	– diffusion coefficient
$F(S_o^*)$	– function of saturation
$g$	– gravity
$GOL$	– gas-oil limit
$GOLO$	– gas-oil limit, originally
$h$	– height
$H$	– total height
$H_g$	– fracture gas invaded height
$J(S_o^*)$	– Leverett function
$K$	– permeability
$K_M$	– transfer coefficient
$K_o$	– effective permeability for oil

$L$	- length of fissure
$m, n$	- horizontal and vertical number of cells
$M$	mobility factor
$OIP$	original oil in place
$P$	- pressure
$P_G$	pressure gradient
$PVT$	pressure – volume – time relationship
$q$	rate
$Q$	- dimensionless rate ( $Q_{SUPP}/Q_{MAX}$ )
$r$	- pore radius
$R_i$	- recovery function of time of block $i$ in a stack
$R_{SF}$	- dissolved gas ratio in fractures
$R_s$	- solution gas ratio
$S$	- saturation
$S_o^*$	- effective saturation for oil (Eq. 10.2)
$t$	- time
$T_G$	- temperature gradient
$v$	velocity
$V_F$	fracture volume
$V_M$	- matrix hydrocarbon volume
$WOLO$	- water-oil limit, originally
$WOL$	- water oil limit
$Z$	- height along axis oz
$x, y$	horizontal and vertical axis parallel to respective oriented fractures

### Greek letters

$\alpha$	- interaction parameter
$\delta_o$	- original volumetric mass
$\delta_p$	- volumetric mass variation under constant pressure
$\delta_T$	- volumetric mass variation under constant temperature
$\epsilon$	- spatial frequency of density distribution
$\varphi$	- porosity
$\kappa$	- Raleigh number
$\lambda$	- coefficient of thermal expansion
$\mu$	- viscosity
$\rho$	- specific mass
$\underline{\rho}$	- unperturbed density
$\sigma$	- interfacial tension
$\omega$	- experimental growth factor for perturbation

### Subscripts

$BL$	- block
$Block$	- matrix block
$Bulk, UZ$	- bulk, undersaturated zone
$C$	- capillary
$DR$	- drainage
$f$	- fracture
$g$	- gas

GR	- gravity
i	- referred to block i
MAX	maximum
mf	matrix fracture
m, M,	matrix
o	oil
oe	- effective for oil
o, uz	oil, undersaturated zone
pass	passing
pm	pores matrix
P, uz	pores, undersaturated zone
RB	reservoir block
REINF	reinfiltration
rg	relative gas
S	static
SI	static reservoir initial
ss	pseudo-steady-state
supp	supply
TH	- threshold
w	- water
wm	- water matrix

## REFERENCES

1. Mattax C.C. and Kyte, J.R. 1962. Imbibition Oil Recovery from Fractured, Water Drive Reservoir. Soc. Petr. Eng. J. (June) 177–184; Trans. AIME, vol. 225
2. Saidi, A.M. and Tehrani, D.H. 1980. Mathematical Simulation of Fractured Reservoir performance, based on Physical Model Experiments. 10th World Petroleum Congress.
3. Saidi, A and Van Golf-Racht T.D. 1971. Consideration on basic producing mechanisms in fractured reservoir. Revue de l'institut Français du Pétrole (December) pp. 1167–1180
4. Dumorè, J.M., 1972. Development of gas saturation during solution-gas drive in an oil layer below a gas cap. Soc. of Petroleum Engineers Journal, AIME, (Sept).
5. Peaceman, D.W. 1976. Convection in a Fractured Reservoir – The Effect of Matrix – Fissure Transfer on the Instability of a Density Inversion in a Vertical Fissures, Soc. Petroleum Eng. J. (October); 269–279
6. Peaceman, D.W., 1976. Convection in a Fractured Reservoir Numerical Calculation of Convection in a Vertical Fissure, Including the Effect of Matrix – Fissure Transfer. Soc. Petroleum Eng. J., AIME, (October), 281–301.
7. Aronofsky, J.S. Masse, L. and Natanson, S.G. «A Model for the Mechanism of Oil Recovery from the Porous Matrix due to Water Invasion in Fractured Reservoir» J. Pet. Tech., AIME, (January); pp 17–19.

This Page Intentionally Left Blank

# CHAPTER 11

## NUMERICAL SIMULATION OF FRACTURED RESERVOIRS

### 11.1. INTRODUCTION

Analytical solutions to the equations of flow through fractured reservoirs, as presented in chapter 6 and this chapter, are limited to relatively simple cases, i.e. one-dimensional or radial flow of one or two phases. More complicated problems can be solved by numerical methods.

Various mathematical models of flow (through fractured reservoirs) were developed by the computer services of the oil companies. The available simulators are known from the publications of the companies offering computer services. Classified as *commercial only*, some information about these computer programs is usually not disclosed to the public.

Here the discussion is limited to numerical simulators presented in the professional and scientific literature, which does not imply their superiority over the others. It is not the aim of this chapter to develop a comparison of the accuracy and efficiency of the different models and simulators.

Details on numerical treatment are not of interest to the reservoir engineer who is *not directly* involved in numerical simulation. And for such details, it is always easier to refer to the original papers.

From the point of view of phase flow simulation the models may be classified as :

- a. one-phase flow
- b. two-phase flow
- c. three-phase flow
- d. multiple component or compositional flow

More comprehensive simulators may be used to solve simple cases, as for example a two-phase flow simulator may easily solve only one-phase flow problems. This is usually less efficient than using the special purpose simulator.

With respect to the simulated formation, the models may be classified as :

- a. single block simulators
- b. discrete simulators of a limited number of blocks and fractures

- c. simulators of the whole fractured reservoir through the equations of continuum.

The *single block simulator* is just a conventional reservoir in which the conditions prevailing in the surrounding fractures are imposed as boundary conditions to the block.

*Discrete simulators* treat the reservoir as a non-homogeneous formation, fractures and blocks of different properties, applying the appropriate boundary conditions at the fracture-block interface.

In the models based on the equations of flow formulated through the continuum approach, the transfer of fracture-block fluids is represented by a *source/sink* function in the equation of conservation of mass in each medium—fracture and block. In some simulators this function is calculated internally, expressed in an implicit or semi-implicit form as a function of the dependent parameters, and *the source function is part of the solution*. Other simulators require that the source/sink, block-fracture transfer function is determined *a priori* by laboratory investigations on cores, single block simulators or by history matching, and supplied as input data.

A common feature of all models presented here is the assumption of a Darcy type flow through both fractures and blocks.

## 11.2. PHASE FLOW SIMULATION

### 11.2.1. One-phase flow simulator

A special idealized fractured reservoir, based on the simplified Warren and Root approach, was used by Kazemi<sup>1</sup> for a two-dimensional radial flow. The approach consists of a well (figure, 11.1) producing from several horizontal matrix slices separated by fractures, so that radical flow-lines in both matrix and fractures converge towards the well. A horizontal fracture, which is equivalent to all the horizontal fractures, is chosen as a first simplification. Other simplified assumptions referring to reservoir characteristics and flow conditions are:

- a. The reservoir matrix has a high storage capacity and a low flowing capacity, while the fracture has a low storage capacity and a high flowing capacity.
- b. As a result the production into the wellbore will be assured mainly through fractures.
- c. The flow takes place under nonsteady-state conditions.
- d. The reservoir is horizontal and both matrix and fractures are homogeneous and isotropic.

The equations considered are :

- for the region of the matrix,

$$\frac{1}{r} \frac{\partial}{\partial r} \left( r \frac{\partial \Psi}{\partial r} \right) + \frac{\partial^2 \Psi}{\partial z^2} = \frac{\Phi_1 \mu C_1}{K_1} \frac{\partial \Psi}{\partial t} \quad (11.1)$$

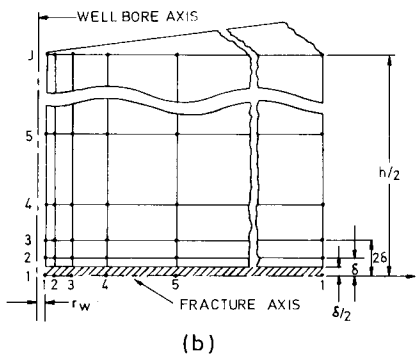
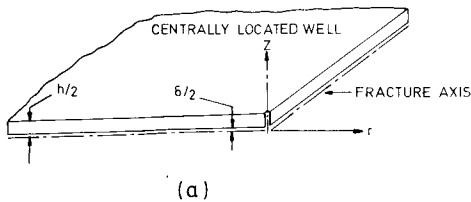
- for the region of fractures of width  $\delta$ ,

$$\frac{1}{r} \frac{\partial}{\partial r} \left( K_2 r \frac{\partial \Psi}{\partial r} \right) + \frac{K_1}{\delta/2} \left( \frac{\partial \Psi}{\partial z} \right)_{z=\delta^+/2} = \Phi_2 \mu C_2 \frac{\partial \Psi}{\partial t} \quad (11.2)$$

where  $\delta^+$  denotes the value of  $\delta$  at the fracture-block interface and potential,

$$\Psi = \rho (o) \left[ \int_o^P \frac{dp}{\rho(p)} + gz \right] \quad (11.3)$$

When equation 11.3 was solved numerically and coded, Kazemi neglected gravity and replaced  $\Psi$  by  $P$ .



11.1 – Kazemi's fractured reservoir model a) well and reservoir b) reservoir modelling (Kazemi<sup>1</sup>, Courtesy AIME)

The boundary conditions are expressed by :

- a. axisymmetrical flow through the block, which corresponds to the validity domain of equation 11.1, is expressed as follows,

$$\frac{\delta}{2} < Z < \frac{h}{2} \quad \text{for} \quad r_w < r < r_e$$

- b. axisymmetrical flow through the fracture, which corresponds to the validity domain of equation 11.2, is expressed as follows,

$$0 < Z < \frac{\delta}{2} \quad \text{for} \quad r_w < r < r_e$$

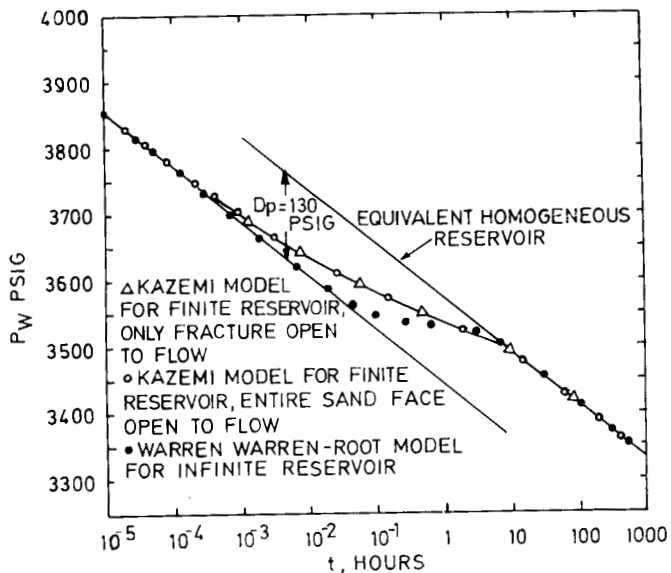
- c. production is only through fractures of height  $\delta$ , expressed as follows,

$$\frac{\partial \Psi}{\partial r} = - \frac{q \mu B}{K_f} \frac{1}{\pi r_w \delta} \quad \text{for} \quad 0 < Z < \frac{\delta}{2}; r = r_w$$

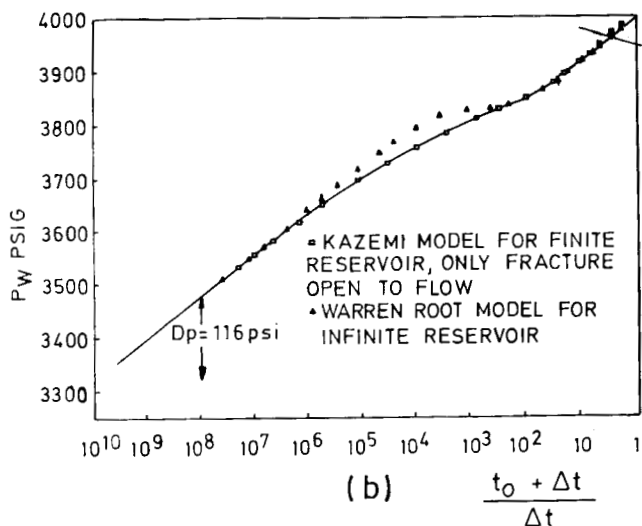
- d. the transfer of fluid at the fracture-block boundary is in a vertical direction only, and is expressed as follows,

$$\frac{\partial \Psi}{\partial r} = 0; \frac{\delta}{2} < Z < \frac{h}{2}; r = r_w \quad \text{and} \quad r = r_e$$

The model was applied to the pressure transient analysis and the results—*pressure drawdown and pressure build-up*—were compared with the Warren and Root solution (figure 11.2). The only difference between the Kazemi and Warren and Root solutions is in the transition zone between the early stages of production and the asymptotic homogeneous behaviour. This difference is attributed to the transient transfer function considered by Kazemi, instead of the quasi-steady-state function considered by Warren and Root. If the entire sand face (blocks and fractures) is open to flow, or only fractures are open to flow, it was observed that the opening thickness has no influence on the results since the contrast between the negligible block transmissivity  $k_1 h_1$  is considerable in comparison with very high fracture transmissivity  $k_2 h_2$ .



(a)



11.2 – Comparison between Kazemi's transient flow simulation and Warren and Root solutions :  
a) Pressure drawdown ; b) Pressure build-up (Kazemi<sup>1</sup>, Courtesy AIME)

### 11.2.2. Two-phase simulators

#### 11.2.2.1. Theoretical basis

Kazemi<sup>2,3</sup> has developed a three-dimensional, multiple-well numerical simulator for oil/water flow in a fractured reservoir. The equations have been developed through the *continuum approach* in which the transfer of fracture-block fluids is presented by a quasi-steady-state source/sink function proportional to potential difference.

Based on Darcy's law and material balance in a unitarian volume of reservoir, the flow through fractures is expressed as follows,

$$\frac{\Phi_2}{B_i} \frac{\partial S_{2,i}}{\partial t} + \frac{S_{2,i} \Phi_2}{B_i} (C_2 + C_i) \frac{\partial \Psi_{2,i}}{\partial t} - \operatorname{div} \left( \frac{K_2 K_{r2i}}{\mu_i B_i} \operatorname{grad} \Psi_{2,i} \right) + \frac{K_1 K_{r1i} s}{\mu_i B_i} (\Psi_{2,i} - \Psi_{1,i}) - q_i \xi (X - X_0) = 0 \quad (11.4)$$

where subscript  $i = w, o$  denotes the water and oil phases, subscript 1 denotes the matrix blocks, and subscript 2 denotes the fractures. The term  $s$  (as discussed in chapter 7) reflects the geometry of the matrix element, and consequently controls the flow between matrix and fractures. The transmissivity in this case is expressed by,

$$\lambda_{2i} = \left( \frac{K \times K_{ir}}{\mu_i B_i} \right)_2 \quad (11.5)$$

for fractures, and by,

$$\lambda_{1,i} \times s = \left( \frac{K \times K_{ir}}{\mu_i B_i} \right)_1 \times s = \lambda'_{1,i} \quad (11.5')$$

for matrix block.

The potential  $\Psi_i$ , mass  $\rho_i$  and volume factor  $B_{oi}$  are expressed by,

$$\begin{aligned} \Psi_i &= P_i + \rho_i g Z \\ \rho_i &= \rho_o [1 + C_i (P_i - P_o)] \\ B_i &= B_{oi} [1 - C_i (P_i - P_o)] \end{aligned} \quad (11.6)$$

while  $q_i$  is the production/injection rate per unit volume at node  $X_o$ .

Under similar notation, flow in the matrix block is expressed by,

$$\frac{\Phi_1}{B_i} \frac{\partial S_{1,i}}{\partial t} + \frac{S_{1,i}}{B_i} \Phi_1 (C_1 + C_i) \frac{\partial \Psi_{1,i}}{\partial t} - \frac{K_i \cdot K_{r,1,i} \cdot s}{\mu_i B_i} (\Psi_{2,i} - \Psi_1) = 0 \quad (11.7)$$

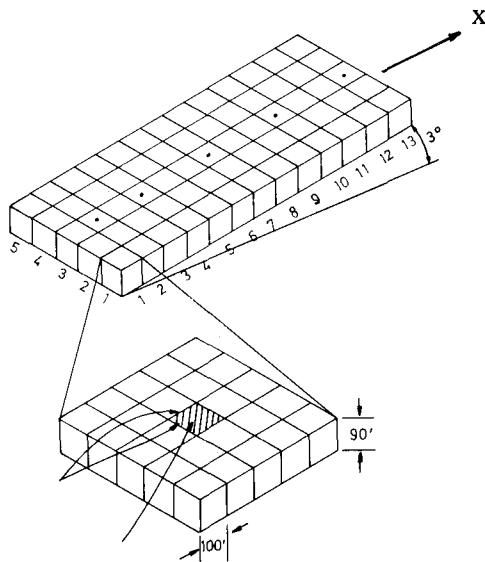
Equations 11.4 and 11.7 have been expressed in semi-implicit finite differences and solved by the block Gauss-Seidel method. Gauss elimination is recommended for large time steps and one of these methods, either SOR, ADIP or SIP, is recommended for a number of nodes exceeding a thousand.

The simulator can handle the imbibition, taking into account gravity, relative permeability and variations in reservoir properties.

#### 11.2.2.2. Application through Kazemi<sup>2</sup> simulator

The Kazemi simulator was applied to a five-spot quadrant and a five-well reservoir.

In the case of five wells in a fractured reservoir, the reservoir properties have been considered as shown in table 11.1. The wells were arranged along a center line in x direction and the reservoir was considered tilted 5° along x direction. Since each node is considered to contain 25 matrix blocks, this would mean there were 1,625 matrix blocks in the reservoir (figure 11.3).



11.3 – Modelling of a reservoir : node arrangement and a single cell containing a fracture (Kazemi<sup>2</sup>, Courtesy AIME)

Table 11.1 Reservoir properties of five-well model (Kazemi<sup>2</sup>)

$K_1 = 1.0 \text{ md}$	$\mu_o = 2.0 \text{ cp}$
$K_f = 21.000 \text{ md}$	$\rho_w = 0.4385 \text{ psi/ft} = 63.14 \text{ lb}_m/\text{cu ft}$
$\Phi_1 = 0.20$	$\rho_o = 0.3611 \text{ psi/ft} = 52.00 \text{ lb}_m/\text{cu ft}$
$\Phi_f = 0.10$	$B_w = 1.0 \text{ at } \rho = 0 \text{ psia}; B_w = 0.9760 \text{ at } \rho = 8,000 \text{ psia}$
$s = 0.0008 \text{ ft}^2$	$B_o = 1.0 \text{ at } \rho = 0 \text{ psia}; B_o = 0.9200 \text{ at } \rho = 8,000 \text{ psia}$
$C\Phi_2 = C\Phi_1 = 3.0 \times 10^{-6} \text{ psi}^{-1}$	$p_i = 3.983.75 \text{ psia}$
$\mu_w = 0.5 \text{ cp}$	

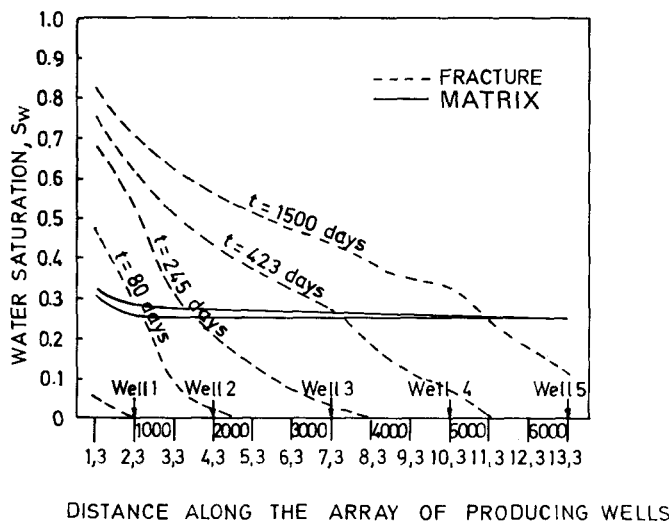
- matrix block size : 100 x 100 x 90 ft

Reservoir grid : 13 x 5 x 1

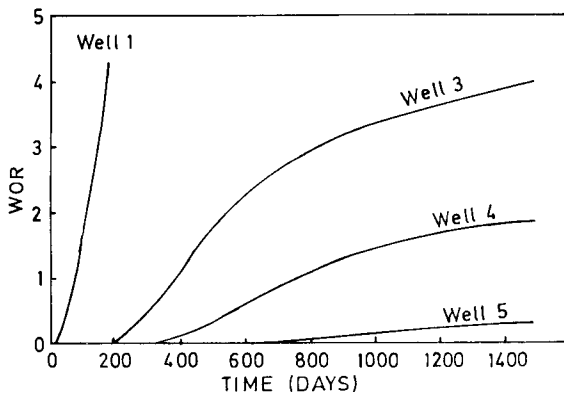
$\Delta x = \Delta y = 500 \text{ ft}, h = \text{ft}$

- Wells 1, 3, 5 produced at rate : 1000 STB/D
- Water influx along 1, 3, 5 line : 2800 STB/D

The results obtained show the saturation distribution along the central axis to be in x direction for both matrix and fractures (figure 11.4), and WOR (water-oil ratio) in wells 1, 3, 4 and 5 vs. time (figure 11.5).



11.4 - Saturation distribution along the array of producing wells (in fracture and matrix) at various time lags (Kazemi<sup>2</sup>, Courtesy AIME)



11.5 – WOR vs. time production wells as effect of their up-dipping location (Kazemi<sup>2</sup>, Courtesy AIME)

### 11.2.2.3. Block imbibition simulation (Kazemi<sup>3</sup>)

The simulation of water imbibition in fractured cores was achieved by a two-dimensional, two-phase semi-implicit, numerical simulator. The matrix geometry used in the model was assumed to be cylindrical or rectangular-shaped, similar to the artificial cores discussed in chapter 9, section 9.5.2.3 and illustrated in figure 9.66. The flow in fractures is then expressed by,

$$\frac{\partial}{\partial x} \left( \lambda_{2,xw} \frac{\partial \Psi_{2w}}{\partial x} \right) - T_{1w} (\Psi_{2w} - \Psi_{1w}) + q_w B_w \xi (X - X_0) = \Phi_2 \frac{\partial S_{2w}}{\partial t} \quad (11.8)$$

where the component on the Z axis was substituted by,

$$\frac{\partial}{\partial z} \left( \lambda_{2zw} \frac{\partial \Psi_{2w}}{\partial z} \right) = -T_{1,w} (\Psi_{2w} - \Psi_{1w}) \quad (11.9)$$

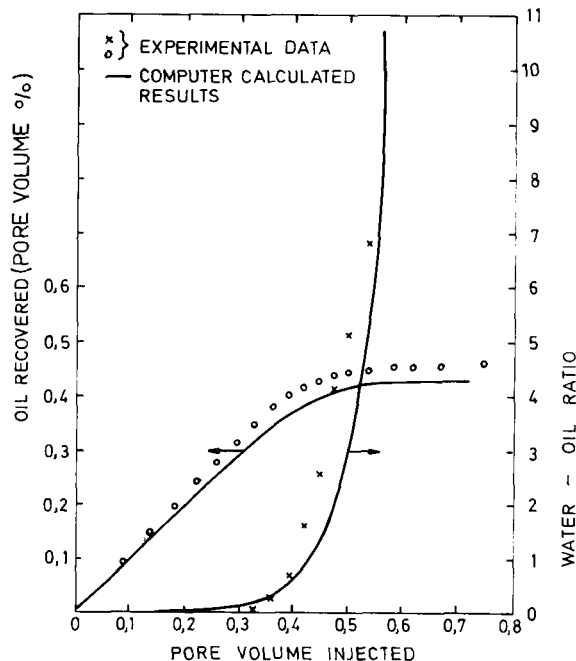
The matrix equation of flow is expressed by,

$$T_{1,w} (\Psi_{2,w} - \Psi_{1,w}) = \Phi_1 \frac{\partial S_{1,w}}{\partial t} \quad (11.10)$$

where  $\lambda_{kw} = 0$ , and,

$$\frac{\partial}{\partial t} \left( \lambda_{1zw} \frac{\partial \Psi_{1,w}}{\partial t} \right) \text{ was replaced by } T_{1,w} (\Psi_{2w} - \Psi_{1w}) \quad (11.11)$$

An example of a displacement test is shown in figure 11.6 ; here the recovery and water-cut if a 1" × 3" Berea core initially 100% saturated with oil, are expressed as functions of injected pore volume. The water was injected at a relatively low rate of 1.07 cm<sup>3</sup>/h and, as observed, the obtained oil recovery and WOR correspond very well with experimental data.



11.6 – Recovery and water-oil ratio vs. pore volume injected (Kazemi<sup>3</sup>, Courtesy AIME)

The basic data are as follows:  $A = 4.76\text{cm}^2$  ;  $L = 7.55\text{cm}$  ;  $\text{PV} = 6.62\text{cc}$  ;  $K = 97\text{mD}$  ;  $\Phi = 0.185$  ;  $q = 1.07\text{cc/hour}$  ; oil (diesel); water = 2000ppm brine ;  $\mu_o = 4.6\text{cP}$  ;  $\mu_w = 10\text{cP}$  ;  $S_{wr} = 0$ . The experimental matrix capillary pressure curves measured resemble those used in the simulator, while the relative permeability in the matrix was calculated by,

$$K_{rw} = S_w^3$$

$$K_{ro} = (S_0 - S_{or})^3$$

and the relative permeability in the fractures was calculated by,

$$K_{rw} = S_w$$

$$K_{ro} = 1 - S_w$$

#### 11.2.2.4. Kleppe's<sup>4</sup> simulation of block imbibition

The differential equations have been written in a similar way by Kleppe for the x, y directions of the oil and water phases for a unitarian block. The equations are as follows,

$$\frac{\partial}{\partial x} \left( CK \frac{K_{ro}}{B_0 \mu_o} \frac{\partial P_o}{\partial x} \right) + \frac{\partial}{\partial y} \left[ CK \frac{K_{ro}}{\mu_o B_0} \left( \frac{\partial P_o}{\partial y} - \rho_o g \right) \right] \\ + q_o = \Phi \frac{\partial}{\partial t} (S_o/B_0) \quad (11.12)$$

$$\frac{\partial}{\partial x} \left[ CK \frac{K_{rw}}{B_w \mu_w} \left( \frac{\partial P_o}{\partial x} - \frac{\partial P_c}{\partial x} \right) \right] + \frac{\partial}{\partial y} \left[ CK \frac{K_{rw}}{B_w \mu_w} \left( \frac{\partial P_o}{\partial y} - \frac{\partial P_c}{\partial y} - \rho_w g \right) \right] \\ + q_w = \Phi \frac{\partial}{\partial t} (S_w/B_w) \quad (11.13)$$

In these equations the derivatives  $dK_{ro}/dS_o$  and  $dK_{rw}/dS_w$  are expressed as slopes of relative permeability curves while capillary pressure terms as a function of saturation are related to capillary pressure curves. The models developed a sequential and simultaneous solution.

The *sequential* solution was found by combining equations 11.12 and 11.13, leaving the pressures as the only unknown variables (on the left hand side of the equation) and then eliminating the saturation terms (on the right hand side of the equation). After each saturation solution, new values were tried for pressure and saturation until a *convergence criterian of pressure or saturation* was reached.

The *simultaneous* solution of pressure and saturation was found by modifying the non-linear terms in order to obtain an equation in terms of pressure and saturation for oil and water.

From the comparison of these two models, the first model performed satisfactorily providing a rapid solution, but was less stable and sometimes failed to reach a rapid convergence. The second model never failed to converge and is therefore of more interest, but the disadvantage is that it requires four times the storage area of the first model.

#### 11.2.3. Three-phase simulator

##### 11.2.3.1. Du Prey's<sup>5</sup> simulator

The model presented by Du Prey<sup>5</sup> is based on general assumptions already

mentioned :

- The *continuum* is the result of a flowing process in fractures governed by Darcy's law and the exchange of fluid between matrix and fractures (transfer function).
- The fluids *flow in fractures* where capillary forces are negligible.
- The *transfer function* may be evaluated separately and associated with the time parameter in the model, or under certain conditions may be evaluated inside the model in parallel with a new distribution of fluids in fractures.

The mass conservation of three phases in fractures (subscript 2) is expressed by,

$$\left. \begin{aligned} \frac{\partial}{\partial t} (\Phi_2 S_{w2} \rho_w) + \nabla \left( \rho_w \vec{U}_{w2} \right) + C_w + q_w &= 0 \\ \frac{\partial}{\partial t} (\Phi_2 S_{o2} \rho_o) + \nabla \left( \rho_o \vec{U}_{o2} \right) + C_o + q_o &= 0 \\ \frac{\partial}{\partial t} (\Phi_2 S_{g2} \rho_g) + \nabla \left( \rho_g \vec{U}_{g2} \right) + \nabla \left( \rho_{gd} \vec{U}_{oz} \right) + C_g + q_g &= 0 \end{aligned} \right\} \quad (11.14)$$

where subscripts w, o and g indicate the water, oil and gas phases respectively, gd indicates dissolved gas,  $C_w$ ,  $C_o$  and  $C_g$  are the transfer functions of fluids between blocks and fractures, and q represents production/injection rate per unit mass while,  $\vec{U}$  represents Darcy's law, i.e.,

$$\left. \begin{aligned} \vec{U}_{wz} &= - K_2 \frac{K_{rwz}}{\mu_w} \nabla \left[ P_2 + \rho_w g z \right] \\ \vec{U}_{oz} &= - K_2 \frac{K_{roz}}{\mu_o} \nabla \left[ P_2 + (\rho_o + \rho_{gd}) g z \right] \\ \vec{U}_{gz} &= - K_2 \frac{K_{rgz}}{\mu_g} \nabla \left[ P_2 + \rho_g g z \right] \end{aligned} \right\} \quad (11.15)$$

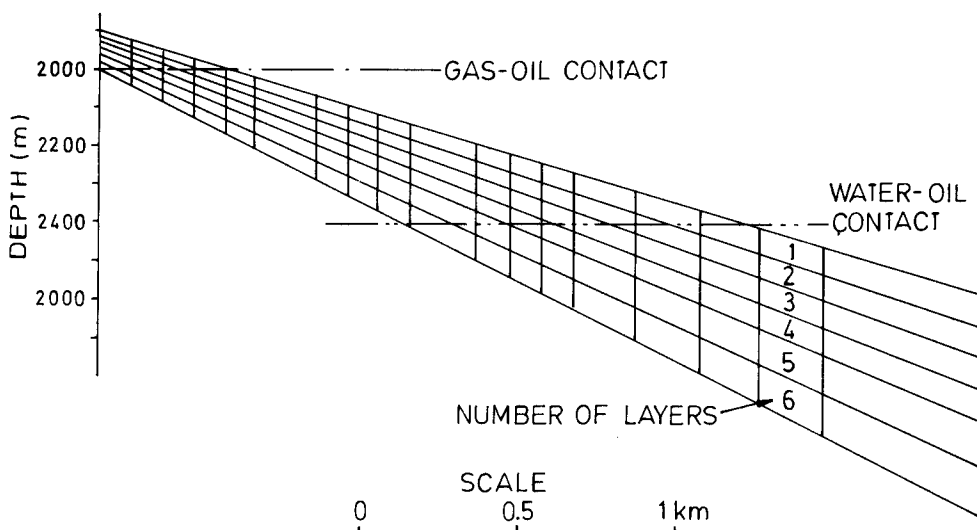
The capillary pressure is negligible in the fractures. The equations were solved by finite differences in two steps : first for pressure with saturation-dependent parameters evaluated at the end of the previous time step, and then for saturation.

Field Simulation Example<sup>5</sup> : A reservoir (figure 11.7) of pay between 100m (top) and 450m (at water-oil contact) has a 400m column of oil limited at the top by a small gas-cap. OOIP =  $21 \times 10^6$  STM<sup>3</sup>. The basic data are as follows:

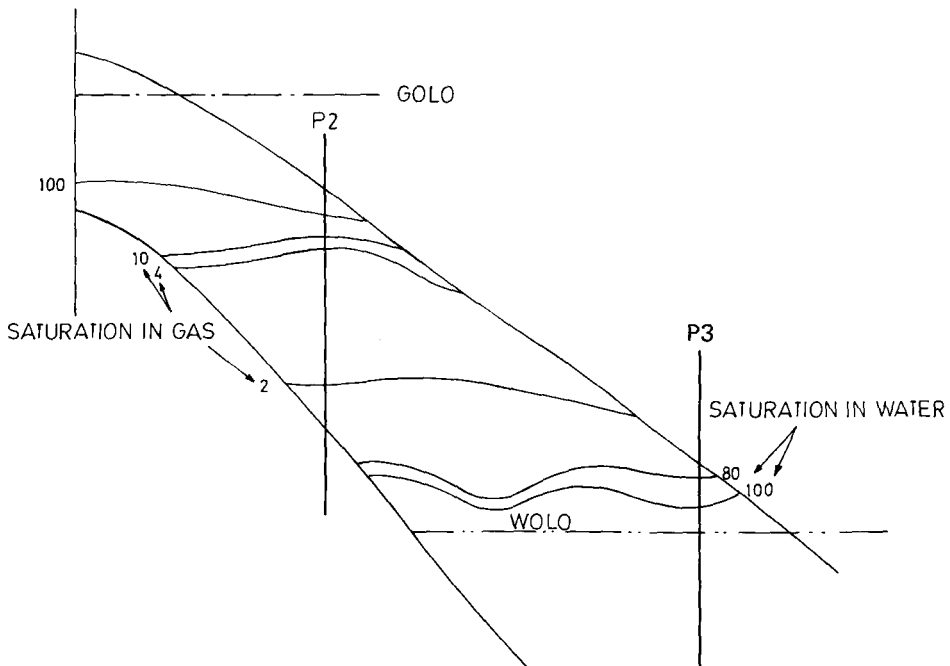
$\Phi_2$	= 0,3 %	${}^\circ\text{API}$	= 40
$K_2$	$\cong 1 \text{ D}$	$P_B$	$= 252,5 \text{ kg/cm}^2$
$\Phi_1$	= 11 %	$\frac{\Delta P_B}{\Delta h}$	$= 0.2 \text{ kg/cm}^2/\text{m}$
$K_1$	$\cong 10 \text{ mD}$		
$S_{wi}$	$\cong 30 \%$	$B_o$	= 1.8 (gas-oil contact)
$h_{BL}$	$\cong 3 \text{ m}$	$R_s$	$= 285 \text{ Nm}^3/\text{m}^3$ (gas-oil contact)

The simulation using  $100 \times 500\text{m}$  grid blocks was actually modelled using a  $18 \times 17 \times 6$  grid. The well denoted  $P_i$  indicates in parenthesis the production (STM<sup>3</sup>/D) of various layers in the following way:  $P_1$  (150 – layer 5,6);  $P_2$  (150 – layer 2) ;  $P_3$  (150 – layer 6) ;  $P_4$  (200 – layers 3 and 4).

After 400 days the water arrives at well  $P_3$ , where water-cut is rapidly increasing to WC = 80%. After 1620 days the entire reservoir is below bubble point and the saturation in water and fluid at this stage is shown in figure 11.8.



11.7 – Simplified cross-section of a simulated reservoir (Du Prey<sup>5</sup>, Courtesy Elsevier)



11.8 – Saturation distribution in fracture obtained in a vertical cross section through wells  $P_2 - P_3$  after 1620 production days. (Du Prey<sup>5</sup>, Courtesy Elsevier)

The single block behaviour has generated a series of *transfer functions* through numerical simulation in such cases as the matrix block located in a gas-invaded zone, gassing zone and water zone. These transfer functions have been introduced as input data in reservoir simulation models.

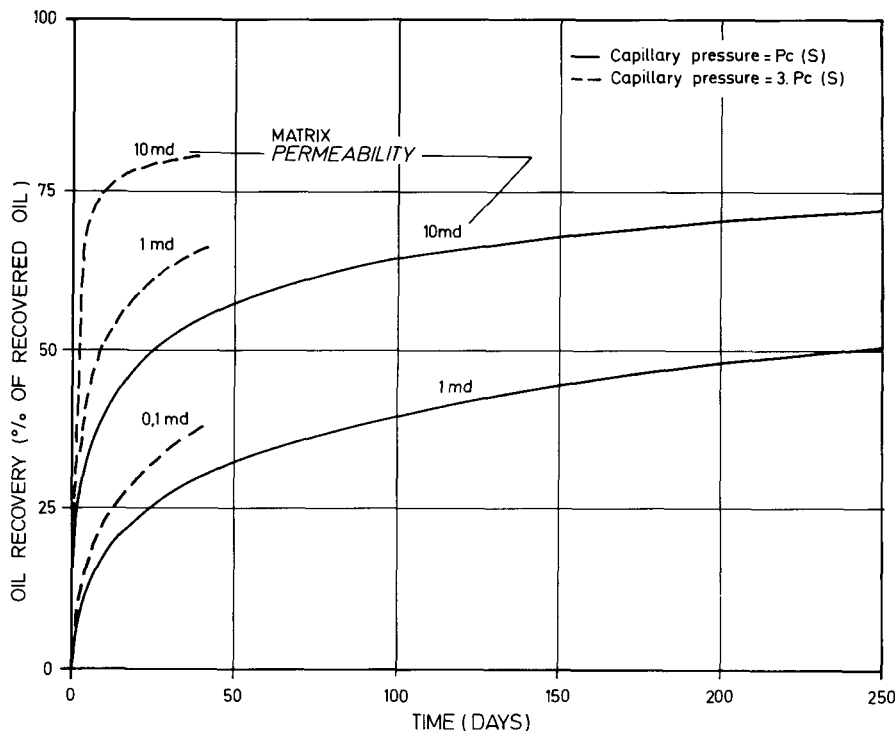
**Transfer Function Example<sup>5</sup>** : The simulations of matrix blocks surrounded by water, oil and gas in the respective water-invaded zone, undersaturated zone and gassing zone are shown below:

a. Oil matrix block surrounded by water

A block having a height of  $h_B = 6\text{m}$ , containing oil  $\mu_o = 0.953 \text{ cP}$  and a density of  $\gamma_o = 0.765 \text{ g/cm}^3$  is surrounded by water with a viscosity of  $\mu_w = 0.620 \text{ cP}$  and a density of  $\gamma_w = 1.140 \text{ g/cm}^3$ . The calculation was developed for three matrix permeabilities  $10\text{mD}$ ;  $1\text{mD}$ ; and  $0.1\text{mD}$  and for two capillary pressures  $P_c(\text{S})$  and  $3P_c(\text{S})$  but for a constant depletion rate of  $5.5\text{Kg/cm}^2/\text{year}$  and a fixed threshold pressure of  $P_{TH} = 0.048\text{Kg/cm}^2$ .

A variation recovery-time, substantially improved for higher matrix permeability and higher capillary pressure will result as shown in figure 11.9.

In the presence of high capillary forces in a block of height  $H_B = 6 \text{ m}$  which corresponds to a tall block, the maximum recovery is reached in one month instead of eight months or more.



11.9 – Recovery vs. time of an oil saturated block surrounded by water examined for various matrix permeabilities and capillary pressure (Du Prey<sup>5</sup>, Courtesy Elsevier)

#### b. Oil matrix block surrounded by oil

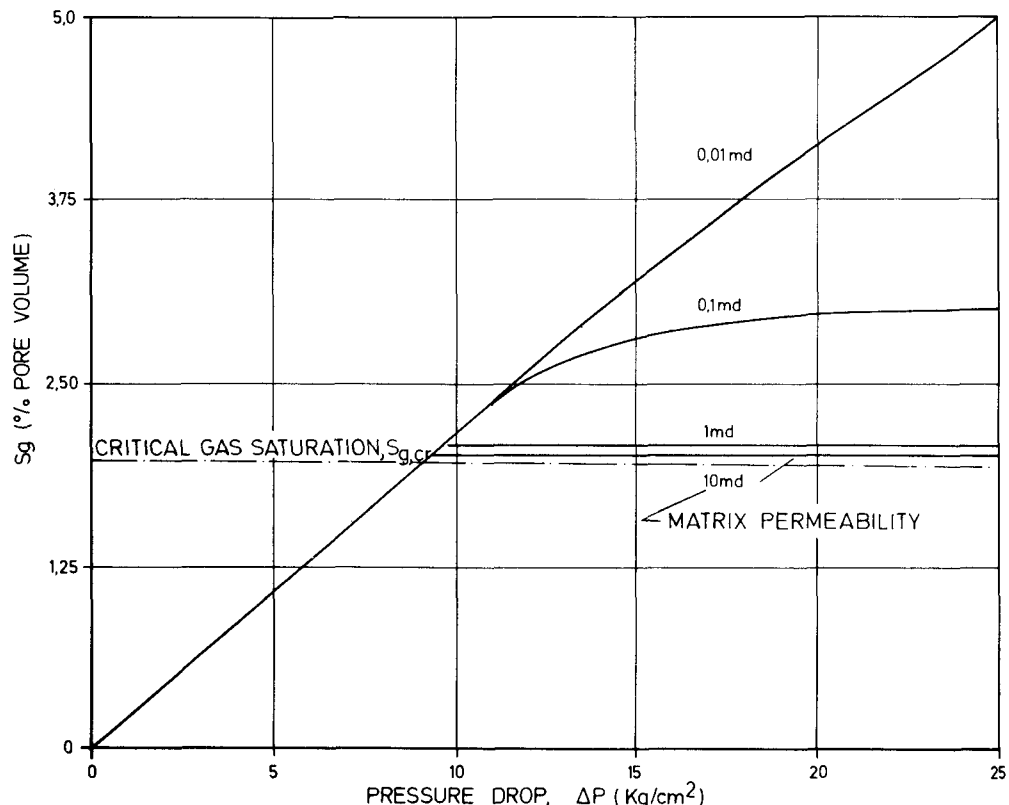
Considering a matrix block of the same size, the fluid characteristics are respectively:

$$\text{oil - } P_b = 252,6 \text{ Kg/cm}^2 ; \mu_o = 0.24 \text{ cP} ; \gamma_o = 0.63 \text{ g/cm}^3 ;$$

$$R_s = 280 \text{ Nm}^3/\text{m}^3 \text{ and } B_o = 1.55.$$

$$\text{gas - } B_g = 3.9 \times 10^{-3} ; \gamma_g = 0.28 \text{ g/cm}^3 ; \mu_g = 0.02 \text{ cP}.$$

For a pressure decline rate  $dp/dt = 5.5 \text{ kg/cm}^2/\text{year}$  and a threshold pressure  $P_{TH} = 0.002 \text{ kg/cm}^2$ , the variation matrix gas saturation vs. time is given in the diagram in figure 11.10.



11.10 – Variation saturation gas vs. time under solution gas drive of an oil saturated block surrounded by oil in case of a given pressure decline rate and various permeabilities (Du Prey<sup>5</sup>, Courtesy Elsevier)

The results are particularly interesting since the role of reimbibition is evident. The desaturation in oil (equivalent to saturation in gas) is continuous in very low permeability ( $K = 0.01 \text{ mD}$ ) where oil reimbibition is non-existent. If permeability is only  $0.1 \text{ mD}$  at a saturation higher than critical the oil produced is compensated for by oil imbibed in a pseudo steady-state condition. If permeability is over  $1\text{mD}$ , the critical gas saturation is the *maximum limit* for desaturation in oil.

### 11.2.3.2. Rossen's<sup>6</sup> simulator

The approach carried out by Rossen follows the general pattern: modelling of flow in fracture network and treating the matrix-fracture fluid transfer by a transfer function. The fluid transfer into the fracture is thus represented by a *source* and the transfer of fluid from the fracture by a *sink*.

- The result of pressure decline in a reservoir will be expansion of matrix fluid in the fracture—a *sink*.
- Gravity drainage and capillary imbibition will represent *sources* for different phases if fluids are transferred from the matrix ; if fluids are transferred into the matrix they will represent *sinks*.
- In addition, a classification of the matrix block in agreement with the magnitude of porosity may be defined as follows :
  1. *wet matrix rock* – if it has a very low porosity and high water saturation and is capable of transferring only water to the fractures.
  2. *net matrix rock* – if it has a high porosity and high oil saturation and is capable of transferring oil toward the fractures.

#### a. General procedure

For the entire fracture-matrix volume, the sum of the contribution of *net* and *wet* matrix blocks represents the *total source* term. Each source term is composed of the three sources-water, gas and oil-expressed as explicit sources, and of three derivatives with respect to  $p$ ,  $S_{gf}$  and  $S_{wf}$ . The explicit source  $Q^*_{om}$  for oil is the sum of the assumed values for the present step and a value which represents the error introduced in the previous step.

#### b. Various cases : Gas environment

The single block saturated by oil and surrounded by gas will give a recovery vs. time as a result of drainage displacement. Defining the drainage time  $t_D$  and referring to the initial gas saturation  $S_{gi}$ , the saturation of the matrix in gas at step  $n + 1$  may be written as,

$$S_{gm}^{n+1} = S_{gi} + S_{gf}^{n+1} \times \left[ R(t_D^{n+1}) - S_{gi} \right] \quad (11.16)$$

where  $R(t_D)$  is the recovery obtained at time  $t_D$ . The time is given by,

$$t_D^{n+1} = \frac{1}{S_{gf}^{n+1}} \left\{ S_{gf}^n \times (t_D^n + \Delta t) + (S_{gf}^{n+1} - S_{gf}^n) \times \left[ \Delta t + R^{-1}(S_{gi}) \right] \right\} \quad (11.17)$$

The fluid transfer expressed implicitly in  $S_{gf}$  is given by,

$$Q_{om}^* = Q_{om} + \frac{\partial Q_{om}}{\partial P_0} \Delta P_0 + \frac{\partial Q_{om}}{\partial S_{gf}} \Delta S_{gf} \quad (11.18)$$

where  $Q_{om}^*$  is the source term if pressure for oil, and fracture gas saturation remains constant.

#### c. Various cases : Water environment

Equations similar to 11.16 and 11.17 are presented below for saturation and time :

$$S_{wm}^{n+1} = S_{wi} + S_{wf}^{n+1} \times \left[ R \left( t_D^{n+1} \right) - S_{wi} \right] \quad (11.19)$$

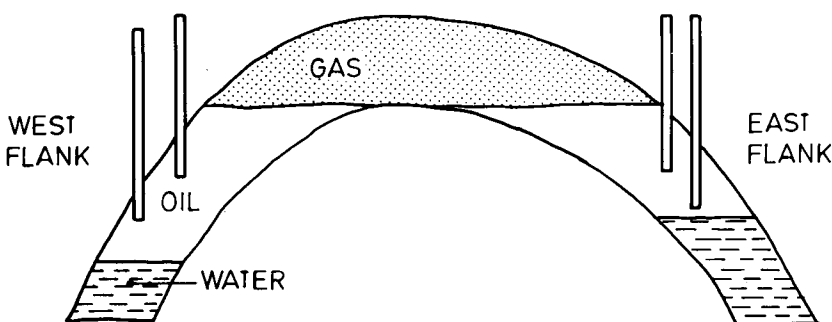
$$t_D^{n+1} = \frac{1}{S_{wf}^{n+1}} \left\{ S_{wf}^n \times \left( t_D^n + \Delta t \right) + \left( S_{wf}^{n+1} - S_{wf}^n \right) \times \left[ \Delta t + R^{-1} \left( S_{wi} \right) \right] \right\} \quad (11.20)$$

#### d. Comments

In Rossen's approach a semi-implicit treatment of the matrix-fracture source terms resulted in a stable procedure for computing both fluid contacts and pressure in the fractures. A hysteresis effect in the maxtrix-fluid saturation was also considered.

#### e. Calculation example

A hypothetical reservoir (figure 11.11) having a gas-cap and an aquifer has the petrophysical and fluid properties shown below :



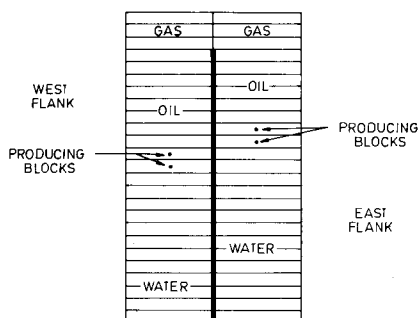
11.11 – Hypothetical oil reservoir delimited by a gas cap and an aquifer (Rossen<sup>6</sup>, Courtesy AIME)

Volume of Gas Cap	$828 \times 10^6$	RB
Original Oil in Place	1696	MMSTB
Original Pressure at Gas-Oil Contact	3000	psi
Original Gas-Oil Contact	5250	feet
Original Saturation Pressure	3000	psi
Original Water-Oil Contacts	6450	feet
	6950	feet
Pressure	250	5250
Oil Formation Volume Factor	1.15	1.60
Water Formation Volume Factor	1.03	1.02
Gas Formation Volume Factor	0.01	0.0006
Solution Gas/Oil Ratio	100	1000

The field was produced at 100,000 STB/D and 75,000 STB/D based on relative volumes of OOIP. The reservoir pressure declined after 500 days by 330 psi. The following two cases have been examined :

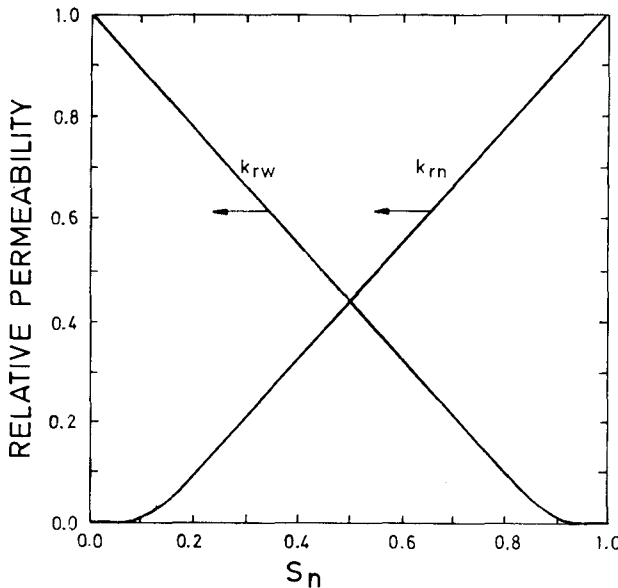
1. Case A - Injection of 200 MMCF/D in gas-cap.
  2. Case B - Injection of 85 - 100 MMDF/D in gas-cap (equal to entire volume of produced gas due to liberation of solution gas).

A comparsion was made by simulating the reservoir by a simple  $2 \times 25$  grid so as to represent the two flanks connected through the gas-cap (figure 11.12). A simplified relative permeability curve, typical for a fracture system where gravitational segregation is governing the flow, was used as shown in figure 11.13.



### 11.12 – Reservoir simulation grid

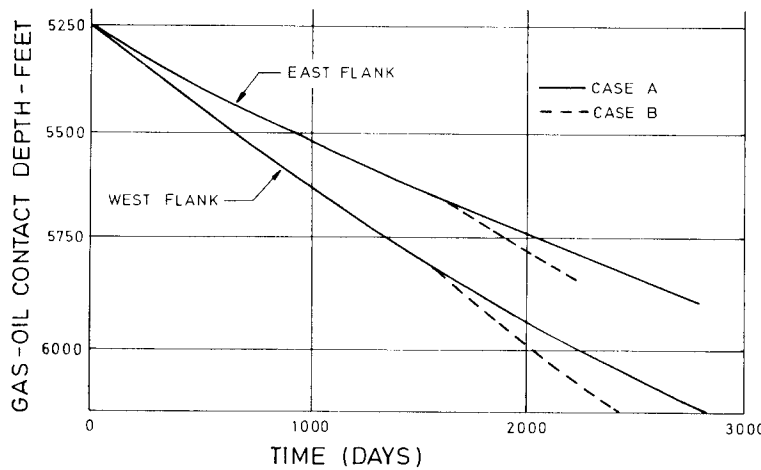
(Rossen<sup>6</sup>, Courtesy AIME)



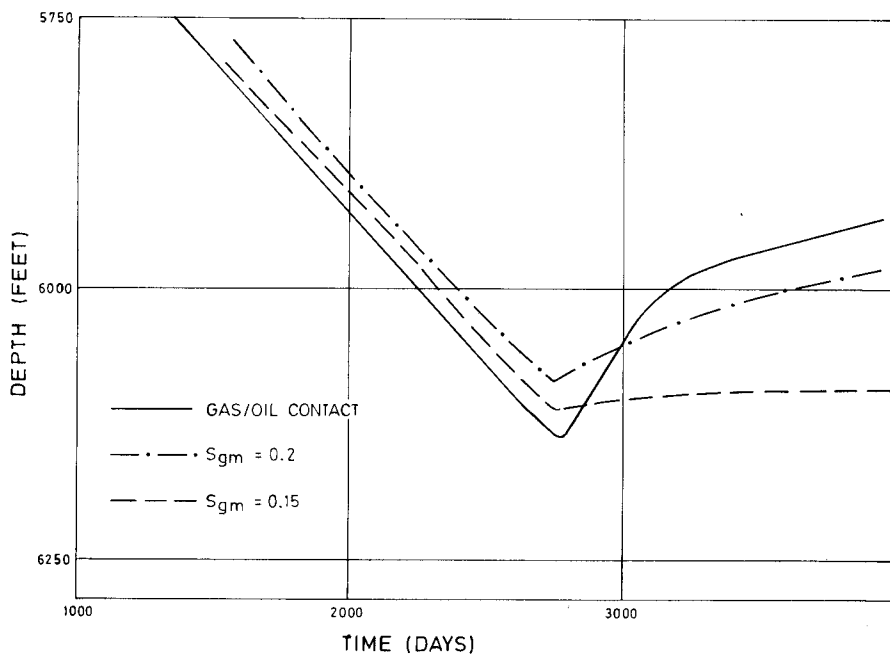
11.13 – Fractured reservoir wetting and non-wetting relative permeabilities ( $K_{rw}$  and  $K_{rn}$ ) vs. saturation (in non-wetting phase  $S_n$ ). (Rosser,<sup>6</sup> courtesy AIME)

The results of simulation determine the following :

- On both flanks higher gas injection (case A) indicated a slower displacement rate of gas-oil contact, which is associated with pressure maintenance at a higher level (figure 11.14).
- When only gas liberated from solution is reinjected into the gas-cap (case B), the gas-oil contact moves faster since the lack of pressure maintenance will help the segregation of larger volumes of gas (figure 11.14).
- If the production wells had been located at a depth of 6,150 feet, the gas breakthrough would have taken place after 2,825 days and 2,450 days in the west flank for cases A and B respectively.
- If after breakthrough in case A (2,825 days), the reservoir production was stopped, contact would retreat to 5,975 feet after two years. This means that a cumulative time of 3,555 days, the gas-oil contact moves 175 feet upwards (figure 11.15).
- As expected, some gas may remain trapped in the matrix blocks, and in this case the upward movement of the water-oil contact will be reduced. This hysteresis, calculated for trapped gas in the matrix  $S_{gm} = 0.2$  and 0.15, is illustrated in figure 11.15.



11.14 – Depth of gas oil contact vs. time in cases: A (pressure maintenance), B (reinjection of produced solution gas). (Rossen<sup>6</sup>, courtesy AIME)



11.15 – Gas-oil contact depth vs. time in case A if after breakthrough (2825 days) the production is stopped for 2 years. Cases : no gas is retained in matrix ; trapped gas in matrix 15 % and 20 % (Rossen<sup>6</sup>, Courtesy AIME)

### 11.2.3.3. Kent Thomas's simulator<sup>7</sup>

The reservoir is assumed, as in other cases, to be formed by a continuous fracture network associated with a discontinuous matrix block, therefore, a local exchange of fluid between fractures and matrix takes place and the fluid moves through the fracture system.

The flow in fractures may be described as in equation 11.14, which, in a finite difference, can be expressed as follows.

for water phase

$$\Delta \left[ T_w \left( \Delta P_{2w} - \gamma_w \Delta D \right) \right] + \lambda'_{1w} (P_{1w} - P_{2w}) - q_w = \frac{V_b}{\Delta t} \bar{\delta} (\Phi B_w S_w)_2 \quad (11.21)$$

for oil phase

$$\Delta \left[ T_o \left( \Delta P_{2o} - \gamma_o \Delta D \right) \right] + \lambda'_{1o} (P_{1o} - P_{2o}) - q_o = \frac{V_b}{\Delta t} \bar{\delta} (\Phi B_o S_o)_2 \quad (11.22)$$

for gas phase

$$\begin{aligned} \Delta \left[ T_g \left( \Delta P_{2g} - \gamma_g \Delta D \right) \right] + \lambda'_{1g} (P_{1g} - P_{2g}) + \Delta \left\{ T_o R_s (\Delta P_{2o} - \gamma_o \Delta D) \right\} + \\ \lambda'_{1,0} R_s (P_{1o} - P_{2o}) - q_g = \frac{V_b}{\Delta t} \bar{\delta} (\Phi B_g S_g + \Phi B_o R_s S_o)_2 \end{aligned} \quad (11.23)$$

The only one term specific to fractured reservoirs is the matrix-fracture fluid exchange expressed as  $\lambda'_1 (P_1 - P_2)$ , which acts as a source/sink term<sup>8</sup> in the fracture network. Parameter  $\lambda$  is dependent on matrix shapes, which may be idealized under certain simple geometrical models.

The equations of matrix fracture transfer for the three phases are then expressed as follows :

$$\left. \begin{aligned} -\lambda'_{1w} (P_{1w} - P_{2w}) &= \frac{V_b}{\Delta t} \bar{\delta} (\Phi B_w S_w)_1 \\ -\lambda'_{1o} (P_{1o} - P_{2o}) &= \frac{V_b}{\Delta t} \bar{\delta} (\Phi B_o S_o)_1 \\ -\lambda'_{1g} (P_{1g} - P_{2g}) &= \lambda' R_s (P_{1o} - P_{2o}) = \frac{V_b}{\Delta t} \bar{\delta} (\Phi B_g S_g + \Phi B_o R_s S_o)_1 \end{aligned} \right\} \quad (11.24)$$

The solution proposed in this simulation for these six equations includes a number of assumed simplifications and procedures among which are the following :

- The right hand terms are expressed as functions of pressure and saturations, where various coefficients represent the partial derivate of the accumulation terms at a given level.
- Terms of *fracture flow* are evaluated *implicitly* for each phase, and relative permeability and PVT properties are calculated at the latest iterate values.
- Terms of *transfer flow* are also expressed *implicitly* with special assumptions for certain terms, such as relative permeability for oil, water and gas.
- The *production* rates are calculated *semi-implicitly* as functions of water and gas saturation and saturation pressure.

a. Calculation example : Single matrix block evaluation.

A matrix block of  $K_i = 1 \text{ mD}$  was simulated for two block heights  $H_{Bi} = 1$  foot and  $H_{Bj} = 10$  feet. The simulator used is a  $7 \times 7 \times 8$  grid with the grid spacing as follows:

for 1 foot block height

$$\Delta x = \Delta y = .001 ; 1 ; 2 ; 4 ; 2 ; 1 ; 001 \text{ ft}$$

$$\Delta z = .001 ; 1 ; 2 ; 2 ; 2 ; 2 ; 1 ; 0.001 \text{ ft}$$

and for 10 foot block height

$$\Delta x = \Delta y = .01 ; .1 ; .2 ; .4 ; .2 ; .1 ; 01 \text{ ft}$$

$$\Delta z = .01 ; .1 ; .2 ; .2 ; .2 ; .2 ; .1 ; .01 \text{ ff}$$

The other characteristics are given below :

#### PVT Data for Single Block and Three Dimensional Examples

Pressure psig	$B_o$ RB/STB	$B_s$ RB/SCF	$R_s$ SCF/STB	$\mu_o$ cP	$\mu_g$ cP	$\sigma$ dynes/cm
1674.	1.3001	.00198	367.	.529	.0162	6.0
2031.	1.3359	.00162	447.	.487	.0171	4.7
2530.	1.3891	.00130	564.	.436	.0184	3.3
2991.	1.4425	.00111	679.	.397	.0197	2.2
3553.	1.5141	.000959	832.	.351	.0213	1.28
4110.	1.5938	.000855	1000.	.310	.0230	.72
4544.	1.6630	.000795	1143.	.278	.0244	.444
4935.	1.7315	.000751	1285.	.248	.0255	.255
5255.	1.7953	.000720	1413.	.229	.0265	.155
5545.	1.8540	.000696	1530.	.210	.0274	.090
7000.	2.1978	.000600	2259.	.109	.0330	.050

## Field properties

Original Bubble Point - 5545 psig

Slope of  $B_o$  above  $P_b$  - .000012 vol/vol-psi

Density of Stock Tank oil - 51.14  $\text{lb}_m/\text{ft}^3$

Slope of  $\mu_o$  above  $P_b$  - .0000172 cp/psi

Gas Density at Standard Conditions -.058  $\text{lb}_m/\text{ft}^3$

Water Formation Volume Factor at 0.0 psig = 1.07

Water Compressibility =  $3.5 \times 10^{-6}$  vol/vol-psi

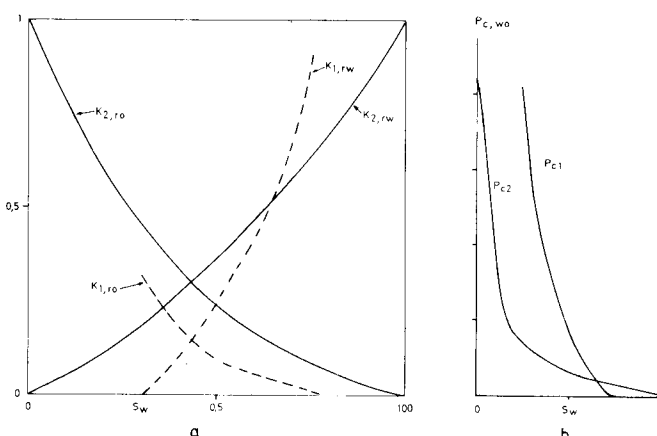
Water Viscosity = .35 cp

Water Density at Standard Conditions = 65  $\text{lb}_m/\text{ft}^3$

Matrix Compressibility =  $3.5 \times 10^{-6}$  vol/vol-psi

Fracture Compressibility =  $3.5 \times 10^{-6}$  vol/vol-psi

Relative permeabilities and capillary pressures for matrix (1) and fractures (2) are given in figures 11.16a and b.



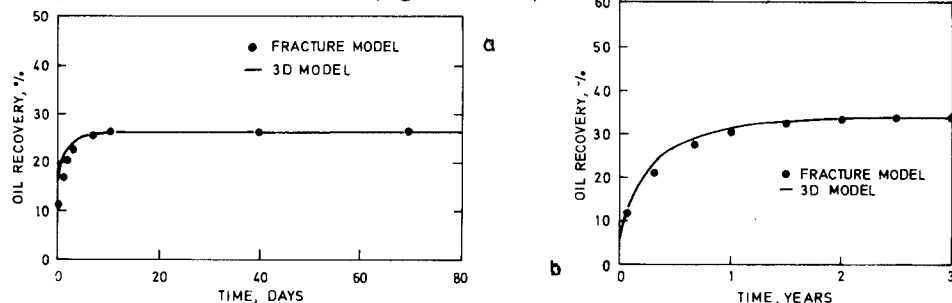
11.16 – Rock properties: a) imbibition relative permeability b) capillary pressure for water-oil, where subscript is matrix (1) and 2 is fractures (Thomas<sup>7</sup>, Courtesy AIME)

b. Calculation example : Water-oil imbibition results (case  $P > P_b$ )

The results obtained are presented as recovery vs. time (figure 11.17a and b) indicating the following :

- Final recovery for a 1 foot block is only 26% compared with the higher value of 34.2% for a 10 foot block; this is due to the contribution of gravity in a taller block (the recovery corresponds to the value of water saturation reached when the water-oil capillary height is equal to half the block height).

- The recovery time for a 1 foot block is only 10 days compared with 2 years for a 10 foot block (figure 11.17).

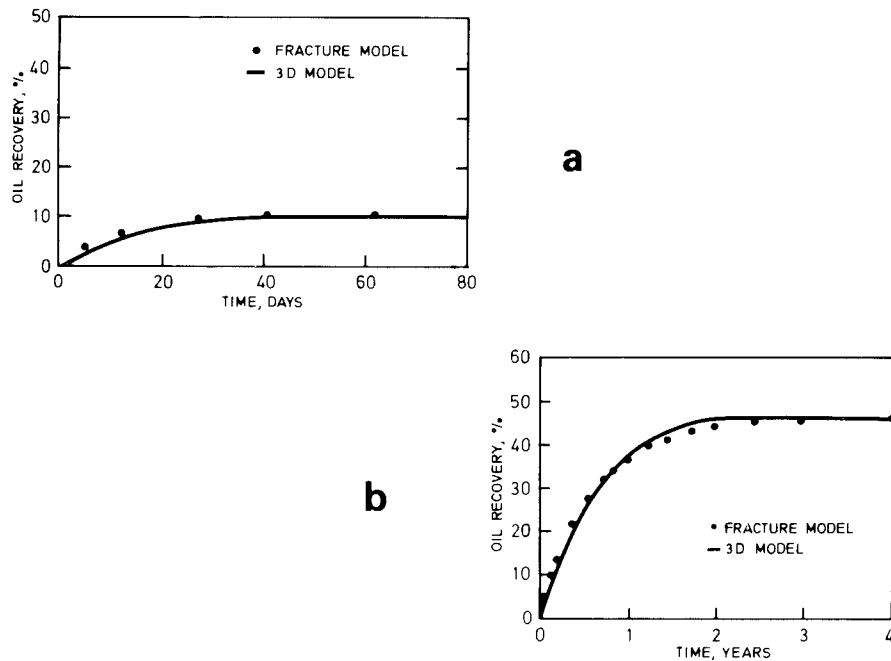


11.17 – Imbibition recovery vs. time a) 1 ft block height, b) 10 ft block height (Thomas<sup>7</sup>, Courtesy AIME)

#### c. Calculation example : Gas-oil drainage results

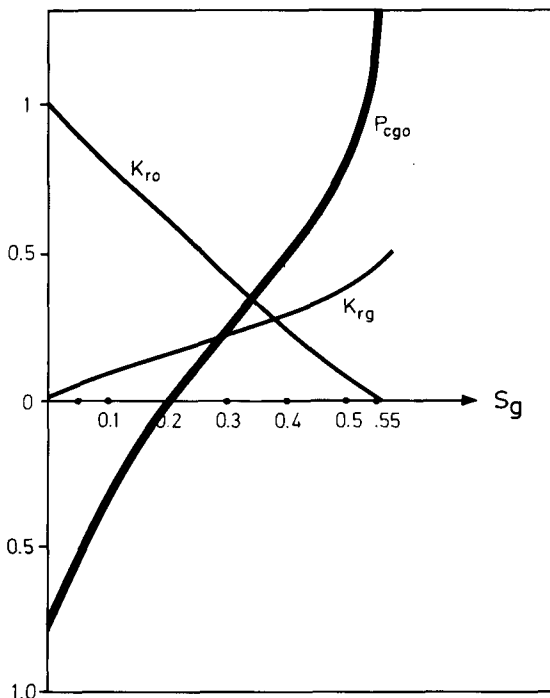
Displacement is governed by gravity forces resulting from the difference in weight between oil and gas. The results obtained (figure 11.18) indicate the following :

- Final recovery corresponds to saturation in water where capillary pressure is equal to gravity force.



11.18 – Gas-oil drainage recovery vs. time a) 1 ft block height and b) 10 ft block height (Thomas<sup>7</sup>, Courtesy AIME)

- The recovery for a 1 foot block is 10 % compared with 46 % for a 10 foot block.
- The recovery time is 60 days in a 1 foot block and 2.5 years in a 10 foot block.
- Between single cell recovery and 3D models the results are in perfect agreement for  $\sigma$  values equal to 2 and 0.2 and for 1 foot and 10 foot block heights. The single cell fracture results were obtained using pseudo gas-oil capillary pressure and relative permeabilities (figure 11.19).



11.19 – Gas-oil pseudo-relative permeability and pseudo-capillary pressure, at 5545 psig (Thomas<sup>7</sup>, Courtesy AIME)

The model can successfully handle three-phase flow as well as water injection or gas and water injection.

### 11.3. COMPOSITIONAL SIMULATORS

The compositional model of a fractured reservoir takes into consideration all the specific features of this type of reservoir and, in addition, introduces the hydrocarbon system through a compositional simulation.

Yamamoto's<sup>10</sup> model simulates the hydrocarbon system in terms of three equivalent components, while Saidi's<sup>11</sup> model may take into account up to ten components.

### 11.3.1. Yamamoto's model

Yamamoto presented a two-dimensional single block model developed under the following assumptions :

- a. immobile water contributing to production only by expansion.
- b. *three equivalent components* simulating the hydrocarbon system-methane, methane through hexanes and heptane plus.
- c. *complete phase equilibrium* is reached in each cell at the end of a time step.
- d. *negligible* capillary pressure takes place in the fracture network.
- e. *negligible* variation in composition of phases takes place in the fracture over the block height interval.

With this last assumption it is possible to represent the conditions prevailing in the surrounding fractures as a boundary condition to the mid-depth node on the lateral face of the block.

The fissure pressure over the full block height is calculated by using the fissure-made pressure. The gas-oil level in the fissure is an assigned parameter.

The equations referred to the components (j) are,

$$\frac{\partial}{\partial t} \left[ \Phi (S_o \rho_o C_{oj} + S_g \rho_g C_{gj}) \right] - \frac{\partial}{\partial x} \left( \frac{K_o \rho_o}{\mu_o} C_{oj} \frac{\partial \Psi_o}{\partial x} + \frac{K_g \rho_g}{\mu_g} C_{gj} \frac{\partial \Psi_g}{\partial x} \right) - \\ (11.25)$$

$$\frac{\partial}{\partial y} \left( \frac{K_o \rho_o}{\mu_o} C_{oj} \frac{\partial \Psi_o}{\partial y} + \frac{K_g \rho_g}{\mu_g} C_{gj} \frac{\partial \Psi_g}{\partial y} \right) = 0$$

where  $C_{oj}$  and  $C_{gj}$  satisfy the phase relationships,

$$\sum_{j=1}^J C_{oj} = 1 \quad \text{and} \quad \sum_{j=1}^J C_{gj} = 1 \quad \text{and} \quad \Psi = p + \rho g z$$

Fluid and rock properties are considered to be known functions of the thermodynamic conditions, i.e.,

$$\left. \begin{array}{l} \rho_0 = \rho_0 (p_0, T, X_j) , \quad \rho_g = \rho_g (p_g, T, X_j) \\ \mu_0 = \mu_0 (p_0, T, X_j) , \quad \mu_g = \mu_g (p_g, T, X_j) \\ k_{ro} = k_{ro} (S_o) \quad k_{rg} = k_{rg} (S_g); p_c = p_c (S_o); \Phi = \Phi (p_0) \end{array} \right\} \quad (11.26)$$

For the mole fractions,

$$\sum_{j=1}^J X_j = 1 ; \quad \sum_{j=1}^J Y_j = 1 \quad \text{and} \quad K_j = Y_j / X_j \quad (j = 1, 2, 3)$$

Equation 11.25 can also be written as,

$$\begin{aligned} & \frac{\partial}{\partial t} \left[ \Phi \left( S_o \rho_0 + S_g \rho_g \right) \right] - \frac{\partial}{\partial x} \left[ \left( \frac{K_o \rho_0}{\mu_0} + \frac{K_g \rho_g}{\mu_0} \right) \frac{\partial P_o}{\partial x} + \frac{K_g \rho_g}{\mu_g} \frac{dP_c}{dS_o} \frac{\partial S_o}{\partial x} \right] \\ & \frac{\partial}{\partial y} \left[ \left( \frac{K_o \rho_0}{\mu_0} + \frac{K_g \rho_g}{\mu_g} \right) \frac{\partial P_o}{\partial y} + \frac{K_g \rho_g}{\mu_g} \frac{dP_c}{dS_o} \frac{\partial S_o}{\partial y} - g \left( \frac{K_o \rho_0^2}{\mu_0} + \frac{K_g \rho_g^2}{\mu_g} \right) \right] = 0 \end{aligned} \quad (11.27)$$

which is expressed in a finite difference form as,

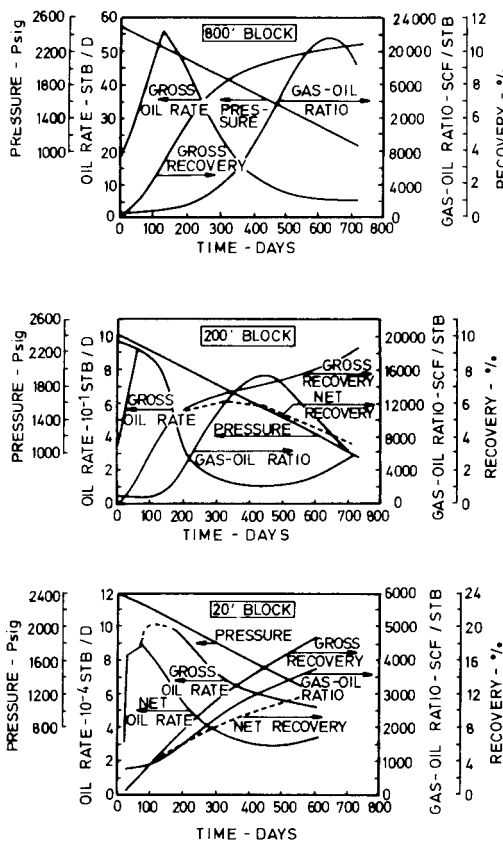
$$\begin{aligned} & \Delta x \Delta y \Delta z \frac{\partial}{\partial t} \left[ \Phi \left( S_o \rho_0 + S_g \rho_0 \right) \right] - \Delta z \cdot \Delta y \left( \frac{K_o \rho_0}{\mu_0} \frac{\partial \Psi_o}{\partial x} + \frac{K_g \rho_g}{\mu_g} \frac{\partial \Psi_g}{\partial x} \right) \Big|_L^R - \\ & \Delta z \Delta x \left( \frac{K_o \rho_0}{\mu_0} \frac{\partial \Psi_o}{\partial y} + \frac{K_g \rho_g}{\mu_g} \frac{\partial \Psi_g}{\partial y} \right) \Big|_B^T - \omega = 0 \end{aligned} \quad (11.28)$$

where L, R, B, and T indicate the left, right, bottom and top boundaries of the block and  $\omega$  indicates the rates of injection/production at the boundary nodes.

Phase behaviour parameters are calculated by using correlations based on pressure, temperature and one of the equivalent components. Capillary pressure imbibition-drainage curves as well as relative permeabilities have to be supplied.

The equations were solved by a semi-implicit scheme by evaluating the coefficients at the end of the previous time step and using upstream mobilities. Yamamoto et al<sup>10</sup> applied their model to the study of performances of blocks of different sizes, under pressure depletion and pressure maintenance.

The performance of a block surrounded by oil under a pressure depletion of 2 psi/day is presented in figure 11.20. The results are different for very tall blocks of 800 feet (figure 11.20a), for tall blocks of 200 feet (figure 11.20b) and for small blocks of only 20 feet (figure 11.20c).

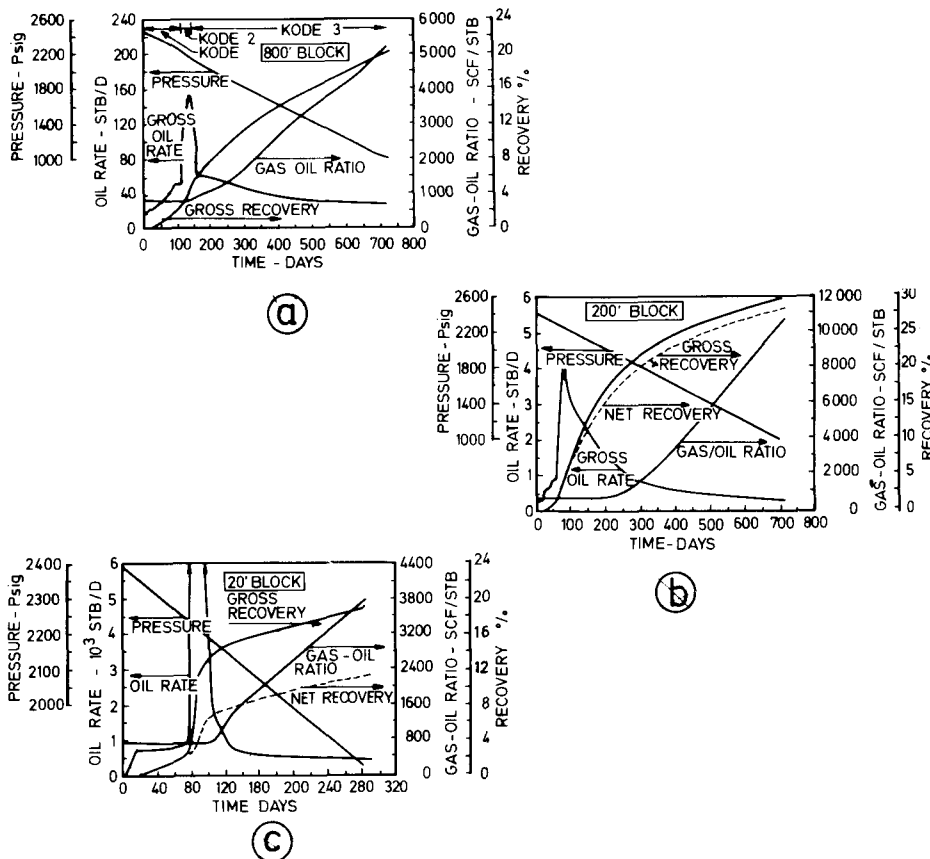


11.20 – Compositional production performance of a single oil-saturated block under pressure depletion in the oil zone : a) 800 ft block b) 200 ft block c) 20 ft block (Yamamoto<sup>10</sup>, Courtesy AIME)

The difference in net and gross recovery indicates the effect of *counterflow* of oil into the block and the results obtained for 200 feet blocks (fig. 11.20b) and 20 feet blocks (fig. 11.20c) show at what scale the *reimbibition* may restore the block oil saturation. Substantially lower effects are observed in 200 feet blocks (fig. 11.20b).

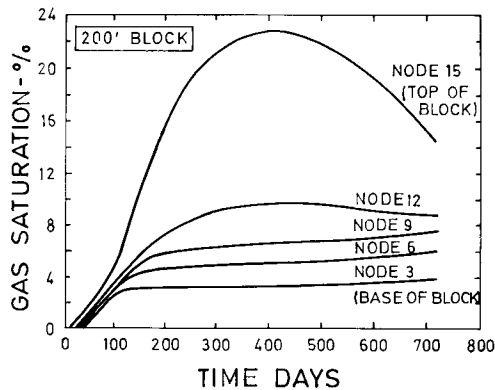
Such behaviour is the direct result of differences in gas-oil gravity segregation processes in small (20 feet) and large (200 - 800 feet) blocks.

In a gas environment (figure 11.21), recoveries are substantially higher than in an oil environment due to gravity drainage and absence of oil counterflow, even if divergence between gross and net recovery is keeping the same order of magnitude.



11.21 – Compositional production performance of an oil saturation block in a gas environment : a) 800 ft block b) 200 ft block c) 20 ft block (Yamamoto<sup>10</sup>, Courtesy AIME).

Figure 11.22 illustrates the results of the calculation of pressure maintenance of an 800 foot block in an oil environment. If after one year production is stopped and the pressure in the fracture is constant, the result is a fast resaturation in oil of the lower part of the block.



11.22 -- Compositional production behaviour of an oil saturated block in an oil zone under depletion conditions of production followed by pressure maintenance (Yamamoto<sup>10</sup>, Courtesy AIME)

### 11.3.2. Saidi's<sup>14</sup> model

Another compositional model was represented by Saidi<sup>11</sup>; this was developed under assumptions appropriate for the oil reservoirs in which pressure and fluid levels are uniform over large areas. The reservoir can then be represented by a relatively small number of blocks and hydrostatic equilibrium of fluids in the fractures can be assumed. Two-dimensional cylindrical blocks are considered sufficiently accurate to describe the actual three-dimensional blocks. This reduces the computational time by a factor of more than two. The model accounts for diffusion of hydrocarbons between block and fractures. Up to ten components may be considered.

The equations considered are those of conservation of mass for water and for the components (subscript i) in the gas, oil and equilibrium relations phases, i., $\lambda$

$$\frac{\partial}{\partial t} \left( \Phi \frac{S_w}{B_w} \right) - \operatorname{div} \left( \frac{K K_{rw}}{B_w \mu_w} \operatorname{grad} \Psi_w \right) - q_w = 0 \quad (11.29)$$

$$\left. \begin{aligned} \frac{\partial}{\partial t} \left[ \Phi (S_0 \rho_0 X_i + S_g \rho_g X_i) \right] - \operatorname{div} \left( \frac{K K_{f0} \rho_0}{\mu_0} X_i \operatorname{grad} \Psi_0 \right) \\ - q_0 X_i + q_v X_i - \operatorname{div} \left( \frac{K K_{rg} \rho_g}{\mu_g} Y_i \operatorname{grad} \Psi_g \right) \\ - q_g Y_i - q_v Y_i - \operatorname{div} \left( \frac{D S_0 \rho_0}{\Phi} \operatorname{grad} X_i \right) = 0 \end{aligned} \right\} \quad (11.30)$$

and

$$Y_i = K_i X_i \quad (i = 1, 2, \dots, N) \text{ with } \sum_{i=1}^N X_i = 1 \text{ and } \sum_{i=1}^N Y_i = 1 \quad (11.31)$$

where the potential  $\Psi = p + \rho g z$  and  $D$  is the diffusivity.

The equations are solved for boundary and initial conditions corresponding to each block. Equations 11.29 through 11.31 were solved by the *implicit pressure explicit saturation method* (IMPES), first for oil pressure by Gauss elimination and then saturations. The model was applied to the Haft Kel field for production after previous matching.

Additional phenomena take place if pressure declines below the saturation pressure and gas is evolved. Loosing part of the dissolved gas, the upper oil reservoir becomes heavier than the oil underneath. As a result of this *density inversion*, a convection current will take place in the fractures, where segregation is relatively fast. Transported downwards through the fracture, heavy oil will come in contact with the block oil containing more dissolved gas. Such a situation will induce transfer of dissolved gas from block to fracture by molecular diffusion and especially by convective mixing.

The convection current and fingering due to density inversion was studied extensively by Peaceman<sup>12</sup>, through perturbation analysis and numerically (discussed in chapter 10). The results showed that in the range of practical values of the diffusion coefficient, density inversion is highly unstable. Matrix-fracture transfer has no influence on stability or instability of the density inversion, on the spacing of the density fingers or on the size of the convection cells.

## SYMBOLS

### Latin letters

A	— flow cross section
B	— volume factor
C	— compressibility
D	— diffusivity
K	— permeability
P	— pressure
PV	— pore volume
r	— radius
s	— shape factor
S	— saturation
T	— piezconductivity
T,R,L,B	— top, right, left, bottom of a matrix block
U	— rate
X	— coordinate of a point
X <sub>o</sub>	— coordinate of injection or production point
x	— cartesian horizontal axis
y	— cartesian horizontal axis
z	— cartesian vertical axis

### Greek letters

$\Psi$	— potential
$\Phi$	— porosity
$\rho$	— specific weight
$\lambda$	— transmissivity/mobility
$\mu$	— viscosity
$\sigma$	— interfacial tension
$\omega$	— rate of injection

### Subscripts

B	— bubble point
c	— capillary
f	— fracture
g	— gas
i	— initial
m	— matrix
o	— oil
j	— components index
r	— relative
w	— water
l	— matrix
2	— fracture

## REFERENCES

1. Kazemi, H., 1969, Pressure transient analysis of naturally fractured reservoirs, SPEJ, December, p. 451 - 462.
2. Kazemi, H., Merrill L.S., Porterfield L., Zeman, P.K., (1976). Numerical simulation of water-oil in Naturally Fractured Reservoirs, SPEJ, September 1976, p. 317 - 323.
3. Kazemi, H., Merril, L.S. (1979) Numerical Simulation of Water Imbibition in Fractured Cores, SPEJ, June, p. 182.
4. Kleppe, J. Morse, R.A. (1974) Oil Production from Fractured Reservoir by Water Displacement, SPE Fall meeting Preprint no. 5084.
5. Lefevre du Prey, E.J. Bossie-Codreana, D.N., (1975) Simulation Numerique de l'exploitation des Reservoirs fissurés, Proceeding of World Petrol Congr. PD 13 (5) vol. 4p. 233 - 246.
6. Rossen, R.H. 1977, Simulation of Naturally Fractured Reservoirs with semi-implicit Source Terms, SPEJ, vol. 17, no. 3, June p. 201 - 210.
7. Thomas L.K., Dixon T.N. (1980), Fractured reservoir Simulation. Paper SPE 9305, 55th Annual Fall meeting, Pallas.
8. Barenblatt, G.L. (1964) On the motion of a Gas-Liquid mixture in a porous fissured media (in Russian). Izv. Akad. Nank U.S.S.R. Mekh. Maskinot. No. 3, 47 - 50.
9. Warren, J.E. and Root, P.J. The Behaviour of Naturally Fractured Reservoir. S.P.E.J. September, 1963 p. 245.
10. Yamamoto R.H., Padgett J.B., Ford W.T., Boubequira A, (1971) Compositional Reservoir Simulation for Fissured Systems - The Single block Model, SPEJ p. 113 - 128.
11. Saidi Ali, M., (1975) Mathematical simulation model describing Iranian Fractured Reservoirs and its application to Haft Kel Field, Ninth World Petrol. Congr. paper I.D. 13 (3) p. 209 - 219.
12. Peaceman, D.W., (1976) Convection in Fractured Reservoirs- The effect of matrix - fissure transfer in the instability of a Density Inversion in a Vertical Fissure SPEJ, p. 264 - 280.
13. Peaceman, D.W. (1976) Convection in Fractured Reservoirs Numerical Calculation of Convection in a Vertical Fissure including the effect of Matrix - Fissure Transfer SPEJ, p. 231 - 301.
14. Saidi, A.M., Martin, R.E. (1965) Applications of Reservoir Engineering in the Development of Iranian Reservoir. Paper presented to the ECAPE symposium of Petroleum, p. 10 - 20.
15. Andersen, K.H., Baker, R.L., Raoofi, J. (1963) The Development of Methods for Analysis of Iranian Asmari Reservoirs. Proceeding of the Sixth World Petroleum Congress, Section II, Paper 14.
16. Khatib, A.K. (1965) Use of mathematical models for the evaluation of a fracture carbonate reservoir. Fifth Arab Petroleum Congress, Cairo, March).

# CHAPTER 12

## FRACTURED RESERVOIR EXAMPLES

In this chapter two categories of examples are considered: existing reservoirs and theoretical calculation examples. The first part of the chapter is influenced by the fact that basic data and information on the past history of fractured reservoirs is very limited as compared to that which is available in the literature concerning conventional reservoirs. Some of this information is, therefore, reviewed as a help in orienting engineering work in the absence of detailed data about a specific reservoir.

The applications developed in the second part of this chapter are based on simplified assumptions and include various problems associated with single block rate, well rate, rate decline and generalized material balance under various production mechanisms.

### 12.1 BASIC DATA AND HISTORY OF CERTAIN FRACTURED RESERVOIRS

#### *12.1.1. Iranian reservoirs*

The Iranian fields have been discussed from a geological point of view in chapter 3, following the geological periods of the Upper Jurassic (Darius-Khang fields) through the Oligocene-Miocene (Asmari limestone) and Pliocene (north and north east of Iran). As mentioned, the fractured Oligocene-Miocene limestones are often underlain by Middle Cretaceous Bangestan limestone.

##### 12.1.1.1. General observations

###### a. Fault contacts

A general characteristic of these reservoirs is that, regardless of the extensive fracturing process developed throughout all of them, the gas-oil and water-oil contacts on the flanks of the reservoirs are located at different levels. This may be explained by the lack of natural communication, especially in very thick formations (over 2,500 feet), such as Agha Jari and Gachsaran.

A description of the reservoirs is provided<sup>1</sup> in table 12.1 and rock and fluid properties are given in Table 12.2.

### b. Aquifer intercommunication

Initially it was believed that a good intercommunication must exist between various fields since a regional pressure gradient (5psi/km) was observed from well data and outcrop studies<sup>2</sup>. This was interpreted as a movement of water from north-east to south-west, but high salt content in water throughout the aquifer, and limited water movement indicate low permeabilities of the aquifer.

Table 12.1

#### RESERVOIR CHARACTERISTICS OF IRANIAN OIL FIELDS

Field	Areal Extent Sq-Mile	Type of Reservoir Rock	Reservoir Thickness Feet	Depth to Producing Formation Feet	Original G.O.L. Feet sub-Sea Average	Original W.O.L. Feet Sub-Sea Average	In Communication with
Agha Jari	95	Asmari Bangestan	1200 2800	4900 - 9800 8800 - 10900	4612	8800 <sup>+</sup>	Bangestan Asmari
Ahwaz	97	Asmari Bangestan	1000 - 1200 2890	7850 Min 10470 Min	8100 None	9225 Unknown	None None
Bibi Hakimeh	110	Asmari Bangestan	1400 2069	3350 Min 6200 Min	3035 None	6500 6500	Bangestan Asmari
Cyrus*	29	Burgan	190	7000	None	7424	
Darius-Kharg*	50	Yamama	1300	10000	10900	12024	
Gachsaran	175	Asmari Bangestan Khami	1550 2322	2745 - 10000 5962	725 None	7850	Bangestan Asmari None
Haft Kel Kel	34	Asmari Bangestan	900	1900 - 4000	1065	3087	Bangestan Asmari
Karanj	64	Asmari Bangestan	1084	6200 - 6700	None	9500 <sup>+</sup>	
Lali	45	Asmari Bangestan	1200 1700	4000 - 7000 7000 - 9000	4267 6500 <sup>+</sup>	6500 8000	
Marun	85	Asmari		7800	8370	12000	
Masjid-Sulaiman	45	Asmari	1000	640 - 3600	None	2200	
Naft-e-Shah	—	Kalhur	250	2400 - 3100	1900	3100	
Naft Safid	26	Asmari	900	3000 - 6000	4425	5500	
Pazanan	100	Asmari	1170	5800 - 9100	7110	7810	

\* Off shore fields + Estimated

Table 12.2

## ROCK AND FLUID CHARACTERISTICS OF IRANIAN OIL FIELDS

Field	2 Average Porosity Percent	4 API Gravity of S.T. crude current	5 G.O.R. SCF/bbl Original	6 Formation Volume factor Original	1 Nature of The Reservoir Rock
Agha Jari	14	34.2	905	1.43	F.L.S.
Ahwaz	12 (F.L.S.) 25 (S.S.)	32.7	950	1.62	F.L.S. and S.S.
Bibi Hakimeh	10	30.4	505	1.34	F.L.S.
Cynus	24	12-19	30	1.08	S.S.
Darius Kharg	14	35	1200	1.55	L.S.
Gachsaran	11	31.3	520	1.25	F.L.S.
Haft kel	16	38.2	403	1.18	F.L.S.
Karanj	10	34.3	850	1.55	F.L.S.
Lali	7	35.3	850	1.37	F.L.S.
Mashjid-i-Sulaiman	11-0	38.9	230	1.11	F.L.S.
Naft-e-Shah		35	780	1.34	F.L.S.
Naft safid	14	35.8	775	1.41	F.L.S.
Pazanan	12	36.0 (Oil) 66.0 (Cond)	1000	1.57	F.L.S.

\* F.L.S. fractured Limestone

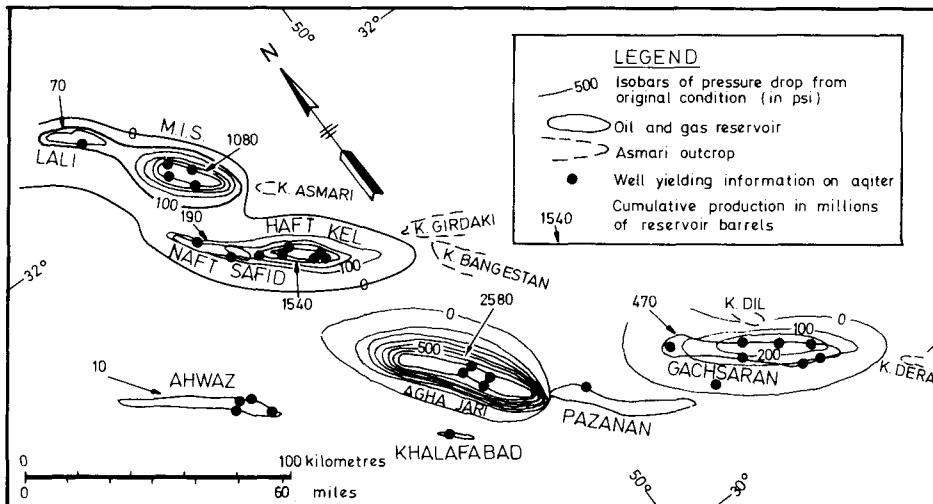
L.S. Limestone

S.S. Sandstone

Measurements of aquifer pressure through wells drilled (figure 12.1) show a poor transmissibility of pressure drop in the water zone, whether or not a single reservoir has been highly depressed (1,000 psi in Agha Jari). In general, with the exception of Haft Kel and Naft Safid where aquifer interaction is evident, it may be concluded that the effect of the water influx on each single reservoir is independent of the surrounding reservoirs.

## c. Behaviour of reservoirs

From early observations<sup>14</sup> on Iranian fields, the following may be concluded:



12.1. — Pressure drop resulting in Asmari aquifer as a result of reservoir production until mid 1962.  
(Andersen<sup>2</sup>, Courtesy Elsevier)

- The single well production capacity, due to a large fracture network and to pressure maintenance (as a result of gas segregation in fractures and aquifer expansion), is kept throughout the entire life of the reservoir.
- If pressure depletion and gas-oil ratio are compared with pressure depletion and gas-oil ratio of a conventional reservoir having the same characteristics, the presence of fractures gives the appearance of a pressure maintenance. A conventional reservoir will only assume a similar behaviour if most of the produced gas is reinjected in the reservoir. The recovery in water and gas-invaded zones of a fractured reservoir is, under the most favourable conditions of oil displacement, the same as that of a conventional reservoir.

## 12.1.1.2. Description of certain Iranian reservoirs

### a. Agha Jari field

The Asmari fractured formation has been examined through well data obtained from cores, mud loss during drilling, productivity index, pressure build-up data and flowmeter surveys<sup>2</sup>. An example of a flowmeter survey in Asmari wells is illustrated in table 12.3. The zones of high percentage of flow on small pay, correspond to the higher fractured interval.

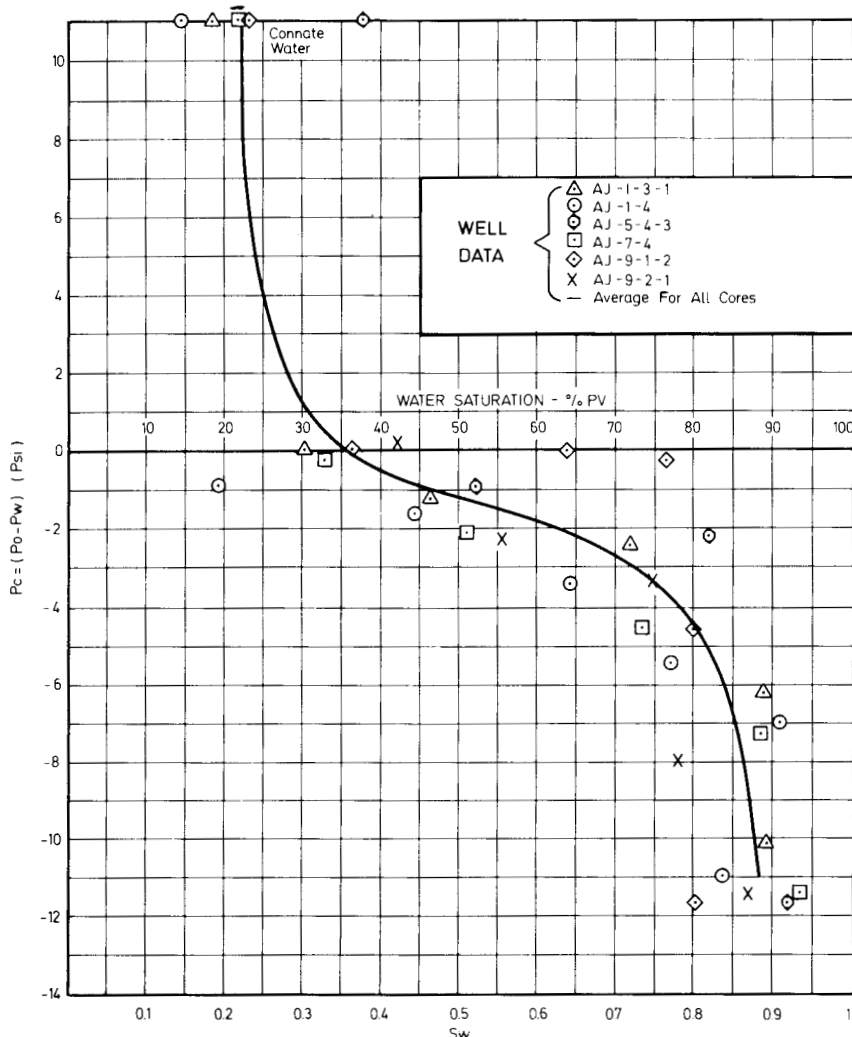
Table 12.3

AGHA JARI: RESULTS OF FLOWMETER SURVEYS

Well Number	Top of Asmari ft.	Total Depth ft.	Inflow Interval ft.	Percent of Total Flow	% Flow per inflow interval
60	8126	8647	8405-19	16	1.14
			8456-61	17	1.13
			8469-74	8	1.60
			8501-08	19	2.70
			8519-23	14	3.50
			8540-46	26	4.33
54	6110	6933	6583-87	7	1.75
			6549-89	23	6.575
			6746-62	5	
			6762-69	13	0.312
			6769-6835	17	0.250
			6835-43	23	2.875
			6843-TD	12	0.133
49	6378	7657	6393-97	5	1.25
			6508-11	35	11.66
			6515-21	9	1.50
			6549-61	8	0.66
			6573-TD	43	0.037
33	7072	7333	7072-78	18	3.00
			7079-83	32	8.00
			7103-12	3	0.33
			7127-46	23	1.21
			7148-7250	23	0.22
			7320-TD	1	0.016

The rate of an average well has been estimated at around 40,000STB/D with a pressure drop of 250psi, which is equivalent to a productivity index of 160STB/D/psi. Since the skin was estimated to be approximately 80 %, the effective productivity index of the fracture network is around 1,000STB/D/psi.

The production mechanism in the water zone, as combined effect of gravitational and capillary imbibition, was examined through a *composite capillary pressure curve* as shown in figure 12.2.



12.2 – Water-oil composite capillary pressure curve for Agha Jari well (obtained on 61 cores, Saidi<sup>14</sup>)

During reservoir depletion the pressure decline rate was small—in the range of  $dP/dt = 3$  atm/year—but the supersaturation in the gasing zone was less evident as a result of high porosity and permeability. A porosity of approximately 20% and a permeability of approximately 20mD indicate the Leverett parameter

$$\sigma\sqrt{\phi/K} = 4 \text{ (dyne/cm)} \sqrt{0.2/0.02 \times 10^{-8} \text{ (cm}^2\text{)}} = 12 \times 10^4 \text{ dyne/cm}^2$$

This value is below  $40 \times 10^4$  dyne/cm<sup>2</sup> (indicated in chapter 10, section 10.3.2.2f), which represents the critical Leverett value of the liberated gas.

#### b. Haft Kel field<sup>11</sup>

The field on the east side of Dezful embayment was discovered in 1928. The Asmari producing formation has a pay of about 900 feet which is in communication with the Naft Safid field.

The oil in place was estimated<sup>11</sup> to be in the range of  $7.2 \times 10^9$  STB in the matrix and  $197 \times 10^6$  STB in the fracture network.

The basic reservoir characteristics are as follows :

- matrix porosity – 7 – 12 %
- matrix permeability – 0.005 – 0.8mD
- matrix block height – 10 – 14 feet
- matrix block extension (radius) – 6 – 8 Feet

Fracture volume along with depth and PVT properties are given in tables 12.4 and 12.5.

Table 12.4

FRACTURE BULK VS. DEPTH

Depth (feet)	Fracture volume $10^6 \text{ Bbl}$
90	4.5
200	10.0
350	55.5
500	85.0
600	97.0
700	107.0
900	127.0
1100	135.0
1400	165.0
1700	193.0
1850	213.0
2136	234.0

Table 12.5

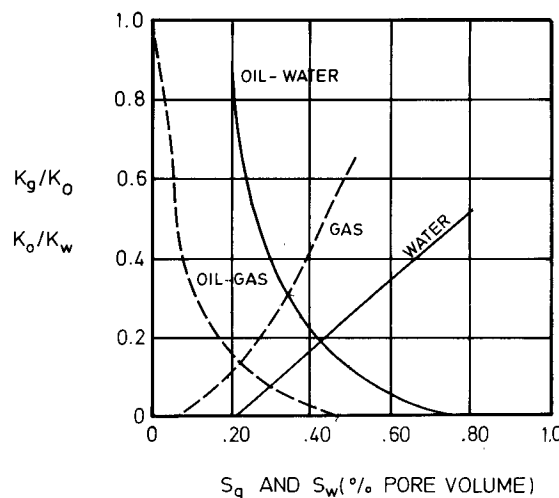
PVT PROPERTIES OF OIL

Pressure (PSI)	$B_o$	Gas FVF (RB/MCF)	$R_s$ (MCF/STB)	$\mu_o$ (cP)	$\mu_g$ (cP)
212	1.065		0.09460	1.590	0.011065
612	1.1037	10.6	0.194934	1.170	0.012059
1012	1.142	4.16	0.295268	0.910	0.013049
1412	1.181	2.40	0.3956	0.785	0.014040
1812	1.1766	1.662	0.3956	0.785	0.015032
2122	1.1723		0.3956	0.785	0.016024

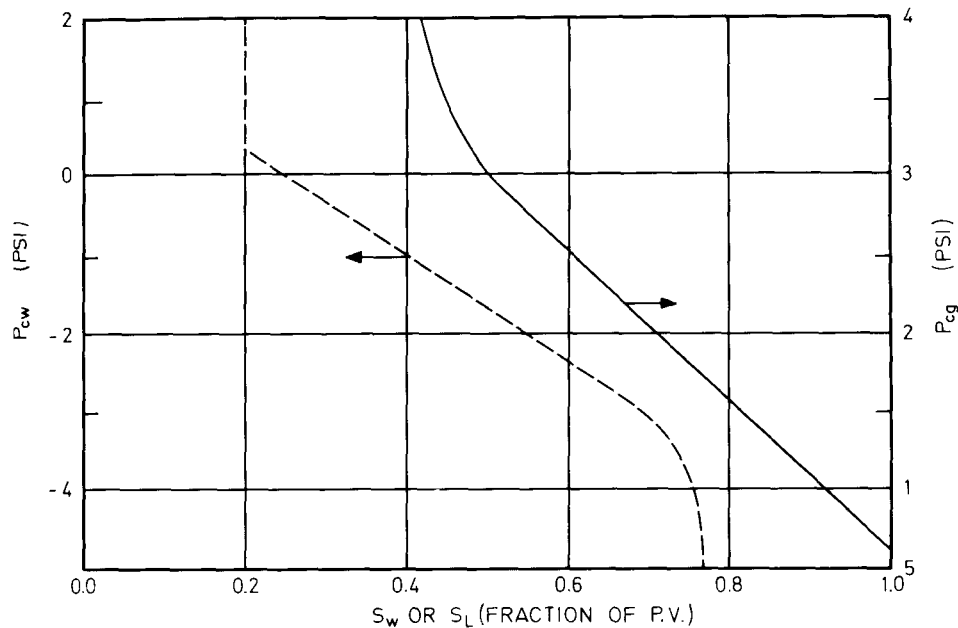
In addition, the following data are known:

- $B_w = 1.002$  (RB/STB)
- $C_o = 3 \times 10^{-6}$  psi $^{-1}$
- $C_r = 4 \times 10^{-6}$  psi $^{-1}$
- $a = \frac{K}{\phi C \mu} 25 \times 10^{-4}$  (ft $^2$ /day)

The relative permeability and capillary pressure are given in figures 12.3 and 12.4, respectively.



12.3 – Relative permeability of water, gas and oil vs. saturation of Haft Kel reservoir (Saidi<sup>1</sup>. Courtesy Elsevier)



12.4 – Average water-oil and gas-oil capillary pressure used for Haft Kel Field (Saidi<sup>1</sup>, Courtesy Elsevier)

After matching the yearly production, the GOR was also matched with cumulative production. Various cases of water and gas injection have been reviewed in case injection might have started from the first year of production; an additional  $800 \times 10^6$  STB would have been recovered if the pressure at the gas-oil contact was kept constant at 1,412 psi.

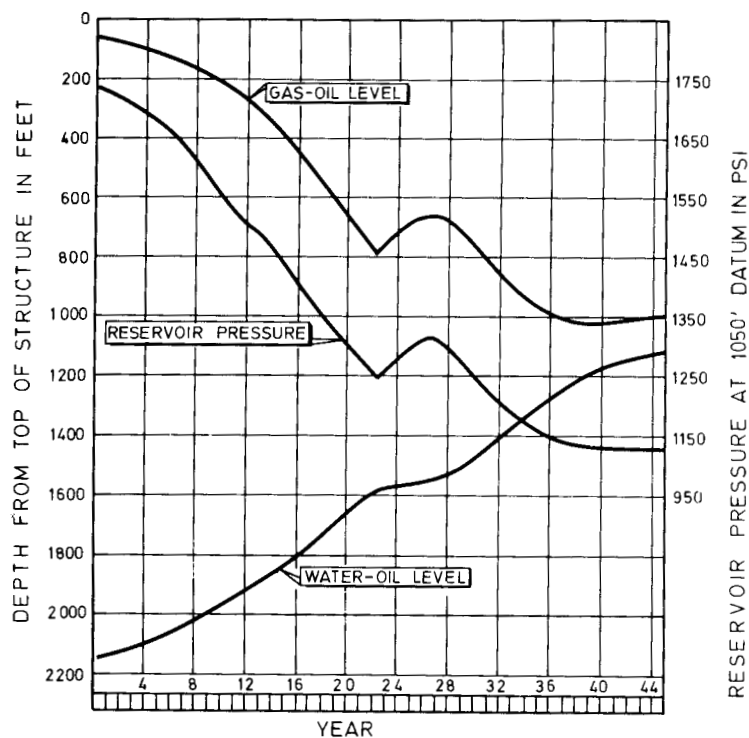
#### 12.1.1.3. Matching reservoir history

The object of history matching<sup>11</sup> was to examine the flow mechanisms such as convection and diffusion, and a sensitivity analysis for parameters such as block height, fracture volume, equilibrium gas saturation, etc.

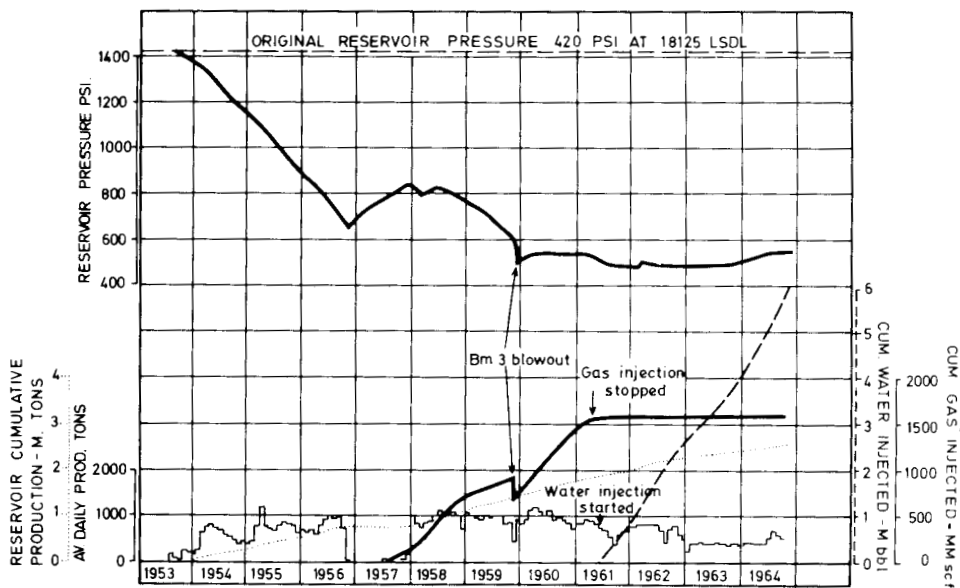
The advantage of this study is also emphasized by the fact that Haft Kel reservoir has a long history where both gas and water-invaded zones have been well developed during reservoir production (figure 12.5).

#### 12.1.2. Irakian reservoir : Butmah<sup>16</sup>

The Butmah reservoir, located in the northern part of Irak, consists of fractured marly limestones where several accumulations of undersaturated



12.5 – Pressure and contacts (gas-oil, water-oil) vs. time of Haft Kel reservoir (Saidi<sup>1</sup>, Courtesy Elsevier)



12.6 – Past history of Butmrah reservoir (Khatib<sup>3</sup>)

oil are connected through the fracture network. A detailed study<sup>16</sup> proved that the fracture connection was good in the crestal part, but very poor down flank.

Basic data :

- matrix porosity = 10 %
- matrix permeability < 2mD
- water salinity = 170,000ppm
- original reservoir pressure @ 19,215 ft. depth = 1,000psi

The production history of the reservoir is given in figure 12.6. An attempt to predict the future behaviour by a type of conventional reservoir approach has proven that water injection had improved the reservoir's behaviour

## 12.2. SIMPLIFIED EXAMPLES OF RESERVOIR CALCULATIONS

### *Application A*

In a fractured reservoir the oil-saturated matrix block is surrounded by fractures saturated with water. In order to examine the imbibition displacement, it is necessary to:

1. Elaborate and discuss the theoretical basis of single matrix block recovery behaviour under imbibition through: 1) the relationship recovery vs. time, 2) the relationship rate vs. recovery, 3) relationship rate vs. time. The examination will be developed assuming in a first case, that the displacement process is under the predominance of *capillary forces only*, then under predominance of *gravity forces only* and finally, under *both capillary and gravity forces*.
2. Elaborate the *dimensionless* relationship *recovery vs. time* for the three cases where the predominant forces are successively: gravity, then capillary and finally gravity & capillary. For the first two cases the mobility will be assumed :  $M = 0.1 ; 0.5 ; 0.8 ; 1.2 ; 2.5$ . For the last case of combined gravity & capillary forces for a mobility  $M = 1.2$  the role of capillary - gravity will be evaluated, assuming  $h_c/H = 0.1 ; 0.3 ; 0.5 ; 0.8 ; 0.9$ .

3. Elaborate the *dimensional* relationship *recovery* vs. *time* for the three cases discussed at point 2. In the case of combined gravity & capillary forces only the case  $M = 1.2$ , and  $h_c = 0.50$  H will be examined.
4. Elaborate the *single block decline rate* vs. *recovery* and *time*, under the following conditions : 1) relationship of decline factor DF vs. recovery for  $M = 1.2$  and  $h_c/H = 1$  ; 2) relationship DF vs. time for  $M = 1.2$  and  $h_c/H = 1$  ; 3) relationship block rate  $Q_{BL}$  vs. time if the block is a cube of 1 m ; 4) relationship well rate vs. time if the drainage area is a square of 1000 m and water table in fractures is raised by 10 m at the same instant that production started.

*Basic data*

Rock properties  $K = 1$  mD.,  $\Phi = .12$ ,  $S_{wi} = .27$

Fluid properties  $B_o = 1.25$  ;  $\mu_o = 1.4$  c.P. ;  $\mu_w = 0.5$  cP ;  $\gamma_o = .82$  kg/dm<sup>3</sup>  
 $\gamma_w = 1.08$  kg/dm<sup>3</sup> ;  $\sigma_{wo} = 48$  dyne/cm ;  $\theta_{wo} = 30^\circ$

- Special data :
- ~ For a given relative permeability curve and viscosities of oil and water ( $\mu_o = 1.4$  CP,  $\mu_w = 0.5$  CP), the saturation in water behind the front resulted :  $\bar{S}_w = 0.52$  (pore fraction).
  - ~ Relative permeabilities at displacement front of two phases are :  $K_{ro} = 0.7$  and  $K_{rw} = 0.3$ .
  - ~ The desaturation in oil behind the front of displacement is equal to difference in water saturation :
- $$\Delta S_w = \bar{S}_w - S_{wi} = 0.52 - 0.27 = 0.25.$$
- ~ Effective porosity is expressed by pores of oil displaced.

$$\Phi_{eff} = \Phi \times \Delta S_w = .12 \times 0.25 = 0.03$$

## SOLUTION

### 1. THEORETICAL APPROACH.

#### 1.1. Definitions and dynamic descriptions

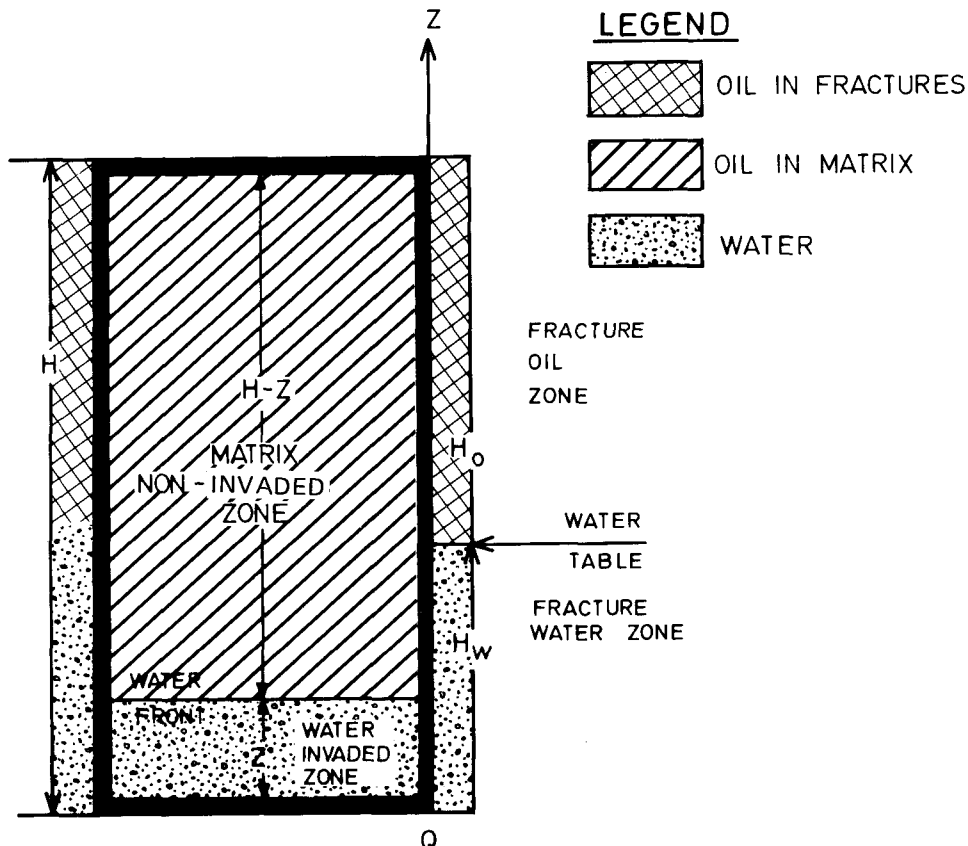
When considering a vertical section in a block, as in figure A.1, the following definitions are generally used :

- *water table* - water-oil contact in fractures.
- *water front* - water-oil contact in matrix during displacement process.

- *water table rate* - advancement velocity of water-oil contact in fractures ( $dH_w/dt$ , figure A.1).
- *water front rate* - advancement of displacement front in matrix.
- *water and oil zones* are defined by the water table position in fractures. The sum of the two heights  $H_w$  and  $H_o$  of water and oil zones are equal to the block height,

$$H_w + H_o = H \quad (\text{A.1})$$

- *the water-invaded zone* and the *non-invaded oil zone* in the matrix are defined by height  $Z$  and  $H - Z$ .
- *recovery* is defined by the ratio  $Z/H = Z_D$ , since the advancement is assumed to be a vertical movement of a horizontal plane (as a piston) during the displacement of oil by water in matrix.



A.1 – Schematic representation of a matrix block saturated with oil and surrounded by water

- the *rate of the water table* and the *water front* may be expressed respectively by,

$$\vartheta = dH_w/dt \sim \text{for water table} \quad (\text{A.2})$$

$$U = \Phi dz/dt \sim \text{for water front} \quad (\text{A.3})$$

- the *forces* which contribute to the oil displacement from the matrix are *capillary* and *gravity* forces. The capillary forces are a result of the specific characteristics of the rock,

$$P_c = h_c \Delta\gamma = J(S_\omega) \sigma \cos \Theta \sqrt{\Phi/K} \quad (\text{A.4})$$

while the gravity forces are always the result of the difference in specific weight between fluids saturating the matrix and fluids saturating the adjacent fractures. In figure A.1 the gravity forces are expressed by,

$$G = (H_w - Z) \Delta\gamma \quad (\text{A.5})$$

In a special case where  $H_w < Z$ , the value G becomes negative and opposes the displacement and vice-versa.

When  $H_w = H$  the gravity forces are expressed as,

$$G = (H - Z) \Delta\gamma \quad (\text{A.6})$$

### 1.2. Basic relationship recovery vs. time (dimensionless)

Very often, and most commonly when the blocks are not very tall, an acceptable assumption is to consider that the water table rises instantaneously from the bottom face to the top face of the block. The filtration velocity  $U_f = U$ , related to the water advancement is expressed by the equation,

$$U = \frac{h_c + (H - Z)}{\frac{\mu_w}{K_w} Z + \frac{\mu_0}{K_0} (H - Z)} \Delta\gamma \quad (\text{A.7})$$

which may also be written

$$U = \frac{k_0}{\mu_0} \times \frac{h_c/H + (1 - Z_D)}{\frac{1}{M} Z_D + (1 - Z_D)} \Delta\gamma \quad (\text{A.8})$$

where,

$$\left. \begin{aligned} M &= \frac{k_w}{\mu_w} \cdot \frac{\mu_0}{k_0} \\ Z_D &= Z/H \end{aligned} \right\} \quad (\text{A.9})$$

The time vs. recovery relationship will result from the combination of equations A.3 and A.8, which will give,

$$dt = \frac{1}{U} \Phi H \cdot d(Z/H) = \frac{\Phi H \mu_0}{k_0 \Delta\gamma} \cdot \frac{\frac{1}{M} Z_D + 1 - Z_D}{h_c/H + 1 - Z_D} \cdot dZ_D \quad (\text{A.10})$$

Based on differential equation A.10 the following will result :  
a. Gravity forces predominate

Neglecting the term  $h_c/H$  in equation A.10 the result is,

$$t = \frac{\Phi H \mu_0}{K_0 \Delta\gamma} \frac{1}{M} \left[ \int \frac{Z_D \, dZ_D}{1 - Z_D} + M \int \frac{dZ_D}{1 - Z_D} - M \int \frac{Z_D \, dZ_D}{1 - Z_D} \right]$$

or,

$$t = \frac{\Phi H \mu_0}{K_0 \Delta\gamma} \frac{1}{M} \left[ -Z_D - \ln(1 - Z_D) - M \ln(1 - Z_D) + MZ_D + M \ln(1 - Z_D) \right]$$

and finally

$$t = \frac{\Phi H \mu_0}{K_0 \Delta\gamma} \frac{1}{M} \left[ Z_D (M - 1) - \ln(1 - Z_D) \right] \quad (\text{A.11})$$

If equation A.11 expresses time as a dimensionless parameter, then:

$$t_{D,G} = (M - 1) Z_D - \ln(1 - Z_D) \quad (\text{A.12})$$

where,

$$t_{D,G} = \frac{K_w \Delta \gamma}{\Phi_{eff} \mu_w H} t \quad (A.13)$$

and,

$$\Phi_{eff} = \Phi \times MDE = \Phi \times \Delta S_0 \quad (A.14)$$

The effective porosity refers to the displacing pore volume in the matrix block.

b. Capillary forces predominate

Neglecting the term  $(1 - Z_D) \Delta \gamma$  the result is,

$$\begin{aligned} dt &= \frac{\Phi \mu_0 H}{K_0 \Delta \gamma} \frac{H}{h_c} \left[ \frac{1}{M} \int z_D dz_D + \int dz_D - \int z_D dz_D \right] \\ t &= \frac{\Phi H \mu_0}{K_0 \Delta \gamma} \frac{H}{h_c} \cdot \frac{1}{M} \left[ Z_D^2 / 2 + MZ_D - MZ_D^2 / 2 \right] \\ t &= \frac{\Phi H \mu_0}{K_0 \Delta \gamma} \frac{H}{h_c} \cdot \frac{1}{M} \left[ MZ_D + (1 - M) Z_D^2 / 2 \right] \end{aligned} \quad (A.15)$$

If time is expressed as a dimensionless parameter

$$t_{D,pc} = MZ_D + (1 - M) Z_D^2 / 2 \quad (A.16)$$

where,

$$t_{D,pc} = \frac{K_0 h_c \Delta \gamma M t}{\mu_0 \Phi_{eff} \mu_w H^2} = \frac{k_w}{\mu_w} \cdot \frac{P_c}{\mu_w} \cdot \frac{1}{H^2} t \quad (A.17)$$

If  $P_c$  is derived from equation A.4 the result is as follows,

$$t_{D,pc} = \frac{k k_{rw} \sigma \cos \Theta \sqrt{\Phi/k}}{\Phi \Delta S_0 \mu_w H^2} t = \frac{\sigma \cos \Theta \sqrt{K/\Phi} k_{rw}}{\Delta S_0 \mu_w H^2} t \quad (A.18)$$

c. Capillary & gravity forces

Based on equation A.10 the differential relationship time vs. recovery may be written as follows,

$$dt = \frac{\Phi H \mu_0}{k_0 \Delta \gamma} \cdot \frac{1}{M} \cdot \left[ \frac{z_D}{\epsilon - z_D} dz_D + M \frac{dz_D}{\epsilon - z_D} - M \frac{z_D}{\epsilon - z_D} dz_D \right] \quad (A.19)$$

where,

$$\epsilon = 1 + h_c/H \quad (\text{A.20})$$

If the equation is integrated, the result is,

$$t = \frac{\Phi H \mu_o}{K_o \Delta \gamma} \cdot \frac{1}{M} \left[ -Z_D - \epsilon \ln(\epsilon - Z_D) - M \ln(\epsilon - Z_D) + M Z_D + M \epsilon \ln(\epsilon - Z_D) \right] \quad (\text{A.21})$$

or, as a function of dimensionless time, as:

$$t_{D,G,Pc} = Z_D (M - 1) - \left[ M + \epsilon (1 - M) \right] \cdot \ln(\epsilon - Z_D) \quad (\text{A.22})$$

where  $t_{D,G,Pc}$  the dimensionless time expressed in terms of gravity will be the same as in equation A.13.

$$t_{D,G,Pc} = t_{D,G} = \frac{k_w}{\mu_w} \cdot \frac{\Delta \gamma}{\Phi H} \cdot t \quad (\text{A.23})$$

Equation A.22 is valid only if  $h_c/H < 1$ , since for prevailing capillary forces  $h_c/H > 1$ , equation A.16 must be used. This observation results from the condition of negative values  $\ln(\epsilon - Z_D)$  when,

$$\ln(\epsilon - Z_D) < 0$$

or,

$$h_c < H \times Z_D$$

Since  $0 < Z_D < 1$ , it results that equation A.22 is used when

$$0 < h_c < H$$

Resuming the results for these three cases discussed, it may be stated that:

For predominant forces	Recovery vs. time is expressed by	Time $t$ vs. $t_D$ is expressed by
Gravity forces	Eq. A.12	Eq. A.13
Capillary forces	Eq. A.16	Eqs. A.17, A.18
Gravity & Capillary forces	Eq. A.22	Eq. A.23 = Eq. A.13

### 1.3. Basic relationship, rate vs. recovery of a matrix block

The water imbibition rate of a block will result from the product between cross-section  $A_{BL}$  and velocity, expressed by equation A.8.

$$Q_{BL} = A_{BL} \times u = A_{BL} \frac{k_0}{\mu_0} \Delta\gamma \frac{\frac{h_c}{H} + (1 - Z_D)}{\frac{1}{M} Z_D + (1 - Z_D)} \quad (A.24)$$

If the expression  $A_{BL} \frac{k_0}{\mu_0} \Delta\gamma$  is considered as defined by Muskat, the (initial) *gravity rate*

$$Q_{GI} = A_{BL} \frac{k_0}{\mu_0} \Delta\gamma \quad (A.25)$$

the remaining fraction of equation A.24 may be assimilated to a decline factor DF expressed by,

$$DF = \frac{\frac{h_c}{H} + 1 - Z_D}{\frac{1}{M} Z_D + 1 - Z_D} \quad (A.26)$$

Thus the equation A.24 may be written,

$$Q_{BL} = A_{BL} \times u = Q_{GI} \times DF = A_{BL} \frac{k_0}{\mu_0} \Delta\gamma \frac{\frac{h_c}{H} + (1 - Z_D)}{\frac{1}{M} Z_D + (1 - Z_D)} \quad (A.27)$$

The value DF expresses the relationship rate vs. recovery as a result of variation of  $Z_D$  between 0 and 1 (equivalent to  $0 < Z < H$ ).

The following table indicates the DF values for various orders of magnitude of mobility M.

M	DF		DF vs. $Z_D$
	$Z_D = 0$	$Z_D = 1$	
below 1	$1 + hc/H$	$\frac{Mhc}{H}$	decreases since $M - \frac{H}{hc} < 1$
equal to 1	$1 + hc/H$	$hc/H$	decreases since $hc/H < 1 + hc/H$
higher than 1	$1 + hc/H$	$\frac{Mhc}{H}$	increases since $M - \frac{H}{hc} > 1$

If  $0 < M < 1$  a continuous decrease of the rate will take place as a result of declining DF with recovery and time. On the contrary, if  $M > 1$  the DF and rate increase vs. time and recovery. The physical explanation of the role of M is the following: when  $M > 1$  (equivalent to case  $\mu_o > \mu_w$ ) the rising z, during advance of the displacement front corresponds to a reduction in height ( $H - Z$ ) of the more viscous fluid zone which consequently reduces the friction losses and thus the rates increase.

Note : The decline factor may be considered as a dimensionless rate of the block ( $Q_{D,BL}$ ) expressed as,

$$DF = Q_{D,BL} = Q_{BL}/Q_{GI} \quad (A.28)$$

#### 1.4. Relationship rate vs. time

The rate vs. time may be obtained indirectly as a result of equations A.26, A.27 combined with equations A.12, A.16, A.22 according to forces which are working in the favour of displacement.

## 2. DIMENSIONLESS RELATIONSHIP RECOVERY VS. TIME (CALCULATION)

A sensitivity calculation is performed hereunder for various values of M and  $h_c/H$ .

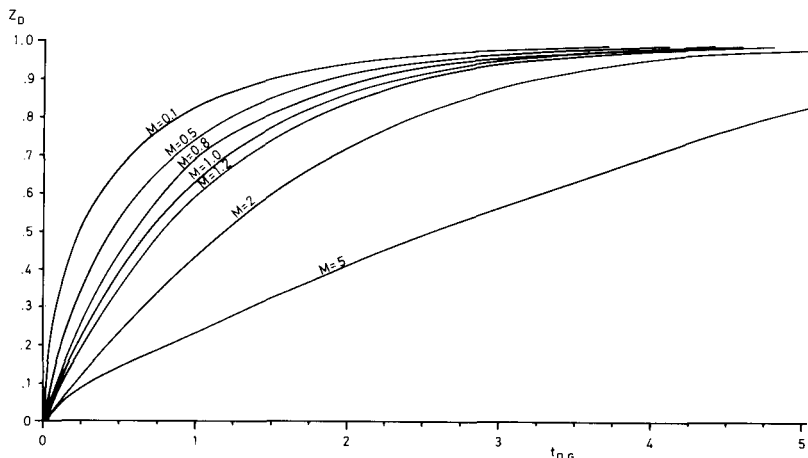
## 2.1. Case of predominance of gravity forces

Assuming the values  $M = 0.1 ; 0.5 ; 0.8 ; 1 ; 1.2 ; 2 ; 5$ , the recovery vs. time will be calculated through equation A.12. Based on Eq. A.12 the results are shown in Table A.1 and Figures A.2 and A.3.

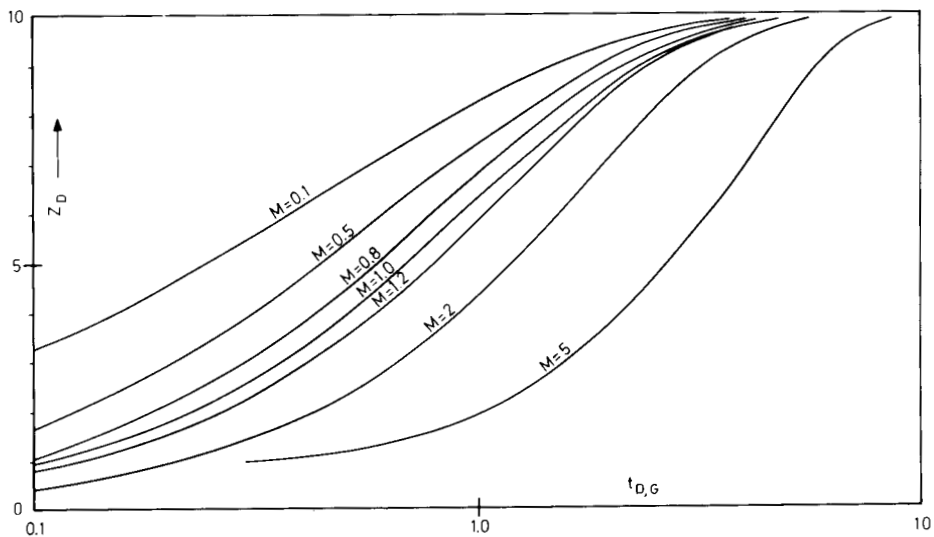
Table A.1. Recovery vs. dimensionless time for various mobility M ((case of predominance of gravity forces)

ZD	$t_{D,G}$ based on Eq. A.12						
	M=0.1	M=0.5	M=0.8	M=1	M=1.2	M=2	M=5
0.0	0	0	0	0	0	0	0
0.1	0.015	0.055	0.085	0.105	0.125	0.205	0.3
0.2	0.043	0.123	0.183	0.223	0.263	0.423	1.023
0.3	0.087	0.207	0.297	0.357	0.417	0.657	1.557
0.4	0.151	0.311	0.431	0.511	0.591	0.911	2.111
0.5	0.243	0.443	0.593	0.693	0.793	1.193	2.693
0.6	0.376	0.616	0.796	0.916	1.036	1.516	3.316
0.7	0.574	0.854	1.064	1.204	1.344	1.904	4.004
0.8	0.889	1.209	1.449	1.609	1.769	2.409	4.809
0.9	1.493	1.853	2.123	2.303	2.483	3.203	5.903

The results obtained are represented in Fig. A.2 on conventional scale while the same results are drawn on a semilog scale in Fig. A.3.

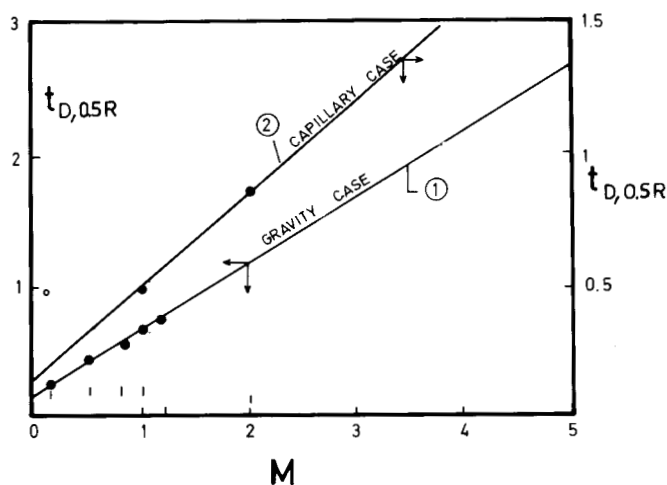


A.2 – Variation recovery ( $Z_D$ ) vs. time ( $t_{D,G}$ ) under predominance of gravity forces (based on Table A.1 data)



A.3. – Variation recovery ( $Z_D$ ) vs. time ( $t_{D,G}$ ) under predominance of gravity forces (semilog scale, Table A.1. data)

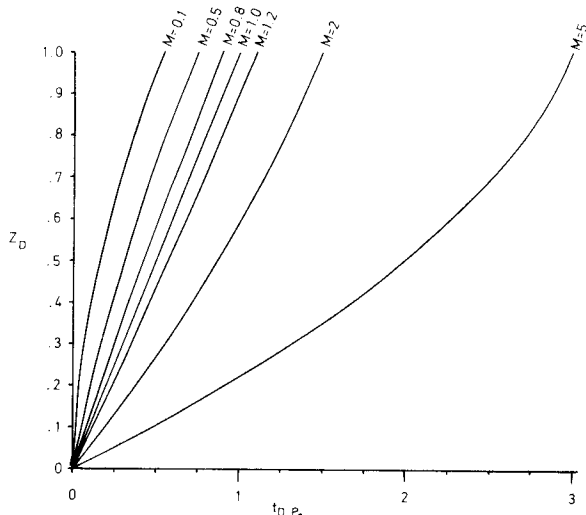
The results in figure A.3 illustrate an S-shaped curve. The role of mobility may also be examined as a function of (dimensionless) time necessary for reaching 50% oil recovery ( $t_{D,0.5R}$ ) and the results obtained for the predominance of gravitational forces show a linear relationship between  $t_{D,0.5R}$  and  $M$ , (figure A.4.).



A.4 – Variation of  $t_{D,0.5R}$  vs.  $M$  under predominant forces : 1) gravitational and 2) capillary.

## 2.2. Case of predominance of capillary pressure

In the case of the predominance of capillary pressure, a similar sensitivity calculation may be developed for the same values of M used in the case of gravitational predominance, but in this case the recovery vs. time will be expressed by equation A.16. The results are given in table A.2 and figure A.5. In the case of capillary pressure predominance the time necessary for 50% recovery ( $t_{D, SR}$ ) indicates the same linear variation with the change in mobility M as illustrated in figure A.4., curve 2.



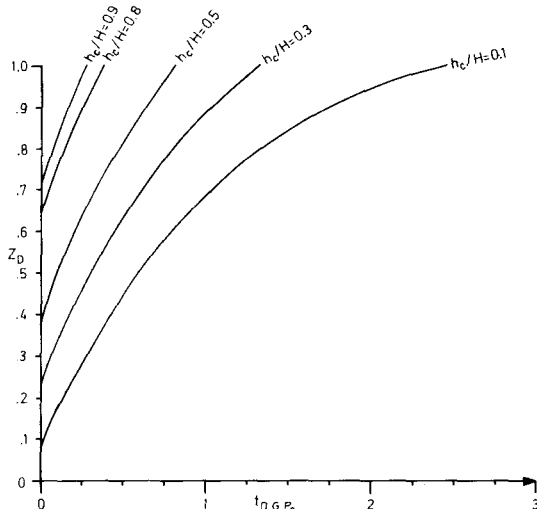
A.5 – Variation recovery ( $Z_D$ ) vs. time ( $t_D$ ) under predominance of capillary forces (Table A.2 data)

Table A.2 Recovery vs. dimensionless time for various mobility M  
(predominance of capillary forces)

$Z_D$	$t_{D, P_c}$ based on Eq. A.16						
	M=0.1	M=0.5	M=0.8	M=1	M=1.2	M=2	M=5
0.0	0	0	0	0	0	0	0
0.1	0.014	0.052	0.081	0.1	0.119	0.195	0.48
0.2	0.038	0.110	0.164	0.2	0.236	0.38	1.92
0.3	0.071	0.173	0.249	0.3	0.351	0.555	1.32
0.4	0.112	0.240	0.336	0.4	0.464	0.720	1.68
0.5	0.163	0.313	0.425	0.5	0.575	0.875	2.00
0.6	0.222	0.390	0.516	0.6	0.684	1.020	2.28
0.7	0.291	0.473	0.609	0.7	0.791	1.155	2.52
0.8	0.368	0.560	0.704	0.8	0.896	1.280	2.72
0.9	0.455	0.653	0.801	0.9	0.999	1.395	2.88
1.0	0.550	0.750	0.900	1.0	1.100	1.50	3.00

### 2.3. Case of capillary & gravity forces

In this specific case the sensitivity calculation refers to the role of  $h_c/H$  for a given mobility. The cases examined in table A.3 refer to mobility  $M = 1.2$  while  $h_c/H = 0.1 ; 0.3 ; 0.5 ; 0.8 ; 0.9$ . The results are shown in figure A.6 where the significant contribution of capillary forces when working together with gravity forces is illustrated.



A.6 - Variation of recovery ( $Z_D$ ) vs. time  $t_{D,G,P_c}$  in case of capillary & gravity driving forces (Table A.3 data)

Table A.3 Recovery vs. dimensionless time for various  $h_c/H$  values and a given mobility  $M = 1.2$

$Z_D$	$t_{D,G,P_c}$ for $M = 1.2$ (Eq. A.22)				
	$h_c/H = 0.1$	$h_c/H = 0.3$	$h_c/H = 0.5$	$h_c/H = 0.8$	$h_c/H = 0.9$
0.00	0.093				
0.10	0.020				
0.20	0.143				
0.30	0.279	0.060			
0.40	0.430	0.179			
0.50	0.601	0.310	0.100		
0.60	0.799	0.455	0.100		
0.70	1.038	0.620	0.341	0.060	
0.80	1.340	0.812	0.481	0.160	0.082
0.90	1.757	1.041	0.640	0.269	0.180
1.00	2.457	1.332	0.824	0.387	0.286

### 3. DIMENSIONAL RELATIONSHIP RECOVERY VS. TIME

In order to transform the results of section 2 in dimensional time, it is necessary to use the following equations:

- In the case of gravity force (equation A.13):

$$t_{D,G} = \frac{Kw \Delta\gamma}{\mu w \Phi_{eff}} \cdot \frac{1}{H} \cdot t$$

- In the case of capillary force (equation A.17)

$$t_{D,Pc} = \frac{Kw \cdot \Delta\gamma \cdot hc}{\mu w \Phi_{eff} H_B^2} \cdot t$$

From basic reservoir data for a block of height  $H_B = 1m$ , the results are as follows :

- Time expressed in terms of gravity force,

$$t_{D,G} = \frac{0.3 \times 10^{-3} \times 0.26 \times 10^{-3}}{0.5 \times 0.12 \times 0.25 \times 100} \cdot t \text{ (sec)}$$

$$t \text{ (days)} = 222,5 t_{DG}$$

- Time expressed in terms of capillary force for  $h_c = 0.5$ ,  $H_B = 100 \text{ cm}$ .

$$t_{D,Pc} = \frac{0.3 \times 10^{-3} \times 0.26 \times 10^{-3} h_c \text{ (cm)}}{0.5 \times 0.12 \times 0.25 \times 10^4} \cdot t \text{ (sec)}$$

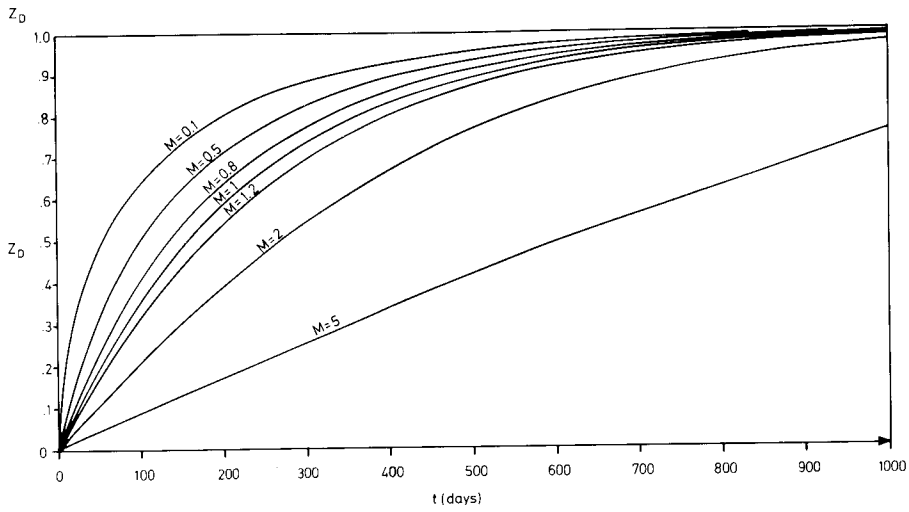
$$t \text{ (days)} = \frac{2.225 \times 10^4}{h_c \text{ (cm)}} \times t_{D,Pc}$$

for capillary height  $h_c = 50 \text{ cm}$

$$t \text{ (days)} = 445 t_{D,Pc}$$

#### 3.1. Predominance of gravity forces

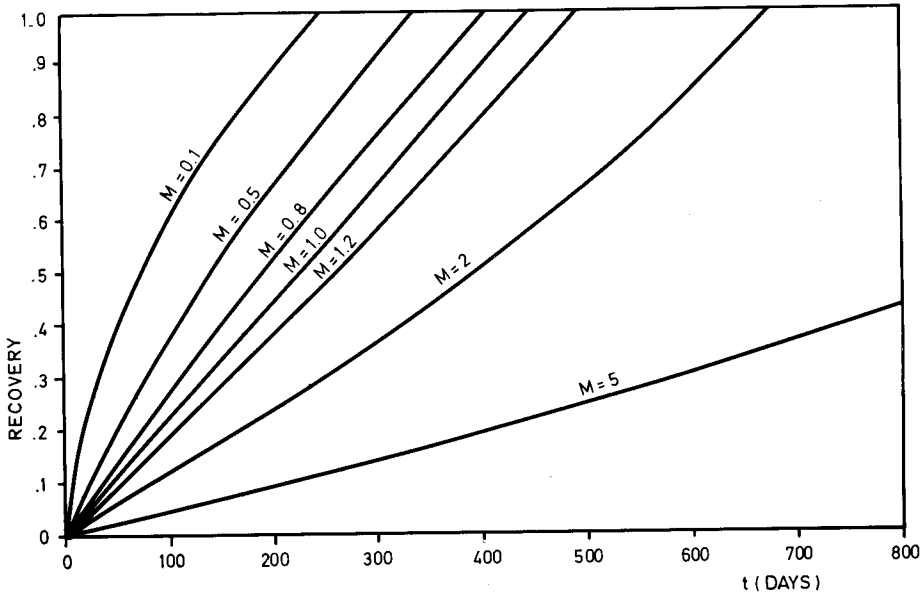
By using the simple relationship of  $t \text{ (days)} = 222.5 t_{D,G}$ , the results of table A.1 will be transformed into the relationship recovery vs. time (days) for various values of M, as shown in figure A.7.



A.7 – Variation of recovery ( $Z_D$ ) vs. dimensional time (days) in case of predominance of gravity driving forces

### 3.2. Predominance of capillary forces

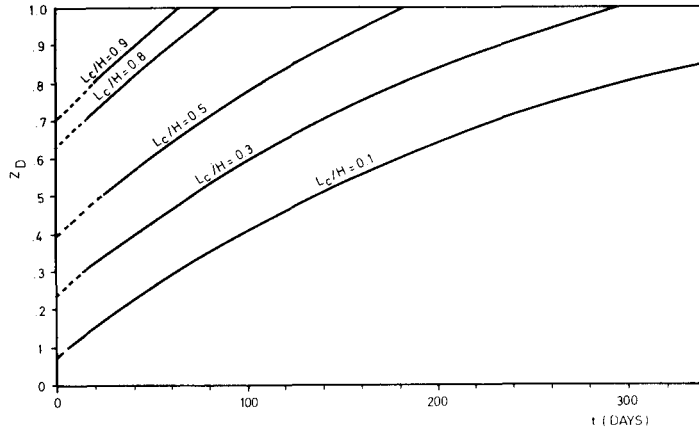
By using the relationship  $t$  (days) =  $445 t_{D,P_c}$  the results of table A.2 will be transformed in a relationship recovery vs. dimensional time, for a ratio  $h_c/H = 0.5$  and various  $M$ . The results are shown in figure A.8.



A.8 – Variation of recovery ( $Z_D$ ) vs. dimensional time (days) in case of predominance of capillary driving forces

### 3.3. Capillary & gravity forces

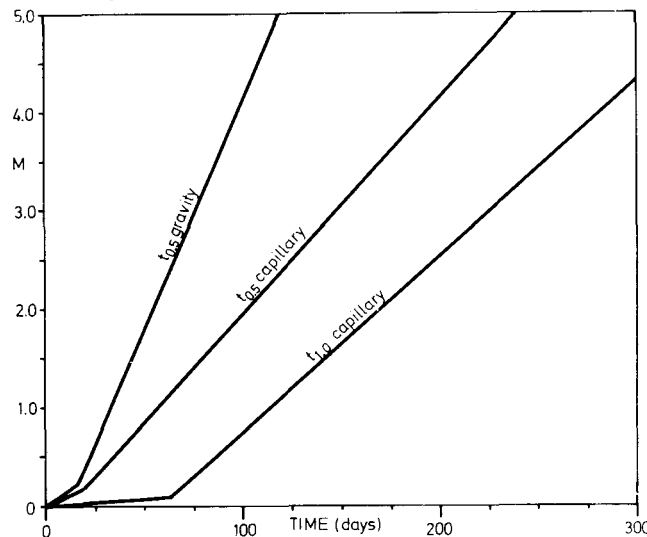
By using the relationship  $t$  (days) = 225.5  $t_{D,G}$  the results of table A.3 will be transformed in a relationship of recovery vs. dimensional time (days) for  $M = 1.2$  and various ratios  $h_c/H$ , as shown in figure A.9



A.9 – Variation of recovery ( $Z_D$ ) vs. dimensional time (days) in case of gravity & capillary driving forces

### 3.4. Comparison of time necessary for a prescribed recovery

From the results obtained in cases 3.2. and 3.3. the necessary time to reach a prescribed recovery ( $R = 0.5$  or  $R = 1$ ), may be evaluated as a relationship  $M$  vs.  $t_{0.5R}$  or  $M$  vs.  $t_{1R}$ . The results have been plotted in Figure A.10 where



A.10 – Variation of  $M$  vs.  $t_{0.5R}$  and  $t_{1R}$  in case of predominance either of gravity or of capillary driving forces

it is observed that for the same  $M$  the time necessary to reach  $R = 0.5$  is less for gravity force predominance than in case of predominance of capillary forces (inversely to Figure A.4) since the capillary forces in the present case are lower ( $h_c = 0.5$  m) than gravity forces ( $h_G = h_{BL} = 1$  m).

#### 4. SINGLE BLOCK RATE BEHAVIOUR

Since the single block rate behaviour may be expressed dimensionlessly by equation A.28, a first evaluation will be developed as a relationship of DF vs. recovery and time.

##### 4.1. DF vs. recovery

As resulted from equation A.26, the decline rate factor is expressed by,

$$DF = \frac{\frac{hc}{H} + 1 - Z_D}{\frac{1}{M} Z_D + 1 - Z_D}$$

where, in the particular case of  $h_c = 0$  (gravitational forces) the DF is reduced to,

$$DF = \frac{1}{\frac{1}{M} \frac{Z_D}{1 - Z_D} + 1}$$

and if  $G = 0$ ,

$$DF = \frac{\frac{hc}{H}}{\frac{1}{M} Z_D + 1 - Z_D}$$

For the two cases  $h_c = 0$  and  $G = 0$  ( $h_c/H = 1$ ), the variation DF vs. recovery  $Z(D)$  as presented in table A.4, demonstrates a different behaviour if  $M > 1$  or if  $M < 1$  as well as if gravity forces or capillary forces are predominant. The results indicate the following :

- If  $M = 1$  under gravity drive conditions, the DF decreases linearly with recovery, while under capillary drive conditions the DF remains constant ( $DF = 1$ ) and independent of recovery.
- Under predominant gravity forces if  $M < 1$  the DF decline is rapid at small RF, while if  $M > 1$  the decline is more significant at a later stage when RF values are large (recovery  $RF = Z_D$ ).

- Under predominance of capillary forces, if  $h_c = H$  the DF increases linearly with recovery for small M and parabolically for large M (when  $M > 1$ ).

The results of table A.4 are shown in figure A.11.

Table A.4 Variation DF vs. recovery in the case of predominant capillary forces and in case of predominant gravity forces

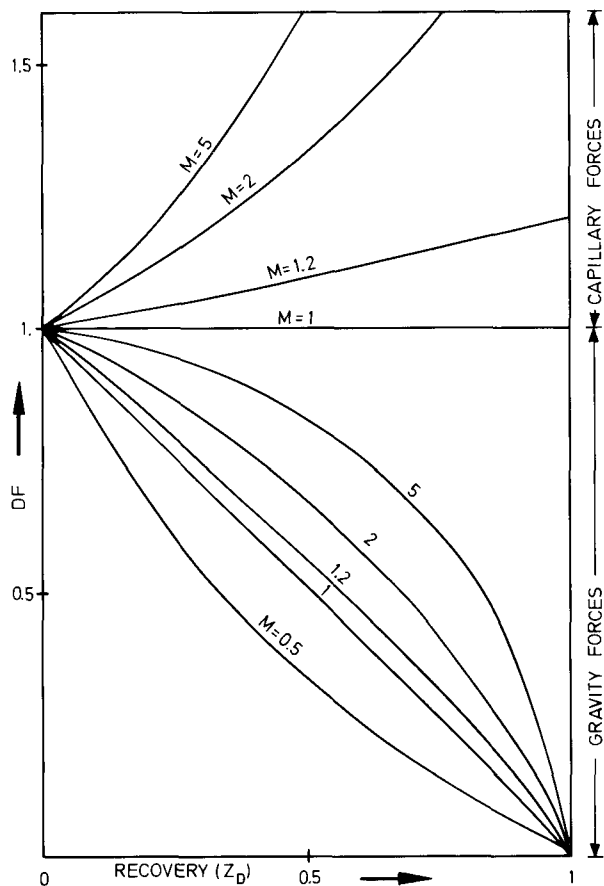
$Z_D$	DF									
	Case $H_c/H = 0$					Case $H_c/H = 1$ and $G = 0$				
	M=0.5	M=1	M=1.2	M=2	M=5	M=0.5	M=1	M=1.2	M=2	M=5
0	1	1	1	1	1	1	1	1	1	1
0.1	0.818	0.9	0.915	0.947	0.978	0.909	1	1.017	1.0	1.087
0.2	0.667	0.8	0.828	0.889	0.952	0.833	1	1.034	1.111	1.190
0.3	0.538	0.7	0.737	0.824	0.921	0.769	1	1.053	1.176	1.316
0.4	0.429	0.6	0.643	0.850	0.882	0.714	1	1.071	1.250	1.471
0.5	0.330	0.5	0.546	0.667	0.833	0.667	1	1.091	1.333	1.667
0.6	0.250	0.4	0.444	0.571	0.769	0.625	1	1.111	1.429	1.923
0.7	0.176	0.3	0.340	0.462	0.682	0.588	1	1.132	1.538	2.273
0.8	0.111	0.2	0.231	0.333	0.556	0.556	1	1.154	1.667	2.778
0.9	0.053	0.1	0.118	0.182	0.357	0.526	1	1.176	1.818	3.571
1.0	~0	~0	~0	~0	~0	0.500	1	1.200	2.000	5.000

#### 4.2. DF vs. dimensional time (case $M = 1.2$ )

Assuming the basic case of  $M = 1.2$ , it is possible to transform the results obtained in columns 4 and 9 of table A.4 in a relationship DF vs. dimensional time (days), based on previous relationship  $Z_D$  vs. time.

##### - Case of predominance of gravity forces

In table A.5 : column 1 represents the recovery ; column 2 the dimensional time (days) obtained from column 6 Table A.1 data and through time relationship  $t$  (days) =  $222.5 t_{D,G}$  ; column 3 is taken directly from column 4 of Table A.4.



A.11 – Variation of DF factor vs. recovery ( $Z_D$ ) in case of predominance of gravity forces  $h_c = 0$ , and predominance of capillary forces ( $G = 0$ ,  $h_c/H = 1$ )

- Case of capillary predominance ( $h_c/H = 1$  ;  $h_c = H = 100$  cm).

In the same table A.5 for the same recovery  $Z_D$ , it will result that: column 4, the dimensional time  $t$  (days) =  $222.5 t_{D,Pc}$  is used for transforming the dimensionless time of column 6, table A.2 ; column 5 gives directly the value DF from column 9 table A.4.

- Discussion of results.

As observed the DF *declines* at 11.8% of initial value in 558 days under predominance of gravity forces, while the value DF *increases* slightly for capillary forces  $h_c/H = 1$  for a period of time of 225 days. The values obtained indicate substantially better results for the case of single capillary

forces drive than single gravity forces dirve, since in the first case the rate does not decline and the *final recovery time required* is shorter.

Table A.5 DF vs. time (days) in case M = 1.2

Z <sub>D</sub>	Predominant Gravity forces		Predominant Capillary forces	
	t (days)	DF	t (days)	DF
0	0	1	0	1
0.1	28.1	0.915	26.7	1.017
0.2	59.1	0.828	53.1	1.034
0.3	93.8	0.737	78.9	1.053
0.4	132.9	0.643	104.5	1.071
0.5	178.4	0.545	130.0	1.091
0.6	233.0	0.444	154.0	1.111
0.7	302.4	0.340	177.0	1.132
0.8	398.0	0.231	201.0	1.154
0.9	558.7	0.118	225.0	1.176
Obtained From	Table A.7	Table A.4	Calculated	Table A.4

#### 4.3. Single block rate vs. time

By using equations A.24 and A.25 and the basic parameters the following will result,

$$Q_{GI} = A_{BL} \frac{K_o}{\mu_o B_o} \Delta \gamma = 10^4 \frac{.7 \times 10^{-3}}{1.4 \times 1.25} \cdot 26 \times 10^{-3} = 1.04 \times 10^{-3} \text{ cm}^3/\text{s}$$

$$= 8.98 \times 10^{-5} (\text{STM}^3/\text{D}) = 5.64 \times 10^{-4} (\text{STB/D})$$

and,

$$Q_{BL} = Q_{GI} \times DF = 8.98 \times 10^{-5} \times DF$$

The relationship rate  $Q_{BL}$  vs. time, based on table A.5, is presented in Table A.6.

#### 4.4. Well rate vs. time

The well rate under prescribed conditions will result from the expression.

$$Q_{well} = n_{BLR} \times n_R \times Q_{BL} = \frac{\text{Area drainage} \times H_{BL}}{V_{BL}} \times n_R \times Q_{BL}$$

where  $n_{BLR}$  and  $n_R$  are respective number of blocks per row and number of rows. This is equivalent to

$$Q_{\text{well}} = \frac{(10^3)^2 \times 1 \text{ (m)}}{1 \text{ (m)}} \times 10 \times Q_{BL} = 10^7 Q_{BL}$$

which will give the variation in time as in Table A.7.

Table A.6 Block rate vs. time

Gravitational case		Capillary imbibition case	
Q <sub>BL</sub> STM <sup>3</sup> /D 10 <sup>-5</sup>	t (days)	Q <sub>BL</sub> STM <sup>3</sup> /D 10 <sup>-5</sup>	t (days)
8.98	0	8.98	0
8.21	27.8	9.13	26.5
7.43	58.5	9.28	52.5
6.61	92.8	9.45	78.1
5.77	131.5	9.61	103.2
4.89	176.5	9.79	127.9
3.98	230.6	9.97	152.2
3.05	299.1	10.16	176.0
2.07	393.6	10.36	199.4
1.05	552.5	10.56	222.3
~	~	~	~

Table A.7 Well rate vs. time

Gravitational case		Capillary imbibition case	
Q <sub>BL</sub> (STM <sup>3</sup> /D)	t (days)	Q <sub>BL</sub> (STM <sup>3</sup> /D)	t (days)
898	0	898	0
821	28.1	913	26.7
743	59.1	928	53.1
661	93.8	945	78.9
577	132.9	961	104.5
489	178.4	979	130.0
398	233.0	997	154.0
305	302.4	1016	177.0
207	398.0	1036	301.0
105	552.7	1056	225.0

Observation: The rate vs. time obtained in table A.7 shows the gravitational and capillary cases when 10 blocks of 1 m are exposed simultaneously to imbibition as a result of instantaneous ( $t = 0$ ) rise of the water table by 10 m.

## APPLICATION B

If the same basic data as have been used in Application A remain valid, it is required to evaluate the well rate, under the conditions specified hereunder:

1. Well rate vs. time in gravitational conditions assuming that  $M = 1.2$ ;  $H_{BL} = .1$  m; 1 m; 10 m; in case of an instantaneous ( $t = 0$ ) rise of the water table by 10 m.
2. Well rate vs. time under the effect of capillary forces, assuming  $h_c/H_{BL} = 5$  or  $h_c = 5$  m, in the case of  $H_{BL} = 1$  m.

Note : The circular drainage area is considered to have a radius  $r_e = 500$  m.

### SOLUTION

#### 1. EVALUATION OF WELL RATE VS. TIME IN GRAVITATIONAL CONDITIONS

##### *1.1. The dimensionless relationship*

By using the basic data from application A, the mobility factor is expressed as,

$$M = \frac{k_{rw}}{k_{ro}} \cdot \frac{\mu_o}{\mu_w} \quad (B1)$$

which gives,

$$M = \frac{0.3}{0.7} \times \frac{1.4}{0.5} = 1.2$$

and therefore, columns 1 and 6 from table A.1 (recopied as columns 1 and 2 in table B.1) will be the dimensionless correlation time-recovery to be used for further calculations.

##### *1.2. The dimensional time*

If it is assumed that for the three block heights the water table rises instantaneously, the time in terms of gravity will give

$$t_{D,G} = \frac{K_w}{\mu_w} \cdot \Delta \gamma \frac{1}{\phi_{eff}} \cdot \frac{1}{H} t(\text{sec}) = \frac{.3 \times 10^{-3}}{0.5} \times .26 \times 10^{-3} \frac{1}{.12 \times 25} \cdot \frac{1}{H(\text{cm})} t(\text{sec})$$

where,

$$\phi_{\text{eff}} = \phi \times \Delta S_w = 0.12 \times 0.25 = .03$$

$$K_w = K_{rw} \times K = 0.3 \times 1 (\text{mD}) = .3 \text{mD}$$

The time vs. height is thus expressed as,

$$t_{D,G} = 5.2 \times 10^{-6} \frac{1}{H} t \text{ (sec)}$$

$$t \text{ (sec)} = 1.92 \times 10^5 \times H \text{ (cm)} \times t_{D,G}$$

$$t \text{ (days)} = 2.225 t_{D,G} \times H \text{ (cm)}$$

which will give,

$$t \text{ (days)} = 2225 \times t_{D,G} \quad \text{for } H = 10 \text{ m}$$

$$t \text{ (days)} = 222.5 \times t_{D,G} \quad \text{for } H = 1 \text{ m}$$

$$t \text{ (days)} = 22.25 \times t_{D,G} \quad \text{for } H = 0.1 \text{ m}$$

The calculated times are presented in table B.1, columns 3, 4 and 5.

### 1.3. The single row well rate

Since the single block rate under gravity is expressed as in table A.6 column 1, this is rewritten in column 6, table B.1. The rate per single row will result as follows if a radial drainage area of 500 m is assumed,

- number of blocks in a row,

$$n_{BL,R} = \frac{\text{Drainage area}}{1 \text{ Block area}} = \frac{\pi \times 500^2 \text{ (m}^2\text{)}}{1 \text{ m}^2} = 7.85 \times 10^5$$

- rate per row,

$$Q_{\text{row}} = Q_{BL} \times n_{BL,R} = Q_{BL} \times 7.85 \times 10^5$$

#### *1.4 Well rate comparison if $H_w = 10 \text{ m}$ at $t \geq 0$*

Based on the number of rows as a function of block height the following will result,

- if  $H_{BL} = 10 \text{ m}$        $n_R = 1 \text{ row}$
- if  $H_{BL} = 1 \text{ m}$        $n_R = 10 \text{ rows}$
- if  $H_{BL} = 0.1 \text{ m}$        $n_R = 100 \text{ rows}$

Consequently, the well rate in all three cases will be expressed by,

$$Q_{well} = n_R \times Q_{row} = n_R \times Q_{BL} \times 7.85 \times 10^5$$

or further

- for  $H_{BL} = 10 \text{ m}$        $Q_{well} = Q_{BL} \times 7.85 \times 10^5$
- for  $H_{BL} = 1 \text{ m}$        $Q_{well} = Q_{BL} \times 7.85 \times 10^6$
- for  $H_{BL} = 0.1 \text{ m}$        $Q_{well} = Q_{BL} \times 7.85 \times 10^7$

and the results are given in columns 7 (for  $H_{BL} = 10 \text{ m}$ ), 8 and 9 (for  $H_{BL} = 1 \text{ m}$  and  $0.1 \text{ m}$ ) of table B.1. Rate vs. time is then presented in figure B.1. The results from table B.1 indicate that if  $H_w = 10 \text{ m}$  at  $t = 0$ , the block height plays an essential role.

$H_{BL} = 10 \text{ m}$  – columns 5 and 7 Table B.1

$H_{BL} = 1 \text{ m}$  – columns 4 and 8 Table B.1

$H_{BL} = 0.1 \text{ m}$  – columns 3 and 9 Table B.1

As observed the existence of small blocks (equivalent to a high fracturing density) implies very high well rates and short recovery time for the same water-table rise. In fact, in the case that blocks of  $0.1 \text{ m}$  height are compared with blocks of  $10 \text{ m}$  height, impressive reduction in time and increase in rates will result in the first case. The time of recovery  $t_{05R}$  is only 17.8 days for  $0.1 \text{ m}$  blocks compared with 1780 days for  $10 \text{ m}$  blocks while the rate is 3830 STMC/D for  $0.1 \text{ m}$  block height compared with only 38.30 STMC/D for blocks of  $10 \text{ m}$  height. Comparison of these results (presented in Table B.1) shows the extraordinary production improvement in the case of a high fracturing density, equivalent to small block heights.

Table B-1 Rate vs. time (predominance of gravity forces)

$Z_D$	$t_{D,G}$		t (days)			$Q_{BL}$	$Q_w$ (STM <sup>3</sup> /D)		
			$H_{BL} = 0.1m$	$H_{BL} = 1m$	$H_{BL} = 10m$		$10^{-5}$ STM <sup>3</sup> /D	$H_{BL} = 10m$	$H_{BL} = 1m$
(1)	2)	(3)	(4)	(5)	(6)	(7)	(8)	(8)	
0	0	0	0	0	8.98	70.4	704	7040	
0.1	0.125	2.78	27.8	278	8.21	64.4	644	7040	
0.2	0.263	5.85	58.5	585	7.43	58.3	583	5830	
0.3	0.417	9.28	92.8	928	6.61	51.8	518	5180	
0.4	0.591	13.15	131.5	1315	5.77	45.2	452	4520	
0.5	0.793	17.65	176.5	1765	4.89	38.3	383	3830	
0.6	1.036	23.06	230.6	2306	3.98	31.2	312	3120	
0.7	1.344	29.91	299.1	2991	3.05	23.9	239	2390	
0.8	1.769	39.36	393.6	3936	2.07	16.2	162	1620	
0.9	2.483	55.25	552.5	5525	1.05	8.24	82.4	824	
1.0	$\infty$								

## 2. EVALUATION OF WELL RATE VS. TIME IN CAPILLARY CONDITIONS

Based on the definition of rate,

$$Q_{well} = n_R \cdot Q_{ROW} = n_R \times n_{BL,R} \times Q_{BL} = n_R \times n_{BL,R} \times Q_{GI} \times DF$$

in the case of capillary forces acting as principal drive, it results that

$$Q_{well} = n_R \times n_{BL,R} \times Q_{GI} \times DF = n_R \times n_{BL,R} \times A_{BL} \times \frac{K_o}{\mu_o B_o} \Delta \gamma \frac{hc/H}{\frac{1}{M} Z_D + 1 - Z_D}$$

In the case that  $H_w = 10$  m (at  $t = 0$ ) and  $H_{BL} = 1$  m, the number of rows, and number of blocks in a row result, respectively, as  $n_{rows} = 10$ ;  $n_{BL,R} = 7.85 \times 10^5$  and thus

$$Q_{well} = 10 \times 7.85 \times 10^5 \times 8.98 \times 10^{-5} \times (h_c/H) / [(1/M) Z_D + 1 - Z_D]$$

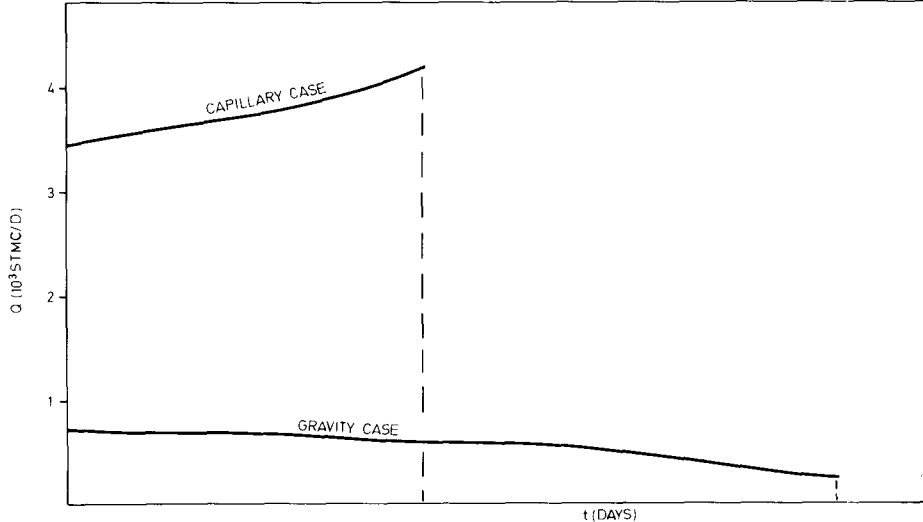
The calculation results shown in table B.2 indicate the following:

- columns 1 and 2, are respectively recovery ( $Z_D$ ) and dimensionless time  $t_{D,P_c}$  for mobility  $M = 1.2$ , both taken respectively from columns 1 and 6 of table A.2.
- column 3 represents the  $Q_{well}$  for  $h_c = 5$  m as a function of  $Z_D$

$$Q_{well} = 3524/(1 - .166 Z_D)$$

- column 4 represents the time based on the equation

$$t_{P_c} (\text{days}) = \frac{222.5 \times 100}{500} \quad t_{D,G} \cong 45 t_{D,P_c}$$



B.1 -- Variation of well rate vs. time under capillary and under gravity drive. (The curve is valid for  $H_{BL} = 1$  m,  $H_w = 10$  m,  $h_c/H = 5$ )

Comparing the two theoretical cases of a block of  $H_{BL} = 1$  m, producing under single gravity driving mechanism (columns 4 and 8 of table B.1) with a high capillary driving force ( $H_c = 5$  m) such as that resulting from columns 3 and 4 of table B.2, it may be concluded that the role of high capillary forces is extremely rate sensitive. As observed in figure B.1, the same volume of oil is produced with high rates in a very short time under the effect of capillary forces while in their absence (only under gravity forces) the rates are small and the time necessary to recover the oil is over ten times as long.

Table B.2 Rate vs. time (predominance of capillary force)

$Z_D$	$t_{D,P_c}$	Q STCM/D	t (days)
(1)	(2)	(3)	(4)
0.0	0	3524	0.00
0.1	0.12	3583	5.40
0.2	0.236	3645	10.60
0.3	0.351	3708	15.80
0.4	0.464	3774	20.80
0.5	0.575	3842	25.80
0.6	0.684	3913	30.78
0.7	0.791	3987	35.60
0.8	0.896	4063	40.3
0.9	0.999	4143	44.9
1.0	1.000	4225	45.0

Note: The results obtained in the present case correspond to very favourable conditions. capillary forces are big ( $h_c/H_{BL} = 5$ ), permeability of matrix is good ( $K = 1$  mD) and block height moderate ( $h_{BL} = 1$  m).

### APPLICATION C

In an undersaturated fractured reservoir, a well having a drainage radius  $r_e = 500$  m was examined in order to evaluate the following :

1. Well productivity index under a simple expansion produt
2. Well daily rate (Q) vs. reservoir pressure decline rate ( $dp/dt$ ) under a simple expansion production mechanism.
3. If  $400\text{STM}^3/\text{D} \cong 2500\text{STB}/\text{D}$  is prescribed as a well rate and the pressure decline rate is  $dp/dt = D_{ps} = 20$  at/year, what is the rate which must be supplied by an additional production mechanism?

4. Assuming there is a gravitational imbibition, what is the water table height  $H_w$  needed in order to assure the conditions required at point 3? The gravitational production conditions are similar to those discussed at point 4 of application A.

Basic data :

Rock properties :  $K_o = 10^{-4}$  mD,  $\phi = 0.12$ ,  $S_{wi} = 0.27$ ,  $C_p = 4.5 \times 10^{-6}$  l/psi,  
 $\phi_{eff} = 0.12 \times 0.73 = 0.087$ ;  $K_{rw} = 0.7$ .

Fluid properties :  $B_o = 1.25$ ;  $\mu_o = 1.4$  cP.;  $\gamma_o = 0.82 K_g/dm^3$ ;  $\gamma_w = 1.08 K_g/dm^3$   
 $C_o = 80 \times 10^{-6}$  l/psi;  $C_w = 3 \times 10^{-6}$  l/psi;  $P_i = 260$  at;  
 $P_B = 180$  at.

Other data : gross pay  $H = 100$  m; block shape and height correspond to a cube of 1 m.

## SOLUTION

### 1. WELL PRODUCTIVITY INDEX

#### 1.1. Theoretical approach

The rate of a single matrix block in the case of a simple expansion is the result of the rates through each of the six surfaces of the cube. The pressure drop  $\Delta P$  between the center of each block (figure C.1) and fracture is developed along an interval  $a/2$ . In this case,

$$Q_{1, \text{BLOCK}} = 6 \frac{k_o}{\mu_o B_o} a^2 \frac{\Delta P}{\Delta L} = 6 \frac{k_o}{\mu_o B_o} a^2 \frac{\Delta P}{a/2} = 12 \frac{k_o}{\mu_o B_o} \times \frac{\Delta P}{1/a} \quad (\text{C.1})$$

The productivity index of a single block is then,

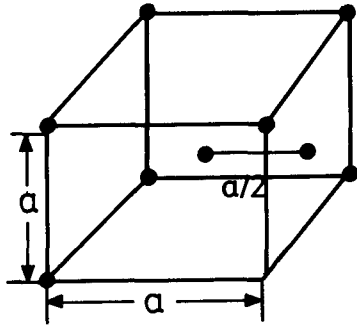
$$PI_{1, \text{BLOCK}} = 12 \frac{k_o}{\mu_o B_o} \frac{1}{1/a} \quad (\text{C.2})$$

The productivity index of the well results from the number  $n$  of blocks. Inside the reservoir where  $H_{reservoir}$  was considered uniform

$$n_{BL} = V_{BULK}/V_{BLOCK} = \frac{\pi r_e^2 H_R}{a^3} \quad (\text{C.3})$$

therefore,

$$PI_{WELL} = 12 \frac{K_0}{\mu_0 B_0 a} \times \frac{\pi r_e^2 H_R}{a^3} \quad (C.4)$$



C.1 – Matrix bulk volume idealized as cube.

### 1.2. Numerical evaluation

The well productivity index through equation C.4 gives,

$$PI_{well} = 12 \frac{0.001 \times 10^{-4}}{1.4 \times 1.25/100} \times \frac{\pi (500)^2 \times 100}{(1)} = 5.38 \times 10^3 \text{ cm}^3/\text{sec/at.}$$

$$PI_{well} = 4.65 \times 10^2 \text{ STM}^3/\text{D/at} = 1.98 \times 10^2 \text{ STB/D/psi}$$

## 2. WELL RATE

The variations of the well rate as the effect of various pressure decline rates between 1 at/year and 80 at/year are given in figure C.2. Considering the case  $\Delta P/\Delta t = 1$  at/year as the yearly pressure decline rate,

$$\Delta P_{daily} = \Delta P_{yearly}/365 = 2.73 \times 10^{-3} \times \Delta P_{yearly} \quad (C.5)$$

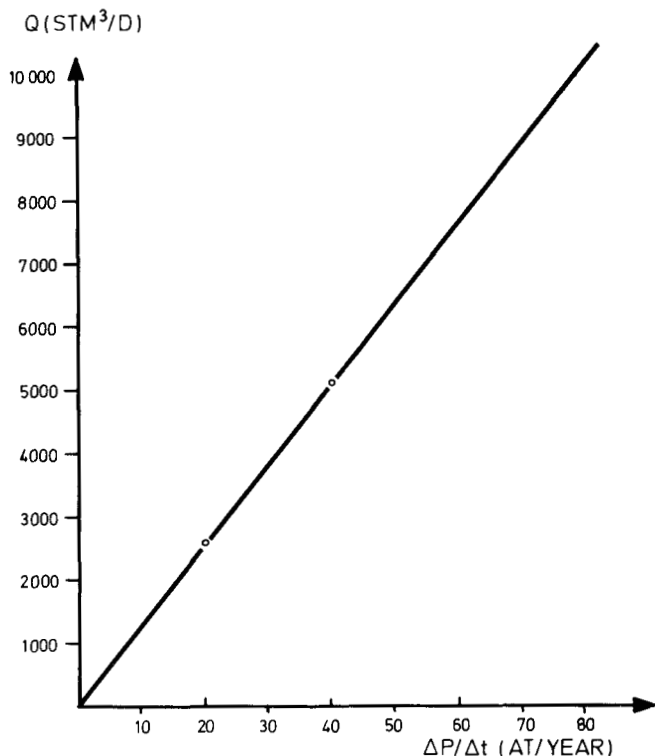
the daily rate will become,

$$Q_{\text{well}} = PI_{\text{well}} \times \Delta P = 4.65 \times 10^2 (\text{STM}^3/\text{D/at}) \times 2.73 \times 10^{-3} (\text{at/D})$$

$$Q_{\text{well}} = 127 (\text{STM}^3/\text{D})$$

As observed from a simple expansion mechanism, the well rate for  $K = 10^{-4}$  mD is very high even for a relatively small pressure decline rate.

In figure C.2 a straight line illustrates the relationship  $Q$  ( $\text{STM}^3/\text{D}$ ) vs.  $\Delta P/\Delta t$  (at/year). As observed for  $\Delta P/\Delta t = 10$  (at/year) and  $\Delta P/\Delta t = 20$  (at/year), rates of  $Q = 1270 \text{ STM}^3/\text{D} \cong 8000 \text{ STB/D}$  and  $Q = 2500 \text{ STM}^3/\text{D} \cong 16,000 \text{ STB/D}$  will result respectively.



C.2 – Relationship well production rate ( $Q$ ) vs. reservoir pressure decline rate ( $\Delta P/\Delta t$ ) in case of simple expansion production mechanism.

### 3. WELL RATE BASED ON EXPANSION PRODUCTION MECHANISM MATERIAL BALANCE

#### 3.1. Theoretical approach

The simple expansion drive mechanism, material balance may be written as

$$N_p B_0 = C_{oe} \times N \times B_{oi} \times (P_{SI} - P_S) \quad (C.6)$$

which further may be expressed in a differential form, as production per unit of pressure decline,

$$\frac{\Delta N_p}{P_{SI} - P_S} = \frac{\Delta N_p}{\Delta P_s} = C_{oe} \times N \times \frac{B_{oi}}{B_o} \quad (C.7)$$

The reservoir production capacity expressed as a rate will depend on reservoir static pressure decline  $D_{ps} = \Delta P_s / \Delta t$ , and therefore, in simple expansion conditions the well rate will be,

$$Q_{w, SE} = \frac{\Delta N_p}{\Delta P_s} \times \frac{\Delta P_s}{\Delta t} = N \frac{B_{oi}}{B_o} \times C_{oe} \times D_{ps} \quad (C.8)$$

Since the oil in place for a well of radius  $r_e$  and gross pay  $H$  is given by,

$$N = \pi r_e^2 H \Phi (1 - S_{wi}) / B_{oi} = \pi r_e^2 H \Phi_{eff} / B_{oi} \quad (C.9)$$

the rate will result from equation C.8 as,

$$Q_{w, SE} = \frac{B_{oi}}{B_o} \times C_{oe} \times \frac{\pi r_e^2 H \Phi_{eff}}{B_{oi}} \times D_{ps} = \pi r_e^2 H \Phi_{eff} \times C_{oe} \times D_{ps} / B_o \quad (C.10)$$

where,

$$C_{oe} = C_o + \frac{C_\omega S_\omega + C_p}{1 - S_{wi}} \quad (C.11)$$

### 3.2. Numerical evaluation

The compressibility  $C_{oe}$  will result from the following equation,

$$C_{oe} = 80 \times 10^{-6} + \frac{3 \times 10^{-6} \times 0.27 + 4.5 \times 10^{-6}}{0.73} \cong 8.72 \times 10^{-5} \left( \frac{1}{\text{psi}} \right) \cong 1.28 \times 10^{-3} \left( \frac{1}{\text{at}} \right)$$

The well rate  $Q_{w,SE}$  (equation C.10) for  $D_{ps} = 20$  at/year, when all other basic data are introduced, becomes,

$$\begin{aligned} Q_{w,SE} &= 3.14 \times 500^2 \times 100 \times 0.087 \times 1.28 \times 10^{-3} \times 20/365/1.25 \\ &= 33 \text{ STM}^3/\text{D} = 207 \text{ STB/D} \end{aligned}$$

*OBSERVATION:* As may be observed, for a pressure decline rate  $D_{ps} = 20$  (at year) = 0.0548 at/days, the resulting rate of 425  $\text{STM}^3/\text{D}$  is substantially lower than the prescribed rate of 400  $\text{STM}^3/\text{D}$ . The prescribed rate  $Q = 400 \text{ STM}^3/\text{D}$  may be reached if another production mechanism is associated to the simple expansion drive.

## 4. COMBINED DRIVE MECHANISM : SIMPLE EXPANSION & IMBIBITION

### 4.1. Theoretical approach

If production is due to simple expansion and imbibition displacement, the well rate is expressed by,

$$Q_w = Q_{w,SE} + Q_{w,IMB} \quad (\text{C.12})$$

which is the result of,

$$Q_{w,SE} = \pi r_e^2 H \Phi(1 - S_{wi}) C_{oe} \times D_{ps}/B_0 \quad (\text{C.13})$$

and,

$$Q_{w,IMB} = n_R \times n_{BL,R} \times Q_{GI} \times DF = \frac{H_w}{H_{BL}} \frac{\pi r_e^2}{a^2} a^2 \frac{k_o}{\mu_0 B_0} \Delta \gamma \times DF \quad (\text{C.14})$$

Since the total number of blocks in the case of a parallelopiped-shaped block is given by

$$n_{\text{Blocks}} = n_R \times n_{BL,R} = \frac{\pi r_e^2 H_w}{a^2 H_{BL}}$$

the equation C.12 becomes

$$Q_w = \frac{\pi r_e^2}{B_0} \left[ H \Phi (1 - S_{wi}) C_{oe} \times D_{ps} + \frac{H_w}{H_{BL}} \cdot \frac{K_o}{\mu_0} \Delta \gamma \times DF \right] \quad (C.15)$$

from which the level of water expressed as a multiple of block height will result

$$H_w/H_{BL} = \left[ Q_w B_0 / \pi r_e^2 \right] - H \Phi (1 - S_{wi}) C_{oe} D_{ps} / (K_o / \mu_0) \Delta \gamma DF \quad (C.16)$$

The value  $H_w$  will indicate the height of rise of water table necessary to assure a prescribed rate for a given  $D_{ps}$

#### 4.2. Numerical evaluation of water table rise $H_w$

Introducing the values indicated in the basic data, the result is as follows :

$$\begin{aligned} H_w/H_{BL} &= \left[ \frac{400 \times 1.25}{3.14 \times 500^2} - 100 \times 0.087 \times 1.28 \times 10^{-3} \times 20/365 \right] \times \\ &1.4/0.7 \times 10^{-3} \times 0.26 \times 10^{-3} \times \frac{86400}{100} \quad DF \end{aligned}$$

$$H_w/H_{BL} = 0.214/DF$$

Note: As observed, the velocity  $\frac{K_o}{\mu_0} \Delta \gamma$  was transformed in m/Day through  $86400/100$  (sec/cm).

#### 4.3. Water table advancement rate

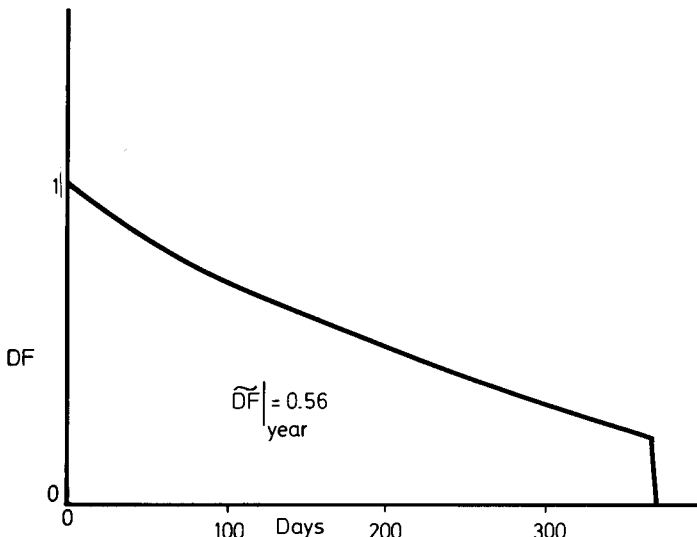
In order to evaluate the water table advancement rate during the first year, the following simplified procedure may be used :

- Since the results of Application A remain valid in the present case, columns 2 and 3 of Table A.5 are used for a diagram which provides an average  $\tilde{DF}_{\text{year}}$  for 365 days (figure C.3.).

$$(\tilde{DF})_{\text{year}} \cong 0.56$$

The average water advancement rate will result in the first year as

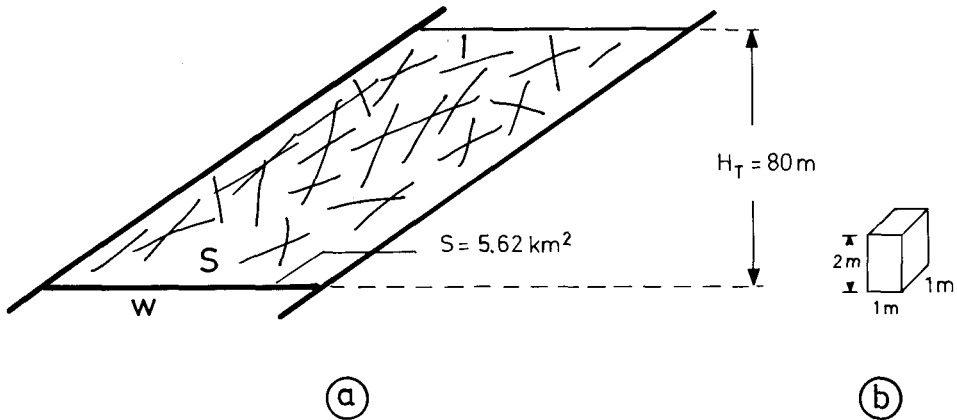
$$(H_w)_{\text{year}} = H_{BL} \times 355 \times 0.214 \cong 54 \text{ m/year (for } H_{BL} = 1 \text{ m.)}$$



C.3 – Average DF value obtained from DF vs. Time (based on table A.5 columns 2.3)

#### APPLICATION D

In an undersaturated reservoir, production is governed by *simple expansion* and *imbibition drive mechanism*. The reservoir is a fractured limestone (figure D.1a) where the blocks have been idealized to parallelepiped shape (figure D.1b).



D.1 – Schematization of a fractured reservoir:a) Vertical cross section b) idealized matrix block

The reservoir has produced for two years and the production data are given below together with other reservoir characteristics. The following is required:

1. Evaluate the reservoir block height by matching the calculated reservoir pressure with recorded reservoir pressure vs. time. Blocks have base area of  $1 \text{ m}^2$  and height  $H_{BL}$  (parallelepiped).
2. Predict reservoir behaviour for the next three years when the reservoir rate is reduced to 1,500,000 STM<sup>3</sup>/year.

*Basic data :*

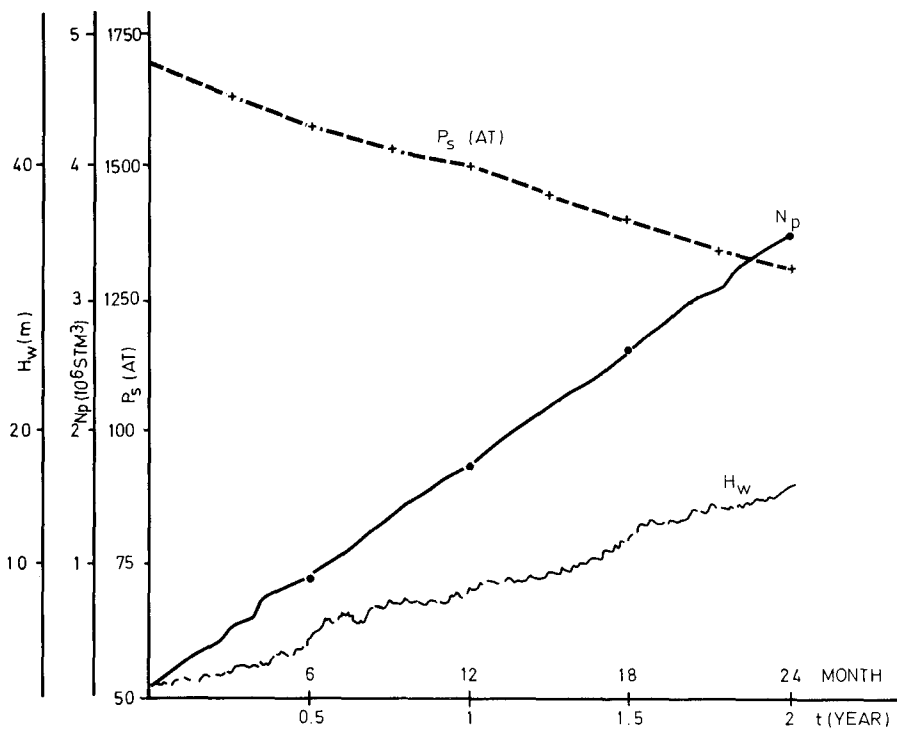
- Surface of water oil contact,  $S = 5.62 \times 10^6 (\text{m}^2)$ .
- Reservoir height,  $H_T = 80 \text{ m}$ .
- Physical properties of rock :
  - Porosity  $\phi = 0.145$ , interstitial water saturation  $S_{wi} = 0.32$  ; residual oil saturation  $S_{or} = 0.26$  ; relative oil permeability  $K_{ro} = 0.7$
- Properties of fluid :
  - Initial reservoir pressure Psi = 268 at ; bubble point pressure 160 at ; original volume factor  $B_o = 1.34$  ; total compressibility for oil  $C_{oe} = 1.48 \times 10^{-9} (1/\text{at})$ .
- Number of wells in production 10..
- Rate produced, water-oil contact recorded in fractures, and reservoir pressure vs. time are given in the table D.1 and in figure D.2.
- From the laboratory experiment, a recovery-time relationship as shown in figure E.3 resulted for an average core of length 8 cm,  $K_{avg} = 1 \text{ mD}$  and  $\phi_{avg} = 0.145$ .

In the experiment, the air was displaced by water having a viscosity of  $\mu_w = 1.05 \text{ cP}$  and interfacial tension  $\sigma_{w-air} = 70 \text{ dyne/cm}$ .

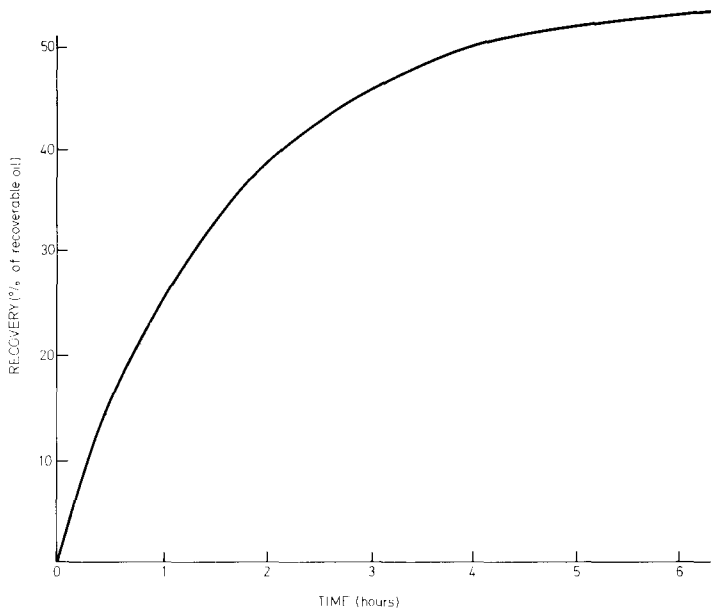
Table D.1

Recorded reservoir data

TIME (months)	$\Delta P$ (at)	$P_s$ (at)	$N_p$ ( $STM^3$ )	$H_w$ (m)
0	0	268	0	0
6	9.00	259	871000	4
12	16.00	252	1442000	8
18	26.00	242	2605000	12
24	33.00	235	3492000	16



D.2 – Variation of basic reservoir parameters,  $H_w$ ,  $N_p$ ,  $P$  versus time for the first 2 years of production history.



D.3 – Recovery vs. time obtained from lab experiments (Basic average values :  $H_{BL} = 8 \text{ cm}$ ,  $K = 1 \text{ mD}$ ,  $\phi = 14,5 \%$ ,  $\mu_w = 1.05 \text{ C.P}$ ,  $\sigma_{w-air} = 70 \text{ dyne/cm}$ )

## SOLUTION

### 1. EVALUATION OF BLOCK HEIGHT THROUGH RESERVOIR PRESSURE MATCHING

The matching of calculated past history and recorded data is developed in relation with reservoir pressure by continuously adjusting the average block height of the matrix. A number of attempts for blocks having a height between 0.3 m to 3 m has been performed, and the best results have been obtained for an average block height  $H_{BL} \approx 2 \text{ m}$ . The results obtained for this case are presented hereunder.

#### 1.1. Scaling lab data for reservoir block of 2 m height

Based on experimental data which are given in figure D.3 and on an assumed "ideal matrix block", the scaling ratio will result from the Mattax equation 9.71 discussed in chap. 9. The experiment was carried out on a reservoir sample.

$$t_M = t_R \left[ \frac{\sigma \cos \theta}{\mu H^2} \sqrt{\frac{k}{\phi}} \right] R \quad / \quad \left[ \frac{\sigma \cos \theta}{\mu H^2} \sqrt{\frac{k}{\phi}} \right] M$$

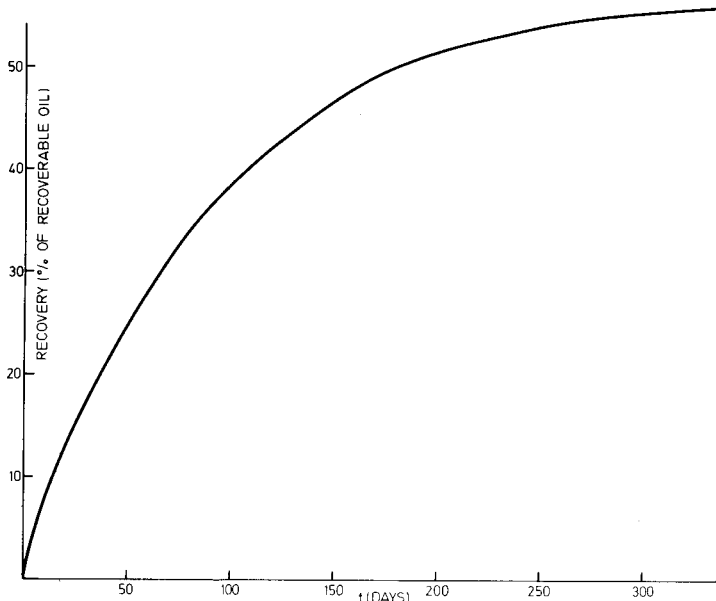
$$t_M = t_R \left[ \frac{32 \times \cos 28^\circ}{0.78 \times 200^2} \right] R \quad / \quad \left[ \frac{70 \times \cos 0^\circ}{1.05 \times 8^2} \right] = t_R \times 8.69 \times 10^{-4}$$

or

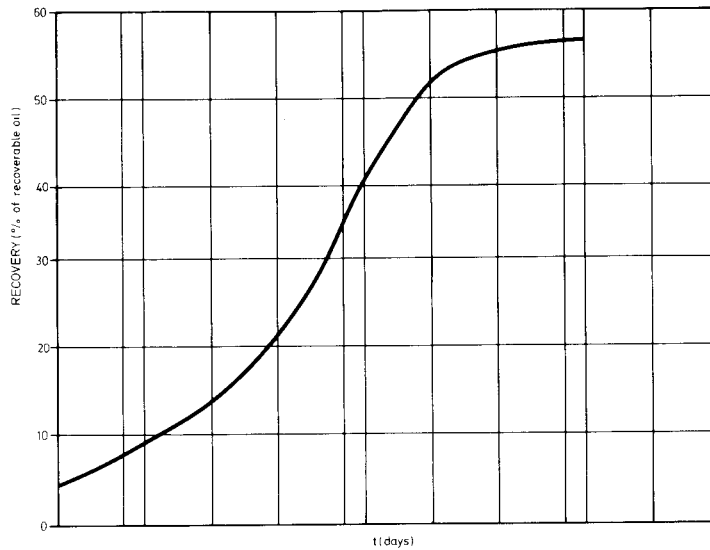
$$t_R \text{ (hours)} = 1150 t_M \text{ (hours)}$$

$$t_R \text{ (days)} = 47.9 t_M \text{ (hours)}$$

For 2 m block height a recovery time curve will result as shown in figure D.4 on a conventional scale and in figure D.5 on a semi-log scale.



D.4 – Recovery vs. time scaled for a block of height  $H_{BL} = 2$  m, for the case of water displacing oil; ( $\sigma_{w-oil} = 32$  dyne/cm),  $\theta = 28^\circ$ , water viscosity  $\mu_w = 0.78$  C.P)



D.5 – Recovery vs. time of block of 2 m height on a semilog scale

### 1.2. Recoverable oil per row of blocks by water imbibition

The recoverable volume of oil in a row is expressed by,

$$S \times H \times \Phi (1 - S_{wi} - S_{or}) / Bo$$

or,

$$5.62 \times 10^6 \times 2 \times 0.145 (1 - 0.32 - 0.26) / 1.34 = 5.11 \times 10^5 \text{ STM}^3$$

where  $S = 5.62 \times 10^6 \text{ m}^2$  represents the water-oil contact surface.

If the matrix blocks are 2 m tall and the water table advancement is 8m/year, the recovery vs. time by imbibition may be calculated for each interval of time per row invaded, by using the diagram in figure D.5.

The results are presented in table D.2 for each 3 months for two years. For each row of blocks (having 2 m height) a recovery will result which is presented as cumulative total recovery.

The cumulative volume of oil produced by imbibition is the result of recovery (% single row recovery) multiplied by  $5.11 \times 10^5 \text{ STM}^3$  (volume of recoverable oil in a single row of blocks). From the table D.2 it may be observed that imbibition on all rows of blocks indicates an average rate of  $10^6 \text{ STM}^3 / \text{year}$ .

Table D.2 Calculated production by imbibition for a fractured reservoir with 2 m block height

TIME (months)	Cumulative recovery per row (%)								Total rows recovery (% of single row)	$N_{p,imb}$ (STM <sup>3</sup> ) Volume produced by imbibition
	1	2	3	4	5	6	7	8		
3	38	—	—	—	—	—	—	—	38	$0.194 \times 10^6$
6	50	38	—	—	—	—	—	—	88	$0.449 \times 10^6$
9	54	50	38	—	—	—	—	—	142	$0.725 \times 10^6$
12	54	54	50	38	—	—	—	—	196	$1.000 \times 10^6$
15	54	54	54	50	38	—	—	—	250	$1.270 \times 10^6$
18	54	54	54	54	50	38	—	—	304	$1.550 \times 10^6$
21	54	54	54	54	54	50	38	—	358	$1.820 \times 10^6$
24	54	54	54	54	54	54	50	38	412	$2.100 \times 10^6$

### 1.3. Matching through material balance

Based on the equivalence between recorded oil production  $N_p$  and oil resulting from the two driving mechanisms, simple expansion ( $N_{p,SE}$ ) and imbibition ( $N_{p,imb}$ ), the following material balance may be written,

$$N_p = N_{p,SE} + N_{p,imb}$$

$$N_{p,SE} = N_p - N_{p,imb} = V_{BULK} \phi (1 - S_{wi}) \times C_{oe} \Delta P \frac{1}{B_o}$$

The bulk volume being expressed as the volume

$$V_{BULK} = \text{Area} (H_{res} - H_w)$$

the reservoir pressure drop results as

$$\Delta P = \frac{(N_p - N_{p,imb}) B_o}{V_{BULK} \phi (1 - S_{wi}) C_{oe}} = \frac{(N_p - N_{p,imb}) \times 1.34}{5.62 \times 10^6 (80 - H_w) \times 0.145 \times (1 - 0.32) 1.48 \times 10^{-3}}$$

$$\Delta P = \frac{N_p - N_{p,imb}}{80 - H_w} \times 1.63 \times 10^{-3} = \frac{N_{p,SE}}{80 - H_w} \times 1.63 \times 10^{-3}$$

Since  $N_p$  and  $H_w$  are recorded (columns 4 and 5 Table D.1) and  $N_{p,imb}$  was calculated (Table 2), it is easy to evaluate the reservoir pressure drop  $\Delta P$ , and further the static reservoir pressure  $P$  (column 7, Table D.3).

Table D.3 Reservoir pressure matching through past history data

Time (month)	$N_p$ $STM^3$ )	$H_w$ (m)	$N_{p, imb}$ $STM^3$ )	$N_{p,SE}$ $STM^3$ )	$\Delta P$ (at)	Calculated $P_s$ (at)	Recorded $P_s$ (at)
0	0	0	0	0		268	2.68
6	871000	4	449000	422000	9.06	258.95	2.59
12	1442000	8	1000000	742000	16.80	251.12	2.52
18	2605000	12	1550000	1055000	25.28	242.72	2.42
24	3492000	16	2100000	1392000	35.45	232.54	2.34

The results (columns 7 and 8, Table D.3) indicate satisfactory agreement between calculated and recorded pressure data.

## 2. PREDICTION OF FUTURE RESERVOIR BEHAVIOUR

If the water table advancement remains the same and the production level is reduced but constant, the pressure decline will result as indicated in the table D.4.

Based on the prescribed yearly production of 1,500,000  $STM^3$ , for a six month step production forecast the rate 750,000  $STM^3/0.5$  year (column 2, Table D.4) will result.

The pressure drop will be calculated with the same equation

$$\Delta P = \frac{N_{p,SE}}{80 - H_w} \times 1.63 \times 10^{-3}$$

In column 3 the cumulative production results from the cumulative of column 2.

In columns 4 and 5 the water table rise and the remaining simple expansion pay zone are given.

In column 6 the constant rise of water table will indicate the cumulative oil produced by imbibition.

Table D.4 Forecast of reservoir behaviour

TIME (month)	$\Delta N_p / \Delta t$ STM <sup>3</sup> / 0,5 year	$N_p$ STM <sup>3</sup>	$H_w$ (m)	$80 - H_w$ (m)	$N_{p,imb}$ STM <sup>3</sup>	$N_{p,SE}$ STM <sup>3</sup>	$\Delta P$ at	$P_s$ at
(1)	(2)	(3)	(4)	(5)	(6)	(7)	(8)	(9)
24	750000	3492000	16	64	210000	1392000	35.45	232.54
30	750000	4242000	20	60	265000	1592000	43.24	224.76
36	750000	4992000	24	56	320000	1792000	52.11	215.90
42	750000	5742000	28	52	3750000	1992000	62.44	205.55
48	750000	6492000	32	48	4300000	2192000	74.44	193.56
54	750000	7242000	36	44	4850000	2392000	88.61	179.38
60	750000	7992000	40	40	5400000	2592000	105.6	162.40

Column 7 shows the oil produced ( $N_{p,SE}$ ) through the simple expansion drive mechanism as a difference between column 3 and 6. In column 8 the reservoir pressure drop ( $\Delta P$ ) is given and in column 9 the reservoir static pressure is obtained as difference between  $P_i$  and  $\Delta P$ .

$$P_s = P_{si} - \Delta P$$

#### APPLICATION E

In a fractured reservoir the production was continuously recorded for 11 years, together with the variation of gas-oil contact and water-oil contact.

- Initial water, oil and gas zones are as in Fig. E.1.
- The reservoir basic data are :

$$\phi = 0.162$$

$$\gamma_o = 0.83 \times 10^{-3} \text{ kg/cm}^2/\text{cm}$$

$$S_{wi} = 0.38$$

$$\gamma_w = 1.03 \times 10^{-3} \text{ kg/cm}^2/\text{cm}$$

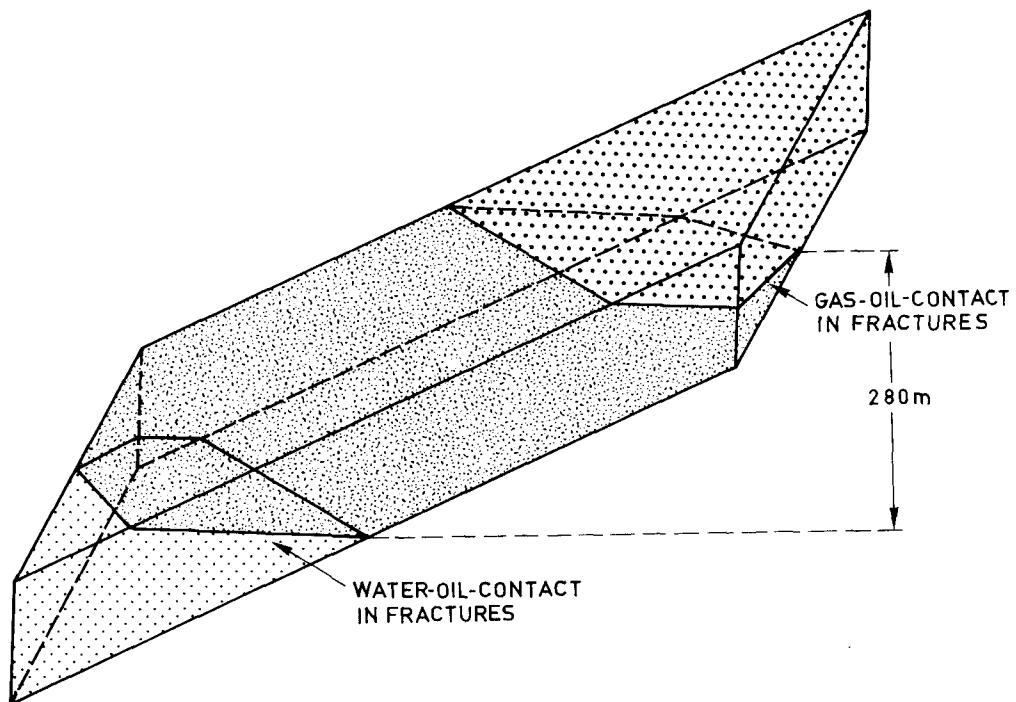
$$B_o = 1.21$$

$$H = 280 \text{ m (total pay)}$$

$$P_B = \text{constant with depth } V_B = 1260 \times 10^6 \text{ (initial bulk of oil zone)}$$

$$P_{oi} = 260 \text{ at}$$

$$V_B \text{ vs. depth (fig. E.2)}$$

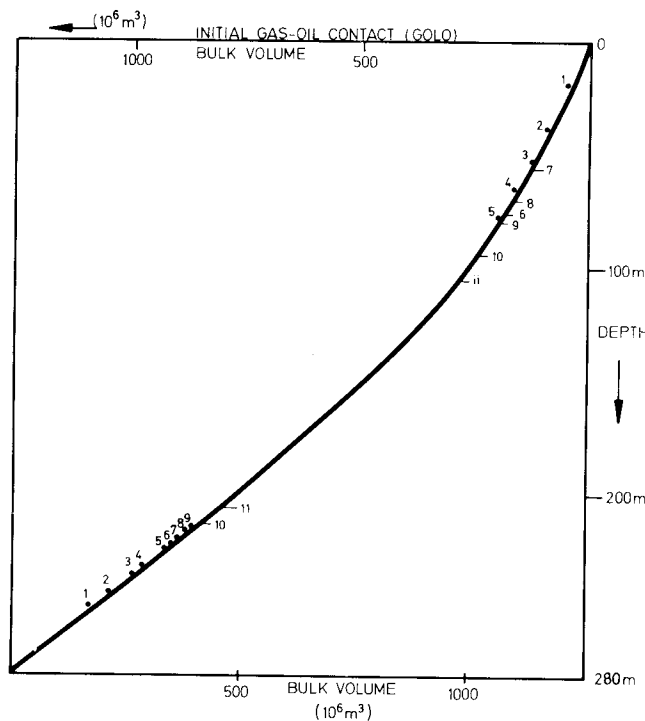


E.1 – Initial distribution of fluid in reservoir

In a second stage the expansion of gas-cap and aquifer (as drawn in Fig. E.3) during reservoir depletion, determine the presence of the gas-invaded, gassing, expansion and water zones.

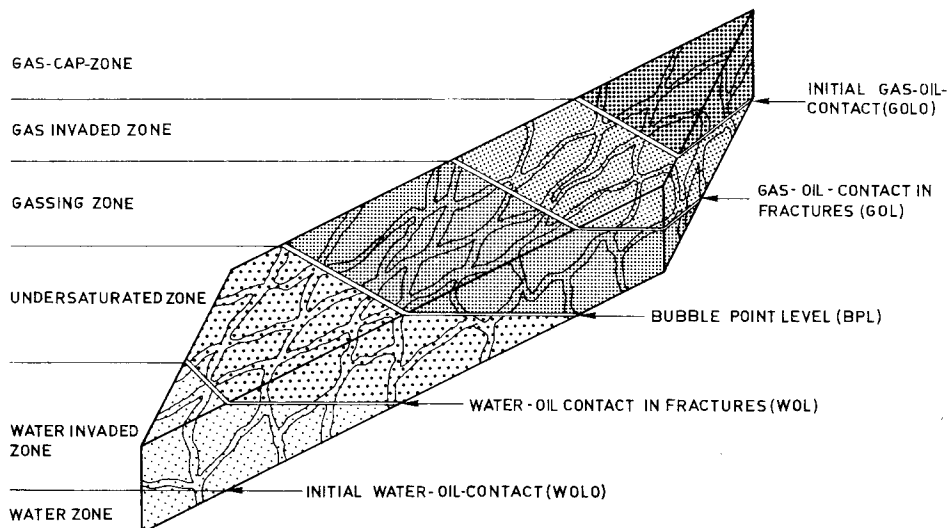
The production developed over 11 years was followed continuously and the recorded data are given in Table E.1. The data recorded are time (columns 1, 2), the cumulative production  $N_p$  (column 3), the average field rate  $Q_{avg}$  (column 4), the gas-oil contact and water-oil contact  $H_G$  and  $H_w$  (columns 5,6).

**OBSERVATION :** both heights of water table and gas-oil contacts measured in the observation wells, are referred to GOLO (original gas-oil contact). Therefore the depth of gas-oil contact is equal to  $H_G$  or to  $1-H_w$ .



E.2 – Rock bulk volume vs. depth

(referred to gas-oil contact)



E.3 – Reservoir zonation after the starting of reservoir production

Determine:

- 1) Original oil volumes in the zones invaded by water and gas.
- 2) Volume of oil produced from gassing and expansion zones.
- 3) Evaluation of oil recovery of entire reservoir.
- 4) Evaluation of recoveries in the invaded zones.

## SOLUTION

### 1. CALCULATION OF ORIGINAL OIL VOLUMES IN THE INVADED ZONES

Based on measurements of gas-oil and water-oil contacts in observation wells (columns 5 and 6, Table E.1), it is possible to evaluate the respective invaded bulk volumes  $VB_{GIZ}$ ,  $VB_{WIZ}$  from diagram figure E.2.

#### *1.1. Calculation of $V_{GIZ}$*

In the gas invaded zone, the gas-oil contact as is observed in column 5 table E.1 shows downward and upward variations during the years 6, 7, 8. The values  $H_G$  indicate the actual level of the gas-oil level (GOL) referred to the original gas-oil level (GOLO).

#### Example

At the end of the 3rd year of production the gas-oil contact is at  $H_G = 51$  m. From figure E.2 the bulk volume of the gas invaded zone is

$$VB_{GIZ} = 127.8 \times 10^6 \text{ m}^3$$

and the original oil volume in this bulk is

$$V_{GIZ} = VB_{GIZ} \times \Phi (1 - Swi) = 127.8 \times 10^6 \times 0.162 \times (1 - 0.38)$$

$$V_{GIZ} = 12.84 \times 10^6 \text{ m}^3$$

The results obtained for each time step are given in column 7 of Table E.1.

#### *1.2. Calculation of $V_{WIZ}$*

A similar procedure was followed for the case of the water invaded zone.

### Example

At the end of the 3 rd year  $H_w = 42$  m indicates the upward distance of the water-oil level (WOL) from the original water-oil level (WOLO).

From figure E.2, the bulk volume of the water invaded zone is given by

$$VB_{WIZ} = 262,5 \times 10^6 \text{ m}^3$$

and further the volume of oil contained in this bulk is

$$V_{WIZ} = 262.5 \times 10^6 \times 0.162 \times (1 - 0.38) = 26.37 \times 10^6 \text{ m}^3$$

The results obtained for each time step are given in column 8 of Table E.1.

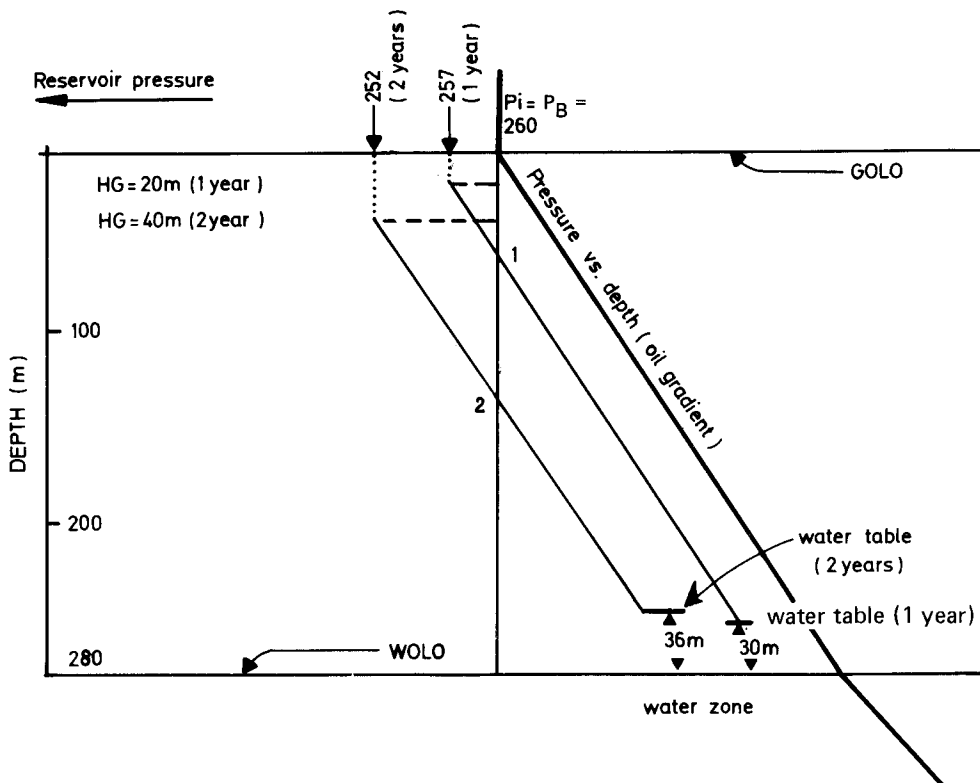
## 2. VOLUME OF OIL PRODUCED FROM GASSING AND EXPANSION ZONES

### 2.1. *Delimitation of gassing and expansion zones*

Based on static reservoir pressure data (column 14, Table E.1) which are referred to at GOLO level, and knowing the gas invaded and water invaded zone, it is possible to estimate the extension of the gassing and expansion zones.

#### Example

The reservoir pressures at the end of the first and second year have been recorded as  $P_s = 257$  at. and  $P_s = 252$  at (at GOLO level) compared with 260 at initial pressure. By using the diagram Figure E.4 (where Bubble Point Pressure Bpp. is assumed to be constant with the depth), for  $P_s = 257$  the pressure will decrease at the end of the first year with the gas gradient inside the gas-cap zone to the new gas-oil contact level  $H_G = 20$  m. It will then decrease with the oil gradient 0.83 towards the actual water-oil contact  $H_w = 30$  m. At the intersection with  $P_s = 260$  at (point 1, Figure E.4) the depth will result which separates the gassing zone in the upper part ( $257 < P < 260$ ) and the expansion zone in the lower part ( $P > 260$  at). A similar procedure, if applied at the end of the second year, when pressure declines to 252 at, will result in an intersection (point 2) which will delimit the same two zones of gassing and simple expansion drive mechanism. (Figure E.4).



E.4 – Graphical evaluation of gassing zone and expansion zone after 1 year and 2 years of production

By using point 1 (Fig. E.4) resulting from the intersection of the vertical line  $P_B = P_i = 260$  at  $= \text{const.}$  and the new pressure gradient after one year, the following zones result:

END	{	- gas invaded zone	: interval 0 - 20 m	pay 20 m
1st year		- gassing zone	: interval 20 - 60 m	pay 40 m
		- undersaturated zone	: interval 60 - 250 m	pay 190 m
		- water invaded zone	: interval 250 - 280 m	pay 30 m

Similarly for point 2 on  $P_B$  straightline,  $P_B$ ,

END	{	- gas invaded zone	: interval 0 - 40 m	pay 40 m
2nd year		- gassing zone	: interval 40 - 141 m	pay 101 m
		- undersaturated zone	: interval 141 - 244 m	pay 103 m
		- water invaded zone	: interval 244 - 280 m	pay 36 m

For all steps during 11 years of production the zones between gas and water invaded zones will be determined with the same procedures.

## 2.2. Evaluation of production $N_{p,EXP}$ and $N_{p,SGD}$

Delimiting the two zone interval, through diagram figure E.4, it is possible to evaluate the bulk volume and the volume of oil in place in both the gassing zone and undersaturated zone.

It will be easy through a conventional procedure to calculate the cumulative produced oil from both zones. For 11 years of past history the calculation results are given in Table E.1, columns 10 and 11.

## 3. Evaluation of total oil recovery

Based on recorded oil production  $N_p$  in column 3, the oil was expressed in reservoir conditions (column 9, Table E.1).

$$N_{p,reservoir} = N_p \times B_o = N_p (\text{STM}^3) \times 1.21$$

Referring to original oil in place

$$OOIP = V_{BULK} \times \phi (1 - Swi) = 1260 \times 10^6 \times 0.162 (1 - 0.38)$$

or

$$OOIP = 126.6 \times 10^6 \text{ m}^3 \text{ in reservoir conditions}$$

the recovery is calculated from column 9 divided by OOIP in reservoir conditions and then reported in column 13, Table E.1.

## 4. Evaluation of recoveries in the invaded zone

### 4.1. Theoretical approach

The procedure is similar to the one discussed in chapter 10 section 10.4. The material balance is associated to the production of oil from the four main zone as : gas invaded, gassing, undersaturated and water invaded. This is expressed by,

$$N_p = R_G \times V_{GIZ} + N_{p,SG} + N_{p,EXP} + R_W \times V_{WIZ} \quad (\text{F.1})$$

which may be written as

$$R_G V_{GIZ} + R_W V_{WIZ} = P_{NET} \quad (E.2)$$

if

$$P_{NET} = N_P - N_{P,SGO} - N_{P,EXP} \quad (E.3)$$

Rearranging the terms by dividing equation E.2 with  $V_{GIZ}$ , it will result that

$$R_G + R_W \frac{V_{WIZ}}{V_{GIZ}} = \frac{P_{NET}}{V_{GIZ}} \quad (E.4)$$

which for n time steps will give

$$nR_G + R_W \sum_1^n \frac{V_{WIZ}}{V_{GIZ}} = \sum_1^n \frac{P_{NET}}{V_{GIZ}} \quad (E.5)$$

If equation E.4 is multiplied by invading ratio coefficient  $V_{WIZ}/V_{GIZ}$  it will give

$$R_G \frac{V_{WIZ}}{V_{GIZ}} + R_W \left( \frac{V_{WIZ}}{V_{GIZ}} \right)^2 = P_{NET} \frac{V_{WIZ}}{(V_{GIZ})^2} \quad (E.6)$$

which for n time steps gives

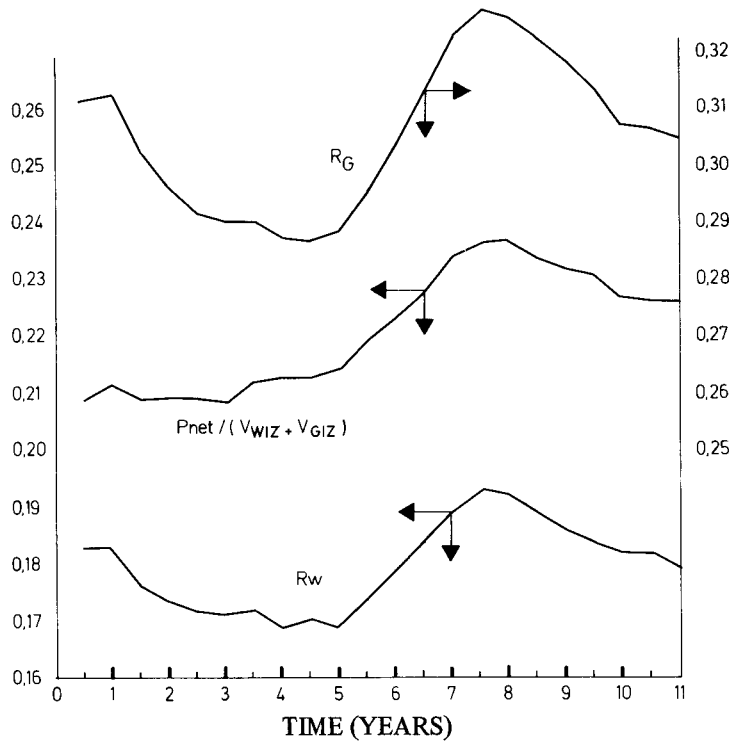
$$R_G \sum_1^n \left( \frac{V_{WIZ}}{V_{GIZ}} \right) + R_W \sum_1^n \left( \frac{V_{WIZ}}{V_{GIZ}} \right)^2 = \sum P_{NET} \frac{V_{WIZ}}{(V_{GIZ})^2} \quad (E.7)$$

#### 4.2. Calculation procedure

By using the equations E.5 and E.7 at each step during 11 years of production (22 steps) the values of recovery  $R_G$  and  $R_W$  for each step will result. The calculations are reported for each time step in Table E.2, including all terms necessary to the equations E.5 and E.7.

Example :

Considering the time at the end of two years of production where the recorded data steps are  $n = 4$ , it will result :



E.5 – Comparison of recoveries toward net production in time

Equation E.5

$$4R_G + R_w \times 12.73 = 3.46$$

Equation E.7

$$R_G \times 12.73 + R_w \times 41.69 = 11.24$$

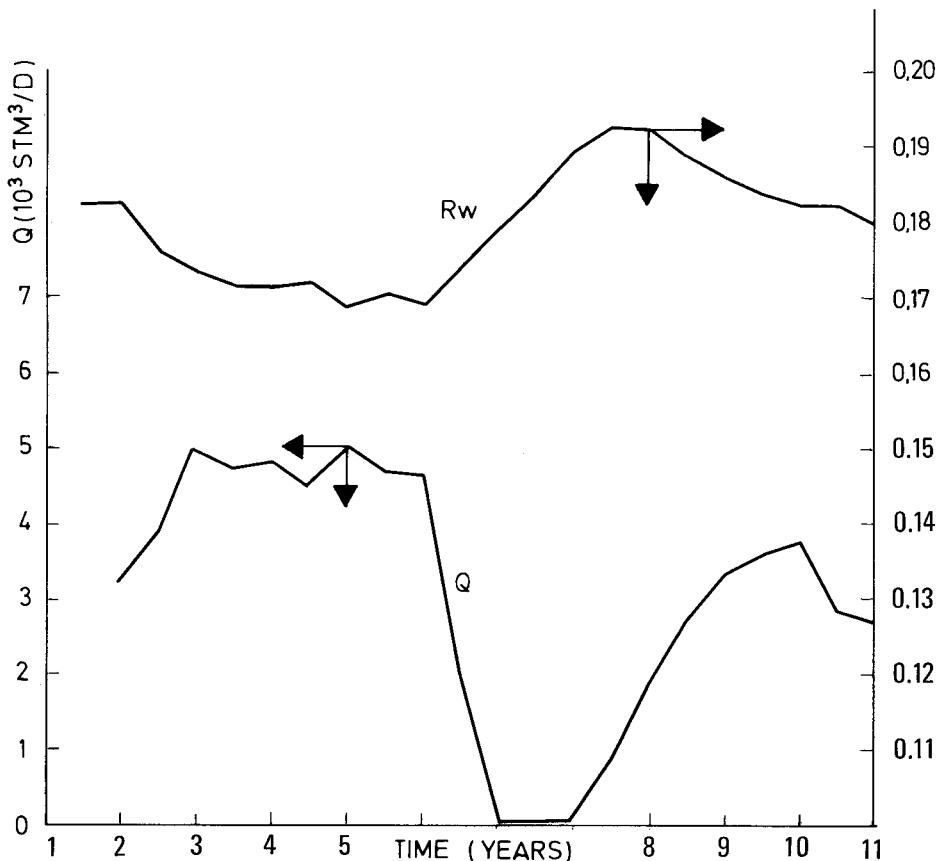
The solutions of these two equations show recovery values

$$R_G = 29.6 \%$$

$$R_w = 17.4 \%$$

#### 4.3. Discussion of results

From the examination of recoveries  $R_G$  and  $R_w$  in the invaded zones during 11 years of production, the following may be concluded :



E.6 – Comparison between water recovery and field production rate versus time

- Comparing  $R_w$ ,  $R_G$  with  $P_{NET}/(V_{WIZ} + V_{GIZ})$  in diagram figure E.5, it is observed that improved recoveries are resulting when  $P_{NET}/(V_{WIZ} + V_{GIZ})$  increases. This is equivalent to an improvement in recovery when the invaded zones are increasing less, or even when those zones are decreasing as during the 6th, 7th and 8th year of production.
- Examining the recovery  $R_G$  and  $R_w$  it is observed that the efficiency in the gas invaded zone is substantially higher than in the water invaded zone As average values

$$\bar{R}_G = 30.5 \%$$

$$\bar{R}_w = 17.87 \%$$

In addition, when the reservoir rate  $Q_{avg}$  (column 4, Table E.1) is reduced, the recoveries are improving as observed in figure E.6. The production reduction directly associated with increasing  $R_w$  and  $R_G$  proves the rate sensitive character of the recovery in a fractured reservoir production mechanism. These results are directly associated with the recovery-time relationship inside the single blocks where gravity and capillary drive mechanisms are operating.

Table E.1

		Recorded data					Calculated data						
End year	End month	Np, ( $10^6 \text{ STM}^3$ ) <sup>1</sup>	Reservoir rate $Q_{avg}, (10^3 \text{ STM}^3/\text{D})$	H <sub>w</sub> , (meters)	V <sub>GIZ</sub> , ( $10^6 \text{ m}^3$ )	V <sub>WIZ</sub> , ( $10^6 \text{ m}^3$ )	Np, ( $10^6 \text{ m}^3$ )	Np <sub>LXP</sub> , ( $10^6 \text{ m}^3$ )	N <sub>p, Sc,b</sub> , $10^6 \text{ m}^3$	P <sub>NFT</sub> , $10^6 \text{ m}^3$	Np/N (%)	Recorded pressure P (at) at GOLO	
1	2	3	4	5	6	7	8	9	10	11	12	13	14
1	6	3.55	3.210	20	4.30	16.27	4.30	0.00	0.00	4.30	3.39	257	
	12	4.13			5.34	17.96	5.00	0.05	0.02	4.93	3.94		
	6	4.83			6.91	20.10	5.85	0.08	0.13	5.64	4.62	255	
2	12	5.75	5.090	40	9.00	21.98	6.96	0.20	0.27	6.49	5.49	252	
	6	6.61			11.05	24.13	8.01	0.28	0.37	7.36	6.52	250	
3	12	7.48	4.810	51	12.84	26.37	9.06	0.38	0.50	8.18	7.15	246	
	6	8.30			14.49	28.11	10.05	0.46	0.58	9.01	7.93	245	
4	12	9.17	5.000	64	16.78	29.92	11.14	0.62	0.60	9.92	8.79	243	
	6	9.58			18.81	31.76	12.16	0.68	0.70	10.78	9.60	241	
5	12	10.88	4.630	78	20.82	33.31	13.17	0.76	0.77	11.64	10.40	241	
	6	11.24			20.52	34.42	13.61	0.76	0.80	12.05	10.75	241	
6	12	11.24	—	76	19.24	34.66	13.61	0.76	0.80	12.06	10.75	242	
	6	11.24			18.04	34.76	13.61	0.76	0.80	12.05	10.75	242	
7	12	11.24	—	56	16.83	34.89	13.61	0.76	0.80	12.04	10.75	243	
	6	11.42			16.53	35.18	13.82	0.72	0.84	12.21	10.91	240	
8	12	11.76	1.920	70	64	17.47	35.80	14.24	0.78	0.88	12.58	11.24	238
	6	12.26			18.78	37.20	14.84	0.83	0.90	13.11	11.72	237	
9	12	12.88	3.430	80	68	20.43	38.71	15.59	0.89	0.96	13.74	12.31	235
	6	13.45			22.23	30.32	16.39	0.93	1.06	14.40	12.94	232	
10	12	14.23	3.850	94	24.42	41.90	17.23	0.98	1.13	15.12	13.60	229	
	6	14.76			25.66	43.12	17.87	1.03	1.26	15.68	14.11	227	
11	12	15.36	2.754	106	27.10	44.49	18.57	1.05	1.28	16.24	14.66	224	

Table E.2 Material balance calculation

Year	Month of year	$V_{WIZ}/V_{GIZ}$	$\Sigma (V_{WIZ}/V_{GIZ})$	$P_{NET}/V_{GIZ}$	$\Sigma (P_{NET}/V_{GIZ})$	$(V_{WIZ}/V_{GIZ})^2$	$\Sigma (V_{WIZ}/V_{GIZ})^2$	$\frac{P_{NET} \cdot V_{WIZ}}{V_{GIZ} \cdot V_{GIZ}}$	$\frac{P_{NET} \cdot V_{WIZ}}{\Sigma V_{GIZ} \cdot V_{GIZ}}$	$R_w (\%)$	$R_G (\%)$	$\frac{P_{NET}}{V_{GIZ} + V_{WIZ}}$
1	6	3.77	3.77	1.00	1.00	14.26	14.25	3.77	3.77	18.3	31.1	0.209
	12	3.36	7.38	.92	1.92	13.00	27.27	3.33	7.10	18.3	31.2	0.2115
2	6	2.90	10.29	.81	2.74	8.45	35.72	2.37	9.48	17.6	30.2	0.2088
	12	2.44	12.73	.72	3.46	5.96	41.69	1.76	11.24	17.4	29.6	0.2094
3	6	2.18	14.91	.66	4.13	4.76	46.45	1.45	12.70	17.2	29.2	0.2092
	12	2.05	16.97	.34	4.77	4.21	50.67	1.31	14.02	17.1	29.0	0.2095
4	6	1.93	18.90	.62	5.39	3.75	54.43	1.20	15.22	17.2	29.0	0.2115
	12	1.78	20.69	.59	5.98	3.17	57.60	1.05	16.27	16.9	28.0	0.2123
5	6	1.69	22.38	.57	6.55	2.86	60.46	.97	17.24	17.0	28.7	0.2131
	12	1.60	23.98	.55	7.11	2.56	63.02	.89	18.14	16.9	28.8	0.2150
6	6	1.67	25.66	.58	7.70	2.81	65.84	.98	19.12	17.4	29.5	0.2190
	12	1.80	27.46	.62	8.32	3.24	69.08	1.12	20.25	17.9	30.4	0.2230
7	6	1.92	29.38	.66	8.99	3.68	72.77	1.27	21.52	18.4	31.3	0.2282
	12	2.07	31.45	.71	9.70	4.29	77.07	1.48	23.00	18.9	32.3	0.2327
8	6	2.12	33.58	.73	10.44	4.52	81.59	1.57	24.58	19.3	32.7	0.2361
	12	2.05	35.63	.72	11.16	4.21	85.80	1.47	26.08	19.8	32.6	0.2361
9	6	1.97	37.61	.69	11.86	3.91	98.72	1.38	27.44	18.9	32.3	0.
	12	1.89	39.50	.67	12.53	3.58	93.30	1.27	28.71	18.6	31.8	0.2323
10	6	1.81	41.31	.64	13.18	3.28	96.59	1.17	29.88	18.4	31.4	0.2302
	12	1.71	43.03	.61	13.80	2.94	99.54	1.06	30.95	18.2	30.7	0.2279
11	6	1.66	44.71	.61	14.41	2.82	102.36	1.02	31.97	18.2	30.6	0.2265
	12	1.63	46.35	.59	15.01	2.68	105.04	.98	32.95	18.0	30.5	0.2268

## SYMBOLS

### Latin letters

- B — volume factor
- C — compressibility
- DF — decline factor
- GOL — gas-oil limit
- GOLO — original gas-oil limit

<b>g</b>	— gravity
<b>H, h</b>	— height
<b>J</b>	— Leverett function
<b>K</b>	— permeability
<b>M</b>	— mobility ratio
<b>n</b>	— number of blocks
<b>P</b>	— pressure
<b>q</b>	— rate
<b>R</b>	— recovery
<b>r</b>	— radius
<b>S</b>	— saturation
<b>t</b>	— time
<b>u</b>	— velocity
<b>GOL</b>	— gas-oil contact
<b>WOLO</b>	— original gas-oil contact
<b>WOL</b>	— water-oil ratio

### Greek letters

<b><math>\gamma</math></b>	— specific weight
<b><math>\mu</math></b>	— viscosity
<b><math>\sigma</math></b>	— interfacial tension
<b><math>\theta</math></b>	— contact angle

### Subscripts

<b>BL</b>	— block
<b>BL, R</b>	— blocks per row
<b>BULK</b>	
<b>D</b>	— dimensionless
<b>D, G</b>	— dimensionless (gravity terms)
<b>D, P<sub>c</sub></b>	— dimensionless (capillary terms)
<b>e</b>	— external boundary
<b>eff</b>	— effective
<b>G</b>	— gravitational
<b>GI</b>	— gravity initial
<b>GIZ</b>	— gas invaded zone
<b>g</b>	— gas
<b>gf</b>	— gas fractures
<b>gd</b>	— gas dissolved

### NET

<b>o</b>	— oil
<b>P</b>	— production
<b>om</b>	— oil-matrix
<b>P.imb</b>	— production imbibition
<b>P, SE</b>	— production, simple expansion

<b>R</b>	— row
<b>r</b>	— relative
<b>res</b>	— reservoir
<b>S</b>	— solution
<b>SE</b>	— simple expansion
<b>SGD</b>	— solution gas drive
<b>w</b>	— water
<b>wf</b>	— water fractures
<b>wi</b>	— interstitial water
<b>WIZ</b>	— water invaded zone
<b>1</b>	— matrix
<b>2</b>	— fracture

## REFERENCES

1. Saidi, A.M., Martin, R.E. (1965) Applications of Reservoir Engineering in the Development of Iranian Reservoir. Paper presented to the ECAPE symposium of Petroleum, p. 10 - 20.
2. Andersen, K.H., Baker, R.L., Raoofi, J. (1963) The Development of Methods for Analysis of Iranian Asmari Reservoirs. Proceeding of the Sixth Wordl Petroleum Congress, Section II, Paper 14.
3. Khatib, A.K. (1965) Use of mathematical models for the evaluation of a fractured carbonate reservoir. Fith Arab Petroleum Congress, Cairo, March).

This Page Intentionally Left Blank

## SUBJECT INDEX

- anisotropy, 434
- Ain Zalah field, 112
- Asmari formation, 124, 126
- Barenblatt, 356
- block height, 80, 90, 687
- block interaction, 567
- block shape, 500, 506
- block stack, 500, 566, 574
- borehole televIEWER, 285
- Braester, 227
- Calculation example**
- capillary pressure, 125
- centrifuge displacement, 517
- coning, 336
- drainage in fracture, 320
- gas flow, 345
- permeability, 41, 170, 174, 183, 185, 197, 320, 328, 389, 400
- porosity, 157, 155, 183, 197, 291, 325, 391, 401
- rates, 185
- relative permeability, 223, 229
- scaling, 497
- simulation example 619, 623, 629
- simplified reservoir calculation, 641
- well 651, 672, 677, 684, 692
- well pressure drawdown, 380, 407
- well pressure build-up, 399, 407, 410
- Californian reservoir, 137
- caliper log, 257
- capillary experiments, 237
- capillary forces 234, 501, 508, 527
- capillary curve, 233
- case history, 111
- caverns, 119
- centrifuge, 509, 248
- confining pressure, 8
- convection, 587
- coning 331, 335, 334
- counterflow, 502
- compositional simulation, 632, 637
- composite capillary curves, 241
- compression wave, 273
- core analysis, 217
- critical coning-height, 335
- critical Reynolds, 324
- critical saturation, 217
- data processing**
- histograms, 87, 187
- table format, 84
- stereograms, 90, 93, 108
- decline factor, 667
- decline rate
- production, 596
- pressure, 552, 582
- density log, 271
- depletion, 554
- diffusion, 576
- dip direction, 19, 74

- dipmeter log, 264
- dispersion, 578
- displacement, 465
  - oil-gas, 476, 496
  - oil-water, 477, 481, 486
  - piston-like, 496
  - theory, 501
- drainage, 566
- dual induction log, 263
- Dukhan field, 121
  
- elasto-visco-plastic state, 45
- expansion mechanism, 562, 585, 681
  
- faulting, 15, 22
- finite elements, 25
- flowchart, 28, 29
- flowmeter, 289
- fluid data, 643
- folding, 17, 19
- fracture
  - classification, 51, 84, 93
  - detection, 51, 102
  - direction, 19, 102
  - evaluation, 66
  - frequency, 57
  
- matrix-block, 59, 80, 245
  - magnitude, 80, 90
  - models, 129, 315
  - shape, 59, 83
- microfracture, 52
- modelling
  - elasto-visco-plastic, 45
  - fracture network, 179, 315
  
- geology, 25
- linear elastic, 44
- single fracture, 320
- multi-block model, 317
- multi-sphere model, 317
- net overburden pressure, 196
- neutron log, 271
- non-linear flow, 309
- numerical simulation, 217, 607
  - block imbibition
  - compositional, 632, 633, 637
  - cross-section, 619
  - gas-oil recovery, 631
  - material balance, 595, 597
  - one phase flow, 612
  - two phase flow, 612
  - three phase flow, 617, 628
  
- observation well, 424
- oil phase simulation, 608
- outcrop fractures, 67
- overburden pressure, 196
  
- permeability, 157, 302
  - conventional, 159
  - empirical, 172
  - evaluation, 389, 400, 414
  - from structural data, 172
  - related to porosity, 175
  - relative, 208
- permeameter, 163
- piezo-conductivity, 349, 420
- Pollard procedure, 374, 408
- porosity, 149
  - porosity evaluation 389, 400
- pore frequency, 209
- pressure

- build-up, 305, 431
- confining, 8
- drawdown, 379, 392
- net overburden, 196
- pore, 197
- production
  - decline, 596
  - free-water oil, 553
  - mechanism, 551, 560
- pseudo-state time, 388
- PVT, 553, 575
  
- radial-symmetric flow, 316, 371, 341
- recovery, 246, 499, 503
- recovery-time
  - critical discussion, 519
  - experiment, 520
  - scaling, 508
  - theory, 536
- relative permeability, 208
  - basic concepts, 209
  - evaluation, 213
  - normalization, 211
- reservoir boundary, 436
- reservoir depletion, 551
- reservoir zoning, 561
  - gas-cap, 561
  - gas-invaded, 560
  - gassing, 561, 576
  - solution gas drive, 572
  - undersaturated, 562, 585, 587
  - waterinvaded zone, 562, 585, 587
  - water invaded zone, 562, 590, 593
  - reservoir history, 649
- resistivity log, 260
  
- Reynolds, 305, 310, 324
- rock
  - data, 643
  - lithology, 64
  - mechanics, 8
  - triaxial testing, 8, 155
  - type, 22
  
- Safe coning, 337
- scaling data, 424
- scaling requirements, 510, 511
- secondary porosity, 281
- shale fractured reservoir, 137
- shale matrix element, 369
- sonic log, 272, 287
- source solution point, 429
- Spraberry field, 131, 133
- sphere matrix element, 369
- stereogram, 93, 98, 108
- storage capacity, 429
- stresses, 9, 10
- strike direction 19, 90
- stylolites
  - classification, 33
  - examples, 120
  - formation, 30, 70
  - type, 32, 71
- stylolithification, 35
- supersaturation, 580
  
- temperature log, 250
- thin section, 79
- three-phase flow simulation, 617, 628
- transient flow, 347
- travel velocity, 273

triaxial testing, 8, 13, 155  
turbulence, 305, 320, 321  
type curve, 453, 455  
two-phase simulator, 612  
undersaturated zone, 562, 585  
undersaturated mechanism, 589  
  
velocity, 301  
vugs, 118, 223, 225  
  
Warren-Root, 359  
water advancement, 498  
water coning, 331  
water front, 472  
water-oil displacement  
water invaded zone, 562, 590, 593  
wettability, 483  
  
Zagros mountain, 103, 125  
Zoning, 555